fractal and fractional

Special Issue Reprint

Numerical Solution and Applications of Fractional Differential Equations, 2nd Edition

Edited by
Libo Feng, Yang Liu and Lin Liu

mdpi.com/journal/fractalfract

Numerical Solution and Applications of Fractional Differential Equations, 2nd Edition

Numerical Solution and Applications of Fractional Differential Equations, 2nd Edition

Guest Editors

Libo Feng
Yang Liu
Lin Liu

MDPI

Basel • Beijing • Wuhan • Barcelona • Belgrade • Novi Sad • Cluj • Manchester

Guest Editors

Libo Feng
School of Mathematical Sciences
Queensland University of Technology
Brisbane
Australia

Yang Liu
School of Mathematical Sciences
Inner Mongolia University
Hohhot
China

Lin Liu
School of Mathematics and Physics
University of Science and Technology Beijing
Beijing
China

Editorial Office
MDPI AG
Grosspeteranlage 5
4052 Basel, Switzerland

This is a reprint of the Special Issue, published open access by the journal *Fractal and Fractional* (ISSN 2504-3110), freely accessible at: https://www.mdpi.com/journal/fractalfract/special_issues/NSAFDE_II.

For citation purposes, cite each article independently as indicated on the article page online and as indicated below:

Lastname, A.A.; Lastname, B.B. Article Title. *Journal Name* **Year**, *Volume Number*, Page Range.

ISBN 978-3-7258-4111-0 (Hbk)
ISBN 978-3-7258-4112-7 (PDF)
https://doi.org/10.3390/books978-3-7258-4112-7

Contents

Preface

Over the past few decades, tremendous interest has been paid to the field of fractional calculus, which finds wide applications in physics, biology, chemistry, finance, signal and image processing, hydrology, non-Newtonian fluids, etc. Given that the analytical solution to fractional models is extremely complicated in terms of transcendental functions and analytically intractable in complex cases, numerical methods become a powerful and useful tool to handle fractional differential equations. This is the motivation for the Special Issue "Numerical Solution and Applications of Fractional Differential Equations" (NSAFDE) in the Journal of *Fractal and Fractional*.

This issue is the 2nd Edition of NSAFDE. It received 48 submissions and produced 12 accepted and published papers, all of which were subject to a rigorous review process. This reprint is a result of these 12 collections, which cover the topics of analytical techniques, numerical methods, and the applications for fractional differential equations.

Regarding the analytical techniques, the complete discriminant system method of polynomials, the traveling wave transformation, the Strang splitting algorithm, the spectral analysis method, the cones fixed point theorem, Filippov's approach, the natural transform, the residual power series method, and the Tikhonov Regularization have been considered.

The numerical methods in the collection include the mixed finite element method, the artificial boundary method, the Chebyshev spectral method, the meshless technique, the compact difference scheme, and the fast Alikhanov method.

Finally, some interesting applications have been presented, such as the second-grade fluid over a semi-infinite plate, biological population dynamics, the liquid crystal model, the Hopfield neural network, the preloaded compliance system and the fractional Cauchy problem in a circular annular region.

All the Guest Editors of this Special Issue are grateful to the authors for their quality contributions, to the reviewers for their valuable comments and advice, and to the administrative staff of MDPI for their support in completing this Special Issue. Special thanks go to the Section Managing Editor, Mr Ethan Zhang, for his excellent collaboration and valuable assistance.

Libo Feng, Yang Liu, and Lin Liu
Guest Editors

fractal and fractional

MDPI

Article

A Dynamical Analysis and New Traveling Wave Solution of the Fractional Coupled Konopelchenko–Dubrovsky Model

Jin Wang and Zhao Li *

College of Computer Science, Chengdu University, Chengdu 610106, China; wj19882009@163.com
* Correspondence: clizhao10.26@163.com

Abstract: The main object of this paper is to study the traveling wave solutions of the fractional coupled Konopelchenko–Dubrovsky model by using the complete discriminant system method of polynomials. Firstly, the fractional coupled Konopelchenko–Dubrovsky model is simplified into nonlinear ordinary differential equations by using the traveling wave transformation. Secondly, the trigonometric function solutions, rational function solutions, solitary wave solutions and the elliptic function solutions of the fractional coupled Konopelchenko–Dubrovsky model are derived by means of the polynomial complete discriminant system method. Moreover, a two-dimensional phase portrait is drawn. Finally, a 3D-diagram and a 2D-diagram of the fractional coupled Konopelchenko–Dubrovsky model are plotted in Maple 2022 software.

Keywords: Konopelchenko–Dubrovsky model; complete discriminant system; traveling wave solution; phase portrait

Citation: Wang, J.; Li, Z. A Dynamical Analysis and New Traveling Wave Solution of the Fractional Coupled Konopelchenko–Dubrovsky Model. *Fractal Fract.* **2024**, *8*, 341. https://doi.org/10.3390/fractalfract8060341

Academic Editor: Nikolay A. Kudryashov

Received: 7 May 2024
Revised: 29 May 2024
Accepted: 4 June 2024
Published: 6 June 2024

1. Introduction

In the present era, nonlinear evolution equations (NLEEs) [1–4] are employed in a number of areas like physics, chemistry, biology, fluid dynamics, engineering, optical fibers, plasma, and hydrodynamics. The analytical solutions of NLEEs can be applied to control complex behavior and difficult phenomena when the system displays [5–23]. While there is no unified method to obtain the exact solution of nonlinear evolution equations, most of the time, NLEEs can be converted into an ordinary differential equation by taken the traveling wave transformation. Based on the efforts of many predecessors, various methods have been imposed to solve NLEEs precisely and analyze various wave phenomena. He and Wu [24] proposed the first-time Exp-function method to seek solitary solutions, periodic solutions and compacton-like solutions of the KdV equation and Dodd–Bullough–Mikhailov equation. By using Hirota's bilinear transformation method, Ma proved the existence of N-soliton solutions of the (2+1)-dimensional KdV equation, the Kadomtsev–Petviashvili equation, the (2+1)-dimensional Hirota–Satsuma–Ito equation, and a combined pKP–BKP equation [25,26], respectively. Li et al. presented the (w/g)-expansion method [27]. Later, Arafat and his collaborators applied the customized (w/g)-expansion method to found the optical soliton solutions of the paraxial nonlinear Schrödinger equation and fractional Biswas–Arshed model [28,29], respectively. Wazwaz has derived the solitons and periodic solution of the Dodd–Bullough–Mikhailov and the Tzitzeica–Dodd–Bullough equations via the tanh-function approach [30]. Seadawy and Iqbal analyzed the nonlinear damped Korteweg–de Vries equation in an unmagnetized collisional dusty plasma via the direct algebraic approach [31]. Arafat also investigated scores of broad-spectral soliton solutions to the stated system via the auxiliary equation technique [32]. However, research on the traveling wave solutions of more complex fractional order NLEEs is still ongoing, and there are still a large number of open issues that need to be addressed by researchers.

In this paper, we consider the fractional coupled Konopelchenko–Dubrovsky model [33]

$$\begin{cases} D_t^\kappa u - u_{xxx} - 6auu_x + \frac{3}{2}b^2u^2u_x - 3v_y + 3bu_xv = 0, \\ v_x = u_y, \end{cases} \tag{1}$$

where $D_t^\kappa u$ is the conformable fractional derivative. $u = u(x, y, t)$ and $v = v(x, y, t)$ represent the velocity components along the horizontal and vertical axes, respectively. a and b stand for the amplitude of the wave. When $\kappa = 1$, Equation (1) become the well-known integer-order Konopelchenko–Dubrovsky model [34]. The main object of this paper is to study the traveling wave solution of the fractional coupled Konopelchenko–Dubrovsky model by using the complete discriminant system method of polynomials. On the one hand, the main effort of this article is to focus on constructing the traveling wave solution of Equation (1). On the other hand, without solving Equation (1), its dynamic branch will be analyzed.

The conformable fractional derivative was first proposed by Khalil et al. [35]. Compared with traditional fractional derivatives, the conformable fractional derivative has a more intuitive physical meaning. At present, it has been widely used in the construction of infectious disease dynamics models, nonlinear system modeling, and thermal science fields. Its definition is usually described as follows.

Definition 1 ([36]). *Let $f : [0, \infty) \to \mathbf{R}$. Then, the conformable derivative of f of order κ is defined as*

$$D_t^\kappa f(t) = \lim_{\varepsilon \to 0} \frac{f(t + \varepsilon t^{1-\kappa}) - f(t)}{\varepsilon}, \forall t \in (0, +\infty), \kappa \in (0, 1], \tag{2}$$

and the function f is κ-conformable differentiable at a point t if the limit in Equation (2) exists.

The remaining sections of this article are arranged as follows: In Section 2, the traveling wave solutions of Equation (1) are constructed by using the complete discriminant system method. Moreover, a two-dimensional phase portrait is drawn. In Section 3, the three-dimensional, two-dimensional, and density plots to some obtained solutions of Equation (1) are plotted. Finally, a brief summary is presented.

2. Dynamical Analysis and Traveling Wave Solutions of Equation (1)

2.1. Traveling Wave Transformation

In this section, we first consider the wave transformation

$$u(x, y, t) = U(\xi), v(x, y, t) = V(\xi), \xi = kx + ly + \mu\frac{t^\kappa}{\kappa}, \tag{3}$$

Substituting Equation (3) into Equation (1), we have

$$\begin{cases} \mu U' - k^3U''' - 6akUU' + \frac{3}{2}kb^2U^2U' - 3lV' + 3kbU'V = 0, \\ kV' = lU'. \end{cases} \tag{4}$$

Integrating the second equation of Equation (4), we obtain

$$V = \frac{l}{k}U. \tag{5}$$

Substituting Equation (5) into the first equation of Equation (4), we have

$$-k^3U'' + \frac{1}{2}kb^2U^3 + (\frac{3lb}{2} - 3ak)U^2 + (\mu - \frac{3l^2}{k})U = d_1, \tag{6}$$

where d_1 is the integral constant.

2.2. Dynamical Analysis

Here, we consider the planar dynamic system of Equation (6) when $d_1 = 0$

$$\begin{cases} \frac{dU}{d\xi} = z, \\ \frac{dz}{d\xi} = \ell_3 U^3 + \ell_2 U^2 + \ell_1 U, \end{cases} \tag{7}$$

where $\ell_3 = \frac{b^2}{2k^2}$, $\ell_2 = \frac{1}{k^3}(\frac{3lb}{2} - 3ak)$, $\ell_1 = \frac{1}{k^3}(\mu - \frac{3l^2}{k})$.

The first integration of Equation (7) is

$$H(U,z) = \frac{1}{2}z^2 - \frac{\ell_3}{4}U^4 - \frac{\ell_2}{3}U^3 - \frac{\ell_1}{2}U^2 = h. \tag{8}$$

By setting the parameter values of fixed Equation (7), we draw the planar phase portrait of Equation (7), as shown in Figure 1.

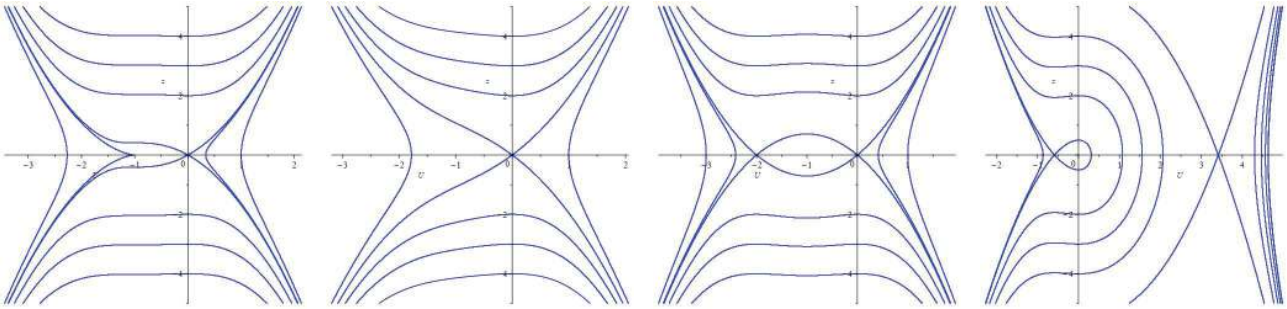

(**a**) $\ell_3 = 1, \ell_2 = 2, \ell_1 = 1$ (**b**) $\ell_3 = 1, \ell_2 = 2, \ell_1 = 2$ (**c**) $\ell_3 = 1, \ell_2 = 3, \ell_1 = 1$ (**d**)$\ell_3 = 1, \ell_2 = -2\sqrt{2}, \ell_1 = -2$

Figure 1. Phase portrait of Equation (7).

2.3. Traveling Wave Solutions of Equation (1)

Multiplying both sides of Equation (6) by U' simultaneously and integrating it yields

$$(U')^2 = b_4 U^4 + b_3 U^3 + b_2 U^2 + b_1 U + b_0, \tag{9}$$

where $b_4 = \frac{b^2}{4k^2}$, $b_3 = \frac{lb}{k^3} - \frac{2a}{k^2}$, $b_2 = \frac{\mu}{k^3} - \frac{3l^2}{k^4}$, $b_1 = -\frac{2d_1}{k^3}$, $b_0 = 2d_2$; here, d_2 is the integral constant.

Here, we make a transformation:

$$\begin{cases} w = (b_4)^{\frac{1}{4}}(U + \frac{b_3}{4b_4}), \\ \chi = (b_4)^{\frac{1}{4}}\xi. \end{cases} \tag{10}$$

Substituting Equation (10) into Equation (9), we obtain:

$$w_\chi^2 = w^4 + c_2 w^2 + c_1 w + c_0, \tag{11}$$

where $c_2 = \frac{b_2}{\sqrt{b_4}}$, $c_1 = (\frac{b_3^3}{8b_4^2} - \frac{b_2 b_3}{2b_4} + b_1)(b_4)^{-\frac{1}{4}}$, $c_0 = \frac{-3b_3^4}{256b_4^3} + \frac{b_2 b_3^2}{16b_4^2} - \frac{b_1 b_3}{4b_4} + b_0$.

By integrating Equation (11) once, one has:

$$\pm(\chi - \chi_0) = \int \frac{dw}{\sqrt{w^4 + c_2 w^2 + c_1 w + c_0}}, \tag{12}$$

where χ_0 denotes an integrating constant.

Denote that $G(w) = w^4 + c_2 w^2 + c_1 w + c_0$. We derive its complete discrimination system in the following form:

$$D_1 = 4, D_2 = -c_2, D_3 = -2c_2^3 + 8c_2c_0 - 9c_1^2, D_4 = -c_2^3c_1^2 + 4c_2^4c_0 + 36c_2c_1^2c_0 - 32c_2^2c_0^2 - \frac{27}{4}c_1^4 + 64c_0^3, \quad E_2 = c_1c_2^2 - 32c_2c_0. \tag{13}$$

According to the root-classifications of Equation (11), we will discuss the traveling wave solutions of Equation (1) under nine cases.

Case 1: $D_2 < 0, D_3 = 0, D_4 = 0$, $G(w) = [w^2 + q^2]^2$.

By combining Equation (9) with Equation (3), the traveling wave solutions of Equation (1) can be expressed as below:

$$u_1(x,y,t) = \frac{2ak - lb}{kb^2} + \frac{\sqrt{2(\mu k - 3l^2)}}{bk}\tan[\frac{\sqrt{2(\mu k - 3l^2)}}{bk^3}(\sqrt{\frac{b}{2k}}(kx + ly + \mu\frac{t^\kappa}{\kappa}) - \chi_0)]. \tag{14}$$

$$v_1(x,y,t) = \frac{2akl - l^2b}{k^2b^2} + \frac{l\sqrt{2(\mu k - 3l^2)}}{bk^2}\tan[\frac{\sqrt{2(\mu k - 3l^2)}}{bk^3}(\sqrt{\frac{b}{2k}}(kx + ly + \mu\frac{t^\kappa}{\kappa}) - \chi_0)]. \tag{15}$$

Case 2: $D_2 = 0, D_3 = 0, D_4 = 0$, $G(w) = w^4$. In this situation, the traveling wave solutions of Equation (1) take the form:

$$u_2(x,y,t) = \frac{2ak - lb}{kb^2} - \sqrt{\frac{2k}{b}}(\sqrt{\frac{b}{2k}}(kx + ly + \mu\frac{t^\kappa}{\kappa}) - \chi_0)^{-1}. \tag{16}$$

$$v_2(x,y,t) = \frac{2akl - l^2b}{k^2b^2} - l\sqrt{\frac{2}{bk}}(\sqrt{\frac{b}{2k}}(kx + ly + \mu\frac{t^\kappa}{\kappa}) - \chi_0)^{-1}. \tag{17}$$

Case 3: $D_2 > 0, D_3 = 0, D_4 = 0$, $G(w) = (w-\alpha)^2(w-\beta)^2$, where α, β are real number, and $\alpha > \beta$.

(i) If $w > \alpha$ or $w < \beta$, the traveling wave solutions of Equation (1) take the form:

$$u_{3,1}(x,y,t) = \alpha\sqrt{\frac{k}{2b}} - \frac{lb - 2ak}{kb^2} + (\beta - \alpha)\sqrt{\frac{k}{2b}}\coth\frac{(\alpha-\beta)\left(\sqrt{\frac{b}{2k}}(kx + ly + \mu\frac{t^\kappa}{\kappa}) - \chi_0\right)}{2}. \tag{18}$$

$$v_{3,1}(x,y,t) = \frac{l\alpha}{\sqrt{2bk}} - \frac{l^2b - 2akl}{k^2b^2} + \frac{l(\beta-\alpha)}{\sqrt{2bk}}\coth\frac{(\alpha-\beta)\left(\sqrt{\frac{b}{2k}}(kx + ly + \mu\frac{t^\kappa}{\kappa}) - \chi_0\right)}{2}. \tag{19}$$

(ii) If $\beta < w < \alpha$, the traveling wave solutions of Equation (1) take the form:

$$u_{3,2}(x,y,t) = \alpha\sqrt{\frac{k}{2b}} - \frac{lb - 2ak}{kb^2} + (\beta - \alpha)\sqrt{\frac{k}{2b}}\tanh\frac{(\alpha-\beta)\left(\sqrt{\frac{b}{2k}}(kx + ly + \mu\frac{t^\kappa}{\kappa}) - \chi_0\right)}{2}. \tag{20}$$

$$v_{3,2}(x,y,t) = \frac{l\alpha}{\sqrt{2bk}} - \frac{l^2b - 2akl}{k^2b^2} + \frac{l(\beta-\alpha)}{\sqrt{2bk}}\tanh\frac{(\alpha-\beta)\left(\sqrt{\frac{b}{2k}}(kx + ly + \mu\frac{t^\kappa}{\kappa}) - \chi_0\right)}{2}. \tag{21}$$

Case 4: $D_2 > 0, D_3 > 0, D_4 = 0$, $G(w) = (w-\alpha)^2(w-\beta)(w-\gamma)$, where α, β and γ are real number, $\beta > \gamma$.

(i) If $\alpha > \beta$ and $w > \beta$, or $\alpha < \gamma$ and $w < \gamma$, the implicit traveling wave solutions of Equation (1) can be expressed as below:

$$\pm\left(\sqrt{\frac{b}{2k}}(kx+ly+\mu\frac{t^{\kappa}}{\kappa})-\chi_0\right)=\frac{1}{(\alpha-\beta)(\alpha-\gamma)}$$
$$\ln\frac{[\sqrt{(kb^2u_{4,1}+lb-2ak-\sqrt{2}(kb)^{\frac{3}{2}}\beta)(\alpha-\gamma)}-\sqrt{(\alpha-\beta)(kb^2u_{4,1}+lb-2ak-\sqrt{2}(kb)^{\frac{3}{2}}\gamma)}]^2}{|kb^2u_{4,1}+lb-2ak-\sqrt{2}(kb)^{\frac{3}{2}}\alpha|}. \tag{22}$$

$$\pm\left(\sqrt{\frac{b}{2k}}(kx+ly+\mu\frac{t^{\kappa}}{\kappa})-\chi_0\right)=\frac{1}{(\alpha-\beta)(\alpha-\gamma)}$$
$$\ln\frac{[\sqrt{(k^2b^2v_{4,1}+l^2b-2alk-\sqrt{2}(kb)^{\frac{3}{2}}l\beta)(\alpha-\gamma)}-\sqrt{(\alpha-\beta)(k^2b^2v_{4,1}+l^2b-2alk-\sqrt{2}(kb)^{\frac{3}{2}}l\gamma)}]^2}{|k^2b^2v_{4,1}+l^2b-2alk-\sqrt{2}(kb)^{\frac{3}{2}}l\alpha|}. \tag{23}$$

(ii) If $\alpha>\beta$ and $w<\gamma$, or $\alpha<\gamma$ and $w<\beta$, the implicit traveling wave solutions of Equation (1) can be expressed as below:

$$\pm\left(\sqrt{\frac{b}{2k}}(kx+ly+\mu\frac{t^{\kappa}}{\kappa})-\chi_0\right)=\frac{1}{(\alpha-\beta)(\alpha-\gamma)}$$
$$\ln\frac{[\sqrt{(kb^2u_{4,2}+lb-2ak-\sqrt{2}(kb)^{\frac{3}{2}}\beta)(\gamma-\alpha)}-\sqrt{(\beta-\alpha)(kb^2u_{4,2}+lb-2ak-\sqrt{2}(kb)^{\frac{3}{2}}\gamma)}]^2}{|kb^2u_{4,2}+lb-2ak-\sqrt{2}(kb)^{\frac{3}{2}}\alpha|}. \tag{24}$$

$$\pm\left(\sqrt{\frac{b}{2k}}(kx+ly+\mu\frac{t^{\kappa}}{\kappa})-\chi_0\right)=\frac{1}{(\alpha-\beta)(\alpha-\gamma)}$$
$$\ln\frac{[\sqrt{(k^2b^2v_{4,2}+l^2b-2alk-\sqrt{2}(kb)^{\frac{3}{2}}l\beta)(\gamma-\alpha)}-\sqrt{(\beta-\alpha)(k^2b^2v_{4,2}+l^2b-2alk-\sqrt{2}(kb)^{\frac{3}{2}}l\gamma)}]^2}{|k^2b^2v_{4,2}+l^2b-2alk-\sqrt{2}(kb)^{\frac{3}{2}}l\alpha|}. \tag{25}$$

(iii) If $\beta>\alpha>\gamma$, the implicit traveling wave solutions of Equation (1) can be expressed as below:

$$\pm\left(\sqrt{\frac{b}{2k}}(kx+ly+\mu\frac{t^{\kappa}}{\kappa})-\chi_0\right)=\frac{1}{(\beta-\alpha)(\alpha-\gamma)}$$
$$\arcsin\frac{(kb^2u_{4,3}+lb-2ak-\sqrt{2}(kb)^{\frac{3}{2}}\beta)(\alpha-\gamma)+(\alpha-\beta)(kb^2u_{4,3}+lb-2ak-\sqrt{2}(kb)^{\frac{3}{2}}\gamma)}{|(kb^2u_{4,3}+lb-2ak-\sqrt{2}(kb)^{\frac{3}{2}}\alpha)(\beta-\gamma)|}. \tag{26}$$

$$\pm\left(\sqrt{\frac{b}{2k}}(kx+ly+\mu\frac{t^{\kappa}}{\kappa})-\chi_0\right)=\frac{1}{(\beta-\alpha)(\alpha-\gamma)}$$
$$\arcsin\frac{(k^2b^2v_{4,3}+l^2b-2alk-\sqrt{2}(kb)^{\frac{3}{2}}l\beta)(\alpha-\gamma)+(\alpha-\beta)(k^2b^2v_{4,3}+l^2b-2alk-\sqrt{2}(kb)^{\frac{3}{2}}l\gamma)}{|(k^2b^2v_{4,3}+l^2b-2alk-\sqrt{2}(kb)^{\frac{3}{2}}l\alpha)(\beta-\gamma)|}. \tag{27}$$

Case 5: $D_2>0, D_3=0, D_4=0, E_2=0, G(w)=(w-\alpha)^3(w-\beta)$, where α,β are real numbers.

When $w > \alpha$ and $w > \beta$, or $w < \alpha$ and $w < \beta$, the traveling wave solutions of Equation (1) take the form:

$$u_5(x,y,t) = \frac{8\sqrt{2}(\alpha-\beta)k^{\frac{3}{2}}}{\sqrt{b}[(\beta-\alpha)^2(\sqrt{b}(kx+ly+\mu\frac{t^\kappa}{\kappa})-\sqrt{2k}\chi_0)^2-4]} + \frac{\sqrt{2}\alpha(kb)^{\frac{3}{2}}+2ak-lb}{kb^2} \tag{28}$$

$$v_5(x,y,t) = \frac{8\sqrt{2}(\alpha-\beta)lk^{\frac{1}{2}}}{\sqrt{b}[(\beta-\alpha)^2(\sqrt{b}(kx+ly+\mu\frac{t^\kappa}{\kappa})-\sqrt{2k}\chi_0)^2-4]} + \frac{\sqrt{2}l\alpha(kb)^{\frac{3}{2}}+2akl-l^2b}{k^2b^2} \tag{29}$$

Case 6: $D_4 = 0, D_2D_3 < 0$, $G(w) = (w-\alpha)^2\left[(w-l_1)^2+s_1^2\right]$. The traveling wave solutions of Equation (1) take the form:

$$u_6(x,y,t) = \frac{2ak-lb}{kb^2} + \sqrt{\frac{2k}{b}}\frac{\left[e^{\pm\sqrt{(\alpha-l_1)^2+s_1^2}(\sqrt{\frac{b}{2k}}(kx+ly+\mu\frac{t^\kappa}{\kappa})-\chi_0)}-\gamma\right]+\sqrt{(\alpha-l_1)^2+s_1^2}(2-\gamma)}{\left[e^{\pm\sqrt{(\alpha-l_1)^2+s_1^2}(\sqrt{\frac{b}{2k}}(kx+ly+\mu\frac{t^\kappa}{\kappa})-\chi_0)}-\gamma\right]^2-1}, \tag{30}$$

$$v_6(x,y,t) = \frac{2akl-l^2b}{k^2b^2} + l\sqrt{\frac{2}{kb}}\frac{\left[e^{\pm\sqrt{(\alpha-l_1)^2+s_1^2}(\sqrt{\frac{b}{2k}}(kx+ly+\mu\frac{t^\kappa}{\kappa})-\chi_0)}-\gamma\right]+\sqrt{(\alpha-l_1)^2+s_1^2}(2-\gamma)}{\left[e^{\pm\sqrt{(\alpha-l_1)^2+s_1^2}(\sqrt{\frac{b}{2k}}(kx+ly+\mu\frac{t^\kappa}{\kappa})-\chi_0)}-\gamma\right]^2-1}, \tag{31}$$

where $\gamma = \frac{\alpha-2l_1}{\sqrt{(\alpha-l_1)^2+s_1^2}}$.

Case 7: $D_4 > 0, D_3 > 0, D_1 > 0$, $G(w) = (w-\alpha_1)(w-\alpha_2)(w-\alpha_3)(w-\alpha_4)$, in which $\alpha_1, \alpha_2, \alpha_3, \alpha_4$ is real number and $\alpha_1 > \alpha_2 > \alpha_3 > \alpha_4$.

When $w > \alpha_1$ or $w < \alpha_4$, the traveling wave solutions of Equation (1) take the form:

$$\begin{aligned}
u_{7,1}(x,y,t) &= \frac{2ak-lb}{kb^2} \\
&+\sqrt{\frac{2k}{b}}\frac{\alpha_2(\alpha_1-\alpha_4)\,\mathrm{sn}^2\left(\frac{\sqrt{(\alpha_1-\alpha_3)(\alpha_2-\alpha_4)}}{2}\left(\sqrt{\frac{b}{2k}}(kx+ly+\mu\frac{t^\kappa}{\kappa})-\chi_0\right),m\right)-\alpha_1(\alpha_2-\alpha_4)}{(\alpha_1-\alpha_4)\,\mathrm{sn}^2\left(\frac{\sqrt{(\alpha_1-\alpha_3)(\alpha_2-\alpha_4)}}{2}\left(\sqrt{\frac{b}{2k}}(kx+ly+\mu\frac{t^\kappa}{\kappa})-\chi_0\right),m\right)-(\alpha_2-\alpha_4)}, \\
v_{7,1}(x,y,t) &= \frac{2akl-l^2b}{k^2b^2} \\
&+l\sqrt{\frac{2}{kb}}\frac{\alpha_2(\alpha_1-\alpha_4)\,\mathrm{sn}^2\left(\frac{\sqrt{(\alpha_1-\alpha_3)(\alpha_2-\alpha_4)}}{2}\left(\sqrt{\frac{b}{2k}}(kx+ly+\mu\frac{t^\kappa}{\kappa})-\chi_0\right),m\right)-\alpha_1(\alpha_2-\alpha_4)}{(\alpha_1-\alpha_4)\,\mathrm{sn}^2\left(\frac{\sqrt{(\alpha_1-\alpha_3)(\alpha_2-\alpha_4)}}{2}\left(\sqrt{\frac{b}{2k}}(kx+ly+\mu\frac{t^\kappa}{\kappa})-\chi_0\right),m\right)-(\alpha_2-\alpha_4)},
\end{aligned} \tag{32}$$

$$
\begin{aligned}
u_{7,2}(x,y,t) &= \frac{2ak-lb}{kb^2} \\
&+\sqrt{\frac{2k}{b}}\frac{\alpha_4(\alpha_2-\alpha_3)\,\mathrm{sn}^2\left(\frac{\sqrt{(\alpha_1-\alpha_3)(\alpha_2-\alpha_4)}}{2}\left(\sqrt{\frac{b}{2k}}(kx+ly+\mu\frac{t^\kappa}{\kappa})-\chi_0\right),m\right)-\alpha_3(\alpha_2-\alpha_4)}{(\alpha_2-\alpha_3)\,\mathrm{sn}^2\left(\frac{\sqrt{(\alpha_1-\alpha_3)(\alpha_2-\alpha_4)}}{2}\left(\sqrt{\frac{b}{2k}}(kx+ly+\mu\frac{t^\kappa}{\kappa})-\chi_0\right),m\right)-(\alpha_2-\alpha_4)}, \\
v_{7,2}(x,y,t) &= \frac{2akl-l^2b}{k^2b^2} \\
&+l\sqrt{\frac{2}{kb}}\frac{\alpha_4(\alpha_2-\alpha_3)\,\mathrm{sn}^2\left(\frac{\sqrt{(\alpha_1-\alpha_3)(\alpha_2-\alpha_4)}}{2}\left(\sqrt{\frac{b}{2k}}(kx+ly+\mu\frac{t^\kappa}{\kappa})-\chi_0\right),m\right)-\alpha_3(\alpha_2-\alpha_4)}{(\alpha_2-\alpha_3)\,\mathrm{sn}^2\left(\frac{\sqrt{(\alpha_1-\alpha_3)(\alpha_2-\alpha_4)}}{2}\left(\sqrt{\frac{b}{2k}}(kx+ly+\mu\frac{t^\kappa}{\kappa})-\chi_0\right),m\right)-(\alpha_2-\alpha_4)},
\end{aligned}
\tag{33}
$$

in which $m^2=\frac{(\alpha_1-\alpha_4)(\alpha_2-\alpha_3)}{(\alpha_1-\alpha_3)(\alpha_2-\alpha_4)}$.

Case 8: $D_4<0, D_2D_3\geqslant 0$, then $G(w)=(w-\alpha)(w-\beta)\left[(w-l_1)^2+s_1^2\right]$, where real number $\alpha>\beta, l_1, s_1>0$.

The traveling wave solutions of Equation (1) take the form:

$$
u_8(x,y,t)=\frac{2ak-lb}{kb^2}+\sqrt{\frac{2k}{b}}\frac{\mathrm{acn}\left(\frac{\sqrt{-2s_1m_1(\alpha-\beta)}}{2mm_1}\left(\frac{b}{2k}(kx+ly+\mu\frac{t^\kappa}{\kappa})-\chi_0\right),m\right)+e_2}{\mathrm{ccn}\left(\frac{\sqrt{-2s_1m_1(\alpha-\beta)}}{2mm_1}\left(\frac{b}{2k}(kx+ly+\mu\frac{t^\kappa}{\kappa})-\chi_0\right),m\right)+e_4}, \tag{34}
$$

$$
v_8(x,y,t)=\frac{2akl-l^2b}{k^2b^2}+l\sqrt{\frac{2}{kb}}\frac{\mathrm{acn}\left(\frac{\sqrt{-2s_1m_1(\alpha-\beta)}}{2mm_1}\left(\frac{b}{2k}(kx+ly+\mu\frac{t^\kappa}{\kappa})-\chi_0\right),m\right)+e_2}{\mathrm{ccn}\left(\frac{\sqrt{-2s_1m_1(\alpha-\beta)}}{2mm_1}\left(\frac{b}{2k}(kx+ly+\mu\frac{t^\kappa}{\kappa})-\chi_0\right),m\right)+e_4}, \tag{35}
$$

in which $e_1=\frac{1}{2}(\alpha+\beta)e_3-\frac{1}{2}(\alpha-\beta)e_4, e_2=\frac{1}{2}(\alpha+\beta)e_4-\frac{1}{2}(\alpha-\beta)e_3, e_3=\alpha-l_1-\frac{s_1}{m_1}$, $e_4=\alpha-l_1-s_1m_1, E=\frac{s_1^2+(\alpha-l_1)(\beta-l_1)}{s_1(\alpha-\beta)}, m_1=E-\sqrt{E^2+1}, m^2=\frac{1}{1+m_1^2}$.

Case 9: $D_4>0, D_2D_3\leqslant 0$, then $G(w)=\left[(w-l_1)^2+s_1^2\right]\left[(w-l_2)^2+s_2^2\right]$, where l_1, l_2, s_1, s_2 are real and $s_1\geqslant s_2>0$. The traveling wave solutions of Equation (1) take the form:

$$
\begin{aligned}
u_9(x,y,t) &= \frac{2ak-lb}{kb^2} \\
&+\sqrt{\frac{2k}{b}}\cdot\frac{e_1\,\mathrm{sn}\left(\eta(\frac{b}{2k}(kx+ly+\mu\frac{t^\kappa}{\kappa})-\chi_0),m\right)+e_2\,\mathrm{cn}\left(\eta(\frac{b}{2k}(kx+ly+\mu\frac{t^\kappa}{\kappa})-\chi_0),m\right)}{e_3\,\mathrm{sn}\left(\eta(\frac{b}{2k}(kx+ly+\mu\frac{t^\kappa}{\kappa})-\chi_0),m\right)+e_4\,\mathrm{cn}\left(\eta(\frac{b}{2k}(kx+ly+\mu\frac{t^\kappa}{\kappa})-\chi_0),m\right)},
\end{aligned}
\tag{36}
$$

$$
\begin{aligned}
v_9(x,y,t) &= \frac{2akl-l^2b}{k^2b^2} \\
&+l\sqrt{\frac{2}{kb}}\cdot\frac{e_1\,\mathrm{sn}\left(\eta(\frac{b}{2k}(kx+ly+\mu\frac{t^\kappa}{\kappa})-\chi_0),m\right)+e_2\,\mathrm{cn}\left(\eta(\frac{b}{2k}(kx+ly+\mu\frac{t^\kappa}{\kappa})-\chi_0),m\right)}{e_3\,\mathrm{sn}\left(\eta(\frac{b}{2k}(kx+ly+\mu\frac{t^\kappa}{\kappa})-\chi_0),m\right)+e_4\,\mathrm{cn}\left(\eta(\frac{b}{2k}(kx+ly+\mu\frac{t^\kappa}{\kappa})-\chi_0),m\right)},
\end{aligned}
\tag{37}
$$

in which $e_1=l_1e_3+s_1e_4, e_2=l_1e_4-s_1e_3, e_3=-s_1-\frac{s_2}{m_1}, e_4=l_1-l_2, E=\frac{(l_1-l_2)^2+s_1^2+s_2^2}{2s_1s_2}$, $m_1=E+\sqrt{E^2-1}, m^2=\frac{m_1^2-1}{m_1^2}, \eta=\frac{s_2\sqrt{\left(e_3^2+e_4^2\right)\left(m_1^2e_3^2+e_4^2\right)}}{e_3^2+e_4^2}$.

3. Numerical Simulation

In order to understand the dynamical processes and mechanisms of complex phenomena of the fractional coupled Konopelchenko–Dubrovsky model, numerical simulations of the obtained soliton solutions are given in this section. As is vividly shown in Figures 2a, 3a and 4a, $u_1(x,y,t), u_2(x,y,t)$ and $u_3(x,y,t)$ stand for the tangent function solutions, the rational function solutions and the hyperbolic function solutions, respectively. Figures 2b, 3b and 4b

denote the level curve at time $t = 1$. Furthermore, Figures 2c, 3c and 4c represent the density plots. Figures 2d, 3d and 4d stand for the contour plots.

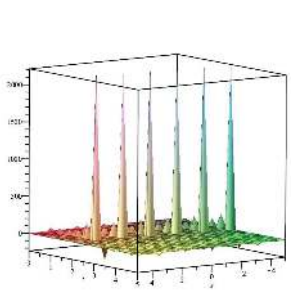

(**a**) Three-dimension graphic

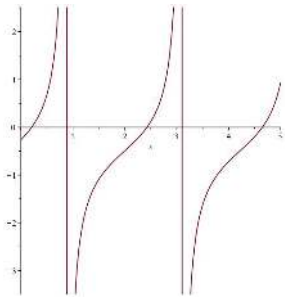

(**b**) Two-dimension graphic

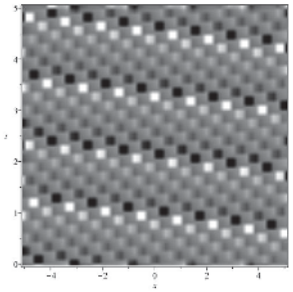

(**c**) Density plot

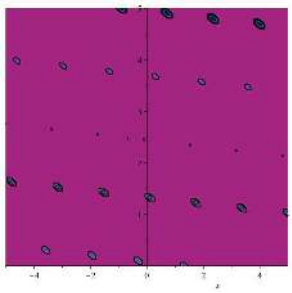

(**d**) Contour plot

Figure 2. Equation (14) for $a = 3, b = 4, k = 1, l = 2, \mu = 16$.

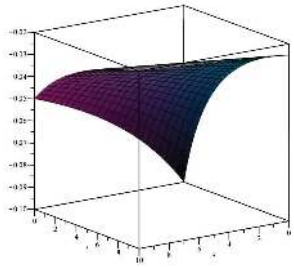

(**a**) Three-dimension graphic

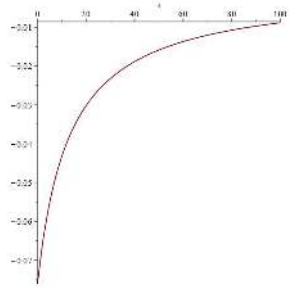

(**b**) Two-dimension graphic

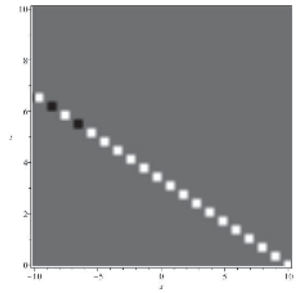

(**c**) Density plot

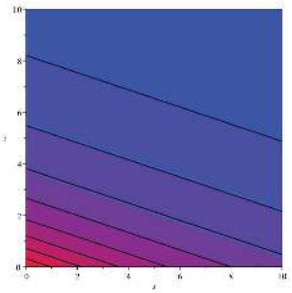

(**d**) Contour plot

Figure 3. Equation (16) for $a = k = l = 1, b = 2, \mu = 3$.

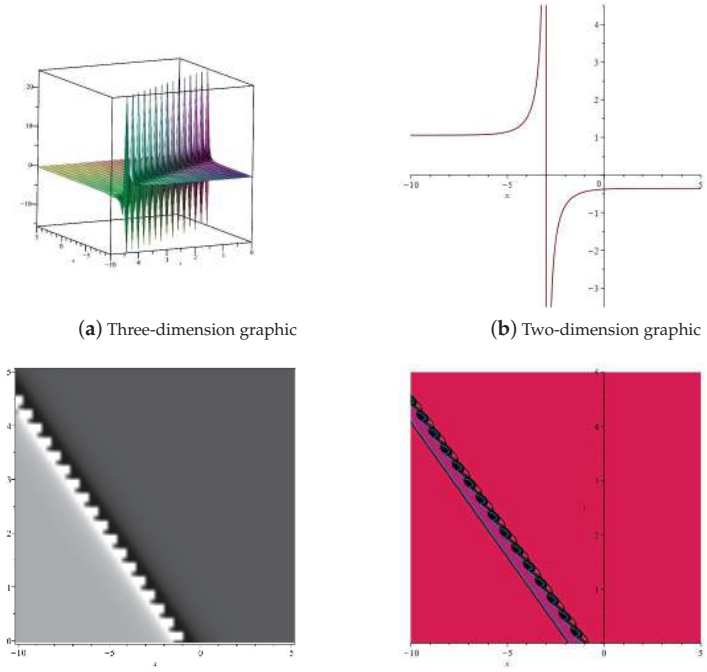

(**a**) Three-dimension graphic (**b**) Two-dimension graphic

(**c**) Density plot (**d**) Contour plot

Figure 4. Equation (18) for $a = k = l = 1, b = 2, \mu = 2, \alpha = \frac{1}{\sqrt{2}}, \beta = \frac{-1}{\sqrt{2}}$.

4. Conclusions

In this article, we have presented the traveling wave solutions of Equation (1) via the complete discriminant system method, which is one of the most useful tools in solving NLEEs. The trigonometric function solutions, the rational function solutions, the hyperbolic function solutions, the exponential function solutions, and the Jacobian elliptic function solutions are obtained. Lastly, in order to understand the mechanisms of physical phenomena for Equation (1), we have also depicted two-dimensional and three-dimensional diagrams. In future work, we will focus on the traveling wave solutions and dynamic behavior of more complex NLEEs. Furthermore, we will also use the Darboux transformations to discuss the N-soliton solutions of more complex NLEEs.

Author Contributions: Software, Z.L.; Writing—original draft, J.W. All authors have read and agreed to the published version of the manuscript.

Funding: This research received no external funding.

Data Availability Statement: No new data were created or analyzed in this study. Data sharing is not applicable to this article.

Conflicts of Interest: The authors declare no conflicts of interest.

References

1. Gu, M.; Peng, C.; Li, Z. Traveling wave solution of (3+1)-dimensional negative-order KdV-Calogero-Bogoyavlenskii-Schiff equation. *Aims Math.* **2024**, *9*, 6699–6708. [CrossRef]
2. Wu, J.; Huang, Y. Boundedness of solutions for an attraction-repulsion model with indirect signal production. *Mathematics* **2024**, *12*, 1143. [CrossRef]
3. Liu, C.; Li, Z. The dynamical behavior analysis and the traveling wave solutions of the stochastic Sasa-Satsuma Equation. *Qual. Theory Dyn. Syst.* **2024**, *23*, 157. [CrossRef]
4. Wu, J.; Yang, Z. Global existence and boundedness of chemotaxis-fluid equations to the coupled Solow-Swan model. *Aims Math.* **2023**, *8*, 17914–17942. [CrossRef]
5. Tang, C.; Li, X.; Wang, Q. Mean-field stochastic linear quadratic optimal control for jump-diffusion systems with hybrid disturbances. *Symmetry* **2024**, *16*, 642. [CrossRef]
6. Chen, T.; Chen, J.; Zhuang, B. Stabilization of coupled delayed nonlinear time fractional reaction diffusion systems using sampled-in-space sensing and actuation. *Int. J. Adapt. Control. Signal Process.* **2024**. [CrossRef]

7. Arfaoui, H.; Makhlouf, A.B. Stability of a time fractional advection-diffusion system. *Chaos Solitons Fractals* **2022**, *157*, 111949. [CrossRef]
8. Khater, M.M.A. In solid physics equations, accurate and novel soliton wave structures for heating a single crystal of sodium fluoride. *Int. J. Mod. Phys.* **2023**, *37*, 2350068. [CrossRef]
9. Li, Z.; Liu, C. Chaotic pattern and traveling wave solution of the perturbed stochastic nonlinear Schrödinger equation with generalized anti-cubic law nonlinearity and spatio-temporal dispersion. *Results Phys.* **2024**, *56*, 107305. [CrossRef]
10. Arafat, S.M.Y.; Fatema, K.; Islam, M.E.; Akbar, M.A. Promulgation on various genres soliton of Maccari system in nonlinear optics. *Opt. Quantum Electron.* **2022**, *54*, 206. [CrossRef]
11. Khater, M.M.A.; Alfalqi, S.H.; Alzaidi, J.F.; Attia, R.A.M. Analytically and numerically, dispersive, weakly nonlinear wave packets are presented in a quasi-monochromaticmedium. *Results Phys.* **2023**, *46*, 106312. [CrossRef]
12. Akinyemi, L.; Rezazadeh, H.; Shi, Q.H.; Inc, M.; Khater, M.M.; Ahmad, H.; Jhangeer, A.; Akbar, M.A. New optical solitons of perturbed nonlinear Schrodinger-Hirota equation with spatio-temporal dispersion. *Results Phys.* **2021**, *29*, 104656. [CrossRef]
13. Li, Z.; Peng, C. Bifurcation, phase portrait and traveling wave solution of time-fractional thin-film ferroelectric material equation with beta fractional derivative. *Phys. Lett.* **2023**, *484*, 129080. [CrossRef]
14. Zhang, K.; Li, Z.; Cao, J. Qualitative analysis and modulation instability for the extended (3+1)-dimensional nonlinear Schrödinger equation with conformable derivative. *Results Phys.* **2024**, *61*, 107713. [CrossRef]
15. Ma, H.; Gao, Y.; Deng, A. Nonlinear superposition of the (2+1)-dimensional generalized Konopelchenko-Dubrovsky-Kaup-Kupershmidt equation. *Nonlinear Dyn.* **2023**, *111*, 619–632. [CrossRef]
16. Khater, M.M.A. Novel computational simulation of the propagation of pulses in optical fibers regarding the dispersion effect. *Int. J. Mod. Phys.* **2023**, *37*, 2350083. [CrossRef]
17. Feng, W.; Chen, L.; Ma, G.; Zhou, Q. Study on weakening optical soliton interaction in nonlinear optics. *Nonlinear Dyn.* **2022**, *108*, 2483–2488. [CrossRef]
18. Ma, H.; Gao, Y.; Deng, A. Fission and fusion solutions of the (2+1)-dimensional generalized Konopelchenko-Dubrovsky-Kaup-Kupershmidt equation: Case of fluid mechanics and plasma physics. *Nonlinear Dyn.* **2022**, *108*, 4123–4137. [CrossRef]
19. Han, T.; Jiang, Y.; Lyu, J. Chaotic behavior and optical soliton for the concatenated model arising in optical communication. *Results Phys.* **2024**, *58*, 107467. [CrossRef]
20. Khater, M.M.A. A hybrid analytical and numerical analysis of ultra-short pulse phase shifts. *Chaos Solitons Fractals* **2023**, *169*, 113232. [CrossRef]
21. Horvath, D.X.; Calabrese, P.; Castro-Alvaredo, O.A. Branch point twist field form factors in the sine-Gordon model II: Composite twist fields and symmetry resolved entanglement. *Sci Post Phys.* **2022**, *12*, 88. [CrossRef]
22. Ismael, H.F.; Bulut, H.; Park, C.; Osman, M.S. M-lump, N-soliton solutions, and the collision phenomena for the (2+1)-dimensional Date-Jimbo-Kashiwara-Miwa equation. *Results Phys.* **2020**, *19*, 103329. [CrossRef]
23. Akbulut, A.; Kaplan, M.; Bekir, A. Auxiliary equation method for fractional differential equations with modified Riemann-Liouville derivative. *Int. J. Nonlinear Sci. Numer. Simul.* **2016**, *17*, 413–420. [CrossRef]
24. He, J.; Wu, X. Exp-function method for nonlinear wave equations. *Chaos Solitons Fractals* **2006**, *30*, 700–708. [CrossRef]
25. Ma, W. N-soliton solution and the Hirota condition of a (2+1)-dimensional combined equation. *Math. Comput. Simul.* **2021**, *190*, 270–279. [CrossRef]
26. Ma, W. N-soliton solution of a combined pKP-BKP equation. *J. Geom. Phys.* **2021**, *165*, 104191. [CrossRef]
27. Li, W.; Chen, H.; Zhang, G. The (w/g)-expansion method and its application to Vakhnenko equation. *Chin. Phys.* **2009**, *18*, 400.
28. Arafat, S.M.Y.; Khan, K.; Islam, S.M.R.; Rahman, M.M. Parametric effects on paraxial nonlinear Schrodinger equation in Kerr media. *Chin. J. Phys.* **2023**, *83*, 361–378. [CrossRef]
29. Arafat, S.M.Y.; Islam, S.M.R.; Rahman, M.M.; Saklayen, M.A. On nonlinear optical solitons of fractional Biswas-Arshed Model with beta derivative. *Results Phys.* **2023**, *48*, 106426. [CrossRef]
30. Wazwaz, A.-M. The tanh method: Solitons and periodic solutions for the Dodd-Bullough-Mikhailov and the Tzitzeica-Dodd-Bullough equations. *Chaos Solitons Fractals* **2005**, *25*, 55–63. [CrossRef]
31. Seadawy, A.R.; Iqbal, M. Propagation of the nonlinear damped Korteweg-de Vries equation in an unmagnetized collisional dusty plasma via analytical mathematical methods. *Math. Methods Appl. Sci.* **2021**, *44*, 737–748. [CrossRef]
32. Yiasir Arafat, S.M.; Fatema, K.; Rayhanul Islam, S.M.; Islam, M.E.; Ali Akbar, M.; Osman, M.S. The mathematical and wave profile analysis of the Maccari system in nonlinear physical phenomena. *Opt. Quantum Electron.* **2023**, *55*, 136. [CrossRef]
33. Aslam, A.; Majeed, A.; Kamran, M.; Inc, M.; Alqahtani, T.R. Dynamical behavior of the fractional coupled Konopelchenko-Dubrovsky and (3+1)-dimensional modified Korteweg-de Vries-Zakharov-Kuznestsov equations. *Opt. Quantum Electron.* **2023**, *55*, 543. [CrossRef]
34. Arafat, S.M.Y.; Rahman, M.M.; Karim, M.F.; Amin, M.R. Wave profile analysis of the (2+1)-dimensional Konopelchenko-Dubrovsky model in mathematical physics. *Partial. Differ. Equ. Appl. Math.* **2023**, *8*, 100573. [CrossRef]
35. Khalil, R.R.; Horani, M.A.H.H.; Yousef, A.; Sababheh, M. A new definition of fractional derivative. *J. Comput. Appl. Math.* **2014**, *264*, 65–70. [CrossRef]

36. Li, Z.; Han, T.; Huang, C. Exact single traveling wave solutions for generalized fractional Gardner equation. *Math. Probl. Eng.* **2020**, *2020*, 8842496. [CrossRef]

fractal and fractional

MDPI

Article

Dynamic Behavior and Optical Soliton for the M-Truncated Fractional Paraxial Wave Equation Arising in a Liquid Crystal Model

Jie Luo [1] and Zhao Li [2,*]

[1] School of Electronic Information and Electrical Engineering, Chengdu University, Chengdu 610106, China; luojie01@cdu.edu.cn
[2] College of Computer Science, Chengdu University, Chengdu 610106, China
* Correspondence: lizhao@cdu.edu.cn; Tel.: +86-183-8207-1390

Abstract: The main purpose of this article is to investigate the dynamic behavior and optical soliton for the M-truncated fractional paraxial wave equation arising in a liquid crystal model, which is usually used to design camera lenses for high-quality photography. The traveling wave transformation is applied to the M-truncated fractional paraxial wave equation. Moreover, a two-dimensional dynamical system and its disturbance system are obtained. The phase portraits of the two-dimensional dynamic system and Poincaré sections and a bifurcation portrait of its perturbation system are drawn. The obtained three-dimensional graphs of soliton solutions, two-dimensional graphs of soliton solutions, and contour graphs of the M-truncated fractional paraxial wave equation arising in a liquid crystal model are drawn.

Keywords: paraxial model; bifurcation; phase portrait; chaos behavior; M-truncated fractional derivative

Citation: Luo, J.; Li, Z. Dynamic Behavior and Optical Soliton for the M-Truncated Fractional Paraxial Wave Equation Arising in a Liquid Crystal Model. *Fractal Fract.* **2024**, *8*, 348. https://doi.org/10.3390/fractalfract8060348

Academic Editor: Carlo Cattani

Received: 22 May 2024
Revised: 3 June 2024
Accepted: 9 June 2024
Published: 12 June 2024

1. Introduction

Fractional partial differential equations (FPDEs) are partial differential equations [1,2] that involve fractional derivatives and are commonly used to describe complex systems with memory effects. FPDEs have wide applications in fluid mechanics, biology, signal processing, and financial mathematics [3]. In general, due to the widespread application of fractional derivatives in multiple fields [4–8], many researchers have proposed many different fractional derivatives from different perspectives. For example, the Riemann–Liouville fractional derivative, the conformable fractional derivative, the Caputo fractional derivative, and the Grünwald–Letnikov fractional derivative. Therefore, with the continuous development of fractional derivative theory, researchers have also delved deeper into the theory of fractional derivatives. Additionally, many different types of FPDEs have been proposed. Due to the complexity and diversity of fractional derivatives, on the one hand, many experts use the finite element method, the spectral method, and the finite difference method to solve the numerical solutions of these equations. On the other hand, many researchers use mathematical analysis methods to construct exact solutions [9,10] to these equations. The main purpose of this article is to study the dynamic behavior and soliton solutions of a very important class of FPDEs.

In this study, the M-truncated fractional paraxial wave equation arising in a liquid crystal model is presented as follows [11]:

$$i\frac{\partial \psi}{\partial y} + \frac{a_1}{2}\,{}_{\kappa}\mathbb{D}_{M,t}^{2\alpha,d}\psi + \frac{a_2}{2}\frac{\partial^2 \psi}{\partial x^2} + a_3|\psi|^2\psi = 0, \tag{1}$$

where a_1, a_2, a_3 are real constants, which represent the coefficients of the dispersal effect, the Kerr nonlinearity effect, and the diffraction effect, respectively. ${}_{\kappa}\mathbb{D}_{M,t}^{2\alpha,d}$ stands for the

M-fractional derivative, which was proposed by Oliveira and Sousa [12]. $\psi = \psi(x, y, t)$, where the variables x, y, t represent the transverse, longitudinal, and temporal propagation, respectively. In [13,14], Hamood, et al. used the ϕ^6 model expansion technique and the Sardar subequation method to study the optical solitons of the paraxial wave model, respectively. In [11], Mannaf et al. studied the optical soliton solutions of Equation (1) by using the extended tanh method and the modified extended tanh method, respectively. However, despite our best efforts, there is still an insufficient body of literature on the dynamic behavior and soliton solutions of Equation (1). Solitons are a special wave phenomenon that occurs in nonlinear physics. Solitons were first proposed in the study of shallow water waves, but were later widely applied in fields such as optics, acoustics, and quantum physics. The optical soliton solution is usually used to describe the mathematical solution of the propagation of optical solitons under specific conditions, for example, the solution to the Schrödinger equation. This article will conduct research from two aspects. On the one hand, by using the method of planar dynamical systems, the dynamic behavior of two-dimensional dynamical systems and their disturbance systems are studied. On the other hand, the optical soliton solution of Equation (1) is constructed using the planar dynamical system method.

The remaining part of this article is arranged as follows: In Section 2, the phase portrait of the two-dimensional dynamical system and its perturbed system are discussed. In Section 3, the optical soliton solutions of Equation (1) are constructed. Finally, a brief conclusion is given.

2. Bifurcation and Chaotic Behaviors

2.1. Preliminary

Definition 1 (M-truncated fractional derivative [15]). *For $\alpha \in (0, 1]$, the M-truncated fractional derivative of $f : [0, +\infty) \to (-\infty, +\infty)$ is defined as*

$$ {}_{\kappa}\mathbb{D}_{M,t}^{2\alpha,d}(f) = \lim_{h \to 0} \frac{f(t_{\kappa}E_d(ht^{\alpha})) - f(t)}{h}, \ \ 0 < \alpha < 1, d > 0. $$

In Definition 1, $E_d(z)$ represents the truncated Mittag-Leffler function of one parameter, which is defined as

$$ {}_{\kappa}E_d(z) = \sum_{j=0}^{\kappa} \frac{z^j}{\Gamma(dj+1)}, \ z \in [0, +\infty). $$

M-truncated fractional derivative has very important properties, and relevant conclusions can be referenced in reference [15].

2.2. Mathematical Derivation

Firstly, let us introduce the the wave transformation

$$ \psi(x, y, t) = \Psi(\xi)e^{i\eta}, \xi = m_1 x + m_2 y + \tfrac{\Gamma(d+1)}{\alpha}\omega t^{\alpha}, \eta = r_1 x + r_2 y + \tfrac{\Gamma(d+1)}{\alpha}\tau t^{\alpha} + \delta. \quad (2) $$

Inserting Equation (2) into Equation (1), we obtain the real and imaginary components of the resultant expression

$$ \begin{cases} (a_1\omega^2 + a_2 m_1^2)\Psi''(\xi) - 2a_3\Psi^3(\xi) - (a_1\tau^2 + a_2 r_1^2 + 2r_2)\Psi(\xi) = 0, \\ (2a_1\tau\omega + 2a_2 m_1 r_1 + 2m_2)\Psi'(\xi) = 0, \end{cases} \quad (3) $$

where $\Psi'(\xi) \neq 0$.

From the second equation of Equation (3), we have

$$ m_2 = -(a_1\tau\omega + a_2 m_1 r_1). \quad (4) $$

In order to further analyze the dynamic behavior and soliton solutions of Equation (1), under the conditions satisfied by Equation (3), we can transform the first equation of Equation (3) into the following ordinary differential equation:

$$\Psi'' - \Im_1 \Psi^3 - \Im_2 \Psi = 0, \tag{5}$$

Here, $\Im_1 = \frac{2a_3}{a_1\omega^2 + a_2 m_1^2}$ and $\Im_2 = \frac{a_1\tau^2 + a_2 r_1^2 + 2r_2}{a_1\omega^2 + a_2 m_1^2}$, where $a_1\omega^2 + a_2 m_1^2 \neq 0$.

2.3. Qualitative Analysis

The two-dimensional dynamic system of Equation (5) can be described as follows:

$$\begin{cases} \frac{d\Psi}{d\xi} = u, \\ \frac{du}{d\xi} = \Im_1 \Psi^3 + \Im_2 \Psi, \end{cases} \tag{6}$$

with its first integral

$$H(\Psi, u) = \frac{1}{2}u^2 - \frac{\Im_1}{4}\Psi^4 - \frac{\Im_2}{2}\Psi^2 = h. \tag{7}$$

Let $F(\Psi_j) = 0$ ($j = 0, 1, 2$) be the abscissa of the equilibrium point, where $F(\Psi_j) = \Im_1 \Psi_j^3 + \Im_2 \Psi_j$. Assume that $\mathbf{M}(\Psi_j, 0) = \begin{pmatrix} 0 & 1 \\ 3\Im_1 \Psi_j^2 + \Im_2 & 0 \end{pmatrix}$ is the coefficient matrix of (6) at the equilibrium point. Then, we obtain

$$\mathbf{det}(\mathbf{M}(\Psi_j, 0)) = -F'(\Psi_j), j = 0, 1, 2. \tag{8}$$

If $\Im_1 \Im_2 > 0$, system (6) has one equilibrium point $(0, 0)$ (see Figure 1a,b). If $\Im_1 \Im_2 < 0$, the system (6) has three equilibrium points: $(0, 0)$, $(\sqrt{-\frac{\Im_2}{\Im_1}}, 0)$, and $(-\sqrt{-\frac{\Im_2}{\Im_1}}, 0)$ (see Figure 1c,d).

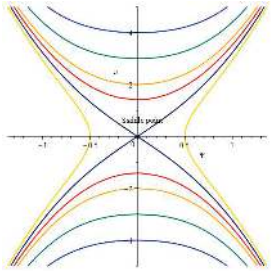

(a) $\Im_1 > 0, \Im_2 > 0$

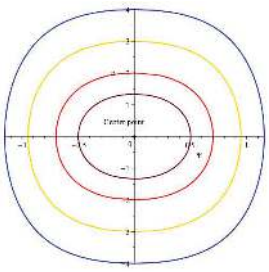

(b) $\Im_1 < 0, \Im_2 < 0$

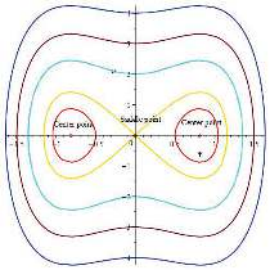

(c) $\Im_1 < 0, \Im_2 > 0$

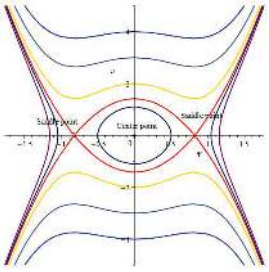

(d) $\Im_1 > 0, \Im_2 < 0$

Figure 1. Two-dimensional phase portrait of system (7).

2.4. Qualitative Analysis with Perturbation Term

In this section, we add the following small perturbation term to system (6):

$$\begin{cases} \frac{d\Psi}{d\xi} = u, \\ \frac{du}{d\xi} = \Im_1 \Psi^3 + \Im_2 \Psi + f(\xi), \end{cases} \tag{9}$$

where $f(\xi) = A\sin(\varpi\xi)$ and $f(\xi) = Ae^{-0.05\xi}$ are the perturbed terms. A stands for the amplitude of system (9). ϖ is the frequency of system (9).

By fixing the parameters $\Im_1, \Im_2, A, \varpi$, we have drawn the two-dimensional, three-dimensional, and Paincaré section diagrams of system (9), as shown in Figures 2–5. Specifically, when drawing two-dimensional and three-dimensional phase diagrams, we consider the graphs under different initial values. In Figure 6, we plotted the branch phase diagram of system (9) when ϖ takes different values. Obviously, it can be seen from Figure 6 that when A reaches a critical point, the phase diagram of system (9) exhibits chaotic behavior.

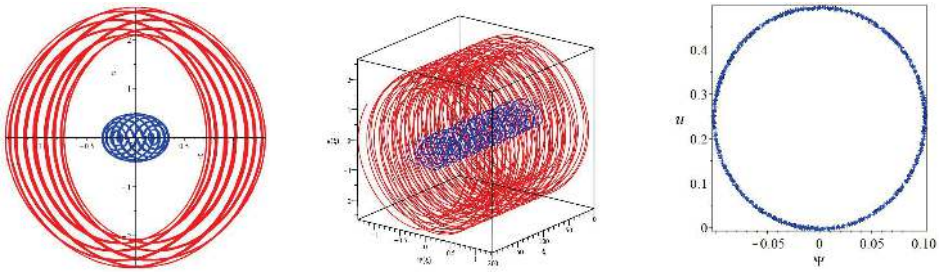

(**a**) 2D phase portrait (**b**) 3D phase portrait (**c**) Paincaré section

Figure 2. The chaotic behaviors of system (9) with $\Im_1 = 1, \Im_2 = -6, A = 1.2, \varpi = 1$.

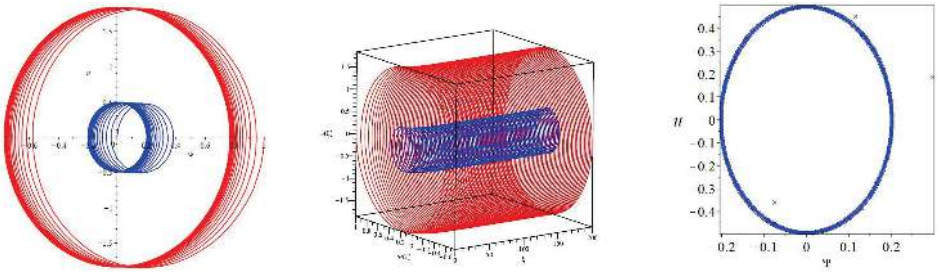

(**a**) 2D phase portrait (**b**) 3D phase portrait (**c**) Paincaré section

Figure 3. The chaotic behaviors of system (9) with $\Im_1 = 1, \Im_2 = -6, A = 1.2$.

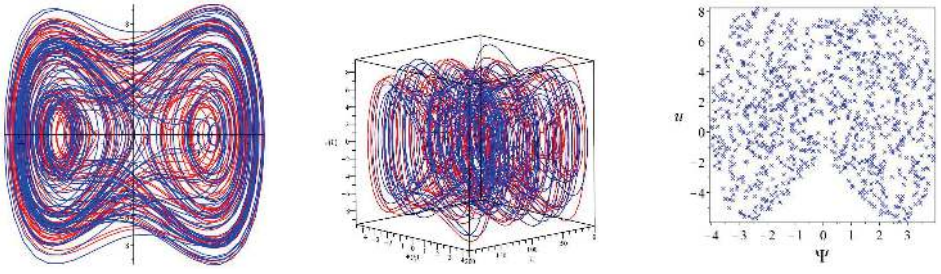

(**a**) 2D phase portrait (**b**) 3D phase portrait (**c**) Paincaré section

Figure 4. The chaotic behaviors of system (9) with $\Im_1 = -1, \Im_2 = 6, A = 6, \varpi = 1$.

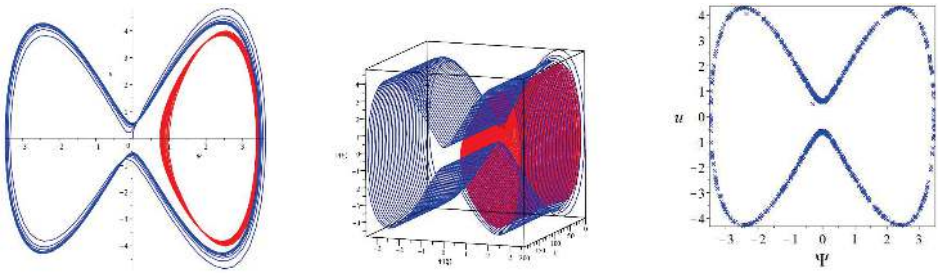

(**a**) 2D phase portrait (**b**) 3D phase portrait (**c**) Paincaré section

Figure 5. The chaotic behaviors of system (9) with $\Im_1 = -1, \Im_2 = 6, A = 1.2$.

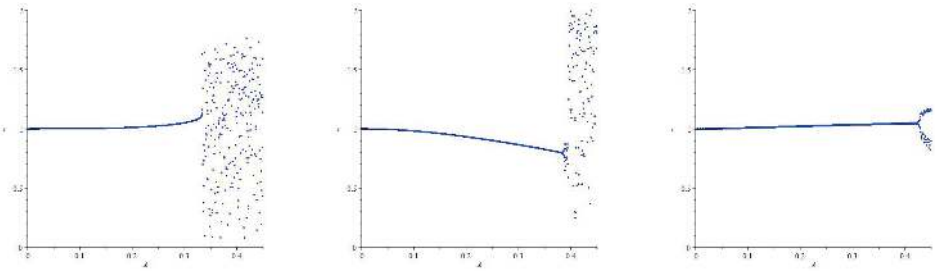

(**a**) $\varpi = \frac{\pi}{8}$ (**b**) $\varpi = \frac{\pi}{4}$ (**c**) $\varpi = \frac{\pi}{2}$

Figure 6. The bifurcation portraits of system (9) with $\Im_1 = -1, \Im_2 = 1, r = \sqrt{u^2 + \Psi^2}$.

3. Optical Soliton Solution of Equation (1)

Let be $h_0 = H(0,0) = 0$, $h_1 = H(\pm\sqrt{-\frac{\Im_2}{\Im_1}}, 0) = \frac{\Im_2^2}{4\Im_1}$.

3.1. $\Im_1 > 0, \Im_2 < 0, 0 < h < \frac{\Im_2^2}{4\Im_1}$

Then, system (7) becomes

$$u^2 = \frac{\Im_1}{2}(\Psi^4 + \frac{2\Im_2}{\Im_1}\Psi^2 + \frac{4h}{\Im_1}) = \frac{\Im_1}{2}(\varrho_{1h}^2 - \Psi^2)(\varrho_{2h}^2 - \Psi^2), \tag{10}$$

where $\varrho_{1h}^2 = \frac{-\Im_2 + \sqrt{\Im_2^2 - 4\Im_1 h}}{\Im_1}$ and $\varrho_{2h}^2 = \frac{-\Im_2 - \sqrt{\Im_2^2 - 4\Im_1 h}}{\Im_1}$.

Substituting (10) into $\frac{d\Phi}{d\xi} = u$ and integrating it, we can present the Jacobian function solutions

$$\psi_1(x,y,t) = \pm\varrho_{1h}\mathbf{sn}(\varrho_{2h}\sqrt{\frac{\Im_1}{2}}(m_1 x + m_2 y + \frac{\Gamma(d+1)}{\alpha}\omega t^\alpha), \frac{\varrho_{1h}}{\varrho_{2h}})\mathbf{e}^{i(r_1 x + r_2 y + \frac{\Gamma(d+1)}{\alpha}\tau t^\alpha + \delta)}. \tag{11}$$

3.2. $\Im_1 > 0, \Im_2 < 0, h = \frac{\Im_2^2}{4\Im_1}$

When $\varrho_{1h}^2 = \varrho_{2h}^2 = -\frac{\Im_2}{\Im_1}$, we can obtain the soliton solution of (1)

$$\psi_2(x,y,t) = \pm\sqrt{-\frac{\Im_2}{\Im_1}}\mathbf{tanh}(\sqrt{-\frac{\Im_2}{2}}(m_1 x + m_2 y + \frac{\Gamma(d+1)}{\alpha}\omega t^\alpha))\mathbf{e}^{i(r_1 x + r_2 y + \frac{\Gamma(d+1)}{\alpha}\tau t^\alpha + \delta)}. \tag{12}$$

3.3. $\Im_1 < 0, \Im_2 > 0, -\frac{\Im_2^2}{4\Im_1} < h < 0$

Then, system (7) becomes

$$u^2 = -\frac{\Im_1}{2}(-\Psi^4 - \frac{2\Im_2}{\Im_1}\Psi^2 - \frac{4h}{\Im_1}) = -\frac{\Im_1}{2}(\Psi^2 - \varrho_{3h}^2)(\varrho_{4h}^2 - \Psi^2), \tag{13}$$

where $\varrho_{3h}^2 = \frac{-\Im_2 + \sqrt{\Im_2^2 - 4\Im_1 h}}{\Im_1}$ and $\varrho_{4h}^2 = \frac{-\Im_2 - \sqrt{\Im_2^2 - 4\Im_1 h}}{\Im_1}$.

Substituting (13) into $\frac{d\Phi}{d\xi} = u$ and integrating it, we can present the Jacobian function solutions

$$\psi_3(x,y,t) = \pm\varrho_{4h}\mathbf{dn}(\varrho_{4h}\sqrt{-\frac{\Im_1}{2}}(m_1x + m_2y + \frac{\Gamma(d+1)}{\alpha}\omega t^\alpha), \frac{\sqrt{\varrho_{4h}^2-\varrho_{3h}^2}}{\varrho_{4h}}) \mathbf{e}^{i(r_1x+r_2y+\frac{\Gamma(d+1)}{\alpha}\tau t^\alpha+\delta)}. \tag{14}$$

3.4. $\Im_1 < 0, \Im_2 > 0, h = 0$

When $\varrho_{3h}^2 = 0, \varrho_{4h}^2 == -\frac{2\Im_2}{\Im_1}$, we can obtain the soliton solution of (1)

$$\psi_4(x,y,t) = \pm\sqrt{-\frac{2\Im_2}{\Im_1}}\mathbf{sech}(\sqrt{\Im_2}(m_1x + m_2y + \frac{\Gamma(d+1)}{\alpha}\omega t^\alpha))\mathbf{e}^{i(r_1x+r_2y+\frac{\Gamma(d+1)}{\alpha}\tau t^\alpha+\delta)}. \tag{15}$$

3.5. $\Im_1 < 0, \Im_2 > 0, h > 0$

Then, system (7) becomes

$$u^2 = -\frac{\Im_1}{2}(-\Psi^4 - \frac{2\Im_2}{\Im_1}\Psi^2 - \frac{4h}{\Im_1}) = -\frac{\Im_1}{2}(\varrho_{5h}^2 + \Psi^2)(\varrho_{6h}^2 - \Psi^2), \tag{16}$$

where $\varrho_{5h}^2 = \frac{\Im_2-\sqrt{\Im_2^2-4\Im_1 h}}{\Im_1}$ and $\varrho_{6h}^2 = \frac{-\Im_2-\sqrt{\Im_2^2-4\Im_1 h}}{\Im_1}$.

Substituting (16) into $\frac{d\Phi}{d\xi} = u$ and integrating it, we can present the Jacobian function solutions

$$\psi_5(x,y,t) = \pm\varrho_{6h}\mathbf{cn}(\sqrt{-\frac{\Im_1(\varrho_{5h}^2+\varrho_{6h}^2)}{2}}(m_1x + m_2y + \frac{\Gamma(d+1)}{\alpha}\omega t^\alpha), \frac{\varrho_{6h}}{\sqrt{\varrho_{5h}^2+\varrho_{6h}^2}}) \mathbf{e}^{i(r_1x+r_2y+\frac{\Gamma(d+1)}{\alpha}\tau t^\alpha+\delta)}. \tag{17}$$

3.6. Numerical Simulations

In this section, we plotted the solutions $\psi_1(x,y,t)$, including the three-dimensional graph, two-dimensional graph, and counter graph, when $a_1 = 1, a_2 = 1, \omega = 1, m_1 = 1, m_2 = 6, \tau = -7, r_1 = 1, r_2 = -\frac{3}{2}, \alpha = \frac{1}{2}, d = 1, h = \frac{3}{16}$ as shown in Figure 7. Obviously, the solution $\psi_1(x,y,t)$ of Equation (1) is a periodic function solution. We plotted the solutions $\psi_2(x,y,t)$, including the three-dimensional graph, two-dimensional graph, and counter graph, when $a_1 = 1, a_2 = 1, \omega = 1, m_1 = 1, m_2 = 6, \tau = -7, r_1 = 1, r_2 = 1, \alpha = \frac{1}{2}$, as shown in Figure 8. Obviously, the solution $\psi_2(x,y,t)$ of Equation (1) is a kink-like soliton. Moreover, we also plot solutions $\psi_3(x,y,t)$, $\psi_4(x,y,t)$, and $\psi_5(x,y,t)$ of Equation (1), as shown in Figures 9–11.

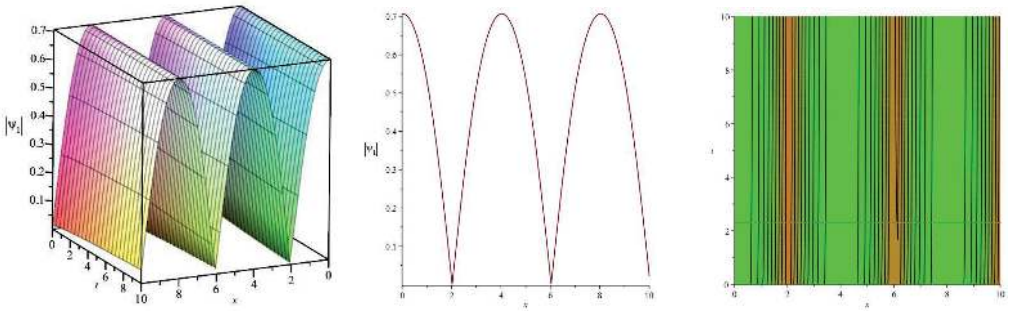

(**a**) 3D graph (**b**) 2D graph (**c**) Contour graph

Figure 7. The solution $\psi_1(x,y,t)$ with $a_1 = 1, a_2 = 1, a_3 = 1, \omega = 1, m_1 = 1, m_2 = 6, \tau = -7, r_1 = 1, r_2 = -25, \alpha = \frac{1}{2}, d = 1, h = \frac{3}{16}$.

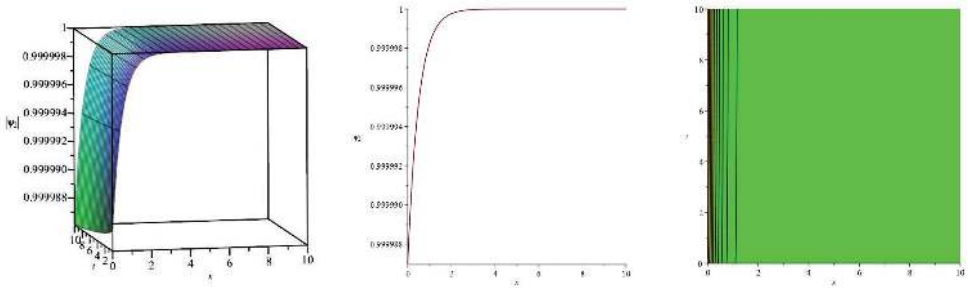

(**a**) 3D graph (**b**) 2D graph (**c**) Contour graph

Figure 8. The solution $\psi_2(x, y, t)$ with $a_1 = 1, a_2 = 1, a_3 = 1, \omega = 1, m_1 = 1, m_2 = 6, \tau = -7, r_1 = 1, r_2 = 1, d = 1, \alpha = \frac{1}{2}, h = \frac{1}{4}$.

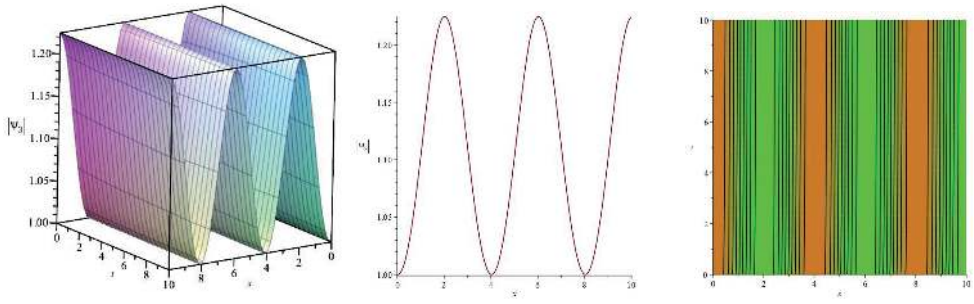

(**a**) 3D graph (**b**) 2D graph (**c**) Contour graph

Figure 9. The solution $\psi_3(x, y, t)$ with $a_1 = 1, a_2 = 1, a_3 = -1, \omega = 1, m_1 = 1, m_2 = 6, \tau = -7, r_1 = 1, r_2 = -24, d = 1, \alpha = \frac{1}{2}, h = -\frac{3}{16}$.

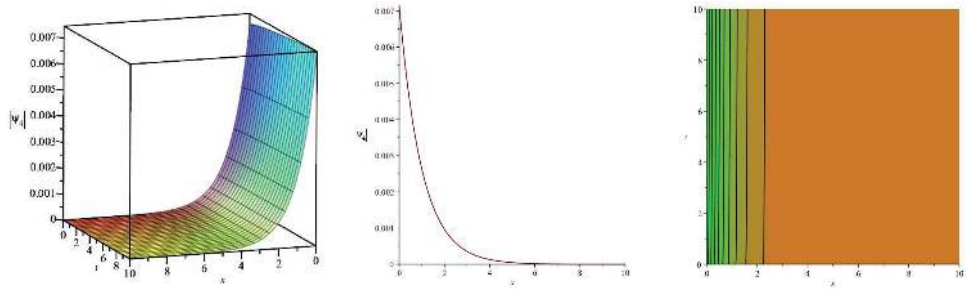

(**a**) 3D graph (**b**) 2D graph (**c**) Contour graph

Figure 10. The solution $\psi_4(x, y, t)$ with $a_1 = 1, a_2 = 1, a_3 = -1, \omega = 1, m_1 = 1, m_2 = 6, \tau = -7, r_1 = 1, r_2 = -24, d = 1, \alpha = \frac{1}{2}, h = 0$.

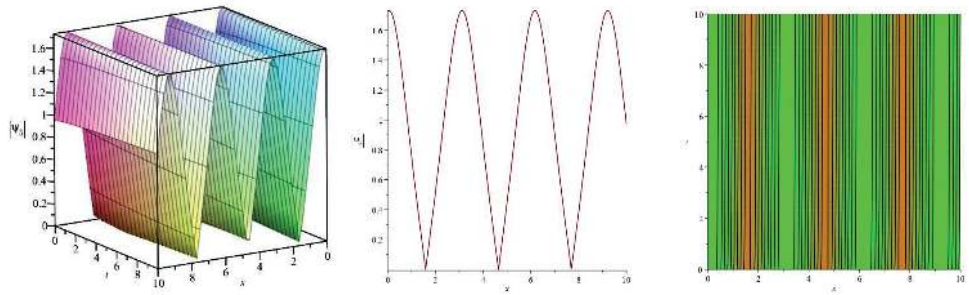

(**a**) 3D graph (**b**) 2D graph (**c**) Contour graph

Figure 11. The solution $\psi_5(x, y, t)$ with $a_1 = 1, a_2 = 1, a_3 = -1, \omega = 1, m_1 = 1, m_2 = 6, \tau = -7, r_1 = 1, r_2 = -\frac{49}{2}, d = 1, \alpha = \frac{1}{2}, h = \frac{3}{4}$.

4. Conclusions

In this article, we use the theory of dynamical systems to study the dynamic behavior and optical soliton for Equation (1) in a liquid crystal model. Furthermore, we used

mathematical software to draw a planar phase diagram of a two-dimensional dynamical system, and we can easily obtain the characteristics of some equilibrium points of the planar dynamical system from the planar phase diagram. And by adding small perturbations, the dynamic behavior of the two-dimensional system is analyzed. Based on different initial values, we have drawn planar phase diagrams using red and blue colors in the same coordinate system. From the perspective of plane dynamics theory, we have drawn a bifurcation phase diagram and Poincaré sections of a disturbance system. And we separately considered the dynamic behavior under periodic and small disturbances. In future research, we will consider the dynamic behavior and optical soliton solutions of more complex FPDEs.

Author Contributions: Software, Z.L.; writing—original draft preparation, J.L.; writing—review and editing, Z.L. All authors have read and agreed to the published version of the manuscript.

Funding: This research received no external funding.

Data Availability Statement: Data are contained within the article.

Conflicts of Interest: The authors declare no conflicts of interest.

References

1. Wu, J.; Yang, Z. Global existence and boundedness of chemotaxis-fluid equations to the coupled Solow-Swan model. *AIMS Math.* **2023**, *8*, 17914–17942. [CrossRef]
2. Wu, J.; Huang, Y.J. Boundedness of solutions for an attraction-repulsion model with indirect signal production. *Mathematics* **2024**, *12*, 1143. [CrossRef]
3. Tang, L. Dynamical behavior and multiple optical solitons for the fractional Ginzburg-Landau equation with β-derivative in optical fibers. *Opt. Quant. Electron.* **2024**, *56*, 175. [CrossRef]
4. Wang, Y.; Qian, Z. Regularizing a two-dimensional time-fractional inverse heat conduction problem by a fractional Landweber iteration method. *Comput. Math. Appl.* **2024**, *164*, 104–115. [CrossRef]
5. Jornet, M. On the Cauchy-Kovalevskaya theorem for Caputo fractional differential equations. *Physica D* **2024**, *462*, 134139. [CrossRef]
6. Yu, J.C.; Feng, Y.Q. On the generalized time fractional reaction-diffusion equation: Lie symmetries, exact solutions and conservation laws. *Chaos Solitons Fractals* **2024**, *182*, 114855. [CrossRef]
7. Espinosa-Paredes, G.; Cruz-López, G.A. A new compartmental fractional neutron point kinetic equations with different fractional orders. *Nucl. Eng. Des.* **2024**, *423*, 113184. [CrossRef]
8. Lu, Y.S.; Hu, Y.Z.; Qiao, Y.; Yuan, M.J.; Xu, W. Sparse least squares via fractional function group fractional function penalty for the identification of nonlinear dynamical systems. *Chaos. Soliton. Fract.* **2024**, *182*, 114733. [CrossRef]
9. Liu, C.Y.; Li, Z. The dynamical behavior analysis and the traveling wave solutions of the stochastic Sasa-Satsuma Equation. *Qual. Theor. Dyn. Syst.* **2024**, *23*, 157. [CrossRef]
10. Gu, M.S.; Chen Peng, C.; Li, Z. Traveling wave solution of (3+1)-dimensional negative-order KdV-Calogero-Bogoyavlenskii-Schiff equation. *AIMS Math.* **2023**, *9*, 6699–6708. [CrossRef]
11. Mannaf, M.A.; Islam, M.E.; Bashar, H.; Basak, U.S.; Akbar, M.A. Dynamical behavior of optical self-control solion in a liquid crystal model. *Results Phys.* **2024**, *57*, 107324. [CrossRef]
12. Usman, Y.; Abdulkadir, S.T.; Ren, J.L. Propagation of M-truncated optical pulses in nonlinear optics. *Opt. Quant. Electron.* **2023**, *55*, 102.
13. Rehman, H.U.; Awan, A.U.; Allahyani, S.A.; Tag-ElDin, E.M.; Binyamin, M.A.; Yasin, S. Exact solution of paraxial wave dynamical model with kerr media by using ϕ^6 model expansion technique. *Results Phys.* **2022**, *42*, 105975. [CrossRef]
14. Rehman, H.U.; Seadawy, A.R.; Younis, M.; Yasi, S.; Raza, S.T.R.; Althobaiti, S. Monochromatic optical beam propagation of paraxial dynamical model in kerr media. *Results Phys.* **2021**, *31*, 105015. [CrossRef]
15. Roshid, M.M.; Uddin, M.; Mostafa, G. Dynamical structure of optical solution for M-fractional paraxial wave equation by using unified technique. *Results Phys.* **2023**, *51*, 106632. [CrossRef]

fractal and fractional

MDPI

Article

Positive Solutions and Their Existence of a Nonlinear Hadamard Fractional-Order Differential Equation with a Singular Source Item Using Spectral Analysis

Cheng Li [1] and Limin Guo [2,*]

[1] School of Automotive Engineering, Changzhou Institute of Technology, Changzhou 213032, China; licheng@czu.cn
[2] School of Science, Changzhou Institute of Technology, Changzhou 213032, China
* Correspondence: guolm@czu.cn

Abstract: Based on the spectral analysis method, Gelfand's formula, and the cones fixed point theorem, some positive solutions with their existence of a nonlinear infinite-point Hadamard fractional-order differential equation is achieved on the interval $[a, b]$ under some conditions, and particularly the nonlinear term allows singularities for time and spatial parameters in the present study. Finally, an analysis case is carried out to reveal the principal results.

Keywords: hadamard; fractional-order differential; positive solution; infinite-point; specral analysis

MSC: 70K50; 34B18

1. Introduction

The fractional-order differential model can exactly depict the physical and mechanical process containing historical memories and thus establish spatial global relationship briefly. Accordingly, the fractional-order differential model is concise in form and the parameter meaning is obvious, so it becomes one of the effective approaches for modeling complex mechanical and physical behaviors. Boulham et al. [1] proposed an adaptive monitor for projective chaotic synchronization of general class fractional-order systems with chaotic uncertainty affected by unknown input nonlinear factors, and the closed-loop stability was strictly verified by two simulation examples and related comparative studies. Wu et al. [2] used a new nonlinear fractional-order damaged pattern with viscosity, elasticity and plasticity for rock and soil materials to characterize three-stage creep behaviors, and their pattern fully calculated and predicted the deformation with hysteresis derived from the rapid creep in tunnel engineering. Ma et al. [3] developed a fractional-order model termed as SEIR type and subsequently the beingness, uniqueness, boundness of such a fractional-order system were determined. The research conclusions indicated that it is difficult for humans to avoid coexistence with the spread of the COVID-19 epidemic. Yang et al. [4] designed a fractional controller of EV hybrid energy storage system that can significantly improve the control performance with good robustness. In addition, fractional-order models have been found to be extensively applied in photovoltaic panels [5], electromagnetic waves [6], electric circuits [7], viscoelastic materials [8], chemical reactions [9] and biological systems [10,11].

Owing to its so many advantages and fine results while simulating the system, the fractional-order differential model has received increasingly research attentions during the past several years. How to get the existence result of positive solution for the fractional-order differential model as well as its related nonlinear dynamics becomes a hot research direction in the field of fractional-order differential models, and many meaningful results are achieved in recent years [12–17]. Xu et al. [18] depicted the positive solutions of a kind of fractional-order differential models as follows

Citation: Li, C.; Guo, L. Positive Solutions and Their Existence of a Nonlinear Hadamard Fractional -Order Differential Equation with a Singular Source Item Using Spectral Analysis. *Fractal Fract.* **2024**, *8*, 377. https://doi.org/10.3390/fractalfract8070377

Academic Editor: Riccardo Caponetto

Received: 27 May 2024
Revised: 23 June 2024
Accepted: 25 June 2024
Published: 26 June 2024

$$^{H}D^{\alpha}_{a^+}x(t) + \hbar(t, x(t)) = 0, t \in (a, b),$$

with the boundary value condition

$$x(a) = x'(a) = 0, x(b) = \int_a^b \chi(t)x(t)\frac{dt}{t},$$

where α, a, b are real positive mumbers, $2 < \alpha < 3$, $a < b < +\infty$, $^{H}D^{\alpha}_{a^+}$ is the Hadamard fractional derivative of order α, $\chi : [a, b] \to \mathbb{R}^+$ with $\chi(t) \not\equiv 0, t \in [a, b]$, and $\int_a^b \chi(t)(\ln \frac{t}{a})^{\alpha-1}\frac{dt}{t} \in [0, (\ln \frac{b}{a})^{\alpha-1})$, $\hbar \in C([a, b] \times \mathbb{R}^+, \mathbb{R}^+)$. Arul and Karthikeyan [19] discussed the existence and uniqueness of solutions with some integral boundary conditions of implicit Hadamard differential equation

$$-^{H} D^{\kappa}_{a^+}v(t) = g(t, v(t),^{H} D^{\kappa}_{a^+}v(t)),\ a < t < b,$$

with boundary value condition

$$v(a) = 0, v(b) = \varsigma \int_0^{\sigma} v(s)ds, a < \sigma < b, \varsigma \in \mathbb{R},$$

where $^{H}D^{\kappa}_{a^+}v$ is the standard Hadamard fractional derivative of order $1 < \kappa \leq 2$, Arul and Karthikeyan [19] investigated the existence and uniqueness based on Banach and Schauder's fixed point theorem. Wang et al. [20] studied a fractional-order iterative functional differential equation containing parameter on the interval $[a, b]$, showed as

$$^{c}D^{\alpha}_{a^+}u(t) = f(t, u(t), u(u^{\nu}(t))) + m, t \in [a, b], \nu \in R\backslash\{0\}, q \in (0, 1), \lambda \in R,$$

with boundary conditions

$$u(t) = \varphi(t), t \in [a_1, a], u(t) = \psi(t), t \in [b, b_1],$$

where $^{c}D^{q}_{a}$ is the Caputo fractional derivative of order q with the oower limit a, $a_1 \leq a < b \leq b_1, a_1 \leq a_1^{v}, b_1^{v} \leq b_1$, $f \in C([a, b] \times [a_1, b_1]^2, R), \varphi \in C([a_1, a], [a_1, b_1])$ and $\psi \in C([b, b_1], [a_1, b_1])$. The existence theorem is established by the method of Schauder's fixed point theorems [20], and Wang et al. [20] obtained data dependence of solutions and related parameters.

In this article, an infinite-point Hadamard fractional-order differential equation is taken into account, shown as

$$-^{H} D^{\flat}_{a^+}\mathcal{V}(t) + \varrho(t)\ell\Big(t, \mathcal{V}(t),^{H} D^{\mu}_{a^+}\mathcal{V}(t)\Big) = 0,\ a < t < b, \tag{1.1}$$

with boundary value conditions

$$^{H}D^{\mu}_{a^+}\mathcal{V}(a) =^{H} D^{\mu+1}_{a^+}\mathcal{V}(a) = 0,^{H} D^{\mu}_{a^+}\mathcal{V}(b) = \sum_{j=1}^{\infty} \kappa_j {}^{H}D^{\mu}_{a^+}\mathcal{V}(\varsigma_j), \tag{1.2}$$

where $2.5 < \flat \leq 3$, $\kappa_j \geq 0$, $0 < \mu < \frac{1}{2}$, $1 < \varsigma_1 < \varsigma_2 < \cdots < \varsigma_{j-1} < \varsigma_j < \cdots < e (j = 1, 2\cdots)$, $\sum_{j=1}^{\infty} \kappa_j \Big(\frac{\ln \varsigma_j - \ln s}{\ln b - \ln s}\Big)^{\flat-1} < 1$ and $\sum_{j=1}^{\infty} \kappa_j (\ln \frac{\varsigma_j}{a})^{\flat-1} < (\ln \frac{b}{a})^{\flat-1}$, $\varrho(t)$ is singular at $t = a$ or/and $t = b$, $\ell : [a, b] \times \mathbb{R} \times \mathbb{R} \to \mathbb{R}$ is a given function and $\ell(t, x, y)$ is continuous, and $^{H}D^{\flat}_{1^+}$ is the standard Hadamard derivative.

Compared with [18,21], the present study contains the the derivative term in the nonlinear term of the equation and we will deal with this difficulty, moreover, and involved infinite points in the boundary conditions. Compared with [19], the nonlinear term is singular in this article, and the method we used is spectral analysis and infinite-points are contained in the boundary conditions. Compared with [22,23], the interval we discussed

is arbitrarily closed interval $[a,b]$, the interval $[1,T]$ or $[0,1]$ in [22,23] are special cases of interval $[a,b]$, considering the solution of the equation on this interval will bring about a series of problems, and we overcome this difficulty.

2. Preliminaries And Lemmas

Some important definitions and lemmas which may be adopted during the certification in the present study, could be reviewed in the newly published papers, e.g., see [24,25], we introduce some of them herein.

Definition 1 ([24,25]). *Let $a > 0$, then the Hadamard-type fractional left integral of order $\beta > 0$ of a function $h : [a,\infty) \to \mathbb{R}$ is defined by*

$$ {}^{H}I^{\beta}_{a^+}h(t) = \frac{1}{\Gamma(\beta)}\int_a^t (\ln\frac{t}{\varsigma})^{\beta-1}h(\varsigma)\frac{d\varsigma}{\varsigma}, t \geq a. $$

Definition 2 ([24,25]). *Let $a > 0$, $h : [a,\infty) \to \mathbb{R}, t^{n-1}h^{(n-1)}(t) \in AC[a,\infty), n \in \mathbb{N}$, $\beta \in (n-1,n)$, then the Hadamard fractional left derivative of from $[a,+\infty)$ is defined by*

$$ {}^{H}D^{\beta}_{a^+}h(t) = \frac{1}{\Gamma(n-\beta)}(t\frac{d}{dt})^n\int_a^t (\ln\frac{t}{\varsigma})^{n-\beta-1}h(\varsigma)\frac{d\varsigma}{\varsigma}, t > a. $$

Lemma 1 ([24,25]). *For $\beta \in (n-1,n), n \in \mathbb{N}, h \in L[a,\infty), a > 0$, the fractional equation ${}^{H}D^{\beta}_{a^+}h(t) + \omega(t) = 0, t > a$ has expression of solution*

$$ x(t) = \sum_{i=1}^{n}\chi_i(\ln\frac{t}{a})^{\beta-i} - \frac{1}{\Gamma(\beta)}\int_a^t (\ln\frac{t}{\varsigma})^{\beta-1}\omega(\varsigma)\frac{d\varsigma}{\varsigma}, t \geq a, $$

where $\chi_i \in \mathbb{R}, k = 1,2,\ldots,n$.

Let $\mathscr{U}(t) = {}^{H}D^{\mu}_{a^+}\mathscr{V}(t), \mathscr{V}(t) \in C[a,b]$, then the BVP (1.1,1.2) can be reduced to a modified model

$$ -{}^{H}D^{\flat-\mu}_{a^+}\mathscr{U}(t) + \varrho(t)\ell\Big(t, {}^{H}I^{\mu}_{a^+}\mathscr{U}(t), \mathscr{U}(t)\Big) = 0,\ a < t < b, \tag{2.1} $$

with boundary value condition

$$ \mathscr{U}(a) = \mathscr{U}'(a) = 0, \mathscr{U}(b) = \sum_{j=1}^{\infty}\kappa_j\mathscr{U}(\varsigma_j). \tag{2.2} $$

Lemma 2. *Given $\mathscr{A} \in L^1(a,b)$, then the model*

$$ {}^{H}D^{\flat-\mu}_{1^+}\mathscr{U}(t) + \mathscr{A}(t) = 0,\ a < t < b, \tag{2.3} $$

with boundary value condition (2.2) can be expressed by

$$ \mathscr{U}(t) = \int_a^b \mathscr{H}(t,s)\mathscr{A}(s)\frac{ds}{s},\ t \in [a,b], \tag{2.4} $$

where

$$ \mathscr{H}(t,s) = \mathscr{G}(t,s) + \frac{(\ln\frac{t}{a})^{\flat-\mu-1}}{\Delta}\sum_{j=1}^{\infty}\kappa_j\mathscr{G}(\varsigma_j,s), $$

$$ \mathscr{G}(t,s) = \frac{1}{(\ln\frac{b}{a})^{\flat-\mu-1}\Gamma(\flat-\mu)}\begin{cases} (\ln t - \ln a)^{\flat-\mu-1}(\ln b - \ln s)^{\flat-\mu-1} \\ -(\ln t - \ln s))^{\flat-\mu-1}(\ln\frac{b}{a})^{\flat-\mu-1},\ a \leq s \leq t \leq b, \\ (\ln t - \ln a)^{\flat-\mu-1}(\ln b - \ln s)^{\flat-\mu-1},\ a \leq t \leq s \leq b, \end{cases} \tag{2.5} $$

in which $\Delta = (\ln \frac{b}{a})^{\flat-\mu-1} - \sum_{j=1}^{\infty} \kappa_j (\ln \frac{\varsigma_j}{a})^{\flat-\mu-1}$.

Proof. By Lemma 1, Formula (2.3) is changed into an equivalent integral equation

$$\mathscr{U}(t) = -{}^{H}I_{a^+}^{\flat-\mu}\mathscr{A}(t) + d_1(\ln \frac{t}{a})^{\flat-\mu-1} + d_2(\ln \frac{t}{a})^{\flat-\mu-2} + d_3(\ln \frac{t}{a})^{\flat-\mu-3}.$$

From $u(a) = 0$, we have $d_3 = 0$, then

$$\mathscr{U}'(t) = -{}^{H}I_{a^+}^{\flat-\mu-1}\mathscr{A}(t) + d_1(\flat-\mu-1)(\ln \frac{t}{a})^{\flat-\mu-2} \cdot \frac{a}{t} + d_2(\flat-\mu-2)(\ln \frac{t}{a})^{\flat-\mu-3}\frac{a}{t},$$

by $\mathscr{U}'(a) = 0$, we have $d_2 = 0$. Hence, we get

$$\begin{aligned}\mathscr{U}(t) =& d_1(\ln \frac{t}{a})^{\flat-\mu-1} - {}^{H}I_{a^+}^{\flat-\mu}\mathscr{A}(t)\\ =& -\frac{1}{\Gamma(\flat-\mu)}\int_a^t (\ln t - \ln s)^{\flat-\mu-1}\mathscr{A}(s)\frac{ds}{s} + d_1(\ln \frac{t}{a})^{\flat-\mu-1},\end{aligned}$$

therefore, $\mathscr{U}(\xi_j) = -\frac{1}{\Gamma(\flat-\mu)}\int_a^{\varsigma_j} (\ln \xi_j - \ln s)^{\flat-\mu-1}\mathscr{A}(s)\frac{ds}{s} + d_1(\ln \frac{\varsigma_j}{a})^{\flat-\mu-1}$. Moreover, by $\mathscr{U}(b) = \sum_{j=1}^{\infty} \kappa_j \mathscr{U}(\varsigma_j)$, we have

$$\begin{aligned}\mathscr{U}(b) =& -\frac{1}{\Gamma(\flat-\mu)}\int_a^b (\ln b - \ln s)^{\flat-\mu-1}\mathscr{A}(s)\frac{ds}{s} + d_1(\ln \frac{b}{a})^{\flat-\mu-1}\\ =& \sum_{j=1}^{\infty}\kappa_j\left(-\frac{1}{\Gamma(\flat-\mu)}\int_a^{\varsigma_j} (\ln \varsigma_j - \ln s)^{\flat-\mu-1}\mathscr{A}(s)\frac{ds}{s} + d_1(\ln \frac{\varsigma_j}{a})^{\flat-\mu-1}\right).\end{aligned}$$

Then, we get

$$\begin{aligned}&d_1\left((\ln \frac{b}{a})^{\flat-\mu-1} - \sum_{j=1}^{\infty}\kappa_j(\ln \frac{\varsigma_j}{a})^{\flat-\mu-1}\right) = \frac{1}{\Gamma(\flat-\mu)}\int_a^b (\ln b - \ln s)^{\flat-\mu-1}\mathscr{A}(s)\frac{ds}{s}\\ &-\frac{1}{\Gamma(\flat-\mu)}\sum_{j=1}^{\infty}\kappa_j\int_a^{\varsigma_j}(\ln \varsigma_j - \ln s)^{\flat-\mu-1}\mathscr{A}(s)\frac{ds}{s},\end{aligned}$$

thus, we have

$$d_1 = \frac{1}{\Gamma(\flat-\mu)\Delta}\int_a^b (\ln b - \ln s)^{\flat-\mu-1}\mathscr{A}(s)\frac{ds}{s} - \frac{1}{\Gamma(\flat-\mu)\Delta}\sum_{j=1}^{\infty}\kappa_j\int_a^{\varsigma_j}(\ln \varsigma_j - \ln s)^{\flat-\mu-1}\mathscr{A}(s)\frac{ds}{s},$$

hence,

$$
\begin{aligned}
\mathscr{U}(t) =& \frac{(\ln\frac{t}{a})^{\flat-\mu-1}}{\Gamma(\flat-\mu)\Delta}\int_a^b(\ln b-\ln s)^{\flat-\mu-1}\mathscr{A}(s)\frac{ds}{s}-\frac{(\ln\frac{t}{a})^{\flat-\mu-1}}{\Gamma(\flat-\mu)\Delta}\sum_{j=1}^{\infty}\kappa_j\int_a^{\varsigma_j}(\ln\varsigma_j-\ln s)^{\flat-\mu-1}\mathscr{A}(s)\frac{ds}{s}\\
&-{}^{H}I_{a^+}^{\flat-\mu}\mathscr{A}(t)\\
=&\frac{(\ln\frac{t}{a})^{\flat-\mu-1}}{\Gamma(\flat-\mu)\Delta}\int_a^b(\ln b-\ln s)^{\flat-\mu-1}\mathscr{A}(s)\frac{ds}{s}-\frac{(\ln\frac{t}{a})^{\flat-\mu-1}}{\Gamma(\flat-\mu)\Delta}\sum_{j=1}^{\infty}\kappa_j\int_a^{\varsigma_j}(\ln\varsigma_j-\ln s)^{\flat-\mu-1}\mathscr{A}(s)\frac{ds}{s}\\
&-\frac{1}{\Gamma(\flat-\mu)}\int_a^t(\ln t-\ln s)^{\flat-\mu-1}\mathscr{A}(s)\frac{ds}{s}\\
&+\frac{1}{\Gamma(\flat-\mu)(\ln\frac{b}{a})^{\flat-\mu-1}}\int_a^b(\ln\frac{t}{a})^{\flat-\mu-1}(\ln\frac{b}{s})^{\flat-\mu-1}\mathscr{A}(s)\frac{ds}{s}\\
&-\frac{1}{\Gamma(\flat-\mu)(\ln\frac{b}{a})^{\flat-\mu-1}}\int_a^b(\ln\frac{t}{a})^{\flat-\mu-1}(\ln\frac{b}{s})^{\flat-\mu-1}\mathscr{A}(s)\frac{ds}{s}\\
=&\int_a^b\mathscr{G}(t,s)\mathscr{A}(s)\frac{ds}{s}+\frac{1}{\Gamma(\flat-\mu)\Delta}\int_a^b(\ln\frac{t}{a})^{\flat-\mu-1}(\ln b-\ln s)^{\flat-\mu-1}\mathscr{A}(s)\frac{ds}{s}\\
&-\frac{1}{\Gamma(\flat-\mu)(\ln\frac{b}{a})^{\flat-\mu-1}}\int_a^b(\ln\frac{t}{a})^{\flat-\mu-1}(\ln\frac{b}{s})^{\flat-\mu-1}\mathscr{A}(s)\frac{ds}{s}\\
&-\frac{(\ln\frac{t}{a})^{\flat-\mu-1}}{\Gamma(\flat-\mu)\Delta}\sum_{j=1}^{\infty}\kappa_j\int_a^{\varsigma_j}(\ln\varsigma_j-\ln s)^{\flat-\mu-1}\mathscr{A}(s)\frac{ds}{s}\\
=&\int_a^b\mathscr{G}(t,s)\mathscr{A}(s)\frac{ds}{s}+\frac{(\ln\frac{b}{a})^{\flat-\mu-1}-\Delta}{\Delta\Gamma(\flat-\mu)(\ln\frac{b}{a})^{\flat-\mu-1}}\int_a^b(\ln\frac{t}{a})^{\flat-\mu-1}(\ln\frac{b}{s})^{\flat-\mu-1}\mathscr{A}(s)\frac{ds}{s}\\
&-\frac{(\ln\frac{t}{a})^{\flat-\mu-1}}{\Gamma(\flat-\mu)\Delta}\sum_{j=1}^{\infty}\kappa_j\int_a^{\varsigma_j}(\ln\varsigma_j-\ln s)^{\flat-\mu-1}\mathscr{A}(s)\frac{ds}{s}\\
=&\int_a^b\mathscr{G}(t,s)\mathscr{A}(s)\frac{ds}{s}\\
&+\frac{(\ln\frac{t}{a})^{\flat-\mu-1}}{\Delta}\left(\frac{1}{\Gamma(\flat-\mu)(\ln\frac{b}{a})^{\flat-\mu-1}}\sum_{j=1}^{\infty}\kappa_j\int_a^b(\ln\frac{\varsigma_j}{a})^{\flat-\mu-1}(\ln\frac{b}{s})^{\flat-\mu-1}\mathscr{A}(s)\frac{ds}{s}\right.\\
&\left.-\frac{1}{\Gamma(\flat-\mu)}\sum_{j=1}^{\infty}\kappa_j\int_a^{\varsigma_j}(\ln\varsigma_j-\ln s)^{\flat-\mu-1}\mathscr{A}(s)\frac{ds}{s}\right)\\
=&\int_a^b\mathscr{G}(t,s)\mathscr{A}(s)\frac{ds}{s}\\
&+\frac{(\ln\frac{t}{a})^{\flat-\mu-1}}{\Delta}\sum_{j=1}^{\infty}\kappa_j\left(\frac{1}{\Gamma(\flat-\mu)(\ln\frac{b}{a})^{\flat-\mu-1}}\int_a^b(\ln\frac{\varsigma_j}{a})^{\flat-\mu-1}(\ln\frac{b}{s})^{\flat-\mu-1}\mathscr{A}(s)\frac{ds}{s}\right.\\
&\left.-\frac{1}{\Gamma(\flat-\mu)}\int_a^{\varsigma_j}(\ln\varsigma_j-\ln s)^{\flat-\mu-1}\mathscr{A}(s)\frac{ds}{s}\right)\\
=&\int_a^b\mathscr{H}(t,s)\mathscr{A}(s)\frac{ds}{s}.
\end{aligned}
$$

Therefore, the expression (2.4) is ritht. □

Lemma 3. *The properties of the Green function (2.4) are as follows:*

(i) $\mathscr{H}(t,s)\leq\frac{\varpi(s)}{\Gamma(\flat-\mu)(\ln\frac{b}{a})}w$;

(ii) $\mathscr{H}(t,s)\geq\frac{\vartheta(t)\varpi(s)}{\Gamma(\flat-\mu)(\ln\frac{b}{a})^{\flat-\mu+1}}$,

where

$$\vartheta(t) = (\ln\frac{t}{a})^{\flat-\mu-1}(\ln\frac{b}{t}), \varpi(t) = (\ln\frac{t}{a})(\ln\frac{b}{t})^{\flat-\mu-1}, w = 1 + \frac{(\ln\frac{b}{a})^{\flat-\mu-1}}{\Delta}\sum_{j=1}^{\infty}\kappa_j. \quad (2.6)$$

Proof. From Lemma 5 of [26], we get

$$\mathscr{G}(t,s) \le \frac{\varpi(s)}{\Gamma(\flat-\mu)(\ln\frac{b}{a})}, \mathscr{G}(t,s) \ge \frac{\vartheta(t)\varpi(s)}{\Gamma(\flat-\mu)(\ln\frac{b}{a})^{\flat-\mu+1}}, \quad (2.7)$$

where $\vartheta(t), \varpi(t)$ is as Lemma 3, $\mathscr{G}(t,s)$ is from (2.5). By (2.7), we get

$$\begin{aligned}\mathscr{H}(t,s) =& \mathscr{G}(t,s) + \frac{(\ln\frac{t}{a})^{\flat-\mu-1}}{\Delta}\sum_{j=1}^{\infty}\kappa_j\mathscr{G}(\xi_j,s)\\ \le& \frac{\varpi(s)}{\Gamma(\flat-\mu)(\ln\frac{b}{a})} + \frac{(\ln\frac{b}{a})^{\flat-\mu-1}}{\Delta}\sum_{j=1}^{\infty}\kappa_j\frac{\varpi(s)}{\Gamma(\flat-\mu)(\ln\frac{b}{a})}\\ \le& \frac{\varpi(s)}{\Gamma(\flat-\mu)(\ln\frac{b}{a})}\left(1 + \frac{(\ln\frac{b}{a})^{\flat-\mu-1}}{\Delta}\sum_{j=1}^{\infty}\kappa_j\right)\\ =& \frac{\varpi(s)}{\Gamma(\flat-\mu)(\ln\frac{b}{a})}w.\end{aligned}$$

On the other hand, we can calculate that

$$\mathscr{H}(t,s) \ge \mathscr{G}(t,s) \ge \frac{\vartheta(t)\varpi(s)}{\Gamma(\flat-\mu)(\ln\frac{b}{a})^{\flat-\mu+1}},$$

then we have (ii) of Lemma 3. As a consequent, we complete the the proof of Lemma 3. □

Let $E = C[a,b]$, $\|\mathscr{U}\| = \max_{a\le t\le b}|\mathscr{U}(t)|$, then $(\mathscr{E}, \|.\|)$ is a Banach space. In this paper,

$$\mathscr{P} = \{u \in E : \mathscr{U}(t) \ge 0,\ t \in [a,b]\},$$

$$\mathscr{K} = \left\{\mathscr{U} \in P : \mathscr{U}(t) \ge \frac{\vartheta(t)}{(\ln\frac{b}{a})^{\flat-\mu}w}\|\mathscr{U}\|,\ t \in [a,b]\right\},$$

where $w = 1 + \frac{(\ln\frac{b}{a})^{\flat-\mu-1}}{\Delta}\sum_{j=1}^{\infty}\kappa_j$. Apparently, $\mathscr{K}$ is a subcone of P, and $(\mathscr{E}, \mathscr{K})$ has an ordering relation. Let $\mathscr{K}_r = \{\mathscr{U} \in \mathscr{K} : \|\mathscr{U}\| < r\}$, $\partial\mathscr{K}_r = \{\mathscr{U} \in \mathscr{K} : \|\mathscr{U}\| = r\}$ and $\overline{\mathscr{K}}_r = \{\mathscr{U} \in \mathscr{K} : \|\mathscr{U}\| \le r\}$.

Now the following conditions is listed which will be used later.

(A_1) $\varrho : (a,b) \to \mathbb{R}^1_+$ is nonnegative, $\varrho(t) \not\equiv 0$ and $\varrho(t)$may be singular at $t = a$, $t = b$, and

$$\int_a^b \varpi(s)\varrho(s)\frac{ds}{s} < +\infty.$$

(A_2) $\ell : [a,b]\times(0,+\infty)\times(0,+\infty) \to \mathbb{R}^1_+$ is continuous, and for any $0 < \iota < \jmath < +\infty$,

$$\begin{aligned}&\limsup_{m\to+\infty}\Big\{\sup\int_{e(m)}\varpi(s)\varrho(s)\ell(s,x_1(s),x_2(s))\frac{ds}{s}\Big|,\\ &x_1 \in \overline{\mathscr{K}}_{\bar{\jmath}} \setminus \mathscr{K}_\iota,\ x_2 \in \overline{\mathscr{K}}_\jmath \setminus \mathscr{K}_\iota\Big\} = 0,\end{aligned}$$

where $e(m) = [0, \frac{1}{m}] \cup [\frac{m-1}{m}, 1]$, $\bar{\jmath} = \frac{1}{\Gamma(\mu+1)}(\ln\frac{b}{a})^\mu\jmath$.

Nonlinear operator $A : \mathscr{K} \setminus \{0\} \to \mathscr{P}$ and linear operator $\mathscr{T} : \mathscr{E} \to \mathscr{E}$ are defined, shown as

$$(A\mathscr{U})(t) = \int_a^b \mathscr{H}(t,s)\varrho(s)\ell\Big(s, {}^H I_{a^+}^{\mu}\mathscr{U}(s), \mathscr{U}(s)\Big)\frac{ds}{s},\ t \in [a,b], \tag{2.8}$$

$$(\mathscr{T}\mathscr{U})(t) = \int_a^b \mathscr{H}(t,s)\varrho(s)\mathscr{U}(s)\frac{ds}{s},\ t \in [a,b]. \tag{2.9}$$

Lemma 4 ([27]). *Assume $\mathscr{T} : \mathscr{E} \to \mathscr{E}$, and $\mathscr{T}$ be a linear operator and is continuous, $\mathscr{T}(\mathscr{K}) \subset \mathscr{K}$, where $\mathscr{K}$ is a total cone. If there exist a positive constant d and $\zeta \in \mathscr{E} \setminus (-\mathscr{K})$ that makes $d\mathscr{T}(\zeta) \geq \zeta$, then the spectral radius of $\mathscr{T}$ be greater than 0, and which has a positive eigenfunction in regard to its the first eigenvalue $\lambda = r(\mathscr{T})^{-1}$. This formula is often called Krein-Rutmann's theorem.*

Lemma 5 ([27]). *The spectral radius of $\mathscr{T}$ meets*

$$r(\mathscr{T}) = \lim_{n \to +\infty} \|\mathscr{T}^n\|^{\frac{1}{n}},$$

where $\mathscr{T}$ is a linear bounded operator, and $\|.\|$ is the norm of operator. This formula is often called Gelfand's formula.

Lemma 6. *$\mathscr{T} : \mathscr{K} \to \mathscr{K}$ defined by (2.9) is a linear operator with complete continuity under the condition (A_1), and the spectral radius $r(\mathscr{T})$ of $\mathscr{T}$ is unequal zero, furthermore, $\mathscr{T}$ exists a positive eigenfunction ζ in regard to its first eigenvalue $\lambda_1 = (r(\mathscr{T}))^{-1}$.*

Proof. For $\forall\ \mathscr{U} \in \mathscr{K}$, from Lemma 3, one arrives

$$\begin{aligned}\|\mathscr{T}\mathscr{U}\| =& \max_{t\in[a,b]} \int_a^b \mathscr{H}(t,s)\varrho(s)\mathscr{U}(s)\frac{ds}{s} \\ \leq& \frac{1}{\Gamma(\flat-\mu)(\ln\frac{b}{a})}\left(1 + \frac{(\ln\frac{b}{a})^{\flat-\mu-1}}{\Delta}\sum_{j=1}^{\infty}\kappa_j\right)\int_a^b \varpi(s)\varrho(s)\mathscr{U}(s)\frac{ds}{s} \\ \leq& \frac{w}{\Gamma(\flat-\mu)(\ln\frac{b}{a})}\int_a^b \varpi(s)\varrho(s)\mathscr{U}(s)\frac{ds}{s}\end{aligned} \tag{2.10}$$

Moreover, by Lemma 3, the following result can be derived

$$\mathscr{T}\mathscr{U}(t) \geq \frac{\vartheta(t)}{\Gamma(\flat-\mu)(\ln\frac{b}{a})^{\flat-\mu+1}}\int_a^b \varpi(s)\varrho(s)\mathscr{U}(s)\frac{ds}{s}, t \in [a,b]. \tag{2.11}$$

Formula (2.10) and Formula (2.11) mean $\mathscr{T}$ from $\mathscr{K}$ to $\mathscr{K}$. One finds that $\mathscr{T}$ has completely continuous property from $\mathscr{K}$ to $\mathscr{K}$ by combing (A_2) and the uniform continuous property of $\mathscr{H}(t,s)$ on $[a,b] \times [a,b]$.

Next, based on Krein-Rutmann's theorem, we prove that $\mathscr{T}$ has the first eigenvalue λ_1 and $\lambda_1 > 0$. In reality, by process of proof Lemma 3, there exists $t_0 \in (a,b)$ that makes $\mathscr{H}(t_0,t_0) > 0$. Therefore, there exists $[m,n] \subset (a,b)$ that makes $t_0 \in (m,n)$ and $\mathscr{H}(t,s) > 0$ for $\forall\ t,s \in [m,n]$. Select $\mathscr{U} \in K$ that makes $\mathscr{U}(t_0) > 0$ and $\mathscr{U}(t) = 0$ for all $t \notin [m,n]$. After that, for $\forall\ t \in [m,n]$, we have

$$(\mathscr{T}\mathscr{U})(t) = \int_a^b \mathscr{H}(t,s)\varrho(s)\mathscr{U}(s)\frac{ds}{s} \geq \int_m^n \mathscr{H}(t,s)\varrho(s)\mathscr{U}(s)\frac{ds}{s} > 0.$$

Hence, there is $d > 0$ such that $d(\mathscr{T}\mathscr{U})(t) \geq \mathscr{U}(t)$ for $t \in [a,b]$, then the spectral radius $r(\mathscr{T}) \neq 0$ according to Lemma 4, furthermore, by Lemma 6, for the given first eigenvalue $\lambda_1 = (r(\mathscr{T}))^{-1}$, there exists a positive eigenfunction $\varphi^\star$ for A that makes

$$\lambda_1 \mathscr{T}\varphi^\star = \varphi^\star.$$

The proof is over. □

Lemma 7. *In case of* (A_1), (A_2) *hold, then* A *acts as an operator with complete continuity from* $\overline{\mathscr{K}_\jmath \setminus \mathscr{K}_\iota}$ *to* $\mathscr{K}$.

Proof. First of all, we show $A(\overline{\mathscr{K}_\jmath \setminus \mathscr{K}_r}) \subset \mathscr{K}$. Actually, for $\forall\, u \in \overline{\mathscr{K}_\jmath \setminus \mathscr{K}_\iota}, t \in [a,b]$, and combing Lemma 3, one has

$$\begin{aligned}(A\mathscr{U})(t) &= \int_a^b \mathscr{H}(t,s)\varrho(s)\ell\Big(s, {}^H I_{a^+}^{\mu}\mathscr{U}(s), \mathscr{U}(s)\Big)\frac{ds}{s}\\ &\leq \frac{w}{\Gamma(\flat-\mu)(\ln\frac{b}{a})}\int_a^b \varpi(s)\varrho(s)\ell\Big(s, {}^H I_{a^+}^{\mu}\mathscr{U}(s), \mathscr{U}(s)\Big)\frac{ds}{s},\end{aligned}$$

Then

$$\|(A\mathscr{U})\| \leq \frac{w}{\Gamma(\flat-\mu)(\ln\frac{b}{a})}\int_a^b \varpi(s)\varrho(s)\ell\Big(s, {}^H I_{a^+}^{\mu}u(s), u(s)\Big)\frac{ds}{s}.$$

On the other side, the following result is obtained from Lemma 3

$$\begin{aligned}(A\mathscr{U})(t) &= \int_a^b \mathscr{H}(t,s)\varrho(s)\ell\Big(s, {}^H I_{a^+}^{\mu}\mathscr{U}(s), \mathscr{U}(s)\Big)\frac{ds}{s}\\ &\geq \frac{\vartheta(t)}{\Gamma(\flat-\mu)(\ln\frac{b}{a})^{\flat-\mu+1}}\int_a^b \varpi(s)\varrho(s)\ell\Big(s, {}^H I_{a^+}^{\mu}\mathscr{U}(s), \mathscr{U}(s)\Big)\frac{ds}{s}\\ &\geq \frac{\vartheta(t)}{(\ln\frac{b}{a})^{\flat-\mu}w}\|A\mathscr{U}\|, t \in [a,b].\end{aligned}$$

Consequently, $A(\overline{\mathscr{K}_\jmath \setminus \mathscr{K}_\iota}) \subset \mathscr{K}$. Next, for $\forall\, \iota > 0$, we prove

$$\sup_{\mathscr{U}\in\overline{\mathscr{K}_\jmath\setminus\mathscr{K}_\iota}}\int_a^b \varpi(s)\varrho(s)\ell\Big(s, {}^H I_{a^+}^{\mu}\mathscr{U}(s), \mathscr{U}(s)\Big)\frac{ds}{s} < +\infty, \tag{2.12}$$

that is to say, $A : \overline{\mathscr{K}_\jmath \setminus \mathscr{K}_\iota} \to \mathscr{K}$ is well defined. As a matter of fact, for $\forall \mathscr{U} \in \overline{\mathscr{K}_\jmath \setminus \mathscr{K}_\iota}$, we have

$$\begin{aligned}{}^H I_{a^+}^{\mu}\mathscr{U}(t) =& \frac{1}{\Gamma(\mu)}\int_a^t (\ln t - \ln s)^{\mu-1}\mathscr{U}(s)\frac{ds}{s}\\ \leq& -\frac{1}{\Gamma(\mu)}\|\mathscr{U}\|\int_a^t (\ln t - \ln s)^{\mu-1}d(\ln t - \ln s)\\ =& \frac{1}{\Gamma(\mu+1)}\|\mathscr{U}\|(\ln t - \ln s)^{\mu}|_a^t = \frac{1}{\Gamma(\mu+1)}(\ln\frac{b}{a})^{\mu}\|\mathscr{U}\|\\ \leq& \frac{1}{\Gamma(\mu+1)}(\ln\frac{b}{a})^{\mu}\jmath, t \in [a,b],\end{aligned} \tag{2.13}$$

Then $\|{}^{H}I^{\mu}_{a^+}\mathscr{U}\| \leq \frac{1}{\Gamma(\mu+1)}(\ln\frac{b}{a})^{\mu}\jmath$, hence, by (A_2), there must be a non-negative integer $v_0 > 1$ such that

$$\sup_{\mathscr{U}\in\overline{K}_{\jmath}\setminus K_{\iota}}\int_{e(v_0)} w(s)\varrho(s)\ell(s,{}^{H}I^{\mu}_{a^+}\mathscr{U}(s),\mathscr{U}(s))\frac{ds}{s} < \frac{\Gamma(\flat-\mu)(\ln\frac{b}{a})}{w}. \tag{2.14}$$

where

$$w = 1 + \frac{(\ln\frac{b}{a})^{\flat-\mu-1}}{\Delta}\sum_{j=1}^{\infty}\kappa_j.$$

Choosing

$$\varrho = \min\left\{\frac{1}{(\ln\frac{b}{a})^{\flat-\mu-1}w}, \frac{(\ln a)^{\flat-\mu}(-1)^{\flat-\mu-1}}{\Gamma(\mu)\gamma(\ln\frac{b}{a})^{\flat-\mu}w}, 1\right\},$$

$$\overline{\varrho} = \max\left\{1, \frac{(\ln\frac{b}{a})^{\mu}}{\Gamma(\mu+1)}\right\}.$$

Hence, for $\forall\ \mathscr{U} \in \overline{\mathscr{K}}_{\jmath}\setminus\mathscr{K}_{\iota}$, we get

$$u(t) \leq \|\mathscr{U}\| \leq \jmath \leq \overline{\varrho}\jmath, \tag{2.15}$$

$$\begin{aligned}\mathscr{U}(t) \geq& \frac{\vartheta(t)\|\mathscr{U}\|}{(\ln\frac{b}{a})^{\flat-\mu}w} = \frac{(\ln\frac{t}{a})^{\flat-\mu-1}(\ln\frac{b}{t})\|\mathscr{U}\|}{(\ln\frac{b}{a})^{\flat-\mu}w}\\ \geq& \frac{(\ln t)^{\flat-\mu-1}}{(\ln\frac{b}{a})^{\flat-\mu-1}w}\|\mathscr{U}\| \geq (\ln t)^{\flat-\mu-1}\overline{\varrho}\|\mathscr{U}\|,\end{aligned} \tag{2.16}$$

by (2.13), we have

$${}^{H}I^{\mu}_{a^+}\mathscr{U}(t) \leq \frac{1}{\Gamma(\mu+1)}(\ln\frac{b}{a})^{\mu}\|\mathscr{U}\| \leq \overline{\varrho}\|\mathscr{U}\|, t\in[a,b], \tag{2.17}$$

$$\begin{aligned}{}^{H}I^{\mu}_{a^+}\mathscr{U}(t) =& \frac{1}{\Gamma(\mu)}\int_a^t(\ln t-\ln s)^{\mu-1}\mathscr{U}(s)\frac{ds}{s}\\ \geq& \frac{1}{\Gamma(\mu)}\int_a^t(\ln t-\ln s)^{\mu-1}\frac{(\ln\frac{s}{a})^{\flat-\mu-1}(\ln\frac{b}{s})}{(\ln\frac{b}{a})^{\flat-\mu}w}\|\mathscr{U}\|\frac{ds}{s}\\ =& \frac{\|\mathscr{U}\|}{\Gamma(\mu)(\ln\frac{b}{a})^{\flat-\mu}w}\int_a^t(\ln t-\ln s)^{\mu-1}(\ln s-\ln a)^{\flat-\mu-1}(\ln b-\ln s)d(\ln s),\\ & t\in[a,b].\end{aligned} \tag{2.18}$$

If $\ln s = \Lambda \ln t$, one gets

$$\begin{aligned}
&\frac{\|\mathscr{U}\|}{\Gamma(\mu)(\ln\frac{b}{a})^{\flat-\mu}w}\int_a^t(\ln t-\ln s)^{\mu-1}(\ln s-\ln a)^{\flat-\mu-1}(\ln b-\ln s)d(\ln s)\\
&=\frac{\|\mathscr{U}\|}{\Gamma(\mu)(\ln\frac{b}{a})^{\flat-\mu}w}\int_{\frac{\ln a}{\ln t}}^1(\ln t-\Lambda\ln t)^{\mu-1}(\iota\ln t-\ln a)^{\flat-\mu-1}(\ln b-\iota\ln t)d\tau\\
&=\frac{\|\mathscr{U}\|}{\Gamma(\mu)(\ln\frac{b}{a})^{\flat-\mu}w}(\ln t)^{\mu-1}\int_{\frac{\ln a}{\ln t}}^1(1-\Lambda)^{\mu-1}(\iota\ln t-\ln a)^{\flat-\mu-1}(\ln b-\iota\ln t)d\tau\\
&\geq\frac{\|\mathscr{U}\|}{\Gamma(\mu)(\ln\frac{b}{a})^{\flat-\mu}w}(\ln t)^{\mu-1}\int_0^1(1-\Lambda)^{\mu-1}(\Lambda\ln b-\ln a)^{\flat-\mu-1}(\ln b-\Lambda\ln a)d\tau\\
&\geq\frac{\|\mathscr{U}\|(\ln a)^{\flat-\mu-1}}{\Gamma(\mu)(\ln\frac{b}{a})^{\flat-\mu}w}(\ln t)^{\mu-1}\int_0^1(1-\Lambda)^{\mu-1}(\Lambda-1)^{\flat-\mu-1}\ln a(1-\Lambda)d\tau\\
&=\frac{\|\mathscr{U}\|(\ln a)^{\flat-\mu}}{\Gamma(\mu)(\ln\frac{b}{a})^{\flat-\mu}w}(\ln t)^{\mu-1}\int_0^1(1-\Lambda)^{\mu-1}(\Lambda-1)^{\flat-\mu-1}d\tau\\
&=\frac{\|\mathscr{U}\|(\ln a)^{\flat-\mu}}{\Gamma(\mu)(\ln\frac{b}{a})^{\flat-\mu}w}(\ln t)^{\mu-1}(-1)^{\flat-\mu-1}\int_0^1(1-\Lambda)^{\flat-1}\\
&=\frac{\|\mathscr{U}\|(\ln a)^{\flat-\mu}}{\gamma\Gamma(\mu)(\ln\frac{b}{a})^{\flat-\mu}w}(\ln t)^{\mu-1}(-1)^{\flat-\mu-1}\\
&\geq\|\mathscr{U}\|(\ln t)^{\mu-1}\varrho\geq\|u\|(\ln t)^{\flat-\mu-1}\varrho, t\in[a,b].
\end{aligned}\tag{2.19}$$

Thus, for $\forall\ a+\frac{1}{v_0}\leq t\leq b-\frac{1}{v_0}$, by (2.15)–(2.19), we obtain

$$r\varrho(\ln(a+\frac{1}{v_0}))^{\flat-\mu-1}\leq\mathscr{U}(t),{}^H I^{\mu}_{a^+}\mathscr{U}(t)\leq\overline{\varrho}_J.\tag{2.20}$$

Combing (2.14) and (2.20), we get

$$\begin{aligned}
&\sup_{\mathscr{U}\in\overline{\mathscr{K}}_J\setminus\mathscr{K}_\iota}\int_a^b\frac{w}{\Gamma(\flat-\mu)(\ln\frac{b}{a})}\varpi(s)\varrho(s)\ell\Big(s,{}^H I^{\mu}_{a^+}\mathscr{U}(s),\mathscr{U}(s)\Big)\frac{ds}{s}\\
&\leq\sup_{\mathscr{U}\in\overline{\mathscr{K}}_J\setminus\mathscr{K}_\iota}\int_{e(v_0)}\frac{w}{\Gamma(\flat-\mu)(\ln\frac{b}{a})}\varpi(s)\varrho(s)\ell\Big(s,{}^H I^{\mu}_{a^+}\mathscr{U}(s),\mathscr{U}(s)\Big)\frac{ds}{s}\\
&+\sup_{\mathscr{U}\in\overline{\mathscr{K}}_J\setminus\mathscr{K}_\iota}\int_{a+\frac{1}{v_0}}^{b-\frac{1}{v_0}}\frac{w}{\Gamma(\flat-\mu)(\ln\frac{b}{a})}\varpi(s)\varrho(s)\ell\Big(s,{}^H I^{\mu}_{a^+}\mathscr{U}(s),\mathscr{U}(s)\Big)\frac{ds}{s}\\
&\leq 1+D_1\int_a^b\frac{w}{\Gamma(\flat-\mu)(\ln\frac{b}{a})}\varpi(s)\varrho(s)\frac{ds}{s}<+\infty,
\end{aligned}\tag{2.21}$$

where

$$w=1+\frac{(\ln\frac{b}{a})^{\flat-\mu-1}}{\Delta}\sum_{j=1}^{\infty}\kappa_j,$$

$$D_1=\max\left\{\ell(t,\varsigma_1,\varsigma_2):(t,\varsigma_1,\varsigma_2)\in\left(\frac{1}{v_0},1-\frac{1}{v_0}\right)\times\left(\iota\varrho(\ln(a+\frac{1}{v_0}))^{\flat-\mu-1},\overline{\varrho}_J\right)^2\right\}.$$

Thus, (2.12) is valid and indicating that A has the uniformly bounded property on any bounded set.

For $\forall\ \epsilon>0$, by (A_2), there must be a non-negative integer $v_0>1$ that makes

$$\sup_{x_1\in\overline{\mathscr{K}}_{\overline{J}}\setminus\mathscr{K}_\iota,x_2\in\overline{\mathscr{K}}_J\setminus\mathscr{K}_\iota}\int_{e(v_0)}w(s)\varrho(s)\ell(s,x_1(s),x_2(s))\frac{ds}{s}<\frac{\varepsilon\Gamma(\flat-\mu)(\ln\frac{b}{a})}{4w}.\tag{2.22}$$

Then, we show that A is continuous from $\overline{\mathscr{K}_J} \setminus \mathscr{K}_\iota$ to $\mathscr{K}$. Let $\mathscr{U}_k, \mathscr{U}_0 \in \overline{\mathscr{K}_J} \setminus \mathscr{K}_\iota$ and $\|\mathscr{U}_k - \mathscr{U}_0\| \to 0$ $(k \to \infty)$. On account of $\ell(t, x_1, x_2)$ has uniformly continuous property on

$$\left(a + \frac{1}{v_0}, b - \frac{1}{v_0}\right) \times \left(r\varrho(\ln(a + \frac{1}{v_0}))^{\flat-\mu-1}, \overline{\varrho}R\right)^2,$$

we have

$$\lim_{k\to+\infty} \left|\ell\Big(s, {}^H I^{\mu}_{a^+} \mathscr{U}_k(s), \mathscr{U}_k(s)\Big) - \ell\Big(s, {}^H I^{\mu}_{a^+} \mathscr{U}_0(s), \mathscr{U}_0(s)\Big)\right| = 0$$

Uniformly holds for $t \in \left[a + \frac{1}{v_0}, b - \frac{1}{v_0}\right]$. Then, by Lebesgue control convergence theorem and (A_2), we have

$$\int_{a+\frac{1}{v_0}}^{b-\frac{1}{v_0}} w(s)\varrho(s)\left|\ell\Big(s, {}^H I^{\mu}_{a^+} \mathscr{U}_k(s), \mathscr{U}_k(s)\Big) - \ell\Big(s, {}^H I^{\mu}_{a^+} \mathscr{U}_0(s), \mathscr{U}_0(s)\Big)\right|\frac{ds}{s} \to 0, \text{ as } k \to \infty.$$

Thus, for the ϵ shown as in (2.18), there is a natural number N, for $k > N$, that makes

$$\begin{aligned} &\int_{a+\frac{1}{v_0}}^{b-\frac{1}{v_0}} w(s)\varrho(s)\left|\ell\Big(s, {}^H I^{\mu}_{a^+} \mathscr{U}_k(s), \mathscr{U}_k(s)\Big) - \ell\Big(s, {}^H I^{\mu}_{a^+} \mathscr{U}_0(s), \mathscr{U}_0(s)\Big)\right|\frac{ds}{s} \\ &< \frac{\varepsilon\Gamma(\flat-\mu)(\ln\frac{b}{a})}{2w}. \end{aligned} \tag{2.23}$$

For $k > N$, by (2.22) and (2.23), one has

$$\begin{aligned} &\|A\mathscr{U}_k - A\mathscr{U}_0\| \\ \leq &\sup_{\mathscr{U}_k\in\overline{\mathscr{K}_J}\setminus\mathscr{K}_\iota} \int_{e(v_0)} \frac{w}{\Gamma(\flat-\mu)(\ln\frac{b}{a})}\varpi(s)\varrho(s)\ell\Big(s, {}^H I^{\mu}_{a^+} \mathscr{U}_k(s), \mathscr{U}_k(s)\Big)\frac{ds}{s} \\ &+ \sup_{\mathscr{U}_k\in\overline{\mathscr{K}_J}\setminus\mathscr{K}_\iota} \int_{e(v_0)} \frac{w}{\Gamma(\flat-\mu)(\ln\frac{b}{a})}\varpi(s)\varrho(s)\ell\Big(s, {}^H I^{\mu}_{a^+} \mathscr{U}_k(s), \mathscr{U}_k(s)\Big)\frac{ds}{s} \\ &+ \int_{a+\frac{1}{v_0}}^{b-\frac{1}{v_0}} \frac{w}{\Gamma(\flat-\mu)(\ln\frac{b}{a})} w(s)\varrho(s)\left|\ell\Big(s, {}^H I^{\mu}_{a^+} \mathscr{U}_k(s), \mathscr{U}_k(s)\Big)\frac{ds}{s}\right. \\ &\left. - \ell\Big(s, {}^H I^{\mu}_{a^+} \mathscr{U}_0(s), \mathscr{U}_0(s)\Big)\frac{ds}{s}\right|\frac{ds}{s} \\ <&2(\frac{w}{\Gamma(\flat-\mu)(\ln\frac{b}{a})}) \times \frac{\varepsilon}{4(\frac{w}{\Gamma(\flat-\mu)(\ln\frac{b}{a})})} + (\frac{w}{\Gamma(\flat-\mu)(\ln\frac{b}{a})})\frac{\varepsilon}{2(\frac{w}{\Gamma(\flat-\mu)(\ln\frac{b}{a})})} = \varepsilon. \end{aligned}$$

Thus, A is continuous from $\overline{\mathscr{K}_J} \setminus \mathscr{K}_\iota$ to K.

For $\forall$ bounded set Ω and $\Omega \subset \overline{\mathscr{K}_J} \setminus \mathscr{K}_\iota$, we show that $A(\Omega)$ is equicontinuous. As a matter of fact, by (A_2), for $\forall\, \epsilon > 0$, there is a natural number $\kappa_0 > 1$ so that

$$\sup_{x_2\in\overline{\mathscr{K}_J}\setminus\mathscr{K}_\iota} \int_{e(\kappa_0)} w(s)\varrho(s)\ell(s, x_1(s), x_2(s))\frac{ds}{s} < \frac{\varepsilon}{4\left(\frac{w}{\Gamma(\flat-\mu)(\ln\frac{b}{a})}\right)}.$$

Taking

$$D_2 = \max\left\{\ell(t, x_1, x_2) : (t, x_1, x_2) \in \left(a + \frac{1}{\kappa_0}, b - \frac{1}{\kappa_0}\right) \times \left(r\varrho(\ln(a + \frac{1}{n_0}))^{\flat-\mu-1}, \overline{\varrho}_J\right)^2\right\}.$$

On account of $\mathscr{H}(t,s)$ is uniformly continuous on $[a,b]\times[a,b]$, for the ϵ which is defined by above, there is $\delta>0$, for $\forall\, s\in[a+\frac{1}{\kappa_0},b-\frac{1}{\kappa_0}]$, we have

$$|\mathscr{H}(t,s)-\mathscr{H}(t',s)|\leq\frac{\varepsilon}{2}\left(D_2\int_{a+\frac{1}{\kappa_0}}^{b-\frac{1}{\kappa_0}}\varrho(s)\frac{ds}{s}\right)^{-1},$$

for $|t-t'|<\delta, t,t'\in[a,b]$. Thus, for $\forall\ |t-t'|<\delta, t,t'\in[a,b]$ and $\mathscr{U}\in\Omega$, we obtain

$$\begin{aligned}
&\|A\mathscr{U}(t)-A\mathscr{U}(t')\|\\
&\leq 2\sup_{\mathscr{U}\in\overline{\mathscr{K}}_J\setminus\mathscr{K}_\iota}\left(\frac{w}{\Gamma(\flat-\mu)(\ln\frac{b}{a})}\right)\int_{e(\kappa_0)}w(s)\varrho(s)\ell\Big(s,{}^H I^{\mu}_{a^+}\mathscr{U}(s),\mathscr{U}(s)\Big)\frac{ds}{s}\\
&+\sup_{\mathscr{U}\in\overline{\mathscr{K}}_J\setminus\mathscr{K}_\iota}\int_{a+\frac{1}{\kappa_0}}^{b-\frac{1}{\kappa_0}}|\mathscr{H}(t,s)-\mathscr{H}(t',s)|\varrho(s)\ell\Big(s,{}^H I^{\mu}_{a^+}\mathscr{U}(s),\mathscr{U}(s)\Big)\frac{ds}{s}\\
&<2\left(\frac{w}{\Gamma(\flat-\mu)(\ln\frac{b}{a})}\right)\times\frac{\varepsilon}{4(\frac{w}{\Gamma(\flat-\mu)(\ln\frac{b}{a})})}+\frac{\varepsilon}{2}=\varepsilon,
\end{aligned}$$

which demonstrates that $A(\Omega)$ is equicontinuous. By the Arzela-Ascoli theorem, A is fully continuous from $\overline{\mathscr{K}}_J\setminus\mathscr{K}_\iota$ to $\mathscr{K}$, then the verification is finished. □

3. Principal Results

In this section, the main results will be provided according to these preliminaries and the following lemmas.

Lemma 8 ([27]). *Suppose $\mathscr{K}$ is a cone within Banach space $\mathscr{E}$. Let $A:\overline{\mathscr{K}}_r\to\mathscr{K}$ is a fully continuous operator. In case of $\mathscr{U}_0\in\mathscr{K}\setminus\{\theta\}$ so that $\mathscr{U}-A\mathscr{U}\neq\mu\mathscr{U}_0$ for an arbitrary $\mathscr{U}\in\partial\mathscr{K}_r$ and $\mu\geq 0$, thus $i(A,\mathscr{K}_r,\mathscr{K})=0$.*

Lemma 9 ([27]). *Suppose $\mathscr{K}$ is a cone within Banach space E. Let $A:\overline{\mathscr{K}}_r\to\mathscr{K}$ is a fully continuous operator. In case of $Au\neq\mu\mathscr{U}$ for an arbitrary $\mathscr{U}\in\partial\mathscr{K}_r$ and $\mu\geq 1$, thus $i(A,\mathscr{K}_r,\mathscr{K})=1$.*

Theorem 1. *Suppose the conditions $(A_1$–$A_2)$ are established, and*

$$\liminf_{\substack{x_i\to 0^+\\ i=1,2}}\min_{t\in[a,b]}\frac{\ell(t,x_1,x_2)}{x_1+x_2}>\lambda_1, \tag{3.1}$$

$$\limsup_{x_2\to+\infty}\max_{t\in[a,b]}\frac{\ell(t,x_1,x_2)}{x_2}<\lambda_1 \tag{3.2}$$

Hold uniformly for $x_i\in[0,+\infty)$ $(i=1,2)$, and λ_1 is the first eigenvalue of $\mathscr{T}$ which is defined by (2.9), then there's at least one positive solution of the BVP (1.1,1.2).

Proof. By (3.1), there exists $\iota>0$, that makes

$$\ell(t,x_1,x_2)\geq\lambda_1(x_1+x_2), 0<x_i\leq\iota, i=1,2,\ t\in[a,b]. \tag{3.3}$$

Choosing $\iota_0=\min\{\iota,\frac{\iota}{\overline{\varrho}}\}$ and for $\forall\ \mathscr{U}\in\partial\mathscr{K}_{\iota_0}$, one has

$$0<{}^H I^{\mu}_{a^+}\mathscr{U}(s)\leq\overline{\varrho}\iota_0\leq\iota, 0<\mathscr{U}(s)\leq\iota,\ s\in[a,b]. \tag{3.4}$$

Accordingly, one can arrive at according to (3.3) and (3.4)

$$\begin{aligned}(A\mathscr{U})(t) &= \int_a^b \mathscr{H}(t,s)\varrho(s)\ell(s,{}^H I^{\mu}_{a^+}\mathscr{U}(s),\mathscr{U}(s))\frac{ds}{s}\\ &\geq \lambda_1\int_a^b \mathscr{H}(t,s)\varrho(s)\Big({}^H I^{\mu}_{a^+}\mathscr{U}(s)+\mathscr{U}(s)\Big)\frac{ds}{s}\\ &\geq \lambda_1(\mathscr{T}\mathscr{U})(t), t\in[a,b].\end{aligned} \tag{3.5}$$

By Lemma 6, $\mathscr{T}$ has a positive eigenfunction ζ in regard to λ_1, i.e., $\zeta = \lambda_1\mathscr{T}\zeta$. Then we will show

$$\mathscr{U} - A\mathscr{U} \neq d\zeta,\ \mathscr{U}\in\partial\mathscr{K}_{\iota_0},\ d\geq 0. \tag{3.6}$$

Otherwise, there is $\mathscr{U}_0\in\partial\mathscr{K}_{\iota_0}$ and $d_0\geq 0$ that makes $\mathscr{U}_0 - A\mathscr{U}_0 = d_0\zeta$, then $d_0 > 0$ and $\mathscr{U}_0 = A\mathscr{U}_0 + d_0\zeta \geq d_0\zeta$. Assume $\overline{d} = \sup\{d|\mathscr{U}_0\geq d\zeta\}$, then $\overline{d}\geq d_0, \mathscr{U}_0\geq\overline{d}\zeta, \lambda_1\mathscr{T}\mathscr{U}_0\geq\lambda_1\overline{d}\mathscr{T}\zeta = \overline{d}\zeta$. Thus, from (3.5), we get

$$\mathscr{U}_0 = A\mathscr{U}_0 + d_0\zeta \geq \lambda_1\mathscr{T}\mathscr{U}_0 + d_0\zeta \geq \overline{d}\zeta + d_0\zeta = (\overline{d}+d_0)\zeta,$$

which is a contradiction with the definition of $\overline{d}$. So (3.6) holds and combing Lemma 8, we have

$$i(A,\mathscr{K}_{\iota_0},\mathscr{K}) = 0. \tag{3.7}$$

Now taking a constant $0<\sigma<1$ makes

$$\limsup_{x_2\to+\infty}\max_{t\in[a,b]}\frac{\ell(t,x_1,x_2)}{x_2} < \omega\lambda_1, \tag{3.8}$$

and a linear operator $\widetilde{\mathscr{T}}\mathscr{U} = \omega\lambda_1\mathscr{T}\mathscr{U}$ is defined, then subsequently $\widetilde{\mathscr{T}}$ is a bounded linear operator from $\mathscr{E}$ to $\mathscr{E}$, and $\widetilde{\mathscr{T}}(\mathscr{K})\subset\mathscr{K}$. Additionally, $\widetilde{\mathscr{T}}\zeta = \omega\lambda_1\mathscr{T}\zeta = \omega\zeta$, and so the spectral radius of $\widetilde{\mathscr{T}}$ is $r(\widetilde{\mathscr{T}}) = \omega$ and $\widetilde{\mathscr{T}}$ also has the first eigenvalue $r^{-1}(\widetilde{\mathscr{T}}) = \omega^{-1} > 1$. Adopting Gelfand's formula, one can obtain

$$\omega = \lim_{n\to+\infty}\|\widetilde{\mathscr{T}}^n\|^{\frac{1}{n}}. \tag{3.9}$$

Let $\varepsilon_0 = \frac{1}{2}(1-\omega)$ and by (3.9), there is a large enough natural number N_0, and when $n\geq N$, we have $\|\widetilde{\mathscr{T}}^n\|\leq[\omega+\epsilon_0]^n$. For $\forall\ \mathscr{U}\in\mathscr{E}$, we define

$$\|\mathscr{U}\|^{\star} = \sum_{i=1}^{N}[\omega+\epsilon_0]^{N-i}\|\widetilde{\mathscr{T}}^{i-1}\mathscr{U}\|, \tag{3.10}$$

where $\widetilde{\mathscr{T}}^0 = I$ is the unit operator. Apparently, $\|.\|^{\star}$ is another norm of $\mathscr{E}$.

In addition, according to (3.2), there is $\jmath_1 > \iota$, we have

$$\ell(t,x_1,x_2)\leq\omega\lambda_1 x_2,\ \text{for } x_2\geq\jmath_1, x_i\geq 0,\ i=1,2,\ t\in[a,b]. \tag{3.11}$$

Choosing

$$\jmath > \max\left\{\jmath_1, \frac{2(\omega+\varepsilon_0^{N-1})^{-1}}{\varepsilon_0}C^{\star}\right\},$$

where $C^{\star} = \|C\|^{\star}$ and

$$\begin{aligned}C &= \sup_{\mathscr{U}\in\mathscr{K}_{\jmath_1}}\int_a^b\frac{w}{\Gamma(\flat-\mu)(\ln\frac{b}{a})}\varpi(s)\varrho(s)\ell(s,{}^H I^{\mu}_{a^+}\mathscr{U}(s),\mathscr{U}(s))\frac{ds}{s}\\ &< +\infty\ (\text{by } (2.11)).\end{aligned} \tag{3.12}$$

Then we prove that

$$A\mathscr{U}\neq\mu\mathscr{U}, \mathscr{U}\in\partial\mathscr{K}_{\jmath},\ \mu\geq 1. \tag{3.13}$$

If not, then there is $\mathscr{U}_1 \in \partial\mathscr{K}_\jmath$ and $d_1 \geq 1$ that makes $A\mathscr{U}_1 = d_1\mathscr{U}_1$. Assume $\widetilde{\mathscr{U}}(t) = \min\{\mathscr{U}_1(t), \jmath_1\}$ and $D(\mathscr{U}_1) = \{t \in [a,b] : \mathscr{U}_1(t) > \jmath_1\}$. Assume

$$\xi(t) = \frac{\Gamma(\flat - \mu)(\ln\frac{b}{a})}{w}\vartheta(t).$$

According to $\widetilde{\mathscr{U}} \in C([a,b],[0,+\infty))$, $\xi(t)\jmath \leq \mathscr{U}_1(t) \leq \|\mathscr{U}_1\| = \jmath$ and $A\mathscr{U}_1 = \mu_1\mathscr{U}_1$, we have $\mathscr{U}_1$ meets boundary conditions, Thus, we get $u_1(0) = 0$, hence, there is $0 < t_0 \leq 1$ that makes $u_1(t_0) = R$. Hence, $\widetilde{\mathscr{U}}(t) = \min\{\mathscr{U}_1(t), \jmath_1\} \leq \min\{\jmath, \jmath_1\} = \jmath_1$ for $t \in [a,b]$, and $\widetilde{\mathscr{U}}(t_0) = \min\{\mathscr{U}_1(t_0), \jmath_1\} = \min\{\jmath, \jmath_1\} = \jmath_1$, then we get $\|\widetilde{\mathscr{U}}\| = \jmath_1$. Because

$$\widetilde{\mathscr{U}}(t) = \min\{\mathscr{U}_1(t), \jmath_1\} \geq \min\{\xi(t)\jmath, \jmath_1\} \geq \jmath_1\xi(t),\ t \in [a,b],$$

Thus, $\widetilde{u} \in \partial\mathscr{K}_{\jmath_1}$. For $t \in D(\mathscr{U}_1)$, $\mathscr{U}_1(t) \geq \jmath_1$, ${}^H I^{\mu}_{a^+}\mathscr{U}_1(t) \geq 0$, by (3.11) and Lemma 2, one gets

$$\begin{aligned}
(A\mathscr{U}_1)(t) &= \int_a^b \mathscr{H}(t,s)\varrho(s)\ell\Big(s, {}^H I^{\mu}_{a^+}\mathscr{U}_1(s), \mathscr{U}_1(s)\Big)\frac{ds}{s} \\
&\leq \int_{D(\mathscr{U}_1)} \mathscr{H}(t,s)\varrho(s)\ell\Big(s, {}^H I^{\mu}_{a^+}\mathscr{U}_1(s), \mathscr{U}_1(s)\Big)\frac{ds}{s} \\
&+ \int_{[a,b]\setminus D(u_1)} \mathscr{H}(t,s)\varrho(s)\ell\Big(s, {}^H I^{\mu}_{a^+}\mathscr{U}_1(s), \mathscr{U}_1(s)\Big)\frac{ds}{s} \\
&\leq \sigma\lambda_1 \int_a^b \mathscr{H}(t,s)\varrho(s)\mathscr{U}_1(s)\frac{ds}{s} \\
&+ \int_a^b \frac{w}{\Gamma(\flat - \mu)(\ln\frac{b}{a})}\varpi(s)\varrho(s)\ell\Big(s, {}^H I^{\mu}_{a^+}\widetilde{\mathscr{U}}(s), \widetilde{\mathscr{U}}(s)\Big)\frac{ds}{s} \\
&\leq (\widetilde{\mathscr{T}}\mathscr{U}_1)(t) + C,\ t \in [a,b].
\end{aligned} \tag{3.14}$$

It is noted that $\widetilde{\mathscr{T}}$ is a bounded linear operator and from $\mathscr{K}$ to $\mathscr{K}$, from (3.14) one arrives

$$0 \leq (\widetilde{\mathscr{T}}^j(A\mathscr{U}_1))(t) \leq (\widetilde{\mathscr{T}}^j(\widetilde{\mathscr{T}}\mathscr{U}_1 + C))(t),\ j = 0,1,2,\cdots,n-1,\ t \in [a,b]. \tag{3.15}$$

Then, by (3.15), we have

$$\|(\widetilde{\mathscr{T}}^j(A\mathscr{U}_1))\| \leq \|(\widetilde{\mathscr{T}}^j(\widetilde{\mathscr{T}}\mathscr{U}_1 + C))\|,\ j = 0,1,2,\cdots,n-1,$$

that gives rise to

$$\begin{aligned}
\|A\mathscr{U}_1\|^\star &= \sum_{i=1}^{n}[\omega + \varepsilon_0]^{n-i}\|\widetilde{\mathscr{T}}^{i-1}(A\mathscr{U}_1)\| \\
&\leq \sum_{i=1}^{n}[\omega + \varepsilon_0]^{n-i}\|\widetilde{\mathscr{T}}^{i-1}(\widetilde{\mathscr{T}}\mathscr{U}_1 + C)\| = \|\widetilde{\mathscr{T}}\mathscr{U}_1 + C\|^\star.
\end{aligned} \tag{3.16}$$

By $\mathscr{U}_1 \in \partial\mathscr{K}_\jmath$, $\|\mathscr{U}_1\| = \jmath$, and (3.10), the following formula can be developed

$$\|\mathscr{U}_1\|^\star > [\omega + \varepsilon_0]^{n-1}\|\mathscr{U}_1\| = [\omega + \varepsilon_0]^{n-1}R > \frac{2}{\varepsilon_0}C^\star,$$

which results in

$$C^\star < \frac{\epsilon_0}{2}\|\mathscr{U}_1\|^\star. \tag{3.17}$$

According to (3.10), (3.16) and (3.17), one obtains

$$\begin{aligned}
\mu_1\|\mathscr{U}_1\|^\star = \|A\mathscr{U}_1\|^\star &\le \|\widetilde{\mathscr{T}}\mathscr{U}_1\|^\star + C^\star = \sum_{i=1}^{n}[\sigma+\epsilon_0]^{n-i}\|\widetilde{\mathscr{T}}^i\mathscr{U}_1\| + C^\star \\
&= [\sigma+\varepsilon_0]\sum_{i=1}^{n-1}[\sigma+\varepsilon_0]^{n-i-1}\|\widetilde{\mathscr{T}}^i\mathscr{U}_1\| + \|\widetilde{\mathscr{T}}^N\mathscr{U}_1\| + C^\star \\
&\le [\sigma+\varepsilon_0]\sum_{i=1}^{N-1}[\sigma+\varepsilon_0]^{n-i-1}\|\widetilde{\mathscr{T}}^i\mathscr{U}_1\| + [\sigma+\epsilon_0]^N\|\mathscr{U}_1\| + C^\star \\
&= [\sigma+\varepsilon_0]\sum_{i=1}^{N}[\sigma+\varepsilon_0]^{n-i}\|\widetilde{\mathscr{T}}^{i-1}\mathscr{U}_1\| + C^\star \\
&= [\sigma+\varepsilon_0]\|u_1\|^\star + C^\star \le [\sigma+\varepsilon_0]\|\mathscr{U}_1\|^\star + \frac{\varepsilon_0}{2}\|\mathscr{U}_1\|^\star \\
&= \left[\frac{1}{4}\sigma+\frac{3}{4}\right]\|\mathscr{U}_1\|^\star.
\end{aligned}$$

Taking care of $d_1 \ge 1$, we have $\frac{1}{4}\omega + \frac{3}{4} \ge 1$, and thus $\omega \ge 1$, which contradict with $0 < \omega < 1$. Thus (3.13) is right, and by Lemma 9 , we have

$$i(A, \mathscr{K}_J, \mathscr{K}) = 1. \tag{3.18}$$

Combing (3.7) with (3.18), we have

$$i(A, \mathscr{K}_J \setminus \overline{\mathscr{K}}_{\iota_0}, J) = i(A, \mathscr{K}_J, \mathscr{K}) - i(A, \mathscr{K}_{\iota_0}, \mathscr{K}) = 1.$$

Hence, A has at least one fixed point in $K_R\backslash\overline{K}_{r_0}$, that is to say, the BVP (2.1, 2.2) has at least one positive solution, which implies that BVP (1.1, 1.2) also has at least one positive solution. Another case for Equations (1.1) and (1.2) will be discussed herein. For this purpose, for $\forall$ small enough $0 < \varepsilon < 1$, we define a linear operator $\mathscr{T}_\varepsilon$

$$(\mathscr{T}_\varepsilon\mathscr{U})(t) = \int_{a+\varepsilon}^{b-\varepsilon}\mathscr{H}(t,s)\varrho(s)\mathscr{U}(s)\frac{ds}{s},\ t \in [a,b].$$

According to Lemma 7, we have$\mathscr{T}_\varepsilon$ form $\mathscr{K}$ to $\mathscr{K}$ denotes a linear operator with complete continuity, too, and the spentral radius $r(\mathscr{T}_\varepsilon)$ of $\mathscr{T}_\varepsilon)$ unequal to 0, and furthermore, $\mathscr{T}_\varepsilon$ has a positive eigenfunction ζ_ε in regard to its first eigenvalue $\lambda_\varepsilon = (r(\mathscr{T}_\varepsilon))^{-1}$. □

Lemma 10. *Assume that (A_1) holds, then $\mathscr{T}$ has an eigenvalue $\widetilde{\lambda}_1$ that makes*

$$\lim_{\varepsilon\to 0^+}\lambda_\varepsilon = \widetilde{\lambda}_1.$$

Proof. Choose $\ldots \le \varepsilon_n \le \ldots \le \varepsilon_2 \le \varepsilon_1$ and ε_n tend to 0 as $n \to +\infty$. Then for $\forall\ n < m$ and $\zeta \in \mathscr{E}$, we get

$$(\mathscr{T}_{\varepsilon_n}\zeta)(t) \le (\mathscr{T}_{\varepsilon_m}\zeta)(t) \le (\mathscr{T}\zeta)(t),\ t \in [a,b],$$

and

$$(\mathscr{T}^k_{\varepsilon_n}\zeta)(t) \le (\mathscr{T}^k_{\varepsilon_m}\zeta)(t) \le (\mathscr{T}^k\zeta)(t),\ t \in [a,b],\ k = 2,3,\cdots,$$

where $\mathscr{T}^k_{\varepsilon_n} = \mathscr{T}(\mathscr{T}^{k-1}_{\varepsilon_n})$ $(k = 2,3,\cdots)$. Thus, $\|\mathscr{T}^k_{\varepsilon_n}\| \le \|\mathscr{T}^k_{\varepsilon_m}\| \le \|\mathscr{T}^k\|$ $(k = 1,2,\cdots)$. By Gelfand's formula, we obtain $\lambda_1 \le \lambda_{\varepsilon_m} \le \lambda_{\varepsilon_n}$, and λ_1 is the first eigenvalue of $\mathscr{T}$. According to $\{\lambda_{\varepsilon_n}\}$ monotonous property with lower boundedness λ_1, assume

$$\lambda_{\varepsilon_n} \to \widetilde{\lambda}_1 (n \to +\infty).$$

Now we prove that $\widetilde{\lambda}_1$ is one of eigenvalue of $\mathscr{T}$. Assume ζ_{ε_n} is one of positive eigenfunction of $\mathscr{T}_{\varepsilon_n}$ in regard to λ_{ε_n} with $\|\zeta_{\varepsilon_n}\| = 1$ $(n = 1, 2, \cdots)$, that is,

$$\varphi_{\varepsilon_n}(t) = \lambda_{\varepsilon_n} \int_{a+\varepsilon_n}^{b-\varepsilon_n} \mathscr{H}(t,s)\varrho(s)\zeta_{\varepsilon_n}(s)\frac{ds}{s} = \lambda_{\varepsilon_n}\mathscr{T}_{\varepsilon_n}\zeta_{\varepsilon_n}(t),\ t \in [a,b]. \tag{3.19}$$

Take notice that

$$\|\mathscr{T}_{\varepsilon_n}\zeta_{\varepsilon_n}\| = \max_{a\le t\le b}\int_{a+\varepsilon_n}^{b-\varepsilon_n} \mathscr{H}(t,s)\varrho(s)\zeta_{\varepsilon_n}(s)\frac{ds}{s} \le \int_a^b \frac{w}{\Gamma(\flat-\mu)(\ln\frac{b}{a})}\varpi(s)\varrho(s)\frac{ds}{s},\ n = 1, 2, \cdots,$$

and hence $\{\mathscr{T}_{\varepsilon_n}\zeta_{\varepsilon_n}\} \subset \mathscr{E}$ is uniform boundedness. In addition, for $\forall\, n \in \mathbb{N}$ and $t_1, t_2 \in [a,b]$, one arrives

$$|\mathscr{T}_{\varepsilon_n}\zeta_{\varepsilon_n}(t_1) - \mathscr{T}_{\varepsilon_n}\zeta_{\varepsilon_n}(t_2)| \le \int_{a+\varepsilon_n}^{b-\varepsilon_n} |\mathscr{H}(t_1,s) - \mathscr{H}(t_2,s)|\varrho(s)\zeta_{\varepsilon_n}(s)\frac{ds}{s}.$$

Since $\mathscr{H}(t,s)$ has uniform continuity property on $[a,b]\times[a,b]$, we have $\{\mathscr{T}_{\varepsilon_n}\zeta_{\varepsilon_n}\} \subset \mathscr{E}$ is equicontinuous. Combing the Arzela-Ascoli theorem, Lemma 3.3 and $\lambda_{\varepsilon_n} \to \widetilde{\lambda}_1 (n \to +\infty)$, we have $\zeta_{\varepsilon_n} \to \zeta_0$ ($n \to +\infty$). This implies $\|\zeta_0\| = 1$, then by using (3.19), we get

$$\zeta_0(t) = \widetilde{\lambda}_1 \int_a^b \mathscr{H}(t,s)\varrho(s)\zeta_0(s)\frac{ds}{s},\ t \in [a,b],$$

in short, $\zeta_0 = \widetilde{\lambda}_1\mathscr{T}\zeta_0$. □

Theorem 2. *Suppose* $(A_1$-$A_2)$ *hold, and*

$$\limsup_{\substack{x_i\to 0^+\\ i=1,2}} \max_{t\in[a,b]} \frac{\ell(t,x_1,x_2)}{x_2} < \lambda_1, \tag{3.20}$$

$$\liminf_{x_1+x_2\to+\infty} \min_{t\in[a,b]} \frac{\ell(t,x_1,x_2)}{x_1+x_2} > \widetilde{\lambda}_1, \tag{3.21}$$

where λ_1 *represents the first appeared eigenvalue of* $\mathscr{T}$ *and* $\widetilde{\lambda}_1$ *is another eigenvalue of* $\mathscr{T}$*, then the BVP (1.1,1.2) has at least one positive solution.*

Proof. First of all, from (3.20), for $\forall\, t \in [a,b]$, there is $\iota_0 > 0$ such that

$$\ell(t,x_1,x_2) \le \lambda_1 x_2, 0 < x_1 \le \frac{(\ln b - \ln a)^\mu}{\Gamma(\mu+1)}\iota_0, 0 < x_2 \le \iota_0,\ t \in [a,b]. \tag{3.22}$$

Hence, for any $\mathscr{U} \in \partial K_{\iota_0}$, noticing ${}^H I_{a^+}^\mu \mathscr{U}(s) \le \frac{(\ln b-\ln a)^\mu}{\Gamma(\mu+1)}\iota_0$, $|\mathscr{U}(s)| \le \|\mathscr{U}\| = \iota_0$. By (3.22), we get

$$\begin{aligned}(A\mathscr{U})(t) &= \int_a^b \mathscr{H}(t,s)\varrho(s)\ell(s, {}^H I_{a^+}^\mu \mathscr{U}(s), \mathscr{U}(s))\frac{ds}{s}\\ &\le \lambda_1 \int_a^b \mathscr{H}(t,s)\varrho(s)\mathscr{U}(s)\frac{ds}{s}\\ &= \lambda_1(\mathscr{T}\mathscr{U})(t),\ t \in [a,b].\end{aligned} \tag{3.23}$$

As a matter of fact, we assume there are no fixed points for on A on $\partial\mathscr{K}_{\iota_0}$. It is necessary to prove

$$A\mathscr{U} \ne d\mathscr{U},\ \text{for any } \mathscr{U} \in \partial\mathscr{K}_{\iota_0},\ d \ge 1. \tag{3.24}$$

If not, there is $\mathscr{U}_0 \in \partial\mathscr{K}_{\iota_0}$ and $d_0 \ge 1$ such that $A\mathscr{U}_0 = d_0\mathscr{U}_0$. Then $d_0 > 1$ and from (3.23), we obtain

$$d_0\mathscr{U}_0 = A\mathscr{U}_0 \le \lambda_1\mathscr{T}\mathscr{U}_0. \tag{3.25}$$

According to induction from (3.25), we achieve

$$d_0^n \mathscr{U}_0 \leq \lambda_1^n \mathscr{T}^n \mathscr{U}_0,\ n = 1, 2, \cdots,$$

we easily get

$$\|\mathscr{T}^n\| \geq \frac{\|\mathscr{T}^n \mathscr{U}_0\|}{\|\mathscr{U}_0\|} \geq \frac{\mu_0^n \|\mathscr{U}_0\|}{\lambda_1^n \|\mathscr{U}_0\|} = \frac{\mu_0^n}{\lambda_1^n}.$$

Additionally, one derives the following result through the Gelfand formula

$$r(\mathscr{T}) = \lim_{n\to\infty} \sqrt[n]{\|\mathscr{T}^n\|} \geq \frac{\mu_0}{\lambda_1} > \frac{1}{\lambda_1},$$

but it contradict with $r(\mathscr{T}) = \lambda_1^{-1}$. So (3.23) holds. Applying Lemma 3.2, one demonstrates

$$i(A, \mathscr{K}_{\iota_0}, \mathscr{K}) = 1. \tag{3.26}$$

According to (3.21) and $\lambda_\varepsilon \to \widetilde{\lambda}_1 (\varepsilon \to 0^+)$, it exists a sufficiently tiny $\varepsilon \in (0, \frac{1}{2})$ and $\jmath > \iota$, we have

$$\ell(t, x_1, x_2) \geq \lambda_\varepsilon (x_1 + x_2) \geq \rho_\varepsilon \jmath,\ t \in [a, b], \tag{3.27}$$

where λ_ε represents the first appeared eigenvalue $\mathscr{T}_\varepsilon$, $\rho_\varepsilon = 2(\ln(a+\varepsilon))^{\flat-\mu-1}$. Assume ζ_ε be the positive eigenfunction of $\mathscr{T}_\varepsilon$ with respect to λ_ε, then $\zeta_\varepsilon = \lambda_\varepsilon \mathscr{T}_\varepsilon \zeta_\varepsilon$.

For an any $\mathscr{U} \in \partial\mathscr{K}_\jmath$, $s \in [a+\varepsilon, b-\varepsilon]$, by (2.13)–(2.15), we achieve

$$\begin{aligned} {}^H I_{a^+}^{\mu} \mathscr{U}(s) + \mathscr{U}(s) =& \frac{1}{\Gamma(\mu)} \int_a^t (\ln t - \ln s)^{\mu-1} \mathscr{U}(s) \frac{ds}{s} + \mathscr{U}(s) \\ &\geq \|\mathscr{U}\| (\ln t)^{\flat-\mu-1} \varrho + \|\mathscr{U}\| (\ln t)^{\flat-\mu-1} \varrho \\ &\geq 2\|\mathscr{U}\| \varrho (\ln(a+\varepsilon))^{\flat-\mu-1} = \rho_\varepsilon \jmath. \end{aligned} \tag{3.28}$$

Combing (3.27) with (3.28) , one has

$$\begin{aligned} (A\mathscr{U})(t) &= \int_a^b \mathscr{H}(t,s) \varrho(s) \ell(s, {}^H I_{a^+}^{\mu} \mathscr{U}(s), \mathscr{U}(s)) \frac{ds}{s} \\ &\geq \int_{a+\varepsilon}^{b-\varepsilon} \mathscr{H}(t,s) \varrho(s) \ell(s, {}^H I_{a^+}^{\mu} \mathscr{U}(s), \mathscr{U}(s)) \frac{ds}{s} \\ &\geq \lambda_\varepsilon \int_{a+\varepsilon}^{b-\varepsilon} \mathscr{H}(t,s) \varrho(s) \left({}^H I_{a^+}^{\mu} \mathscr{U}(s) + \mathscr{U}(s) \right) \frac{ds}{s} \\ &\geq \lambda_\varepsilon \int_{a+\varepsilon}^{b-\varepsilon} \mathscr{H}(t,s) \varrho(s) \mathscr{U}(s) \frac{ds}{s} \\ &= \lambda_\varepsilon (\mathscr{T}_\varepsilon \mathscr{U})(t),\ t \in [a, b]. \end{aligned}$$

By the similar method with the proof of Theorem 1, one gets

$$\mathscr{U} - A\mathscr{U} \neq d\zeta_\varepsilon,\ \mathscr{U} \in \partial\mathscr{K}_\jmath,\ d \geq 0,$$

by using Lemma 8, one arrives at

$$i(A, \mathscr{K}_\jmath, \mathscr{K}) = 0. \tag{3.29}$$

Combing (3.26) with (3.29), one obtains

$$i(A, \mathscr{K}_\jmath \setminus \overline{\mathscr{K}}_{\iota_0}, \mathscr{K}) = i(A, \mathscr{K}_\jmath, \mathscr{K}) - i(A, \mathscr{K}_{\iota_0}, \mathscr{K}) = -1.$$

Hence, A at least has one fixed point in $K_R \setminus \overline{K}_{r_0}$, which means BVP (2.1,2.2) at least has a positive solution, i.e., the BVP (1.1,1.2) has at least one positive solution. The proof is completed. □

4. Example

Example 1. *For a boundary value problem show as follows*

$$\begin{cases} -{}^{H}D_{a^+}^{\frac{5}{2}}v(t) = g(t)\ell\Big(t, v(t), {}^{H}D_{a^+}^{\frac{1}{4}}v(t)\Big),\ a < t < b, \\ {}^{H}D_{a^+}^{\frac{1}{4}}v(a) = {}^{H}D_{a^+}^{\frac{5}{4}}v(a) = 0, \\ {}^{H}D_{a^+}^{\frac{1}{4}}v(b) = \sum\limits_{j=1}^{\infty}\eta_j {}^{H}D_{a^+}^{\frac{1}{4}}v(\xi_j), \end{cases} \tag{4.1}$$

where $\flat = \frac{5}{2}$, $\mu = \frac{1}{4}, a = 1, b = 3$, $a = 1, b = 3$, $\kappa_j = \frac{1}{16}\frac{1}{j^4}, \varsigma_j = e^{\frac{1}{j^4}}$, $\varrho(t) = \frac{1}{3(1-t)(t-3)}$, $\ell(t,x,y) = (x+y)^{-\frac{1}{3}} + |\ln y|$. *Clearly,* $\varrho(t)$ *is singular at* $t = a$ *or/and* $t = b$, $\ell(t,x,y)$ *is singular at* $x = y = 0$. *Let* $\mathscr{U}(t) = {}^{H}D_{a^+}^{\frac{1}{4}}\mathscr{V}(t)$, *the BVP (4.1) can be reduced to an amended boundary value problem shown as follows*

$$\begin{cases} -{}^{H}D_{a^+}^{\frac{9}{4}}\mathscr{U}(t) = \varrho(t)\ell(t, {}^{H}I_{a^+}^{\frac{1}{4}}\mathscr{U}(t), \mathscr{U}(t)),\ a < t < b, \\ \mathscr{U}(a) = \mathscr{U}'(a) = 0, \mathscr{U}(b) = \sum\limits_{j=1}^{\infty}\eta_j\mathscr{U}(\xi_j), \end{cases} \tag{4.2}$$

by simple calculations, we have

$$\Delta = (\ln\frac{b}{a})^{\flat-\mu-1} - \sum_{j=1}^{\infty}\kappa_j(\ln\frac{\varsigma_j}{a})^{\flat-\mu-1} = 0.1554,$$

clearly, we have

$$\mathscr{G}(t,s) = \frac{1}{(\ln 3)^{\frac{5}{4}}\Gamma(\frac{9}{4})}\begin{cases} (\ln t)^{\frac{5}{4}}(\ln 3 - \ln s)^{\frac{5}{4}} - (\ln t - \ln s))^{\frac{5}{4}}(\ln 3)^{\frac{5}{4}},\ 1 \le s \le t \le 3, \\ (\ln t)^{\frac{5}{4}}(\ln 3 - \ln s)^{\frac{5}{4}},\ 1 \le t \le s \le 3, \end{cases} \tag{4.3}$$

$$\mathscr{H}(t,s) = \mathscr{G}(t,s) + \frac{(\ln t)^{\frac{5}{4}}}{\Delta}\sum_{j=1}^{\infty}\kappa_j\mathscr{G}(\varsigma_j, s),$$

$$w = 1 + \frac{(\ln\frac{b}{a})^{\flat-\mu-1}}{\Delta}\sum_{j=1}^{\infty}\eta_j = 1 + \frac{(\ln 3)^{\frac{5}{4}}}{0.1554}\sum_{j=1}^{\infty}\frac{1}{16}\frac{1}{j^4} \approx 1.4895,$$

then the cone

$$\mathscr{K} = \{\mathscr{U} \in C[1,e] : \mathscr{U}(t) \ge \frac{\vartheta(t)}{(\ln 3)w}\|\mathscr{U}\| \ge 0.6150\vartheta(t)\|\mathscr{U}\|\}.$$

For any $0 < r < R < +\infty$ *and* $u \in \overline{\mathscr{K}}_R \setminus \mathscr{K}_r$, *we have*

$$(\ln t)^{\frac{5}{4}}\varrho r \le \mathscr{U}(t) \le R\overline{\varrho},$$

$$(\ln t)^{\frac{5}{4}}\varrho r \le \|u\|(\ln t)^{\flat-\mu-1}\varrho \le v(t) = {}^{H}I_{1^+}^{\frac{1}{4}}\mathscr{U}(t) \le \frac{1}{\Gamma(\frac{5}{4})}(\ln 3)^{\frac{1}{4}}\|\mathscr{U}\| \le \overline{\varrho}\|\mathscr{U}\|,\ t \in [1,3],$$

$$\varrho = \min\left\{\frac{1}{(\ln\frac{b}{a})^{\gamma-\mu-1}w}, \frac{(\ln a)^{\flat-\mu}(-1)^{\flat-\mu-1}}{\Gamma(\mu)\gamma(\ln\frac{b}{a})^{\flat-\mu}w}, 1\right\} = \min\left\{\frac{1}{(\ln 3)^{\frac{5}{4}}w}, \frac{(-1)^{\frac{5}{4}}}{\Gamma(\frac{1}{4})\gamma(\ln 3)^{\frac{9}{4}}w}, 1\right\},$$

$$\overline{\varrho} = \max\left\{1, \frac{(\ln\frac{b}{a})^{\mu}}{\Gamma(\mu+1)}\right\} = \max\left\{1, \frac{(\ln 3)^{\frac{1}{4}}}{\Gamma(\frac{5}{4})}\right\}. \tag{4.4}$$

Since $|\ln u|$ *decreases on* $(0,1)$*, and increases on* $(1,+\infty)$*, one must have*

$$|\ln u(t)| \leq 2|\ln R| + |(\ln t)^4|, t \in [1,e],$$

$$[x(t)+y(t)]^{-\frac{1}{3}} \leq \left[(\ln t)^4 r + \frac{B(5,\frac{1}{2})}{\Gamma(\mu)} r(\ln t)^{-\frac{1}{2}}\right]^{-\frac{1}{3}}, \ t \in [1,e].$$

where $B(5,\frac{1}{2})$ *is a Beta function. By considering the absolute continuity of the obtained integral, one can derive that*

$$\lim_{m\to\infty} \int_{e(m)} \varpi(s)\varrho(t)\left((\ln t)^4 r + \left[(\ln t)^4 r + B(5,\frac{1}{2}) r(\ln t)^{-\frac{1}{2}}\right]^{-\frac{1}{3}}\right)\frac{ds}{s} = 0.$$

Hence,

$$\begin{aligned}
&\limsup_{m\to+\infty} \sup_{\substack{x_1\in\overline{K}_{\overline{R}}\setminus K_r \\ x_2\in\overline{K}_R\setminus K_r}} \int_{e(m)} \varpi(s)\varrho(s) f(s,x_1(s),x_2(s))\frac{ds}{s} \\
\leq &\limsup_{m\to+\infty} \sup_{\substack{x_1\in\overline{K}_{\overline{R}}\setminus K_r \\ x_2\in\overline{K}_R\setminus K_r}} \int_{e(m)} (\ln\frac{s}{a})(\ln\frac{b}{s})^{\flat-\mu-1}\frac{1}{3(1-s)(s-3)}\left[(x_1+x_2)^{-\frac{1}{3}} + |\ln x_2|\right]\frac{ds}{s} \\
\leq &\limsup_{m\to+\infty} \int_{e(m)} (\ln\frac{s}{a})(\ln\frac{b}{a})^{\frac{5}{4}}\frac{1}{3(1-s)(s-3)}\left((\ln t)^4 r + \left[(\ln t)^4 r + B(5,\frac{1}{2}) r(\ln t)^{-\frac{1}{2}}\right]^{-\frac{1}{3}}\right)\frac{ds}{s} = 0,
\end{aligned}$$

where $\overline{R} = \frac{1}{\Gamma(\mu+1)}(\ln\frac{b}{a})^\mu R = \frac{1}{\Gamma(\frac{5}{4})}(\ln 3)^{\frac{1}{4}} R$*. So* (H_1) *holds. On the other hand, it is obvious that*

$$\begin{aligned}
&\liminf_{\substack{x_1\to0^+ \\ x_2\to0^+}} \inf_{t\in[1,3]} \frac{f(t,x_1,x_2)}{x_1+x_2} = \liminf_{\substack{x_1\to0^+ \\ x_2\to0^+}} \frac{(x_1+x_2)^{-\frac{1}{3}} + |\ln x_2|}{x_1+x_2} = +\infty, \\
&\limsup_{\substack{x_1+x_2\to+\infty \\ x_2\to+\infty}} \sup_{t\in[1,3]} \frac{f(t,x_1,x_2)}{x_2} = \limsup_{\substack{x_1+x_2\to+\infty \\ x_2\to+\infty}} \sup_{t\in[1,3]} \frac{((x_1+x_2)^{-\frac{1}{3}} + |\ln x_2|)}{x_2} = 0,
\end{aligned}$$

which implies that

$$\liminf_{\substack{x_1\to0^+ \\ x_2\to0^+}} \inf_{t\in[1,3]} \frac{f(t,x_1,x_2)}{x_1+x_2} > \lambda_1 > \limsup_{\substack{x_1+x_2\to+\infty \\ x_2\to+\infty}} \sup_{t\in[1,3]} \frac{f(t,x_1,x_2)}{x_2}.$$

So far, all the condition proposed in Theorem 1 have been meet. Consequently, Theorem 1 ensures that there must be one or more positive solutions to Equation (4.2). Equivalently, one or more positive solutions can be determined for Equation (4.2). It is worth mentioning that the calculation of fractional derivatives generally involves the beta function. In this example, because a specific explicit expression is provided, the beta function appears. However, in the general setting, if the function is abstract, then such the beta function will not appear.

5. Conclusions

The present study was concerned with the positive solutions and their existence for a nonlinear infinite-point Hadamard fractional differential equation. Using the fixed point theorem in cones, the nonlinear singularities on time and spatial variables are achieved through the spectral analysis of the relevant linear operator and Gelfand's formula. Compared with some existing literature discussing the same interval we derived herein, we overcome a significant difficulty that the consideration of solutions on this interval brings

about a series of problems. Compared with some other existing literature, the nonlinear term of the equation contains the derivative term, and the infinite point is involved in the boundary conditions. These are the main contributions and innovations of the present research.

Author Contributions: C.L.: Conceptualization, Investigation, Formal analysis, Writing—original draft; L.G.: Methodology, Validation, Project administration, Resources, Writing—review and editing, Funding acquisition. All authors have read and agreed to the published version of the manuscript.

Funding: This research was supported by the National Natural Science Foundation ofChina (12272064, 12101086), Major Project of Basic Science (Natural Science) Research in Colleges andUniversities of Jiangsu Province (23KJA580001), and Young and Middle-aged Academic Leaders ofthe Blue Project in Colleges and Universities in Jiangsu Province (31120223005).

Institutional Review Board Statement: Not applicable.

Informed Consent Statement: All authors have read and agreed to the published version of the manuscript.

Data Availability Statement: No new data were created or analyzed in this study. Data sharing is not applicable to this article.

Acknowledgments: We appreciate the constructive comments and suggestions from the anonymous reviewers.

Conflicts of Interest: The authors declare no conflicts of interest.

References

1. Boulham, I.; Boubakir, A.; Labiod, S. Fuzzy L1 adaptive controller for chaos synchronization of uncertain fractional-order chaotic systems with input nonlinearities. *Tran. Inst. Meas. Cont.* **2023**, *45*, 2310–2323. [CrossRef]
2. Wu, J.; Wang, W.; Cao, Y.; Liu, S.; Zhang, Q.; Chu, W. A novel nonlinear fractional viscoelastic–viscoplastic damage creep model for rock-like geomaterials. *Compu. Geot.* **2023**, *163*, 105726. [CrossRef]
3. Ma, W.; Ma, N.; Dai, C.; Chen, Y.; Wang, X. Fractional modeling and optimal control strategies for mutated COVID-19 pandemic. *Math. Meth. Appl. Sci.* **2023**. [CrossRef]
4. Yang, B.; Zhu, T.; Zhang, X.; Wang, J.; Shu, H.; Li, S.; He, T.; Yang, L.; Yu, T. Design and implementation of Battery/SMES hybrid energy storage systems used in electric vehicles: A nonlinear robust fractional-order control approach. *Energy* **2020**, *191*, 116510. [CrossRef]
5. Ouhsaine, L.; Boukal, Y.; Ganaoui, M.; Darouach, M.; Zasadzinski, M.; Mimet, A.; Eddine Radhy, N. A General fractional-order heat transfer model for Photovoltaic/Thermal hybrid systems and its observer design. *Energy Procedia* **2017**, *139*, 49–54. [CrossRef]
6. Tomasz, P.; Jacek, G. Signal propagation in electromagnetic media described by fractional-order models. *Commun. Nonlinear Sci. Nume. Simul.* **2020**, *82*, 105029.
7. Piotrowska, E.; Rogowski, K. Analysis of fractional electrical circuit using Caputo and Conformable derivative definitions. *Non-Integer Order Calc. Appl.* **2019**, *15*, 183–194.
8. Huang, P.; Zhang, J.; Damascene, N.; Dong, C.; Wang, Z. A fractional order viscoelastic-plastic creep model for coal sample considering initial damage accumulation. *Alex. Engi. J.* **2021**, *60*, 3921–3930. [CrossRef]
9. Jena, R.; Chakraverty, S.; Rezazadeh, H.; Domiri Ganji, D. On the solution of time- fractional dynamical model of Brusselator reaction-diffusion system arising in chemical reactions. *Bull. Sci. Math.* **2020**, *43*, 3903–3913. [CrossRef]
10. Munoz-Pacheco, J.; Posadas-Castillo, C.; Zambrano-Serrano, E. The Effect of a Non-Local Fractional Operator in an Asymmetrical Glucose-Insulin Regulatory System: Analysis, Synchronization and Electronic Implementation. *Symmetry* **2020**, *12*, 1395. [CrossRef]
11. Yusuf, A.; Acay, B.; Tasiu, U.; Mustafa, I.; Baleanu, D. Mathematical modeling of pine wilt disease with Caputo fractional operator. *Chaos Solitons Fractals* **2021**, *143*, 110569. [CrossRef]
12. Guo, L.; Li, C.; Zhao, J. Existence of monotone positive solutions for Caputo-Hadamard nonlinear fractional differential equation with infinite-point boundary value conditions. *Symmetry* **2023**, *15*, 970. [CrossRef]
13. Li, C.; Zhu, C.; Lim, C.; Li, S. Nonlinear in-plane thermal buckling of rotationally restrained functionally graded carbon nanotube reinforced composite shallow arches under uniform radial loading. *Appl. Math. Mech. Engl. Ed.* **2022**, *43*, 1821–1840. [CrossRef]
14. Guo, L.; Cai, J.; Xie, Z.; Li, C. Mechanical responses of symmetric straight and curved composite microbeams. *J. Vibr. Eng. Technol.* **2024**, *12*, 1537–1549. [CrossRef]
15. Li, C.; Zhu, C.; Zhang, N.; Sui, S.; Zhao, J. Free vibration of self-powered nanoribbons subjected to thermal-mechanical-electrical fields based on a nonlocal strain gradient theory. *Appl. Math. Model.* **2022**, *110*, 583–602. [CrossRef]
16. Chabane, F.; Abbas, S.; Benbachir, M.; Benchohra, M.; N'Guérékata, G. Existence of Concave Positive Solutions for Nonlinear Fractional Differential Equation with p-Laplacian Operator. *Viet. J. Math.* **2023**, *51*, 505–543. [CrossRef]

17. Guo, L.; Zhao, J.; Liao, L.; Liu, L. Existence of multiple positive solutions for a class of infinite-point singular p-Laplacian fractional differential equation with singular source terms. *Nonli. Anal. Model. Control* **2022**, *27*, 609–629. [CrossRef]
18. Xu, J.; Liu, J.; O'Regan, D. Solvability for a Hadamard-type fractional integral boundary value problem. *Nonli. Anal. Model. Control* **2023**, *4*, 1–25. [CrossRef]
19. Arul, R.; Karthikeyan, P. Integral boundary value problems for implicit fractional differential equations involving Hadamard and Caputo-Hadamard fractional derivatives. *Krag. J. Math.* **2019**, *45*, 331–341.
20. Wang, J.; Feckan, M.; Zhou, Y. Fractional order iterative functional differential equations with parameter. *Appl. Math. Model.* **2013**, *37*, 6055–6067. [CrossRef]
21. Ardjouni, A.; Djoudi, A. Positive solutions for nonlinear Caputo-Hadamard fractional differential equations with integral boundary conditions. *Open J. Math. Anal.* **2019**, *3*, 62–69. [CrossRef]
22. Zhang, S. Positive solutions for a class of singular fractional differential equation with infinite-point boundary value conditions. *Appl. Math. Lett.* **2015**, *39*, 22–27. [CrossRef]
23. Boutiara, A.; Benbachir, M.; Guerbati, K. Boundary value problem for nonlinear Caputo-Hadamard fractional differential equation with Hadamard fractional integral and anti-periodic conditions. *Facta. Univer. Seri. Math. Infor.* **2021**, *36*, 735–748.
24. Ahmad, B.; Alsaedi, A.; Ntouyas, S.; Tariboon, J. *Hadamard-Type Fractional Differential Equations, Inclusions and Inequalities*; Springer: Cham, Switzerland, 2017.
25. Kilbas, A.; Srivastava, H.; Trujillo, J. *Theory and Applications of Fractional Differential Equations*; Elsevier Science BV: Amsterdam, The Netherlands, 2006.
26. Naseer, A. Positive solution for a Hadamard fractional singular boundary value problem of order $\mu \in (2, 3)$. *arXiv* **2021**, arXiv:2108.13127.
27. Guo, D.; Lakshmikantham, V. *Nonlinear Problems in Abstract Cones*; Academic Press: Boston, MA, USA, 1988.

fractal and fractional

MDPI

Article

Well-Posedness of the Mild Solutions for Incommensurate Systems of Delay Fractional Differential Equations

Babak Shiri

Data Recovery Key Laboratory of Sichuan Province, College of Mathematics and Information Science, Neijiang Normal University, Neijiang 641100, China; shiribabak2018@gmail.com

Abstract: Systems of incommensurate delay fractional differential equations (DFDEs) with non-vanishing constant delay of retarded type are investigated. It is shown that the mild solutions are well-posed in Hadamard sense on the space of continuous functions. The analysis is local and carried out for finite intervals. The strong results are obtained with weak conditions by using state-of-the-art new methods. No condition on the Lipschitz parameter is added for well-posedness results. Application of this theorem for the Hopfield neural network is carried out.

Keywords: fractional differential equation; well-posed in Hadamard sense; non-vanishing constant delay of retarded type; incommensurate systems; Hopfield neural networks

Academic Editors: Libo Feng, Yang Liu and Lin Liu

Received: 29 December 2024
Revised: 11 January 2025
Accepted: 19 January 2025
Published: 21 January 2025

Citation: Shiri, B. Well-Posedness of the Mild Solutions for Incommensurate Systems of Delay Fractional Differential Equations. *Fractal Fract.* **2025**, *9*, 60. https://doi.org/10.3390/fractalfract9020060

1. Introduction

Fractional differential equations (FDEs) have found extensive use in the modeling of complex systems, primarily due to their ability to represent memory in systems dynamics [1,2]. Fortunately, there are various fractional derivatives, each having different memory kernels. This diversity, provide us with a rich set of operators capable of capturing the intricate dynamics of complex natural systems [3].

Similar to FDEs, delay differentiate equations (DDEs) have been widely applied in mathematical models, especially in biological phenomena [4]. However, DDEs are rarely studied and well-analyzed in connection to FDEs. The analysis of the linear delay fractional differential equation (DFDE),

$$\mathfrak{D}^{\psi}y(t) = ay(\theta(t)) + by(t) + f(t), \quad t > 0, \quad \psi \in (0,1), \quad a,b \in \mathbb{R}, \quad f \in \mathcal{C}[0,\mathfrak{T}], \qquad (1)$$

has been explored in [5]. In their paper, the lag term is defined by $\theta(t) := t - \tau$ with a constant time delay $\tau > 0$. This study covers the uniqueness of the mild solution and the dependency of the mild solution on its parameters. The stability of the problem (1) has also been studied [6].

We note that such DFDEs are known as retarded ones since the lag term does not involve fractional derivatives. If the equation involves terms like $\mathfrak{D}^{\psi}y(\theta(t))$, the equation becomes a neutral type, which we do not study here. The existence result of fractional-order neutral time-delay systems can be found in [7].

Most applied problems can not be modeled by a simple one-D equations like (1). A state of natural systems involves more than one component that are connected to each other to achieve an aim. In mathematics, a system is described by more than one equation. If the dynamics of each state depend on other states, it is called a coupled system. FDEs and DFDEs are utilized in diverse modeling. Currently, there is abundant work in biology, mechanics, electronics, and other branch of science that use systems of FDEs in their modeling.

However, they usually use a common order for all equations. But there is no need for all states to have the same memory and thus the same order of derivatives [8,9]. Therefore, the systems that may have different orders for each equation must be important for modeling. Such systems are known as incommensurate systems [10,11]. Incommensurate FDEs have been used in the structure of fractional Hopfield neural networks (FHNNs) [11–13].

A linear incommensurate system of DFDEs with multiple delays (multi-delay) can be described by

$$\begin{cases} {}^{C}\mathfrak{D}^{\psi_1} y_1(t) &= a_{11}y_1(t) + \ldots + a_{1\nu}y_\nu(t) + b_{11}y_1(\theta_1(t)) + \ldots + b_{1\nu}y_\nu(\theta_\nu(t)) + f_1(t), \\ &\vdots \\ {}^{C}\mathfrak{D}^{\psi_\nu} y_\nu(t) &= a_{\nu 1}y_1(t) + \ldots + a_{\nu\nu}y_\nu(t) + b_{\nu 1}y_1(\theta_1(t)) + \ldots + b_{\nu\nu}y_\nu(\theta_\nu(t)) + f_\nu(t), \end{cases} \tag{2}$$

where $\psi_i \in (0,1)$, $a_{ij}, b_{i,j} \in \mathbb{R}$ and $f_i : [0,\mathfrak{T}] \to \mathbb{R} \in \mathcal{C}[0,\mathfrak{T}]$, $y_i : [0,\mathfrak{T}] \to \mathbb{R} \in \mathcal{C}[0,\mathfrak{T}]$, for $i,j = 1,\ldots,\nu$. This system can be expressed in shorthand as

$$\mathfrak{D}^{\Psi} Y(t) = AY(t) + BY(\Theta(t)) + F(t) \tag{3}$$

where $\Psi = [\psi_1,\ldots,\psi_\nu]^T \in (0,1)^\nu$, $Y = [y_1,\ldots,y_\nu]^T \in (\mathcal{C}[0,\mathfrak{T}])^\nu$, $F = [f_1,\ldots,f_\nu]^T \in (\mathcal{C}[0,\mathfrak{T}])^\nu$, $\Theta = [\theta_1,\ldots,\theta_\nu]^T$, $\theta_i(t) = t - \tau_i$, $\tau_i \in \mathbb{R}$, $A = (a_{ij})$ and $B = (b_{ij})$. The meaning of such vector operators later will be recalled. Problem (2) has been studied subject to delay condition

$$y_i(t) = g_i(t), \quad t \in (-\tau_i, 0]. \tag{4}$$

If we assume that all delays are equal (i.e., $\tau_i = \tau$ where $\tau > 0$ is a positive constant), then the initial condition and prehistoric conditions (4) can be expressed as

$$Y(t) = G(t), \quad t \in (-\tau, 0]. \tag{5}$$

Such delays are also referred to as a single/constant delay. In this case, the lag term is a single function, and we simply use θ to represent it, where $\theta(t) := t - \tau$. The nonlinear DFDE with a constant delay can be described by

$$\begin{cases} {}^{C}\mathfrak{D}^{\psi_1} y_1(t) &= u_1(t, y_1(t),\ldots,y_\nu(t), y_1(\theta(t)),\ldots,y_\nu(\theta(t))), \\ &\vdots \\ {}^{C}\mathfrak{D}^{\psi_\nu} y_\nu(t) &= u_\nu(t, y_1(t),\ldots,y_\nu(t), y_1(\theta(t)),\ldots,y_\nu(\theta(t))), \end{cases} \tag{6}$$

subject to condition (5). It can be written in a compact form as

$$\mathfrak{D}^{\Psi} Y(t) = U(t, Y(t), Y(\Theta(t))). \tag{7}$$

where $\Theta(t) = [\theta,\ldots,\theta]^T$. We note that the related operations of $Y(\Theta(t))$ are explained for the algebra of the vector-valued function in the next sections, and they are not composite functions.

There are studies on systems with various delays for each state [14]. Specifically, ref. [14] addresses the stability of a class of incommensurate DFDEs with multiple delays. A numerical method for nonlinear systems of DFDE with a single/constant delay $\tau_i = \tau$ and commensurate order $\psi_i = \psi$ has been studied in [15]. The stability of a class of commensurate systems (3) with a constant delay, where A is a zero matrix, is studied in [16].

The objective of this paper is to study System (6) with constant delay. Such systems may appear in research papers, but fundamental questions regarding these systems, such

as the existence of a unique solution and well-posedness are still unstudied. Existence results for systems of fractional equations typically utilize fixed-point theorems like the Banach fixed-point or Schauder fixed-point theorems. However, as discussed in [17] and other relative works, these types of theorems impose additional conditions on U or even $\mathfrak{T}$. Therefore, we apply the state-of-the-art method used in [17] to obtain strong results under weaker conditions. In the main theorems, we will find that continuity of the functions U and G and Lipschitz continuity of the function U with respect to Y is sufficient to guaranty the existence of the unique mild solution. Moreover, we show it is sufficient to ensure the continuous dependency of the mild solution to G, if we assume U is also Lipschitz continuous with respect to W.

Remark 1. *The fractional derivative and integral operators have two parameters. For example, in RL integral*

$$\mathfrak{I}^{\psi} y(t)(s) = \frac{1}{\Gamma(\psi)} \int_0^s (s-t)^{1-\psi} y(t) dt.$$

the variable t is the dummy variable, and s is the active variable. Usually, in the literature, the active variable is deleted. However, in this paper, for clarity, we may add the second variable to separate the dummy variable and active variable.

2. Vector-Valued Operational Algebra

Here, we clarify the algebra of vector-valued functions and their related operations through exact definitions. Suppose $\mathcal{Y}$ is a space of functions, and

$$F = [f_1, \dots, f_\nu]^T : [0, \mathfrak{T}] \to \mathbb{R}^\nu \in \mathcal{Y}^\nu$$

is a vector-valued function. For operators $o_i : \mathcal{Y} \to \mathcal{Y}$, we define the vector-operator

$$\mathfrak{O} = [o_1, \dots, o_\nu]^T : \mathcal{Y}^\nu \to \mathcal{Y}^\nu$$

by

$$\mathfrak{O}(F) = [o_1(f_1), \dots, o_\nu(f_\nu)]^T = \mathrm{Diag}([o_1, \dots, o_\nu])F.$$

Such an $\mathfrak{O}$ can be ${}^{C}D^{\Psi} = [{}^{C}D^{\psi_1}, \dots, {}^{C}D^{\psi_\nu}]^T$ or $\mathcal{I}^{\Psi} = [\mathcal{I}^{\psi_1}, \dots, \mathcal{I}^{\psi_\nu}]^T$.

The elementary operations such as addition, difference, product, division, and power operations of vector-valued functions are performed element-wise. For example, if $G = [g_1, \dots, g_\nu] : [0, \mathfrak{T}] \to \mathbb{R}^\nu$ is another vector-valued function

$$F \pm G = [f_1 \pm g_1, \dots, f_\nu \pm g_\nu]^T.$$

Let $\Theta = [\theta_1, \dots, \theta_\nu]^T : [0, \mathfrak{T}] \to \mathbb{R}^\nu$ be a vector-lag term. Clearly, $F(\Theta)$ is not well-defined as a composite function. However, we define it as vector-wise composite functional,

$$F(\Theta) = [f_1(\theta_1), \dots, f_\nu(\theta_\nu)]^T. \tag{8}$$

We note that, in our study $\Theta = [\theta, \dots, \theta]^T$ can be substituted by θ and serve as a composite function! Consequently, in our study, $F(\Theta) = F(\theta)$. However, in multi-delay cases, the use of element-wise composition is indispensable.

The operation of one-dimensional functions and operators with a scalar is inherited by all elements of the vector. For example, if $f : [0, \mathfrak{T}] \to \mathbb{R}$ is a scalar function, as well as $\Psi = [\psi_1, \dots, \psi_\nu]$, then $G = f^{\Psi}$ is defined by

$$G = [f^{\psi_1}, \dots, f^{\psi_\nu}]^T.$$

Example 1. *For* $\Psi = [\psi_1, \dots, \psi_\nu]^T$ *and* $P = [p_1, \dots, p_\nu]^T$, *we have*

$$\mathfrak{I}^{\Psi} t^{P} = \frac{\Gamma(P+1)}{\Gamma(P+\Psi+1)} t^{\Psi+P}. \tag{9}$$

We note that this equation is exactly similar to the computation of the non-vector case of $I^{\alpha} t^{\beta}$. *However, we should note that the notation here has a different meaning. To be more clear, the right-hand side of Equation* (9) *is*

$$[\frac{\Gamma(p_1+1)}{\Gamma(p_1+\psi_1+1)} t^{p_1+\psi_1}, \dots, \frac{\Gamma(p_\nu+1)}{\Gamma(p_\nu+\psi_\nu+1)} t^{p_\nu+\psi_\nu}]^T!$$

Theorem 1. *Let* $0 < \psi_i \leq 1$, $i = 1, \dots, \nu$ *and* $Y \in (\mathcal{AC}[0, \mathfrak{T}])^{\nu}$. *Then,*

$$\mathfrak{I}^{\Psi}\, {}^{C}D^{\Psi} Y = Y(t) - Y(0) \tag{10}$$

and

$${}^{C}D^{\Psi} \mathfrak{I}^{\Psi} Y(t) = Y(t). \tag{11}$$

Theorem 2 (Generalized Gronwall inequality [18,19]). *Suppose* $q, \mathfrak{T} > 0$, $c \geq 0$ *and* $y : [0, \mathfrak{T}] \to \mathbb{R}$ *is a locally integrable and no-negative function satisfying*

$$y(t) \leq c + M \int_0^t (t-a)^{\psi-1} y(s) ds \tag{12}$$

Then, $y(t) \leq c E_{\psi}(M\Gamma(\psi) t^{\psi})$.

3. Existence of a Unique Continuous Mild Solution with Single Delay

Applying the RL integral $\mathfrak{I}^{\Psi}$ to both sides of (3), we obtain

$$Y(t) = Y(0) + \mathfrak{I}^{\Psi} AY(t) + \mathfrak{I}^{\Psi} BY(\Theta(t)). \tag{13}$$

It is well-known that the solution to (13) may not be differentiated, or may not be in $\mathcal{AC}$ (see, for example, [20]). So, the solution of (13) may not satisfies the original Equation (3). But, in most applied mathematics, we need a solution of the model based on (3). Therefore, we use the adjective "mild" before the word solution to emphasize that the solution of associate integral may not be the solution of the original Equation (3).

We should note that interchanging the place of the fractional integral and constant matrix in System (13) can be problematic. While this interchange is valid for commensurate systems, it is incorrect for incommensurate systems. In particular, we have

$$\mathfrak{I}^{\Psi} AY \neq A\mathfrak{I}^{\Psi} Y. \tag{14}$$

This leads to additional complexities for incommensurate FDEs compared to commensurate FDEs.

Similarly, and in general, from (7), we can infer that the mild solution satisfies

$$Y(t) = Y(0) + \mathfrak{I}^{\Psi} U(t, Y(t), Y(\Theta(t))). \tag{15}$$

Definition 1. *We define* Y *as a mild solution of* (7) *under Condition* (5) *if it fulfills System* (15).

Remark 2. *A solution to* (15) *might not be differentiable and, therefore, might not satisfy the original Problem* (7) *under Condition* (5). *However, the solution to the original problem satisfies* (15).

The existence of a mild solution of incommensurate systems of FDEs has been established in [17]. Based on the discussion in that paper, the existence of a mild solution based on the Banach fixed-point theorem and the Schauder fixed-point theorem require stronger conditions. To obtain the weaker condition, the authors of [17] proposed a direct method using Cauchy sequences. They first established the result on the interval $[0, 1]$ and then extended the global existence using the tail part of the RL integral.

Now, consider a single delay, τ. Let $t \in (0, \tau]$, which implies that $t - \tau \in (-\tau, 0]$. Then, $Y(\Theta(t)) = G(\Theta(t))$, and Equation (15) becomes equivalent to

$$Y(t) = G(0) + \mathfrak{I}^{\Psi} U(t, Y(t), G(\Theta(t))), \quad t \in [0, \tau]. \tag{16}$$

We note that $G(\Theta(0)) = G(-\tau)$ is not defined. We assume $G(\Theta(0^+)) = G(-\tau^+) < \infty$, and extend G on $[-\tau, 0]$ by $G(-\tau) = G(-\tau^+)$ to use compactness of interval. It follows immediately that $G \in \mathcal{C}[-\tau, 0]$. Also, it is clear the value of $\mathfrak{I}^{\Psi}$ at $t = 0$ is zero for any continuous function.

We use the absolute value notation as a norm in $\mathbb{R}^{\nu}$, defined by

$$|Y| = \max_{i=1,\dots,\nu} |y_i|.$$

However, we use the norm notation for spaces of functions, especially for $F \in (C[0, \mathfrak{T}])^{\nu}$

$$\|F\| = \sup_{t \in [0,\mathfrak{T}]} |F(t)| = \sup_{t \in [0,\mathfrak{T}]} \max_{i=1,\dots,\nu} |f_i(t)|.$$

Now, consider the following hypotheses:

(H1) U is globally Lipschitz continuous with respect to Y, i.e., $\exists\, L_i \in \mathbb{R}$, such that

$$|u_i(t, Y, W) - u_i(t, Z, W)| \leq L_i |Y - Z|$$

for all $t \in [0, \mathfrak{T}]$, and for all $Z, Y, W \in \mathbb{R}^{\nu}$.

(H2) $U : [0, \mathfrak{T}] \times \mathbb{R}^{\nu} \times \mathbb{R}^{\nu} \to \mathbb{R}^{\nu}$ is continuous with respect to its domain.

(H3) G is a continuous function on $(-\tau, 0]$ and $\lim_{t \to \tau} g_i(t) < \infty$.

Remark 3. *Letting $L = \max_{i=1,\dots,\nu} |L_i|$, it follows from (H1) that*

$$|U(t, Y, W) - U(t, Z, W)| \leq L|Y - Z|, \quad \forall t \in [0, \mathfrak{T}], \forall Z, Y, W \in \mathbb{R}^{\nu}.$$

Remark 4. *More precisely, (H3) states that if we extend G to $[-\tau, 0]$ by $G(-\tau) = \lim_{t \to \tau} G(t)$, then it is continuous on $[-\tau, 0]$. Thus, the condition (H3) can be expressed as "G is continuous on $[-\tau, 0]$".*

Theorem 3. *Let Hypotheses (H1)–(H3) hold. Then, System* (7) *subject to Condition* (5) *processes a mild continuous solution on $[0, \tau]$.*

Proof. The proof is similar to Theorem 7 of [17], so we provide a proof sketch here. First, we assume $\tau \leq 1$, introduce a Picard operator $\mathfrak{P}$ by

$$\mathfrak{P}Y = G(0) + \mathfrak{I}^{\Psi} U(t, Y(t), G(\Theta(t))) \tag{17}$$

and we show that the functions

$$Y_{n+1} = \mathfrak{P}Y_n, \quad Y_0 = G_0, \quad n = 0, 1, \dots$$

are Cauchy sequences in $(\mathcal{C}[0,\tau])^{\nu}$. Consequently, they have a uniform limit, say Y. By the uniform convergence theorem for fractional integrals, we have

$$\begin{aligned}\lim_{N\to\infty} Y_{n+1} &= \lim_{N\to\infty} \mathfrak{P}Y_n = G(0) + \mathfrak{I}^{\Psi}U(t, Y_N(t), G(\Theta(t)))\\ &= G(0) + \mathfrak{I}^{\Psi}\lim_{N\to\infty} U(t, Y_N(t), G(\Theta(t))).\end{aligned} \tag{18}$$

Since U is continuous, we can rewrite the above as

$$\lim_{N\to\infty} Y_{n+1} = G(0) + \mathfrak{I}^{\Psi}U(t, \lim_{N\to\infty} Y_N(t), G(\Theta(t))). \tag{19}$$

Thus, Y satisfies Equation (16). Now, assume that $1 < \tau \leq 2$. Given that a solution exists on $[0,1]$, w can decompose the $\mathfrak{I}^{\Psi}$ into two operators: the Fredholm operator $\mathfrak{F}^{\Psi}$ and the Volterra operator $\mathfrak{V}^{\Psi}$. The Fredholm operator is defined as

$$\mathfrak{F}^{\Psi}Y(t) = \frac{1}{\Gamma(\Psi)}\int_0^1 (t-z)^{\Psi-1}Y(z)dz \tag{20}$$

and the Volterra operator is defined as

$$\mathfrak{V}^{\Psi}Y(t) = \frac{1}{\Gamma(\Psi)}\int_1^t (t-z)^{\Psi-1}Y(z)dz. \tag{21}$$

We know that $\mathfrak{I}^{\Psi} = \mathfrak{F}^{\Psi} + \mathfrak{V}^{\Psi}$. Therefore, Equation (16) can be written as

$$Y(t) = G(0) + \mathfrak{F}^{\Psi}U(.,Y(.),G(\Theta(.)))(t) + \mathfrak{V}^{\Psi}U(.,Y(.),G(\Theta(.)))(t), \quad t\in[0,\tau]. \tag{22}$$

We have already established the existence of a solution of (16) on $[0,1]$. For convenience, we rename Y on $[0,1]$ by Y_1. Then, the tail of Equation (22) is known function say Z, i.e.,

$$Z(t) := G(0) + \mathfrak{F}^{\Psi}U(.,Y_1(.),G(\Theta(.)))(t).$$

Thus,

$$Y(t) = Z(t) + \mathfrak{V}^{\Psi}U(.,Y(.),G(\Theta(.)))(t), \quad t\in[1,\tau]. \tag{23}$$

Substituting $t = s+1$ gives

$$Y(s+1) = Z(s+1) + \frac{1}{\Gamma(\Psi)}\int_1^{s+1} (s+1-z)^{\Psi-1}U(z,Y(z),G(\Theta(z)))dz, \tag{24}$$

where $s\in[0,\tau-1]$. If we substitute $z = r+1$, we obtain

$$Y(s+1) = Z(s+1) + \frac{1}{\Gamma(\Psi)}\int_0^{s} (s-r)^{\Psi-1}U(r+1,Y(r+1),G(\Theta(r+1)))dr. \tag{25}$$

It is interesting to note that when considering the Volterra operator at the peak of dynamical System (25), it becomes an RL integral operate, and by renaming $Y_2(s) = Y(s+1)$, we obtain

$$Y_2(s) = Z(s+1) + \mathfrak{J}^{\Psi}U(r+1,Y_2(r),G(\Theta(r+1)))(s), \quad s\in[0,\tau-1]. \tag{26}$$

Equation (26) is of the same form as (16). Consequently, the existence of a unique $Y_2 \in (\mathcal{C}[0,\tau-1])^{\nu}$ is guaranteed in the same way. Conclusively,

$$Y(t) = \begin{cases} Y_1(t), & t\in[0,1],\\ Y_2(t-1), & t\in[1,\tau].\end{cases} \tag{27}$$

Clearly, $Y_2(1-1) = Y_2(0) = Z(1) = Y_1(1)$ and Y is a continuous solution to (16) on $[0, \tau]$. By induction, (16) has a unique continuous solution for any $\tau > 0$. □

The uniqueness of the solution follows from the generalized Gronwall inequality.

Theorem 4. *Let Hypotheses (H1)–(H3) hold. Then, System* (7) *subject to condition* (5) *has a unique mild continuous solution on* $[0, \tau]$.

Proof. The proof is similar to Theorem 10 of [17]. First, we show the uniqueness for $\tau \leq 1$. Let X and Y be two solutions. Then,

$$|x_i(t) - y_i(t)| \leq |\mathfrak{I}^{\psi_i} u_i(t, x_i(t), g_i(\theta_i(t))) - \mathfrak{I}^{\psi_i} u_i(t, y_i(t), g_i(\theta_i(t)))|, \quad t \in [0, \tau] \subseteq [0, 1].$$

Since $t \leq 1$, it follows from Hypotheses (H1) that

$$\begin{aligned} |x_i(t) - y_i(t)| &\leq \frac{L_i}{\Gamma(\alpha_i)} \int_0^t (t-z)^{\psi_i - 1} |X(z) - Y(z)| dz \\ &\leq M^* \int_0^t (t-z)^{\psi^* - 1} |X(z) - Y(z)| dz \end{aligned} \tag{28}$$

where $M* = \max_{i=1,\dots,\nu} \frac{L_i}{\Gamma(\alpha_i)}$ and $\psi^* = \min_{i=1,\dots,\nu} \psi_i$. We note that Inequality (28) is independent of i. Thus,

$$|X(t) - Y(t)| \leq M^* \int_0^t (t-z)^{\psi^* - 1} |X(z) - Y(z)| dz. \tag{29}$$

Immediately, it follows from the generalized Gronwall inequity that $|X(t) - Y(t)| = 0$, and $X(t) = Y(t)$ for all $t \in [0, 1]$. Now, let $\tau \in [0, 2]$. From a previous argument, we already know that $X(t) = Y(t)$ for $t \in [0, 1]$. From an argument similar to the proof of Theorem (3), Y and X satisfies Equation (25) while the definition of Z only uses the information of $Y(t)$ on $[0, 1]$. Since Y is unique on $[0, 1]$, the tail function Z is unique for all $t \in [0, \tau]$. It follows from (25) that

$$|X(s+1) - Y(s+1)| \leq M^* \int_0^s (s-z)^{\psi^* - 1} |X(r+1) - Y(r+1)| dr, \tag{30}$$

for $s \in [0, \tau - 1] \subseteq [0, 1]$. Therefore, from the generalized Gronwall inequality,

$$X(s+1) = Y(s+1), \quad s \in [0, \tau - 1]$$

or, equivalently, $X(t) = Y(t)$ on $[1, \tau]$ and, thus, on $[0, \tau]$. Similar induction can be used to prove that $X(t) = Y(t)$ for any delay $\tau > 0$. □

Up to this point, we have determined that System (1) has a unique mild solution within the interval $[0, \tau]$, and this solution is continuous. Now, we establish the existence of a unique continuous solution for any arbitrary interval $[0, \mathfrak{T}]$.

Theorem 5. *Let Hypotheses (H1)–(H3) hold. Then, System* (7) *subject to Condition* (5) *processes a unique mild continuous solution on* $[0, \mathfrak{T}]$.

Proof. If $\mathfrak{T} < \tau$, the claim follows from Theorem 4. Suppose $\tau < \mathfrak{T} \leq 2\tau$. We already know that there exists a solution on $[0, \tau]$. Denote this solution as Y_1. Then, System (15) is equivalent to

$$Y(t) = G(0) + \mathfrak{F}_\tau^\Psi U(z, Y_1(z), G(z-\tau))(t) + \mathfrak{V}_\tau^\Psi U(z, Y(z), Y_1(z-\tau))(t) \tag{31}$$

for $t \in [\tau, \mathfrak{T}]$, where

$$\mathfrak{F}_{\tau}^{\Psi} Y(t) = \frac{1}{\Gamma(\Psi)} \int_0^{\tau} (t-z)^{\Psi-1} Y(z) dz \tag{32}$$

is a Fredholm operator, and

$$\mathfrak{V}_{\tau}^{\Psi} Y(t) = \frac{1}{\Gamma(\Psi)} \int_{\tau}^{t} (t-z)^{\Psi-1} Y(z) dz \tag{33}$$

is a Volterra operator. For the tail of System (31) $Z(t) = G(0) + \mathfrak{F}_{\tau}^{\Psi} U(s, Y_1(s), G(s-\tau))(t)$ the Fredholm operator only depends on the values of $Y_1(s)$ and $G_1(s-\tau)$ on $s \in [0, \tau]$. Since Y_1 is known to be a unique, Z is well-defined unique function. Conclusively, by substituting $t = r + \tau$, we have (31),

$$Y(r+\tau) = Z(r+\tau) + \mathfrak{V}_{\tau}^{\Psi} U(s, Y(s), Y_1(s-\tau))(r+\tau). \tag{34}$$

Regarding the peak operator, by substituting $z = s + \tau$, we obtain

$$\begin{aligned} \mathfrak{V}_{\tau}^{\Psi} U(s, Y(s), Y_1(s-\tau))(r+\tau) =& \frac{1}{\Gamma(\Psi)} \int_{\tau}^{r+\tau} (r+\tau-z)^{\Psi-1} U(z, Y(z), Y_1(z-\tau)) dz \\ =& \frac{1}{\Gamma(\Psi)} \int_0^{r} (t-z)^{\Psi-1} U(s+\tau, Y(s+\tau), Y_1(s)) ds \\ =& \mathfrak{J}^{\Psi} U(s+\tau, Y(s+\tau), Y_1(s))(r). \end{aligned} \tag{35}$$

If we rename $Y_2(t) := Y(t+\tau)$ and consider Equation (35), then Equation (34) can be written as

$$Y_2(r) = Z(r+\tau) + \mathfrak{J}^{\Psi} U(s+\tau, Y_2(s), Y_1(s))(r), \quad r \in [0, \mathfrak{T}-\tau]. \tag{36}$$

Noticeably, we convert an equation on $[\tau, \mathfrak{T}]$ into a similar type of equation on the interval $[0, \mathfrak{T}-\tau] \subseteq [0, \tau]$. Therefore, we can use the same reasoning as in Theorems 3 and 4 to show that System (36) has a unique continuous solution on $[0, \mathfrak{T}-\tau]$.

We note that the only difference between Equations (16) and (36) is that $G(0)$ is replaced by $Z(r+\tau)$, which does not effect the proof. Thus, System (15) has a unique solution, given by

$$y(t) = \begin{cases} G(t), & t \in (-\tau, 0], \\ Y_1(t), & t \in (0, \tau], \\ Y_2(t-\tau), & t \in (\tau, \mathfrak{T}]. \end{cases} \tag{37}$$

It is clear that $Y(\tau^+) = Y_2(0^+) = Z(\tau^+) = Z(\tau) = Y_1(\tau)$, indicating that Y is continuous at τ. Moreover, $Y(0^+) = Y_1(0^+) = Y_1(0) = G(0) = Y(0)$, showing that Y is also continuous at 0. Conclusively, $Y \in (\mathcal{C}[0, \mathfrak{T}])^{\nu}$. This completes the proof for this case. The same recursive argument can be applied to prove the cases when $\mathfrak{T}$ belongs to $[2\tau, 3\tau]$, $[3\tau, 4\tau]$ and so on, thereby completing the proof. □

4. Transforming DFDEs into Fractional Integral Equations Without Delays

The existence analysis above presents a constructive approach to study DFDEs. Let $n = \text{Ciel}\left(\frac{T}{\tau}\right)$, meaning that $n - 1 < \frac{T}{\tau} \leq n$. Let Y_j represent the solution on the interval $[(j-1)\tau, j\tau]$ for $j = 1, \ldots, n$. As stated previously, for $j < n$, we can define the Fredholem operators related to the system's memory on $[(j-1)\tau, j\tau]$ as follows:

$$\mathfrak{F}_{j\tau}^{\Psi} Y(t) = \frac{1}{\Gamma(\Psi)} \int_{(j-1)\tau}^{j\tau} (t-z)^{\Psi-1} Y_j(z) dz. \tag{38}$$

It should be noted that while this operator utilizes the information of Y at $[(j-1)\tau, j\tau]$, the variable t can take on arbitrary values. In particular, this operator is well-defined for $[0, \infty)$. Consequently, the contribution of Y within the jth interval regarded to the memory of the Fredholm operator (38) is distributed over future time.

Theorem 6. *The memory associated with the fixed interval j is fading as t increases.*

Proof. From Theorem (5), Y_j is continuous. Assume $t_2 > t_1 \geq 1 + j\tau$. Then, $t_2 - z > t_1 - z > 1$ and $(t_2 - z)^{1-\psi_i} > (t_1 - z)^{1-\psi_i} \geq 1$ for $z \in [(j-1)\tau, j\tau]$. Therefore,

$$(t_2 - z)^{\Psi-1}|Y(z)| < (t_1 - z)^{\Psi-1}|Y(z)| \leq 1$$

where the inequities are component-wise. Thus,

$$\mathfrak{F}_{j\tau}^{\Psi}|Y|(t_2) \leq \mathfrak{F}_{j\tau}^{\Psi}|Y|(t_1).$$

Therefore, $\mathfrak{F}_{j\tau}^{\Psi}|Y|$ is decreasing component-wise for $t > 1 + j\tau$. Since Y is continuous, and $(t-z)^{\Psi-1}Y(z) \to [0, \ldots, 0]^T$ uniformly as $t \to \infty$, we conclude that

$$\mathfrak{F}_{j\tau}^{\Psi}Y(t) \to [0, \ldots, 0]^T$$

as $t \to \infty$. This indicates that the memory of jth interval fades to zero. □

Finally, we can define the peak information of $\mathfrak{J}^{\Psi}$ by Volterra operator,

$$\mathfrak{V}_{j\tau}^{\Psi}Y(t) = \frac{1}{\Gamma(\Psi)}\int_{j\tau}^{t}(t-z)^{\Psi-1}Y(z)dz \tag{39}$$

where $t \in [j\tau, (j+1)\tau]$, for $j = 0, \ldots, n-2$, and $t \in [(n-1)\tau, \mathfrak{T}]$ when $j = n-1$. We show that the translation of the peak operator is precisely the RL operator of a translation of Y.

Theorem 7. *For $j = 0, \ldots, n-1$, we have*

$$\mathfrak{V}_{j\tau}^{\Psi}Y(t + j\tau) = \mathfrak{J}^{\Psi}Y(s + j\tau)(t). \tag{40}$$

Proof. Substitute $s = z - j\tau$ into (39). This gives

$$\mathfrak{V}_{j\tau}^{\Psi}Y(t) = \frac{1}{\Gamma(\Psi)}\int_{0}^{t-j\tau}(t - s - j\tau)^{\Psi-1}Y(s + j\tau)ds. \tag{41}$$

Now, consider the value of this operator when t is replaced by $t + j\tau$,

$$\mathfrak{V}_{j\tau}^{\Psi}Y(t + j\tau) = \frac{1}{\Gamma(\Psi)}\int_{0}^{t}(t-s)^{\Psi-1}Y(s + j\tau)ds = \mathfrak{J}^{\Psi}Y(s + j\tau)(t) \tag{42}$$

where $t \in [0, \tau]$ for $j < n-1$ and $t \in [0, \mathfrak{T} - (n-1)\tau]$ if $j = n-1$. □

For convenience, we define $Y_0(t) = G(t)$ on the interval $(-\tau, 0]$. Then, we have the following series of equations: For $t \in (0, \tau]$, Y_1 is given by

$$Y_1(t) = G(0) + \mathfrak{J}^{\Psi}U(s, Y_1(s), Y_0(\Theta(s)))(t), \tag{43}$$

for $t \in (\tau, 2\tau]$, Y_2 is expressed as

$$Y_2(t) = G(0) + \mathfrak{F}_{\tau}^{\Psi}U(s, Y_1(s), Y_0(\Theta(s)))(t) + \mathfrak{V}_{\tau}^{\Psi}U(s, Y_2(s), Y_1(\Theta(s)))(t),$$

and for $j < n$, and $t \in ((j-1)\tau, j\tau]$, Y_j is obtained by

$$\begin{aligned} Y_j(t) =& G(0) + \sum_{i=1}^{j-1} \mathfrak{F}_{i\tau}^{\Psi} U(s, Y_i(s), Y_{i-1}(\Theta(s)))(t) \\ &+ \mathfrak{V}_{(j-1)\tau}^{\Psi} U(s, Y_j(s), Y_{j-1}(\Theta(s)))(t), \end{aligned} \tag{44}$$

For final interval $t \in ((n-1)\tau, \mathfrak{T}]$, where $j = n$, we have

$$\begin{aligned} Y_n(t) =& G(0) + \sum_{i=1}^{n-1} \mathfrak{F}_{i\tau}^{\Psi} U(s, Y_i(s), Y_{i-1}(\Theta(s)))(t) \\ &+ \mathfrak{V}_{(n-1)\tau}^{\Psi} U(s, Y_n(s), Y_{n-1}(\Theta(s)))(t). \end{aligned} \tag{45}$$

We define the tail function as

$$Z_j(t) = G(0) + \sum_{i=1}^{j-1} \mathfrak{F}_{i\tau}^{\Psi} U(s, Y_i(s), Y_{i-1}(\Theta(s)))(t).$$

By using Theorem 7, we obtain integral equations

$$Y_j(t + j\tau) = Z_j(t + j\tau) + \mathfrak{J}^{\Psi} U(s + j\tau, Y_j(s + j\tau), Y_{j-1}(\Theta(s + j\tau)))(t) \tag{46}$$

for $j = 1, \ldots, n-1$, $t \in (0, \tau]$, and $j = n$, $t \in (0, \mathfrak{T} - (n-1)\tau] \subseteq (0, \tau]$. It is clear that Equation (46) is an integral equation with respect to $Y_j(t + j\tau)$.

5. Well-Posedness

The well-posedness of a mathematical problem in the Hadamard sense requires three conditions: existence, uniqueness, and stability. Until now, we have provided the first two conditions. In this section, we investigated the third condition. The stability for the well-posedness of a problem implies that the solution depends continuously to the data. In particular, for initial value problems, the data consists of initial conditions. Here, the given data are a function G which is well-defined at $(-\tau, 0]$. To ensure the stability, let emphasize the dependence of Y to G through $Y(t, G)$. Let $\tilde{Y}(t, \tilde{G})$ be a solution to (46) corresponding with $\tilde{G}$. This implies $\tilde{Y}_0(t) = \tilde{G}(t)$ for $t \in (0, \tau]$ and $\tilde{Y}_j$ satisfies the systems described by (46). To establish well-posedness we need a slightly stronger assumption than (H1). This assumption involves adding Lipschitz continuity for the third parameter of U.

(H4) U is globally Lipschitz continuous with respect to Y and W, i.e., $\exists\, L_i \in \mathbb{R}$, such that

$$|u_i(t, Y, W) - u_i(t, \hat{Y}, \hat{W})| \leq L_i \max\{|Y - \hat{Y}|, |W - \hat{W}|\}$$

for all $t \in [0, \mathfrak{T}]$ and for all $Y, W, \hat{Y}, \hat{W} \in \mathbb{R}^{\nu}$.

Theorem 8. *Let Hypotheses (H2)–(H4) hold. Then, the mild solution of System* (7) *subject to Condition* (5) *is Lipschitz continuous with respect to G on the finite interval* $[0, \mathfrak{T}]$.

Proof. Let $M = \max \frac{L_i}{\Gamma(\alpha_i)}$. Then,

$$\begin{aligned} |Y_1(t) - \tilde{Y}_1(t)| \leq& |G(0) - \tilde{G}(0)| \\ &+ M \int_0^t (t-z)^{\psi^*-1} \max\{|Y_1(z) - \hat{Y}_1(z)|, |G(z) - \hat{G}(z)|\} \end{aligned} \tag{47}$$

for $t \leq 1$, where $\psi^* = \min \psi_i$. Therefore,

$$\begin{aligned}|Y_1(t) - \tilde{Y}_1(t)| \leq & |G(0) - \tilde{G}(0)| \\ & + M \int_0^t (t-z)^{\psi^*-1} |Y_1(z) - \hat{Y}_1(z)| dz \\ & + M \int_0^t (t-\tau)^{\psi^*-1} |G(z) - \hat{G}(z)| dz\end{aligned}$$

for $t \leq 1$. Thus,

$$\begin{aligned}|Y_1(t) - \tilde{Y}_1(t)| \leq & |G(0) - \tilde{G}(0)| + M \int_0^t (t-z)^{\psi^*-1} |Y_1(z) - \hat{Y}_1(z)| dz \\ & + M \int_0^t (t-\tau)^{\psi^*-1} |G(z) - \hat{G}(z)| dz.\end{aligned}$$

It follows that

$$|Y_1(t) - \tilde{Y}_1(t)| \leq \left(1 + \frac{Mt^{\psi^*}}{\psi^*}\right) \|G - \tilde{G}\| + M \int_0^t (t-z)^{\psi^*-1} |Y_1(z) - \hat{Y}_1(z)| dz \tag{48}$$

and, thus,

$$|Y_1(t) - \tilde{Y}_1(t)| \leq \left(1 + \frac{Mt^{\psi^*}}{\psi^*}\right) E_{\psi^*}(M\Gamma(\psi^*) t^{\psi^*}) \|G - \tilde{G}\|. \tag{49}$$

Consequently,

$$|Y_1(t) - \tilde{Y}_1(t)| = C_1 \|G - \tilde{G}\|, \quad t \in [0,1], \tag{50}$$

where $C_1 := \max_{t \in [0,1]} \left(1 + \frac{Mt^{\psi^*}}{\psi^*}\right) E_{\psi^*}(M\Gamma(\psi^*) t^{\psi^*})$. This completes the proof on $[0, \tau]$ when $\tau \leq 1$. Now, consider $\tau \in [0,2]$. For $t > 1$, we have

$$\begin{aligned}|Y_1(t) - \tilde{Y}_1(t)| \leq & |G(0) - \tilde{G}(0)| + M \int_0^t |(t-z)^{\Psi-1}| |Y_1(z) - \hat{Y}_1(z)| dz \\ & + M \int_0^t |(t-z)^{\Psi-1}| |G(z) - \hat{G}(z)| dz \\ \leq & |G(0) - \tilde{G}(0)| + M \int_0^1 |(t-z)^{\Psi-1}| |Y_1(z) - \hat{Y}_1(z)| dz \\ & + M \int_1^t |(t-z)^{\Psi-1}| |Y_1(z) - \hat{Y}_1(z)| dz + M \int_0^t |(t-z)^{\Psi-1}| |G(z) - \hat{G}(z)| dz \\ \leq & \|G - \tilde{G}\| + M \max_{z \in [0,1]} |Y_1(z) - \hat{Y}_1(z)| \Omega + M \int_1^t |(t-z)^{\Psi-1}| |Y_1(z) - \hat{Y}_1(z)| dz \\ & + M \|G - \hat{G}\| \Omega \\ \leq & (1 + MC_1\Omega + M\Omega) \|G - \hat{G}\| + M \int_1^t |(t-z)^{\Psi-1}| |Y_1(z) - \hat{Y}_1(z)| dz\end{aligned} \tag{51}$$

where

$$\Omega := \max_{t \in [0,2]} \int_0^t |(t-z)^{\Psi-1}| dz$$

and, clearly, $\Omega < \infty$. It immediately follows that

$$|Y_1(t+1) - \tilde{Y}_1(t+1)| \leq C_2 \|G - \hat{G}\| + M \int_0^t (t-s)^{\psi^*-1} |Y_1(s+1) - \hat{Y}_1(s+1)| ds \tag{52}$$

for $t \in [0,1]$ where $C_2 = 1 + MC_1\Omega + M\Omega$. By applying the generalized Gronwall inequality, we obtain

$$|Y_1(t+1) - \tilde{Y}_1(t+1)| \leq C_2 E_{\psi^*}(M\Gamma(\psi^*)t^{\psi^*})\|G - \hat{G}\|, \quad t \in [0,1] \tag{53}$$

and, thus,

$$|Y_1(t) - \tilde{Y}_1(t)| \leq C_2 E_{\psi^*}(M\Gamma(\psi^*)(t-1)^{\psi^*})\|G - \hat{G}\|, \quad t \in [1,2]. \tag{54}$$

Particularly, by defining $C_3 = \max\{C_1, \max_{t\in[0,1]} C_2 E_{\psi^*}(M\Gamma(\psi^*)(t-1)^{\psi^*})\}$, we have

$$|Y_1(t) - \tilde{Y}_1(t)| \leq C_3\|G - \hat{G}\|, \quad t \in [0,\tau]. \tag{55}$$

Using the same induction, Equation (55) holds for any $\tau < \infty$. Now we consider the dynamics of the system for $t > \tau$. Suppose that

$$|Y(t) - \tilde{Y}(t)| \leq C\|G - \hat{G}\|, \quad t \in [0,(j-1)\tau], j \geq 1 \tag{56}$$

for some constant C. We provide the same result on $[(j-1)\tau, j\tau]$. We note that, by definition of Z_j,

$$Z_j(t) = G(0) + \frac{1}{\Gamma(\Psi)}\sum_{i=1}^{j-1}\int_{(i-1)\tau}^{i\tau}(t-s)^{\Psi-1}U(s, Y_i(s), Y_{i-1}(\Theta(s)))ds. \tag{57}$$

Thus,

$$\begin{aligned}|Z_j(t) - \tilde{Z}_j(t)| \leq & |G(0) - \tilde{G}(0)| \\ & + M\sum_{i=1}^{j-1}\int_{(i-1)\tau}^{i\tau}|(t-s)^{\Psi-1}|\max\{|Y_i(s) - \tilde{Y}_i|, |Y_{i-1}(\Theta(s)) - \tilde{Y}_{i-1}(\Theta(s))|\}ds\end{aligned} \tag{58}$$

For $i \leq j-1$, based on the assumption, $|Y_i(s) - \tilde{Y}_i| \leq C\|G - \hat{G}\|$ and $|Y_{i-1}(\Theta(s)) - Y_{i-1}(\Theta(s))| \leq C\|G - \hat{G}\|$. Therefore, for $t \in [(j-1)\tau, j\tau]$,

$$\begin{aligned}|Z_j(t) - \tilde{Z}_j(t)| \leq & |G(0) - \tilde{G}(0)| + MC\|G - \hat{G}\|\sum_{i=1}^{j-1}\int_{(i-1)\tau}^{i\tau}|(t-s)^{\Psi-1}|ds \\ \leq & \|G - \tilde{G}\| + MC\|G - \hat{G}\|\int_0^{(j-1)\tau}|(t-s)^{\Psi-1}|ds, \\ \leq & (1 + MC\Omega_j)\|G - \tilde{G}\|\end{aligned} \tag{59}$$

where

$$\Omega_j := \max_{t\in[(j-1)\tau, j\tau]}\int_0^t |(t-z)^{\Psi-1}|dz \leq \infty.$$

Using (46), we obtain

$$\begin{aligned}&|Y_j(j\tau + t) - \tilde{Y}_j(j\tau + t)| \leq |Z_j(j\tau + t) - \tilde{Z}_j(j\tau + t)| \\ &\quad + M\int_0^t |(t-s)^{\Psi-1}|\max\{|Y_i(j\tau + s) - \tilde{Y}_i(j\tau + s)|, |Y_{i-1}(\Theta(s)) - \tilde{Y}_{i-1}(\Theta(j\tau + s))|\}ds \\ &\leq (1 + MC\Omega_j)\|G - \tilde{G}\| \\ &\quad + M\int_0^t |(t-s)^{\Psi-1}|\max\{|Y_i(j\tau + s) - \tilde{Y}_i(j\tau + s)|, |Y_{i-1}(\Theta(j\tau + s)) - \tilde{Y}_{i-1}(\Theta(j\tau + s))|\}ds\end{aligned} \tag{60}$$

This equation is similar to (47). A similar analysis shows that $|Y_j(j\tau + t) - \tilde{Y}_j(j\tau + t)|$ is proportional to $\|G - \tilde{G}\|$. We need prove this separately for τ in $[0,1]$, $[1,2]$, and so

on. We briefly carry the proof for the case $\tau \in [0,1]$, while it is also similar to previous discussions. From (60), we have

$$\begin{aligned}|Y_j(j\tau+t)-\tilde{Y}_j(j\tau+t)| \leq & (1+MC\Omega_j)\|G-\tilde{G}\| \\ & + M\int_0^t |(t-s)^{\psi^*-1}||Y_i(j\tau+s)-\tilde{Y}_i(j\tau+s)|ds \\ & + M\int_0^t |(t-s)^{\psi^*-1}||Y_{i-1}(\Theta(j\tau+s))-\tilde{Y}_{i-1}(\Theta(j\tau+s))|\}ds \\ \leq & (1+MC\Omega_j+\frac{MCt^{\psi^*}}{\psi^*})\|G-\tilde{G}\| \\ & + M\int_0^t |(t-s)^{\psi^*-1}||Y_i(j\tau+s)-\tilde{Y}_i(j\tau+s)|ds\end{aligned} \tag{61}$$

By applying the generalized Gronwall inequality, we obtain

$$|Y_j(j\tau+t)-\tilde{Y}_j(j\tau+t)| \leq (1+MC\Omega_j+\frac{MCt^{\psi^*}}{\psi^*})E_{\psi^*}(M\Gamma(\psi^*)t^{\psi^*})\|G-\tilde{G}\|. \tag{62}$$

This shows that

$$|Y_j(t)-\tilde{Y}_j(t)| \leq C_4\|G-\tilde{G}\|, \quad t \in j\tau+[0,\tau]=[j\tau,(j+1)\tau], \quad \tau \leq 1, \tag{63}$$

where C_4 is a finite constant, defined by

$$C_4 = \max_{t\in[0,1]}(1+MC\Omega_j+\frac{MCt^{\psi^*}}{\psi^*})E_{\psi^*}(M\Gamma(\psi^*)t^{\psi^*}).$$

□

6. Examples and Applications

6.1. Applications in Hopfield Neural Network

An interesting incommensurate system of DFDEs is used in [11] to describe a Hopfield neural network (HNN). HNNs, a form of recurrent artificial neural network, are particularly known for their ability to store and retrieve memory patterns efficiently, making them suitable for numerous practical uses.

In this section, we aim to study the well-posedness of a class of such HNNs. In terms of our notation, such HNNs can be described by the incommensurate System (6), with

$$\begin{aligned}u_1(t,Y,W) &= -0.1y_1+1.5\tanh(w_3)+0.8\tanh(w_4)+1.9\tanh(w_5),\\ u_2(t,Y,W) &= -0.6y_2-0.6\tanh(w_3)-0.5\tanh(w_4)+2.2\tanh(w_5),\\ u_3(t,Y,W) &= -0.1y_3-1.5\tanh(y_1)+2.5\tanh(y_2),\\ u_4(t,Y,W) &= -0.8y_4+0.5\tanh(y_1)-0.8\tanh(y_2),\\ u_5(t,Y,W) &= -1.3y_5+\tanh(y_1)-2\tanh(y_2).\end{aligned} \tag{64}$$

The stability of such systems has been studied in [11]. The hyperbolic tangent function tanh is a Lipschitz continuous function with Lipschitz constant 1. Therefore, the functions u_i for $i=1,\ldots,5$ are also Lipschitz continuous with respect to Y and W. Thus, Hypotheses (H1) and (H4) automatically hold. Particularly, $L_1=\max\{0.1,1.5,0.8,1.9\}=1.9$, $L_2=\max\{0.6,0.5,2.2\}=2.2$, $L_3=\max\{0.1,1.5,2.5\}=2.5$, $L_4=\max\{0.8,0.5\}=0.8$, and $L_5=\max\{1.3,1,2\}=2$. Also, each u_i is continuous with respect to its variable, thus (H2) holds. Assuming that G satisfies (H3), according to Theorem 5, the Hopfield neural network (64) has a unique mild solution. According to Theorem 8, the solution is Lips-

chitz continuous with respect to G, indicating that the Hopfield neural network (64) is well-posed.

6.2. A General Linear Case

Equation (3) represents a linear incommensurate systems of DFDEs with constant coefficients. However, this equation can be generalized to the form with variable coefficients as follows:

$$\mathfrak{D}^{\Psi} Y(t) = A(t)Y(t) + B(t)Y(\Theta(t)) + F(t) \tag{65}$$

where $A \in (\mathcal{C}[0,\mathfrak{T}])^{\nu\times\nu}$ and $B \in (\mathcal{C}[0,\mathfrak{T}])^{\nu\times\nu}$.

In terms of presentations (7), we have

$$U(t,Y,W) = A(t)Y + B(t)W + F(t).$$

Since a_{ij} and b_{ij} are assumed to be continuous, they are bounded on the compact interval $[0,\mathfrak{T}]$. Therefore,

$$L_i = \max_{j=1,\dots,\nu} \{ \max_{t\in[a,b]} |a_{ij}(t)|, \max_{t\in[a,b]} |b_{ij}(t)| \}$$

is a well-defined real number, and Hypothesis (H4) holds with this L_i for all $i = 1,\dots,\nu$. Consequently, according to Theorems 5 and 8, it has a unique continuous mild solution, and the solution is Lipschitz continuous with respect to any continuous G. For instance, a complex system described by

$$\begin{aligned} \mathfrak{D}^{0.5} y_1(t) &= \sin(t)y_1(t) - \exp(t)y_2(t-0.5) + \cos(t), \\ \mathfrak{D}^{0.5} y_2(t) &= \cos(t)y_1(t) - t^2(t)y_2(t-0.5) + |t|, \end{aligned} \tag{66}$$

with prehistoric conditions

$$\begin{aligned} y_1(t) &= t\sin(t), \quad t \in (-0.5, 0], \\ y_2(t) &= t^2 + t + 1, \quad t \in (-0.5, 0], \end{aligned} \tag{67}$$

has a unique solution. This example demonstrates the strength of Theorems 5–8, which imposes no further requirements for well-posedness of such systems. Due to the significance of this example, we add the following corollary for reference in future research.

Corollary 1. *Assume* $A, B, F \in (\mathcal{C}[0,\mathfrak{T}])^{\nu\times\nu}$, $G \in (\mathcal{C}[-\tau,0])^{\nu\times\nu}$, $\tau, \mathfrak{T} > 0$ *and* $\Psi \in (0,1)^{\nu}$. *Then, System* (65) *has a unique mild solution, and is Lipschitz continuous with respect to* G *on* $[0,\mathfrak{T}]$.

Proof. The proof is a straightforward conclusion of Theorems 5–8. □

7. Conclusions and Remaining Works on This Topic

We have demonstrated that the mild solutions of incommensurate systems for DFDEs satisfy delay RL integral equations. To ensure well-posedness, we divided the interval into $[0,\tau]$, $[\tau,2\tau]$, ..., $[(n-1)\tau,\mathfrak{T}]$, and transformed studied integral equations into RL integral equations without delays as described by (46). This decomposition has been utilized throughout the analysis. Then, we proceed by assuming $\tau \in [0,1]$, and extended it for $\tau < \infty$ in any interval $[n, n+1]$, through induction. To obtain the existence result, we used Picard iterations to obtain a sequence of Cauchy continuous functions. We employed the completeness of the space of continuous functions to establish uniform convergence of

such Cauchy sequences. Subsequently, we showed that the limit of the Cauchy sequence satisfies the original RL integral equation. Thus, we have established the existence of a solution. For uniqueness and stability with respect to G, we applied generalized Gronwall inequality. The results of this paper can be summarized as follows.

Theorem 9. *Assume $\psi_i \in (0,1)$, G is continuous function on $(-\tau,0]$, $\lim_{t\to-\tau} G(t) < \infty$, and $0 \leq \tau < \infty$. Additionally, assume that U is a continuous vector-valued function and each component of U is Lipschitz continuous with respect to both the second and third variables. Then, the incommensurate system of DFDEs* (6) *with prehistoric condition* (5) *has a unique solution. Furthermore, this solution is continuously dependent on G.*

While we provided a well-posedness of the problem on the spaces of continuous functions, there are fundamental questions regarding the need to investigated in dynamic of the solution. One key question is related to the regularity of the solutions. In terms of the classical analysis, regularity speaks about the existence and behavior of derivatives of the solution. Knowledge of the differentiability of the solution is crucial for constructing efficient numerical solutions. In the context of wider analysis, regularity speaks about the existence of a solution within a specific space. Studies by Liang and Stynes [21] have investigated the regularity of a wide class of singular Volterra integral equations of the second kind in weighted space $\mathcal{C}^{m,\alpha}$. It is an ongoing area of research related to unified theories for weakly singular integrals (including logarithm singularity and singularity with power function), mainly performed in the past three decades by Vainikko and Pedas [22–24]. Recently, in a book published by Brunner [19], the regularity of the solution of a weakly singular integral equation is studied in detail. Among the related books, this book devotes a chapter to this topic. We hope to investigate the regularity of DFDEs in future studies.

Funding: This research is supported by the Neijiang Normal University school-level science and technology project (key project, No. XJ2024008301).

Data Availability Statement: The original contributions presented in this study are included in the article. Further inquiries can be directed to the corresponding author.

Conflicts of Interest: The author declares no conflicts of interest.

Abbreviations

The following abbreviations are used in this manuscript:

FDEs	Fractional differential equations
DFDEs	delay fractional differential equations
DDEs	delay differentiate equations
HNNs	Hopfield Neural Network

References

1. Diethelm, K.; Ford, N.J. *The Analysis of Fractional Differential Equations*; Lecture Notes in Mathematics; Springer: New York, NY, USA, 2010.
2. Kilbas, A.A.; Srivastava, H.M.; Trujillo, J.J. *Theory and Applications of Fractional Differential Equations*; Elsevier: Amsterdam, The Netherlands, 2006; Volume 204, pp. 1–523.
3. Shiri, B.; Baleanu, D. All linear fractional derivatives with power functions' convolution kernel and interpolation properties. *Chaos Solit. Fractals* **2023**, *2023*, 113399. [CrossRef]
4. Smith, H.L. *An Introduction to Delay Differential Equations with Applications to the Life Sciences*; Springer: New York, NY, USA, 2011.
5. Morgado, M.L.; Ford, N.J.; Lima, P.M. Analysis and numerical methods for fractional differential equations with delay. *J. Comput. Appl. Math.* **2013**, *252*, 159–168. [CrossRef]
6. Čermák, J.; Došlá, Z.; Kisela, T. Fractional differential equations with a constant delay: Stability and asymptotics of solutions. *Appl. Math. Comput.* **2017**, *1*, 336–350. [CrossRef]

7. Huseynov, I.T.; Mahmudov, N.I. Analysis of positive fractional-order neutral time-delay systems. *J. Franklin Inst.* **2022**, *359*, 294–330. [CrossRef]
8. Shiri, B.; Baleanu, D. Numerical solution of some fractional dynamical systems in medicine involving non-singular kernel with vector order. *Res. Nonlinear Anal.* **2019**, *2*, 160–168.
9. Das, S; Gupta, P.K. A mathematical model on fractional Lotka–Volterra equations. *J. Theor. Biol.* **2011**, *277*, 1–6. [CrossRef] [PubMed]
10. Tavazoei, M; Asemani, M.H. On robust stability of incommensurate fractional-order systems. *Commun. Nonlinear Sci. Numer. Simul.* **2020**, *90*, 105–344. [CrossRef]
11. Zhang, Y.; Li L.; Huang, J.; Gorbachev, S.; Aravind, R.V. Exploration on bifurcation for an incommensurate five-neuron fractional-order BAM neural network involving multiple delays. *Phys. D Nonlinear Phenom.* **2024**, *460*, 134047. [CrossRef]
12. Kaslik, E.; Sivasundaram, S. Nonlinear dynamics and chaos in fractional-order neural networks. *Neural Netw.* **2012**, *32*, 245–256. [CrossRef] [PubMed]
13. Karoun, R.C.; Ouannas, A.; Horani, M.A.; Grassi, G. The effect of Caputo fractional variable difference operator on a discrete-time hopfield neural network with non-commensurate order. *Fractal. Fract.* **2022**, *6*, 575. [CrossRef]
14. Deng, W.; Li, C.; Lu, J. Stability analysis of linear fractional differential system with multiple time delays. *Nonlinear Dyn.* **2007**, *48*, 409–416. [CrossRef]
15. Nouri, K.; Nazari, M.; Torkzadeh, L. Numerical approximation of the system of fractional differential equations with delay and its applications. *Eur. Phys. J. Plus.* **2020**, *135*, 1–4. [CrossRef]
16. Čermák, J.; Horníček, J.; Kisela, T. Stability regions for fractional differential systems with a time delay. *Commun. Nonliner Sci. Numer. Simul.* **2016**, *31* 108–123. [CrossRef]
17. Shiri, B.; Shi, Y.G.; Baleanu, D. The Well-Posedness of Incommensurate FDEs in the space of continuous functions. *Symmetry* **2024**, *16*, 1058. [CrossRef]
18. Ye, H.; Gao, J.; Ding, Y. A generalized Gronwall inequality and its application to a fractional differential equation. *J. Math. Anal. Appl.* **2007**, *328*, 1075–1081. [CrossRef]
19. Brunner, H. *Volterra Integral Equations: An Introduction to Theory and Applications*; Cambridge University Press: Cambridge, UK, 2017.
20. Lan, K.; Webb, J.R. A new Bihari inequality and initial value problems of first order fractional differential equations. *Fract. Calc. Appl. Anal.* **2023**, *26*, 962–988. [CrossRef] [PubMed]
21. Liange, H.; Stynes, M. Regularity of the solution of a nonlinear Volterra integral equation of the second kind. *Discret. Contin. Dyn.-Syst.-Ser. B* **2023**, *28*, 2211. [CrossRef]
22. Gennadi, V. *Multidimensional Weakly Singular Integral Equations*; Lecture Notes in Mathematics; Springer: Berlin/Heidelberg, Germany, 1993; p. 1549.
23. Pedas, A.; Vainikko, G. The smoothness of solutions to nonlinear weakly singular integral equations. *Z. Anal. Anwendungen* **1994**, *13*, 463–476. [CrossRef]
24. Hermann, B.; Arvet, P.; Gennadi, V. The piecewise polynomial collocation method for nonlinear weakly singular Volterra equations. *Math. Comp.* **1999**, *68*, 1079–1095.

fractal and fractional

MDPI

Article

Certain Analytic Solutions for Time-Fractional Models Arising in Plasma Physics via a New Approach Using the Natural Transform and the Residual Power Series Methods

Asad Freihat [1], Mohammed Alabedalhadi [1], Shrideh Al-Omari [2,*], Sharifah E. Alhazmi [3], Shaher Momani [4,5] and Mohammed Al-Smadi [1,5,6]

[1] Department of Applied Science, Ajloun College, Al-Balqa Applied University, Ajloun 26816, Jordan; asad.freihat@bau.edu.jo (A.F.); mohmdnh@bau.edu.jo (M.A.); malsmadi@lu.edu.qa (M.A.-S.)
[2] Department of Mathematics, Faculty of Science, Al Balqa Applied University, Salt 19117, Jordan
[3] Department of Mathematics, College of Education for Girls at Al-Qunfudah, Umm Al-Qura University, Mecca 11942, Saudi Arabia; sehazmi@uqu.edu.sa
[4] Department of Mathematics, Faculty of Science, University of Jordan, Amman 11942, Jordan; s.momani@ju.edu.jo
[5] Nonlinear Dynamics Research Center (NDRC), Ajman University, Ajman 20550, United Arab Emirates
[6] College of Commerce and Business, Lusail University, Lusail 9717, Qatar
* Correspondence: shridehalomari@bau.edu.jo; Tel.: +962-772-061-029

Abstract: This paper studies three time-fractional models that arise in plasma physics: the modified Korteweg–deVries–Zakharov–Kuznetsov equation, the stochastic potential Korteweg–deVries equation, and the forced Korteweg–deVries equation. These equations are significant in plasma physics for modeling nonlinear ion acoustic waves and thus helping us to understand wave dynamics in plasmas. We introduce a new approach that relies on a new fractional expansion in the natural transform space and residual power series method to construct analytical solutions to the governing models. We investigate the theoretical analysis of the proposed method for these equations to expose this approach's applicability, efficiency, and effectiveness in constructing analytical solutions to the governing equations. Moreover, we present a comparative discussion between the solutions derived during the work and those given in the literature to confirm that the proposed approach generates analytical solutions that rapidly converge to exact solutions, which proves the effectiveness of the proposed method.

Keywords: fractional model; plasma physics; Korteweg–deVries equation; natural transform; residual power series method

Academic Editors: Libo Feng, Yang Liu and Lin Liu

Received: 26 January 2025
Revised: 21 February 2025
Accepted: 23 February 2025
Published: 28 February 2025

Citation: Freihat, A.; Alabedalhadi, M.; Al-Omari, S.; Alhazmi, S.E.; Momani, S.; Al-Smadi, M. Certain Analytic Solutions for Time-Fractional Models Arising in Plasma Physics via a New Approach Using the Natural Transform and the Residual Power Series Methods. *Fractal Fract.* **2025**, *9*, 152. https://doi.org/10.3390/fractalfract9030152

1. Introduction

Nonlinear wave phenomena are of fundamental importance in the context of physics in general and plasma dynamics in particular [1]. A comprehensive understanding of ion acoustic waves and their behavior is essential for many applications in the context of plasma physics, such as energy transfer, plasma containment, and wave–particle interactions [2,3]. In light of this, many mathematical models have been presented to describe such phenomena, including the Korteweg–de Vries (KdV) equation [4], the nonlinear Schrödinger equation [5], Burgers' equation [6], the Zakharov system [7], the sine-Gordon equation [8], the Benjamin–Bona–Mahony equation [9], the Kadomtsev–Petviashvili equation [10], and others. Since the emergence of the concept of fractional differential and integral calculus and the work carried out by researchers in studying its impact on mathematical systems in various fields of science, researchers have turned their attention to researching

the importance of fractional differential and integral calculus in plasma physics [11,12]. It has been shown that fractional calculations have great importance for the effects of memory and generic properties of systems, which play a prominent role in providing an accurate description of complex plasma dynamics [13,14]. Considering the long-term interactions in plasma systems, the fractional derivative provides a more general approach than classical derivatives, which in turn helps in modeling the wave propagation, diffusion processes, and anomalous transport phenomena that may not be available in standard models to capture the complex behavior of plasma [15]. This enables scientists to gain a deeper understanding of plasma behavior in physical environments and laboratories by developing fractional mathematical models for ion acoustic waves, plasma turbulence, and other nonlinear phenomena [16]. The main interest of this work is to study three important equations in the context of plasma physics: the fractional modified Korteweg–deVries–Zakharov–Kuznetsov (mKdV-ZK) equation, the fractional stochastic potential Korteweg–deVries (spKdV) equation, and the fractional forced Korteweg–deVries (FKdV) equation. We consider the following time-fractional KdV-ZK equation [17]:

$$\mathcal{D}_t^{\alpha}\psi + \mu^2\psi\frac{\partial\psi}{\partial x} + \frac{\partial^3\psi}{\partial x^3} + \frac{\partial^3\psi}{\partial x\partial y^2} + \frac{\partial^3\psi}{\partial x\partial z^2} = 0,\ t \geq 0,\ x, y, z \in \mathbb{R}, \tag{1.1}$$

subject to the initial condition:

$$\psi(x, y, z, 0) = f(x, y, z), x, y, z \in \mathbb{R}, \tag{1.2}$$

where $\mathcal{D}_t^{\alpha}\psi$ represents the Caputo derivative of the electric field potential $\psi(x, y, z, t)$ with respect to the time t of the fractional derivative order $\alpha \in (0, 1]$. The variables x, y and z are the scaled space coordinates, while μ is the dispersion coefficient that stands for positive correlation with negative correlation, Boltzmann distribution, and fluid species. The Korteweg–DeVries–Zakharov–Kuznetsov equation was introduced by the authors [18] with the aim of using the reductive perturbation approach for mixing both warm adiabatic fluids and cold stationary isothermal solid background species in a magnetized plasma where they discussed acoustic electron, acoustic ion, and acoustic dust waves. In Ref. [19], the mKdV-ZK equation is presented using the reductive perturbation approach to control the diagonal diffusion in nonlinear electrostatic modes. In Ref. [20], multiple-soliton solutions for the mKdV-ZK equation were obtained. Solitary solutions were explored using the modified extended direct algebraic method for the mKdV-ZK equation in Ref. [21]. Younas et al. constructed traveling wave solutions by utilizing two different approaches to the mKdV-ZK equation [22]. The second equation considered in this work is the time-fractional spKdV equation [23]:

$$\mathcal{D}_t^{\alpha}\psi + \omega\frac{\partial\psi}{\partial x} + \beta\left(\frac{\partial\psi}{\partial x}\right)^2 + \gamma\frac{\partial^3\psi}{\partial x^3} = 0,\ t \geq 0,\ x \in \mathbb{R}, \tag{1.3}$$

subject to the initial condition:

$$\psi(x, 0) = g(x), x \in \mathbb{R}, \tag{1.4}$$

where ω is the stochastic parameter, β is the nonlinearity coefficient, and γ refers to the dispersion coefficient. Equation (1.3) is a nonlinear model that appears in applications of multicomponent plasmas and electrical circuits and is used to predict the weak dispersive effects on the propagation of nonlinear optical waves and photons. The spKdV equation is presented in Ref. [23], where the authors obtained lumps, breathers, and multi-soliton solutions using the simplified Hirota method and the Cole–Hopf transformation. In Ref. [24],

the authors suggested the fractional spKdV equation and they constructed closed-form solutions for the proposed model. In Ref. [25], the spKdV equation was investigated and the Lie symmetry approach was utilized to carry out the symmetry generators to obtain traveling wave solutions and conservation laws for the proposed model. The final equation that will be investigated in our paper is the following fractional FKdV equation [26]:

$$\frac{1}{c}\mathcal{D}_t^{\alpha}\psi + \left((\mathcal{F}_r - 1) - \frac{3}{2\chi}\psi\right)\frac{\partial\psi}{\partial x} - \frac{\chi^2}{6}\frac{\partial^3\psi}{\partial x^3} = \frac{1}{2}\frac{d\phi(x)}{dx},\ t \geq 0,\ x \in \mathbb{R}, \tag{1.5}$$

subject to the initial condition:

$$\psi(x, 0) = h(x), x \in \mathbb{R}. \tag{1.6}$$

The term $\left((\mathcal{F}_r - 1) - \frac{3}{2\chi}\psi\right)\frac{\partial\psi}{\partial x}$ describes nonlinear interactions in a wave that are measured using the parameter χ which arises from the amplitude of the plasma wave where higher amplitudes affect the wave velocity. The parameter $\mathcal{F}_r$ represents some force or property of the plasma. The term $\frac{1}{2}\frac{d\phi(x)}{dx}$ represents an external influence on the plasma wave such as an electric or magnetic field or any other disturbance. The importance of Equation (1.5) lies in allowing the integration of external forces, memory effects, nonlinearity, and dispersion to model the propagation of nonlinear ion-acoustic waves, as these components are necessary to accurately describe the wave behavior in plasma environments. This model is of great value in many contexts such as astrophysical plasmas affected by large-scale forces, fusion plasmas affected by electric and magnetic fields, and the study of stability and turbulence in plasma systems. In Ref. [26], the authors investigated the fractional FKdV equation to construct traveling wave solutions using the fractional natural decomposition method. The distributed-order time-fractional FKdV equation is presented in Ref. [27], where the authors used the shifted Legendre operational matrix to infer approximate solutions for the proposed model. In Ref. [28], the authors studied the FKdV equation and obtained approximate solutions for the model using the q-homotopy analysis transform technique. The fractional FKdV equation was discussed with the help of the Yang homotopy perturbation method and the Yang transform decomposition method to construct approximate solutions for the model in Ref. [29].

With the wide development in scientific research regarding mathematical systems that describe and model physical phenomena and the emergence and discovery of complex systems in various fields of science, the need to develop methods to derive accurate and approximate solutions for these presented systems arose. Researchers worked to develop such techniques, including the reproducing kernel Hilbert space method [30], the multi-step reduced differential transformation method [31], the Atangana–Baleanu fractional framework for the reproducing kernel technique [32], the multistep generalized differential transform method [33], the homotopy analysis method [34], the shifted Jacobi polynomials method [35], the Chebyshev polynomials method [36], auxiliary equation method [37], the B-spline schemes method [38], the fractional variational iteration method [39–41], the Kudryashov method [42], and others. Abu Arqub et al. [43] presented a new analytical method, the residual power series (RPS) method, for obtaining solitary wave solutions of time-fractional dispersive partial differential equations based on the generalized Taylor series formula and residual error function. Researchers have employed this method to derive analytical solutions for a wide range of fractional equations as it is an effective method [44,45]. In Ref. [46], El-Ajou proposed a new technique that combines the Laplace transform and RPS method, called the Laplace residual power series (LRPS) method, where the proposed method was utilized to explore exact solitary solutions to the nonlinear time-fractional dispersive partial differential equations (PDEs). The main goal of this work

is to suggest a new attractive approach, the natural residual power series (NRPS) method, that depends on the natural transformation and RPS method. Moreover, we seek to utilize the NRPS method to infer analytical solutions for the governing Equations (1.1)–(1.6). The NRPS method is based on using natural transformation to transform the time-fractional differential equation into the natural space, then using a suitable expansion to deal with the newly obtained equation together with the RPS method, which in turn helps in deducing the expansion coefficients based on the concept of limit, which reduces the calculations required to reach accurate approximate solutions to the governing equation.

We organized the paper with the introduction as the first section. Section 2 presents some preliminaries about the Caputo fractional derivative. Section 3 is devoted to introducing the definition of natural transformation and investigating its essential properties, then presenting the natural fractional expansion. In Section 4, we introduce the steps of the proposed method. Applications of the NRPS method to construct approximate solutions for the governing models are introduced in Section 5. Some conclusions are presented in Section 6.

2. Preliminaries

Since the advent of fractional calculus, many fractional operators have appeared, such as the Riemann–Liouville operator [47], the Caputo operator [48], Atangana–Baleanu operator [49], and others. Here, we present the definition of the Caputo fractional derivative and some of its essential properties that are useful in our work.

Definition 1 ([49]). *The Caputo derivative of fractional order $\alpha > 0$ of an integrable function $\psi(t)$ is given by:*

$$\mathcal{D}_t^{\alpha}\psi(t,x) = \frac{1}{\Gamma(k-\alpha)}\int_0^t \frac{\frac{\partial^k \psi(\tau,x)}{\partial \tau^k}}{(t-\tau)^{\alpha-k+1}} d\tau, \tag{2.1}$$

where $t \geq 0$, $k = [\alpha] + 1$. The Riemann–Liouville fractional integral of order α, $Re(\alpha) > 0$ is given by:

$$\mathcal{J}_t^{\alpha}\psi(t) = \frac{1}{\Gamma(\alpha)}\int_0^t (t-\tau)^{\alpha-1}\psi(\tau,x)d\tau. \tag{2.2}$$

Lemma 1 ([49]). *For $\alpha > 0$, $\eta > -1$, $p \in \mathbb{R}$ and $t \geq 0$, the Caputo fractional derivative has the property:*

(a) $\mathcal{D}_t^{\alpha} p = 0.$ (2.3)

(b) $\mathcal{D}_t^{\alpha} t^{\eta} = \frac{\Gamma(\eta+1)}{\Gamma(\eta+1-\alpha)} t^{\eta-\alpha}.$ (2.4)

(c) $\mathcal{D}_t^{\alpha}\mathcal{J}_t^{\alpha}\psi(t,x) = \psi(t,x).$ (2.5)

(d) $\mathcal{J}_t^{\alpha}\mathcal{D}_t^{\alpha}\psi(t,x) = \psi(t,x) - \sum_{i=0}^{k-1} \frac{\partial^i \psi(0^+,x)}{\partial t^i} \frac{t^i}{i!}.$ (2.6)

3. Natural Transformation and Fractional Expansion

The natural transformation combines the features of the Laplace and the Sumudu transforms into a powerful tool for dealing with a variety of differential and integral equations. Natural transformation provides a simple and flexible approach to transforming functions from the time domain to the complex domain, making it powerful for dealing with problems involving fractional time models. Furthermore, the natural transform can handle a wide range of functions with singularities and simplifies the process of finding analytical solutions to complex problems. Therefore, it is considered a valuable tool widely

used in applied mathematics, engineering, and physics [50–54]. The general integral transform of the function $\psi(t,x),\ t,x \in \mathbb{R}$ is defined as:

$$\mathcal{T}\{\psi(t,x)\} = \int_{-\infty}^{\infty} \mathcal{K}(s,t)\psi(t,x)dt, \tag{3.1}$$

where $\mathcal{K}(s,t)$ is the kernel of the transform and s represents the real (complex) number that is independent of t. The Laplace transform, Mellin transform, and Hankel transform can be obtained by letting the kernel of the transform in (3.1) be: $e^{-st},\ t^{s-1}(st)$, and $tJ_n(st)$, respectively. To define the natural transformation, we define the following set:

$$\mathcal{C} = \left\{ \psi(t,x) : \exists\ B,\ \sigma_1,\sigma_2,\ |\psi(t,x)| < Be^{(\frac{|t|}{\sigma_i})}, t \in (-1)^i \times [0,\infty),\ x \in A \subseteq \mathbb{R}, i \in \mathbb{Z}^+ \right\} \tag{3.2}$$

Definition 2 ([51]). *Let $\psi(t,x) \in \mathcal{C}$. The natural transformation of the function $\psi(t,x)$ is defined as:*

$$\Psi(s,w,x) = \mathcal{N}\{\psi(t,x)\} = \int_0^{\infty} e^{-st}\psi(wt,x)dt,\ s,w \in (0,\infty), \tag{3.3}$$

where $\mathcal{N}\{\psi(t,x)\}$ is the natural transformation of $\psi(t,x)$ and the variables s and w are the natural transform variables. The inverse natural transformation of the function $\Psi(s,w,x)$ is defined as follows:

$$\psi(t,x) = \mathcal{N}^{-1}\{\Psi(s,w,x)\} = \frac{1}{2\pi i}\int_{u-i\infty}^{u+i\infty} e^{-\frac{st}{w}}\Psi(s,w,x)ds,\ t \in [0,\infty), \tag{3.4}$$

where the integral is applied for a complex number $s = a + ib$ along $s = u$.

The following theorem shows the existence of natural transformations.

Theorem 1 ([51]). *Let $\psi(t,x) \in \mathcal{C}$ be piecewise continuous on $[0,\infty) \times A$ and of an exponential order $\frac{\theta}{w}$ as $t \to \infty$. Then, the natural transformation of $\psi(t,x)$ exists for all $s \in (\theta,\infty), w \in (0,\infty)$.*

Remark 1. *The Laplace and Sumudu transforms can be obtained by letting $w = 1$ and $s = 1$, respectively, in the natural transform (3.3).*

Remark 2. *Let $\Psi(s,w,x) = \mathcal{N}\{\psi(t,x)\}$ be the natural transform of the function and let*

$$\Psi_L(s,x) = \mathcal{L}\{\psi(t,x)\} = \int_0^{\infty} e^{-st}\psi(t,x)dt,$$

$$\Psi_S(w,x) = \mathcal{S}\{\psi(t,x)\} = \int_0^{\infty} e^{-t}\psi(wt,x)dt,$$

be the Laplace and Sumudu transforms of the function $\psi(t,x)$, respectively. Then, the duality relationship between the Natural-Laplace and Natural-Sumudu transforms is given by:

$$\mathcal{N}\{\psi(t,x)\} = \Psi(s,w,x) = \frac{1}{w}\Psi_L\Big(\frac{s}{w},x\Big), \tag{3.5}$$

$$\mathcal{N}\{\psi(t,x)\} = \Psi(s,w,x) = \frac{1}{s}\Psi_S\Big(\frac{w}{s},x\Big). \tag{3.6}$$

Lemma 2 ([52]). *Let $\psi_1(t,x), \psi_2(t,x) \in \mathcal{C}$ be piecewise continuous on $[0,\infty) \times A$ and of an exponential order $\frac{\theta_1}{w}$ and $\frac{\theta_2}{w}$, respectively, with $\theta_1 < \theta_2$. Then, the natural transform satisfies the following properties:*

$$\text{(i)} \quad \mathcal{N}(1) = \frac{1}{s}. \tag{3.7}$$

$$\text{(ii)} \quad \mathcal{N}\left(t^{k\eta}\right) = \frac{\Gamma(k\eta+1)w^{k\eta}}{s^{k\eta+1}},\ \eta > -1. \tag{3.8}$$

$$\text{(iii)} \quad \mathcal{N}(p_1\psi_1(t,x) + p_2\psi_2(t,x)) = p_1\Psi_1(s,w,x) + p_2\Psi_2(s,w,x),\ p_1, p_2 \in \mathbb{R}. \tag{3.9}$$

$$\text{(iv)} \quad \mathcal{N}^{-1}(p_1\Psi_1(s,w,x) + p_2\Psi_2(s,w,x)) = p_1\psi_1(t,x) + p_2\psi_1(t,x),\ p_1, p_2 \in \mathbb{R}. \tag{3.10}$$

Lemma 3. *Let $\psi(t,x) \in \mathcal{C}$ be piecewise continuous on $[0,\infty) \times A$ and of exponential order $\frac{\theta}{w}$. Then, the natural transform satisfies the following properties:*

$$\text{(i)} \quad \mathcal{N}\left\{\frac{\partial^k}{\partial t^k}\psi(t,x)\right\} = \frac{s^k}{w^k}\Psi(s,w,x) - \sum_{i=0}^{k-1}\frac{s^{k-i-1}}{w^{k-i}}\frac{\partial^i}{\partial t^i}\psi(0,x), k \in \mathbb{Z}. \tag{3.11}$$

$$\text{(ii)} \quad \lim_{s\to\infty} s\Psi(s,w,x) = \psi(0,x). \tag{3.12}$$

$$\text{(iii)} \quad \mathcal{N}\{\mathcal{D}_t^\alpha\psi(t,x)\} = \frac{s^\alpha}{w^\alpha}\Psi(s,w,x) - \frac{s^{\alpha-1}}{w^\alpha}\psi(0,x), 0 < \alpha < 1. \tag{3.13}$$

$$\text{(iv)} \quad \mathcal{N}\left\{\mathcal{D}_t^{k\alpha}\psi(t,x)\right\} = \frac{s^{k\alpha}}{w^{k\alpha}}\Psi(s,w,x) - \sum_{i=0}^{k-1}\frac{s^{(k-i)\alpha-1}}{w^{(k-i)\alpha}}\mathcal{D}_t^{i\alpha}\psi(0,x), 0 < \alpha < 1. \tag{3.14}$$

where $\mathcal{D}_t^{k\alpha} = \mathcal{D}_t^\alpha\mathcal{D}_t^\alpha \ldots \mathcal{D}_t^\alpha$ (k-times).

Proof. The properties (i) can be found in Ref. [48]. To prove (ii), we use the property (i) at $k = 1$, we obtain:

$$\mathcal{N}\left\{\frac{\partial}{\partial t}\psi(t,x)\right\} = \frac{s}{w}\Psi(s,w,x) - \frac{1}{w}\psi(0,x). \tag{3.15}$$

Which gives:

$$s\Psi(s,w,x) = w\int_{-\infty}^{\infty} e^{-st}\frac{\partial}{\partial t}\psi(wt,x)dt + \psi(0,x). \tag{3.16}$$

Taking the limit for both sides of (3.16) as $s \to \infty$ to obtain the property (ii). To prove (iii), we use the following fact for the Sumudu transform for the Caputo fractional derivative:

$$\Psi_S^*(w,x) = \mathcal{S}\{\mathcal{D}_t^\alpha\psi(t,x)\} = \frac{1}{w^\alpha}(\Psi_S(w,x) - \psi(0,x)). \tag{3.17}$$

Substitute $w = \frac{w}{s}$ in (3.17) to obtain:

$$\Psi_S^*\left(\frac{w}{s},x\right) = \frac{s^\alpha}{w^\alpha}\left(\Psi_S\left(\frac{w}{s},x\right) - \psi(0,x)\right). \tag{3.18}$$

Multiply (3.18) by $\frac{1}{s}$, we have:

$$\frac{1}{s}\Psi_S^*\left(\frac{w}{s},x\right) = \frac{s^\alpha}{w^\alpha}\frac{1}{s}\,\Psi_S\left(\frac{w}{s},x\right) - \frac{s^{\alpha-1}}{w^\alpha}\psi(0,x). \tag{3.19}$$

Therefore, using the relationship (3.6) to obtain the property (iii):

$$\mathcal{N}\{\mathcal{D}_t^\alpha\psi(t,x)\} = \frac{s^\alpha}{w^\alpha}\Psi(s,w,x) - \frac{s^{\alpha-1}}{w^\alpha}\psi(0,x). \tag{3.20}$$

We use mathematical induction to verify the property (iv). For $k = 1$, the property is proved in (iii). We assume the formula is satisfied at $k = n$, then we have:

$$\mathcal{N}\{\mathcal{D}_t^{n\alpha}\psi(t,x)\} = \frac{s^{n\alpha}}{w^{n\alpha}}\Psi(s,w,x) - \sum_{i=0}^{n-1}\frac{s^{(n-i)\alpha-1}}{w^{(n-i)\alpha}}\mathcal{D}_t^{i\alpha}\psi(0,x). \tag{3.21}$$

We seek to verify it at $k = n+1$. Now,

$$\mathcal{N}\left\{\mathcal{D}_t^{(n+1)\alpha}\psi(t,x)\right\} = \mathcal{N}\{\mathcal{D}_t^{\alpha}(\mathcal{D}_t^{n\alpha}\psi(t,x))\} = \mathcal{N}\{\mathcal{D}_t^{\alpha}\phi(t,x)\}, \tag{3.22}$$

where $\phi(t,x) = \mathcal{D}_t^{n\alpha}\psi(t,x)$. Using (iii), we obtain:

$$\mathcal{N}\{\mathcal{D}_t^{\alpha}\phi(t,x)\} = \frac{s^{\alpha}}{w^{\alpha}}\mathcal{N}\{\mathcal{D}_t^{n\alpha}\psi(t,x)\} - \frac{s^{\alpha-1}}{w^{\alpha}}\mathcal{D}_t^{n\alpha}\psi(0,x). \tag{3.23}$$

Using (3.21) into (3.23) to infer:

$$\begin{aligned}\mathcal{N}\{\mathcal{D}_t^{\alpha}\phi(t,x)\} = \;& \frac{s^{\alpha}}{w^{\alpha}}\left(\frac{s^{n\alpha}}{w^{n\alpha}}\Psi(s,w,x) - \sum_{i=0}^{n-1}\frac{s^{(n-i)\alpha-1}}{w^{(n-i)\alpha}}\mathcal{D}_t^{i\alpha}\psi(0,x)\right) - \frac{s^{\alpha-1}}{w^{\alpha}}\mathcal{D}_t^{n\alpha}\psi(0,x)\\ &= \frac{s^{(n+1)\alpha}}{w^{(n+1)\alpha}}\Psi(s,w,x) - \sum_{i=0}^{n-1}\frac{s^{(n+1-i)\alpha-1}}{w^{(n+1-i)\alpha}}\mathcal{D}_t^{i\alpha}\psi(0,x) - \frac{s^{\alpha-1}}{w^{\alpha}}\mathcal{D}_t^{n\alpha}\psi(0,x)\\ &= \frac{s^{(n+1)\alpha}}{w^{(n+1)\alpha}}\Psi(s,w,x) - \sum_{i=0}^{n}\frac{s^{(n+1-i)\alpha-1}}{w^{(n+1-i)\alpha}}\mathcal{D}_t^{i\alpha}\psi(0,x).\end{aligned} \tag{3.24}$$

From (3.22) and (3.24), we obtain:

$$\mathcal{N}\left\{\mathcal{D}_t^{(n+1)\alpha}\psi(t,x)\right\} = \frac{s^{(n+1)\alpha}}{w^{(n+1)\alpha}}\Psi(s,w,x) - \sum_{i=0}^{n}\frac{s^{(n+1-i)\alpha-1}}{w^{(n+1-i)\alpha}}\mathcal{D}_t^{i\alpha}\psi(0,x). \tag{3.25}$$

Therefore, the poof is complete. □

The next theorem presents a new fractional expansion which is essential for our proposed method, the NRPS method.

Theorem 2. *Let $\psi(t,x) \in \mathcal{C}$ be piecewise continuous on $[0,\infty) \times A$ and of an exponential order $\frac{\theta}{w}$, and let $\Psi(s,w,x) = \mathcal{N}\{\psi(t,x)\}$ have the following fractional expansion:*

$$\Psi(s,w,x) = \sum_{k=0}^{\infty}\frac{\Pi_k(x)w^{k\alpha}}{s^{1+k\alpha}},\ \alpha \in (0,1], x \in A,\ s \in (\theta,\infty), w \in (0,\infty). \tag{3.26}$$

Then, the coefficients $\Pi_k(x) = \mathcal{D}_t^{k\alpha}\psi(0,x), k = 0,1,2,\ldots$. Consequently, $\psi(t,x)$ can be written in the following fractional Taylor's formula:

$$\psi(t,x) = \sum_{k=0}^{\infty}\frac{\mathcal{D}_t^{k\alpha}\psi(0,x)t^{k\alpha}}{\Gamma(1+k\alpha)}, \alpha \in (0,1], x \in \mathbb{R}, t \in (0,\infty). \tag{3.27}$$

Proof. Assume that $\Psi(s,w,x)$ has the fractional expansion in (3.26). Multiply both sides of (3.26) by s, then take the limit as $s \to \infty$ to obtain:

$$\lim_{s\to\infty} s\Psi(s,w,x) = \lim_{s\to\infty} s\sum_{k=0}^{\infty}\frac{\Pi_k(x)w^{k\alpha}}{s^{1+k\alpha}} = \lim_{s\to\infty}\left(\Pi_0(x) + \sum_{k=1}^{\infty}\frac{\Pi_k(x)w^{k\alpha}}{s^{k\alpha}}\right) = \Pi_0(x).$$

Using (3.12), it is possible to obtain $\Pi_0(x) = \psi(0,x)$. Hence, we can write the fractional expansion (3.26) in the form:

$$\Psi(s,w,x) = \frac{\psi(0,x)}{s} + \sum_{k=1}^{\infty} \frac{\Pi_k(x) w^{k\alpha}}{s^{1+k\alpha}},\ \alpha \in (0,1], x \in \mathbb{R}, s \in (\theta,\infty), w \in (0,\infty). \tag{3.28}$$

Now, multiply both sides of (3.28) by $s^{\alpha+1}$ to obtain:

$$s^{\alpha+1}\Psi(s,w,x) = s^{\alpha}\psi(0,x) + \Pi_1(x)w^{\alpha} + \sum_{k=2}^{\infty} \frac{\Pi_k(x) w^{k\alpha}}{s^{(k-1)\alpha}}. \tag{3.29}$$

Consequently, with the aid of (3.13), we have:

$$\begin{aligned}\Pi_1(x) &= \frac{s^{\alpha+1}}{w^{\alpha}}\Psi(s,w,x) - \frac{s^{\alpha}}{w^{\alpha}}\psi(0,x) - \sum_{k=2}^{\infty} \frac{\Pi_k(x) w^{(k-1)\alpha}}{s^{(k-1)\alpha}} \\ &= s\left(\frac{s^{\alpha}}{w^{\alpha}}\Psi(s,w,x) - \frac{s^{\alpha-1}}{w^{\alpha}}\psi(0,x)\right) - \sum_{k=2}^{\infty} \frac{\Pi_k(x) w^{(k-1)\alpha}}{s^{(k-1)\alpha}} \\ &= s\mathcal{N}\{\mathcal{D}_t^{\alpha}\psi(t,x)\} - \sum_{k=2}^{\infty} \frac{\Pi_k(x) w^{(k-1)\alpha}}{s^{(k-1)\alpha}}.\end{aligned} \tag{3.30}$$

Take the limit as $s \to \infty$ for both sides of (3.30) with the aid of (3.12) to infer:

$$\Pi_1(x) = \lim_{s\to\infty} s\mathcal{N}\{\mathcal{D}_t^{\alpha}\psi(t,x)\} = \mathcal{D}_t^{\alpha}\psi(0,x). \tag{3.31}$$

To find $\Pi_2(x)$, multiply both sides of (3.28) by $s^{2\alpha+1}$ to obtain:

$$s^{2\alpha+1}\Psi(s,w,x) = s^{2\alpha}\psi(0,x) + s^{\alpha}\Pi_1(x)w^{\alpha} + \Pi_2(x)w^{2\alpha} + \sum_{k=3}^{\infty} \frac{\Pi_k(x) w^{k\alpha}}{s^{(k-2)\alpha}}. \tag{3.32}$$

Thus, using (3.31) and (3.14), we infer:

$$\begin{aligned}\Pi_2(x) &= \frac{s^{2\alpha+1}}{w^{2\alpha}}\Psi(s,w,x) - \frac{s^{2\alpha}}{w^{2\alpha}}\psi(0,x) - \frac{s^{\alpha}\Pi_1(x)}{w^{\alpha}} - \sum_{k=3}^{\infty} \frac{\Pi_k(x) w^{(k-2)\alpha}}{s^{(k-2)\alpha}} \\ &= s\left(\frac{s^{2\alpha}}{w^{2\alpha}}\Psi(s,w,x) - \frac{s^{2\alpha-1}}{w^{2\alpha}}\psi(0,x) - \frac{s^{\alpha-1}\mathcal{D}_t^{\alpha}\psi(0,x)}{w^{\alpha}}\right) - \sum_{k=3}^{\infty} \frac{\Pi_k(x) w^{(k-2)\alpha}}{s^{(k-2)\alpha}} \\ &= s\mathcal{N}\left\{\mathcal{D}_t^{2\alpha}\psi(t,x)\right\} - \sum_{k=3}^{\infty} \frac{\Pi_k(x) w^{(k-2)\alpha}}{s^{(k-2)\alpha}}.\end{aligned} \tag{3.33}$$

Take the limit as $s \to \infty$ for both sides of (3.33) with the aid of (3.12) to obtain:

$$\Pi_2(x) = \lim_{s\to\infty} s\mathcal{N}\left\{\mathcal{D}_t^{2\alpha}\psi(t,x)\right\} = \mathcal{D}_t^{2\alpha}\psi(0,x). \tag{3.34}$$

Now, we use the induction to complete the proof. Then, assume that $\Pi_k(x) = \mathcal{D}_t^{k\alpha}\psi(0,x), k = 0,1,2,\ldots,n$. Then, the fractional expansion (3.28) can be written as:

$$\Psi(s,w,x) = \frac{\psi(0,x)}{s} + \sum_{k=1}^{n} \frac{\mathcal{D}_t^{k\alpha}\psi(0,x) w^{k\alpha}}{s^{1+k\alpha}} + \frac{\Pi_{n+1}(x) w^{(n+1)\alpha}}{s^{1+(n+1)\alpha}} + \sum_{k=n+2}^{\infty} \frac{\Pi_k(x) w^{k\alpha}}{s^{1+k\alpha}}. \tag{3.35}$$

To find the coefficient $\Pi_{n+1}(x)$, we multiply both sides of (3.35) by $s^{(n+1)\alpha+1}$, one has:

$$
\begin{aligned}
&s^{(n+1)\alpha+1}\Psi(s,w,x)\\
&\quad= s^{(n+1)\alpha}\psi(0,x)+\sum_{k=1}^{n}\frac{\mathcal{D}_t^{k\alpha}\psi(0,x)w^{k\alpha}}{s^{(k-n-1)\alpha}}+\Pi_{n+1}(x)w^{(n+1)\alpha}\\
&\quad+\sum_{k=n+2}^{\infty}\frac{\Pi_k(x)w^{k\alpha}}{s^{(k-n-1)\alpha}}.
\end{aligned}
\tag{3.36}
$$

Consequently, with the aid of (3.14), we obtain:

$$
\begin{aligned}
\Pi_{n+1}(x)&=\frac{s^{(n+1)\alpha+1}}{w^{(n+1)\alpha}}\Psi(s,w,x)-\frac{s^{(n+1)\alpha}}{w^{(n+1)\alpha}}\psi(0,x)-\sum_{k=1}^{n}\frac{\mathcal{D}_t^{k\alpha}\psi(0,x)s^{(n+1-k)\alpha}}{w^{(n+1-k)\alpha}}-\sum_{k=n+2}^{\infty}\frac{\Pi_k(x)w^{(k-n-1)\alpha}}{s^{(k-n-1)\alpha}}\\
&=s\left(\frac{s^{(n+1)\alpha}}{w^{(n+1)\alpha}}\Psi(s,w,x)-\frac{s^{(n+1)\alpha-1}}{w^{(n+1)\alpha}}\psi(0,x)-\sum_{k=1}^{n}\frac{\mathcal{D}_t^{k\alpha}\psi(0,x)s^{(n+1-k)\alpha-1}}{w^{(n+1-k)\alpha}}\right)\\
&-\sum_{k=n+2}^{\infty}\frac{\Pi_k(x)w^{(k-n-1)\alpha}}{s^{(k-n-1)\alpha}}=s\mathcal{N}\left\{\mathcal{D}_t^{(n+1)\alpha}\psi(t,x)\right\}-\sum_{k=n+2}^{\infty}\frac{\Pi_k(x)w^{(k-n-1)\alpha}}{s^{(k-n-1)\alpha}}.
\end{aligned}
\tag{3.37}
$$

Take the limit as $s\to\infty$ for both sides of (3.37) with the aid of (3.12) to obtain:

$$
\Pi_{n+1}(x)=\lim_{s\to\infty}s\mathcal{N}\left\{\mathcal{D}_t^{(n+1)\alpha}\psi(t,x)\right\}=\mathcal{D}_t^{(n+1)\alpha}\psi(0,x).
\tag{3.38}
$$

Which prove that $\Pi_k(x)=\mathcal{D}_t^{k\alpha}\psi(0,x), k=0,\ 1,\ 2,\ldots..$ Hence, the function $\Psi(s,w,x)$ can be written as:

$$
\Psi(s,w,x)=\sum_{k=0}^{\infty}\frac{\mathcal{D}_t^{k\alpha}\psi(0,x)w^{k\alpha}}{s^{1+k\alpha}},\ \alpha\in(0,1], x\in A,\ s\in(\theta,\infty), w\in(0,\infty).
\tag{3.39}
$$

Take the inverse natural transform of (3.39) with the aid of (3.8) to obtain:

$$
\psi(t,x)=\sum_{k=0}^{\infty}\frac{\mathcal{D}_t^{k\alpha}\psi(0,x)t^{k\alpha}}{\Gamma(1+k\alpha)}, \alpha\in(0,1], x\in\mathbb{R}, t\in(0,\infty).
\tag{3.40}
$$

Which completes the proof. □

We are now going to prove that the fractional expansion for $\Psi(s,w,x)$ in (3.26) converges under certain conditions.

Theorem 3. *Let $\psi(t,x)\in\mathcal{C}$ be piecewise continuous on $[0,\infty)\times A$ and of an exponential order $\frac{\theta}{w}$, and let $\Psi(s,w,x)=\mathcal{N}\{\psi(t,x)\}$ have the fractional expansion (3.26). Then, the reminder $\mathfrak{R}_{\mathcal{K}}(s,w,x)$ of (3.26) is satisfied:*

$$
|\mathfrak{R}_{\mathcal{K}}(s,w,x)|\leq\frac{w^{(\mathcal{K}+1)\alpha}}{s^{(\mathcal{K}+1)\alpha+1}}\mathfrak{M}(x),\ \alpha\in(0,1], x\in A,\ s\in(\theta,\theta^*], w\in(0,\infty),
\tag{3.41}
$$

provided that:

$$
\left|s\mathcal{N}\left\{\mathcal{D}_t^{(\mathcal{K}+1)\alpha}\psi(t,x)\right\}\right|\leq\mathfrak{M}(x),\ \alpha\in(0,1], x\in A,\ s\in(\theta,\theta^*], w\in(0,\infty).
\tag{3.42}
$$

Proof. The reminder $\mathfrak{R}_k(s,w,x)$ of the fractional expansion (3.26) can be written as:

$$
\mathfrak{R}_{\mathcal{K}}(s,w,x)=\Psi(s,w,x)-\sum_{k=0}^{\mathcal{K}}\frac{\mathcal{D}_t^{k\alpha}\psi(0,x)w^{k\alpha}}{s^{1+k\alpha}}.
\tag{3.43}
$$

Multiply both sides of (3.43) by $\frac{s^{(\mathcal{K}+1)\alpha+1}}{w^{(\mathcal{K}+1)\alpha}}$; with the aid of (3.14) we obtain:

$$\begin{aligned}\frac{s^{(\mathcal{K}+1)\alpha+1}}{w^{(\mathcal{K}+1)\alpha}}\mathfrak{R}_{\mathcal{K}}(s,w,x) &= \frac{s^{(\mathcal{K}+1)\alpha+1}}{w^{(\mathcal{K}+1)\alpha}}\Psi(s,w,x) - \sum_{k=0}^{\mathcal{K}}\frac{\mathcal{D}_t^{k\alpha}\psi(0,x)s^{(\mathcal{K}+1-k)\alpha}}{w^{(\mathcal{K}+1-k)\alpha}}\\ &= s\left(\frac{s^{(\mathcal{K}+1)\alpha}}{w^{(\mathcal{K}+1)\alpha}}\Psi(s,w,x) - \sum_{k=0}^{\mathcal{K}}\frac{\mathcal{D}_t^{k\alpha}\psi(0,x)s^{(\mathcal{K}+1-k)\alpha-1}}{w^{(\mathcal{K}+1-k)\alpha}}\right)\\ &= s\mathcal{N}\left\{\mathcal{D}_t^{(\mathcal{K}+1)\alpha}\psi(t,x)\right\}.\end{aligned} \tag{3.44}$$

Using (3.42) and (3.44), we obtain the result in (3.41). □

4. A Description of the Proposed NRPS Method

This section is devoted to presenting the NRPS method to establish approximate solutions to the nonlinear fractional PDE:

$$\mathcal{D}_t^{\alpha}\psi(t,x) = \mathcal{G}_x[\psi(t,x)],\ \alpha \in (0,1], x \in A, t \geq 0, \tag{4.1}$$

with the initial condition:

$$\psi(0,x) = g(x), x \in A. \tag{4.2}$$

The symbol $\mathcal{G}_x$ denotes a nonlinear operator relative to the x of degree $r, x \in A, t \geq 0$, $\mathcal{D}_t^{\alpha}$ refers to the α-th Caputo fractional derivative for $\alpha \in (0,1]$, and $\psi(t,x)$ is an unknown function to be determined. To obtain the desired analytical solution for (4.1)–(4.2) using the NRPS method, we can perform the following steps:

Step 1. Apply the natural transformation for both sides of (4.1) by taking advantage of the facts in Lemmas 2 and 3, we obtain:

$$\Psi(s,w,x) - \frac{1}{s}g(x) - \frac{w^{\alpha}}{s^{\alpha}}\mathcal{N}\left\{\mathcal{G}_x\left[\mathcal{N}^{-1}\{\Psi(s,w,x)\}\right]\right\} = 0,\ \alpha \in (0,1], x \in A,\ s \in (\theta,\infty), w \in (0,\infty), \tag{4.3}$$

where $\Psi(s,w,x) = \mathcal{N}\{\psi(t,x), x \in A, s \in (\theta,\infty), w \in (0,\infty)\}$.

Step 2. Suppose that the solution of (4.3) can be written in the following expansion:

$$\Psi(s,w,x) = \sum_{k=0}^{\infty}\frac{\Pi_k(x)w^{k\alpha}}{s^{1+k\alpha}},\ \alpha \in (0,1], x \in A,\ s \in (\theta,\infty), w \in (0,\infty). \tag{4.4}$$

Define the $\mathcal{K}$th truncated series of $\Psi(s,w,x)$ as:

$$\Psi_{\mathcal{K}}(s,w,x) = \sum_{k=0}^{\mathcal{K}}\frac{\Pi_k(x)w^{k\alpha}}{s^{1+k\alpha}},\ \alpha \in (0,1], x \in A,\ s \in (\theta,\infty), w \in (0,\infty). \tag{4.5}$$

Using the results in Theorem 2, we deduce that the initial guess $\Pi_0(x) = g(x)$. Upon this fact, we write the $\mathcal{K}$th truncated series of $\Psi(s,w,x)$ as:

$$\Psi_{\mathcal{K}}(s,w,x) = \frac{g(x)}{s} + \sum_{k=1}^{\mathcal{K}}\frac{\Pi_k(x)w^{k\alpha}}{s^{1+k\alpha}},\ \alpha \in (0,1], x \in A,\ s \in (\theta,\infty), w \in (0,\infty). \tag{4.6}$$

Step 3. We define the so-called natural residual function (NRF) as:

$$\begin{aligned}\mathcal{N}Res(s,w,x) = \Psi(s,w,x) - \tfrac{1}{s}g(x) - \tfrac{w^{\alpha}}{s^{\alpha}}\mathcal{N}\{\mathcal{G}_x[\mathcal{N}^{-1}\{\Psi(s,w,x)\}]\}, \alpha\\ \in (0,1], x \in A,\ s \in (\theta,\infty), w \in (0,\infty),\end{aligned} \tag{4.7}$$

and the $\mathcal{K}$th truncated NRF as:

$$\mathcal{N}Res_{\mathcal{K}}(s,w,x) = \Psi_{\mathcal{K}}(s,w,x) - \frac{1}{s}g(x) - \frac{w^{\alpha}}{s^{\alpha}}\mathcal{N}\{\mathcal{G}_x[\mathcal{N}^{-1}\{\Psi_{\mathcal{K}}(s,w,x)\}]\}, \ \alpha \in (0,1], x \in A, \ s \in (\theta,\infty), w \in (0,\infty), \tag{4.8}$$

Now, we introduce some essential facts to obtain the desired coefficients $\Pi_k(x)$ in the expansion (4.6).

Remark 3. *The NRF and the $\mathcal{K}$th truncated NRF in (4.7) and (4.8), respectively, satisfy the following properties:*

(i) $\mathcal{N}Res(s,w,x) = 0, x \in A, s \in (\theta,\infty), w \in (0,\infty).$ (4.9)

(ii) $\lim_{k\to\infty}\mathcal{N}Res_{\mathcal{K}}(s,w,x) = \mathcal{N}Res(s,w,x), x \in A, \ s \in (\theta,\infty), w \in (0,\infty).$ (4.10)

(iii) $\lim_{s\to\infty} s^{1+\mathcal{K}\alpha}\mathcal{N}Res_{\mathcal{K}}(s,w,x) = 0, \ \mathcal{K} = 1,2,\ldots, x \in A, \ s \in (\theta,\infty), w \in (0,\infty).$ (4.11)

Proof. The properties (i) and (ii) are clear. To prove (iii), we represent the NRF (4.7) in fractional expansion as:

$$\mathcal{N}Res(s,w,x) = \sum_{k=1}^{\infty}\frac{\left(\Pi_k(x) - \mathcal{G}_x^{(k)}[\Pi_i(x)]\right)w^{k\alpha}}{s^{1+k\alpha}}, \ \alpha \in (0,1], x \in A, \ s \in (\theta,\infty), w \in (0,\infty), \ i \in \{0,1,2,\ldots,k-1\}, \tag{4.12}$$

where $\mathcal{G}_x^{(k)}, k = 1,2,3,\ldots$ are differential operators related to the x of degree r. Using (4.9), we obtain $\Pi_k(x) - \mathcal{G}_x^{(k)}[\Pi_i(x)] = 0$ for $k = 1,2,3,\ldots$ and $i \in \{0,1,2,\ldots,k-1\}$. Substitute the $\mathcal{K}$th truncated series $\Psi_{\mathcal{K}}(s,w,x)$ into (4.12) that can be written in the following expression:

$$\mathcal{N}Res_{\mathcal{K}}(s,w,x) = \sum_{k=1}^{\mathcal{K}}\frac{\left(\Pi_k(x) - \mathcal{G}_x^{(k)}[\Pi_i(x)]\right)w^{k\alpha}}{s^{1+k\alpha}} + \sum_{k=\mathcal{K}+1}^{\mathcal{K}r+1}\frac{\left(\Pi_k(x) - \mathcal{G}^{*(\mathcal{K}k)}_x[\Pi_j(x)]\right)w^{k\alpha}}{s^{1+k\alpha}}, \tag{4.13}$$

where $i \in \{0,1,2,\ldots,k-1\}, j \in \{0,1,2,\ldots,\mathcal{K}\}$, and $\mathcal{G}^{*(\mathcal{K}k)}_x, k = \mathcal{K}+1, \mathcal{K}+2,\ldots,\mathcal{K}r+1$ are differential operators related to x and $\Pi_k(x) - \mathcal{G}^{*(\mathcal{K}k)}_x[\Pi_j(x)] \neq 0$. By multiplying both sides of (4.13) by $s^{1+k\alpha}$ and taking the limit as $s \to \infty$, we obtain:

$$\lim_{s\to\infty} s^{1+k\alpha}\mathcal{N}Res_k(s,w,x) = \left(\Pi_k(x) - \mathcal{G}_x^{(k)}[\Pi_i(x)]\right)w^{k\alpha} = 0, \ k = 1,2,\ldots,i \in \{0,1,2,\ldots,k-1\}. \tag{4.14}$$

Step 4. Substitute the $\mathcal{K}$th truncated series $\Psi_{\mathcal{K}}(s,w,x)$ in (4.6) into the $\mathcal{K}$th truncated NRF (4.8).

Step 5. To determine the coefficients $\Pi_k(x), \ k = 1,2,\ldots,\mathcal{K}$, we solve the system that was obtained using $\lim_{s\to\infty} s^{1+k\alpha}\mathcal{N}Res_k(s,w,x) = 0, k = 1,2,\ldots,\mathcal{K}$ and collect the results into the $\mathcal{K}$th truncated series $\Psi_{\mathcal{K}}(s,w,x)$ in (4.6).

Step 6. Apply the inverse natural operator for both sides of the inferred $\mathcal{K}$th truncated series $\Psi_{\mathcal{K}}(s,w,x)$ to obtain the $\mathcal{K}$th approximate solution for the nonlinear fractional PDE (4.1). □

5. Applications

In this section, we investigate the time-fractional KdV-ZK Equations (1.1) and (1.2), the time-fractional spKdV Equations (1.3) and (1.4), and the fractional FKdV E quations (1.5) and (1.6) using the proposed NRPS method. We used the mathematical software package Mathematica 13 to implement all symbolic and numerical computations.

Application 1. *Consider the time-fractional KdV-ZK equation [17]:*

$$\mathcal{D}_t^{\alpha}\psi + 36\psi\frac{\partial\psi}{\partial x} + \frac{\partial^3\psi}{\partial x^3} + \frac{\partial^3\psi}{\partial x\partial y^2} + \frac{\partial^3\psi}{\partial x\partial z^2} = 0,\ t \geq 0,\ x, y, z \in \mathbb{R}, \tag{5.1}$$

subject to the initial condition:

$$\psi(0, x, y, z) = \frac{1}{\sqrt{2}}\text{sech}(x + y + z), x, y, z \in \mathbb{R}. \tag{5.2}$$

Apply the natural transformation for both sides of (5.1) with the aid of (3.13) to obtain:

$$\begin{aligned}\frac{s^{\alpha}}{w^{\alpha}}\Psi(s, w, x, y, z) - \frac{s^{\alpha-1}}{w^{\alpha}}\psi(0, x, y, z) + 36\mathcal{N}\left\{\mathcal{N}^{-1}\{\Psi(s, w, x, y, z)\}\frac{\partial}{\partial x}\mathcal{N}^{-1}\{\Psi(s, w, x, y, z)\}\right\}\\ +\mathcal{N}\left\{\frac{\partial^3}{\partial x^3}\mathcal{N}^{-1}\{\Psi(s, w, x, y, z)\}\right\} + \mathcal{N}\left\{\frac{\partial^3}{\partial x\partial y^2}\mathcal{N}^{-1}\{\Psi(s, w, x, y, z)\}\right\}\\ +\mathcal{N}\left\{\frac{\partial^3}{\partial x\partial z^2}\mathcal{N}^{-1}\{\Psi(s, w, x, y, z)\}\right\} = 0,\end{aligned} \tag{5.3}$$

where $\Psi(s, w, x, y, z) = \mathcal{N}\{\psi(t, x, y, z)\}$. *Using (5.2) in (5.3), we obtain:*

$$\begin{aligned}\Psi(s, w, x, y, z) - \ & \frac{1}{s\sqrt{2}}\text{sech}(x + y + z)\\ & +\frac{w^{\alpha}}{s^{\alpha}}\left(36\mathcal{N}\left\{\mathcal{N}^{-1}\{\Psi(s, w, x, y, z)\}\frac{\partial}{\partial x}\mathcal{N}^{-1}\{\Psi(s, w, x, y, z)\}\right\}\right.\\ & +\mathcal{N}\left\{\frac{\partial^3}{\partial x^3}\mathcal{N}^{-1}\{\Psi(s, w, x, y, z)\}\right\}\\ & +\mathcal{N}\left\{\frac{\partial^3}{\partial x\partial y^2}\mathcal{N}^{-1}\{\Psi(s, w, x, y, z)\}\right\}\\ & \left.+\mathcal{N}\left\{\frac{\partial^3}{\partial x\partial z^2}\mathcal{N}^{-1}\{\Psi(s, w, x, y, z)\}\right\}\right) = 0,\end{aligned} \tag{5.4}$$

Suppose that the solution of (5.4) can be written in the following expansion:

$$\Psi(s, w, x, y, z) = \sum_{k=0}^{\infty}\frac{\Pi_k(x, y, z)w^{k\alpha}}{s^{1+k\alpha}},\ \alpha \in (0, 1], x, y, z \in A,\ s \in (\theta, \infty), w \in (0, \infty). \tag{5.5}$$

Define the $\mathcal{K}$*th truncated series of* $\Psi(s, w, x, y, z)$ *as:*

$$\Psi_{\mathcal{K}}(s, w, x, y, z) = \sum_{k=0}^{\mathcal{K}}\frac{\Pi_k(x, y, z)w^{k\alpha}}{s^{1+k\alpha}},\ \alpha \in (0, 1], x, y, z \in A,\ s \in (\theta, \infty), w \in (0, \infty). \tag{5.6}$$

Using the results in Theorem 2, we deduce that the initial guess $\Pi_0(x, y, z) = \sqrt{\frac{1}{2}}sech((x + y + z))$. *Upon this fact, we write the* $\mathcal{K}$*th truncated series of* $\Psi(s, w, x, y, z)$ *as:*

$$\Psi_{\mathcal{K}}(s, w, x, y, z) = \frac{1}{s\sqrt{2}}\text{sech}(x + y + z) + \sum_{k=1}^{\mathcal{K}}\frac{\Pi_k(x, y, z)w^{k\alpha}}{s^{1+k\alpha}}. \tag{5.7}$$

We define the NRF as:

$$\begin{aligned}&\mathcal{N}Res(s,w,x,y,z)\\&\quad=\Psi(s,w,x,y,z)-\tfrac{1}{s\sqrt{2}}\mathrm{sech}(x+y+z)\\&\quad+\tfrac{w^{\alpha}}{s^{\alpha}}\Big(36\mathcal{N}\Big\{\mathcal{N}^{-1}\{\Psi(s,w,x,y,z)\}\tfrac{\partial}{\partial x}\mathcal{N}^{-1}\{\Psi(s,w,x,y,z)\}\Big\}\\&\quad+\mathcal{N}\Big\{\tfrac{\partial^3}{\partial x^3}\mathcal{N}^{-1}\{\Psi(s,w,x,y,z)\}\Big\}\\&\quad+\mathcal{N}\Big\{\tfrac{\partial^3}{\partial x\partial y^2}\mathcal{N}^{-1}\{\Psi(s,w,x,y,z)\}\Big\}\\&\quad+\mathcal{N}\Big\{\tfrac{\partial^3}{\partial x\partial z^2}\mathcal{N}^{-1}\{\Psi(s,w,x,y,z)\}\Big\}\Big),\end{aligned}\tag{5.8}$$

and the $\mathcal{K}$th truncated NRF as:

$$\begin{aligned}&\mathcal{N}Res_{\mathcal{K}}(s,w,x,y,z)\\&\quad=\Psi_{\mathcal{K}}(s,w,x,y,z)-\tfrac{1}{s\sqrt{2}}\mathrm{sech}(x+y+z)\\&\quad+\tfrac{w^{\alpha}}{s^{\alpha}}\Big(36\mathcal{N}\Big\{\mathcal{N}^{-1}\{\Psi_{\mathcal{K}}(s,w,x,y,z)\}\tfrac{\partial}{\partial x}\mathcal{N}^{-1}\{\Psi_{\mathcal{K}}(s,w,x,y,z)\}\Big\}\\&\quad+\mathcal{N}\Big\{\tfrac{\partial^3}{\partial x^3}\mathcal{N}^{-1}\{\Psi_{\mathcal{K}}(s,w,x,y,z)\}\Big\}\\&\quad+\mathcal{N}\Big\{\tfrac{\partial^3}{\partial x\partial y^2}\mathcal{N}^{-1}\{\Psi_{\mathcal{K}}(s,w,x,y,z)\}\Big\}\\&\quad+\mathcal{N}\Big\{\tfrac{\partial^3}{\partial x\partial z^2}\mathcal{N}^{-1}\{\Psi_{\mathcal{K}}(s,w,x,y,z)\}\Big\}\Big).\end{aligned}\tag{5.9}$$

For $\mathcal{K}=1$, we obtain the 1st NRF with using (5.7) as follows:

$$\begin{aligned}&\mathcal{N}Res_1(s,w,x,y,z)\\&\quad=\tfrac{\Pi_1(x,y,z)w^{\alpha}}{s^{1+\alpha}}\\&\quad+\tfrac{w^{\alpha}}{s^{\alpha}}\Big(36\mathcal{N}\Big\{\mathcal{N}^{-1}\Big\{\tfrac{1}{s\sqrt{2}}\mathrm{sech}(x+y+z)+\tfrac{\Pi_1(x,y,z)w^{\alpha}}{s^{1+\alpha}}\Big\}\tfrac{\partial}{\partial x}\mathcal{N}^{-1}\Big\{\tfrac{1}{s\sqrt{2}}\mathrm{sech}(x+y+z)\\&\quad+\tfrac{\Pi_1(x,y,z)w^{\alpha}}{s^{1+\alpha}}\Big\}\Big\}+\mathcal{N}\Big\{\tfrac{\partial^3}{\partial x^3}\mathcal{N}^{-1}\Big\{\tfrac{1}{s\sqrt{2}}\mathrm{sech}(x+y+z)+\tfrac{\Pi_1(x,y,z)w^{\alpha}}{s^{1+\alpha}}\Big\}\Big\}\\&\quad+\mathcal{N}\Big\{\tfrac{\partial^3}{\partial x\partial y^2}\mathcal{N}^{-1}\Big\{\tfrac{1}{s\sqrt{2}}\mathrm{sech}(x+y+z)+\tfrac{\Pi_1(x,y,z)w^{\alpha}}{s^{1+\alpha}}\Big\}\Big\}\\&\quad+\mathcal{N}\Big\{\tfrac{\partial^3}{\partial x\partial z^2}\mathcal{N}^{-1}\Big\{\tfrac{1}{s\sqrt{2}}\mathrm{sech}(x+y+z)+\tfrac{\Pi_1(x,y,z)w^{\alpha}}{s^{1+\alpha}}\Big\}\Big\}\Big).\end{aligned}\tag{5.10}$$

By multiplying both sides of (5.10) by $s^{1+\alpha}$ and using $\lim_{s\to\infty}s^{1+\alpha}\mathcal{N}Res_1(s,w,x)=0$, we obtain:

$$\Pi_1(x,y,z)=3\sqrt{3}\mathrm{sech}(x+y+z)\tanh(x+y+z).\tag{5.11}$$

Similarly, we can obtain the following:

$$\Pi_2(x,y,z)=\frac{9}{2}\sqrt{3}(-3+\cosh(2(x+y+z)))\mathrm{sech}(x+y+z)^3.\tag{5.12}$$

$$\Pi_3(x,y,z)=\frac{27}{4}\sqrt{3}\mathrm{sech}(x+y+z)^4(-23\sinh(x+y+z)+\sinh(3(x+y+z))).\tag{5.13}$$

$$\Pi_4(x,y,z)=\frac{81\sqrt{3}}{8}(115-76\cosh(2(x+y+z))+\cosh(4(x+y+z)))\mathrm{sech}(x+y+z)^5.\tag{5.14}$$

The CPU time that is needed to obtain these results (5.11)–(5.14) was 35.390625 *s. Substitute (5.11)–(5.14) into (5.7) to obtain the $\mathcal{K}$th truncated series of $\Psi(s,w,x)$ as:*

$$\begin{aligned}\Psi_{\mathcal{K}}(s,w,x,y,z)=&\tfrac{1}{s\sqrt{2}}\mathrm{sech}(x+y+z)+\tfrac{\Pi_1(x,y,z)w^{\alpha}}{s^{1+\alpha}}+\tfrac{\Pi_2(x,y,z)w^{2\alpha}}{s^{1+2\alpha}}\\&+\tfrac{\Pi_3(x,y,z)w^{3\alpha}}{s^{1+3\alpha}}+\tfrac{\Pi_4(x,y,z)w^{4\alpha}}{s^{1+4\alpha}}+\ldots+\tfrac{\Pi_{\mathcal{K}}(x,y,z)w^{\mathcal{K}\alpha}}{s^{1+\mathcal{K}\alpha}}.\end{aligned}\tag{5.15}$$

Apply the inverse natural operator of (5.15) to obtain the $\mathcal{K}$th NRPS solution for the time-fractional KdV-ZK equation as:

$$\psi_{\mathcal{K}}(t,x,y,z) = \frac{1}{\sqrt{2}}\operatorname{sech}(x+y+z) + \frac{\Pi_1(x,y,z)t^{\alpha}}{\Gamma(1+\alpha)} + \frac{\Pi_2(x,y,z)t^{2\alpha}}{\Gamma(1+2\alpha)} + \frac{\Pi_3(x,y,z)t^{3\alpha}}{\Gamma(1+3\alpha)} + \frac{\Pi_4(x,y,z)t^{4\alpha}}{\Gamma(1+4\alpha)} + \ldots + \frac{\Pi_{\mathcal{K}}(x,y,z)t^{\mathcal{K}\alpha}}{\Gamma(1+\mathcal{K}\alpha)}. \tag{5.16}$$

We present a numerical simulation of the results obtained. We assume that $y = z = 0$. Table 1 compares the exact solution for the time-fractional KdV-ZK Equation (5.1) and the inferred fourth NRPS solution (5.16) where the absolute and relative errors are presented. Figure 1 presents the absolute error between the exact solution and the explored approximate fourth NRPS solution (5.16) for the time-fractional KdV-ZK Equation (5.1). To our knowledge, no works in the literature have been presented to deduce approximate solutions to Equation (5.1). Still, all the works presented are concerned with deriving exact solutions to the equation. From Table 1 and Figure 1, we can see the convergence of the numerical solutions derived through the proposed method with the exact solutions, which provides insight into the high accuracy of the proposed method. Figure 2 shows the surfaces of the exact and the fourth NRPS solutions (5.16) at $\alpha = 1$. Figure 3 presents the fourth NRPS solution (5.16) surfaces at different fractional orders $\alpha = 0.95$ and $\alpha = 0.9$ to demonstrate the effect of the fractional derivative on the established surfaces. For more explanation, we depicted, in Figures 4–6, the NRPS solutions explored in 2D plots at different fractional orders α where the time t is considered at various values.

Table 1. A comparison between the exact solution and the NRPS solution for the time-fractional KdV-ZK equation.

x	t	Exact Solution	NRPS Solution	Absolute Error	Relative Error	CPU Time
-1	0.0	1.122462928047994	1.122462928047995	2.220446×10^{-16}	1.978190×10^{-16}	0.015625
	0.1	0.878805774963547	0.878736016940593	6.975802×10^{-5}	7.937820×10^{-5}	
	0.2	0.671997937091220	0.669464247695219	2.533689×10^{-3}	3.770382×10^{-3}	
	0.3	0.506783751732631	0.486544390701797	2.023936×10^{-2}	3.993687×10^{-2}	
0	0.0	1.732050807568877	1.732050807568877	2.220446×10^{-16}	1.281975×10^{-16}	0.015625
	0.1	1.656928147349753	1.657031356966050	1.032096×10^{-5}	6.228973×10^{-5}	
	0.2	1.461072649720631	1.467047034010839	5.974384×10^{-3}	4.089039×10^{-3}	
	0.3	1.208615771635065	1.267319925263052	5.870415×10^{-2}	4.857139×10^{-2}	
1	0.0	1.122462928047994	1.122462928047995	2.220446×10^{-16}	1.978190×10^{-16}	0.015625
	0.1	1.379934335375192	1.379959423861089	2.508848×10^{-5}	1.818092×10^{-5}	
	0.2	1.602159904080592	1.601751160457130	4.087436×10^{-4}	2.551203×10^{-4}	
	0.3	1.723426491772224	1.709575007146963	1.385148×10^{-2}	8.037177×10^{-3}	

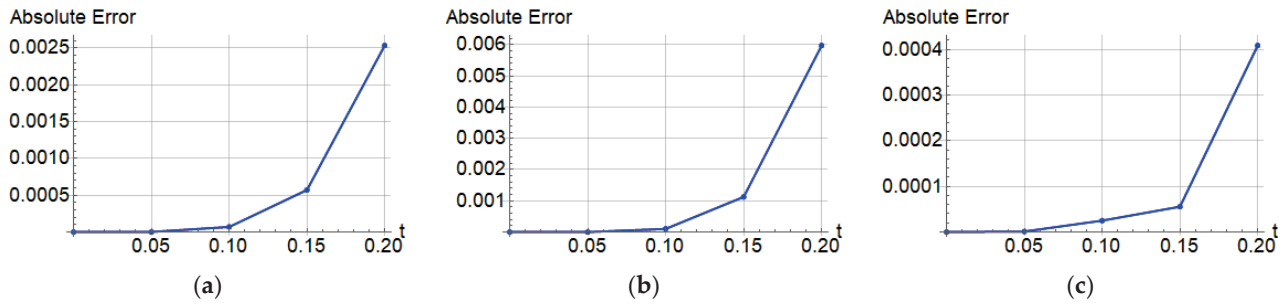

(**a**) (**b**) (**c**)

Figure 1. The absolute error between the approximate and exact solutions for the time-fractional KdV-ZK Equation (5.1) at $\alpha = 1$: (**a**) $x = -1$, (**b**) $x = 0$, and (**c**) $x = 1$.

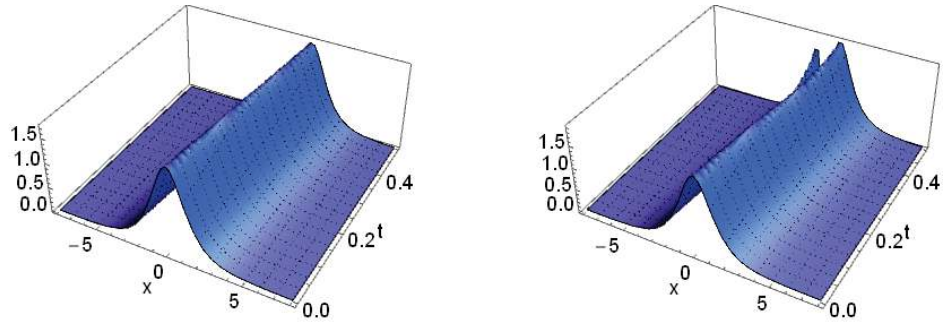

(**a**) (**b**)

Figure 2. The solution of the time-fractional KdV-ZK Equation (5.1) at $\alpha = 1$: (**a**) exact solution, (**b**) 4th NRPS solution (5.16).

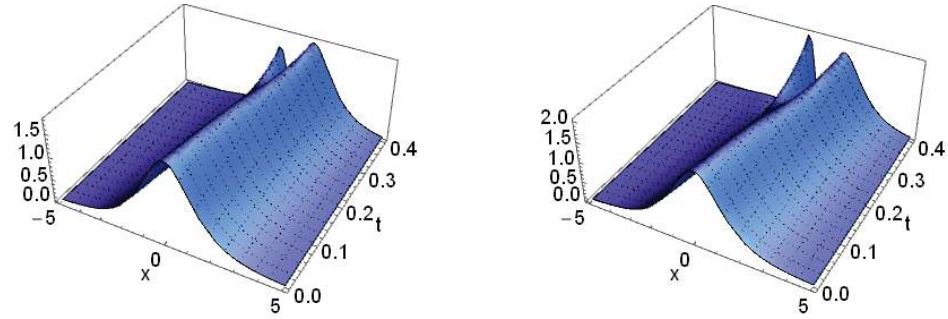

(**a**) (**b**)

Figure 3. The 4th NRPS solution (5.16) of the time-fractional KdV-ZK Equation (5.1): (**a**) $\alpha = 0.95$; (**b**) $\alpha = 0.9$.

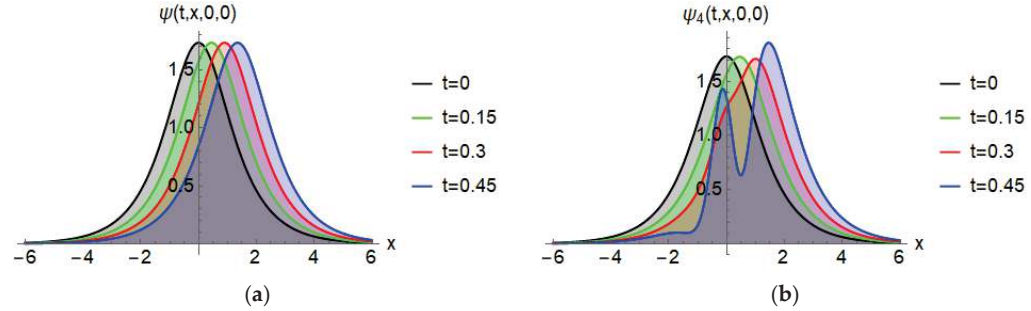

(**a**) (**b**)

Figure 4. Solution of the time-fractional KdV-ZK Equation (5.1) at $\alpha = 1, t \in \{0, 0.15, 0.3, 0.45\}$: (**a**) exact solution; (**b**) 4th NRPS solution (5.16).

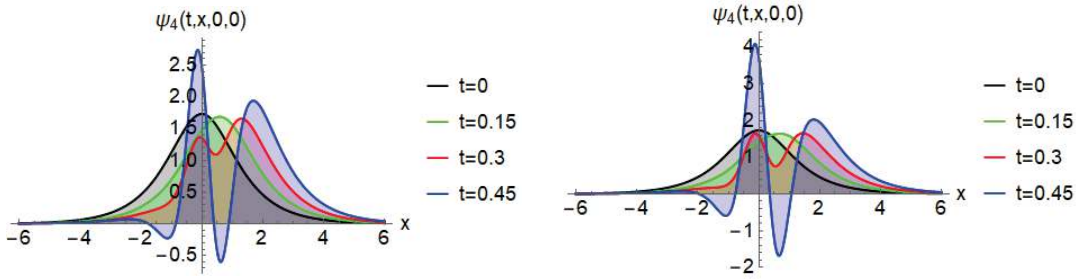

(**a**) (**b**)

Figure 5. The 4th NRPS solution (5.16) of the time-fractional KdV-ZK Equation (5.1) at $t \in \{0,\ 0.15,\ 0.3,\ 0.45\}$: (**a**) $\alpha = 0.9$; (**b**) $\alpha = 0.85$.

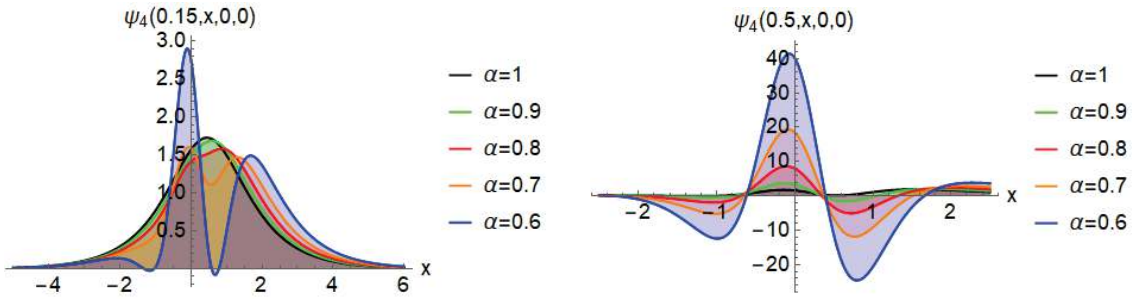

(**a**) (**b**)

Figure 6. The 4th NRPS solution (5.16) of the time-fractional KdV-ZK Equation (5.1) at different fractional orders $\alpha \in \{1,\ 0.9,\ 0.8,\ 0.7,\ 0.6\}$: (**a**) $t = 0.15$; (**b**) $t = 0.5$.

Applications 2. *Consider the following time-fractional spKdV equation:*

$$\mathcal{D}_t^{\alpha}\psi - 8\frac{\partial\psi}{\partial x} + \left(\frac{\partial\psi}{\partial x}\right)^2 + 2\frac{\partial^3\psi}{\partial x^3} = 0,\ t \geq 0,\ x \in \mathbb{R}, \tag{5.17}$$

subject to the initial condition:

$$\psi(x,0) = g(x) = 1 + 12\tanh(x), x \in \mathbb{R}. \tag{5.18}$$

Apply the natural transformation for both sides of (5.17) with the aid of (3.13) to obtain:

$$\begin{aligned}\tfrac{s^{\alpha}}{w^{\alpha}}\Psi(s,w,x) - \tfrac{s^{\alpha-1}}{w^{\alpha}}\psi(0,x) - 8\mathcal{N}\left\{\tfrac{\partial}{\partial x}\mathcal{N}^{-1}\{\Psi(s,w,x)\}\right\} + \mathcal{N}\left\{\left(\tfrac{\partial}{\partial x}\mathcal{N}^{-1}\{\Psi(s,w,x)\}\right)^2\right\}\\ +2\mathcal{N}\left\{\tfrac{\partial^3}{\partial x^3}\mathcal{N}^{-1}\{\Psi(s,w,x)\}\right\} = 0,\end{aligned} \tag{5.19}$$

where $\Psi(s,w,x) = \mathcal{N}\{\psi(t,x)\}$. *Using (5.18) in (5.19), we obtain:*

$$\begin{aligned}\Psi(s,w,x) - \tfrac{1}{s}(1+12\tanh(x))\\ +\tfrac{w^{\alpha}}{s^{\alpha}}\left(-8\mathcal{N}\left\{\tfrac{\partial}{\partial x}\mathcal{N}^{-1}\{\Psi(s,w,x)\}\right\} + \mathcal{N}\left\{\left(\tfrac{\partial}{\partial x}\mathcal{N}^{-1}\{\Psi(s,w,x)\}\right)^2\right\}\right.\\ \left.+2\mathcal{N}\left\{\tfrac{\partial^3}{\partial x^3}\mathcal{N}^{-1}\{\Psi(s,w,x)\}\right\}\right) = 0,\end{aligned} \tag{5.20}$$

Suppose that the solution of (5.20) can be written in the following expansion:

$$\Psi(s,w,x) = \sum_{k=0}^{\infty}\frac{\Pi_k(x)w^{k\alpha}}{s^{1+k\alpha}},\ \alpha \in (0,1], x \in A,\ s \in (\theta,\infty), w \in (0,\infty). \tag{5.21}$$

Define the $\mathcal{K}$*th truncated series of* $\Psi(s,w,x)$ *as:*

$$\Psi_{\mathcal{K}}(s,w,x) = \sum_{k=0}^{\mathcal{K}}\frac{\Pi_k(x)w^{k\alpha}}{s^{1+k\alpha}},\ \alpha \in (0,1], x \in A,\ s \in (\theta,\infty), w \in (0,\infty). \tag{5.22}$$

Using the results in Theorem 2, we deduce that the initial guess $\Pi_0(x) = 1 + 12tanh(x)$. *Based on this fact, we write the* $\mathcal{K}$*th truncated series of* $\Psi(s,w,x)$ *as:*

$$\Psi_{\mathcal{K}}(s,w,x) = \frac{1}{s}(1+12\tanh(x)) + \sum_{k=1}^{\mathcal{K}}\frac{\Pi_k(x)w^{k\alpha}}{s^{1+k\alpha}}. \tag{5.23}$$

We define the NRF as:

$$\begin{aligned}\mathcal{N}Res(s,w,x) &= \Psi(s,w,x) - \tfrac{1}{s}(1+12\tanh(x)) \\ &+\tfrac{w^{\alpha}}{s^{\alpha}}\left(-8\mathcal{N}\left\{\tfrac{\partial}{\partial x}\mathcal{N}^{-1}\{\Psi(s,w,x)\}\right\}+\mathcal{N}\left\{\left(\tfrac{\partial}{\partial x}\mathcal{N}^{-1}\{\Psi(s,w,x)\}\right)^2\right\}\right. \\ &\left.+2\mathcal{N}\left\{\tfrac{\partial^3}{\partial x^3}\mathcal{N}^{-1}\{\Psi(s,w,x)\}\right\}\right),\end{aligned} \tag{5.24}$$

and the $\mathcal{K}$th truncated NRF as:

$$\begin{aligned}\mathcal{N}Res_{\mathcal{K}}(s,w,x) &= \Psi_{\mathcal{K}}(s,w,x) - \tfrac{1}{s}(1+12\tanh(x)) \\ &+\tfrac{w^{\alpha}}{s^{\alpha}}\left(-8\mathcal{N}\left\{\tfrac{\partial}{\partial x}\mathcal{N}^{-1}\{\Psi_{\mathcal{K}}(s,w,x)\}\right\}+\mathcal{N}\left\{\left(\tfrac{\partial}{\partial x}\mathcal{N}^{-1}\{\Psi_{\mathcal{K}}(s,w,x)\}\right)^2\right\}\right. \\ &\left.+2\mathcal{N}\left\{\tfrac{\partial^3}{\partial x^3}\mathcal{N}^{-1}\{\Psi_{\mathcal{K}}(s,w,x)\}\right\}\right),\end{aligned} \tag{5.25}$$

Using the fact that $\lim_{s\to\infty} s^{1+k\alpha}\mathcal{N}Res_k(s,w,x) = 0,\ k = 1,2,\ldots$, *we obtain:*

$$\Pi_1(x) = 8g'(x) - \left(g'(x)\right)^2 - 2g'''(x). \tag{5.26}$$

$$\Pi_2(x) = 8\Pi_1'(x) - 2g'(x)\Pi_1'(x) - 2\Pi_1'''(x). \tag{5.27}$$

$$\Pi_3(x) = \frac{-\Gamma(1+2\alpha)\left(\Pi_1'(x)\right)^2 - \left(\Gamma(1+\alpha)\right)^2\left(-8\Pi_2'(x) + 2g'(x)\Pi_2'(x) + 2\Pi_2'''(x)\right)}{\left(\Gamma(1+\alpha)\right)^2}. \tag{5.28}$$

$$\Pi_4(x) = \frac{-2\Gamma(1+3\alpha)\Pi_1'(x)\Pi_2'(x) + 8\Gamma(1+\alpha)\Gamma(1+2\alpha)\left(-8\Pi_3'(x) + 2g'(x)\Pi_3'(x) + 2\Pi_3'''(x)\right)}{\Gamma(1+\alpha)\Gamma(1+2\alpha)}. \tag{5.29}$$

The CPU time needed to obtain these results (5.26)–(5.29) was 8.53125 *s. Substitute (5.26)–(5.29) into (5.23) to obtain the $\mathcal{K}$th truncated series of $\Psi(s,w,x)$ as:*

$$\Psi_{\mathcal{K}}(s,w,x) = \frac{1}{s}(1+12\tanh(x)) + \frac{\Pi_1(x)w^{\alpha}}{s^{1+\alpha}} + \frac{\Pi_2(x)w^{2\alpha}}{s^{1+2\alpha}} + \frac{\Pi_3(x)w^{3\alpha}}{s^{1+3\alpha}} + \frac{\Pi_4(x)w^{4\alpha}}{s^{1+4\alpha}} + \ldots + \frac{\Pi_{\mathcal{K}}(x)w^{\mathcal{K}\alpha}}{s^{1+\mathcal{K}\alpha}}. \tag{5.30}$$

Apply the inverse natural operator of (5.30) to obtain the $\mathcal{K}$th NRPS solution for the time-fractional spKdV equation as:

$$\psi_{\mathcal{K}}(t,x,y,z) = 1 + 12\tanh(x) + \frac{\Pi_1(x)t^{\alpha}}{\Gamma(1+\alpha)} + \frac{\Pi_2(x)t^{2\alpha}}{\Gamma(1+2\alpha)} + \frac{\Pi_3(x)t^{3\alpha}}{\Gamma(1+3\alpha)} + \frac{\Pi_4(x)t^{4\alpha}}{\Gamma(1+4\alpha)} + \ldots + \frac{\Pi_{\mathcal{K}}(x)t^{\mathcal{K}\alpha}}{\Gamma(1+\mathcal{K}\alpha)}. \tag{5.31}$$

Table 2 shows the absolute and relative errors for the constructed numerical results to demonstrate the accuracy of the NRPS method. Figure 7 presents the absolute error between the exact solution and the explored approximate 4th NRPS solution (5.31) for the time-fractional spKdV Equation (5.17). When comparing the solution explored using the proposed method and the exact solution and calculating the absolute error and relative error, it becomes clear that the proposed method achieves an accuracy within 10^{-4} in dealing with Equation (5.17), which is a suitable level for numerical modeling applications that require accurate and stable solutions. It is worth noting here that based on the literature review, it was found that there are no works that focused on extracting approximate solutions to Equation (5.17), which prompted us to compare the approximate solutions derived here with the exact solutions to the equation. This may be a strong motivation to work on presenting other works that focus on deducing approximate solutions to the equation using new techniques and comparing them with the numerical solutions presented in this work. Figure 8 depicts the exact and 4th NRPS solution surfaces in (5.31) for the time-fractional spKdV Equation (5.17) where we can note the harmony between them, which ensures the efficiency of the proposed method. In Figure 9, we present the 2D plots for the exact and 4th NRPS solutions for the time-fractional spKdV Equation (5.17) at $t = 0.1$ and $t = 1$. Note that the harmony between the depicted solutions reduces

with time. This harmony can be increased for a longer time by increasing the terms of the NRPS solution (5.17). To illustrate the effect of the fractional order α on the behavior of the constructed approximate solution, we present Figure 10 which depicts the 4th NRPS solution (5.17) at different fractional orders $\alpha = 0.95, 0.75, 0.5, 0.25$.

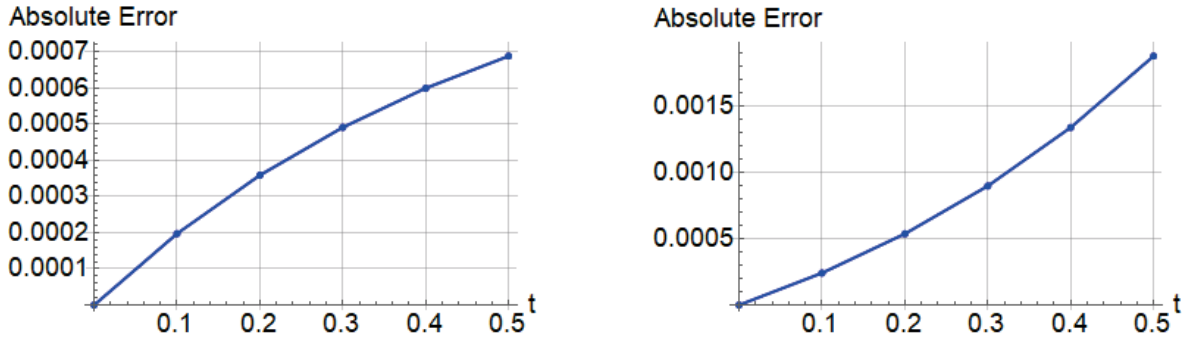

(**a**) (**b**)

Figure 7. Absolute error between the approximate and exact solutions for the time-fractional spKdV Equation (5.17) at $\alpha = 1$ where (**a**) $x = -5$; (**b**) $x = 5$.

Table 2. Comparison between the exact solution and NRPS solution for the time-fractional sp-KdV equation.

x	t	Exact Solution	NRPS Solution	Absolute Error	Relative Error	CPU Time
-5	0.0	-10.99891045115114	-10.998910451151142	0.0	0.0	2.328125
	0.1	-10.99866923540665	-10.998910451151142	2.412157×10^{-4}	2.193135×10^{-5}	
	0.2	-10.99837462040912	-10.998910451151142	5.358307×10^{-4}	4.871908×10^{-5}	
	0.3	-10.99801478665156	-10.998910451151142	8.956644×10^{-4}	8.143874×10^{-5}	
	0.4	-10.99757529934621	-10.998910451151142	1.335151×10^{-3}	1.214041×10^{-4}	
	0.5	-10.99703853017633	-10.998910451151142	1.871920×10^{-3}	1.702204×10^{-4}	
5	0.0	12.99891045115114	12.998910451151142	0.0	0.0	1.703125
	0.1	12.99910794550953	12.998910451151142	1.974943×10^{-4}	1.519291×10^{-5}	
	0.2	12.99926964263438	12.998910451151142	3.591914×10^{-4}	2.763166×10^{-5}	
	0.3	12.99940203066545	12.998910451151142	4.915795×10^{-4}	3.781554×10^{-5}	
	0.4	12.99951042190528	12.998910451151142	5.999707×10^{-4}	4.615333×10^{-5}	
	0.5	12.99959916587564	12.998910451151142	6.887147×10^{-4}	5.297968×10^{-5}	

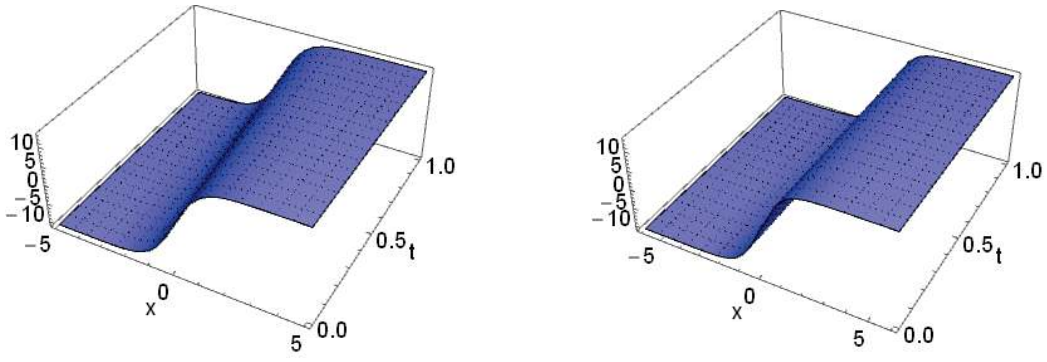

(**a**) (**b**)

Figure 8. Solution of the time-fractional spKdV Equation (5.17) at $\alpha = 1$ where (**a**) exact solution; (**b**) 4th NRPS solution (5.31).

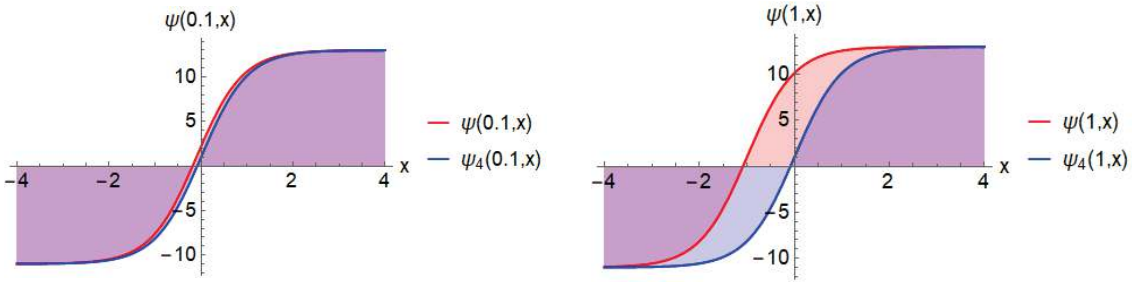

(**a**) (**b**)

Figure 9. Solution of the time-fractional spKdV Equation (5.17) at $\alpha = 1$ where (**a**) $t = 0.1$; (**b**) $t = 1$.

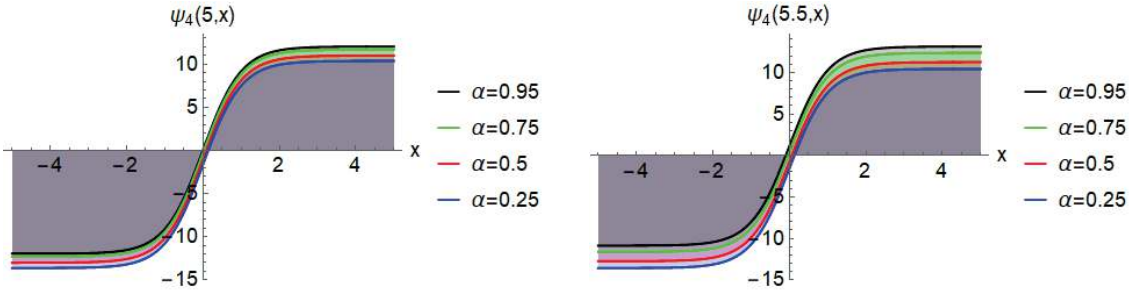

(**a**) (**b**)

Figure 10. The 4th NRPS solution (5.31) of the time-fractional spKdV Equation (5.17) at different fractional orders $\alpha \in \{0.95,\ 0.75,\ 0.5,\ 0.25\}$ where (**a**) $t = 5$; (**b**) $t = 5.5$.

Application 3. *Consider the time-fractional FKdV equation:*

$$\frac{1}{\sqrt{9.8}}\mathcal{D}_t^{\alpha}\psi + \left(-2 - \frac{3}{2}\psi\right)\frac{\partial\psi}{\partial x} - \frac{1}{6}\frac{\partial^3\psi}{\partial x^3} = \frac{-x}{40}e^{\frac{-x^2}{4}},\ t \geq 0,\ x \in \mathbb{R}, \tag{5.32}$$

where $\phi(x) = 1 + 0.1e^{\frac{-x^2}{4}}$. *We assume the initial condition as follows:*

$$\psi(x,0) = h(x) = \frac{-2e^x}{(1+e^x)^2}, x \in \mathbb{R}. \tag{5.33}$$

By applying the same argument above for the NRPS method, we obtain the following results:

$$\Pi_1(x) = \frac{\sqrt{9.8}}{6}\left(3\phi'(x) + 6h'(x) + 6h'(x) + 9h(x)h'(x) + h'''(x)\right). \tag{5.34}$$

$$\Pi_2(x) = \frac{\sqrt{9.8}}{6}\left(6\Pi_1'(x) + 6\Pi_1'(x) + 9h(x)\Pi_1'(x) + 9\Pi_1(x)h\prime(x) + \Pi_1'''(x)\right). \tag{5.35}$$

$$\begin{aligned}\Pi_3(x) = \frac{\sqrt{9.8}}{6(\Gamma(1+\alpha))^2}\Big(&9\Gamma(1+2\alpha)\Pi_1(x)\Pi_1'(x)\\ &+(\Gamma(1+\alpha))^2\left(12\Pi_2'(x) + 9h(x)\Pi_2'(x) + 9\Pi_2(x)h'(x) + \Pi_2'''(x)\right)\Big).\end{aligned} \tag{5.36}$$

$$\begin{aligned}\Pi_4(x) = \frac{\sqrt{9.8}}{6\Gamma(1+\alpha)\Gamma(1+2\alpha)}\Big(&9\Gamma(1+3\alpha)\left(\Pi_2(x)\Pi_1'(x) + \Pi_1(x)\Pi_2'(x)\right)\\ &+\Gamma(1+\alpha)\Gamma(1+2\alpha)\left(12\Pi_3'(x) + 9h(x)\Pi_3'(x) + 9h'(x)\Pi_3(x) + \Pi_3'''(x)\right)\Big).\end{aligned} \tag{5.37}$$

The CPU time needed to obtain these results (5.34)–(5.37) was 16.59375 *s. Using these results, we obtain the* $\mathcal{K}$*th NRPS solution for the time-fractional FKdV equation as:*

$$\psi_{\mathcal{K}}(t,x,y,z) = \frac{-2e^{x}}{(1+e^{x})^{2}} + \frac{\Pi_1(x)t^{\alpha}}{\Gamma(1+\alpha)} + \frac{\Pi_2(x)t^{2\alpha}}{\Gamma(1+2\alpha)} + \frac{\Pi_3(x)t^{3\alpha}}{\Gamma(1+3\alpha)} + \frac{\Pi_4(x)t^{4\alpha}}{\Gamma(1+4\alpha)} + \ldots + \frac{\Pi_{\mathcal{K}}(x)t^{\mathcal{K}\alpha}}{\Gamma(1+\mathcal{K}\alpha)}. \tag{5.38}$$

Table 3 shows the numerical results at $x \in \{-0.05, 0, 0.05\}$ and $t \in \{0, 0.01, 0.02, 0.03, 0.04, 0.05\}$ and the absolute and relative errors correspond to these numerical results which show convergences between the approximate and exact solutions for the time-fractional FKdV Equation (5.38). Figure 11 presents the absolute error between the exact solution and the explored approximate fourth NRPS solution (5.31) for the time-fractional FKdV Equation (5.32). It is clear from Table 3 that the absolute and relative errors were calculated at different values of the variable x and the variable t, and the accuracy of the proposed method was within 10^{-3}, which is a suitable level to confirm that the proposed method in this work is effective and suitable for dealing with such issues in the context of numerical modeling. Moreover, the approximate solutions presented here are in agreement with those presented in Ref. [28]. It is worth noting here that the work in Ref. [28] did not present the absolute or relative error of the derived solutions and did not provide a reading for comparing the solutions with other approximate solutions of Equation (5.32). Figures 12 and 13 present the surface of the fourth NRPS approximate solution and the exact solution to be able to observe the harmony between them. In Figure 9, we consider $\alpha = 1$, while we consider different fractional orders $\alpha \in \{0.9, 0.8\}$ in Figure 13. Figure 14 compares the exact solution and the fourth NRPS solution (5.38) at $t = 0.05$ and $t = 0.15$. The harmony between the depicted solutions is a little larger at $t = 0.05$ than at $t = 0.15$. To further illustrate the effect of the fractional derivative on the behavior of the solution derived using the proposed method for the time-fractional FKdV Equation (5.32), we present Figures 15–17. Figure 15 was performed by considering $t \in \{0, 0.1, 0.2\}$ at $\alpha = 0.9$ and $\alpha = 0.75$, while we performed Figure 16 by considering $t \in \{0, 0.15, 0.3, 0.5\}$ where $\alpha = 0.95$ and $\alpha = 0.75$. Figure 17 depicts the fourth NRPS solution at $t \in \{0.05, 0.15, 0.25, 0.5\}$ where $\alpha \in \{0.95, 0.8, 0.7, 0.6\}$.

Table 3. A comparison between the exact solution and NRPS solution for the time-fractional FKdV equation.

x	t	Exact Solution	NRPS Solution	Absolute Error	Relative Error	CPU Time
-0.05	0.0	-0.49968763016223	-0.49968763016223	0.0	0.0	41.265625
	0.01	-0.49968763016223	-0.49987856920723	1.909390×10^{-4}	3.821168×10^{-4}	
	0.02	-0.49968763016223	-0.49981332801340	1.256978×10^{-4}	2.515528×10^{-4}	
	0.03	-0.49968763016223	-0.49949449146807	1.931386×10^{-4}	3.865188×10^{-4}	
	0.04	-0.49968763016223	-0.49892579802621	7.618321×10^{-4}	1.524616×10^{-3}	
	0.05	-0.49968763016223	-0.49811213971041	1.575490×10^{-3}	3.152950×10^{-3}	
0	0.0	-0.5	-0.5	0.0	0.0	58.0625
	0.01	-0.5	-0.49987108520902	1.289147×10^{-4}	2.578295×10^{-4}	
	0.02	-0.5	-0.49948494667779	5.150533×10^{-4}	1.030106×10^{-3}	
	0.03	-0.5	-0.49884340193134	1.156598×10^{-3}	2.313196×10^{-3}	
	0.04	-0.5	-0.49794948017807	2.050519×10^{-3}	4.101039×10^{-3}	
	0.05	-0.5	-0.49680742230976	3.192577×10^{-3}	6.385155×10^{-3}	
0.05	0.0	-0.49968763016223	-0.49968763016223	0.0	0.0	39.9375
	0.01	-0.49968763016223	-0.49923907955869	4.485506×10^{-4}	8.976620×10^{-4}	
	0.02	-0.49968763016223	-0.49853263964456	1.154990×10^{-3}	2.311425×10^{-3}	
	0.03	-0.49968763016223	-0.49756918623542	2.118443×10^{-3}	4.239536×10^{-3}	
	0.04	-0.49968763016223	-0.49635074871447	3.336881×10^{-3}	6.677934×10^{-3}	
	0.05	-0.49968763016223	-0.49488051003255	4.807120×10^{-3}	9.620250×10^{-3}	

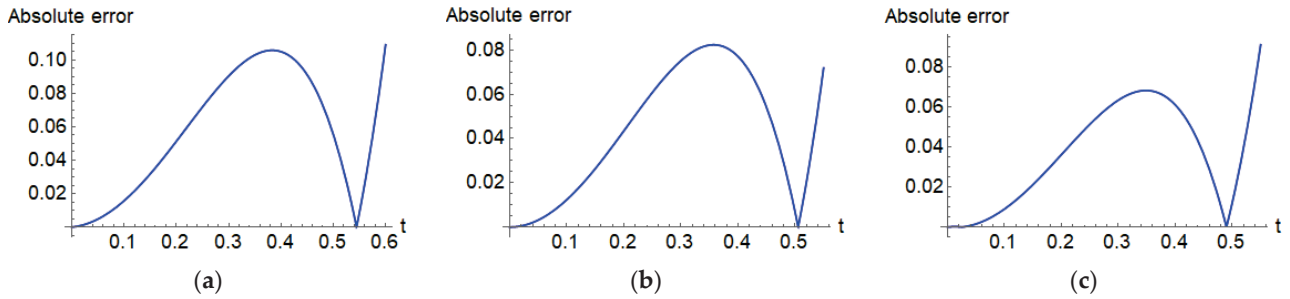

(**a**) (**b**) (**c**)

Figure 11. The absolute error between the approximate and exact solutions for the time-fractional FKdV Equation (5.32) at $\alpha = 1$: (**a**) $x = -0.05$, (**b**) $x = 0$, and (**c**) $x = 0.05$.

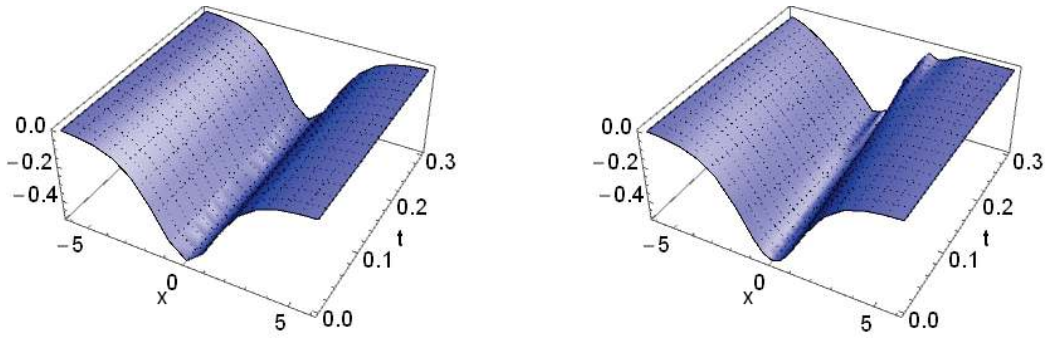

(**a**) (**b**)

Figure 12. The solution of the time-fractional FKdV Equation (5.32) at $\alpha = 1$: (**a**) exact solution, (**b**) 4th NRPS solution (5.38).

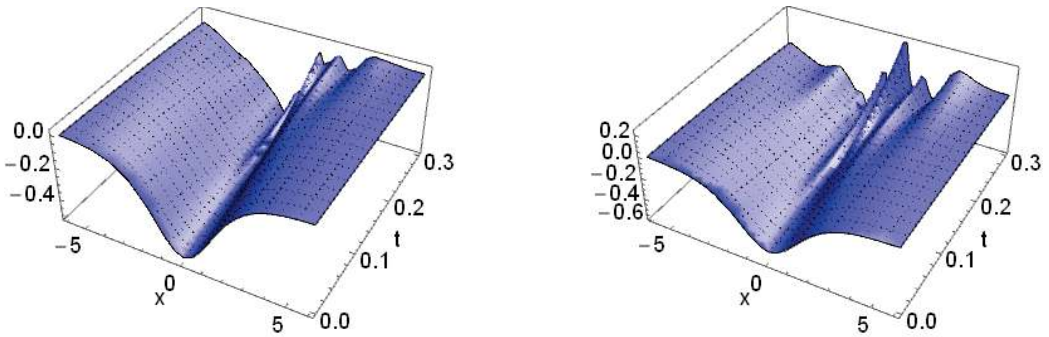

(**a**) (**b**)

Figure 13. The 4th NRPS solution (5.38) of the time-fractional FKdV Equation (5.32): (**a**) $\alpha = 0.9$; (**b**) $\alpha = 0.8$.

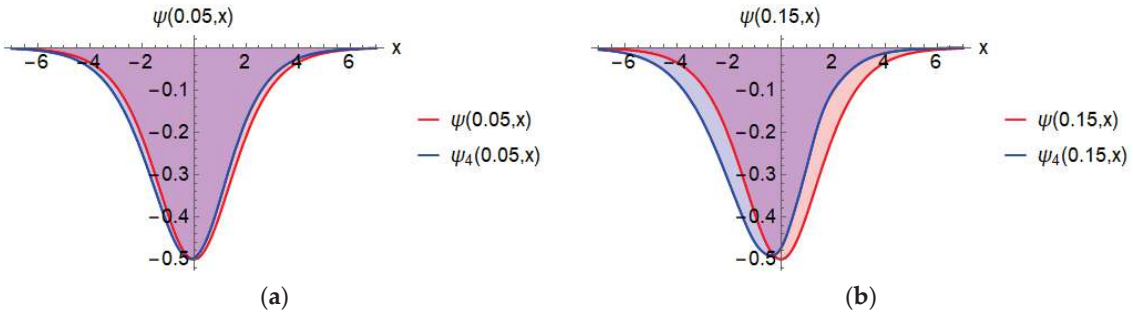

(**a**) (**b**)

Figure 14. The solution of the time-fractional FKdV Equation (5.32) at $\alpha = 1$: (**a**) $t = 0.05$, (**b**) $t = 0.15$ on (5.38).

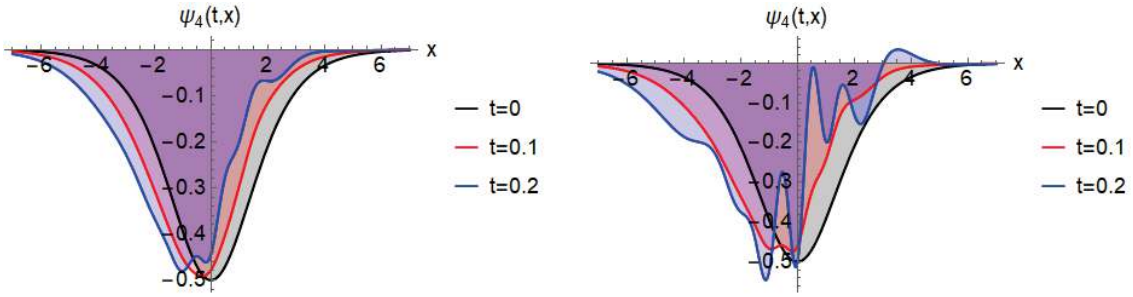

Figure 15. The 4th NRPS solution (5.38) of the time-fractional FKdV Equation (5.32) at $t \in \{0, 0.1, 0.2\}$: (**a**) $\alpha = 0.9$, (**b**) $\alpha = 0.75$.

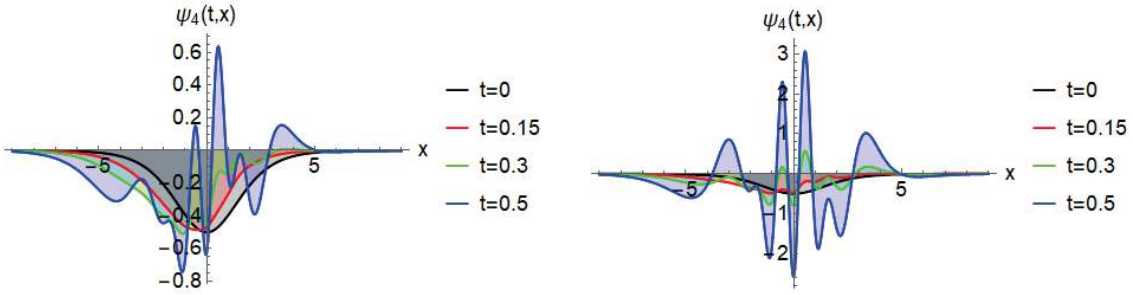

Figure 16. The 4th NRPS solution (5.38) of the time-fractional FKdV Equation (5.32) at $t \in \{0,\ 0.15,\ 0.3,\ 0.5\}$: (**a**) $\alpha = 0.95$, (**b**) $\alpha = 0.75$.

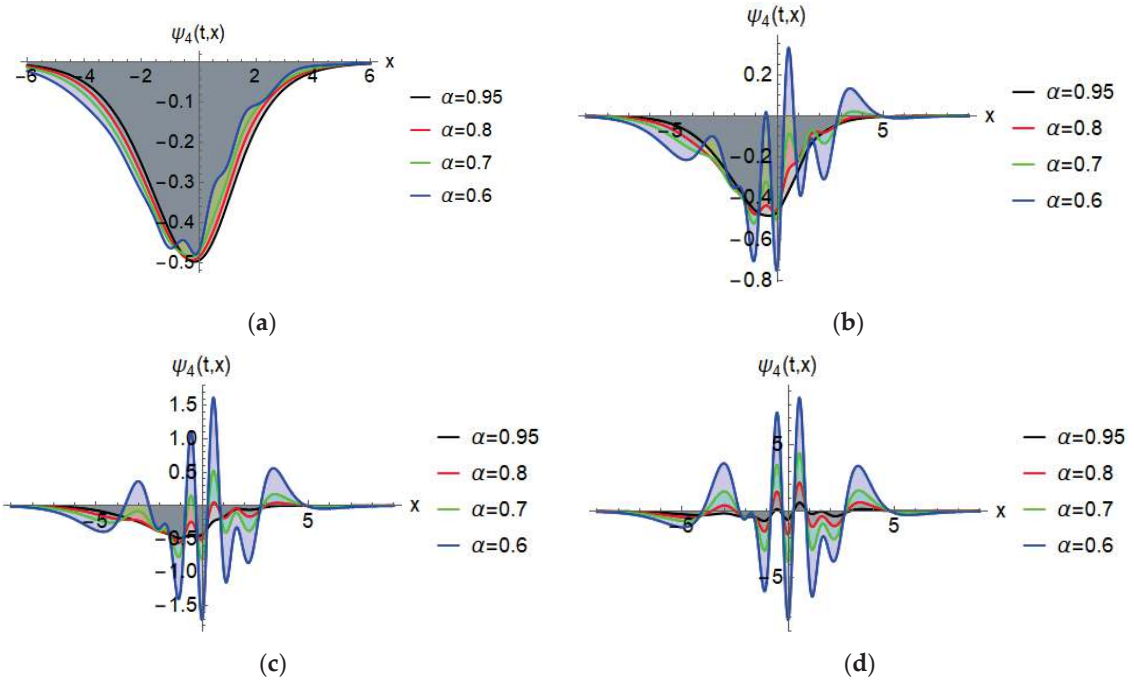

Figure 17. The 4th NRPS solution (5.38) of the time-fractional FKdV Equation (5.32) at different fractional orders $\alpha \in \{0.95,\ 0.8,\ 0.7,\ 0.6\}$: (**a**) $t = 0.05$, (**b**) $t = 0.15$, (**c**) $t = 0.25$, and (**d**) $t = 0.5$.

From the introduced numerical and graphical results, we can deduce that the proposed NRPS method is efficient in dealing with the governing models by noticing the harmony and convergences between the approximate and exact solutions. We utilized four terms

of the NRPS solutions to show their efficiency and we can achieve higher efficiency by obtaining further terms of the approximate solutions.

6. Conclusions

This work investigated three time-fractional models that arise in plasma physics: the mKdV-ZK equation, the spKdV equation, and the FKdV equation. The governing equations in this work are of considerable importance in plasma physics by modeling nonlinear ion acoustic waves which play a fundamental role in understanding wave dynamics in plasma. We considered the fractional derivative in the Caputo sense. In this work, we investigate a new work based on the new fractional expansion in the natural transformation space and the RPS method to construct analytical solutions for the governing models. The RPS method is one of the important methods in deriving approximate solutions for fractional models, but it may require complex calculations to deal with more complex fractional models. To address this point, the Laplace transform was integrated with the RPS method in the literature. In this work, we seek to compose the natural transformation with the RPS method, as the natural transformation is more general than the Laplace transform, which enables us to deal with a wider range of complex fractional systems. To achieve our goal, we investigated the theoretical analysis of the proposed method to reveal the applicability, efficiency, and effectiveness of this approach to dealing with the governing models. Clear steps were set for the proposed method to obtain analytical solutions that are consistent and close to the exact solutions. These steps were implemented for the three governing equations, and an analytical study of the derived solutions for each equation was presented to confirm that the proposed approach generates analytical solutions that converge quickly to exact solutions, which proves the effectiveness of the proposed method.

Author Contributions: Conceptualization, S.M. and S.A.-O.; methodology, M.A.; software, S.E.A.; validation, M.A. and S.M.; formal analysis, S.A.-O.; investigation, M.A.-S.; writing—original draft preparation, S.A.-O. and M.A.-S.; writing—review and editing, A.F.; visualization, A.F.; supervision and project administration, S.E.A.; funding acquisition, S.A.-O. All authors have read and agreed to the published version of the manuscript.

Funding: This research work was funded by Umm Al-Qura University, Saudi Arabia under grant number: 25UQU4282396GSSR01.

Data Availability Statement: Data are contained within the article.

Acknowledgments: The authors extend their appreciation to Umm Al-Qura University, Saudi Arabia for funding this research work through grant number: (25UQU4282396GSSR01).

Conflicts of Interest: The authors declare no conflict of interest.

References

1. Saha, A.; Banerjee, S. *Dynamical Systems and Nonlinear Waves in Plasmas*; CRC Press: Boca Raton, FL, USA, 2021.
2. Varghese, S.S.; Singh, K.; Kourakis, I. Electrostatic Supersolitary Waves: A Challenging Paradigm in Nonlinear Plasma Science and Beyond—State of the Art and Overview of Recent Results. *Fundam. Plasma Phys.* **2024**, *10*, 100048. [CrossRef]
3. Altuijri, R.; Abdel-Aty, A.H.; Nisar, K.S.; Khater, M. Exploring novel wave characteristics in a nonlinear model with complexity arising in plasma physics. *Opt. Quantum Electron.* **2024**, *56*, 1128. [CrossRef]
4. Johnson, R.S. Water waves and Korteweg–de Vries equations. *J. Fluid Mech.* **1980**, *97*, 701–719. [CrossRef]
5. Seadawy, A.R.; Alsaedi, B. Contraction of variational principle and optical soliton solutions for two models of nonlinear Schrodinger equation with polynomial law nonlinearity. *AIMS Math.* **2024**, *9*, 6336–6367.
6. Mubaraki, A.M.; Nuruddeen, R.I.; Ali, K.K.; Gómez-Aguilar, J.F. Additional solitonic and other analytical solutions for the higher-order Boussinesq-Burgers equation. *Opt. Quantum Electron.* **2024**, *56*, 165. [CrossRef]
7. Gulay, T.A.; Zakharov, V.V.; Kron, R.V.; Popova, S.V.; Shibaev, V.P. Algorithmic support of the integrated aircraft control system using the systems embedding technology. *AIP Conf. Proc.* **2024**, *2969*, 060009.

8. Halcrow, C.; John, R.R.; Anusree, N. Modified sine-Gordon theory with static multikinks. *Phys. Rev. D* **2024**, *110*, 065010. [CrossRef]
9. Sagib, M.; Hossain, M.A.; Saha, B.K.; Khan, K. On traveling wave solutions with stability and phase plane analysis for the modified Benjamin-Bona-Mahony equation. *PLoS ONE* **2024**, *19*, e0306196.
10. Hosseini, K.; Hincal, E.; Sadri, K.; Rabiei, F.; Ilie, M.; Akgül, A.; Osman, M.S. The positive multi-complexiton solution to a generalized Kadomtsev–Petviashvili equation. *Partial Differ. Equ. Appl. Math.* **2024**, *9*, 100647.
11. Faridi, W.A.; Iqbal, M.; Riaz, M.B.; AlQahtani, S.A.; Wazwaz, A.M. The fractional soliton solutions of dynamical system arising in plasma physics: The comparative analysis. *Alex. Eng. J.* **2024**, *95*, 247–261. [CrossRef]
12. Alam, M.M.; Alam, M.S. Study of Time-Fractional Dust Ion Acoustic Waves Propagation in Collisionless Unmagnetized Dusty Plasmas. *Braz. J. Phys.* **2024**, *54*, 192.
13. Phoosree, S.; Khongnual, N.; Sanjun, J.; Kammanee, A.; Thadee, W. Riccati sub-equation method for solving fractional flood wave equation and fractional plasma physics equation. *Partial Differ. Equ. Appl. Math.* **2024**, *10*, 100672. [CrossRef]
14. Abdelwahed, H.G.; El-Shewy, E.K.; Alghanim, S.; Abdelrahman, M.A. On the physical fractional modulations on Langmuir plasma structures. *Fractal Fract.* **2022**, *6*, 430. [CrossRef]
15. Poolcharuansin, P.; Bradley, J.W. Short-and long-term plasma phenomena in a HiPIMS discharge. *Plasma Sources Sci. Technol.* **2010**, *19*, 025010. [CrossRef]
16. Alsatami, K.A. Exploring Nonlinear Fractional (2+1)-Dimensional KP–Burgers Model: Derivation and Ion Acoustic Solitary Wave Solution. *Int. J. Anal. Appl.* **2024**, *22*, 147. [CrossRef]
17. Alabedalhadi, M.; Al-Omari, S.; Al-Smadi, M.; Alhazmi, S. Traveling wave solutions for time-fractional mKdV-ZK equation of weakly nonlinear ion-acoustic waves in magnetized electron–positron plasma. *Symmetry* **2023**, *15*, 361. [CrossRef]
18. Lazarus, I.J.; Bharuthram, R.; Hellberg, M.A. Modified Korteweg–de Vries–Zakharov–Kuznetsov solitons in symmetric two-temperature electron–positron plasmas. *J. Plasma Phys.* **2008**, *74*, 519–529. [CrossRef]
19. Verheest, F.; Mace, R.L.; Pillay, S.R.; Hellberg, M.A. Unified derivation of Korteweg-de Vries-Zakharov-Kuznetsov equations in multispecies plasmas. *J. Phys. A Math. Gen.* **2002**, *35*, 795.
20. Zhou, T.Y.; Tian, B.; Zhang, C.R.; Liu, S.H. Auto-Bäcklund transformations, bilinear forms, multiple-soliton, quasi-soliton and hybrid solutions of a (3+1)-dimensional modified Korteweg-de Vries-Zakharov-Kuznetsov equation in an electron-positron plasma. *Eur. Phys. J. Plus* **2022**, *137*, 912. [CrossRef]
21. Rehman, H.U.; Seadawy, A.R.; Younis, M.; Rizvi ST, R.; Anwar, I.; Baber, M.Z.; Althobaiti, A. Weakly nonlinear electron-acoustic waves in the fluid ions propagated via a (3+1)-dimensional generalized Korteweg–de-Vries–Zakharov–Kuznetsov equation in plasma physics. *Results Phys.* **2022**, *33*, 105069.
22. Younas, U.; Ren, J.; Baber, M.Z.; Yasin, M.W.; Shahzad, T. Ion-acoustic wave structures in the fluid ions modeled by higher dimensional generalized Korteweg-de Vries–Zakharov–Kuznetsov equation. *J. Ocean Eng. Sci.* **2023**, *8*, 623–635. [CrossRef]
23. Alhami, R.; Alquran, M. Extracted different types of optical lumps and breathers to the new generalized stochastic potential-KdV equation via using the Cole-Hopf transformation and Hirota bilinear method. *Opt. Quantum Electron.* **2022**, *54*, 553. [CrossRef]
24. Alquran MA RW, A.N. Investigating the revisited generalized stochastic potential-KdV equation: Fractional time-derivative against proportional time-delay. *Rom. J. Phys.* **2023**, *68*, 106.
25. Abbas, N.; Hussain, A.; Riaz, M.B.; Ibrahim, T.F.; Birkea, F.O.; Tahir, R.A. A discussion on the Lie symmetry analysis, travelling wave solutions and conservation laws of new generalized stochastic potential-KdV equation. *Results Phys.* **2024**, *56*, 107302. [CrossRef]
26. Wu TY, T. Generation of upstream advancing solitons by moving disturbances. *J. Fluid Mech.* **1987**, *184*, 75–99.
27. Derakhshan, M.H.; Aminataei, A. A numerical method for finding solution of the distributed-order time-fractional forced Korteweg–de Vries equation including the Caputo fractional derivative. *Math. Methods Appl. Sci.* **2022**, *45*, 3144–3165. [CrossRef]
28. Veeresha, P.; Yavuz, M.; Baishya, C. A computational approach for shallow water forced Korteweg–De Vries equation on critical flow over a hole with three fractional operators. *Int. J. Optim. Control Theor. Appl. (IJOCTA)* **2021**, *11*, 52–67. [CrossRef]
29. Alhejaili, W.; Az-Zo'bi, E.; Shah, R.; El-Tantawy, S.A. On the analytical soliton approximations to fractional forced Korteweg-de Vries equation arising in fluids and Plasmas using two novel techniques. *Commun. Theor. Phys.* **2024**, *76*, 085001. [CrossRef]
30. Abu Arqub, O.; Al-Smadi, M.; Momani, S.; Hayat, T. Numerical solutions of fuzzy differential equations using reproducing kernel Hilbert space method. *Soft Comput.* **2016**, *20*, 3283–3302. [CrossRef]
31. Al-Smadi, M.; Freihat, A.; Khalil, H.; Momani, S.; Ali Khan, R. Numerical multistep approach for solving fractional partial differential equations. *Int. J. Comput. Methods* **2017**, *14*, 1750029. [CrossRef]
32. Hasan, S.; El-Ajou, A.; Hadid, S.; Al-Smadi, M.; Momani, S. Atangana-Baleanu fractional framework of reproducing kernel technique in solving fractional population dynamics system. *Chaos Solitons Fractals* **2020**, *133*, 109624.
33. Momani, S.; Freihat, A.; Al-Smadi, M. Analytical Study of Fractional-Order Multiple Chaotic FitzHugh-Nagumo Neurons Model Using Multistep Generalized Differential Transform Method. *Abstr. Appl. Anal.* **2014**, *2014*, 276279. [CrossRef]

34. Al-Smadi, M.; Gumah, G. On the homotopy analysis method for fractional SEIR epidemic model. *Res. J. Appl. Sci. Eng. Technol.* **2014**, *7*, 3809–3820.
35. Khalil, H.; Khan, R.A.; HAl-Smadi, M.; Freihat, A.A. Approximation of solution of time fractional order three-dimensional heat conduction problems with Jacobi Polynomials. *Punjab Univ. J. Math.* **2020**, *47*, 35–56.
36. Heydari, M.H.; Zhagharian, S.; Razzaghi, M. Discrete Chebyshev polynomials for the numerical solution of stochastic fractional two-dimensional Sobolev equation. *Commun. Nonlinear Sci. Numer. Simul.* **2024**, *130*, 107742. [CrossRef]
37. Sivasankar, K.; Nadhaprasadh, M.; Sathish, K.; Al-Omari, S.; Udhayakuma, R. New study on Cauchy problems of fractional stochastic evolution systems on an infinite interval. *Math. Methods Appl. Sci.* **2024**, *48*, 890–904.
38. Roul, P.; Rohil, V. A high-accuracy computational technique based on L 2-1 σ and B-spline schemes for solving the nonlinear time-fractional Burgers' equation. *Soft Comput.* **2024**, *28*, 6153–6169.
39. Nawaz, R.; Fewster-Young, N.; Katbar, N.M.; Ali, N.; Zada, L.; Ibrahim, R.W.; Alqahtani, H. Numerical inspection of (3 + 1)-perturbed Zakharov–Kuznetsov equation via fractional variational iteration method with Caputo fractional derivative. *Numer. Heat Transf. Part B Fundam.* **2024**, *85*, 1162–1177.
40. Momani, S.; Odibat, Z.; Alawneh, A. Variational iteration method for solving the space-and time-fractional KdV equation. *Numer. Methods Partial Differ. Equ. Int. J.* **2008**, *24*, 262–271.
41. El-Wakil, S.A.; Abulwafa, E.M.; Zahran, M.A.; Mahmoud, A.A. Time-fractional KdV equation: Formulation and solution using variational methods. *Nonlinear Dyn.* **2011**, *65*, 55–63.
42. Bulut, H.; Pandir, Y.; Demiray, S.T. Exact solutions of time-fractional KdV equations by using generalized Kudryashov method. *Int. J. Model. Optim.* **2014**, *4*, 315.
43. Arqub, O.A.; El-Ajou, A.; Momani, S. Constructing and predicting solitary pattern solutions for nonlinear time-fractional dispersive partial differential equations. *J. Comput. Phys.* **2015**, *293*, 385–399.
44. Abu Arqub, O. Application of residual power series method for the solution of time-fractional Schrödinger equations in one-dimensional space. *Fundam. Inform.* **2019**, *166*, 87–110. [CrossRef]
45. Tchier, F.; Inc, M.; Korpinar, Z.S.; Baleanu, D. Solutions of the time fractional reaction–diffusion equations with residual power series method. *Adv. Mech. Eng.* **2016**, *8*, 1687814016670867.
46. El-Ajou, A. Adapting the Laplace transform to create solitary solutions for the nonlinear time-fractional dispersive PDEs via a new approach. *Eur. Phys. J. Plus* **2021**, *136*, 229.
47. Džrbašjan, M.M. A generalized Riemann-Liouville operator and some of its applications. *Math. USSR-Izv.* **1968**, *2*, 1027.
48. Farman, M.; Alfiniyah, C. A constant proportional caputo operator for modeling childhood disease epidemics. *Decis. Anal. J.* **2024**, *10*, 100393.
49. Trujillo, J.J.; Scalas, E.; Diethelm, K.; Baleanu, D. *Fractional Calculus: Models and Numerical Methods*; World Scientific: Singapore, 2016; Volume 5.
50. Sivasankar, S.; Udhayakumar, R.; Muthukumaran, V.; Gokul, G.; Al-Omari, S. Existence of Hilfer fractional neutral stochastic differential systemswith infinite delay, Bulletin of the Karaganda University. *Math. Ser.* **2024**, *1*, 119–174.
51. Belgacem FB, M.; Silambarasan, R.; Sivasundaram, S. Advances in the natural transform. *AIP Conf. Proc.-Am. Inst. Phys.* **2012**, *1493*, 106.
52. Rawashdeh, M.S.; Al-Jammal, H. New approximate solutions to fractional nonlinear systems of partial differential equations using the FNDM. *Adv. Differ. Equ.* **2016**, *2016*, 235.
53. Maitama, S.; Zhao, W. Beyond Sumudu transform and natural transform: J-transform properties and applications. *J. Appl. Anal. Comput.* **2020**, *10*, 1223–1241.
54. Rawashdeh, M.S.; Maitama, S. Solving nonlinear ordinary differential equations using the NDM. *J. Appl. Anal. Comput.* **2015**, *5*, 77–88.

fractal and fractional

MDPI

Article

A Mixed Finite Element Method for the Multi-Term Time-Fractional Reaction–Diffusion Equations

Jie Zhao [1], Shubin Dong [2] and Zhichao Fang [2,*]

[1] School of Statistics and Mathematics, Inner Mongolia University of Finance and Economics, Hohhot 010070, China; zhaoj@imufe.edu.cn
[2] School of Mathematical Sciences, Inner Mongolia University, Hohhot 010021, China; madongshubin@126.com
* Correspondence: zcfang@imu.edu.cn

Abstract: In this work, a fully discrete mixed finite element (MFE) scheme is designed to solve the multi-term time-fractional reaction–diffusion equations with variable coefficients by using the well-known $L1$ formula and the Raviart–Thomas MFE space. The existence and uniqueness of the discrete solution is proved by using the matrix theory, and the unconditional stability is also discussed in detail. By introducing the mixed elliptic projection, the error estimates for the unknown variable u in the discrete $L^{\infty}\left(L^{2}(\Omega)\right)$ norm and for the auxiliary variable $\boldsymbol{\lambda}$ in the discrete $L^{\infty}\left(\left(L^{2}(\Omega)\right)^{2}\right)$ and $L^{\infty}(\boldsymbol{H}(\mathrm{div},\Omega))$ norms are obtained. Finally, three numerical examples are given to demonstrate the theoretical results.

Keywords: multi-term time-fractional reaction–diffusion equations; mixed finite element method; $L1$ formula; unconditional stability; error estimate

1. Introduction

Fractional calculus and fractional partial differential equations (FPDEs) have been confirmed to be very important tools in describing some anomalous phenomena and processes with memory and nonlocal properties [1–6]. Moreover, some underlying and complex processes can be described more appropriately by multi-term FPDEs [7–9], as they contains multiple fractional derivative or calculus terms. In recent years, many numerical methods have been increasingly used by scholars to solve multi-term FPDEs. Liu et al. [10] constructed some finite difference (FD) schemes to solve the multi-term time-fractional wave-diffusion equations by using two fractional predictor–corrector methods. Dehghan et al. [11] devised two high-order numerical schemes to solve the multi-term time-fractional diffusion-wave equations by using the compact FD method and Galerkin spectral technique. Ren and Sun [12] established an efficient compact FD scheme for the multi-term time-fractional diffusion-wave equation by using the $L1$ formula. Zheng et al. [13] proposed a high-order space–time spectral method for the multi-term time-fractional diffusion equations by using the Legendre polynomials in the temporal direction and the Fourier-like basis functions in the spatial direction. Du and Sun [14] constructed an FD scheme for multi-term time-fractional mixed diffusion and wave equations by using the $L2-1_{\sigma}$ formula. Hendy and Zaky [15] proposed a spectral method for a coupled system of nonlinear multi-term time–space fractional diffusion equations by using the $L1$ formula on a time-graded mesh. Liu et al. [16] developed an ADI Legendre spectral method for solving a multi-term time-fractional Oldroyd-B fluid-type diffusion equation. Wei and Wang [17] constructed a higher-order numerical scheme for the multi-term variable-order time-fractional diffusion equation by using the local discontinuous Galerkin method. She et al. [18] considered a spectral method for solving the multi-term time-fractional diffusion problem by using a modified $L1$ formula.

Meanwhile, many scholars selected the finite element (FE) method for solving the multi-term FPDEs and have achieved excellent results. Jin et al. [19] developed an FE

Citation: Zhao, J.; Dong, S.; Fang, Z. A Mixed Finite Element Method for the Multi-Term Time-Fractional Reaction–Diffusion Equations. *Fractal Fract.* **2024**, *8*, 51. https://doi.org/10.3390/fractalfract8010051

Academic Editor: Jordan Hristov

Received: 5 December 2023
Revised: 4 January 2024
Accepted: 8 January 2024
Published: 12 January 2024

method for a multi-term time-fractional diffusion equation and considered the case of smooth and nonsmooth initial data. Li et al. [20] proposed an FE method to solve a higher-dimensional multi-term fractional diffusion equation on nonuniform time meshes. Zhou et al. [21] developed a weak Galerkin FE method for solving multi-term time-fractional diffusion equations by using a convolution quadrature formula. Bu et al. [22] proposed a space–time FE method for solving the multi-term time–space fractional diffusion equation based on the suitable graded time mesh. Feng et al. [23] proposed an FE method for a multi-term time-fractional mixed subdiffusion and diffusion-wave equation on the convex domain by using mixed L-type schemes. Meng and Stynes [24] considered an $L1$ FE method for a multi-term time-fractional initial-boundary value problem on the temporal graded mesh. Yin et al. [25] constructed a class of efficient time-stepping FE schemes for multi-term time-fractional reaction–diffusion-wave equations by using the shifted convolution quadrature method. Huang et al. [26] proposed an α-robust FE method for a multi-term time-fractional diffusion problem on a graded mesh by using the $L1$ formula. Liu et al. [27] proposed an FE method for solving a multi-term variable-order time-fractional diffusion equation and developed an efficient parallel-in-time algorithm to reduce the computational costs.

In this work, we will construct a fully discrete mixed finite element (MFE) scheme for the following multi-term time-fractional reaction–diffusion (TFRD) equations with variable coefficients:

$$\begin{cases} P(D_t)u(\boldsymbol{x},t) - \operatorname{div}(\mathcal{A}(\boldsymbol{x})\nabla u(\boldsymbol{x},t)) + p(\boldsymbol{x})u(\boldsymbol{x},t) = f(\boldsymbol{x},t), & (\boldsymbol{x},t) \in \Omega \times J, \\ u(\boldsymbol{x},t) = 0, & (\boldsymbol{x},t) \in \partial\Omega \times \overline{J}, \\ u(\boldsymbol{x},0) = u_0(\boldsymbol{x}), & \boldsymbol{x} \in \overline{\Omega}, \end{cases} \tag{1}$$

where $\Omega \subset R^2$ is a convex and bounded polygon region with boundary $\partial\Omega$, $J = (0, T]$ with $0 < T < \infty$. We assume that the source function $f(\boldsymbol{x}, t)$, initial data $u_0(\boldsymbol{x})$, and non-negative coefficient $p(\boldsymbol{x})$ are smooth enough. Specifically, for the symmetric diffusion coefficient matrix $\mathcal{A}(\boldsymbol{x})$, we should assume that there exist two constants A_0, $A_1 > 0$ such that

$$A_0 \boldsymbol{z}^T \boldsymbol{z} \le \boldsymbol{z}^T \mathcal{A}(\boldsymbol{x}) \boldsymbol{z} \le A_1 \boldsymbol{z}^T \boldsymbol{z}, \forall \boldsymbol{z} \in R^2, \forall \boldsymbol{x} \in \overline{\Omega}.$$

Moreover, the multi-term time-fractional derivative $P(D_t)u(\boldsymbol{x}, t)$ is defined by

$$P(D_t)u(\boldsymbol{x},t) = \sum_{i=1}^{m} b_i D_t^{\alpha_i} u(\boldsymbol{x},t), 0 < \alpha_m < \alpha_{m-1} < \cdots < \alpha_1 < 1,$$

where $b_i \quad (i = 1, 2, \cdots, m)$ are the positive real numbers and $D_t^{\alpha_i} u$ is the Caputo time-fractional derivative as follows:

$$D_t^{\alpha_i} u(\boldsymbol{x},t) = \frac{1}{\Gamma(1-\alpha_i)} \int_0^t \frac{\partial u(x,s)}{\partial s} \frac{1}{(t-s)^{\alpha_i}} \mathrm{d}s,$$

where $\Gamma(\cdot)$ denotes the Γ-function.

It should be noted that the MFE method, as an important numerical calculation method, has been widely used to solve FPDEs [28–32], and some scholars have also used this method to solve the multi-term FPDEs [33–35]. In [33], Shi et al. proposed an H^1 -Galerkin mixed finite element (MFE) method for the multi-term time-fractional diffusion equations and gave a superconvergence result. In [34], Li et al. proposed an MFE method for the multi-term time-fractional diffusion and diffusion-wave equations by using an MFE space contained in $\left(L^2(\Omega)\right)^d \times H_0^1(\Omega)$, where $d = 2, 3$. In [35], Cao et al. constructed a nonconforming MFE scheme for the multi-term time-fractional mixed diffusion and diffusion-wave equations. Motivated by the above excellent works, we will construct a fully discrete MFE scheme for the multi-term TFRD equation (1) by using the Raviart–Thomas MFE space and the $L1$ formula, analyze the existence, uniqueness, and unconditional

stability in detail, and give error estimates for u (in discrete $L^\infty\left(L^2(\Omega)\right)$ norm) and auxiliary variable $\boldsymbol{\lambda}$ (in discrete $L^\infty\left(\left(L^2(\Omega)\right)^2\right)$ and discrete $L^\infty(\boldsymbol{H}(\mathrm{div},\Omega))$ norms). Finally, we give numerical experiments to demonstrate the efficiency of the proposed method.

The remainder of this paper is arranged as follows. In Section 2, we construct a fully discrete MFE scheme for the multi-term TFRD equations by using the Raviart–Thomas MFE space and the $L1$ -formula. In Section 3, we give a fractional Grönwall inequality and analyze the existence and uniqueness of the discrete solution. We derive the unconditional stability results and a priori error estimates in detail in Sections 4 and 5, respectively. Finally, three numerical examples are given to verify the theoretical results.

2. Mixed Finite Element Method

We introduce the flux $\boldsymbol{\lambda}(\boldsymbol{x},t) = -\mathcal{A}(\boldsymbol{x})\nabla u(\boldsymbol{x},t)$ as the auxiliary variable. Then, the original problem (1) can be rewritten as follows:

$$\begin{cases} (a)P(D_t)u(\boldsymbol{x},t) + \mathrm{div}\boldsymbol{\lambda}(\boldsymbol{x},t) + p(\boldsymbol{x})u(\boldsymbol{x},t) = f(\boldsymbol{x},t), & (\boldsymbol{x},t) \in \Omega \times J, \\ (b)\mathcal{A}^{-1}(x)\boldsymbol{\lambda}(\boldsymbol{x},t) + \nabla u(\boldsymbol{x},t) = 0, & (\boldsymbol{x},t) \in \Omega \times J, \\ (c)u(\boldsymbol{x},t) = 0, & (\boldsymbol{x},t) \in \partial\Omega \times \overline{J}, \\ (d)u(\boldsymbol{x},0) = u_0(\boldsymbol{x}), & \boldsymbol{x} \in \overline{\Omega}. \end{cases} \tag{2}$$

Let $V = L^2(\Omega)$ and $\boldsymbol{W} = \boldsymbol{H}(\mathrm{div},\Omega) = \left\{\boldsymbol{w} \in \left(L^2(\Omega)\right)^2 : \mathrm{div}\boldsymbol{w} \in L^2(\Omega)\right\}$. Then, we obtain the mixed variational formulation of (2): find $(u,\boldsymbol{\lambda}) \in V \times \boldsymbol{W}$ such that

$$\begin{cases} (a)(P(D_t)u, v) + (\mathrm{div}\boldsymbol{\lambda}, v) + (pu, v) = (f, v), & \forall v \in V, \\ (b)\left(\mathcal{A}^{-1}\boldsymbol{\lambda}, \boldsymbol{w}\right) - (u, \mathrm{div}\boldsymbol{w}) = 0, & \forall \boldsymbol{w} \in \boldsymbol{W}, \\ (c)u(\boldsymbol{x},0) = u_0(\boldsymbol{x}), & \forall \boldsymbol{x} \in \overline{\Omega}. \end{cases} \tag{3}$$

Let K_h be a quasi-uniform triangulation of the domain Ω, h_T be the diameter of the triangle $T \in K_h$ and denote $h = \max\{h_T\}$. We select the Raviart–Thomas MFE space $V_h \times \boldsymbol{W}_h \subset V \times \boldsymbol{W}$, that is,

$$\begin{aligned} V_h(K) &= \{v_h \in V : v_h|_T \in P_r(T), \forall T \in K_h\}, \\ \boldsymbol{W}_h(K) &= \left\{\boldsymbol{w}_h \in \boldsymbol{W} : \boldsymbol{w}_h\Big|_T \in (P_r(T))^2 \oplus (\boldsymbol{x}P_r(T)), \forall T \in K_h\right\}, \end{aligned}$$

where the notation $\oplus$ indicates a direct sum, $\boldsymbol{x}P_r(T) = (x_1P_r(T), x_2P_r(T)), \boldsymbol{x} = (x_1, x_2)$ and $r \geq 0$ is a given integer.

Let $\tau = T/N$ and $t_n = n\tau$ for $n = 0, 1, 2, \cdots, N$, where N is a positive integer. For the parameters α_i and $i = 1, 2, \cdots, m$, the Caputo time-fraction derivative $D_t^{\alpha_i}u(\boldsymbol{x},t)$ at $t = t_n$ is approximated by using the well-known $L1$ formula [36,37] as follows:

$$\begin{aligned} D_t^{\alpha_i}u(\boldsymbol{x},t_n) =& \frac{1}{\Gamma(1-\alpha_i)}\int_0^{t_n}\frac{\partial u(x,s)}{\partial s}\frac{1}{(t_n-s)^{\alpha_i}}ds \\ =& \frac{1}{\Gamma(2-\alpha_i)}\sum_{k=0}^{n-1}\frac{u^{k+1}-u^k}{\tau}\left[(t_n-t_k)^{1-\alpha_i} - (t_n-t_{k+1})^{1-\alpha_i}\right] + Q_{\alpha_i}^n(x) \\ =& \frac{1}{\Gamma(2-\alpha_i)}\left[d_{\alpha_i,1}^n u^n + \sum_{k=1}^{n-1}\left(d_{\alpha_i,k+1}^n - d_{\alpha_i,k}^n\right)u^{n-k} - d_{\alpha_i,n}^n u^0\right] + Q_{\alpha_i}^n(x) \\ =& \frac{1}{\Gamma(2-\alpha_i)}\sum_{k=0}^{n}\widetilde{d}_{\alpha_i,k}^n u^k + Q_{\alpha_i}^n(x), \end{aligned} \tag{4}$$

where $d^n_{\alpha_i,k} = \frac{(t_n-t_{n-k})^{1-\alpha_i}-(t_n-t_{n-k+1})^{1-\alpha_i}}{\tau}$, $\widetilde{d}^n_{\alpha_i,0} = -d^n_{\alpha_i,n}$, $\widetilde{d}^n_{\alpha_i,n} = -d^n_{\alpha_i,1}$, and $\widetilde{d}^n_{\alpha_i,k} = d^n_{\alpha_i,n-k+1} - d^n_{\alpha_i,n-k}(0 < k \le n-1)$. Setting $D^{\alpha_i}_N u^n = \frac{1}{\Gamma(2-\alpha_i)} \sum\limits_{k=0}^{n} \widetilde{d}^n_{\alpha_i,k} u^k$, we have $D^{\alpha_i}_t u(\boldsymbol{x}, t_n) = D^{\alpha_i}_N u^n + Q^n_{\alpha_i}(x)$, where $Q^n_{\alpha_i}(x)$ is the truncation error.

Based on the above definitions, and setting u^n_h and $\boldsymbol{\lambda}^n_h$ to be the discrete solutions of u and $\boldsymbol{\lambda}$ at $t = t_n$, respectively, then we can design a fully discrete MFE scheme for the original problem (1): find $\left(u^n_h, \lambda^n_h\right) \in V_h \times \boldsymbol{W}_h$ such that

$$\begin{cases} (a)\left(\sum\limits_{i=1}^{m} b_i D^{\alpha_i}_N u^n_h, v_h\right) + \left(\mathrm{div}\boldsymbol{\lambda}^n_h, v_h\right) + \left(p u^n_h, v_h\right) = (f^n, v_h), & \forall v_h \in V_h, \\ (b)\left(\mathcal{A}^{-1}\boldsymbol{\lambda}^n_h, \boldsymbol{w}_h\right) - \left(u^n_h, \mathrm{div}\boldsymbol{w}_h\right) = 0, & \forall \boldsymbol{w}_h \in \boldsymbol{W}_h, \end{cases} \tag{5}$$

where $\left(u^0_h, \boldsymbol{\lambda}^0_h\right) \in V_h \times \boldsymbol{W}_h$ satisfies

$$\begin{cases} (a)\left(\mathcal{A}^{-1}\boldsymbol{\lambda}^0_h, \boldsymbol{w}_h\right) - \left(u^0_h, \mathrm{div}\boldsymbol{w}_h\right) = 0, & \forall \boldsymbol{w}_h \in \boldsymbol{W}_h, \\ (b)\left(\mathrm{div}\boldsymbol{\lambda}^0_h, v_h\right) = (\mathrm{div}\boldsymbol{\lambda}_0, v_h), & \forall v_h \in V_h, \end{cases} \tag{6}$$

where $\boldsymbol{\lambda}_0(\boldsymbol{x}) = -\mathcal{A}(\boldsymbol{x})\nabla u_0(\boldsymbol{x})$.

Remark 1. *(I) In the MFE scheme (5)–(6), we particularly emphasize the calculation of initial values $\left(u^0_h, \boldsymbol{\lambda}^0_h\right)$, as this calculation will be used in stability and convergence analyses. Moreover, from the mixed elliptic projection R_h defined in Section 5, we can see that $\left(u^0_h, \boldsymbol{\lambda}^0_h\right) = (R_h u_0, R_h \boldsymbol{\lambda}_0)$.*

(II) Compared with the standard FE methods, it is well known that the MFE method can not only reduce the smoothness requirement of the finite element space, but also simultaneously calculate multiple physical quantities. These advantages are very important and popular in practical applications.

3. Existence and Uniqueness

In this section, we shall prove the existence and uniqueness for the MFE scheme (5)–(6). We first give some lemmas, which are important in subsequent theoretical analysis.

Lemma 1 ([38])**.** *There exist two positive constants μ_0 and μ_1 such that*

$$\mu_0 \| \boldsymbol{w} \|^2 \le \| \boldsymbol{w} \|^2_{\mathcal{A}^{-1}} \le \mu_1 \| \boldsymbol{w} \|^2, where \| \boldsymbol{w} \|^2_{\mathcal{A}^{-1}} = \left(\mathcal{A}^{-1}\boldsymbol{w}, \boldsymbol{w}\right), \forall \boldsymbol{w} \in \boldsymbol{W}.$$

Lemma 2 ([28])**.** *Let $\{z^n\}_{n=0}^{\infty}$ be a sequence on $\boldsymbol{W}_h$. Then, the following identity holds:*

$$\begin{aligned} \sum_{k=0}^{n} \widetilde{d}^n_{\alpha_i,k}\left(\mathcal{A}^{-1}z^k, z^n\right) =& \frac{1}{2}[\widetilde{d}^n_{\alpha_i,n}\left(\mathcal{A}^{-1}z^n, z^n\right) + \sum_{k=0}^{n-1} \widetilde{d}^n_{\alpha_i,k}\left(\mathcal{A}^{-1}z^k, z^k\right) \\ &+ \sum_{k=0}^{n-1} \widetilde{d}^n_{\alpha_i,k}\left(\mathcal{A}^{-1}\left(z^n - z^k\right), z^n - z^k\right]. \end{aligned}$$

Lemma 3. *Let $\left\{\varphi^k : 0 \le k \le N\right\}$ be a non-negative sequence, $\left\{\xi^k : 0 \le k \le N\right\}$ be a nondecreasing positive sequence, and $C_0 \ge 1$ be a constant, which satisfy*

$$\sum_{i=1}^{m} \frac{b_i}{\Gamma(2-\alpha_i)} \widetilde{d}^n_{\alpha_i,n} \varphi^n \le -C_0 \sum_{i=1}^{m} \frac{b_i}{\Gamma(2-\alpha_i)} \sum_{k=0}^{n-1} \widetilde{d}^n_{\alpha_i,k} \varphi^k + \xi^n, 1 \le n \le N. \tag{7}$$

Then, we have

$$\varphi^n \le C_0^n\left(\varphi^0 + \frac{1}{\sum\limits_{i=1}^{m} \frac{b_i}{\Gamma(2-\alpha_i)} d^n_{\alpha_i,n}} \xi^n\right), 1 \le n \le N. \tag{8}$$

Further, we can further write (8) as

$$\varphi^n \le C_0^n(\varphi^0 + \sum_{i=1}^{m} \frac{\Gamma(1-\alpha_i)t_n^{\alpha_i}}{b_i}\xi^n), 1 \le n \le N. \tag{9}$$

Proof. When $n = 1$ in (7), we have

$$\sum_{i=1}^{m} \frac{b_i}{\Gamma(2-\alpha_i)} \widetilde{d}^1_{\alpha_i,1}\varphi^1 \le -C_0 \sum_{i=1}^{m} \frac{b_i}{\Gamma(2-\alpha_i)} \widetilde{d}^1_{\alpha_i,0}\varphi^0 + \xi^1. \tag{10}$$

Noting that $\widetilde{d}^n_{\alpha_i,0} = -d^n_{\alpha_i,n}, \widetilde{d}^n_{\alpha_i,n} = d^n_{\alpha_i,1}$, we have

$$\sum_{i=1}^{m} \frac{b_i}{\Gamma(2-\alpha_i)} d^1_{\alpha_i,1}\varphi^1 \le C_0 \sum_{i=1}^{m} \frac{b_i}{\Gamma(2-\alpha_i)} d^1_{\alpha_i,1}\varphi^0 + \xi^1. \tag{11}$$

Then, we can obtain

$$\varphi^1 \le C_0(\varphi^0 + \frac{1}{\sum\limits_{i=1}^{m} \frac{b_i}{\Gamma(2-\alpha_i)} d^1_{\alpha_i,1}}\xi^1). \tag{12}$$

It means that the conclusion (8) is valid for the case of $n = 1$. Assume that (8) is valid for $n = 1, 2, \cdots, r$. We now need to prove that it also holds for $n = r + 1$. Selecting $n = r + 1$ in (7), we obtain

$$\begin{aligned}
&\sum_{i=1}^{m} \frac{b_i}{\Gamma(2-\alpha_i)} \widetilde{d}^{j+1}_{\alpha_i,j+1}\varphi^{j+1} \\
\le& -C_0 \sum_{i=1}^{m} \frac{b_i}{\Gamma(2-\alpha_i)} \sum_{k=0}^{j} \widetilde{d}^{j+1}_{\alpha_i,k}\varphi^k + \xi^{j+1} \\
=& C_0 \sum_{i=1}^{m} \frac{b_i}{\Gamma(2-\alpha_i)} \sum_{k=1}^{j} \left(d^{j+1}_{\alpha_i,j-k+1} - d^{j+1}_{\alpha_i,j-k+2}\right)\varphi^k + C_0 \sum_{i=1}^{m} b_i d^{j+1}_{\alpha_i,j+1}\varphi^0 + \xi^{j+1} \\
=& C_0 \sum_{i=1}^{m} \frac{b_i}{\Gamma(2-\alpha_i)} \sum_{k=0}^{j-1} \left(d^{j+1}_{\alpha_i,k+1} - d^{j+1}_{\alpha_i,k+2}\right)\varphi^{j-k} + C_0 \sum_{i=1}^{m} \frac{b_i}{\Gamma(2-\alpha_i)} d^{j+1}_{\alpha_i,j+1}\varphi^0 + \xi^{j+1}.
\end{aligned} \tag{13}$$

Noting that $0 < d^{k+1}_{\alpha_i,k+1} < d^k_{\alpha_i,k}$ and $0 < d^n_{\alpha_i,k+1} < d^n_{\alpha_i,k}, (k = 0, 1 \cdots j)$, we have

$$\begin{aligned}
&\sum_{i=1}^{m} \frac{b_i}{\Gamma(2-\alpha_i)} \widetilde{d}^{j+1}_{\alpha_i,j+1}\varphi^{j+1} \\
\le& C_0 \sum_{i=1}^{m} \frac{b_i}{\Gamma(2-\alpha_i)} \sum_{k=0}^{j-1} \left(d^{j+1}_{\alpha_i,k+1} - d^{j+1}_{\alpha_i,k+2}\right)[C_0^{j-k}(\varphi^0 + \frac{1}{\sum\limits_{i=1}^{m} \frac{b_i}{\Gamma(2-\alpha_i)} d^{j-k}_{\alpha_i,j-k}}\xi^{j-k})] \\
&+ C_0 \sum_{i=1}^{m} \frac{b_i}{\Gamma(2-\alpha_i)} \mathrm{d}^{j+1}_{\alpha_i,j+1}(\varphi^0 + \frac{1}{\sum\limits_{i=1}^{m} \frac{b_i}{\Gamma(2-\alpha_i)} d^{j+1}_{\alpha_i,j+1}}\xi^{j+1}) \\
\le& C_0^{j+1} \sum_{i=1}^{m} \frac{b_i}{\Gamma(2-\alpha_i)} [\sum_{k=0}^{j-1} \left(d^{j+1}_{\alpha_i,k+1} - d^{j+1}_{\alpha_i,k+2}\right) + d^{j+1}_{\alpha_i,j+1}](\varphi^0 + \frac{1}{\sum\limits_{i=1}^{m} \frac{b_i}{\Gamma(2-\alpha_i)} d^{j+1}_{\alpha_i,j+1}}\xi^{j+1}) \\
\le& C_0^{j+1} \sum_{i=1}^{m} \frac{b_i}{\Gamma(2-\alpha_i)} d^{j+1}_{\alpha_i,1}(\varphi^0 + \frac{1}{\sum\limits_{i=1}^{m} \frac{b_i}{\Gamma(2-\alpha_i)} d^{j+1}_{\alpha_i,j+1}}\xi^{j+1}).
\end{aligned} \tag{14}$$

Therefore, using the mathematical induction method, we can complete the proof of (8). From [37], we know $n^{\alpha_i}\left(n^{1-\alpha_i}-(n-1)^{1-\alpha_i}\right)\geq 1-\alpha_i$, and then

$$d^n_{\alpha_i,n}=\frac{(n\tau)^{1-\alpha_i}-(n\tau-\tau)^{1-\alpha_i}}{\tau}=\frac{\left(n^{1-\alpha_i}-(n-1)^{1-\alpha_i}\right)}{\tau^{\alpha_i}}\geq\frac{(1-\alpha_i)}{\tau^{\alpha_i}n^{\alpha_i}}. \tag{15}$$

Thus, making use of (8) and (15), we can complete the proof of (9). □

Next, we give the existence and uniqueness results for the MFE scheme (5).

Theorem 1. *The MFE scheme (5) has a unique solution.*

Proof. Let $V_h=\text{span}\{\phi_1,\phi_2,\cdots,\phi_{M_1}\}$ and $\boldsymbol{W}_h=\text{span}\{\boldsymbol{\psi}_1,\boldsymbol{\psi}_2,\cdots,\boldsymbol{\psi}_{M_2}\}$. Then, u^n_h and $\boldsymbol{\lambda}^n_h$ can be written as

$$u^n_h=\sum_{i=1}^{M_1}\widetilde{u}^n_i\phi_i,\boldsymbol{\lambda}^n_h=\sum_{j=1}^{M_2}\widetilde{s}^n_j\boldsymbol{\psi}_j. \tag{16}$$

Substituting 16 into (5) and selecting $v_h=\phi_i\ \ (i=1,2,\cdots,M_1)$ and $\boldsymbol{w}_h=\boldsymbol{\psi}_j\ \ (j=1,2,\cdots,M_2)$, we have

$$\begin{bmatrix}\sum\limits_{i=1}^{m}\frac{b_i}{\Gamma(2-\alpha_i)}\widetilde{d}^n_{\alpha_i,n}B_1+B_3 & D^T\\ -D & B_2\end{bmatrix}\begin{bmatrix}U^n\\L^n\end{bmatrix}=\begin{bmatrix}F^n-\sum\limits_{i=1}^{m}\frac{b_i}{\Gamma(2-\alpha_i)}\sum\limits_{k=0}^{n-1}\widetilde{d}^n_{\alpha_i,k}B_1U^k\\0\end{bmatrix}, \tag{17}$$

where

$$\begin{aligned}&U^n=\left(\widetilde{u}^n_1,\widetilde{u}^n_2,\cdots,\widetilde{u}^n_{M_1}\right)^T, && L^n=\left(\widetilde{s}^n_1,\widetilde{s}^n_2,\cdots,\widetilde{s}^n_{M_2}\right)^T,\\ &B_1=\left((\phi_i,\phi_j)\right)_{M_1\times M_1}, && B_2=\left((\mathcal{A}^{-1}\boldsymbol{\psi}_i,\boldsymbol{\psi}_j)\right)_{M_2\times M_2},\\ &B_3=\left((p\phi_i,\phi_j)\right)_{M_1\times M_1}, && D=\left((\text{div}\boldsymbol{\psi}_i,\phi_j)\right)_{M_2\times M_1},\\ &F^n=\left((f^n,\phi_i)\right)_{M_1\times 1},\end{aligned}$$

Noting that B_1 and B_2 are symmetric positive definite matrices and B_3 is a symmetric semi-positive matrix, we have

$$\begin{bmatrix}E & -D^TB_2^{-1}\\0 & E\end{bmatrix}\begin{bmatrix}\sum\limits_{i=1}^{m}\frac{b_i}{\Gamma(2-\alpha_i)}\widetilde{d}^n_{\alpha_i,n}B_1+B_3 & D^T\\ -D & B_2\end{bmatrix}=\begin{bmatrix}G & 0\\-D & B_2\end{bmatrix}. \tag{18}$$

where $G=\sum\limits_{i=1}^{m}\frac{b_i}{\Gamma(2-\alpha_i)}\widetilde{d}^n_{\alpha_i,n}B_1+B_3+D^TB_2^{-1}D$. It is easy to see that G is invertible, so the coefficient matrix of linear Equation (17) is invertible. This means that the MFE scheme (5) has a unique solution. □

Remark 2. *For Lemma 3, when $C_0=1$, a similar conclusion can be seen from the proof of Theorem 3.1 in [20]. When $C_0>1$, some special applications can be seen from [39]. It should be noted that this lemma can be considered a fractional Grönwall inequality without any other conditions for its existence, which will play a crucial role in the subsequent proof process of stability and convergence analyses.*

4. Stability Analysis

In this section, we will discuss the unconditional stability for the MFE scheme (5)–(6).

Theorem 2. *Let* $\left(u_h^n, \boldsymbol{\lambda}_h^n\right)_{n=1}^N$ *be the solutions of the MFE scheme (5). Then, there exists a constant* $C > 0$ *independent of* h *and* N *such that*

$$\| u_h^n \| \leq \| u_h^0 \| + \sum_{i=1}^{m} \frac{\Gamma(1-\alpha_i) t_n^{\alpha_i}}{b_i} \sup_{t\in[0,T]} \| f(t) \| \triangleq U_h^{\diamond},$$

$$\| \boldsymbol{\lambda}_h^n \| \leq C \left(\| \boldsymbol{\lambda}_h^0 \| + \left(\sum_{i=1}^{m} \frac{\Gamma(1-\alpha_i) t_n^{\alpha_i}}{b_i} \right)^{1/2} \left(\sup_{t\in[0,T]} \| f(t) \| + \| p \|_{\infty} U_h^{\diamond} \right) \right).$$

Proof. Taking $v_h = u_h^n$ and $w_h = \boldsymbol{\lambda}_h^n$ in (5), we have

$$\left(\sum_{i=1}^{m} b_i D_N^{\alpha_i} u_h^n, u_h^n \right) + \left(\mathcal{A}^{-1} \boldsymbol{\lambda}_h^n, \boldsymbol{\lambda}_h^n \right) + (p u_h^n, u_h^n) = (f^n, u_h^n). \tag{19}$$

Using Lemma 1 and the definition of $D_N^{\alpha_i} u_h^n$, we have

$$\sum_{i=1}^{m} \frac{b_i}{\Gamma(2-\alpha_i)} \widetilde{d}_{\alpha_i,n}^n (u_h^n, u_h^n) + \mu_0 \| \boldsymbol{\lambda}_h^n \|^2 \leq \sum_{i=1}^{m} \frac{b_i}{\Gamma(2-\alpha_i)} \sum_{k=0}^{n-1} \widetilde{d}_{\alpha_i,k}^n \left(u_h^k, u_h^n \right) + (f^n, u_h^n). \tag{20}$$

Applying the Cauchy–Schwarz inequality yields

$$\sum_{i=1}^{m} \frac{b_i}{\Gamma(2-\alpha_i)} \widetilde{d}_{\alpha_i,n}^n \| u_h^n \| \leq \sum_{i=1}^{m} \frac{b_i}{\Gamma(2-\alpha_i)} \sum_{k=0}^{n-1} \widetilde{d}_{\alpha_i,k}^n \| u_h^k \| + \| f^n \|. \tag{21}$$

Using Lemma 3, we obtain

$$\| u_h^n \| \leq \| u_h^0 \| + \sum_{i=1}^{m} \frac{\Gamma(1-\alpha_i) t_n^{\alpha_i}}{b_i} \sup_{t\in[0,T]} \| f(t) \| \triangleq U_h^{\diamond}. \tag{22}$$

Next, using (5) (b) and (6) (a), we have

$$\left(A^{-1} \sum_{i=1}^{m} b_i D_N^{\alpha_i} \boldsymbol{\lambda}_h^n, \boldsymbol{w}_h \right) - \left(\sum_{i=1}^{m} b_i D_N^{\alpha_i} u_h^n, \mathrm{div} \boldsymbol{w}_h \right) = 0, \forall \boldsymbol{w}_h \in \boldsymbol{W}_h. \tag{23}$$

Choosing $v_h = \sum_{i=1}^{m} b_i D_N^{\alpha_i} u_h^n$ and $\boldsymbol{w}_h = \boldsymbol{\lambda}_h^n$ in (5) (a) and (23), respectively, we obtain

$$\| \sum_{i=1}^{m} b_i D_N^{\alpha_i} u_h^n \|^2 + \left(A^{-1} \sum_{i=1}^{m} b_i D_N^{\alpha_i} \boldsymbol{\lambda}_h^n, \boldsymbol{\lambda}_h^n \right) + \left(p u_h^n, \sum_{i=1}^{m} b_i D_N^{\alpha_i} u_h^n \right) = \left(f^n, \sum_{i=1}^{m} b_i D_N^{\alpha_i} u_h^n \right). \tag{24}$$

Using Lemma 2 in (24) yields

$$\begin{aligned} &\| \sum_{i=1}^{m} b_i D_N^{\alpha_i} u_h^n \|^2 + \frac{1}{2} \sum_{i=0}^{m} \frac{b_i}{\Gamma(2-\alpha_i)} \left[\widetilde{d}_{\alpha_i,n}^n \left(A^{-1} \boldsymbol{\lambda}_h^n, \boldsymbol{\lambda}_h^n \right) + \sum_{k=0}^{n-1} \widetilde{d}_{\alpha_i,k}^n \left(A^{-1} \boldsymbol{\lambda}_h^k, \boldsymbol{\lambda}_h^k \right) \right. \\ &\left. - \sum_{k=0}^{n-1} \widetilde{d}_{\alpha_i,k}^n \left(A^{-1} \left(\boldsymbol{\lambda}_h^n - \boldsymbol{\lambda}_h^k \right), \boldsymbol{\lambda}_h^n - \boldsymbol{\lambda}_h^k \right) \right] = \left(f^n, \sum_{i=1}^{m} b_i D_N^{\alpha_i} u_h^n \right) - \left(p u_h^n, \sum_{i=1}^{m} b_i D_N^{\alpha_i} u_h^n \right). \end{aligned} \tag{25}$$

Because of $\widetilde{d}^n_{\alpha_i,k} < 0, 0 < k \le n-1$, we have

$$\begin{aligned}
&\| \sum_{i=1}^{m} b_i D_N^{\alpha_i} u_h^n \|^2 + \frac{1}{2} \sum_{i=0}^{m} \frac{b_i}{\Gamma(2-\alpha_i)} \widetilde{d}^n_{\alpha_i,n} \left(A^{-1} \boldsymbol{\lambda}_h^n, \boldsymbol{\lambda}_h^n \right) \\
\le & -\frac{1}{2} \sum_{i=0}^{m} \frac{b_i}{\Gamma(2-\alpha_i)} \sum_{k=0}^{n-1} \widetilde{d}^n_{\alpha_i,k} \left(A^{-1} \boldsymbol{\lambda}_h^k, \boldsymbol{\lambda}_h^k \right) \\
& + \left(f^n, \sum_{i=1}^{m} b_i D_N^{\alpha_i} u_h^n \right) - \left(p u_h^n, \sum_{i=1}^{m} b_i D_N^{\alpha_i} u_h^n \right).
\end{aligned} \tag{26}$$

Apply the Cauchy–Schwarz inequality and the Young inequality in (26) to obtain

$$\begin{aligned}
&\| \sum_{i=1}^{m} b_i D_N^{\alpha_i} u_h^n \|^2 + \frac{1}{2} \sum_{i=0}^{m} \frac{b_i}{\Gamma(2-\alpha_i)} \widetilde{d}^n_{\alpha_i,n} \left(A^{-1} \boldsymbol{\lambda}_h^n, \boldsymbol{\lambda}_h^n \right) \\
\le & -\frac{1}{2} \sum_{i=0}^{m} \frac{b_i}{\Gamma(2-\alpha_i)} \sum_{k=0}^{n-1} \widetilde{d}^n_{\alpha_i,k} \left(A^{-1} \boldsymbol{\lambda}_h^k, \boldsymbol{\lambda}_h^k \right) \\
& + \frac{1}{2} \| \sum_{i=1}^{m} b_i D_N^{\alpha_i} u_h^n \|^2 + \| f^n \|^2 + \| p \|_\infty^2 \| u_h^n \|^2.
\end{aligned} \tag{27}$$

Using Lemma 3 in (27), we obtain

$$\| \boldsymbol{\lambda}_h^n \| \le C \left(\| \boldsymbol{\lambda}_h^0 \| + \left(\sum_{i=1}^{m} \frac{\Gamma(1-\alpha_i) t_n^{\alpha_i}}{b_i} \right)^{1/2} \left(\sup_{t \in [0,T]} \| f(t) \| + \| p \|_\infty U_h^\diamond \right) \right). \tag{28}$$

Thus, we complete the proof. □

5. Convergence Analysis

In this section, we will present the convergence results. For this purpose, we first introduce the mixed elliptic projection $(R_h u, R_h \boldsymbol{\lambda}) \in V_h \times \boldsymbol{W}_h$ defined by

$$\begin{cases} (a)(\mathcal{A}^{-1}(\boldsymbol{\lambda} - R_h \boldsymbol{\lambda}), \boldsymbol{w}_h) - (u - R_h u, \mathrm{div} \boldsymbol{w}_h) = 0, & \forall w_h \in \boldsymbol{W}_h, \\ (b)(\mathrm{div}(\boldsymbol{\lambda} - R_h \boldsymbol{\lambda}), v_h) = 0, & \forall v_h \in V_h. \end{cases} \tag{29}$$

Then, the above projection satisfies the classical estimates as follows.

Lemma 4 ([40,41])**.** *There exists a constant $C > 0$ independent of h and N such that*

$$\begin{aligned}
&\| \boldsymbol{\lambda} - R_h \boldsymbol{\lambda} \| \le C h^{r+1} \| \boldsymbol{\lambda} \|_{r+1}, for \boldsymbol{\lambda} \in \left(H^{r+1}(\Omega) \right)^2, \\
&\| \mathrm{div}(\boldsymbol{\lambda} - R_h \boldsymbol{\lambda}) \| \le C h^{r+1} \| \mathrm{div} \boldsymbol{\lambda} \|_{r+1}, for \mathrm{div} \boldsymbol{\lambda} \in H^{r+1}(\Omega), \\
&\| u - R_h u \| \le C h^{r+1} \left(\| u \|_{r+1} + \| \boldsymbol{\lambda} \|_{r+1} \right), for u \in H^{r+1}(\Omega), \boldsymbol{\lambda} \in \left(H^{r+1}(\Omega) \right)^2.
\end{aligned}$$

For the truncation error $Q^n_{\alpha_i}$ $(i = 1, 2, \cdots, m)$ of the $L1$ formula, from [36,37], we give the following estimates.

Lemma 5. *Let $u \in \mathcal{C}^2(\overline{J}, L^2(\Omega))$. Then, we have*

$$\begin{aligned}
&\| Q^n_{\alpha_i} \| \le C N^{-(2-\alpha_i)}, i = 1, 2, \cdots, m, \\
&\| \sum_{i=1}^{m} b_i Q^n_{\alpha_i} \| \le C N^{-(2-\alpha_1)},
\end{aligned}$$

where $C > 0$ is a constant independent of h and N.

Now, we write the errors $u(t_n) - u_h^n = u(t_n) - R_h u(t_n) + R_h u(t_n) - u_h^n = \rho^n + \theta^n$ and $\boldsymbol{\lambda}(t_n) - \boldsymbol{\lambda}_h^n = \boldsymbol{\lambda}(t_n) - R_h\boldsymbol{\lambda}(t_n) + R_h\boldsymbol{\lambda}(t_n) - \boldsymbol{\lambda}_h^n = \boldsymbol{\xi}^n + \boldsymbol{\eta}^n$. From (3) and (5), making use of the mixed elliptic projection R_h, we have the following error equations:

$$\begin{cases} (a)\left(\sum\limits_{i=1}^{m} b_i D_N^{\alpha_i}(\theta^n + \rho^n), v_h\right) + (\mathrm{div}\boldsymbol{\eta}^n, v_h) + (p(\theta^n + \rho^n), v_h) \\ = -\left(\sum\limits_{i=1}^{m} b_i Q_{\alpha_i}^n, v_h\right), & \forall v_h \in V_h, \\ (b)\left(\mathcal{A}^{-1}\boldsymbol{\eta}^n, \boldsymbol{w}_h\right) - (\theta^n, \mathrm{div}\boldsymbol{w}_h) = 0, & \forall \boldsymbol{w}_h \in \boldsymbol{W}_h. \end{cases} \tag{30}$$

Noting that $\left(u_h^0, \boldsymbol{\lambda}_h^0\right) = (R_h u_0, R_h\boldsymbol{\lambda}_0)$, we have $\theta^0 = 0$ and $\boldsymbol{\eta}^0 = \mathbf{0}$. We next give the convergence results for the MFE scheme (5)–(6).

Theorem 3. *Let $(u^n, \boldsymbol{\lambda}^n) \in V \times \boldsymbol{W}$ and $\left(u_h^n, \boldsymbol{\lambda}_h^n\right) \in V_h \times \boldsymbol{W}_h$ be the solutions of (3) and (5), respectively. Assume that $u, div\boldsymbol{\lambda} \in \mathcal{C}^2\left(\overline{J}, H^{r+1}(\Omega)\right)$, $\boldsymbol{\lambda} \in \mathcal{C}^2\left(\overline{J}, \left(H^{r+1}(\Omega)\right)^2\right)$. Then, we have*

$$\begin{aligned} &\max_{1\le n\le N} \| u(t_n) - u_h^n \| + \max_{1\le n\le N} \| \boldsymbol{\lambda}(t_n) - \boldsymbol{\lambda}_h^n \| \le C\left(h^{r+1} + N^{-(2-\alpha_1)}\right), \\ &\max_{1\le n\le N} \| \boldsymbol{\lambda}(t_n) - \boldsymbol{\lambda}_h^n \|_{\boldsymbol{H}(\mathrm{div},\Omega)} \le C\left(1 + N^{\frac{\alpha_m}{2}}\right)\left(h^{r+1} + N^{-(2-\alpha_1)}\right), \end{aligned}$$

where $C > 0$ is a constant independent of h and N.

Proof. Taking $v_h = \theta^n$ and $\boldsymbol{w}_h = \boldsymbol{\eta}^n$ in (30), we can obtain

$$\begin{aligned} &\left(\sum_{i=1}^{m} b_i D_N^{\alpha_i}\theta^n, \theta^n\right) + \left(\mathcal{A}^{-1}\boldsymbol{\eta}^n, \boldsymbol{\eta}^n\right) + (p\theta^n, \theta^n) \\ =&-\left(\sum_{i=1}^{m} b_i Q_{\alpha_i}^n, \theta^n\right) - (p\rho^n, \theta^n) - \left(\sum_{i=1}^{m} b_i D_N^{\alpha_i}\rho^n, \theta^n\right). \end{aligned} \tag{31}$$

Noting that $p(\boldsymbol{x}) \ge 0$, using the Lemma 1 and the definition of $D_N^{\alpha_i} u_h^n$, we have

$$\begin{aligned} &\sum_{i=1}^{m} \frac{b_i}{\Gamma(2-\alpha_i)} \widetilde{d}_{\alpha_i,n}^n(\theta^n, \theta^n) + \mu_0 \| \boldsymbol{\eta}^n \|^2 \\ \le&-\sum_{i=1}^{m} \frac{b_i}{\Gamma(2-\alpha_i)} \sum_{k=0}^{n-1} \widetilde{d}_{\alpha_i,k}^n\left(\theta^k, \theta^n\right) - \left(\sum_{i=1}^{m} b_i Q_{\alpha_i}^n, \theta^n\right) - (p\rho^n, \theta^n) - \left(\sum_{i=1}^{m} b_i D_N^{\alpha_i}\rho^n, \theta^n\right). \end{aligned} \tag{32}$$

Applying the Cauchy–Schwarz inequality, we obtain

$$\begin{aligned} &\sum_{i=1}^{m} \frac{b_i}{\Gamma(2-\alpha_i)} \widetilde{d}_{\alpha_i,n}^n \| \theta^n \|^2 + \mu_0 \| \boldsymbol{\eta}^n \|^2 \\ \le&-\sum_{i=1}^{m} \frac{b_i}{\Gamma(2-\alpha_i)} \sum_{k=0}^{n-1} \widetilde{d}_{\alpha_i,k}^n \| \theta^k \| \| \theta^n \| \\ &+(\| \sum_{i=1}^{m} b_i Q_{\alpha_i}^n \| + \| p \|_\infty \| \rho \| + \| \sum_{i=1}^{m} b_i D_N^{\alpha_i}\rho^n \|) \| \theta^n \|, \end{aligned} \tag{33}$$

and then

$$\begin{aligned}&\sum_{i=1}^{m}\frac{b_i}{\Gamma(2-\alpha_i)}\widetilde{d}^{n}_{\alpha_i,n}\| \theta^n \|^2\\ \leq&-\sum_{i=1}^{m}\frac{b_i}{\Gamma(2-\alpha_i)}\sum_{k=0}^{n-1}\widetilde{d}^{n}_{\alpha_i,k}\| \theta^k \| + (\| \sum_{i=1}^{m} b_i Q^n_{\alpha_i} \| + \| p \|_\infty \| \rho \| + \| \sum_{i=1}^{m} b_i D^{\alpha_i}_N \rho^n \|).\end{aligned} \tag{34}$$

Using Lemmas 4 and 5, we obtain

$$\sum_{i=1}^{m}\frac{b_i}{\Gamma(2-\alpha_i)}\widetilde{d}^{n}_{\alpha_i,n}\| \theta^n \| \leq -\sum_{i=1}^{m}\frac{b_i}{\Gamma(2-\alpha_i)}\sum_{k=0}^{n-1}\widetilde{d}^{n}_{\alpha_i,k}\| \theta^k \| + C\Big(N^{-(2-\alpha_1)}+h^{r+1}\Big). \tag{35}$$

Noting that $\theta^0 = 0$ and using Lemma 3, we obtain

$$\| \theta^n \| \leq C\Big(h^{r+1}+N^{-(2-\alpha_1)}\Big). \tag{36}$$

Now, from (30) (b), we obtain

$$\left(\mathcal{A}^{-1}\sum_{i=1}^{m} b_i D^{\alpha_i}_N \boldsymbol{\eta}^n, \boldsymbol{w}_h\right) - \left(\sum_{i=1}^{m} b_i D^{\alpha_i}_N \theta^n, \mathrm{div}\boldsymbol{w}_h\right) = 0, \forall \boldsymbol{w}_h \in \boldsymbol{W}_h. \tag{37}$$

Choosing $v_h = \sum\limits_{i=1}^{m} b_i D^{\alpha_i}_N \theta^n$ and $\boldsymbol{w}_h = \boldsymbol{\eta}^n$ in (30) (a) and (37), respectively, we can obtain

$$\begin{aligned}&\| \sum_{i=1}^{m} b_i D^{\alpha_i}_N \theta^n \|^2 + \left(\mathcal{A}^{-1}\sum_{i=1}^{m} b_i D^{\alpha_i}_N \boldsymbol{\eta}^n, \boldsymbol{\eta}^n\right)\\ =&-\left(\sum_{i=1}^{m} b_i D^{\alpha_i}_N \rho^n, \sum_{i=1}^{m} b_i D^{\alpha_i}_N \theta^n\right) - \left(p(\rho^n+\theta^n), \sum_{i=1}^{m} b_i D^{\alpha_i}_N \theta^n\right) - \left(\sum_{i=1}^{m} b_i Q^n_{\alpha_i}, \sum_{i=1}^{m} b_i D^{\alpha_i}_N \theta^n\right).\end{aligned} \tag{38}$$

Using Lemma 2, we have

$$\begin{aligned}&\| \sum_{i=1}^{m} b_i D^{\alpha_i}_N \theta^n \|^2 + \frac{1}{2}\sum_{i=1}^{m}\frac{b_i}{\Gamma(2-\alpha_i)}\Big[\widetilde{d}^{n}_{\alpha_i,n}\Big(\mathcal{A}^{-1}\boldsymbol{\eta}^n, \boldsymbol{\eta}^n\Big) - \sum_{k=0}^{n-1}\widetilde{d}^{n}_{\alpha_i,k}\Big(\mathcal{A}^{-1}\Big(\boldsymbol{\eta}^n-\boldsymbol{\eta}^k, \boldsymbol{\eta}^n-\boldsymbol{\eta}^k\Big)\Big]\\ =&-\frac{1}{2}\sum_{i=1}^{m}\frac{b_i}{\Gamma(2-\alpha_i)}\sum_{k=0}^{n-1}\widetilde{d}^{n}_{\alpha_i,k}\Big(\mathcal{A}^{-1}\boldsymbol{\eta}^k, \boldsymbol{\eta}^k\Big) - \left(\sum_{i=1}^{m} b_i D^{\alpha_i}_N \rho^n, \sum_{i=1}^{m} b_i D^{\alpha_i}_N \theta^n\right)\\ &-\left(\sum_{i=1}^{m} b_i Q^n_{\alpha_i}, \sum_{i=1}^{m} b_i D^{\alpha_i}_N \theta^n\right) - \left(p(\rho^n+\theta^n), \sum_{i=1}^{m} b_i D^{\alpha_i}_N \theta^n\right).\end{aligned} \tag{39}$$

Noting that $\widetilde{d}^{n}_{\alpha_i,k} < 0, 0 < k \leq n-1$ and using Lemma 1, we obtain

$$\begin{aligned}&\| \sum_{i=1}^{m} b_i D^{\alpha_i}_N \theta^n \|^2 + \frac{1}{2}\sum_{i=1}^{m}\frac{b_i}{\Gamma(2-\alpha_i)}\widetilde{d}^{n}_{\alpha_i,n}\Big(\mathcal{A}^{-1}\boldsymbol{\eta}^n, \boldsymbol{\eta}^n\Big)\\ \leq&-\frac{1}{2}\sum_{i=1}^{m}\frac{b_i}{\Gamma(2-\alpha_i)}\sum_{k=0}^{n-1}\widetilde{d}^{n}_{\alpha_i,k}\Big(\mathcal{A}^{-1}\boldsymbol{\eta}^k, \boldsymbol{\eta}^k\Big) - \left(\sum_{i=1}^{m} b_i D^{\alpha_i}_N \rho^n, \sum_{i=1}^{m} b_i D^{\alpha_i}_N \theta^n\right)\\ &-\left(\sum_{i=1}^{m} b_i Q^n_{\alpha_i}, \sum_{i=1}^{m} b_i D^{\alpha_i}_N \theta^n\right) - \left(p(\rho^n+\theta^n), \sum_{i=1}^{m} b_i D^{\alpha_i}_N \theta^n\right).\end{aligned} \tag{40}$$

Applying the Cauchy–Schwarz and the Young inequality in (40) yields

$$\begin{aligned}
&\| \sum_{i=1}^{m} b_i D_N^{\alpha_i}\theta^n \|^2 + \frac{1}{2}\sum_{i=1}^{m}\frac{b_i}{\Gamma(2-\alpha_i)}\widetilde{d}^n_{\alpha_i,n}\Big(\mathcal{A}^{-1}\boldsymbol{\eta}^n,\boldsymbol{\eta}^n\Big)\\
\leq&-\frac{1}{2}\sum_{i=1}^{m}\frac{b_i}{\Gamma(2-\alpha_i)}\sum_{k=0}^{n-1}\widetilde{d}^n_{\alpha_i,k}\Big(\mathcal{A}^{-1}\boldsymbol{\eta}^k,\boldsymbol{\eta}^k\Big)+\frac{1}{2}\| \sum_{i=1}^{m} b_i D_N^{\alpha}\theta^n \|^2\\
&+2\Bigg(\| \sum_{i=1}^{m} b_i D_N^{\alpha_i}\rho^n \| + \| \sum_{i=1}^{m} b_i Q^n_{\alpha_i} \|^2 + \| p \|^2_\infty(\| \rho^n \|^2 + \| \theta^n \|^2)\Bigg).
\end{aligned} \tag{41}$$

Using Lemmas 4 and 5, we obtain

$$\begin{aligned}
&\sum_{i=1}^{m}\frac{b_i}{\Gamma(2-\alpha_i)}\widetilde{d}^n_{\alpha_i,n}\Big(\mathcal{A}^{-1}\boldsymbol{\eta}^n,\boldsymbol{\eta}^n\Big)\\
\leq&-\sum_{i=1}^{m}\frac{b_i}{\Gamma(2-\alpha_i)}\sum_{k=0}^{n-1}\widetilde{d}^n_{\alpha_i,k}\Big(\mathcal{A}^{-1}\boldsymbol{\eta}^k,\boldsymbol{\eta}^k\Big)+C\Big(N^{-2(2-\alpha_1)}+h^{2r+2}\Big).
\end{aligned} \tag{42}$$

Noting that $\boldsymbol{\eta}^0=\mathbf{0}$ and using Lemma 3, we obtain

$$\| \boldsymbol{\eta}^n \| \leq C\Big(h^{r+1}+N^{-(2-\alpha_1)}\Big). \tag{43}$$

We now estimate $\| \boldsymbol{\lambda}^n-\boldsymbol{\lambda}^n_h \|_{\boldsymbol{H}(\mathrm{div},\Omega)}$. Taking $v_h=\sum\limits_{i=1}^{m} b_i D_N^{\alpha_i}\theta^n$ and $\boldsymbol{w}_h=\boldsymbol{\eta}^n$ in (30) (a) and (37), respectively, we have

$$\begin{aligned}
\| \mathrm{div}\boldsymbol{\eta}^n \|^2=&-\Bigg(\mathcal{A}^{-1}\sum_{i=1}^{m} b_i D_N^{\alpha_i}\boldsymbol{\eta}^n,\boldsymbol{\eta}^n\Bigg)-\Bigg(\sum_{i=1}^{m} b_i D_N^{\alpha_i}\rho^n,\mathrm{div}\boldsymbol{\eta}^n\Bigg)\\
&-(p(\rho^n+\theta^n),\mathrm{div}\boldsymbol{\eta}^n)-\Bigg(\sum_{i=1}^{m} b_i Q^n_{\alpha_i},\mathrm{div}\boldsymbol{\eta}^n\Bigg).
\end{aligned} \tag{44}$$

For the term $-\Bigg(\mathcal{A}^{-1}\sum\limits_{i=1}^{m} b_i D_N^{\alpha_i}\boldsymbol{\eta}^n,\boldsymbol{\eta}^n\Bigg)$, noting that $\sum\limits_{k=0}^{n-1}\Big(-\widetilde{d}^n_{\alpha_i,k}\Big)=T^{-\alpha_i}N^{\alpha_i}$, we obtain

$$\begin{aligned}
-\Bigg(\mathcal{A}^{-1}\sum_{i=1}^{m} b_i D_N^{\alpha_i}\boldsymbol{\eta}^n,\boldsymbol{\eta}^n\Bigg)=&-\sum_{i=1}^{m}\frac{b_i}{\Gamma(2-\alpha_i)}\Bigg(\sum_{k=0}^{n-1}\widetilde{d}^n_{\alpha_i,k}\Big(\mathcal{A}^{-1}\boldsymbol{\eta}^k,\boldsymbol{\eta}^n\Big)+\widetilde{d}^n_{\alpha_i,n}\Big(\mathcal{A}^{-1}\boldsymbol{\eta}^n,\boldsymbol{\eta}^n\Big)\Bigg)\\
\leq&\mu_1\sum_{i=1}^{m}\frac{b_i}{\Gamma(2-\alpha_i)}\sum_{k=0}^{n-1}\Big(-\widetilde{d}^n_{\alpha_i,k}\Big)\| \boldsymbol{\eta}^k \|\| \boldsymbol{\eta}^n \|\\
\leq&C\sum_{i=1}^{m}\frac{b_i}{\Gamma(2-\alpha_i)}T^{-\alpha_i}N^{\alpha_i}\Big(N^{-(2-\alpha_1)}+h^{r+1}\Big)^2.
\end{aligned} \tag{45}$$

Then, it holds from (45) that

$$\begin{aligned}
\| \mathrm{div}\boldsymbol{\eta}^n \|^2=&2\Bigg(\| \sum_{i=1}^{m} b_i D_N^{\alpha_i}\rho^n \| + \| \sum_{i=1}^{m} b_i Q^n_{\alpha_i} \|^2 + \| p \|^2_\infty(\| \rho^n \|^2 + \| \theta^n \|^2)\Bigg)\\
&+C\sum_{i=1}^{m}\frac{b_i}{\Gamma(2-\alpha_i)}T^{-\alpha_i}N^{\alpha_i}\Big(N^{-(2-\alpha_1)}+h^{r+1}\Big)^2+\frac{1}{2}\| \mathrm{div}\boldsymbol{\eta}^n \|^2.
\end{aligned} \tag{46}$$

Using Lemmas 4 and 5, we have

$$\| \mathrm{div}\boldsymbol{\eta}^n \| \leq C\Big(1+N^{\frac{\alpha m}{2}}\Big)\Big(h^{r+1}+N^{-(2-\alpha_1)}\Big). \tag{47}$$

Then, we finish the proof. □

Remark 3. *(I) For variables u and $\boldsymbol{\lambda}$, we define the discrete norms of the errors as follows:*

$$\begin{aligned}
&\| u-u_h \|_{\hat{L}^\infty(L^2(\Omega))}= \max_{1\le n\le N} \| u(t_n)-u_h^n \|,\\
&\| \boldsymbol{\lambda}-\boldsymbol{\lambda}_h \|_{\hat{L}^\infty((L^2(\Omega))^2)}= \max_{1\le n\le N} \| \boldsymbol{\lambda}(t_n)-\boldsymbol{\lambda}_h^n \|,\\
&\| \boldsymbol{\lambda}-\boldsymbol{\lambda}_h \|_{\hat{L}^\infty(\boldsymbol{H}(\mathrm{div},\Omega))}= \max_{1\le n\le N} \| \boldsymbol{\lambda}(t_n)-\boldsymbol{\lambda}_h^n \|_{\boldsymbol{H}(\mathrm{div},\Omega)}.
\end{aligned}$$

From Theorem 3, we obtain the optimal a priori error estimate results for u in the discrete $L^\infty\big(L^2(\Omega)\big)$ norm and $\boldsymbol{\lambda}$ in the discrete $L^\infty\Big(\big(L^2(\Omega)\big)^2\Big)$ norm and obtain the suboptimal error estimate for $\boldsymbol{\lambda}$ in the discrete $L^\infty(\boldsymbol{H}(div,\Omega))$ norm. In the actual calculation in the next section, we achieve the optimal convergence rates for variables u and $\boldsymbol{\lambda}$ based on the above discrete norms.

(II) It should be pointed out that the solutions of many FPDEs have an initial layer at $t=0$ (see [42,43]). To overcome this difficulty, some scholars have adopted nonuniform mesh methods and achieved excellent results [24,26,42,44–46]. Moreover, it is noted that $\big\{\xi^k : 0\le k\le N\}$ in Lemma 3 is required to be a nondecreasing positive sequence, so the error estimates for the MFE scheme (5)–(6) with the temporal nonuniform method should adopt some other techniques. It is gratifying that the numerical results in Example 3 show that the MFE scheme (5)–(6) with the temporal graded mesh is feasible and effective.

6. Numerical Examples

In this section, we given three test examples to verify the effectiveness and convergence accuracy of the proposed MFE scheme (5)–(6) and adopt the lowest-order Raviart–Thomas MFE space for variables u and $\boldsymbol{\lambda}$ in the numerical experiments.

Example 1. *Consider the following two-term TFRD equation:*

$$\begin{cases}
D_t^{\alpha_1}u(\boldsymbol{x},t)+D_t^{\alpha_2}u(\boldsymbol{x},t)-\Delta u(\boldsymbol{x},t)+p(\boldsymbol{x})u(\boldsymbol{x},t)=f(\boldsymbol{x},t), & (\boldsymbol{x},t)\in\Omega\times J,\\
u(\boldsymbol{x},t)=0, & (\boldsymbol{x},t)\in\partial\Omega\times\overline{J},\\
u(\boldsymbol{x},0)=u_0(\boldsymbol{x}), & \boldsymbol{x}\in\overline{\Omega},
\end{cases} \tag{48}$$

where $J=(0,1]$, $\Omega=(0,1)^2$, $p(\boldsymbol{x})=1+x_1^2+x_2^2$, $\boldsymbol{x}=(x_1,x_2)\in\Omega$, $u(\boldsymbol{x},0)=0$, and the source function f is taken by

$$\begin{aligned}
f(\boldsymbol{x},t)=&\Big(\frac{\Gamma(3+\alpha_1+\alpha_2)}{\Gamma(3+\alpha_2)}t^{2+\alpha_2}+\frac{\Gamma(3+\alpha_1+\alpha_2)}{\Gamma(3+\alpha_1)}t^{2+\alpha_1}+\Big(2\pi^2+p(\boldsymbol{x})\Big)t^{2+\alpha_1+\alpha_2}\Big)\\
&\times\sin(\pi x_1)\sin(\pi x_2).
\end{aligned}$$

And we can find the analytical solutions for variables u and $\boldsymbol{\lambda}$ as follows:

$$\begin{aligned}
&u(\boldsymbol{x},t)=t^{2+\alpha_1+\alpha_2}\sin(\pi x_1)\sin(\pi x_2),\\
&\boldsymbol{\lambda}(\boldsymbol{x},t)=-\pi t^{2+\alpha_1+\alpha_2}(\cos(\pi x_1)\sin(\pi x_2),\sin(\pi x_1)\cos(\pi x_2)).
\end{aligned}$$

In the numerical simulation, we select fractional parameters $\alpha_1=0.9, 0.7, 0.5$ and $\alpha_2=0.1, 0.4$ in Equation (48) and know that among these different fractional parameters, the convergence rates are only related to the largest fractional parameter α_1 from Theorem 3. By taking $N=5, 8, 10, 16$ and the corresponding $h=\sqrt{2}/N^{2-\alpha_1}$, we give the error results and convergence rates in Tables 1–3 for the MFE scheme (5)–(6), which show that the convergence rates in the temporal direction for u (in the discrete $L^\infty\big(L^2(\Omega)\big)$ norm) and $\boldsymbol{\lambda}$ (in the discrete $L^\infty\Big(\big(L^2(\Omega)\big)^2\Big)$ and $L^\infty(\boldsymbol{H}(\mathrm{div},\Omega))$ norms) are close to $2-\alpha_1$. Moreover, in order to test convergence rates in the spatial direction, by fixing $N=100$ and taking $h=\sqrt{2}/4$, $\sqrt{2}/8$, $\sqrt{2}/16$, $\sqrt{2}/32$, we give the error results and convergence rates in Tables 4–6, which show that the convergence rates in the spatial direction for u (in the

discrete $L^\infty\left(L^2(\Omega)\right)$ norm) and $\boldsymbol{\lambda}$ (in the discrete $L^\infty\left(\left(L^2(\Omega)\right)^2\right)$ and $L^\infty(\boldsymbol{H}(\mathrm{div},\Omega))$ norms) are close to 1.

Table 1. Numerical results with $h \approx \sqrt{2}/N^{2-\alpha_1}$ and $\alpha_1 = 0.9$ in Example 1.

α_2	N	u–$\hat{L}^\infty(L^2)$	Rates	λ–$\hat{L}^\infty((L^2)^2)$	Rates	λ–$\hat{L}^\infty(H(\mathrm{div}))$	Rates
0.1	5	8.6930×10^{-2}	–	3.3630×10^{-1}	–	$1.7545 \times 10^{+0}$	–
	8	5.2424×10^{-2}	1.0760	2.0229×10^{-1}	1.0814	$1.0569 \times 10^{+0}$	1.0784
	10	4.0389×10^{-2}	1.1687	1.5578×10^{-1}	1.1709	8.1390×10^{-1}	1.1708
	16	2.3908×10^{-2}	1.1157	9.2174×10^{-2}	1.1165	4.8141×10^{-1}	1.1172
0.4	5	8.7218×10^{-2}	–	3.3776×10^{-1}	–	$1.7631 \times 10^{+0}$	–
	8	5.2624×10^{-2}	1.0750	2.0332×10^{-1}	1.0799	$1.0619 \times 10^{+0}$	1.0786
	10	4.0555×10^{-2}	1.1674	1.5663×10^{-1}	1.1692	8.1786×10^{-1}	1.1704
	16	2.4011×10^{-2}	1.1153	9.2701×10^{-2}	1.1160	4.8371×10^{-1}	1.1175

Table 2. Numerical results with $h \approx \sqrt{2}/N^{2-\alpha_1}$ and $\alpha_1 = 0.7$ in Example 1.

α_2	N	u–$\hat{L}^\infty(L^2)$	Rates	λ–$\hat{L}^\infty((L^2)^2)$	Rates	λ–$\hat{L}^\infty(H(\mathrm{div}))$	Rates
0.1	5	6.5262×10^{-2}	–	2.5184×10^{-1}	–	$1.3146 \times 10^{+0}$	–
	8	3.4916×10^{-2}	1.3308	1.3451×10^{-1}	1.3344	7.0291×10^{-1}	1.3321
	10	2.6204×10^{-2}	1.2863	1.0092×10^{-1}	1.2875	5.2740×10^{-1}	1.2873
	16	1.4175×10^{-2}	1.3073	5.4581×10^{-2}	1.3077	2.8520×10^{-1}	1.3080
0.4	5	6.5379×10^{-2}	–	2.5244×10^{-1}	–	$1.3184 \times 10^{+0}$	–
	8	3.4998×10^{-2}	1.3296	1.3493×10^{-1}	1.3328	7.0499×10^{-1}	1.3318
	10	2.6269×10^{-2}	1.2858	1.0125×10^{-1}	1.2869	5.2895×10^{-1}	1.2875
	16	1.4212×10^{-2}	1.3070	5.4771×10^{-2}	1.3073	2.8602×10^{-1}	1.3081

Table 3. Numerical results with $h \approx \sqrt{2}/N^{2-\alpha_1}$ and $\alpha_1 = 0.5$ in Example 1.

α_2	N	u–$\hat{L}^\infty(L^2)$	Rates	λ–$\hat{L}^\infty((L^2)^2)$	Rates	λ–$\hat{L}^\infty(H(\mathrm{div}))$	Rates
0.1	5	4.7518×10^{-2}	–	1.8311×10^{-1}	–	9.5625×10^{-1}	–
	8	2.2765×10^{-2}	1.5657	8.7633×10^{-2}	1.5679	4.5800×10^{-1}	1.5663
	10	1.6367×10^{-2}	1.4786	6.2996×10^{-2}	1.4792	3.2925×10^{-1}	1.4791
	16	8.1859×10^{-3}	1.4742	3.1504×10^{-2}	1.4743	1.6465×10^{-1}	1.4744
0.4	5	4.7568×10^{-2}	–	1.8337×10^{-1}	–	9.5799×10^{-1}	–
	8	2.2802×10^{-2}	1.5645	8.7824×10^{-2}	1.5662	4.5893×10^{-1}	1.5658
	10	1.6396×10^{-2}	1.4781	6.3145×10^{-2}	1.4785	3.2993×10^{-1}	1.4790
	16	8.2016×10^{-3}	1.4738	3.1585×10^{-2}	1.4739	1.6499×10^{-1}	1.4744

Table 4. Numerical results with $\tau = T/N = 1/100$ and $\alpha_1 = 0.9$ in Example 1.

α_2	h	u–$\hat{L}^\infty(L^2)$	Rates	λ–$\hat{L}^\infty((L^2)^2)$	Rates	λ–$\hat{L}^\infty(H(\mathrm{div}))$	Rates
0.1	$\sqrt{2}/4$	1.2927×10^{-1}	–	5.0254×10^{-1}	–	$2.5970 \times 10^{+0}$	–
	$\sqrt{2}/8$	6.5234×10^{-2}	0.9867	2.5171×10^{-1}	0.9975	$1.3118 \times 10^{+0}$	0.9853
	$\sqrt{2}/16$	3.2696×10^{-2}	0.9965	1.2589×10^{-1}	0.9996	6.5762×10^{-1}	0.9963
	$\sqrt{2}/32$	1.6361×10^{-2}	0.9989	6.2964×10^{-2}	0.9996	3.2908×10^{-1}	0.9988
0.4	$\sqrt{2}/4$	1.2926×10^{-1}	–	5.0244×10^{-1}	–	$2.5971 \times 10^{+0}$	–
	$\sqrt{2}/8$	6.5231×10^{-2}	0.9866	2.5169×10^{-1}	0.9973	$1.3119 \times 10^{+0}$	0.9853
	$\sqrt{2}/16$	3.2696×10^{-2}	0.9964	1.2589×10^{-1}	0.9995	6.5766×10^{-1}	0.9962
	$\sqrt{2}/32$	1.6363×10^{-2}	0.9987	6.2973×10^{-2}	0.9994	3.2913×10^{-1}	0.9987

Table 5. Numerical results with $\tau = T/N = 1/100$ and $\alpha_1 = 0.7$ in Example 1.

α_2	h	u–$\hat{L}^\infty(L^2)$	Rates	λ–$\hat{L}^\infty((L^2)^2)$	Rates	λ–$\hat{L}^\infty(H(\mathrm{div}))$	Rates
0.1	$\sqrt{2}/4$	1.2929×10^{-1}	–	5.0266×10^{-1}	–	$2.5969 \times 10^{+0}$	–
	$\sqrt{2}/8$	6.5241×10^{-2}	0.9867	2.5174×10^{-1}	0.9976	$1.3118 \times 10^{+0}$	0.9853
	$\sqrt{2}/16$	3.2698×10^{-2}	0.9966	1.2590×10^{-1}	0.9997	6.5757×10^{-1}	0.9963
	$\sqrt{2}/32$	1.6359×10^{-2}	0.9991	6.2954×10^{-2}	0.9999	3.2900×10^{-1}	0.9991
0.4	$\sqrt{2}/4$	1.2928×10^{-1}	–	5.0258×10^{-1}	–	$2.5970 \times 10^{+0}$	–
	$\sqrt{2}/8$	6.5239×10^{-2}	0.9867	2.5173×10^{-1}	0.9975	$1.3118 \times 10^{+0}$	0.9853
	$\sqrt{2}/16$	3.2697×10^{-2}	0.9966	1.2590×10^{-1}	0.9996	6.5758×10^{-1}	0.9963
	$\sqrt{2}/32$	1.6359×10^{-2}	0.9991	6.2954×10^{-2}	0.9999	3.2900×10^{-1}	0.9990

Table 6. Numerical results with $\tau = T/N = 1/100$ and $\alpha_1 = 0.5$ in Example 1.

α_2	h	u–$\hat{L}^\infty(L^2)$	Rates	λ–$\hat{L}^\infty((L^2)^2)$	Rates	λ–$\hat{L}^\infty(H(\mathrm{div}))$	Rates
0.1	$\sqrt{2}/4$	1.2930×10^{-1}	–	5.0273×10^{-1}	–	$2.5969 \times 10^{+0}$	–
	$\sqrt{2}/8$	6.5243×10^{-2}	0.9868	2.5176×10^{-1}	0.9977	$1.3118 \times 10^{+0}$	0.9852
	$\sqrt{2}/16$	3.2699×10^{-2}	0.9966	1.2591×10^{-1}	0.9997	6.5756×10^{-1}	0.9963
	$\sqrt{2}/32$	1.6359×10^{-2}	0.9991	6.2955×10^{-2}	0.9999	3.2899×10^{-1}	0.9991
0.4	$\sqrt{2}/4$	1.2929×10^{-1}	–	5.0266×10^{-1}	–	$2.5969 \times 10^{+0}$	–
	$\sqrt{2}/8$	6.5242×10^{-2}	0.9867	2.5175×10^{-1}	0.9976	$1.3118 \times 10^{+0}$	0.9853
	$\sqrt{2}/16$	3.2698×10^{-2}	0.9966	1.2590×10^{-1}	0.9997	6.5757×10^{-1}	0.9963
	$\sqrt{2}/32$	1.6359×10^{-2}	0.9991	6.2955×10^{-2}	0.9999	3.2899×10^{-1}	0.9991

Example 2. *Consider the following three-term TFRD equation:*

$$\begin{cases} D_t^{\alpha_1} u(\boldsymbol{x},t) + D_t^{\alpha_2} u(\boldsymbol{x},t) + D_t^{\alpha_3} u(\boldsymbol{x},t) - \Delta u(\boldsymbol{x},t) + p(\boldsymbol{x}) u(\boldsymbol{x},t) = f(\boldsymbol{x},t), & (\boldsymbol{x},t) \in \Omega \times J, \\ u\,(\boldsymbol{x},t) = 0, & (\boldsymbol{x},t) \in \partial\Omega \times \overline{J}, \\ u(\boldsymbol{x},0) = u_0(\boldsymbol{x}), & \boldsymbol{x} \in \overline{\Omega}, \end{cases} \tag{49}$$

where the spatial domain Ω, temporal domain J, coefficient $p(\boldsymbol{x})$, and initial data $u(\boldsymbol{x},0)$ are as in Example 1 and the source function f is taken by

$$\begin{aligned} f(\boldsymbol{x},t) = & \Bigg(\frac{\Gamma(3+\alpha_1+\alpha_2+\alpha_3)}{\Gamma(3+\alpha_2+\alpha_3)} t^{2+\alpha_2+\alpha_3} + \frac{\Gamma(3+\alpha_1+\alpha_2+\alpha_3)}{\Gamma(3+\alpha_1+\alpha_3)} t^{2+\alpha_1+\alpha_3} \\ & + \frac{\Gamma(3+\alpha_1+\alpha_2+\alpha_3)}{\Gamma(3+\alpha_1+\alpha_2)} t^{2+\alpha_1+\alpha_2} + \Big(2\pi^2 + p(\boldsymbol{x})\Big) t^{2+\alpha_1+\alpha_2+\alpha_3} \Bigg) \sin(\pi x_1) \sin(\pi x_2). \end{aligned}$$

And we can also find the analytical solutions for variables u and $\boldsymbol{\lambda}$ as follows:

$$\begin{aligned} u(\boldsymbol{x},t) &= t^{2+\alpha_1+\alpha_2+\alpha_3} \sin(\pi x_1) \sin(\pi x_2), \\ \boldsymbol{\lambda}(\boldsymbol{x},t) &= -\pi t^{2+\alpha_1+\alpha_2+\alpha_3} (\cos(\pi x_1) \sin(\pi x_2), \sin(\pi x_1) \cos(\pi x_2)). \end{aligned}$$

In this example, since the Equation (49) contains three Caputo time-fractional derivative terms, we specifically take the fractional parameters $\alpha_1 = 0.9, 0.7, 0.5$ and $(\alpha_2, \alpha_3) = (0.4, 0.2), (0.3, 0.1)$. From Theorem 3, we also point out that the convergence rates are only related to the maximum fractional parameter α_1. In Tables 7–9, for different $N = 5, 8, 10, 16$, we give the error results and convergence rates for the MFE scheme (5)–(6), where the spatial grid sizes are also taken as $h = \sqrt{2}/N^{2-\alpha_1}$. We can also see that the convergence rates in the temporal direction for u (in the discrete $L^\infty\big(L^2(\Omega)\big)$ norm) and $\boldsymbol{\lambda}$ (in the discrete $L^\infty\Big(\big(L^2(\Omega)\big)^2\Big)$ and $L^\infty(\boldsymbol{H}(\mathrm{div}, \Omega))$ norms) are close to $2 - \alpha_1$. Furthermore, in Tables 10–12, we also fix $N = 100$ and take $h = \sqrt{2}/4$, $\sqrt{2}/8$, $\sqrt{2}/16$, $\sqrt{2}/32$, give

the error results and convergence rates, and see that the convergence rates in the spatial direction for u and $\boldsymbol{\lambda}$ in the above corresponding discrete norms are also close to 1.

Table 7. Numerical results with $h \approx \sqrt{2}/N^{2-\alpha_1}$ and $\alpha_1 = 0.9$ in Example 2.

α_2	α_3	N	u–$\hat{L}^\infty(L^2)$	Rates	λ–$\hat{L}^\infty((L^2)^2)$	Rates	λ–$\hat{L}^\infty(H(\mathrm{div}))$	Rates
0.4	0.2	5	8.7400×10^{-2}	–	3.3868×10^{-1}	–	$1.7681 \times 10^{+0}$	–
		8	5.2741×10^{-2}	1.0747	2.0392×10^{-1}	1.0795	$1.0648 \times 10^{+0}$	1.0790
		10	4.0650×10^{-2}	1.1670	1.5711×10^{-1}	1.1686	8.2004×10^{-1}	1.1704
		16	2.4067×10^{-2}	1.1152	9.2988×10^{-2}	1.1159	4.8494×10^{-1}	1.1177
0.3	0.1	5	8.7138×10^{-2}	–	3.3735×10^{-1}	–	$1.7608 \times 10^{+0}$	–
		8	5.2567×10^{-2}	1.0753	2.0303×10^{-1}	1.0804	$1.0605 \times 10^{+0}$	1.0788
		10	4.0507×10^{-2}	1.1679	1.5638×10^{-1}	1.1698	8.1673×10^{-1}	1.1706
		16	2.3980×10^{-2}	1.1154	9.2546×10^{-2}	1.1162	4.8304×10^{-1}	1.1175

Table 8. Numerical results with $h \approx \sqrt{2}/N^{2-\alpha_1}$ and $\alpha_1 = 0.7$ in Example 2.

α_2	α_3	N	u–$\hat{L}^\infty(L^2)$	Rates	λ–$\hat{L}^\infty((L^2)^2)$	Rates	λ–$\hat{L}^\infty(H(\mathrm{div}))$	Rates
0.4	0.2	5	6.5465×10^{-2}	–	2.5288×10^{-1}	–	$1.3208 \times 10^{+0}$	–
		8	3.5052×10^{-2}	1.3291	1.3521×10^{-1}	1.3321	7.0629×10^{-1}	1.3319
		10	2.6310×10^{-2}	1.2857	1.0146×10^{-1}	1.2868	5.2989×10^{-1}	1.2877
		16	1.4234×10^{-2}	1.3070	5.4886×10^{-2}	1.3073	2.8651×10^{-1}	1.3083
0.3	0.1	5	6.5343×10^{-2}	–	2.5225×10^{-1}	–	$1.3173 \times 10^{+0}$	–
		8	3.4972×10^{-2}	1.3300	1.3479×10^{-1}	1.3334	7.0434×10^{-1}	1.3321
		10	2.6247×10^{-2}	1.2860	1.0114×10^{-1}	1.2872	5.2845×10^{-1}	1.2876
		16	1.4200×10^{-2}	1.3071	5.4707×10^{-2}	1.3075	2.8575×10^{-1}	1.3082

Table 9. Numerical results with $h \approx \sqrt{2}/N^{2-\alpha_1}$ and $\alpha_1 = 0.5$ in Example 2.

α_2	α_3	N	u–$\hat{L}^\infty(L^2)$	Rates	λ–$\hat{L}^\infty((L^2)^2)$	Rates	λ–$\hat{L}^\infty(H(\mathrm{div}))$	Rates
0.4	0.2	5	4.7614×10^{-2}	–	1.8360×10^{-1}	–	9.5930×10^{-1}	–
		8	2.2831×10^{-2}	1.5638	8.7972×10^{-2}	1.5654	4.5961×10^{-1}	1.5656
		10	1.6417×10^{-2}	1.4779	6.3255×10^{-2}	1.4782	3.3041×10^{-1}	1.4790
		16	8.2126×10^{-3}	1.4738	3.1641×10^{-2}	1.4738	1.6523×10^{-1}	1.4745
0.3	0.1	5	4.7550×10^{-2}	–	1.8327×10^{-1}	–	9.5743×10^{-1}	–
		8	2.2788×10^{-2}	1.5650	8.7752×10^{-2}	1.5669	4.5859×10^{-1}	1.5661
		10	1.6385×10^{-2}	1.4783	6.3087×10^{-2}	1.4788	3.2967×10^{-1}	1.4791
		16	8.1952×10^{-3}	1.4740	3.1552×10^{-2}	1.4742	1.6486×10^{-1}	1.4745

Table 10. Numerical results with $\tau = T/N = 1/100$ and $\alpha_1 = 0.9$ in Example 2.

α_2	α_3	h	u–$\hat{L}^\infty(L^2)$	Rates	λ–$\hat{L}^\infty((L^2)^2)$	Rates	λ–$\hat{L}^\infty(H(\mathrm{div}))$	Rates
0.4	0.2	$\sqrt{2}/4$	1.2924×10^{-1}	–	5.0230×10^{-1}	–	$2.5973 \times 10^{+0}$	–
		$\sqrt{2}/8$	6.5229×10^{-2}	0.9865	2.5168×10^{-1}	0.9970	$1.3119 \times 10^{+0}$	0.9853
		$\sqrt{2}/16$	3.2696×10^{-2}	0.9964	1.2589×10^{-1}	0.9994	6.5768×10^{-1}	0.9962
		$\sqrt{2}/32$	1.6364×10^{-2}	0.9986	6.2979×10^{-2}	0.9992	3.2916×10^{-1}	0.9986
0.3	0.1	$\sqrt{2}/4$	1.2925×10^{-1}	–	5.0236×10^{-1}	–	$2.5972 \times 10^{+0}$	–
		$\sqrt{2}/8$	6.5231×10^{-2}	0.9865	2.5169×10^{-1}	0.9971	$1.3119 \times 10^{+0}$	0.9853
		$\sqrt{2}/16$	3.2696×10^{-2}	0.9964	1.2589×10^{-1}	0.9995	6.5765×10^{-1}	0.9962
		$\sqrt{2}/32$	1.6362×10^{-2}	0.9988	6.2971×10^{-2}	0.9994	3.2912×10^{-1}	0.9987

Table 11. Numerical results with $\tau = T/N = 1/100$ and $\alpha_1 = 0.7$ in Example 2.

α_2	α_3	h	u–$\hat{L}^\infty(L^2)$	Rates	λ–$\hat{L}^\infty((L^2)^2)$	Rates	λ–$\hat{L}^\infty(H(\mathrm{div}))$	Rates
0.4	0.2	$\sqrt{2}/4$	1.2926×10^{-1}	–	5.0244×10^{-1}	–	$2.5971 \times 10^{+0}$	–
		$\sqrt{2}/8$	6.5237×10^{-2}	0.9866	2.5172×10^{-1}	0.9972	$1.3118 \times 10^{+0}$	0.9853
		$\sqrt{2}/16$	3.2697×10^{-2}	0.9965	1.2590×10^{-1}	0.9996	6.5758×10^{-1}	0.9963
		$\sqrt{2}/32$	1.6359×10^{-2}	0.9991	6.2954×10^{-2}	0.9999	3.2901×10^{-1}	0.9990
0.3	0.1	$\sqrt{2}/4$	1.2927×10^{-1}	–	5.0249×10^{-1}	–	$2.5970 \times 10^{+0}$	–
		$\sqrt{2}/8$	6.5238×10^{-2}	0.9866	2.5172×10^{-1}	0.9973	$1.3118 \times 10^{+0}$	0.9853
		$\sqrt{2}/16$	3.2697×10^{-2}	0.9965	1.2590×10^{-1}	0.9996	6.5758×10^{-1}	0.9963
		$\sqrt{2}/32$	1.6359×10^{-2}	0.9991	6.2954×10^{-2}	0.9999	3.2900×10^{-1}	0.9991

Table 12. Numerical results with $\tau = T/N = 1/100$ and $\alpha_1 = 0.5$ in Example 2.

α_2	α_3	h	u–$\hat{L}^\infty(L^2)$	Rates	λ–$\hat{L}^\infty((L^2)^2)$	Rates	λ–$\hat{L}^\infty(H(\mathrm{div}))$	Rates
0.4	0.2	$\sqrt{2}/4$	1.2927×10^{-1}	–	5.0252×10^{-1}	–	$2.5970 \times 10^{+0}$	–
		$\sqrt{2}/8$	6.5240×10^{-2}	0.9866	2.5173×10^{-1}	0.9973	$1.3118 \times 10^{+0}$	0.9853
		$\sqrt{2}/16$	3.2698×10^{-2}	0.9965	1.2590×10^{-1}	0.9996	6.5757×10^{-1}	0.9963
		$\sqrt{2}/32$	1.6359×10^{-2}	0.9991	6.2955×10^{-2}	0.9999	3.2899×10^{-1}	0.9991
0.3	0.1	$\sqrt{2}/4$	1.2928×10^{-1}	–	5.0257×10^{-1}	–	$2.5970 \times 10^{+0}$	–
		$\sqrt{2}/8$	6.5241×10^{-2}	0.9866	2.5174×10^{-1}	0.9974	$1.3118 \times 10^{+0}$	0.9853
		$\sqrt{2}/16$	3.2698×10^{-2}	0.9966	1.2590×10^{-1}	0.9996	6.5757×10^{-1}	0.9963
		$\sqrt{2}/32$	1.6359×10^{-2}	0.9991	6.2955×10^{-2}	0.9999	3.2899×10^{-1}	0.9991

Based on the numerical results in Tables 1–12 obtained from the above two test examples, we can see that the convergence rates in the spatial and temporal directions for u (in the discrete $L^\infty\big(L^2(\Omega)\big)$ norm) and $\boldsymbol{\lambda}$ (in the discrete $L^\infty\Big(\big(L^2(\Omega)\big)^2\Big)$ norm) are in agreement with the theoretical results in Theorem 3, and those for $\boldsymbol{\lambda}$ (in the discrete $L^\infty(\boldsymbol{H}(\mathrm{div},\Omega))$ norm) are higher than the theoretical result. These results fully demonstrate that the proposed MFE method for the multi-term TFRD equations is effective.

Example 3. *Consider the two-term TFRD equation in Example 1 with weak regularity solutions near the initial time $t = 0$, where the source function f is taken by*

$$\begin{aligned} f(\boldsymbol{x},t) =& \Big(\frac{2}{\Gamma(3-\alpha_1)}t^{2-\alpha_1} + \Gamma(1+\alpha_1) + \frac{\Gamma(2+\alpha_2)}{\Gamma(2+\alpha_2-\alpha_1)}t^{1+\alpha_2-\alpha_1} \\ &+ \frac{2}{\Gamma(3-\alpha_2)}t^{2-\alpha_2} + \frac{\Gamma(1+\alpha_1)}{\Gamma(1+\alpha_1-\alpha_2)}t^{\alpha_1-\alpha_2} + \Gamma(2+\alpha_2)t \\ &+ \Big(2\pi^2 + p(\boldsymbol{x})\Big)\Big(t^2 + t^{\alpha_1} + t^{1+\alpha_2}\Big)\Big)\sin(\pi x_1)\sin(\pi x_2). \end{aligned}$$

And we can also find the analytical solutions for variables u and $\boldsymbol{\lambda}$ as follows:

$$\begin{aligned} u(\boldsymbol{x},t) &= \Big(t^2 + t^{\alpha_1} + t^{1+\alpha_2}\Big)\sin(\pi x_1)\sin(\pi x_2), \\ \boldsymbol{\lambda}(\boldsymbol{x},t) &= -\pi\Big(t^2 + t^{\alpha_1} + t^{1+\alpha_2}\Big)(\cos(\pi x_1)\sin(\pi x_2), \sin(\pi x_1)\cos(\pi x_2)). \end{aligned}$$

In this example, we will select the graded mesh to discretize the interval $[0,T]$ and set $t_n = T(n/N)^\gamma$, for $n = 0, 1, 2, \cdots, N$, where constant $\gamma \geq 1$ is the temporal graded mesh parameter. The ideal optimal error estimates for u (in the discrete $L^\infty\big(L^2(\Omega)\big)$ norm) and $\boldsymbol{\lambda}$ (in the discrete $L^\infty\Big(\big(L^2(\Omega)\big)^2\Big)$ and $L^\infty(\boldsymbol{H}(\mathrm{div},\Omega))$ norms) should be $O\Big(N^{-\min\{\gamma\alpha_1, 2-\alpha_1\}} + h\Big)$. Here, we will mainly test the convergence rates in the temporal direction with the graded mesh parameter $\gamma = 1$ and $(2-\alpha_1)/\alpha_1$. We first conduct numerical experiments with

$\gamma = 1$. Then, the optimal convergence rate in the temporal direction is α_1. For fractional parameters $\alpha_1 = 0.9, 0.7, 0.5$ and $\alpha_2 = 0.1, 0.4$, we take the time mesh parameter $N = 20, 40, 80, 160$ and special spatial grid parameters: (i) when $\alpha_1 = 0.9$, take $h \approx 2\sqrt{2}/N^{\alpha_1}$; (ii) when $\alpha_1 = 0.7$, take $h \approx \sqrt{2}/N^{\alpha_1}$; (iii) when $\alpha_1 = 0.5$, take $h \approx \sqrt{2}/(2N^{\alpha_1})$. Then, we give the numerical results in Tables 13–15, which show that the convergence rates in the temporal direction for u (in the discrete $L^\infty\big(L^2(\Omega)\big)$ norm) and $\boldsymbol{\lambda}$ (in the discrete $L^\infty\Big(\big(L^2(\Omega)\big)^2\Big)$ and $L^\infty(\boldsymbol{H}(\mathrm{div},\Omega))$ norms) are close to α_1.

Table 13. Numerical results with $\alpha_1 = 0.9$ and graded mesh parameter $\gamma = 1$ in Example 3.

α_2	N	u–$\hat{L}^\infty(L^2)$	Rates	λ–$\hat{L}^\infty((L^2)^2)$	Rates	λ–$\hat{L}^\infty(H(\mathrm{div}))$	Rates
0.1	20	1.9572×10^{-1}	–	7.5520×10^{-1}	–	$3.9354 \times 10^{+0}$	–
	40	1.1208×10^{-1}	0.8042	4.3165×10^{-1}	0.8070	$2.2539 \times 10^{+0}$	0.8041
	80	6.0396×10^{-2}	0.8920	2.3245×10^{-1}	0.8930	$1.2146 \times 10^{+0}$	0.8920
	160	3.2722×10^{-2}	0.8842	1.2591×10^{-1}	0.8845	6.5806×10^{-1}	0.8842
0.4	20	1.9571×10^{-1}	–	7.5516×10^{-1}	–	$3.9354 \times 10^{+0}$	–
	40	1.1208×10^{-1}	0.8042	4.3164×10^{-1}	0.8069	$2.2540 \times 10^{+0}$	0.8041
	80	6.0396×10^{-2}	0.8920	2.3244×10^{-1}	0.8929	$1.2146 \times 10^{+0}$	0.8920
	160	3.2722×10^{-2}	0.8842	1.2591×10^{-1}	0.8845	6.5806×10^{-1}	0.8842

Table 14. Numerical results with $\alpha_1 = 0.7$ and graded mesh parameter $\gamma = 1$ in Example 3.

α_2	N	u–$\hat{L}^\infty(L^2)$	Rates	λ–$\hat{L}^\infty((L^2)^2)$	Rates	λ–$\hat{L}^\infty(H(\mathrm{div}))$	Rates
0.1	20	1.9573×10^{-1}	–	7.5526×10^{-1}	–	$3.9353 \times 10^{+0}$	–
	40	1.2068×10^{-1}	0.6976	4.6487×10^{-1}	0.7002	$2.4269 \times 10^{+0}$	0.6974
	80	7.4765×10^{-2}	0.6908	2.8779×10^{-1}	0.6918	$1.5035 \times 10^{+0}$	0.6907
	160	4.4872×10^{-2}	0.7365	1.7268×10^{-1}	0.7369	9.0241×10^{-1}	0.7365
0.4	20	1.9572×10^{-1}	–	7.5523×10^{-1}	–	$3.9354 \times 10^{+0}$	–
	40	1.2068×10^{-1}	0.6976	4.6486×10^{-1}	0.7001	$2.4269 \times 10^{+0}$	0.6974
	80	7.4765×10^{-2}	0.6908	2.8779×10^{-1}	0.6918	$1.5035 \times 10^{+0}$	0.6907
	160	4.4872×10^{-2}	0.7365	1.7268×10^{-1}	0.7369	9.0241×10^{-1}	0.7365

Table 15. Numerical results with $\alpha_1 = 0.5$ and graded mesh parameter $\gamma = 1$ in Example 3.

α_2	N	u–$\hat{L}^\infty(L^2)$	Rates	λ–$\hat{L}^\infty((L^2)^2)$	Rates	λ–$\hat{L}^\infty(H(\mathrm{div}))$	Rates
0.1	20	1.7410×10^{-1}	–	6.7141×10^{-1}	–	$3.5006 \times 10^{+0}$	–
	40	1.2069×10^{-1}	0.5286	4.6487×10^{-1}	0.5303	$2.4269 \times 10^{+0}$	0.5285
	80	8.7212×10^{-2}	0.4687	3.3576×10^{-1}	0.4694	$1.7538 \times 10^{+0}$	0.4686
	160	6.2812×10^{-2}	0.4735	2.4175×10^{-1}	0.4739	$1.2632 \times 10^{+0}$	0.4735
0.4	20	1.7410×10^{-1}	–	6.7139×10^{-1}	–	$3.5006 \times 10^{+0}$	–
	40	1.2069×10^{-1}	0.5286	4.6487×10^{-1}	0.5303	$2.4269 \times 10^{+0}$	0.5285
	80	8.7212×10^{-2}	0.4687	3.3576×10^{-1}	0.4694	$1.7538 \times 10^{+0}$	0.4686
	160	6.2812×10^{-2}	0.4735	2.4175×10^{-1}	0.4739	$1.2632 \times 10^{+0}$	0.4735

Next, we conduct numerical experiments with $\gamma = (2 - \alpha_1)/\alpha_1$. Then, the optimal convergence rate is $2 - \alpha_1$. We take the time mesh parameter $N = 5, 8, 10, 16$ and the spatial grid parameter $h = \sqrt{2}/N^{2-\alpha_1}$. Then, we give the numerical results in Tables 16–18 and find that the convergence rates in the temporal direction for u (in the discrete $L^\infty\big(L^2(\Omega)\big)$ norm) and $\boldsymbol{\lambda}$ (in the discrete $L^\infty\Big(\big(L^2(\Omega)\big)^2\Big)$ and $L^\infty(\boldsymbol{H}(\mathrm{div},\Omega))$ norms) are close to $2 - \alpha_1$. Based on the above discussion, we know that the MFE scheme (5)–(6) with the temporal graded mesh for solving the multi-term TFRD equations with the initial layer is also feasible and effective.

Table 16. Numerical results with $\alpha_1 = 0.9$ and graded mesh parameter $\gamma = \frac{2-\alpha_1}{\alpha_1}$ in Example 3.

α_2	N	u–$\hat{L}^\infty(L^2)$	Rates	λ–$\hat{L}^\infty((L^2)^2)$	Rates	λ–$\hat{L}^\infty(H(\mathrm{div}))$	Rates
0.1	5	2.6024×10^{-1}	–	$1.0062 \times 10^{+0}$	–	$5.2342 \times 10^{+0}$	–
	8	1.5673×10^{-1}	1.0789	6.0412×10^{-1}	1.0855	$3.1526 \times 10^{+0}$	1.0787
	10	1.2067×10^{-1}	1.1718	4.6479×10^{-1}	1.1750	$2.4273 \times 10^{+0}$	1.1718
	16	7.1368×10^{-2}	1.1175	2.7470×10^{-1}	1.1189	$1.4355 \times 10^{+0}$	1.1176
0.4	5	2.6021×10^{-1}	–	$1.0060 \times 10^{+0}$	–	$5.2351 \times 10^{+0}$	–
	8	1.5673×10^{-1}	1.0787	6.0410×10^{-1}	1.0852	$3.1531 \times 10^{+0}$	1.0787
	10	1.2067×10^{-1}	1.1716	4.6479×10^{-1}	1.1748	$2.4276 \times 10^{+0}$	1.1718
	16	7.1372×10^{-2}	1.1174	2.7472×10^{-1}	1.1188	$1.4357 \times 10^{+0}$	1.1176

Table 17. Numerical results with $\alpha_1 = 0.7$ and graded mesh parameter $\gamma = \frac{2-\alpha_1}{\alpha_1}$ in Example 3.

α_2	N	u–$\hat{L}^\infty(L^2)$	Rates	λ–$\hat{L}^\infty((L^2)^2)$	Rates	λ–$\hat{L}^\infty(H(\mathrm{div}))$	Rates
0.1	5	1.9568×10^{-1}	–	7.5499×10^{-1}	–	$3.9360 \times 10^{+0}$	–
	8	1.0462×10^{-1}	1.3323	4.0284×10^{-1}	1.3365	$2.1043 \times 10^{+0}$	1.3323
	10	7.8497×10^{-2}	1.2872	3.0217×10^{-1}	1.2887	$1.5789 \times 10^{+0}$	1.2873
	16	4.2450×10^{-2}	1.3079	1.6336×10^{-1}	1.3086	8.5380×10^{-1}	1.3081
0.4	5	1.9566×10^{-1}	–	7.5492×10^{-1}	–	$3.9370 \times 10^{+0}$	–
	8	1.0462×10^{-1}	1.3320	4.0289×10^{-1}	1.3361	$2.1049 \times 10^{+0}$	1.3323
	10	7.8506×10^{-2}	1.2870	3.0221×10^{-1}	1.2885	$1.5793 \times 10^{+0}$	1.2874
	16	4.2457×10^{-2}	1.3078	1.6339×10^{-1}	1.3084	8.5400×10^{-1}	1.3081

Table 18. Numerical results with $\alpha_1 = 0.5$ and graded mesh parameter $\gamma = \frac{2-\alpha_1}{\alpha_1}$ in Example 3.

α_2	N	u–$\hat{L}^\infty(L^2)$	Rates	λ–$\hat{L}^\infty((L^2)^2)$	Rates	λ–$\hat{L}^\infty(H(\mathrm{div}))$	Rates
0.1	5	1.4253×10^{-1}	–	5.4923×10^{-1}	–	$2.8673 \times 10^{+0}$	–
	8	6.8272×10^{-2}	1.5661	2.6278×10^{-1}	1.5685	$1.3733 \times 10^{+0}$	1.5663
	10	4.9083×10^{-2}	1.4788	1.8890×10^{-1}	1.4794	9.8727×10^{-1}	1.4790
	16	2.4548×10^{-2}	1.4742	9.4464×10^{-2}	1.4744	4.9373×10^{-1}	1.4744
0.4	5	1.4255×10^{-1}	–	5.4933×10^{-1}	–	$2.8688 \times 10^{+0}$	–
	8	6.8306×10^{-2}	1.5654	2.6296×10^{-1}	1.5675	$1.3743 \times 10^{+0}$	1.5659
	10	4.9113×10^{-2}	1.4783	1.8905×10^{-1}	1.4788	9.8804×10^{-1}	1.4787
	16	2.4567×10^{-2}	1.4739	9.4561×10^{-2}	1.4740	4.9416×10^{-1}	1.4742

7. Conclusions

This work presents a Raviart–Thomas MFE method for solving the multi-term TFRD equations with variable coefficients by using the well-known $L1$ formula. The existence, uniqueness, and unconditional stability of the discrete solution are discussed, and the optimal a priori error estimates for u (in the discrete $L^\infty\left(L^2(\Omega)\right)$ norm) and $\boldsymbol{\lambda}$ (in the discrete $L^\infty\left(\left(L^2(\Omega)\right)^2\right)$ norm) and the suboptimal a priori error estimate for $\boldsymbol{\lambda}$ (in the discrete $L^\infty(\boldsymbol{H}(\mathrm{div},\Omega))$ norm) are obtained in this work. In addition, some numerical results are given to demonstrate the effectiveness of the proposed MFE method. In future research, we will try to give theoretical analysis for the MFE method with the temporal graded mesh to solve some FPDEs with the initial layer at $t = 0$ and apply the MFE method to solve more FPDEs in scientific and engineering fields.

Author Contributions: Conceptualization, J.Z. and S.D.; methodology, Z.F.; software, Z.F.; validation, J.Z., S.D. and Z.F.; formal analysis, J.Z. and S.D.; writing—original draft preparation, J.Z. and S.D.; writing—review and editing, J.Z. and Z.F.; funding acquisition, J.Z. and Z.F. All authors have read and agreed to the published version of the manuscript.

Funding: This work was supported by the National Natural Science Foundation of China (11701299), the Scientific Research Projection of Higher Schools of the Inner Mongolia Autonomous Region

(NJZY23055), and the Central Government Guided Local Science and Technology Development Fund Project of China (2022ZY0175).

Data Availability Statement: Data are contained within the article.

Acknowledgments: The authors are very grateful to the editors and reviewers for their helpful comments and suggestions on improving this work.

Conflicts of Interest: The authors declares no conflicts of interest.

References

1. Ross, B. *Fractional Calculus and Its Applications*; Lecture Notes in Mathematics; Springer: Berlin/Heidelberg, Germany, 1975.
2. Hilfer, R. *Applications of Fractional Calculus in Physics*; World Scientific: Singapore, 2000.
3. Diethelm, K. *The Analysis of Fractional Differential Equations*; Springer: Berlin/Heidelberg, Germany, 2010.
4. Hendy, M.H.; Amin, M.M.; Ezzat, M.A. Two-dimensional problem for thermoviscoelastic materials with fractional order heat transfer. *J. Therm. Stress.* **2019**, *42*, 1298–1315. [CrossRef]
5. Zhou, J.C.; Salahshour, S.; Ahmadian, A.; Senu, N. Modeling the dynamics of COVID-19 using fractal-fractional operator with a case study. *Results Phys.* **2022**, *33*, 105103. [CrossRef] [PubMed]
6. Shymanskyi, V.; Sokolovskyy, I.; Sokolovskyy, Y.; Bubnyak, T. Variational Method for Solving the Time-Fractal Heat Conduction Problem in the Claydite-Block Construction. In *Advances in Computer Science for Engineering and Education. ICCSEEA 2022*; Hu, Z., Dychka, I., Petoukhov, S., He, M., Eds.; Lecture Notes on Data Engineering and Communications Technologies; Springer: Cham, Switzerland, 2022; Volume 134.
7. Bagley, R.L.; Torvik, R.J. On the appearance of the fractional derivative in the behaviour of real materials. *Appl. Mech.* **1984**, *51*, 294–298.
8. Ming, C.Y.; Liu, F.W.; Zheng, L.C.; Turner, I.; Anh, V. Analytical solutions of multi-term time fractional differential equations and application to unsteady flows of generalized viscoelastic fluid. *Comput. Math. Appl.* **2006**, *72*, 2084–2097. [CrossRef]
9. Fetecau, C.; Athar, M.; Fetecau, C. Unsteady flow of a generalized Maxwell fluid with fractional derivative due to a constantly accelerating plate. *Comput. Math. Appl.* **2009**, *57*, 596–603. [CrossRef]
10. Liu, F.W.; Meerschaert, M.M.; McGough, R.J.; Zhuang, P.H.; Liu, Q.X. Numerical methods for solving the multi-term time-fractional wave-diffusion equation. *Fract. Calc. Appl. Anal.* **2013**, *16*, 9–25. [CrossRef]
11. Dehghan, M.; Safarpoor, M.; Abbaszadeh, M. Two high-order numerical algorithms for solving the multi-term time fractional diffusion-wave equations. *J. Comput. Appl. Math.* **2015**, *290*, 174–195. [CrossRef]
12. Ren, J.C.; Sun, Z.Z. Efficient Numerical Solution of the Multi-Term Time Fractional Diffusion-Wave Equation. *East Asian J. Appl. Math.* **2015**, *5*, 1–28. [CrossRef]
13. Zheng, M.; Liu, F.W.; Anh, V.; Turner, I. A high-order spectral method for the multi-term time-fractional diffusion equations. *Appl. Math. Model.* **2016**, *40*, 4970–4985. [CrossRef]
14. Du, R.L.; Sun, Z.Z. Temporal second-order difference methods for solving multi-term time fractional mixed diffusion and wave equations. *Numer. Algorithms* **2021**, *88*, 191–226. [CrossRef]
15. Hendy, A.S.; Zaky, M.A. Graded mesh discretization for coupled system of nonlinear multi-term time-space fractional diffusion equations. *Eng. Comput.* **2022**, *38*, 1351–1363. [CrossRef]
16. Liu, Y.Q.; Yin, X.L.; Liu, F.W.; Xin, X.Y.; Shen, Y.F.; Feng, L.B. An alternating direction implicit Legendre spectral method for simulating a 2D multi-term time-fractional Oldroyd-B fluid type diffusion equation. *Comput. Math. Appl.* **2022**, *113*, 160–173. [CrossRef]
17. Wei, L.L.; Wang, H.H. Local discontinuous Galerkin method for multi-term variable-order time fractional diffusion equation. *Math. Comput. Simulat.* **2023**, *203*, 685–698. [CrossRef]
18. She, M.F.; Li, D.F.; Sun, H.W. A transformed $L1$ method for solving the multi-term time-fractional diffusion problem. *Math. Comput. Simulat.* **2022**, *193*, 584–606. [CrossRef]
19. Jin, B.T.; Lazarov, R.; Liu, Y.K.; Zhou, Z. The Galerkin finite element method for a multi-term time-fractional diffusion equation. *J. Comput. Phys.* **2015**, *281*, 825–843. [CrossRef]
20. Li, M.; Huang, C.M.; Jiang, F.Z. Galerkin finite element method for higher dimensional multi-term fractional diffusion equation on non-uniform meshes. *Appl. Anal.* **2017**, *96*, 1269–1284. [CrossRef]
21. Zhou, J.; Xu, D.; Chen, H.B. A Weak Galerkin Finite Element Method for Multi-Term Time-Fractional Diffusion Equations. *East Asian J. Appl. Math.* **2018**, *8*, 181–193. [CrossRef]
22. Bu, W.P.; Shu, S.; Xue, X.Q.; Xiao, A.G.; Zeng, W. Space-time finite element method for the multi-term time-space fractional diffusion equation on a two-dimensional domain. *Comput. Math. Appl.* **2019**, *78*, 1367–1379. [CrossRef]
23. Feng, L.B.; Liu, F.W.; Turner, I. Finite difference/finite element method for a novel 2D multi-term time-fractional mixed sub-diffusion and diffusion-wave equation on convex domains. *Commun. Nonlinear Sci. Numer. Simulat.* **2019**, *70*, 354–371. [CrossRef]
24. Meng, X.Y.; Stynes, M. Barrier function local and global analysis of an $L1$ finite element method for a multiterm time-fractional initial-boundary value problem. *J. Sci. Comput.* **2020**, *84*, 5. [CrossRef]

25. Yin, B.L.; Liu, Y.; Li, H.; Zeng, F.H. A class of efficient time-stepping methods for multi-term time-fractional reaction-diffusion-wave equations. *Appl. Numer. Math.* **2021**, *165*, 56–82. [CrossRef]
26. Huang, C.B.; Stynes, M.; Chen, H. An α-robust finite element method for a multi-term time-fractional diffusion problem. *J. Comput. Appl. Math.* **2021**, *389*, 113334. [CrossRef]
27. Liu, H.; Zheng, X.C.; Fu, H.F. Analysis of a multi-term variable-order time-fractional diffusion equation and its Galerkin finite element approximation. *J. Comput. Math.* **2022**, *40*, 814–834. [CrossRef]
28. Zhao, Y.M.; Chen, P.; Bu, W.P.; Liu, X.T.; Tang, Y.F. Two mixed finite element methods for time-fractional diffusion equations. *J. Sci. Comput.* **2017**, *70*, 407–428. [CrossRef]
29. Liu, Y.; Fang, Z.C.; Li, H.; He, S. A mixed finite element method for a time-fractional fourth-order partial differential equation. *Appl. Math. Comput.* **2014**, *243*, 703–717. [CrossRef]
30. Li, X.C.; Yang, X.Y.; Zhang, Y.H. Error estimates of mixed finite element methods for time-fractional Navier-Stokes equations. *J. Sci. Comput.* **2017**, *70*, 500–515. [CrossRef]
31. Liu, Y.; Du, Y.W.; Li, H.; Li, J.C.; He, S. A two-grid mixed finite element method for a nonlinear fourth-order reaction-diffusion problem with time-fractional derivative. *Comput. Math. Appl.* **2015**, *70*, 2474–2492. [CrossRef]
32. Li, X.W.; Tang, Y.L. Interpolated coefficient mixed finite elements for semilinear time fractional diffusion equations. *Fractal Fract.* **2023**, *7*, 482. [CrossRef]
33. Shi, Z.G.; Zhao, Y.M.; Tang, Y.F.; Wang, F.L.; Shi, Y.H. Superconvergence analysis of an H^1-Galerkin mixed finite element method for two-dimensional multi-term time fractional diffusion equations. *Int. J. Comput. Math.* **2018**, *95*, 1845–1857. [CrossRef]
34. Li, M.; Huang, C.M.; Ming, W.Y. Mixed finite-element method for multi-term time-fractional diffusion and diffusion-wave equations. *Comp. Appl. Math.* **2018**, *37*, 2309–2334. [CrossRef]
35. Cao, F.F.; Zhao, Y.M.; Wang, F.L.; Shi, Y.H.; Yao, C.H. Nonconforming mixed FEM analysis for multi-term time-fractional mixed sub-diffusion and diffusion-wave equation with time-space coupled derivative. *Adv. Appl. Math. Mech.* **2023**, *15*, 322–358. [CrossRef]
36. Sun, Z.Z.; Wu, X.N. A fully discrete scheme for a diffusion-wave system. *Appl. Numer. Math.* **2006**, *56*, 193–209. [CrossRef]
37. Lin, Y.M.; Xu, C.J. Finite difference/spectral approximations for the time-fractional diffusion equation. *J. Comput. Phys.* **2007**, *225*, 1533–1552. [CrossRef]
38. Sinha, R.K.; Ewing, R.E.; Lazarov, R.D. Mixed finite element approximations of parabolic integro-differential equations with nonsmooth initial data. *SIAM J. Numer. Anal.* **2009**, *47*, 3269–3292. [CrossRef]
39. Fang, Z.C.; Zhao, J.; Li, H.; Liu, Y. Finite volume element methods for two-dimensional time fractional reaction-diffusion equations on triangular grids. *Appl. Anal.* **2023**, *102*, 2248–2270. [CrossRef]
40. Douglas, J.; Roberts, J.E. Global Estimates for Mixed Methods for Second Order Elliptic Equations. *Math. Comput.* **1985**, *44*, 39–52. [CrossRef]
41. Durán, R.G. *Mixed Finite Element Methods*; Lecture Notes in Mathematics; Springer: Berlin/Heidelberg, Germany, 2008; Volume 1939.
42. Stynes, M.; O'Riordan, E.; Gracia, J.L. Error analysis of a finite difference method on graded meshes for a time-fractional diffusion equation. *SIAM J. Numer. Anal.* **2017**, *55*, 1057–1079. [CrossRef]
43. Jin, B.T.; Li, B.Y.; Zhou, Z. Numerical analysis of nonlinear subdiffusion equations. *SIAM J. Numer. Anal.* **2018**, *56*, 1–23. [CrossRef]
44. Liao, H.L.; Li, D.F.; Zhang, J.W. Sharp error estimate of the nonuniform $L1$ formula for linear reaction-subdiffusion equations. *SIAM J. Numer. Anal.* **2018**, *56*, 1112–1133. [CrossRef]
45. Ren, J.C.; Liao, H.L.; Zhang, Z.M. Superconvergence error estimate of a finite element method on nonuniform time meshes for reaction-subdiffusion equations. *J. Sci. Comput.* **2020**, *84*, 38. [CrossRef]
46. Huang, C.B.; Stynes, M. Optimal H^1 spatial convergence of a fully discrete finite element method for the time-fractional Allen-Cahn equation. *Adv. Comput. Math.* **2020**, *46*, 63. [CrossRef]

fractal and fractional

MDPI

Article

Fractional Second-Grade Fluid Flow over a Semi-Infinite Plate by Constructing the Absorbing Boundary Condition

Jingyu Yang [1], Lin Liu [1,*], Siyu Chen [1], Libo Feng [2] and Chiyu Xie [3]

[1] School of Mathematics and Physics, University of Science and Technology Beijing, Beijing 100083, China; yjy20030104@163.com (J.Y.); csy15110422531@163.com (S.C.)
[2] School of Mathematical Sciences, Queensland University of Technology, GPO Box 2434, Brisbane, QLD 4001, Australia; l6.feng@qut.edu.au
[3] School of Astronautics, Beihang University, Beijing 100191, China; chiyuxie@ustb.edu.cn
* Correspondence: liulin1020@126.com

Abstract: The modified second-grade fluid flow across a plate of semi-infinite extent, which is initiated by the plate's movement, is considered herein. The relaxation parameters and fractional parameters are introduced to express the generalized constitutive relation. A convolution-based absorbing boundary condition (ABC) is developed based on the artificial boundary method (ABM), addressing issues related to the semi-infinite boundary. We adopt the finite difference method (FDM) for deriving the numerical solution by employing the L1 scheme to approximate the fractional derivative. To confirm the precision of this method, a source term is added to establish an exact solution for verification purposes. A comparative evaluation of the ABC versus the direct truncated boundary condition (DTBC) is conducted, with their effectiveness and soundness being visually scrutinized and assessed. This study investigates the impact of the motion of plates at different fluid flow velocities, focusing on the effects of dynamic elements influencing flow mechanisms and velocity. This research's primary conclusion is that a higher fractional parameter correlates with the fluid flow. As relaxation parameters decrease, the delay effect intensifies and the fluid velocity decreases.

Keywords: absorbing boundary condition; second-grade fluid; fractional derivative; finite difference method

Citation: Yang, J.; Liu, L.; Chen, S.; Feng, L.; Xie, C. Fractional Second-Grade Fluid Flow over a Semi-Infinite Plate by Constructing the Absorbing Boundary Condition. *Fractal Fract.* **2024**, *8*, 309. https://doi.org/10.3390/fractalfract8060309

Academic Editor: Riccardo Caponetto

Received: 28 March 2024
Revised: 16 May 2024
Accepted: 21 May 2024
Published: 23 May 2024

1. Introduction

Viscoelastic fluid is widely used in petroleum exploitation, medicine, biology, and other fields [1–3]. Viscoelastic fluid combines the viscosity of the fluid and the elasticity of the elastic solid, which shows the complex behavior between them and makes it a typical non-Newtonian fluid. Viscoelastic fluid has a time-dependent stress–strain response, showing shear rate-dependent viscosity and elastic recovery after unloading. Second-grade fluids are a specialized subclass of non-Newtonian fluids [4,5] which exhibit unique viscoelastic characteristics. A feature of these fluids is that their velocity field includes two derivatives within the correlation linking stress to strain, whereas the velocity field of Newtonian fluid contains only a first-order derivative. To better understand the flow characteristics of second-grade fluids, scholars often choose a simple model for analysis, which is helpful to understand the motion nature of second-grade fluid more deeply and provide theoretical support for related industrial applications. Ho et al. [6] investigated the migration of rigid spheres in a flowing second-grade fluid by simplifying the fluid flow problem between parallel plane walls. Khan et al. [7] gave an exact analytical solution for the fluid flow of a generalized second-grade fluid between two walls perpendicular to a flat plate. Tassaddiq [8] analyzed the flow of a second-grade fluid by simplifying the problem to a non-constant flow of the incompressible fluid over an inclined plate with an inclined magnetic field. Further studies are cited in references [9,10]. This paper focuses on the behavior of generalized second-grade fluids over a semi-infinite plate which contains

broad applications in various fields, as noted in references [11–14], including the flow of biological fluids, liquid metals and alloys, plasma, and blood.

The traditional second-grade fluid constitutive relation is grounded in integer differentials [15,16]. By considering the historical memory during their flow process, meaning that their current state is not solely determined by the present stress state but is also influenced by the stress history of the past, the fractional second-grade fluid is developed. The fractional differential equations [17–20] surpass the capabilities of integer-based models and offer a more precise capture of the historical dependency. Furthermore, the fractional derivatives possess a nonlocal nature; the derivative value at any given instant is intimately connected to the entire historical trajectory. This attribute equips fractional differential equations with the ability to describe physical processes exhibiting long-range or spatially extensive correlations [21]. The fractional operator addresses the significant inconsistencies between classical integer differential models and experimental outcomes, which compensates for their serious shortcomings. Consequently, it can achieve superior fitting results with experimental data by utilizing a reduced number of parameters. Sene et al. [22] used the double integration method to solve the fractional differential equation in the two-level fluid model. Chan et al. [23] carried out research into the behavior of deformable droplets when suspended within a second-grade fluid environment. Jiang et al. [24] made contributions to the field by examining the unsteady magnetohydrodynamic flow of a modified second-grade fluid by taking into account the Hall effect, as it pertains to movement through porous media. For more research on fractional derivatives in the field of viscoelastic fluids, the readers are encouraged to refer to [25–27]. In this work, we integrate the fundamental equation governing fluid dynamics with a model representing a modified second-grade fluid which includes the application of Riemann–Liouville time fractional derivative (RLTFD) operators.

Numerical simulations, when analyzing flow mechanisms, can demonstrate the flow properties of complex fluid models, eliminating the necessity of experimental procedures. Within this study, the formulation of the equation is achieved through the application of the FDM, as introduced in references [28,29]. The FDM is a numerical technique that divides a continuous domain into discrete grids and approximates the equation at these grid points. This method is adept at transforming a partial differential equation into a collection of either linear or nonlinear algebraic equation. This conversion facilitates straightforward numerical solutions that can be efficiently computed with the aid of computer systems. The FDM is not only intuitive in concept and easy to implement in programming, but also can flexibly handle problems with various boundary conditions and complex geometric shapes. Mei et al. [30] studied the flow around a sphere with free flow velocity oscillation and unsteady resistance under a finite Reynolds number by using FDM. Dennis et al. [31] proposed a new FDM for calculating steady flow in curved pipes. Kim et al. [32] developed a computational approach specifically tailored for the second-grade gradient theory of incompressible fluid dynamics. For more related research, one can refer to [33–35]. In addition, in the numerical simulation of the fractional derivatives, a variety of interpolation approximation methods has been reported, such as Grünwald–Letnikov definition [36], the L1 scheme [37], the L2 $-$ 1_σ scheme [38] and the fast algorithm [39].

The critical challenge in numerical methods pertains to the effective reduction of the effects that the unbounded regions exert on computational outcomes. Historically, the prevalent approach to dealing with the unbounded regions is through the employment of a direct truncation method (DTM), as documented in reference [40]. This approach involves selecting an exceedingly large value at the boundary, rather than attempting to define an actual infinite boundary condition. The DTM is less favorable for performing computer-based numerical simulations, notably for those that are extended over a long duration. In this paper, we employ an alternative strategy referred to as the artificial boundary method to establish the ABC. The core concept of this approach entails partitioning the unbounded domain into two distinct regions: a confined computational zone, which is the internal area, and an unbounded zone, representing the external area. The chosen boundary points

need to ensure that the source term is compactly supported within a finite truncation area. Subsequently, the relation at the truncation point is determined through the use of the Laplace transform in the external region. The use of this approach retains the effect exerted by the external area on the truncated boundary, which ensures the restricted area has a more reasonable boundary condition. The mentioned approach has been utilized extensively in various studies. For instance, Barucq et al. [41] analyzed the Helmholtz equation numerically by using ABC. They conducted an in-depth analysis of the impact of various parameters on these numerical results. Li et al. [42] solved the effective second-grade Schrödinger equation with the FDM by constructing ABCs. Muhr et al. [43] applied the ABC to address the Westervelt wave equation related to sound velocity potential, and the effectiveness and efficiency were confirmed. Further information on ABC is available in [44–46].

This paper studies the impulsive motion of a modified second-grade fluid on a plate of semi-infinite extent by introducing an ABC. In Section 2, we propose the constitutive relation and formulate the governing equation. Section 3 details the development and construction of the ABC. In Section 4, the numerical framework for the governing equation, along with its initial and boundary conditions (IBCs), is presented. In Section 5, four numerical instances are provided, detailing numerical methods' efficacy, the dynamic parameters' impacts on velocity, the ABC, and a comparison of this study with other methods. Section 6 offers a summary of these findings.

2. The Construction of the Governing Equation

We are now focusing on an infinitely extended flat plate with a fluid situated on a single side of the plate. In the initial state, the plate and the fluid above it remain stationary. Suddenly, the flat plate initiates movement with a velocity denoted as $u_w(t)$. As Figure 1 shows, we use a coordinate system where the flow progresses in the x direction, while the y direction is perpendicular to the plate. The positions of the plate are denoted as $y = 0$. The fluid's velocity on the surface of the plate is equal to the plate's velocity, which considers the no-slip condition. The fluid is regarded as a generalized second-grade fluid with stresses that depend not only on the current strain rate, but also possibly on the historical one. We neglect sidewall effects because the plate is considered to be infinitely long, such that the flow problem is mainly controlled by the motion of the plate and the viscoelastic properties of the fluid. In addition, the fluid is considered incompressible. The flow is supposed to be laminar, and no turbulence occurs. Finally, the deformation of the fluid is small and can be analyzed using linear theory. Collectively, these stipulations and suppositions constitute the foundational framework upon which the problem's analysis and resolution are predicated.

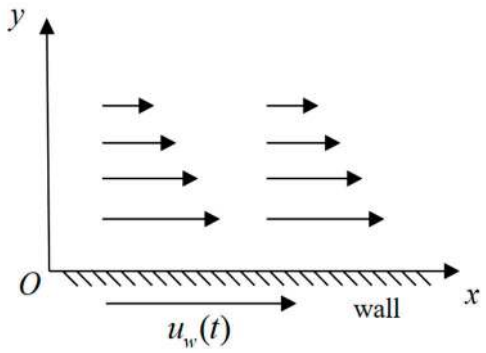

Figure 1. Schematic diagram of fractional second-grade fluid flow problem on a plate of semi-infinite extent.

The constitutive relation for a second-grade fluid satisfies [45]:

$$\mathbf{T} = -p\mathbf{I} + \mu\mathbf{A_1} + \alpha_1\mathbf{A_2} + \alpha_2\mathbf{A_1}^2 \tag{1}$$

in which the identity tensor is expressed as $\mathbf{I}$, the hydrostatic pressure is expressed as p, the stress tensor is expressed as $\mathbf{T}$, μ represents the coefficients of viscosity, α_1 and α_2 denote as the normal stress moduli, and the symbols $\mathbf{A_1}$ and $\mathbf{A_2}$ refer to the kinematic tensors [47] separately described by the following equation.

$$\mathbf{A}_1 = \nabla\mathbf{V} + (\nabla\mathbf{V})^{\mathrm{T}} \tag{2}$$

$$\mathbf{A}_2 = \frac{\partial\mathbf{A}_1}{\partial t} + \mathbf{A}_1(\nabla\mathbf{V}) + (\nabla\mathbf{V})^{\mathrm{T}}\mathbf{A}_1 \tag{3}$$

in which $\frac{\partial}{\partial t}$ is indicative of the material time partial derivative, $\mathbf{V}$ expresses the velocity vector field, and ∇ is the operator of the gradient. Suppose that the fluid described by Equation (1) conforms to thermodynamics, then all motions of the fluid satisfy the Clausius–Duhem inequality. Assume that the specific Helmholtz free energy of the fluid is minimized when the fluid is locally stationary [48]; then,

$$\mu \geqslant 0,\ \alpha_1 \geqslant 0,\ \alpha_1 + \alpha_2 = 0 \tag{4}$$

The fractional derivatives are able to describe the nonlocality and memory effects [17,21] of the generalized second-grade fluid. Since the fractional derivatives are nonlocal, this allows fractional differential equations to describe physical processes with long-range correlations or spatial-extent correlations. In general, the constitutive relation for the fractional second-grade fluid [49,50] also assumes the form (1), yet $\mathbf{A}_2$ satisfies

$$\mathbf{A}_2 = {}_0^{RL}\mathcal{D}_t^{\beta}\mathbf{A}_1 + \mathbf{A}_1(\nabla\mathbf{V}) + (\nabla\mathbf{V})^{\mathrm{T}}\mathbf{A}_1 \tag{5}$$

in which ${}_0^{RL}\mathcal{D}_t^{\beta}$ denotes the RLTFD operator [51].

The RLTFD operator ${}_0^{RL}\mathcal{D}_t^{\beta}$ satisfies

$${}_0^{RL}\mathcal{D}_t^{\beta}u(y,t) = \frac{\partial}{\partial t}\left(\frac{1}{\Gamma(1-\beta)}\int_0^t \frac{u(y,\tau)d\tau}{(t-\tau)^{\beta}}\right),\ 0 < \beta < 1 \tag{6}$$

where $\Gamma(\cdot)$ denotes the Gamma function. When $\beta = 1$, using the RLTFD's property, one obtains ${}_0^{RL}\mathcal{D}_t^{\beta}f(t) = {}_0^{RL}\mathcal{D}_t^{1}\left({}_0^{RL}\mathcal{D}_t^{0}f(t)\right) = \frac{\mathrm{d}f(t)}{\mathrm{d}t}$, namely, Equation (5) simplifies to Equation (3). When $\alpha_1 = 0$ and $\alpha_2 = 0$, the classical viscous Newtonian fluid is recovered [52,53]. It should be indicated that we have kept the same notation for the constant α_1 in (1) for the sake of simplicity, but it refers to a new material constant with the dimensions $kg \cdot m^{-1} \cdot s^{\beta-1}$. It reduces to $kg \cdot m^{-1}$ for $\beta \to 1$. For the other relations between (1) and (3), they remain formally unchanged under the above dimensional understanding [54].

Neglecting the external forces, the equation of motion satisfies

$$\rho\frac{\mathrm{D}\mathbf{V}}{\mathrm{D}t} = \nabla \cdot \mathbf{T} \tag{7}$$

in which the fluid's density is expressed as ρ, and the material derivative is represented as $\frac{\mathrm{D}}{\mathrm{D}t}$.

The continuity equation for velocity is expressed as

$$\nabla \cdot \mathbf{V} = 0 \tag{8}$$

Consider a modified second-grade fluid flowing close to a plate, moving with the velocity $u_w(t)$ within its own plane suddenly. The x-axis is defined following the motion adjacent to the wall, and the y-axis and the wall are perpendicular. Assuming the effects of

the side walls can be disregarded and implying the wall is infinitely long, we aim to find solutions in the form of the velocity field as

$$\mathbf{V} = u(y,t)\mathbf{i} \tag{9}$$

in which the x-direction unit vector is represented as $\mathbf{i}$, and the x-direction velocity is expressed as u.

The stresses exerted on the plate initiate the movement of the fluid, which is given by (1), (2), (4), and (5). Substituting (9) into (1)–(6), we obtain

$$\mathbf{T}_{xy} = \mu\frac{\partial u}{\partial y} + \alpha_1 {}_0^{RL}\mathcal{D}_t^{\beta}\frac{\partial u}{\partial y} \tag{10}$$

where $\mathbf{T}_{xy} = \mathbf{T}_{yx}$ and $\mathbf{T}_{xx} = \mathbf{T}_{yy} = \mathbf{T}_{zz} = \mathbf{T}_{xz} = \mathbf{T}_{yz} = 0$. Note that we have kept the same notation for the constant α_1 in (10), but it refers to a new material constant with the dimensions $kg \cdot m^{-1} \cdot s^{\beta-1}$.

By introducing (9) and (10) into (7), it yields

$$\rho\frac{\partial u}{\partial t} = \mu\frac{\partial^2 u}{\partial y^2} + \alpha_1 {}_0^{RL}\mathcal{D}_t^{\beta}\frac{\partial^2 u}{\partial y^2} \tag{11}$$

The IBCs satisfy

$$u(y,0) = 0,\ y > 0 \tag{12}$$

$$u(0,t) = u_w(t),\ u(+\infty,t) = 0,\ t \in [0,T] \tag{13}$$

where $u_w(t)$ is the velocity of the plate.

Dimensionless variables are introduced to facilitate the analysis

$$\widehat{u} = \frac{u}{U},\ \widehat{y} = \frac{yU\rho}{\mu},\ \widehat{t} = \frac{tU^2\rho}{\mu},\ \widehat{u}_w(\widehat{t}) = \frac{u_w(t)}{U} \tag{14}$$

where U represents the characteristic velocity.

For generalization purposes, the form of $f(y,t)$ is presented. Subsequently, the dimensionless governing equation along with its IBCs are presented as follows (the superscript "$\widehat{\ }$" is omitted)

$$\frac{\partial u(y,t)}{\partial t} = \frac{\partial^2 u(y,t)}{\partial y^2} + \eta_0^{RL}\mathcal{D}_t^{\beta}\frac{\partial^2 u(y,t)}{\partial y^2} + f(y,t) \tag{15}$$

$$u(y,0) = 0,\ y > 0 \tag{16}$$

$$u(0,t) = u_w(t),\ u(+\infty,t) = 0,\ t \in [0,T] \tag{17}$$

where $\eta = \frac{\alpha_1 U^{2\beta}\rho^{\beta}}{\mu^{\beta+1}}$.

3. The Establishment of the ABC

By using the ABM, we formulate the exact ABC. First, the unbounded region $\Omega := \{y|0 \le y < +\infty\}$ is truncated by the point y_r. In such a case, we divide the unbounded region as the unbounded area $\Omega_r := \{y|y_r \le y < +\infty\}$ located to the right, and the bounded area $\Omega_c := \{y|0 \le y \le y_r\}$ is designated for calculation. The selection of y_r demands that the initial conditions and the source term be compactly supported in region Ω_c.

In the unbounded region Ω_r, we have

$$\frac{\partial u(y,t)}{\partial t} = \frac{\partial^2 u(y,t)}{\partial y^2} + \eta_0^{RL}\mathcal{D}_t^{\beta}\frac{\partial^2 u(y,t)}{\partial y^2} + f(y,t) \tag{18}$$

$$u(y,0) = 0 \text{ for } y > 0 \tag{19}$$

$$u(+\infty,t) = 0 \text{ when } t \in [0,T] \tag{20}$$

Since β is between zero and one, the Laplace transform for ${}_0^{RL}\mathcal{D}_t^{\beta}$ [55] has the form $L\left\{{}_0^{RL}\mathcal{D}_t^{\beta} f(t), s\right\} = s^{\beta} L\{f(t), s\} - \left[{}_0^{RL}\mathcal{D}_t^{\beta-1} f(t)\right]_{t=0}$. By referring to the principle of the Laplace transform for the RLTFD, we obtain

$$\frac{\partial^2 \hat{u}(y,s)}{\partial y^2} - \frac{s}{1+\eta s^{\beta}} \hat{u}(y,s) = 0 \tag{21}$$

in which the Laplace transform of $u(y,t)$ is represented as $\hat{u}(y,s)$.

Solving the above equation yields

$$\hat{u}(y,s) = e^{-\sqrt{\frac{s}{1+\eta s^{\beta}}} y} \tag{22}$$

For Equation (22), we take the derivative for y

$$\frac{\partial \hat{u}(y,s)}{\partial y} = -\frac{1}{\left(1+\eta s^{\beta}\right)^{\frac{1}{2}}} \hat{u}(y,s) \tag{23}$$

Before performing the inverse Laplace transform, it is crucial to define the generalized Mittag–Leffler function [55]:

$$E_{k,l}^{\gamma}(z) = \sum_{n=0}^{\infty} \frac{(\gamma)_n}{n!\Gamma(nk+l)} z^n, \ \mathrm{Re}k > 0, \ l \in C, \ \gamma > 0 \tag{24}$$

where $(\gamma)_n = \gamma(\gamma+1)\cdots(\gamma+n-1) = \Gamma(\gamma+n)/\Gamma(\gamma)$.

The Mittag–Leffler function [55] has the following property:

$$\mathcal{L}\left\{t^{l-1} E_{k,l}^{\gamma}\left(-\lambda t^k\right), s\right\} = \frac{s^{k\gamma-l}}{\left(\lambda + s^k\right)^{\gamma}} \tag{25}$$

where Re$k > 0$ and Re$l > 0$.

By conducting the inverse Laplace transformation for (23), we infer the ABC at $y = y_r$

$$\frac{\partial u(y_r,t)}{\partial y} = -\sqrt{\frac{1}{\eta}} \left[t^{\frac{1}{2}\beta-1} E_{\beta,\frac{1}{2}\beta}^{\frac{1}{2}}\left(-\frac{1}{\eta} t^{\beta}\right)\right] * {}_0^{RL}\mathcal{D}_t^{\frac{1}{2}} u(y_r,t) \tag{26}$$

where $*$ stands for the convolution.

To facilitate explanation, we introduce the notation as

$$K_1(t) = \sqrt{\frac{1}{\eta}} \left[t^{\frac{1}{2}\beta-1} E_{\beta,\frac{1}{2}\beta}^{\frac{1}{2}}\left(-\frac{1}{\eta} t^{\beta}\right)\right] \tag{27}$$

After introducing the symbol $K_1(t)$, the Equation (26) changes:

$$\frac{\partial u(y_r,t)}{\partial y} = \int_0^t -K_1(t-\tau) * {}_0^{RL}\mathcal{D}_{\tau}^{\frac{1}{2}} u(y_r,\tau) d\tau \tag{28}$$

Taking Equation (28) as the exact ABC, we formulate the governing equation based on the IBCs:

$$\frac{\partial u(y,t)}{\partial t} = \frac{\partial^2 u(y,t)}{\partial y^2} + \eta {}_0^{RL}\mathcal{D}_t^{\beta} \frac{\partial^2 u(y,t)}{\partial y^2} + f(y,t) \tag{29}$$

$$u(y,0) = 0 \tag{30}$$

$$u(0,t) = 0 \tag{31}$$

$$\frac{\partial u(y_r,t)}{\partial y} = \int_0^t -K_1(t-\tau) * {}_0^{RL}\mathcal{D}_\tau^{\frac{1}{2}} u(y_r,\tau)d\tau \tag{32}$$

Now, we discuss the well-posedness of the considered problem. Since the initial condition of our question is zero, ${}_0^{RL}\mathcal{D}_t^\beta u(t)$ and ${}_0^{C}\mathcal{D}_t^\beta u(t)$ are equivalent. Then, the property for the Caputo fractional derivative is also applicable to the RLTFD. Initially, we introduce the following lemma.

Lemma 1. *Assume $u(t)$ to be an absolutely continuous function on $[0,T]$. Considering $0 < \beta < 1$ and $u(0) = 0$, it yields [56]*

$$u(t){}_0^{RL}\mathcal{D}_t^\beta u(t) \geq \frac{1}{2}{}_0^{RL}\mathcal{D}_t^\beta u^2(t) \tag{33}$$

Theorem 1. *The problem (29)–(32) is L^2 -stable and adheres to the subsequent estimation:*

$$\left\| \frac{\partial u(y,t)}{\partial y} \right\|^2_{L^2[0,y_r]} \leq \|f(y,t)\|^2_{L^2[0,y_r]} \tag{34}$$

where $\|u(y,t)\|^2_{L^2[a,b]}(t) = \int_a^b |u(y,t)|^2 \mathrm{d}y$.

Proof. In the outer region $(y_r, +\infty]$, the source term becomes zero due to the compactly supported assumption in $[0, y_r]$. Multiplying both sides of Equation (29) simultaneously by $\frac{\partial^2 u(y,t)}{\partial y^2}$ and integrating over y from y_r to $+\infty$ and t from 0 to T, it yields:

$$\begin{aligned} &\int_0^T \int_{y_r}^{+\infty} \frac{\partial u(y,t)}{\partial t} \frac{\partial^2 w(y,t)}{\partial y^2} \mathrm{d}y\mathrm{d}t = \int_0^T \int_{y_r}^{+\infty} \frac{\partial^2 u(y,t)}{\partial y^2} \frac{\partial^2 u(y,t)}{\partial y^2} \mathrm{d}y\mathrm{d}t \\ &+\eta \int_0^T \int_{y_r}^{+\infty} \frac{\partial^2 u(y,t)}{\partial y^2} {}_0^{RL}\mathcal{D}_t^\beta \frac{\partial^2 u(y,t)}{\partial y^2} \mathrm{d}y\mathrm{d}t. \end{aligned} \tag{35}$$

Employing the method of integration by parts and Lemma 1 yields:

$$\int_0^T \int_{y_r}^{+\infty} \frac{\partial u(y,t)}{\partial t} \frac{\partial^2 u(y,t)}{\partial y^2} \mathrm{d}y\mathrm{d}t = -\int_0^T \frac{\partial u(y_r,t)}{\partial t} \frac{\partial u(y_r,t)}{\partial y} \mathrm{d}t - \frac{1}{2}\int_0^T \frac{\partial}{\partial t} \left\| \frac{\partial u(y,t)}{\partial y} \right\|^2_{L^2(y_r,+\infty]} \mathrm{d}t \tag{36}$$

Considering (30) and (31), we have:

$$\begin{aligned} &-\int_0^T \frac{\partial u(y_r,t)}{\partial t} \frac{\partial u(y_r,t)}{\partial y} \mathrm{d}t - \frac{1}{2}\int_0^T \frac{\partial}{\partial t} \left\| \frac{\partial u(y,t)}{\partial y} \right\|^2_{L^2(y_r,+\infty]} \mathrm{d}t \\ &= -\int_0^T \frac{\partial u(y_r,t)}{\partial t} \frac{\partial u(y_r,t)}{\partial y} \mathrm{d}t - \frac{1}{2} \left\| \frac{\partial u(y,T)}{\partial y} \right\|^2_{L^2(y_r,+\infty]} \\ &\leq -\int_0^T \frac{\partial u(y_r,t)}{\partial t} \frac{\partial u(y_r,t)}{\partial y} \mathrm{d}t. \end{aligned} \tag{37}$$

The second term satisfies that:

$$\int_0^T \int_{y_r}^{+\infty} \frac{\partial^2 u(y,t)}{\partial y^2} \frac{\partial^2 u(y,t)}{\partial y^2} \mathrm{d}y\mathrm{d}t \geq 0 \tag{38}$$

By using Lemma 1, we obtain:

$$\begin{aligned}
&\eta\int_0^T\int_{y_r}^{+\infty}\frac{\partial^2u(y,t)}{\partial y^2}\,{}_0^{RL}\mathcal{D}_t^{\beta}\frac{\partial^2u(y,t)}{\partial y^2}\mathrm{d}y\mathrm{d}t \geq \frac{\eta}{2}\int_0^T {}_0^{RL}\mathcal{D}_t^{\beta}\left\|\frac{\partial^2u(y,t)}{\partial y^2}\right\|^2_{L^2(y_r,+\infty]}\mathrm{d}t\\
&=\frac{\eta}{2}\int_0^T\frac{\mathrm{d}}{\mathrm{d}t}\left(\frac{1}{\Gamma(1-\beta)}\int_0^t\left\|\frac{\partial^2u(y,\tau)}{\partial y^2}\right\|^2_{L^2(y_r,+\infty]}\frac{1}{(t-\tau)^{\beta}}\mathrm{d}\tau\right)\mathrm{d}t\\
&=\frac{\eta}{2}\left(\frac{1}{\Gamma(1-\beta)}\int_0^T\left\|\frac{\partial^2u(y,\tau)}{\partial y^2}\right\|^2_{L^2(y_r,+\infty]}\frac{1}{(T-\tau)^{\beta}}\mathrm{d}\tau\right)\geq 0.
\end{aligned}\tag{39}$$

Combining (35)–(39), we can deduce:

$$\int_0^T\frac{\partial u(y_r,t)}{\partial t}\frac{\partial u(y_r,t)}{\partial y}\mathrm{d}t\leq 0\tag{40}$$

Consider the inner region $[0,y_r]$. Both sides of Equation (29) are simultaneously multiplied by $\frac{\partial^2u(y,t)}{\partial y^2}$ and integrated over y in region $[0,y_r]$ and t in region $[0,T]$. Then, we have

$$\begin{aligned}
&\int_0^T\int_0^{y_r}\frac{\partial u(y,t)}{\partial t}\frac{\partial^2u(y,t)}{\partial y^2}\mathrm{d}y\mathrm{d}t=\int_0^T\int_0^{y_r}\frac{\partial^2u(y,t)}{\partial y^2}\frac{\partial^2u(y,t)}{\partial y^2}\mathrm{d}y\mathrm{d}t\\
&+\eta\int_0^T\int_0^{y_r}{}_0^{RL}\mathcal{D}_t^{\beta}\frac{\partial^2u(y,t)}{\partial y^2}\frac{\partial^2u(y,t)}{\partial y^2}\mathrm{d}y\mathrm{d}t+\int_0^T\int_0^{y_r}f(y,t)\frac{\partial^2u(y,t)}{\partial y^2}\mathrm{d}y\mathrm{d}t.
\end{aligned}\tag{41}$$

For the first term, considering the boundary condition, we can derive:

$$\begin{aligned}
&\int_0^T\int_0^{y_r}\frac{\partial w(y,t)}{\partial t}\frac{\partial^2w(y,t)}{\partial y^2}\mathrm{d}y\mathrm{d}t=\int_0^T\int_0^{y_r}\frac{\partial w(y,t)}{\partial t}\mathrm{d}\frac{\partial w(y,t)}{\partial y}\mathrm{d}t\\
&=\int_0^T\frac{\partial w(y_r,t)}{\partial t}\frac{\partial w(y_r,t)}{\partial y}\mathrm{d}t-\int_0^T\int_0^{y_r}\frac{\partial w(y,t)}{\partial y}\frac{\partial}{\partial t}\frac{\partial w(y,t)}{\partial y}\mathrm{d}y\mathrm{d}t.
\end{aligned}\tag{42}$$

Considering the initial condition, it yields:

$$-\int_0^T\int_0^{y_r}\frac{\partial w(y,t)}{\partial y}\frac{\partial}{\partial t}\frac{\partial w(y,t)}{\partial y}\mathrm{d}y\mathrm{d}t\leq-\int_0^{y_r}\left(\frac{\partial w(y,T)}{\partial y}\right)^2\mathrm{d}y+\int_0^{y_r}\left[\int_0^T\frac{\partial w(y,t)}{\partial y}\frac{\partial}{\partial t}\frac{\partial w(y,t)}{\partial y}\mathrm{d}t\right]\mathrm{d}y\tag{43}$$

then one can obtain

$$-\int_0^T\int_0^{y_r}\frac{\partial w(y,t)}{\partial y}\frac{\partial}{\partial t}\frac{\partial w(y,t)}{\partial y}\mathrm{d}y\mathrm{d}t\leq-\frac{1}{2}\int_0^{y_r}\left(\frac{\partial w(y,T)}{\partial y}\right)^2\mathrm{d}y\leq 0\tag{44}$$

Combining (40), (42) and (44), the first term changes:

$$\int_0^T\int_0^{y_r}\frac{\partial w(y,t)}{\partial t}\frac{\partial^2w(y,t)}{\partial y^2}\mathrm{d}y\mathrm{d}t\leq 0\tag{45}$$

The second term satisfies that:

$$\int_0^T\int_0^{y_r}\frac{\partial^2w(y,t)}{\partial y^2}\frac{\partial^2w(y,t)}{\partial y^2}\mathrm{d}y\mathrm{d}t\geq 0\tag{46}$$

Using Lemma 1, the third term satisfies

$$\eta\int_0^T\int_0^{y_r}\frac{\partial^2w(y,t)}{\partial y^2}\,{}_0^{RL}\mathcal{D}_t^{\beta}\frac{\partial^2w(y,t)}{\partial y^2}\mathrm{d}y\mathrm{d}t\geq\frac{\eta}{2}\int_0^T\int_0^{y_r}{}_0^{RL}\mathcal{D}_t^{\beta}\left(\frac{\partial^2w(y,t)}{\partial y^2}\right)^2\mathrm{d}y\mathrm{d}t\tag{47}$$

Considering the definition (6), we obtain

$$\begin{aligned}&\frac{\eta}{2}\int_0^T\int_0^{y_r}{}_0^{RL}\mathcal{D}_t^{\beta}\left(\frac{\partial^2 w(y,t)}{\partial y^2}\right)^2\mathrm{d}y\mathrm{d}t\\&=\frac{\eta}{2}\int_0^T\int_0^{y_r}\frac{\mathrm{d}}{\mathrm{d}t}\left(\frac{1}{\Gamma(1-\beta)}\int_0^t\frac{1}{(t-\tau_1)^{\beta}}\left(\frac{\partial^2 w(y,\tau_1)}{\partial y^2}\right)^2\mathrm{d}\tau_1\right)\mathrm{d}y\mathrm{d}t\\&=\frac{\eta}{2}\int_0^{y_r}\left(\frac{1}{\Gamma(1-\beta)}\int_0^t\frac{1}{(T-\tau_1)^{\beta}}\left(\frac{\partial^2 w(y,\tau_1)}{\partial y^2}\right)^2\mathrm{d}\tau_1\right)\mathrm{d}y\geq 0.\end{aligned}\tag{48}$$

According to the Cauchy–Schwartz inequality, one can estimate the fourth term as

$$-\int_0^T\int_0^{y_r}f(y,t)\frac{\partial^2 u(y,t)}{\partial y^2}\mathrm{d}y\mathrm{d}t\leq\frac{1}{2}\int_0^T\int_0^{y_r}(f(y,t))^2\mathrm{d}y\mathrm{d}t+\frac{1}{2}\int_0^T\int_0^{y_r}\left(\frac{\partial^2 u(y,t)}{\partial y^2}\right)^2\mathrm{d}y\mathrm{d}t\tag{49}$$

Then, Equation (41) changes:

$$\int_0^T\int_0^{y_r}\frac{\partial^2 u(y,t)}{\partial y^2}\frac{\partial^2 u(y,t)}{\partial y^2}\mathrm{d}y\mathrm{d}t\leq\int_0^T\int_0^{y_r}(f(y,t))^2\mathrm{d}y\mathrm{d}t\tag{50}$$

Therefore, the proof is complete and Equation (34) has been proven. □

Theorem 2. *Given that $u(y,t)$ and $v(y,t)$ are solutions to (29)–(32), it is concluded that $u(y,t)$ and $v(y,t)$ are identical, ensuring the uniqueness of the solution.*

Proof. Denote $w(y,t)=u(y,t)-v(y,t)$. $w(y,t)$ satisfies the following equation:

$$\frac{\partial w(y,t)}{\partial t}=\frac{\partial^2 w(y,t)}{\partial y^2}+\eta_0^{RL}\mathcal{D}_t^{\beta}\frac{\partial^2 w(y,t)}{\partial y^2}\tag{51}$$

which is subjected to IBCs:

$$w(y,0)=0\tag{52}$$

$$w(0,t)=0\tag{53}$$

$$\frac{\partial w(y_r,t)}{\partial y}=\int_0^t -K_1(t-\tau)*{}_0^{RL}\mathcal{D}_t^{\frac{1}{2}}w(y_r,\tau)\mathrm{d}\tau\tag{54}$$

According to Theorem 1, it follows that

$$\int_0^t\left\|\frac{\partial^2 w(\cdot,\tau)}{\partial y^2}\right\|^2\mathrm{d}\tau\leq 0\tag{55}$$

where $\|w(\cdot,t)\|^2$ is defined as $\|w(\cdot,t)\|^2=\int_0^{y_r}w^2(y,t)\mathrm{d}y$.

Since $\left\|\frac{\partial^2 w(\cdot,\tau)}{\partial y^2}\right\|^2$ is no less than zero, we obtain

$$\frac{\partial^2 w(\cdot,\tau)}{\partial y^2}=0\tag{56}$$

According to (56), we assume that $w(y,t)$ has the form

$$w(y,t)=C_1(t)y+C_2(t)\tag{57}$$

Then, one can obtain

$$\frac{\partial w(y,t)}{\partial y}=C_1(t)\tag{58}$$

Considering the boundary condition (53), we have:

$$C_2(t) = 0 \tag{59}$$

Combining Equations (54)–(58), we can deduce:

$$C_1(t) = -y_r \int_0^t K_1(t-\tau) * {}_0^{RL}\mathcal{D}_\tau^{\frac{1}{2}} C_1(\tau) \mathrm{d}\tau. \tag{60}$$

Since the parameter y_r is arbitrary, the following condition must hold for (60):

$$C_1(t) = 0 \tag{61}$$

which means $w(y,t) = 0$. The uniqueness of the solution has been established. The proof of Theorem 2 has been finished. □

4. Construction of the FDM

This section is dedicated to formulating a numerical scheme based on Equation (29) to Equation (32), with the aim of solving the problem on a bounded domain Ω_c. In the domain $\Omega_c \times [0,T]$, we define the temporal step size as $\tau = T/N$ and the spatial step size as $h = \frac{y_r}{M}$, where the integers N and M correspond to the count of grid points in the temporal and spatial dimensions, respectively. The grid points are defined as $t_n := n\tau$ for $0 \le n \le N$ and $y_j = jh_y$ for $0 \le j \le M$. Furthermore, $u(y_j, t_n)$ and u_j^n represent the exact solutions and numerical solutions of the velocity at grid points (y_j, t_n) for $0 \le n \le N$ and $0 \le j \le M$, respectively. For clarity, we introduce some notations below [28,29]

$$\delta_t u_j^n = \frac{u_j^n - u_j^{n-1}}{\tau},\ \delta_y^2 u_j^n = \frac{u_{j+1}^n - 2u_j^n + u_{j-1}^n}{h^2} \tag{62}$$

At $t = t_n$, the time-fractional derivative of order α in the RLTFD is approximated by the L1 scheme [49] by considering the equivalent relationship between the RLTFD and the Caputo fractional derivative:

$${}_0^{RL}\mathcal{D}_t^\alpha u^n = {}_0^C\widetilde{D}_t^\alpha u^n + R_1 = \frac{\tau^{-\alpha}}{\Gamma(2-\alpha)}\left[a_0^{(\alpha)}u^n - \sum_{k=1}^{n-1}\left(a_{n-k-1}^{(\alpha)} - a_{n-k}^{(\alpha)}\right)u^k - a_{n-1}^{(\alpha)}u^0 + \frac{1-\alpha}{n^\alpha}u^0\right] + R_1 \tag{63}$$

where $a_0^{(\alpha)} = 1$ and $a_k^{(\alpha)} = (k+1)^{1-\alpha} - k^{1-\alpha}$, $k = 1, 2, \ldots, n-1$. The symbol R_1 refers to the error and satisfies $|R_1| \le C\tau^{2-\alpha}$.

Apart from that, the central difference formula is utilized to approximate $\frac{\partial^2 u}{\partial y^2}$, and the error terms are disregarded. Subsequently, the discretized scheme of the equation is obtained as follows:

$$\delta_t u_j^n = \frac{\tau^{-\beta}}{\Gamma(2-\beta)}\left[a_0{}^{(\beta)}\delta_y^2 u_j^n - \sum_{k=1}^{n-1}\left(a_{n-k-1}^{(\beta)} - a_{n-k}^{(\beta)}\right)\delta_y^2 u_j^k - a_{n-1}^{(\beta)}\delta_y^2 u_j^0 + \frac{1-\beta}{n^\beta}u_j^0\right] + \delta_y^2 u_j^n \tag{64}$$

Furthermore, using the definitions given by Equation (62), the aforementioned equation can be rearranged as:

$$\begin{aligned}&-\left(\frac{\eta\tau^{-\beta}}{\Gamma(2-\beta)}a_0{}^{(\beta)}+1\right)\frac{u_{j+1}^n}{h^2}+\left(\frac{\eta\tau^{-\beta}}{\Gamma(2-\beta)}a_0{}^{(\beta)}\frac{2}{h^2}+\frac{2}{h^2}+\frac{1}{\tau}\right)u_j^n-\left(\frac{\eta\tau^{-\beta}}{\Gamma(2-\beta)}a_0{}^{(\beta)}+1\right)\frac{u_{j-1}^n}{h^2}\\&=-\frac{\eta\tau^{-\beta}}{\Gamma(2-\beta)}\left[\sum_{k=1}^{n-1}\left(a_{n-k-1}^{(\beta)}-a_{n-k}^{(\beta)}\right)\delta_y^2u_j^k+a_{n-1}^{(\beta)}\delta_y^2u_j^0-\frac{1-\beta}{n^\beta}u_j^0\right]+\frac{u_j^{n-1}}{\tau}.\end{aligned}\tag{65}$$

The integral term (32) under the ABC is approximated using the following form:

$$\begin{aligned}&\textstyle\int_{t_{k-1}}^{t_k}K_1(t-\tau)*{}_0^{RL}\mathcal{D}_t^{1/2}u d\tau\\&\approx\tau K_1(t_n-t_k)\frac{\tau^{-1/2}}{\Gamma(3/2)}\left[a_0^{(1/2)}u^k-\sum_{j=1}^{k-1}\left(a_{k-j-1}^{(1/2)}-a_{k-j}^{(1/2)}\right)u^j-a_{k-1}^{(1/2)}u^0-\frac{1}{2n^{1/2}}u_j^0\right].\end{aligned}\tag{66}$$

By using the backward difference scheme with first-order spatial derivatives, we derive the final difference scheme for the ABC:

$$\frac{u_j^n-u_{j-1}^n}{h}=-\sum_{k=1}^{n}K_1((n-k)\tau)\frac{\tau^{1/2}}{\Gamma(3/2)}\left[a_0^{(1/2)}u^k-\sum_{j=1}^{k-1}\left(a_{k-j-1}^{(1/2)}-a_{k-j}^{(1/2)}\right)u^j-a_{k-1}^{(1/2)}u^0+\frac{1}{2n^{1/2}}u_j^0\right]\tag{67}$$

Subsequently, the remaining conditions can be discretized as follows:

$$u_j^0=0,\ j=0,1,2,\ldots,M,\ u_0^n=u_w(t_n),\ n=0,1,2,\ldots.$$

Remark 1. *Since the governing equation in this work constitutes a particular instance of the issue in [57] with new boundary condition, the stability and convergence of the proposed numerical scheme can be proved through a comparable approach. This paper primarily focuses on the formulation of the ABC and an evaluation of its advantages. As such, a detailed theoretical analysis of the numerical scheme has been excluded.*

5. Numerical Examples

5.1. The Verification of the Solution and the ABC

The first step is to validate the numerical solution by contrasting it with the exact solution. According to (29) to (32), the governing equation with a source term $f(y,t)$ is as follows:

$$\frac{\partial u(y,t)}{\partial t}=\frac{\partial^2u(y,t)}{\partial y^2}+\eta_0^{RL}\mathcal{D}_t^\beta\frac{\partial^2u(y,t)}{\partial y^2}+f(y,t)\tag{68}$$

subsequently, the IBCs are presented by

$$u(y,0)=0\text{ for }y>0\tag{69}$$

$$u(0,t)=Wt^2\text{and }\frac{\partial u(y_r,t)}{\partial y}+\int_0^t K_1(t-\tau)*{}_0^{RL}\mathcal{D}_\tau^{1/2}u(y_r,\tau)d\tau=0,\text{ for }t>0\tag{70}$$

where y_r is selected to be $y_r=1$.

We define the exact solution as

$$u(y,t)=\begin{cases}W(1-y)^6(1+y)^6t^6, & \text{for}\quad 0\le y\le 1,\\0, & \text{elsewhere.}\end{cases}\tag{71}$$

Bringing the above exact solution (71) into Equation (68) yields the expression for the source term:

$$f(y,t)=\begin{cases}6Wt^5(1-y)^6(y+1)^6-Wt^6(30(y+1)^6(y-1)^4 \\ +72(y+1)^5(y-1)^5+30(y+1)^4(y-1)^6)\left[\frac{\Gamma(7)t^{-\beta}}{\Gamma(7-\beta)}+1\right], & \text{for} \quad 0\le y\le 1, \\ 0, & \text{elsewhere.}\end{cases}$$

It should be indicated that the source term complies with the condition of the ABC that it is compactly supported in the inner region $[0,1]$.

In conjunction with the matrix form of the difference scheme, which can be deduced by (65), we use MATLAB to solve the governing equation. This aims at generating the numerical solutions on successive time levels. The computational domain is specified as $[0,1]$, with a termination time denoted by $T=1$. The calculation parameters are set to $\beta=0.5$ and $\eta=1$, while the temporal and spatial steps are $\tau=1/2^{10}$ and $h=1/2^{10}$, respectively. As apparently revealed in Figure 2, the comparative velocity profiles of the numerical and analytical solutions at $t=1$ exhibit similar distribution patterns, which is sufficient to prove that the numerical scheme we developed is precise.

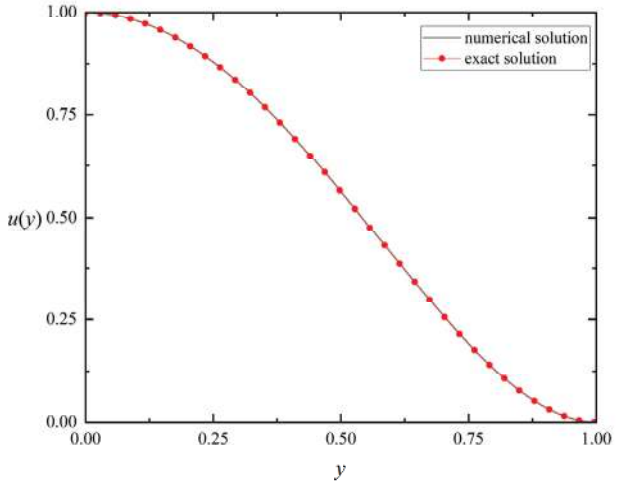

Figure 2. The comparison curve of error distribution for $T=1$ between the numerical solution and the exact solution when $\beta=0.5$, $\eta=1$ and $W=1$.

Figure 3 provides a clear visualization of the disparities in velocity distribution when comparing the ABC against the DTBC, facilitated by the choice of $f(y,t)=0$. Notably, the distribution curves exhibit significant divergence at the right boundary. This difference stems from the fact that the DTBC specifies zero velocity at the selected right boundary, whereas the velocity at the right boundary follows a specific functional relationship when subject to the ABC, which is determined through meticulous derivation. In numerous practical situations, the velocity at the boundary on the right does not maintain a constant zero over time, which potentially results in imprecise numerical solutions based on the DTBC. However, the ABC averts the artificial error at the truncation point and is consistent with the zero boundary condition at infinite locations. This proves that the ABC can effectively deal with problems related to extension to infinite domains.

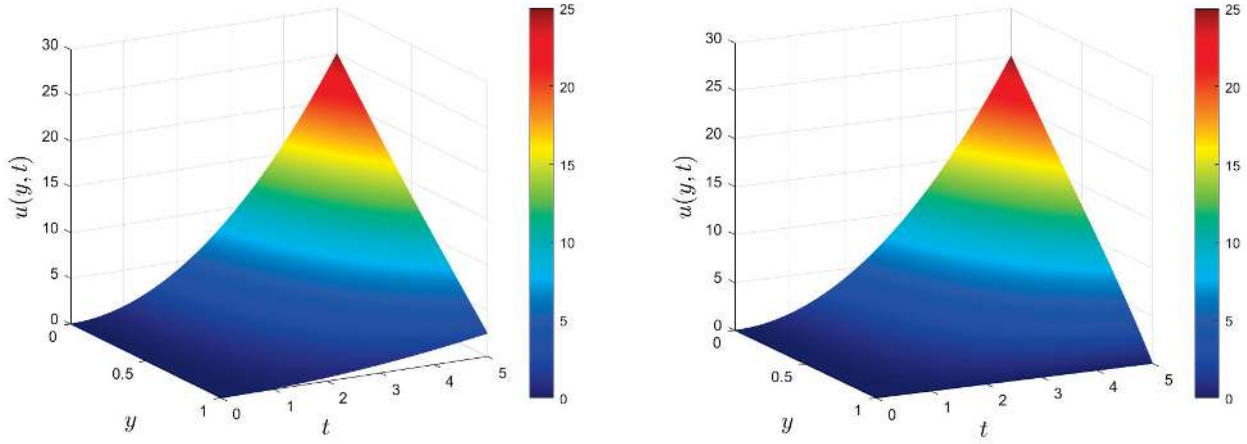

Figure 3. The velocity distribution between the ABC (**left**) and the DTBC (**right**) when $f(y,t) = 0$, $T = 5$, $\beta = 0.5$, $\eta = 1$, and $W = 1$.

5.2. Impact of Parameter Variations on the Velocity Field Induced by a Moving Plate

We assume that the fluid is set in motion by a plate moving at the velocity $u_w(t) = Wt^2$. With this assumption, the governing equation with its associated IBCs reduces to:

$$\frac{\partial u(y,t)}{\partial t} = \frac{\partial^2 u(y,t)}{\partial y^2} + \eta_0^{RL}\mathcal{D}_t^{\beta}\frac{\partial^2 u(y,t)}{\partial y^2} \tag{72}$$

$$u(y,0) = 0 \text{ for } y > 0 \tag{73}$$

$$u(0,t) = Wt^2 \text{ and } \frac{\partial u(y_r,t)}{\partial y} + \int_0^t K_1(t-\tau) * {}_0^{RL}\mathcal{D}_\tau^{1/2} u(y_r,\tau)\mathrm{d}\tau = 0 \tag{74}$$

The examination of parameter influence on the velocity field is conducted. In this example, we select the cut-off point as $y_r = 8$. Figure 4 illustrates the impact of the varying time parameter on the velocity distribution. Comparing multiple curves at different time points, it can be found that the fluid velocity at the same location increases with time. Analyzing a single curve, it can be observed that the closer the fluid is to the plate, the greater the velocity will be. The figure describes the time evolution of the velocity well.

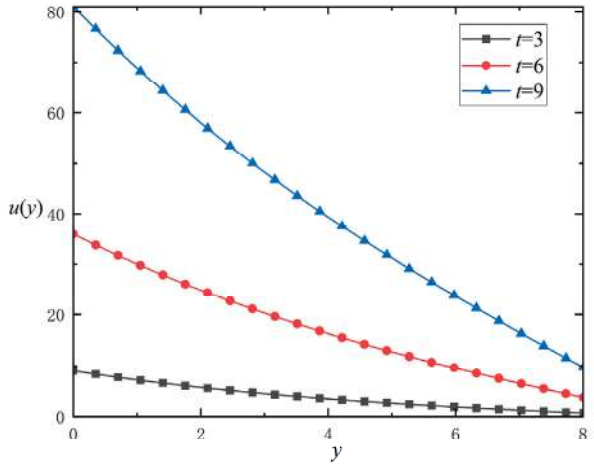

Figure 4. The impacts exerted by the time parameters on the velocity distribution for $\beta = 0.5$, $\eta = 1$, and $W = 1$.

As shown in Figure 5 for y (left) and t (right), the variation in fractional orders significantly influences the velocity distribution. This plate's motion changes the shear force, causing the fluid near the plate to begin to flow. Therefore, it can be observed that

in the actual image, the velocity at the starting point is very high, whereas the velocity at locations further away is relatively low. A trend is observable in these images, where the flow velocity diminishes with an increase in y. And at a fixed position, the velocity rises with the augmentation of t. As shown in the figure on the left of Figure 5, at a fixed time, the increase in the fractional parameter results in a smaller value of the distribution curve. From this, it can be observed that as the fractional parameter diminishes, the fluid's memory properties become more pronounced, and the velocity transmission occurs more rapidly. Regarding the relationship between the distribution curve and time, when the spatial position is fixed, the larger fractional parameter results in the decreasing velocity of the fluid.

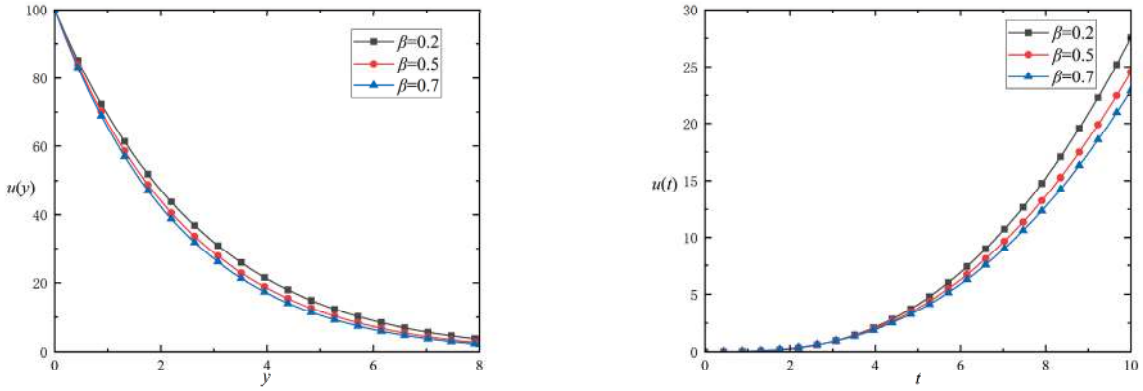

Figure 5. The impacts exerted of the fractional parameters on the velocity distribution versus y ($t = 1$) and t ($y = 1$) for $\eta = 1$ and $W = 1$.

In Figure 6, the effect of relaxation parameters on the velocity distribution is shown. The relaxation time parameter exerts a delayed impact on the fluid's flow. As illustrated on the left side of Figure 6, at a fixed time, an increase in the relaxation parameter results in a higher value of the distribution curve. From this observation, a conclusion can be drawn that there is a correlation between the larger relaxation parameter and the delay effect. For the relationship between the distribution curve and time, when the space y is fixed, the velocity increases as the relaxation parameter becomes larger.

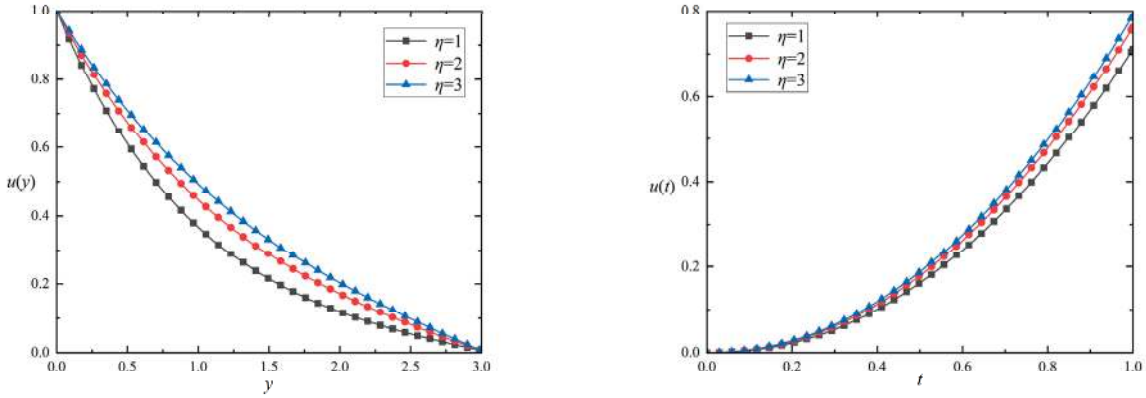

Figure 6. The impacts of the relaxation parameters on the velocity distribution versus y ($t = 1$) and t ($y = 1$) for $\beta = 0.5$ and $W = 1$.

Figure 7 demonstrates the distribution versus β with the influence of various relaxation time parameters, highlighting the relaxation time parameter's delayed influence on fluid flow. As depicted in Figure 7, for a constant fractional parameter β, an increase in the relaxation parameter leads to a higher value of the distribution curve. Concurrently, with the fractional parameter increasing, the fluid velocity diminishes progressively. It

is inferred that a larger relaxation parameter results in a diminished delay effect and an increased velocity.

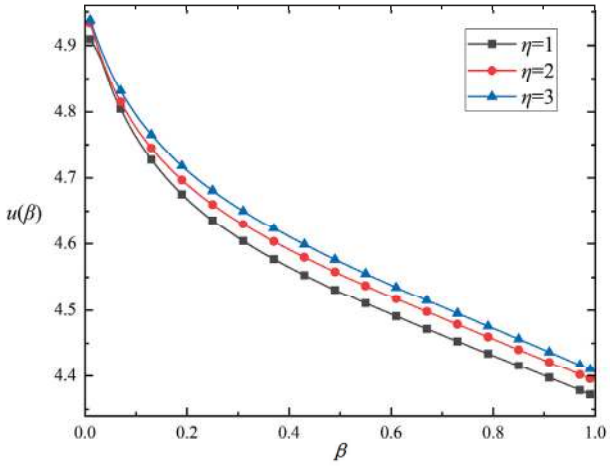

Figure 7. The impacts of the relaxation parameters on the velocity distribution versus β for $W = 1$.

5.3. Various Velocities Induced by Vibrating Plates with Different Physical Parameters

In this example, the emphasis is placed on the impact of dynamic parameters on the flow mechanism of fluid, propelled by a plate with oscillating velocity. The governing equation for the IBCs is presented below

$$\frac{\partial u(y,t)}{\partial t} = \frac{\partial^2 u(y,t)}{\partial y^2} + \eta_0^{RL} D_t^{\beta} \frac{\partial^2 u(y,t)}{\partial y^2} \tag{75}$$

$$u(y,0) = 0 \text{ for } y > 0 \tag{76}$$

$$u(0,t) = U \sin\left(\omega t^2\right) \text{ and } \frac{\partial u(y_r,t)}{\partial y} + \int_0^t K_1(t-\tau) * {}_0^{RL}\mathcal{D}_\tau^{1/2} u(y_r,\tau) \mathrm{d}\tau = 0 \tag{77}$$

Figure 8 shows the velocity distribution of y and t. Contrary to previous numerical instances, the observations from the figure reveal that the oscillating distribution results directly from a moving plate exhibiting oscillatory velocity. The effects of frequency ω and amplitude U on the velocity distribution on y and t are shown in Figures 9 and 10. It should be noted that we took the space calculation region as $[0, 5]$, and the termination time of the analysis was $T = 5$.

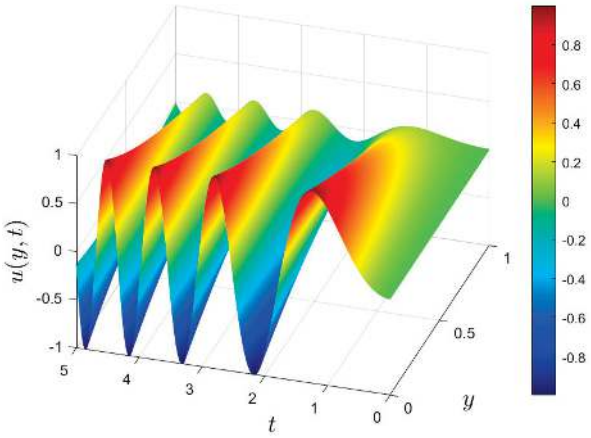

Figure 8. The velocity distributions with y and t for $\beta = 0.5$, $\eta = 1$, $\omega = 1$, and $U = 1$.

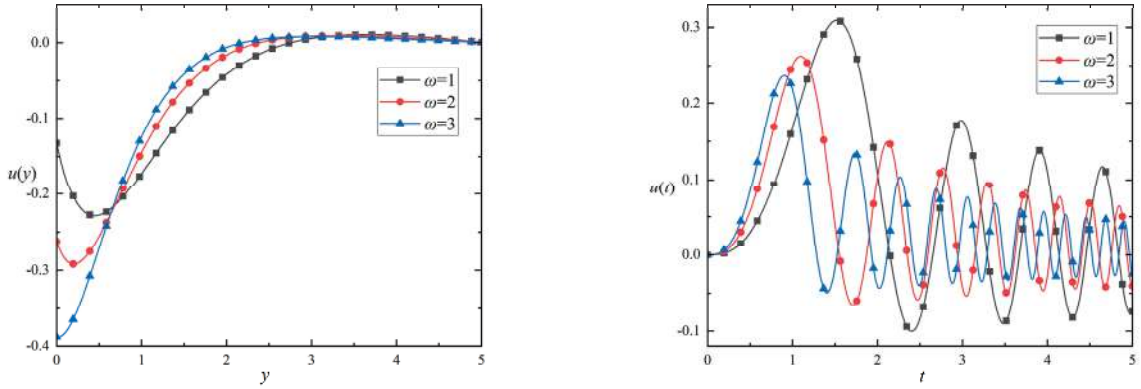

Figure 9. The velocity distributions with different frequency ω versus y ($t = 5$) and t ($y = 1$) for $\beta = 0.5$, $U = 1$, and $\eta = 1$.

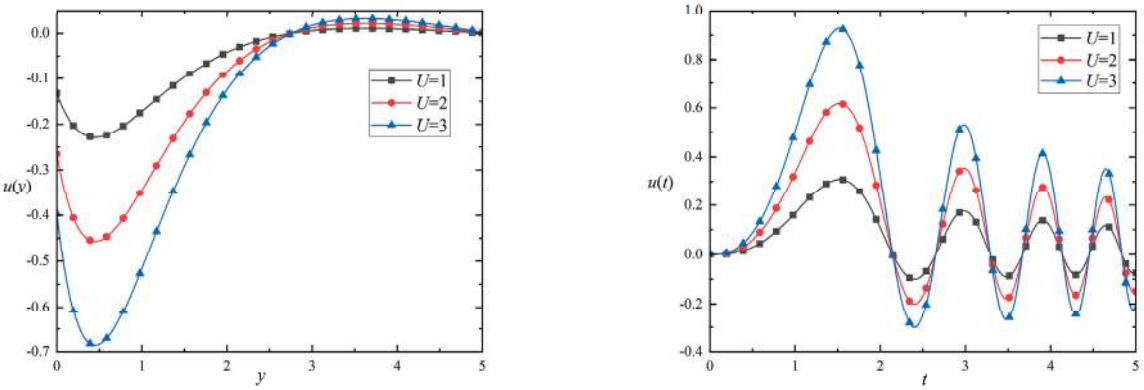

Figure 10. The velocity distributions with different amplitudes U versus y ($t = 5$) and t ($y = 1$) for $\beta = 0.5$, $\omega = 1$, and $\eta = 1$.

Figure 9 illustrates the impact of the oscillation frequency ω on the velocity distribution. In the left figure, at a fixed time, the fluid near the moving plate has a larger negative velocity in the initial position. The fluid's velocity increases with the moving plate's vibration frequency ω. Due to the vibration of the moving plate, the peak value of the velocity distribution curve occurs within a certain distance from the plate when $\omega = 1$ and $\omega = 2$, while the curve does not oscillate when $\omega = 3$. With the increase in y, the influence of oscillations on the fluid weakens and the fluid velocity decreases in the negative direction. By comparing the velocity distribution curves at different frequencies, it can be observed that the velocity distribution curve of the fluid changes more rapidly as the frequency ω of the moving plate increases. Finally, when the distance from the plate is far enough, the vibration of the plate has no effect on the fluid. The velocity distribution curve of the fluid becomes smoother, and the velocity distribution curves of different vibration frequencies tend to be close. In the figure on the right, the time change of the fluid near the plate, which is affected by the moving plate, is described. For the same vibration frequency ω, the amplitude of the velocity distribution curve and the vibration period gradually decrease with the passage of time, because the moving plate whose velocity oscillates in the form of a sinusoidal function causes the fluctuation of the velocity distribution. The peak value of the velocity distribution curve is earlier for a larger vibration frequency ω. The results show that, as the frequency ω increases, both the period and the amplitude of the distribution curve decrease.

Figure 10 depicts the impact of the amplitude on the velocity distribution. Similar to Figure 9, the negative velocity of the fluid close to the moving plate first increases to the peak and then decreases. At a fixed position, the oscillation period and amplitude of the fluid decrease gradually with the passage of time. By comparing the velocity distribution

curves of different amplitudes, the larger the amplitude U is, the greater the peak value of the velocity distribution curve at a fixed time is, and the faster the curve changes. In a fixed position, the velocity distribution curve's amplitude is directly proportional to the amplitude U.

5.4. Comparison of This Study with Other Methods in Ref. [58]

To further verify the accuracy of the numerical solutions presented in this paper, other studies on generalized second-order fluid flow on a semi-infinite plate are selected for comparison. Shahed [58] studied the impulsive flow of a fractional second-grade fluid on a flat plate. The IBCs were $u(y,0) = 0$, $y > 0$, $u(0,t) = 1$, $u(+\infty,t) = 0$, and $t \in [0,T]$.

Since the initial condition is zero, the equation containing the Caputo fractional derivative in reference [58] is equivalent to the equation with RLTFD in this paper. The ABC (32) is applied. By selecting the same parameters and comparing them with Figure 2 in [58], the comparison curve with the numerical solution in our study is given in Figure 11. The red dotted line is the curve derived from the method of this study, and the black solid line is the curve given by Shahed [58]. The comparison shows that the curves derived from the two methods match very well, which indicates the accuracy of our numerical method.

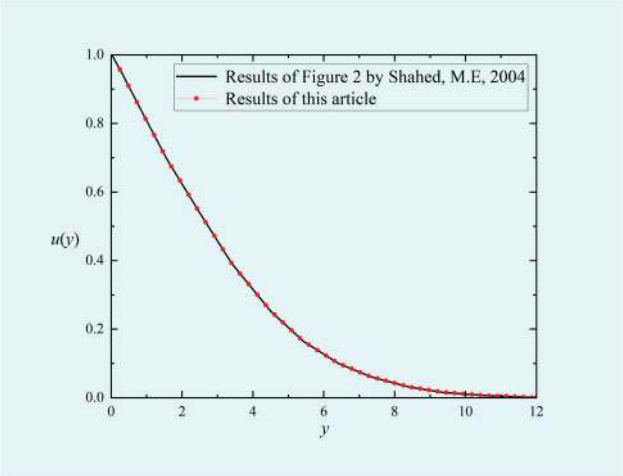

Figure 11. Comparison between the numerical solution in our study and other methods in Ref. [58] by selecting parameters $\eta = 1$, $t = 2$, and $\beta = 0.5$.

6. Conclusions

In this study, the fractional governing equation that describes generalized second-grade fluid's flow over semi-infinite plates, induced by varying plate velocities, was rigorously derived. For semi-bounded domains, the study employed the ABM. This resulted in the formulation of ABC as convolutions within a finite region. The use of the artificial boundary method made the numerical simulation of this fractional governing equation highly applicable. Subsequently, the governing equation was numerically discretized by incorporating the initial condition and the ABC by utilizing the L1 scheme. The paper then presented four numerical examples: the first one validated the difference scheme's effectiveness through introducing the source term and demonstrated the superiority of the ABC compared to the DTBC, and the second one examined how dynamic parameters within the governing equation affect velocity distribution. In the third example, a numerical example was given to analyze the flow mechanism arising from an oscillating plate, and the effects of the frequency and amplitude on velocity were described, respectively. Finally, the comparison of the numerical example with the ABC and the results in Ref. [58] was discussed. Some of the major findings are summarized below.

(i) A higher fractional parameter leads to a slower rate of fluid flow;

(ii) The delay effect increases with the decrease in relaxation parameters, and the fluid velocity rises as the relaxation parameter increases;
(iii) The higher the oscillation frequency is, the faster the velocity will change, and the velocity distribution curve will exhibit a decreased period and amplitude;
(iv) With a greater amplitude, the fluid velocity changes more rapidly and the amplitude of the velocity distribution curve also increases.

The important conclusions drawn from this study not only advance the theory of non-Newtonian fluid dynamics, but also extend to its engineering applications in a broad spectrum of fields, including chemical, petroleum, aerospace, and biomedical engineering. In addition, this research contributes to the design and optimization of new materials in materials science, the prediction of pollutant dispersion in environmental science, and the diagnosis and treatment of cardiovascular diseases in the medical field. It also promotes the advancement of numerical simulation technology to solve the problem of infinite boundaries using artificial boundary techniques and provides a theoretical basis and computational methods for the simulation of complex fluid systems. We intend to explore more comprehensive non-Newtonian fluid models with ABC is our future work.

Author Contributions: Conceptualization, J.Y.; Methodology, L.L., S.C. and C.X.; Validation, J.Y.; Formal analysis, J.Y. and S.C.; Writing—original draft, J.Y.; Writing—review & editing, J.Y., L.L., S.C., L.F. and C.X.; Visualization, J.Y. and C.X.; Supervision, L.L. and L.F.; Project administration, L.L. All authors have read and agreed to the published version of the manuscript.

Funding: The work is supported by the Project funded by the National Natural Science Foundation of China (Nos. 11801029, 12302326), Fundamental Research Funds for the Central Universities (Nos. QNXM20220048, FRF-EYIT-23-07), and Beijing Natural Science Foundation (No. IS23027), 2023 Fund for Fostering Young Scholars of the School of Mathematics and Physics, USTB (No. FRF-BR-23-01B).

Data Availability Statement: The data that support the findings of this study are available from the corresponding author upon reasonable request.

Conflicts of Interest: The authors declare no conflicts of interest.

References

1. Mohamed, A.A.; Khishvand, M.; Piri, M. Entrapment and mobilization dynamics during the flow of viscoelastic fluids in natural porous media: A micro-scale experimental investigation. *Phys. Fluids* **2023**, *35*, 047119. [CrossRef]
2. Steinhaus, B.; Shen, A.Q.; Sureshkumar, R. Dynamics of viscoelastic fluid filaments in microfluidic devices. *Phys. Fluids* **2007**, *19*, 073103. [CrossRef]
3. Lauga, E. Propulsion in a viscoelastic fluid. *Phys. Fluids* **2007**, *19*, 083104. [CrossRef]
4. VeeraKrishna, M.; Chamkha, A.J. Hall effects on unsteady MHD flow of second grade fluid through porous medium with ramped wall temperature and ramped surface concentration. *Phys. Fluids* **2018**, *30*, 053101. [CrossRef]
5. Wang, S.; Tai, C.W.; Narsimhan, V. Dynamics of spheroids in an unbound quadratic flow of a general second-grade fluid. *Phys. Fluids* **2020**, *32*, 113106. [CrossRef]
6. Ho, B.P.; Leal, L.G. Migration of rigid spheres in a two-dimensional unidirectional shear flow of a second-grade fluid. *J. Fluid Mech.* **1976**, *76*, 783–799. [CrossRef]
7. Khan, M.; Wang, S. Flow of a generalized second-grade fluid between two side walls perpendicular to a plate with a fractional derivative model. *Nonlinear Anal. Real World Appl.* **2009**, *10*, 203–208. [CrossRef]
8. Tassaddiq, A. MHD flow of a fractional second grade fluid over an inclined heated plate. *Chaos Soliton. Fract.* **2019**, *123*, 341–346. [CrossRef]
9. Metzne, A.B.; Park, M.G. Turbulent flow characteristics of viscoelastic fluids. *J. Fluid Mech.* **1964**, *20*, 291–303. [CrossRef]
10. Li, G.; McKinley, G.H.; Ardekani, A.M. Dynamics of particle migration in channel flow of viscoelastic fluids. *J. Fluid Mech.* **2015**, *785*, 486–505. [CrossRef]
11. Billingham, J.; King, A.C. The interaction of a moving fluid/fluid interface with a flat plate. *J. Fluid Mech.* **1995**, *296*, 325–351. [CrossRef]
12. Traugott, S.C. Impulsive Motion of an Infinite Plate in a Compressible Fluid with Non-Uniform External Flow. *J. Fluid Mech.* **1962**, *13*, 400–416. [CrossRef]
13. Jaworski, J.W.; Peake, N. Aerodynamic noise from a poroelastic edge with implications for the silent flight of owls. *J. Fluid Mech.* **2013**, *723*, 456–479. [CrossRef]
14. Sahoo, T.; Yip, T.L.; Chwang, A.T. Scattering of surface waves by a semi-infinite floating elastic plate. *Phys. Fluids* **2001**, *13*, 3215–3222. [CrossRef]

15. Baranovskii, E.S. Exact solutions for non-isothermal flows of second grade fluid between parallel plates. *Nanomaterials* **2023**, *13*, 1409. [CrossRef] [PubMed]
16. Baranovskii, E.S. Analytical Solutions to the Unsteady Poiseuille Flow of a Second Grade Fluid with Slip Boundary Conditions. *Polymers* **2024**, *16*, 179. [CrossRef] [PubMed]
17. Du, M.; Wang, Z.; Hu, H. Measuring memory with the grade of fractional derivative. *Sci. Rep.* **2013**, *3*, 3431. [CrossRef] [PubMed]
18. Carpinteri, A.; Francesco, M. *Fractals and Fractional Calculus in Continuum Mechanics*; Springer: Berlin/Heidelberg, Germany, 2014; Volume 378.
19. Uchaikin, V.; Renat, S. *Fractional Kinetics in Space: Anomalous Transport Models*; World Scientific: Singapore, 2018.
20. Tarasov, V.E. *Fractional Dynamics: Applications of Fractional Calculus to Dynamics of Particles, Fields and Media*; Springer Science & Business Media: Berlin/Heidelberg, Germany, 2011.
21. Shen, M.; Chen, L.; Zhang, M.; Liu, F. A renovated Buongiorno's model for unsteady Sisko nanofluid with fractional Cattaneo heat flux. *Int. J. Heat Mass Transf.* **2018**, *126*, 277–286. [CrossRef]
22. Sene, N. Second-grade fluid model with Caputo-Liouville generalized fractional derivative. *Chaos Soliton. Fract.* **2020**, *133*, 109631. [CrossRef]
23. Chan, P.C.H.; Leal, L.G. The motion of a deformable drop in a second-grade fluid. *J. Fluid Mech.* **1979**, *92*, 131–170. [CrossRef]
24. Jiang, X.; Zhang, H.; Wang, S. Unsteady magnetohydrodynamic flow of generalized second grade fluid through porous medium with Hall effects on heat and mass transfer. *Phys. Fluids* **2020**, *32*, 113105. [CrossRef]
25. Deswal, S.C.R.; Kalkal, K.K. Fractional grade heat conduction law in micropolar thermo-viscoelasticity with two temperatures. *Int. J. Heat Mass Transf.* **2013**, *66*, 451–460. [CrossRef]
26. Wang, X.; Xu, H.; Qi, H. Transient magnetohydrodynamic flow and heat transfer of fractional Oldroyd-B fluids in a microchannel with slip boundary condition. *Phys. Fluids* **2020**, *32*, 103104. [CrossRef]
27. Awad, E. Dual-phase-lag in the balance Sufficiency bounds for the class of Jeffreys' equations to furnish physical solutions. *Int. J. Heat Mass Transf.* **2020**, *158*, 119742. [CrossRef]
28. Coppola, G.; Veldman, A.E.P. Global and local conservation of mass, momentum and kinetic energy in the simulation of compressible flow. *J. Comput. Phys.* **2023**, *475*, 111879. [CrossRef]
29. Tamim, S.; Bostwick, J.B. Spreading of a thin droplet on a soft substrate. *J. Fluid Mech.* **2023**, *971*, A32. [CrossRef]
30. Mei, R.; Adrian, R.J. Flow past a sphere with an oscillation in the free-stream velocity and unsteady drag at finite Reynolds number. *J. Fluid Mech.* **1992**, *237*, 323–341. [CrossRef]
31. Dennis, S.C.R. Calculation of the steady flow through a curved tube using a new finite-difference method. *J. Fluid Mech.* **1980**, *99*, 449–467. [CrossRef]
32. Kim, T.Y.; Dolbow, J.; Fried, E. A numerical method for a second-gradient theory of incompressible fluid flow. *J. Comput. Phys.* **2007**, *223*, 551–570. [CrossRef]
33. Gilmanov, A.; Sotiropoulos, F. A hybrid Cartesian/immersed boundary method for simulating flows with 3D, geometrically complex, moving bodies. *J. Comput. Phys.* **2005**, *207*, 457–492. [CrossRef]
34. Li, B.; Zhang, J.; Zheng, C. Stability and error analysis for a second-grade fast approximation of the one-dimensional Schrödinger equation under absorbing boundary conditions. *SIAM J. Sci. Comput.* **2018**, *40*, A4083–A4104. [CrossRef]
35. Uhlmann, M. An immersed boundary method with direct forcing for the simulation of particulate flows. *J. Comput. Phys.* **2005**, *209*, 448–476. [CrossRef]
36. Özdemir, N.; Karadeniz, D.; İskender, B.B. Fractional optimal control problem of a distributed system in cylindrical coordinates. *Phys. Lett. A* **2009**, *373*, 221–226. [CrossRef]
37. Yan, Y.; Khan, M.; Ford, N.J. An analysis of the modified L1 scheme for time-fractional partial differential equations with nonsmooth data. *SIAM J. Numer. Anal.* **2018**, *56*, 210–227. [CrossRef]
38. Lyu, P.; Vong, S. A nonuniform L2 formula of Caputo derivative and its application to a fractional Benjamin-Bona-Mahony-type equation with nonsmooth solutions. *Numer. Meth. Part Differ. Equ.* **2020**, *36*, 579–600. [CrossRef]
39. Xing, Z.; Wen, L. Numerical Analysis of the Nonuniform Fast L1 Formula for Nonlinear Time-Space Fractional Parabolic Equations. *J. Sci. Comput.* **2023**, *95*, 58. [CrossRef]
40. Chen, Z.; Zheng, W. Convergence of the uniaxial perfectly matched layer method for time-harmonic scattering problems in two-layered media. *SIAM J. Numer. Anal.* **2010**, *48*, 2158–2185. [CrossRef]
41. Barucq, H.; Rouxelin, N.; Tordeux, S. Low-grade Prandtl-Glauert-Lorentz based Absorbing Boundary Conditions for solving the convected Helmholtz equation with Discontinuous Galerkin methods. *J. Comput. Phys.* **2022**, *468*, 111450. [CrossRef]
42. Li, B.; Zhang, J.; Zheng, C. An efficient second-grade finite difference method for the one-dimensional Schrödinger equation with absorbing boundary conditions. *SIAM J. Numer. Anal.* **2018**, *56*, 766–791. [CrossRef]
43. Muhr, M.; Nikolić, V.; Wohlmuth, B. Self-adaptive absorbing boundary conditions for quasilinear acoustic wave propagation. *J. Comput. Phys.* **2019**, *388*, 279–299. [CrossRef]
44. Fu, W.; Wang, W.; Li, C.; Huang, S. An investigation of natural convection in parallel square plates with a heated bottom surface by an absorbing boundary condition. *Int. J. Heat Mass Transf.* **2013**, *56*, 35–44. [CrossRef]
45. Baffet, D.; Grote, M.J. On wave splitting, source separation and echo removal with absorbing boundary conditions. *J. Comput. Phys.* **2019**, *387*, 589–596. [CrossRef]

46. Hwang, J.; Jang, J.; Jung, J. The Fokker-Planck equation with absorbing boundary conditions in bounded domains. *SIAM J. Math. Anal.* **2018**, *50*, 2194–2232. [CrossRef]
47. Tan, W.; Masuoka, T. Stokes' first problem for a second grade fluid in a porous half-space with heated boundary. *Int. J. Non-Linear Mech.* **2005**, *40*, 515–522. [CrossRef]
48. Rivlin, R.S.; Ericksen, J.L.V. *Stress-Deformation Relations for Isotropic Materials*; Collected Papers of RS Rivlin Volume I and II; Springer: Berlin/Heidelberg, Germany, 1997; pp. 911–1013.
49. Tan, W.; Xu, M. The impulsive motion of flat plate in a generalized second grade fluid. *Mech. Res. Commun.* **2002**, *29*, 3–9. [CrossRef]
50. Khan, M.; Nadeem, S.; Hayat, T.; Siddiqui, A.M. Unsteady motions of a generalized second-grade fluid. *Math. Comput.* **2005**, *41*, 629–637. [CrossRef]
51. Hilfer, R. *Applications of Fractional Calculus in Physics*; World Scientific: Singapore, 2000.
52. Hristov, J. Linear viscoelastic responses and constitutive equations in terms of fractional operators with non-singular kernels-pragmatic approach, memory kernel correspondence requirement and analyses. *Eur. Phys. J. Plus* **2019**, *134*, 283. [CrossRef]
53. Li, C.; Qian, D.; Chen, Y. On Riemann-Liouville and Caputo derivatives. *Discrete. Dyn. Nat. Soc.* **2011**, *2011*, 562494. [CrossRef]
54. Mahmood, A.; Fetecau, C.; Khan, N.A.; Jamil, M. Some exact solutions of the oscillatory motion of a generalized second grade fluid in an annular region of two cylinders. *Acta Mech. Sin.* **2010**, *26*, 541–550. [CrossRef]
55. Podlubny, I. *Fractional Differential Equation*; Academic Press: San Diego, LA, USA, 1999.
56. Alikhanov, A.A. A priori estimates for solutions of boundary value problems for fractional-grade equations. *Differ. Equ.* **2010**, *46*, 660–666. [CrossRef]
57. Feng, L.; Liu, F.; Turner, I.; Zheng, L. Novel numerical analysis of multi-term time fractional viscoelastic non-Newtonian fluid models for simulating unsteady MHD Couette flow of a generalized Oldroyd-B fluid. *Fract. Calc Appl. Anal.* **2018**, *21*, 1073–1103. [CrossRef]
58. Shahed, M.E. On the impulsive motion of flat plate in a generalized second grade fluid. *Z. Naturfors. Sect. A-J. Phys. Sci.* **2004**, *59*, 829–837.

fractal and fractional

MDPI

Article

Dynamical Analysis of Two-Dimensional Fractional-Order-in-Time Biological Population Model Using Chebyshev Spectral Method

Ishtiaq Ali

Department of Mathematics and Statistics, College of Science, King Faisal University, P.O. Box 400, Al-Ahsa 31982, Saudi Arabia; iamirzada@kfu.edu.sa

Abstract: In this study, we investigate the application of fractional calculus to the mathematical modeling of biological systems, focusing on fractional-order-in-time partial differential equations (FTPDEs). Fractional derivatives, especially those defined in the Caputo sense, provide a useful tool for modeling memory and hereditary characteristics, which are problems that are frequently faced with integer-order models. We use the Chebyshev spectral approach for spatial derivatives, which is known for its faster convergence rate, in conjunction with the $L1$ scheme for time-fractional derivatives because of its high accuracy and robustness in handling nonlocal effects. A detailed theoretical analysis, followed by a number of numerical experiments, is performed to confirmed the theoretical justification. Our simulation results show that our numerical technique significantly improves the convergence rates, effectively tackles computing difficulties, and provides a realistic simulation of biological population dynamics.

Keywords: fractional-order-in-time biological population model; Chebyshev spectral method; error analysis; numerical examples

Citation: Ali, I. Dynamical Analysis of Two-Dimensional Fractional-Order-in-Time Biological Population Model Using Chebyshev Spectral Method. *Fractal Fract.* **2024**, *8*, 325. https://doi.org/10.3390/fractalfract8060325

Academic Editors: Libo Feng, Lin Liu and Yang Liu

Received: 28 April 2024
Revised: 23 May 2024
Accepted: 27 May 2024
Published: 29 May 2024

1. Introduction

Fractional calculus is an extension of conventional calculus that explores the possibility of taking real-numbered powers of the differentiation and integration operators. Unlike classical calculus, which only works with integer orders, fractional calculus accepts integrals and derivatives of any fractional order, positive or negative. The fractional integral of order α is a generalization of the n-fold integral applied n times, where α can be any real number. It is typically defined using a convolution with a power function, leading to an integral operator known as the Riemann–Liouville integral. Fractional calculus has a wide range of applications in disciplines including biology, engineering, physics, economics, and more. It is employed in physics to simulate systems that have memory and inherited characteristics, such as viscoelastic materials or processes in which the system's future state is dependent on both its past behavior and its current state. Fractional calculus is helpful to engineers in control theory, especially for designing controllers that provide reliable performance under a variety of circumstances [1–3]. Fractional derivatives are incorporated into standard partial differential equations in order to generate fractional partial differential equations (FPDEs), which enable the modeling of memory and hereditary features in a variety of materials and systems. Time-fractional differential equations, in which the order of the time derivative is a fraction instead of an integer, are the subject of this research. When modeling systems where the rate of change is not constant but rather depends on the process's whole history, these equations are especially helpful. Most recently, the application of fractional-order equation-based vegetation–water in an arid flat environment has been studied in [4].

The most common form of a time-fractional partial differential equation involves the Caputo or Riemann–Liouville definition of fractional derivatives. Time-fractional PDEs

are extensively used to model physical phenomena exhibiting anomalous diffusion, which is diffusion where the flux at any point in space depends on the historical states of the system, rather than being directly proportional to the gradient of concentration as in classical diffusion. These models have been used to simulate subdiffusion or superdiffusion processes in complex systems where particle trajectories diverge from those of traditional Brownian motion in domains like physics. When molecular movement is impeded by barriers or binding effects that lead to anomalous diffusion, biology uses it to describe the transport dynamics within cells. In finance, on the other hand, it is employed to capture memory and hereditary effects in financial markets, enhancing asset price and risk management modeling [5–8].

The goal of the latest developments in fractional calculus has been to enhance the numerical techniques for solving fractional differential equations, which are crucial for real-world applications across a range of industries. Several novel techniques have been presented by researchers in an effort to more effectively handle the nonlocal characteristics included in fractional derivatives. Adaptive methods are among them; they improve accuracy and save computing costs by modifying the time steps based on the behavior of the answer. The ability to numerically solve differential equations with fractional derivatives, which are more difficult by nature because of their nonlocal nature, has been made possible by advances in computational mathematics. Modern numerical techniques and algorithms are still developing, which makes fractional calculus more useful in both industry and scientific study [9–14]. As fractional calculus advances, it will offer a more comprehensive mathematical framework that goes beyond the constraints of traditional differential and integral calculus, providing up new possibilities for modeling and understanding the natural world.

Biological population models are crucial and have contributed significantly to our understanding of ecology, public health, and the behavior of the environment. Because they aid in forecasting and controlling species interactions, population growth, and the impact of changing environmental circumstances on ecosystems, these models are crucial to ecology. They serve as crucial tools in conservation biology as well, helping scientists identify a species' vulnerability and develop effective conservation strategies. In order to evaluate programs, predict the beginning of epidemics, and comprehend how infectious diseases propagate, biological population models are essential to public health research [15,16]. A more comprehensive study on the role of fractional calculus in modeling a biological phenomena can be found in [17]. Fractional derivatives are used in biology to simulate anomalous diffusion, which deviates from the standard equations of diffusion in cells and tissues due to its ability to capture memory and hereditary properties inherent in such systems as compared to the integer-order differential equation. Due to the fact that these mathematical models, which consist of fractional-order derivatives, have a nonlocal nature, involve complicated boundary conditions and memory effects, and therefore lack closed-form solutions, the analytical solution of fractional differential equations is more complicated, and sometimes it is even not possible to find it. These models are especially helpful in ecosystems where organisms have lengthy lifespans or where environmental changes occur slowly, which reduces the efficacy of standard models.

A sophisticated method of applying fractional calculus to study biological population dynamics is introduced by the idea of a two-dimensional fractional-order-in-time biological population model. By utilizing fractional derivatives, which are expansions of ordinary derivatives, this mathematical framework expands upon the traditional population models by including memory and hereditary features. This model takes into account both the history and present population sizes when determining each population's growth rate. This is accomplished through the use of fractional differential equations, in which the degree to which the past influences the dynamics of the present is indicated by the derivative's order, typically between 0 and 1. These models are better able to capture the intricacies of biological processes that, as is common in many ecological systems, display long-term memory or power-law waiting times. Predators and prey are two examples of interacting

animals that could be included in a two-dimensional model. Fractional derivatives are useful in modeling scenarios in which the dynamics of both populations in the future are influenced throughout time by the residual effects of past interactions (e.g., resource competition or predation rates). When contrasted to traditional models, this may result in oscillations and stability conditions that are more realistic. In general, biologists and ecologists can benefit greatly from the use of two-dimensional fractional-order models in biological populations since they offer a greater understanding of the dynamics of intricate ecosystems where past conditions have a substantial influence on future states. Analytically solving population models is often infeasible for complex boundary and initial conditions; thus, numerical solutions such as finite difference methods, finite element methods, and spectral methods are employed. These methods involve discretizing the time and space variables and approximating the fractional derivatives using techniques adapted for their nonlocal nature. The integration of fractional calculus into partial differential equations offers a powerful tool for exploring and describing dynamic systems with memory and hereditary characteristics, which are not adequately modeled by classical PDEs for these models. The development of robust numerical methods continues to be a vital area of research, enabling the practical application of FPDEs across various scientific disciplines [18,19].

Fractional-order diffusion equations, which are generalizations of classical diffusion equations and address super-diffusive flow processes, are among the most basic instances of the former. A large portion of published work on FPDEs has been focused on fractional diffusion equations. In [20], Agrawal uses a finite sine transform method to find the general solution of fractional-order diffusion equations. A theoretical framework using the least-squares finite element technique has been investigated in [21], while a spectral collocation scheme for two-dimensional nonlinear fractional diffusion equations and a radial basis function approximation method is used in [22,23], respectively. A mathematical model based on nonlinear fractional-order equations for the description of the behavior of viscoplastic materials was developed in [24], while a fractional advection–dispersion equation has been numerically investigated in [25,26]. In order to find the scale-invariant solution of the TFDE in terms of the Wright function, Gorenflo et al. employed the similarity approach and the Laplace transform method [27,28]. Numerous authors have examined these models in analytical and numerical frameworks. A few of these researchers have attempted to find analytical solutions for differential equations using temporal fractions. For instance, time-fractional diffusion-wave equations were taken into consideration by Schneider and Wyss and Wyss [29,30]. The temporal fractional PDE using finite difference in fractional time and a higher numerical scheme was investigated in detail in [31]. Capturing memory and hereditary properties is crucial in biological systems due to their inherent dependence on past states. Fractional differential equations are particularly adept at modeling these characteristics because they incorporate nonlocal properties, meaning the rate of change at any point in time depends on all previous states. However, these equations are complex and often lack closed-form solutions, making analytical solutions challenging and necessitating robust numerical methods. The complexity of fractional derivatives, especially their nonlocal nature, poses significant computational challenges that need to be addressed with efficient numerical techniques.

In this work, we consider solving numerically a fractional-order-in-time biological population model in two dimensions. We use the $L1$ scheme for fractional-order-in-time derivatives. This scheme is very useful in handling the nonlocal properties of fractional-order-in-time derivatives. For spatial derivatives, we use an efficient numerical scheme based on the Chebyshev spectral method. Spectral methods are a class of techniques used in numerical analysis to solve differential equations whose solutions are essentially represented by the sum of globally defined basis functions. These functions are typically orthogonal or trigonometric polynomials, depending on the boundary conditions and nature of the problem. When the solution has smooth properties, spectral methods are well known for their high accuracy and exponential rates of convergence, which greatly exceed

the performance provided by conventional finite difference or finite element methods. The most notable method among these is the Chebyshev spectral method due to its particular effectiveness in handling problems with complex geometries or boundary conditions. This method utilizes Chebyshev polynomials, which are a set of orthogonal polynomials defined on the interval $[-1, 1]$. The main advantage of Chebyshev polynomials is their near-minimal property for polynomial approximation. This property significantly minimizes the maximum error between the numerical solution and the true solution. The efficiency of this approach is further increased by the employment of Chebyshev nodes, or the roots of these polynomials, which assist prevent the Runge phenomenon and guarantee stability and dependability in numerical approximations [32–40]. Several studies have applied fractional calculus to model biological systems. For instance, fractional derivatives have been used to simulate anomalous diffusion in cells and tissues, capturing more realistic dynamics than traditional models. Hattaf and Yousfi explored the global stability of fractional diffusion equations in biological systems, highlighting the advantages of fractional models in capturing complex biological behaviors [41]. However, many of these studies focus on one-dimensional models or rely on analytical solutions, which are not feasible for complex systems. This paper addresses this gap by developing a numerical scheme for a two-dimensional fractional-order-in-time biological population model [42,43].

The rest of the paper is organized as follows: In Section 2, we present some preliminaries and some basic definitions, which play a key role in the analysis of the scheme, followed by the mathematical description of the model and the discretization scheme. Section 4 consists of a detailed error analysis, followed by numerical examples in Section 5. Section 6 consists of concluding remarks.

2. Preliminaries and Some Basic Definitions

In this section, we present some basic definitions related to fractional calculus theory and orthogonal polynomials that are useful in the error analysis of our proposed numerical scheme [44–47].

Definition 1. *A real function $g(\tau)$, $\tau > 0$ is defined to belong to the space C_ν, $\nu \in \mathbb{R}$, if there exists a real number $q > \nu$, such that $g(\tau) = \tau^q g_1(\tau)$, where $g_1(\tau) \in C(0, \infty)$, and g is in the space $C_{n\nu}$ if and only if $g^{(n)} \in C_\nu$, $n \in \mathbb{N}$.*

Definition 2. *The Riemann–Liouville fractional integral operator I^β ($\beta \geq 0$) of a function $g \in C_\nu$, $\nu \geq -1$ is given by*

$$I^\beta g(\tau) = \frac{1}{\Gamma(\beta)} \int_0^\tau (\tau - s)^{\beta-1} g(s)\, ds, \quad (\beta \geq 0) \tag{1}$$

where $\Gamma(\cdot)$ is the gamma function. The properties of the operator I^β include

$$I^\beta I^\gamma g(\tau) = I^{\beta+\gamma} g(\tau), \quad (\beta \geq 0, \gamma \geq 0) \tag{2}$$

$$I^\beta \tau^\delta = \frac{\Gamma(1+\delta)}{\Gamma(1+\delta+\beta)} \tau^{\beta+\delta}, \quad (\delta \geq -1) \tag{3}$$

Definition 3. *The Caputo fractional derivative C^α of a function $g(\tau)$ is defined as*

$${}^C D_\tau^\alpha g(\tau) = \frac{1}{\Gamma(n-\alpha)} \int_0^\tau g^{(n)}(s) \frac{ds}{(\tau - s)^{\alpha+1-n}}, \quad (n - 1 < Re(\alpha) \leq n, n \in \mathbb{N}) \tag{4}$$

The properties of the Caputo fractional derivative include

$${}^C D_\tau^\alpha \tau^\beta = \frac{\Gamma(1+\beta)}{\Gamma(1+\beta-\alpha)} \tau^{\beta-\alpha}, \tag{5}$$

$$(I^{\alpha\,C}D^{\alpha})g(\tau) = g(\tau) - \sum_{k=0}^{n-1} \frac{g^{(k)}(0+)}{k!}\tau^k, \tag{6}$$

The Caputo fractional derivative is chosen for its ability to incorporate conventional initial and boundary conditions in problem formulations.

Definition 4. *The Mittag–Leffler function $E_{\alpha,\beta}(z)$ for complex numbers z and parameters α and β is defined by the series*

$$E_{\alpha,\beta}(z) = \sum_{k=0}^{\infty} \frac{z^k}{\Gamma(\alpha k + \beta)}, \tag{7}$$

where $\alpha > 0$ and β are real numbers, and $\Gamma(\cdot)$ denotes the Gamma function. This function generalizes the exponential function, which is recovered as a special case when $\alpha = 1$ and $\beta = 1$.

$E_{\alpha,\beta}(z)$ represents a two-parameter family of functions, where α and β allow for various forms of convergence and divergence characteristics depending on their values. When $\alpha = 1$ and $\beta = 1$, the Mittag–Leffler function simplifies to the exponential function e^z, that is $E_{1,1}(z) = e^z$.

Definition 5. *Chebyshev polynomials, represented as $C_n(x)$, are established over the domain $[-1, 1]$ and can be formulated by the expression*

$$C_n(x) = \cos(n \arccos(x)), \quad n = 0, 1, 2, \ldots \tag{8}$$

Definition 6. *The collection of Chebyshev polynomials $\{C_n(x)\}$ set within the interval $[-1, 1]$ adhere to this orthogonality condition with respect to the weighted scalar product*

$$\langle C_i, C_j \rangle_\omega := \int_{-1}^{1} C_i(x) C_j(x) \omega(x)\, dx = \begin{cases} 0, & \text{if } i \neq j, \\ \pi, & \text{if } i = j = 0, \\ \frac{\pi}{2}, & \text{if } i = j \neq 0. \end{cases} \tag{9}$$

where the weighting function $\omega(x)$ is defined by

$$\omega(x) = \frac{1}{\sqrt{1 - x^2}}. \tag{10}$$

Definition 7. *Let δ_n denote the scaling coefficients for orthogonality:*

$$\delta_n = \begin{cases} 2, & \text{if } n = 0, \\ 1, & \text{if } n > 0. \end{cases} \tag{11}$$

Considering practical approaches in mathematical representations, when examining polynomials of a degree at most N, the matrix representation of the weighted scalar product can be succinctly illustrated as

$$H = \operatorname{diag}\{h_{ii}\}, \quad h_{ii} := \frac{\sigma}{2}\delta_n \tag{12}$$

Here, the matrix H is diagonal with size $(N+1) \times (N+1)$, and each diagonal element h_{ii} is influenced by the coefficient δ_n from the previous equation.

Definition 8. *A smooth, continuous function $\sigma(\theta)$, defined on $[-1, 1]$, can be approximated using Chebyshev polynomials $C_n(\theta)$ as follows:*

$$\sigma(\theta) \approx \sum_{n=0}^{N} \widetilde{\sigma}_n C_n(\theta), \tag{13}$$

where N represents the truncation level in the spectral method, and $\widetilde{\sigma}_n$ is the Chebyshev expansion coefficient for σ. This coefficient is calculated by

$$\widetilde{\sigma}_n = \frac{1}{\delta_n}\int_{-1}^{1}\sigma(\theta)C_n(\theta)\omega(\theta)\,d\theta, \quad \delta_n = \int_{-1}^{1}C_n^2(\theta)\sqrt{1-\theta^2}\,d\theta = \begin{cases}\pi, & \text{if } n=0,\\ \frac{\pi}{2}, & \text{if } n>0.\end{cases} \tag{14}$$

Definition 9. *In the computational process known as the Chebyshev forward transformation, the Gauss–Lobatto integration method is typically employed for computing the weighted integral:*

$$\widetilde{\sigma}_n \approx \frac{1}{\delta_n}\sum_{i=0}^{N}\sigma(\theta_i)C_n(\theta_i)w_i \tag{15}$$

where N represents the number of integration nodes, matching the truncation level. These nodes and weights are specified as

$$\theta_0 = 1, \theta_N = -1, \theta_i = \cos\left(\frac{\pi i}{N}\right), w_0 = w_N = \frac{\pi}{2N}, w_i = \frac{\pi}{N} \tag{16}$$

Definition 10. *For any continuous and smooth function $\sigma(\theta)$ defined over the interval $[-1,1]$, if the derivative $\sigma'(\theta)$ maintains smoothness, it can be expanded using $C_n(\theta)$ as*

$$\sigma'(\theta) \approx \sum_{n=0}^{N}\widetilde{\sigma}'_n C_n(\theta), \tag{17}$$

It is established that the expansion coefficient $\widetilde{\sigma}'_n$ for the derivative $\sigma'(\theta)$ and the coefficient $\widetilde{\sigma}_n$ for the original function satisfy the relation

$$\widetilde{\sigma}'_n \approx \frac{2}{\delta_n}\sum_{q=n+1,\, q+n\ odd}^{N} q\widetilde{\sigma}_q, \quad n \geq 0 \tag{18}$$

This relation can then be reformulated in matrix terminology:

$$\widetilde{\sigma}' = D\widetilde{\sigma}, \tag{19}$$

where $\widetilde{\sigma}'$ and $\widetilde{\sigma}$ are arrays with dimensions $1\times(N+1)$, defined as $\widetilde{\sigma}' = [\widetilde{\sigma}'_0, \widetilde{\sigma}'_1, \ldots, \widetilde{\sigma}'_N]$ and $\widetilde{\sigma} = [\widetilde{\sigma}_0, \widetilde{\sigma}_1, \ldots, \widetilde{\sigma}_N]$. The matrix D is an upper triangular square matrix, sized $(N+1)\times(N+1)$.

Definition 11. *The natural Sobolev norms, appropriate for gauging approximation errors within the Chebyshev framework, integrate the Chebyshev weight into the quadratic means of the error and its derivatives over the span $(-1,1)$. Thus, we establish the weighted Sobolev norm as*

$$\|g\|_{\mathcal{H}_m^w(-1,1)} = \left(\sum_{n=0}^{m}\|g^{(n)}\|^2_{L_w^2(-1,1)}\right)^{1/2}. \tag{20}$$

The associated Hilbert space is denoted $\mathcal{H}_m^w(-1,1)$, where:

- *$\|g^{(n)}\|_{L_w^2(-1,1)}$ signifies the L^2-norm of the n-th derivative of g, weighted over the interval $(-1,1)$.*
- *$\mathcal{H}_m^w(-1,1)$ is the weighted Sobolev space capturing the behavior of functions and their derivatives up to order m under the weighted norm.*

3. Fractional-Order-in-Time Dispersal in Population Dynamics

According to biologists, migration or dispersal has a significant impact on the regulation of species populations. The diffusion of a biological species in a given region C is described by three functions of position $\mathbf{x} = (\eta, \xi)$ and time t: the population supply $s(\mathbf{x}, t)$,

the diffusion velocity $\mathbf{u}(\mathbf{x}, t)$, and the population density $\rho(\mathbf{x}, t)$. The population density $\rho(\mathbf{x}, t)$ quantifies the number of individuals per unit volume at position $\mathbf{x}$ and at time t. By integrating ρ over any subregion D of C, the total population in D at time t is obtained. The term $s(\mathbf{x}, t)$ indicates the rate at which individuals are added or removed per unit volume at position $\mathbf{x}$ due to births and deaths. The diffusion velocity $\mathbf{u}(\mathbf{x}, t)$ represents the mean velocity of individuals at position $\mathbf{x}$ at time t, facilitating the description of population movement from one location to another.

The following equation governs the dynamics:

$$\frac{\partial^\alpha}{\partial t^\alpha} \int_D \rho \, dV + \int_{\partial D} \rho \mathbf{u} \cdot \mathbf{n} \, dA = \int_D s \, dV, \tag{21}$$

where $\mathbf{n}$ is the outward unit normal on the boundary ∂D. The Caputo fractional derivative is used to interpret the derivative. This basic equation means that the rate at which new individuals are delivered directly to D must equal the rate at which the population within D changes plus the rate at which people leave D over its boundary. With $s = s(\rho)$ and $\mathbf{u} = \lambda(\rho)\nabla\rho$ as assumptions, one can derive the following two-dimensional nonlinear degenerate parabolic partial differential equation for ρ, where $\lambda(\rho) > 0$ for $\rho > 0$ and ∇ is the gradient operator:

$$\frac{\partial^\alpha \rho}{\partial t^\alpha} = \Delta(s(\rho)) + s(\rho), \quad t > 0, \quad (\eta, \xi) \in \mathbb{R}^2, \tag{22}$$

where the order of the fractional derivative with respect to time t is denoted by α. The temporal fractional-order biological population model (TFBPM) is the name given to this equation. The analysis presents $\phi(\rho) = \rho^2$ as a specific instance for modeling animal populations, as explored by Gurney and Nisbet [48]. The migrations usually happen as a result of individuals traveling down the population density gradient, which moves more quickly at higher densities, in search of less congested areas to breed in a model that took into account an animal walking through a rectangular grid was created to mimic this behavior. With each step, the animal might either remain in the same spot or migrate toward the area with the lowest density. The size of the population density gradient at the relevant grid boundary determines the probability distribution for these movements. This model leads to

$$\frac{\partial^\alpha \rho}{\partial t^\alpha} = \Delta(\rho^2) + s(\rho), \quad t > 0, \quad (\eta, \xi) \in \mathbb{R}^2, \tag{23}$$

with the initial condition $\rho(\eta, \xi, 0)$ provided. When $\alpha = 1$, this equation simplifies to the normal biological population model (NBPM):

$$\frac{\partial^\alpha \rho}{\partial t^\alpha} = \Delta(\rho^2) + s(\rho), \quad t > 0, \quad (\eta, \xi) \in \mathbb{R}^2. \tag{24}$$

Additionally, various properties such as Hölder estimates and solutions of this model have been explored.

Constitutive equations for $s(\rho)$ may include the following:

- Malthusian Law: $s(\rho) = c\rho$, where c is a constant.
- Verhulst Law: $s(\rho) = c_1\rho - c_2\rho^2$, where c_1, c_2 are positive constants.
- Porous Media: $s(\rho) = c\rho^q$, where $c > 0$ and $0 < q < 1$.

For a generalized form, consider

$$\frac{\partial^\alpha \rho}{\partial t^\alpha} = \frac{\partial^2 \rho^2}{\partial \eta^2} + \frac{\partial^2 \rho^2}{\partial \xi^2} + h\rho^a(1 - \ell\rho^b), \quad t > 0, \quad (\eta, \xi) \in \mathbb{R}^2, \tag{25}$$

subject to some appropriate initial conditions and where h, a, ℓ, b are real numbers. Under some specific parameter conditions, both the Verhulst and the Malthusian laws are covered by Equation (25).

Discretization Methodology

We consider the time-fractional partial differential equation given by Equation (25):

The $L1$ scheme is used to discretize the fractional time derivative $\frac{\partial^\alpha \rho}{\partial t^\alpha}$. This scheme is particularly suitable for fractional derivatives due to its capability to handle the memory effect inherent in such derivatives. The $L1$ approximation at a time t_n is defined as: The $L1$ scheme approximates the fractional time derivative as follows:

$$\frac{\partial^\alpha \rho_{n+1}}{\partial t^\alpha} = \frac{(\delta t)^{-\alpha}}{\Gamma(2-\alpha)} \sum_{k=0}^{n} (\rho_{n+1-k} - \rho_{n-k}) \Big((k+1)^{1-\alpha} - k^{1-\alpha} \Big) + O(\delta t^{2-\alpha}), \tag{26}$$

where δt is the time step, and α is the fractional order of the derivative.

The correction term B_n, defined as

$$B_n = \frac{(\delta t)^{-\alpha}}{\Gamma(2-\alpha)} \sum_{k=1}^{n} \Big((k+1)^{1-\alpha} - k^{1-\alpha} \Big) (\rho_{n+1-k} - \rho_{n-k}), \tag{27}$$

becomes zero when $n = 0$. Therefore, the discretization formula simplifies as

$$\frac{\partial^\alpha \rho_{n+1}}{\partial t^\alpha} = \begin{cases} \frac{(\delta t)^{-\alpha}}{\Gamma(2-\alpha)} (\rho_{n+1} - \rho_n) + B_n + O(\delta t^{2-\alpha}), & \alpha \in (0,1), \\ \frac{\rho_{n+1} - \rho_n}{\delta t} + O(\delta t), & \alpha = 1. \end{cases} \tag{28}$$

The Chebyshev spectral method involves representing the solution ρ as a series expansion in terms of Chebyshev polynomials. These polynomials are particularly effective for approximating functions on bounded intervals due to their excellent approximation properties and the clustering of nodes at the endpoints, which can help in resolving boundary layer effects. The approximation of ρ at a fixed time t_n is given by

$$\rho(\eta, \xi, t_n) \approx \sum_{i=0}^{N} \sum_{j=0}^{N} c_{ij}^n T_i(\eta) T_j(\xi), \tag{29}$$

where T_i are Chebyshev polynomials and c_{ij}^n are the spectral coefficients.

The derivatives in the spatial domain are computed using the derivative properties of Chebyshev polynomials:

$$\frac{\partial^2 \rho^2}{\partial \eta^2} \approx \sum_{i=0}^{N} \sum_{j=0}^{N} \Big(c_{ij}^n \Big)^2 \frac{d^2}{d\eta^2} T_i(\eta) T_j(\xi), \tag{30}$$

$$\frac{\partial^2 \rho^2}{\partial \xi^2} \approx \sum_{i=0}^{N} \sum_{j=0}^{N} \Big(c_{ij}^n \Big)^2 T_i(\eta) \frac{d^2}{d\xi^2} T_j(\xi). \tag{31}$$

Combining the discretized forms of the time and space derivatives, we obtain the fully discretized version of the the model Equation (25), given by

$$\begin{aligned} \frac{1}{\Gamma(2-\alpha)} \sum_{k=0}^{n} \frac{\rho^{k+1} - \rho^k}{\Delta t^\alpha} &((k+1)\Delta t)^{1-\alpha} - (k\Delta t)^{1-\alpha} \\ &= \sum_{i=0}^{N} \sum_{j=0}^{N} \left[(c_{ij}^n)^2 \left(\frac{d^2}{d\eta^2} T_i(\eta) + \frac{d^2}{d\xi^2} T_j(\xi) \right) \right] \\ &\quad + h \left(\sum_{i=0}^{N} \sum_{j=0}^{N} c_{ij}^n T_i(\eta) T_j(\xi) \right)^a \left(1 - \ell \left(\sum_{i=0}^{N} \sum_{j=0}^{N} c_{ij}^n T_i(\eta) T_j(\xi) \right)^b \right). \end{aligned} \tag{32}$$

4. Error Analysis

This section deals with the error analysis of our proposed numerical scheme. Before the main results, we state some useful results in the form of lemmas [49].

Lemma 1 (Estimate for the Truncation Error)**.** *Consider the truncation error of a function u when approximated by its truncated Chebyshev series, denoted as $P_N u$, where*

$$P_N u = \sum_{k=0}^{N} \hat{u}_k T_k,$$

and $\hat{u}_k$ represents the Chebyshev-series coefficients of u. The truncation error $u - P_N u$, measured in the weighted L^2 norm over the interval $(-1, 1)$, satisfies the inequality

$$\|u - P_N u\|_{L^2_w(-1,1)} \leq CN^{-m} \|u\|_{\mathcal{H}^w_{m;N}(-1,1)}, \tag{33}$$

for all functions u belonging to the weighted Sobolev space $\mathcal{H}^w_m(-1, 1)$ with $m \geq 0$. Here, C is a constant that depends on N and m, and $\mathcal{H}^w_{m;N}(-1, 1)$ represents the Sobolev space characterized by integrating the function and its derivatives up to order m, each weighted by the Chebyshev weight.

Lemma 2 (Interpolation Error Estimate)**.** *The interpolation error associated with approximating a function u by its interpolant $I_N u$, which is defined at Chebyshev Gauss points across three different families. For this interpolant, which belongs to the polynomial space P_N, an important error estimates. The error between the function u and its interpolant, measured in the weighted L^2 norm over the interval $[-1, 1]$, adheres to the following bound:*

$$\|u - I_N u\|_{L^2_w(-1,1)} \leq CN^{-m} \|u\|_{H^w_{m;N}(-1,1)}, \tag{34}$$

$$\|u - I_N u\|_{L^\infty_w(-1,1)} \leq CN^{\frac{1}{2}-m} \|u\|_{H^w_{m;N}(-1,1)}, \tag{35}$$

where C represents a constant and $m \geq 1$ reflects the smoothness level of the function. This estimate is valid under the condition that u is an element of the weighted Sobolev space $H^w_m(-1, 1)$. This space is characterized by considering functions that maintain their derivatives up to the m-th order, each weighted appropriately over the interval.

Lemma 3 (Integration Error Estimate)**.** *Given a function u from the weighted Sobolev space $H^w_m(-1, 1)$ with $m \geq 1$ and a polynomial φ from the space P_N, the error produced by applying a Gauss-type quadrature formula for integration relative to the Chebyshev weight can be estimated as follows. Consider the integral of the product of u and φ, weighted by the Chebyshev weight $w(x)$, and its approximation by the quadrature formula:*

$$\left| \int_{-1}^{1} u(x)\varphi(x)w(x)\,dx - (u, \varphi)_N \right| \leq CN^{-m} \|u\|_{H^w_{m;N}(-1,1)} \|\varphi\|_{L^2_w(-1,1)}, \tag{36}$$

where

- *$(u, \varphi)_N$ denotes the approximation of the integral by the Gauss-type quadrature.*
- *C is a constant dependent on N and m, indicating the rate at which the error diminishes as the polynomial degree N or the smoothness m of the function u increases.*
- *$\|u\|_{H^w_{m;N}(-1,1)}$ and $\|\varphi\|_{L^2_w(-1,1)}$ are the norms measuring the magnitude of u and φ in their respective function spaces.*

One can state and prove the following error estimates for the fractional-order time discretization.

Theorem 1 ([31]). *Let ρ be the exact solution of the model Equation (25), and let $\{\rho_k\}_{k=0}^{K}$ be the time-discrete solution of with the initial condition $\rho_0(x) = \rho(x,0)$; then, the following error estimates hold:*

1. *For $0 \leq a < 1$,*
$$\|\rho(t_k) - \rho_k\|_1 \leq c_{u,a} T^a \Delta t^{2-a}, \quad k = 1, 2, \ldots, K, \tag{37}$$
where $c_{u,a} := \frac{c_u}{1-a}$ with c_u a constant defined in (3.3).
2. *As $a \to 1$,*
$$\|\rho(t_k) - \rho_k\|_1 \leq c_u T \Delta t, \quad k = 1, 2, \ldots, K. \tag{38}$$

Similarly for the space discretization, using Lemmas 1–3, one can state and prove the following results of exponential order of convergence.

Theorem 2. *Let $\{\rho_k^N\}_{k=0}^{K}$ be the solution of the problem given in Equation (25) with the initial condition ρ_0^N taken to be $I_N\rho(0)$, and $\{\rho_k\}_{k=0}^{K}$ be the numerical solution. Suppose $\rho_k \in H^m(K) \cap H_1^0(K)$, $m > 1$; then,*

- *For $0 \leq \alpha < 1$,*
$$\|\rho_k - \rho_k^N\|_{L_2} \leq c_\alpha \Delta t^\alpha N^{-m} \max_{0 \leq j \leq k} \|\rho_j\|_m, \quad k = 1, 2, \ldots, K, \tag{39}$$
where $c_\alpha = \frac{c}{1-\alpha}$ with c a constant.
- *As $\alpha \to 1$,*
$$\|\rho_k - \rho_k^N\|_{L_2} \leq c \Delta t^{-1} N^{-m} \max_{0 \leq j \leq k} \|\rho_j\|_m, \quad k = 1, 2, \ldots, K, \tag{40}$$
where c only depends on T.

Proof. Assume $r^N = \rho_{k+1}^N - w^N$ where w^N is any function in $P_0^N(K)$. By direct calculation,

$$A^N(r^N, r^N) = A(\rho_{k+1} - w^N, r^N) + A(w^N, r^N) - A^N(w^N, r^N) + F^N(r^N) - F(r^N), \tag{41}$$

which leads to

$$\begin{aligned} \|r^N\|_{1,N}^2 \leq \|\rho_{k+1} - w^N\|_1 \|r^N\|_1 + \Big|A(w^N, r^N) - A^N(w^N, r^N)\Big| \\ + \Big|F(r^N) - F^N(r^N)\Big| \quad \forall w^N \in P_0^{N-1}(K). \end{aligned} \tag{42}$$

$$\begin{aligned} \Big|F(r^N) - F^N(r^N)\Big| = \Big|(1-b_1)\Big[(\rho_k, r^N) - (\rho_k^N, r^N)^N\Big] \\ + \sum_{j=1}^{k-1} (b_j - b_{j+1})\Big[(\rho_{k-j}, r^N) - (\rho_{k-j}^N, r^N)^N\Big] \\ + b_k\Big[(\rho_0, r^N) - (\rho_0^N, r^N)^N\Big]\Big|. \end{aligned} \tag{43}$$

$$(g, r^N) - (g^N, r^N)^N \leq (cN^{-m}\|g\|_m + \|g - g^N\|_{L_2})\|r^N\|_{L_2}. \tag{44}$$

Applying this to $g = \rho_j$; $g^N = \rho_j^N$ for all $j = 1, 2, \ldots, k$, we derive

$$\begin{aligned} \Big|F(r^N) - F^N(r^N)\Big| \leq (1-b_1)\|e_k^N\|_{L_2} + \sum_{j=1}^{k-1} (b_j - b_{j+1})\|e_{k-j}^N\|_{L_2} \\ + b_k\|e_0^N\|_{L_2} + cN^{-m} \max_{0 \leq j \leq k} \|\rho_j\|_m \|r^N\|_{L_2}. \end{aligned} \tag{45}$$

This shows that the order of convergence of our combined numerical scheme is $O(\delta t^{2-\alpha} + N^{-m})$ in the L_2 norm in the case of spatial coordinates. Similarly, if we use the L_∞ norm in the space coordinate, then the error estimate is of $O(\delta t^{2-\alpha} + N^{\frac{1}{2}-m})$. □

5. Numerical Results

We present in this section a number of numerical examples to confirm our theoretical justification, as given in Theorems 1 and 2. In our simulations, we use a fixed time $t = 0.1$ in comparison between the exact solution and the solution obtained by using the proposed scheme. In addition to this, in all of our simulations, we use a PC with processor 12th Gen Intel(R) Core(TM) i7-1255U and 16 GB RAM. The average CPU time in all these simulations is 0.03 s for collocation points from 15–50. The algorithm for these simulations is given in Appendix A.

Example 1. *Consider the model Equation (25) with $a = 0, b = 1$, that is, we have the following linear fractional-order-in-time biological population model of the form*

$$\frac{\partial^\alpha \rho}{\partial t^\alpha} = \frac{\partial^2 \rho^2}{\partial \eta^2} + \frac{\partial^2 \rho^2}{\partial \xi^2} + h\rho, \tag{46}$$

subject to the initial condition:

$$\rho_0 = \sqrt{\eta\xi}. \tag{47}$$

Equation (46), subject to the initial condition given in Equation (47), corresponds to Malthusian law. The exact solution is given by

$$\rho(\eta, \xi, t) = \sqrt{\eta\xi} e^{ht} \mathcal{E}_\alpha h t^\alpha, \tag{48}$$

where $\mathcal{E}_\alpha h t^\alpha$ is the Mittag–Leffler function. When $\alpha \to 1$, then the exact solution becomes

$$\rho(\eta, \xi, t) = \sqrt{\eta\xi} \sum_{n=0}^{\infty} \frac{(ht)^n}{\Gamma(1+n)} = \sqrt{\eta\xi} e^{ht}. \tag{49}$$

In our simulations, we use the fractional-order $\alpha = 0.5$. We compare our results for different collocation points with the exact solution as shown in Figures 1–3. The error behavior between the exact and numerical solution is shown in Figure 4. One can see that the error between the exact and approximate solution decays exponentially by increasing the number of collocation points. These results emphasize the reliability of our numerical scheme, which is crucial for accurately predicting population dynamics in more detailed biological studies, making it practical for real-world biological population models where computational resources may be limited.

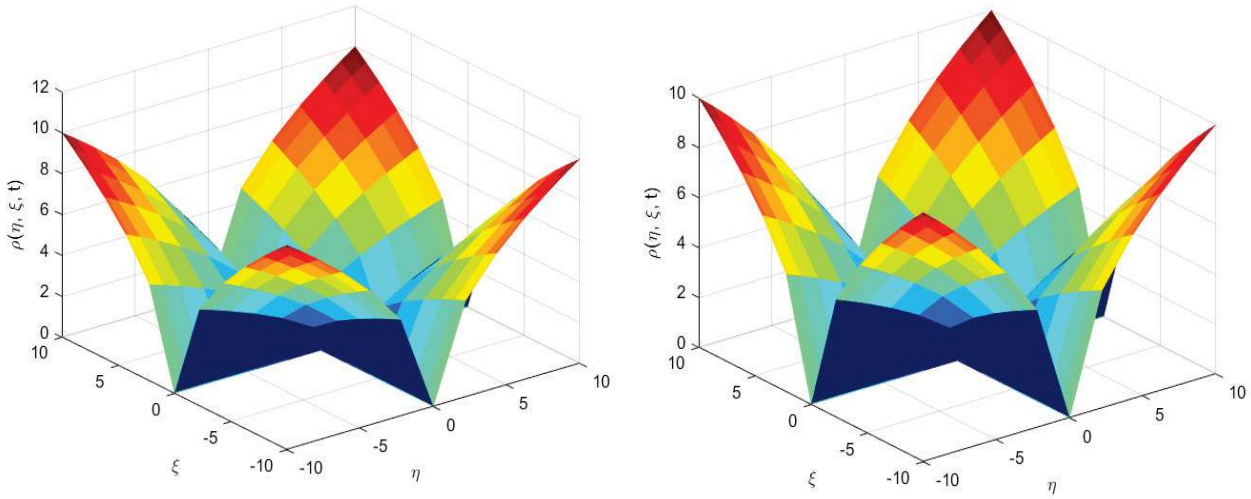

Figure 1. Example 1: Exact (**left**) vs. numerical solution (**right**) at $N = 15$ collocation points.

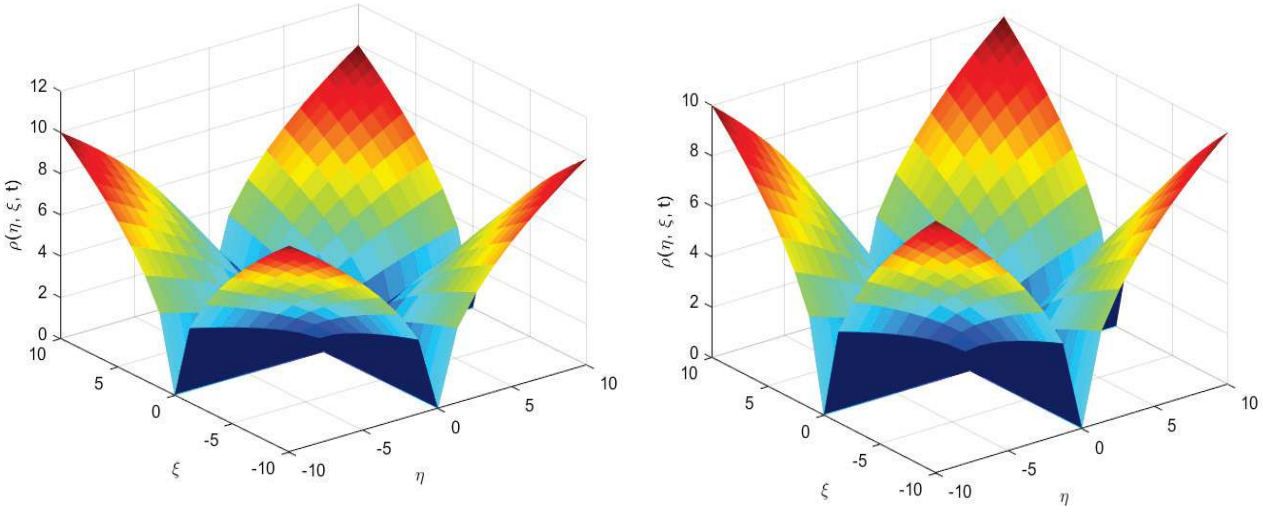

Figure 2. Example 1: Exact (**left**) vs. numerical solution (**right**) at $N = 25$ collocation points.

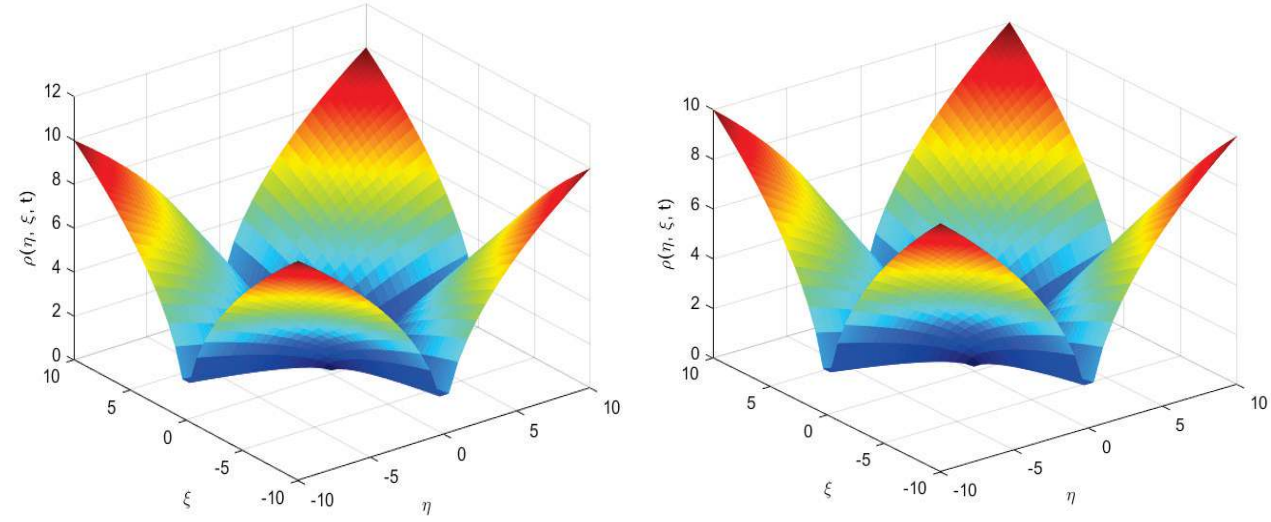

Figure 3. Example 1: Exact (**left**) vs. numerical solution (**right**) at $N = 50$ collocation points.

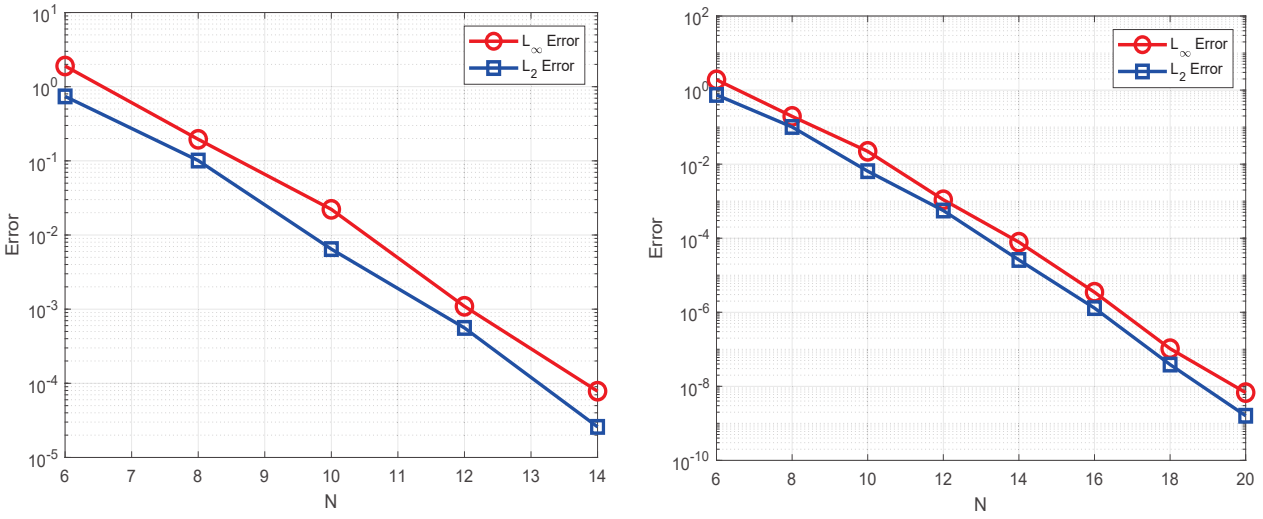

Figure 4. Example 1: Error behavior of exact solution vs. numerical solution at $N = 15$ (**left**) and at $N = 20$ (**right**).

Example 2. *Consider the model Equation (25) with $a = 1, b = 1$. This gives us Verhulst law, and the model Equation (25) becomes*

$$\frac{\partial^{\alpha}\rho}{\partial t^{\alpha}} = \frac{\partial^2\rho^2}{\partial\eta^2} + \frac{\partial^2\rho^2}{\partial\xi^2} + h\rho(1-\ell\rho), \tag{50}$$

subject to the initial condition

$$\rho_0 = e^{\sqrt{\frac{h\ell}{8}}(\eta+\xi)}, \tag{51}$$

The exact solution is given by

$$\rho_0 = e^{\sqrt{\frac{h\ell}{8}}(\eta+\xi)}\mathcal{E}_{\alpha}ht^{\alpha} \tag{52}$$

For $\alpha \to 1$, the exact solution has the form

$$\rho_0 = e^{\sqrt{\frac{h\ell}{8}}(\eta+\xi)+ht}. \tag{53}$$

The numerical experiments are performed between exact and approximate solution for $\alpha = 0.5$ and different collocations points, as shown in Figures 5–7. The error behavior between the exact and numerical solution is given in Table 1. Again, one can see how fast the error is decreasing while increasing the number of collocation points. The numerical solution accurately captures the behavior of the exact solution, which represents the population growth with a carrying capacity, highlighting how the population stabilizes over time, which is a key aspect in ecological studies. The high-level accuracy is essential for making reliable predictions, especially in scenarios involving critical decisions about species conservation or resource management.

Table 1. Example 2: Error behavior of exact vs. numerical solution.

N	L_∞	L_2	N	L_∞	L_2
6	9.541×10^{-1}	4.086×10^{-1}	8	4.842×10^{-2}	2.485×10^{-2}
10	8.145×10^{-3}	3.139×10^{-3}	12	2.670×10^{-4}	1.210×10^{-4}
14	1.650×10^{-5}	7.114×10^{-6}	16	4.706×10^{-7}	2.099×10^{-7}
18	2.132×10^{-8}	6.028×10^{-9}	20	5.213×10^{-10}	1.906×10^{-10}

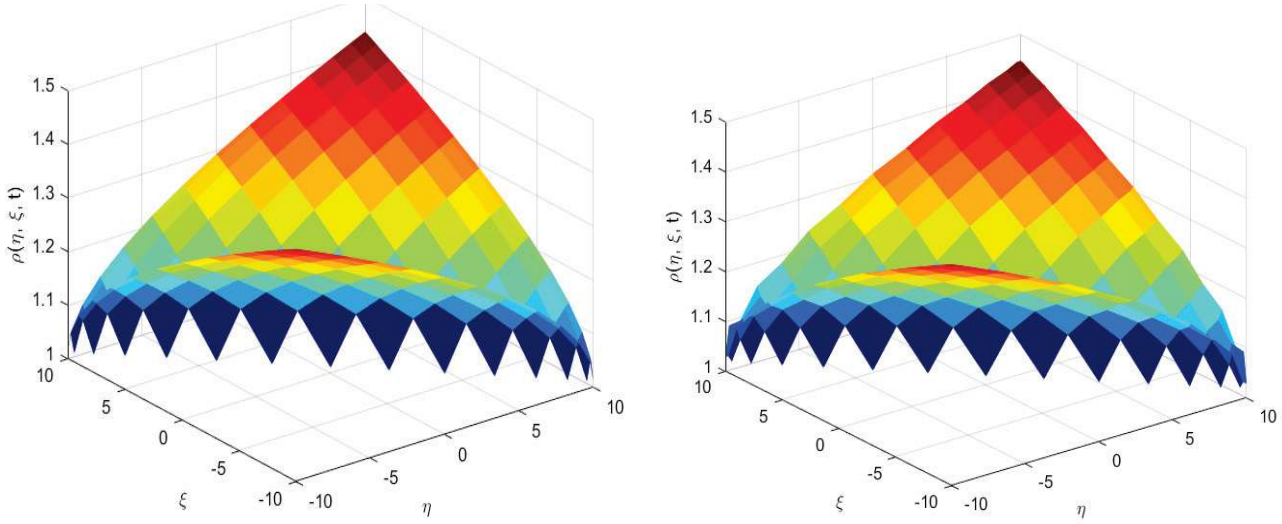

Figure 5. Example 2: Exact (**left**) vs. numerical solution (**right**) at $N = 15$ collocation points.

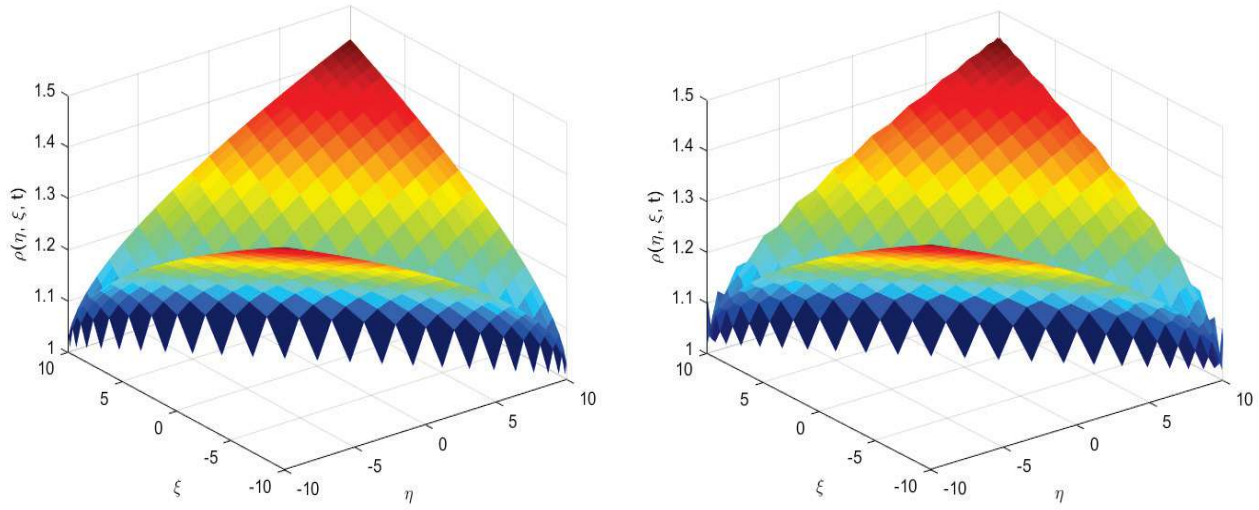

Figure 6. Example 2: Exact (**left**) vs. numerical solution (**right**) at $N = 25$ collocation points.

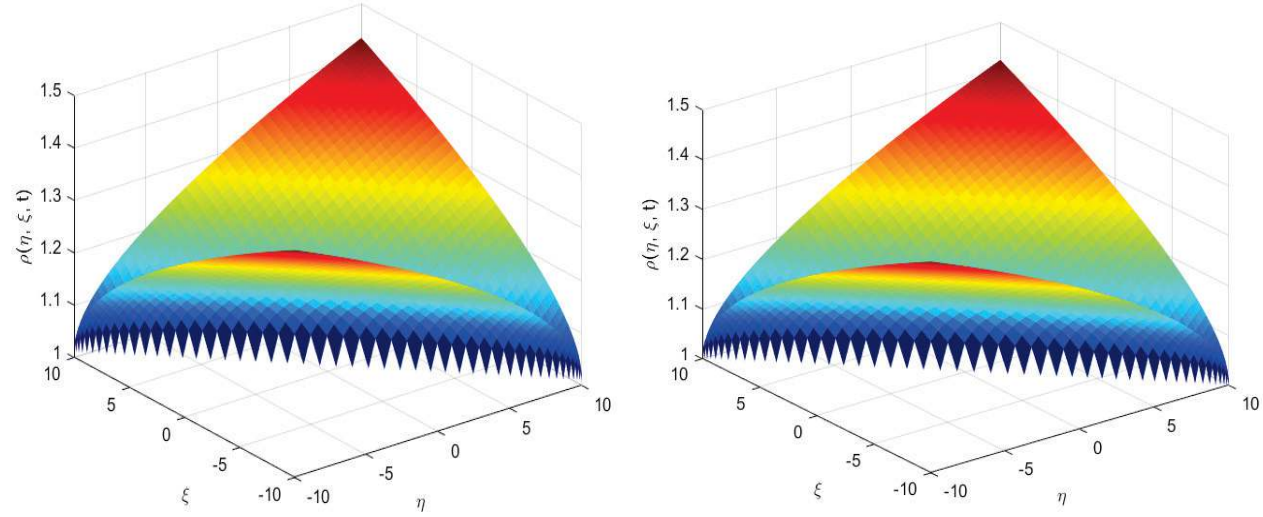

Figure 7. Example 2: Exact (**left**) vs. numerical solution (**right**) at $N = 50$ collocation points.

Example 3. *In this example, we choose* $a = -1, b = 1$. *This gives us the model Equation (25) of the form*

$$\frac{\partial^\alpha \rho}{\partial t^\alpha} = \frac{\partial^2 \rho^2}{\partial \eta^2} + \frac{\partial^2 \rho^2}{\partial \xi^2} + h(\rho^{-1} - \ell), \tag{54}$$

subject to the initial condition

$$\rho_0 = \sqrt{\frac{h\ell}{4}\eta^2 + \frac{h\ell}{4}\xi^2 + \xi + 5}, \tag{55}$$

The exact solution is given by

$$\rho(\eta, \xi, t) = \rho_0 + \sum_{n=0}^{\infty} \frac{(ht^\alpha)\rho_0}{\Gamma(1 + (n+1)\alpha)} + \left(\frac{ht^\alpha}{\rho_0^2}\right)^n \tag{56}$$

For $\alpha \to 1$, *the transform exact solution is*

$$\rho(\eta, \xi, t) = \rho_0 + \frac{ht}{\rho_0} e^{\frac{ht}{\rho_0^2}}. \tag{57}$$

Figures 8–10 show the comparison between the actual and numerical solution for $\alpha = 0.5$ with different collocations points. Our simulations confirmed that our numerical method performed very well against the exact solution. Further validation of exponential error decays is shown in Table 2. These results illustrate the model's capability to handle nonlinear dynamics, which are common in biological systems where interactions between species or within populations can lead to complex behaviors.

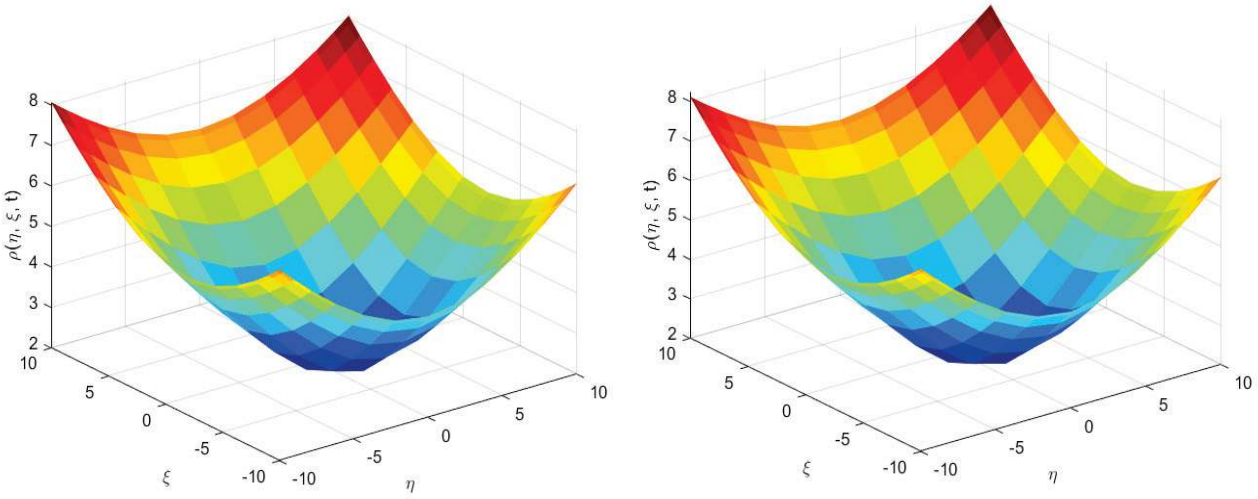

Figure 8. Example 3: Exact (**left**) vs. numerical solution (**right**) at $N = 15$ collocation points.

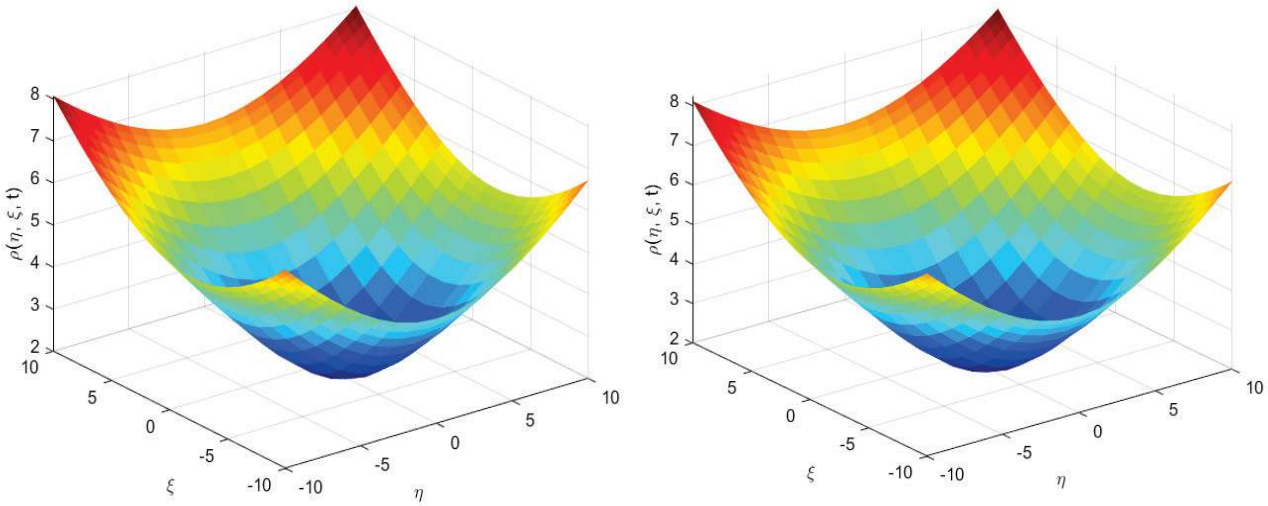

Figure 9. Example 3: Exact (**left**) vs. numerical solution (**right**) at $N = 25$ collocation points.

Table 2. Example 3: Error behavior of exact vs. numerical solution.

N	L_∞	L_2	N	L_∞	L_2
6	1.901×10^{0}	7.400×10^{-1}	8	1.951×10^{-1}	1.009×10^{-1}
10	2.218×10^{-2}	6.456×10^{-3}	12	1.093×10^{-3}	5.585×10^{-4}
14	7.824×10^{-5}	2.584×10^{-5}	16	3.480×10^{-6}	1.295×10^{-6}
18	1.039×10^{-7}	3.863×10^{-8}	20	6.763×10^{-9}	1.602×10^{-9}

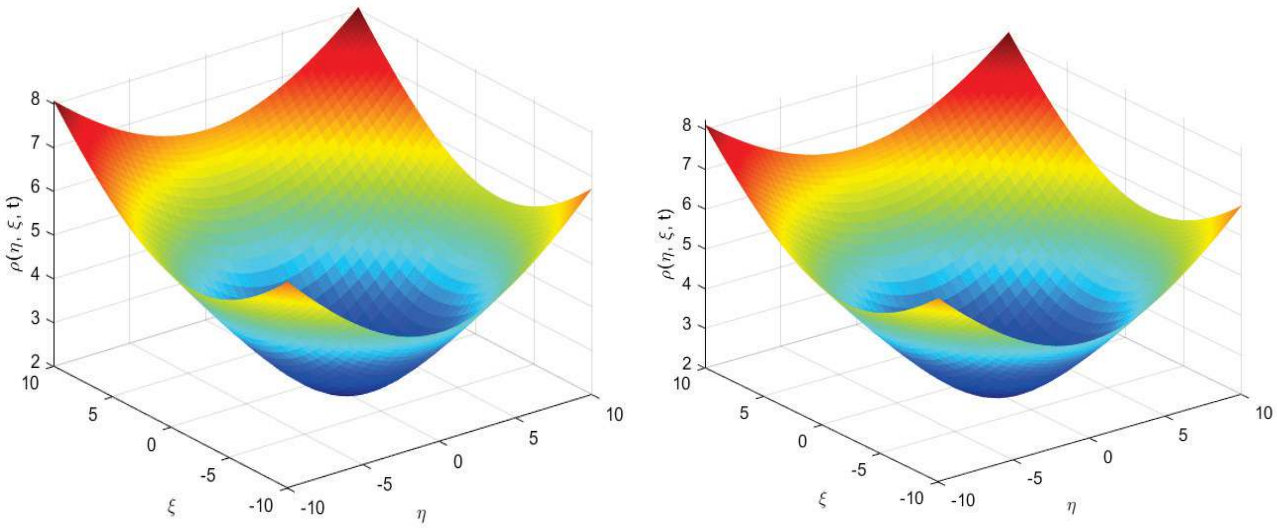

Figure 10. Example 3: Exact (**left**) vs. numerical solution (**right**) at $N = 50$ collocation points.

6. Conclusions

This study has successfully shown how fractional calculus may be used to describe fractional-order-in-time partial differential equations, which are used to simulate the dynamic behavior of biological populations. It has been shown that using the $L1$ scheme for time-fractional derivatives is a reliable and accurate way to deal with the nonlocal properties included in these kinds of equations. This method is especially crucial for capturing the genetic and memory components that are essential to biological systems. Additionally, it has been demonstrated that the Chebyshev spectral method for spatial derivatives is a highly effective method that offers an exponential rate of convergence, making it perfect for managing intricate boundary conditions and geometries that are common in biological modeling. Our algorithms provide a powerful tool for approximation solutions in situations where analytical methods are not sufficient, as confirmed by our theoretical and numerical investigation. Our approach is accurate and reliable, as evidenced by the well-aligned numerical experiments with the theoretical predictions.

Funding: This research received no external funding.

Data Availability Statement: The original contributions presented in the study are included in the article, further inquiries can be directed to the corresponding author.

Conflicts of Interest: The author declares no conflicts of interest.

Appendix A

Algorithm A1 Algorithm for Solving the Fractional PDE (25):

1. **Parameter Initialization:**
   - Define h, a, ℓ, b, and fractional order α.
   - Define time step size Δt and total simulation time T.
2. **Spatial Domain Discretization:**
   - Define Chebyshev nodes $\eta_j = \cos\left(\frac{j\pi}{N_\eta}\right)$ and $\xi_i = \cos\left(\frac{i\pi}{N_\xi}\right)$ for $j, i = 0, 1, \ldots, N$.
   - Construct Chebyshev differentiation matrices D_η and D_ξ.
3. **Initial Condition:**

$$\rho(\eta, \xi, 0) = \text{given initial condition.} \tag{A1}$$

Algorithm A1 *Cont.*

4. **Time Discretization Using L1 Scheme:**

$$\frac{\partial^\alpha \rho}{\partial t^\alpha} \approx \frac{1}{\Gamma(2-\alpha)} \sum_{k=0}^{n} w_k (\rho^{n-k} - \rho^{n-k-1}), \tag{A2}$$

where $w_k = (\Delta t)^\alpha (k^{1-\alpha} - (k-1)^{1-\alpha})$.

5. **Assembling the System:**

$$\frac{1}{\Gamma(2-\alpha)} \sum_{k=0}^{n} w_k \rho^{n-k} = D_\eta^2 (\rho^n)^2 + D_\xi^2 (\rho^n)^2 + h(\rho^n)^a (1 - \ell(\rho^n)^b), \tag{A3}$$

6. **Matrix Formulation:**
   - Represent the problem in matrix form to prepare for numerical solving:

$$A\rho^{n+1} = b^n, \tag{A4}$$

   where A is derived from the $L1$ and Chebyshev methods, and b^n contains the known terms from time step n.

7. **Iterative Solving:**
   - Solve the matrix equation using an appropriate iterative method:

$$\rho^{n+1} = A^{-1} b^n. \tag{A5}$$

8. **Advance Time Step:**
   - Increment n and repeat from step 4 until $t = T$.

9. **Postprocessing:**
   - Plot $\rho(\eta, \xi, t)$.

References

1. Singh, H.; Srivastava, H.M.; Nieto, J.J. *Handbook of Fractional Calculus for Engineering and Science*; Chapman and Hall/CRC: Boca Raton, FL, USA, 2022.
2. Inoue, T. *The Advanced Theory of Fractional Calculus*, 3rd ed.; Academic Research Publication: New York, NY, USA, 2021.
3. Hilfer, R. *Applications of Fractional Calculus in Physics*; World Scientific: Singapore, 2000.
4. Gao, X.-L.; Zhang, H.-L.; Wang, Y.-L.; Li, Z.-Y. Research on Pattern Dynamics Behavior of a Fractional Vegetation-Water Model in Arid Flat Environment. *Fractal Fract.* **2024**, *8*, 264. [CrossRef]
5. Magin, R.L. Fractional Calculus Models of Complex Dynamics in Biological Tissues. *Comput. Math. Appl.* **2010**, *59*, 1586–1593. [CrossRef]
6. Hattaf, K. On the Stability and Numerical Scheme of Fractional Differential Equations with Application to Biology. *Computation* **2022**, *10*, 97. [CrossRef]
7. Hattaf, K. A New Mixed Fractional Derivative with Applications in Computational Biology. *Computation* **2024**, *12*, 7. [CrossRef]
8. Nguyen Tien, D. Fractional Stochastic Differential Equations with Applications to Finance. *J. Math. Anal. Appl.* **2013**, *397*, 334–348. [CrossRef]
9. Wu, Z.; Zhang, X.; Wang, J.; Zeng, X. Applications of Fractional Differentiation Matrices in Solving Caputo Fractional Differential Equations. *Fractal Fract.* **2023**, *7*, 374. [CrossRef]
10. Podlubny, I. *Fractional Differential Equations: An Introduction to Fractional Derivatives, Fractional Differential Equations, to Methods of Their Solution and Some of Their Applications*; Elsevier: Amsterdam, The Netherlands, 1998.
11. Bin Jebreen, H. The Müntz–Legendre Wavelet Collocation Method for Solving Weakly Singular Integro-Differential Equations with Fractional Derivatives. *Fractal Fract.* **2023**, *7*, 763. [CrossRef]
12. Xu, Y.; Liu, Y.; Yin, X.; Feng, L.; Wang, Z. A Compact Scheme Combining the Fast Time Stepping Method for Solving 2D Fractional Subdiffusion Equations. *Fractal Fract.* **2023**, *7*, 186. [CrossRef]
13. Sytnyk, D.; Wohlmuth, B. Exponentially Convergent Numerical Method for Abstract Cauchy Problem with Fractional Derivative of Caputo Type. *Mathematics* **2023**, *11*, 2312. [CrossRef]
14. Caputo, M. Linear Models of Dissipation Whose Q Is Almost Frequency Independent II. *Geophys. J. Int.* **1967**, *13*, 529–539. [CrossRef]

15. Djilali, S. Threshold Asymptotic Dynamics for a Spatial Age-Dependent Cell-to-Cell Transmission Model with Nonlocal Disperse. *Discret. Contin. Dyn. Syst. Ser. B* **2023**, *28*, 4108–4143. [CrossRef]
16. Hathout, F.Z.; Touaoula, T.M.; Djilali, S. Efficiency of Protection in the Presence of Immigration Process for an Age-Structured Epidemiological Model. *Acta Appl. Math.* **2023**, *185*, 3. [CrossRef]
17. Ionescu, C.; Lopes, A.; Copot, D.; Machado, J.A.T.; Bates, J.H.T. The role of fractional calculus in modeling biological phenomena: A review. *Commun. Nonlinear Sci. Numer. Simul.* **2017**, *51*, 141–159. [CrossRef]
18. Caputo, M.; Fabrizio, M. A New Definition of Fractional Derivative without Singular Kernel. *Prog. Fract. Differ. Appl.* **2015**, *1*, 1–13.
19. Chen, Y.-G.; Yang, F.; Tian, F. The Landweber Iterative Regularization Method for Identifying the Unknown Source of Caputo-Fabrizio Time Fractional Diffusion Equation on Spherically Symmetric Domain. *Symmetry* **2023**, *15*, 1468. [CrossRef]
20. Agrawal, O.P. Solution for a Fractional Diffusion-Wave Equation Defined in a Bounded Domain. *J. Nonlinear Dynam.* **2002**, *29*, 145–155. [CrossRef]
21. Fix, G.J.; Roop, J.P. Least Squares Finite Element Solution of a Fractional Order Two-Point Boundary Value Problem. *Comput. Math. Appl.* **2004**, *48*, 1017–1033. [CrossRef]
22. Ali, I.; Haq, S.; Hussain, M.; Nisar, K.S.; Ul Arifeen, S. On the Analysis and Application of a Spectral Collocation Scheme for the Nonlinear Two-Dimensional Fractional Diffusion Equation. *Results Phys.* **2024**, *56*, 107222. [CrossRef]
23. Alam, M.; Haq, S.; Ali, I.; Ebadi, M.J.; Salahshour, S. Radial Basis Functions Approximation Method for Time-Fractional FitzHugh–Nagumo Equation. *Fractal Fract.* **2023**, *7*, 882. [CrossRef]
24. Diethelm, K.; Freed, A.D. On the Solution of Nonlinear Fractional-Order Differential Equations Used in the Modeling of Viscoplasticity. In *Proceedings of the Second Conference on Scientific Computing in Chemical Engineering*; Springer: Berlin/Heidelberg, Germany, 1999; pp. 217–224.
25. Deng, Z.; Singh, V.P.; Bengtsson, L. Numerical Solution of Fractional Advection–Dispersion Equation. *J. Hydraul. Eng.* **2004**, *130*, 422–431. [CrossRef]
26. Meerschaert, M.; Tadjeran, C. Finite Difference Approximations for Fractional Advection-Dispersion Flow Equations. *J. Comp. Appl. Math.* **2004**, *172*, 65–77. [CrossRef]
27. Gorenflo, R.; Mainardi, F.; Moretti, D.; Paradisi, P. Time Fractional Diffusion: A Discrete Random Walk Approach. *Nonlinear Dyn.* **2002**, *29*, 129–143. [CrossRef]
28. Gorenflo, R.; Luchko, Y.; Mainardi, F. Wright Function as Scale-Invariant Solutions of the Diffusion-Wave Equation. *J. Comp. Appl. Math.* **2000**, *118*, 175–191. [CrossRef]
29. Schneider, W.R.; Wyss, W. Fractional Diffusion and Wave Equations. *J. Math. Phys.* **1989**, *30*, 134–144. [CrossRef]
30. Wyss, W. The Fractional Diffusion Equation. *J. Math. Phys.* **1986**, *27*, 2782–2785. [CrossRef]
31. Lin, Y.; Xu, C. Finite Difference/Spectral Approximations for the Time-Fractional Diffusion Equation. *J. Comput. Phys.* **2007**, *225*, 1533–1552. [CrossRef]
32. Gottlieb, D.; Hussaini, M.Y.; Orszag, S.A. Theory and application of spectral methods. In *Spectral Methods for Partial Differential Equations*; Voigt, R.G., Gotlieb, D., Hussaini, M.Y., Eds.; SIAM: Philadelphia, PA, USA, 1984; pp. 1–55.
33. Gottlieb, D.; Orszag, S.A. *Numerical Analysis of Spectral Methods: Theory and Applications*; SIAM: Philadelphia, PA, USA, 1977.
34. Trefethen, L.N. *Spectral Methods in MATLAB*; SIAM: Philadelphia, PA, USA, 2000.
35. Mason, J.C.; Handscomb, D.C. *Chebyshev Polynomials*; CRC Press LLC: New York, NY, USA, 2003.
36. Ali, I.; Saleem, M.T. Applications of Orthogonal Polynomials in Simulations of Mass Transfer Diffusion Equation Arising in Food Engineering. *Symmetry* **2023**, *15*, 527. [CrossRef]
37. Ali, I.; Khan, S.U. Asymptotic Behavior of Three Connected Stochastic Delay Neoclassical Growth Systems Using Spectral Technique. *Mathematics* **2022**, *10*, 3639. [CrossRef]
38. Ali, I.; Khan, S.U. Threshold of Stochastic SIRS Epidemic Model from Infectious to Susceptible Class with Saturated Incidence Rate Using Spectral Method. *Symmetry* **2022**, *14*, 1838. [CrossRef]
39. Ali, I.; Khan, S.U. Dynamics and Simulations of Stochastic COVID-19 Epidemic Model Using Legendre Spectral Collocation Method. *AIMS Math.* **2023**, *8*, 4220–4236. [CrossRef]
40. Khan, S.U.; Ali, I. Convergence and Error Analysis of a Spectral Collocation Method for Solving System of Nonlinear Fredholm Integral Equations of Second Kind. *Comp. Appl. Math.* **2019**, *38*, 125. [CrossRef]
41. Hattaf, K.; Yousfi, N. Global Stability for Fractional Diffusion Equations in Biological Systems. *Complexity* **2020**, *2020*, 5476842. [CrossRef]
42. Rida, S.Z.; Arafa, A.A.M. Exact Solutions of Fractional-Order Biological Population Model. *Commun. Theor. Phys.* **2009**, *52*, 992–996.
43. Shakeri, E.; Dehghan, M. Numerical Solutions of a Biological Population Model Using He's Variational Iteration Method. *Comput. Math. Appl.* **2007**, *54*, 1197–1207. [CrossRef]
44. Liu, Y.; Li, Z.; Zhang, Y. Homotopy Perturbation Method to Fractional Biological Population Equation. *Fract. Differ. Calc.* **2011**, *1*, 117–124. [CrossRef]
45. Ma, X.; Wang, Y.; Zhu, X.; Liu, W.; Lan, Q.; Xiao, W. A Spectral Method for Two-Dimensional Ocean Acoustic Propagation. *J. Mar. Sci. Eng.* **2021**, *9*, 892. [CrossRef]
46. Shen, J.; Tang, T. *Spectral and High-Order Methods with Applications*; Science Press: Beijing, China, 2006.
47. Boyd, J.P. *Chebyshev and Fourier Spectral Methods*, 2nd ed.; Dover: New York, NY, USA, 2001.

48. Gurney, W.S.C.; Nisbet, R.M. *Ecological Dynamics*; Oxford University Press: Oxford, UK, 1998.
49. Canuto, C.; Hussaini, M.Y.; Quarteroni, A.; Zang, T.A. *Spectral Methods: Fundamentals in Single Domains*; Springer Series in Scientific Computation; Springer: New York, NY, USA, 2006.

fractal and fractional

MDPI

Article

An Efficient Numerical Solution of a Multi-Dimensional Two-Term Fractional Order PDE via a Hybrid Methodology: The Caputo–Lucas–Fibonacci Approach with Strang Splitting

Imtiaz Ahmad [1,*], Abdulrahman Obaid Alshammari [2], Rashid Jan [3], Normy Norfiza Abdul Razak [3] and Sahar Ahmed Idris [4]

[1] Institute of Informatics and Computing in Energy (IICE), Universiti Tenaga Nasional (UNITEN), Kajang 43000, Selangor, Malaysia
[2] Department of Mathematics, College of Science, Jouf University, Sakaka 72388, Saudi Arabia; aoshammari@ju.edu.sa
[3] Institute of Energy Infrastructure (IEI), Department of Civil Engineering, College of Engineering, Universiti Tenaga Nasional (UNITEN), Putrajaya Campus, Jalan IKRAM-UNITEN, Kajang 43000, Selangor, Malaysia; rashid.jan@uniten.edu.my (R.J.); normy@uniten.edu.my (N.N.A.R.)
[4] Faculty of Engineering, Department of Industrial Engineering, King Khalid University, Abha 61421, Saudi Arabia; smohammedali@kku.edu.sa
* Correspondence: imtiazkakakhil@gmail.com

Abstract: The utilization of time-fractional PDEs in diverse fields within science and technology has attracted significant interest from researchers. This paper presents a relatively new numerical approach aimed at solving two-term time-fractional PDE models in two and three dimensions. We combined the Liouville–Caputo fractional derivative scheme with the Strang splitting algorithm for the temporal component and employed a meshless technique for spatial derivatives utilizing Lucas and Fibonacci polynomials. The rising demand for meshless methods stems from their inherent mesh-free nature and suitability for higher dimensions. Moreover, this approach demonstrates the effective approximation of solutions across both regular and irregular domains. Error norms were used to assess the accuracy of the methodology across both regular and irregular domains. A comparative analysis was conducted between the exact solution and alternative numerical methods found in the contemporary literature. The findings demonstrate that our proposed approach exhibited better performance while demanding fewer computational resources.

Keywords: Strang splitting algorithm; Caputo derivative; Fibonacci polynomials; Lucas polynomials; two-term fractional-order PDE

Citation: Ahmad, I.; Alshammari, A.O.; Jan, R.; Razak, N.N.A.; Idris, S.A. An Efficient Numerical Solution of a Multi-Dimensional Two-Term Fractional Order PDE via a Hybrid Methodology: The Caputo–Lucas–Fibonacci Approach with Strang Splitting. *Fractal Fract.* **2024**, *8*, 364. https://doi.org/10.3390/fractalfract8060364

Academic Editors: Ricardo Almeida, Libo Feng, Lin Liu and Yang Liu

Received: 29 May 2024
Revised: 13 June 2024
Accepted: 17 June 2024
Published: 20 June 2024

1. Introduction

Over the last decade, there has been considerable interest in fractional partial differential equations (PDEs), making it a vibrant research field for scientists and engineers. PDEs possess the capability to describe numerous complex phenomena across diverse fields, including biology, fluid mechanics, plasma physics, optics, acoustics, financial mathematics, climate modeling, materials science, and electromagnetics [1,2]. Fractional calculus, which deals with derivatives and integrals of non-integer order, finds broad applications in science and technology. In physics, it models complex systems with non-local behavior, such as anomalous diffusion in fluid dynamics and memory effects in viscoelastic materials [3]. Engineering benefits from fractional calculus are found in signal processing, control theory, and optimization, offering robustness and efficiency in dynamic systems. Telecommunications utilize it for modeling wireless communication channels and improving channel estimation algorithms. Fractional calculus enables advancements in understanding and optimizing real-world processes and systems across various domains [4]. The fractional spatio-temporal PDE models are crucial in describing complex phenomena [5], whereas the

two-scale fractal PDE models are essential for simulating intricate structures in materials science and physics, offering insights into multiscale behaviors and enhancing our understanding of fractal geometries in natural and engineered systems [6]. In particular, the Sobolev model equation is integral across various scientific fields, providing a robust framework for investigating phenomena with spatial variations. Its relevance extends across disciplines, encompassing physics, engineering, biology, and finance. In physics, Sobolev PDEs are commonly utilized to model phenomena such as heat conduction, fluid dynamics, and quantum mechanics [7,8]. Engineers employ them to analyze structural mechanics, electromagnetism, and signal-processing problems [7]. Furthermore, Sobolev PDEs find applications in image processing, medical imaging, and geophysical exploration. Their adaptability lies in their capacity to handle irregular domains and boundary conditions while providing solutions that demonstrate smoothness properties.

Numerous studies explored the applications and theoretical foundations of Sobolev PDEs, underscoring their significance in both theoretical and applied contexts. However, numerous researchers faced challenges in deriving and formulating various complex phenomena within nonlinear PDEs with integer orders [9]. In response, fractional calculus is regarded as a viable solution to this issue, as it incorporates a nonlocal property that is absent in nonlinear PDEs with integer orders [10]. Observations indicate that multi-term time-fractional PDEs were proposed to enhance the modeling accuracy in depicting anomalous diffusion processes, capturing various types of viscoelastic damping, accurately representing power-law frequency dependence, and simulating the flow of a fractional Maxwell fluid [11]. This study focused on the two-term time-fractional Sobolev equation in two and three dimensions, defined as follows:

$$\begin{aligned}&\frac{\partial^{\xi_1}\mathcal{U}}{\partial t^{\xi_1}}+\frac{\partial^{\xi_2}\mathcal{U}}{\partial t^{\xi_2}}-\beta\frac{\partial}{\partial t}\left(\frac{\partial^2\mathcal{U}}{\partial r^2}+\frac{\partial^2\mathcal{U}}{\partial s^2}\right)-\delta\left(\frac{\partial^2\mathcal{U}}{\partial r^2}+\frac{\partial^2\mathcal{U}}{\partial s^2}\right)+\eta\left(\mathcal{U}\left(\frac{\partial^2\mathcal{U}}{\partial r^2}+\frac{\partial^2\mathcal{U}}{\partial s^2}\right)\right)\\&+\eta\left(\frac{\partial\mathcal{U}}{\partial r}+\frac{\partial\mathcal{U}}{\partial s}\right)^2+\gamma\mathcal{U}=F(r,s,t),\ \ r,s\in\Omega\subset\mathbb{R}^2,\ \ 0<\xi_2\leq\xi_1\leq 1,\ \ t>0,\end{aligned}\tag{1}$$

and

$$\begin{aligned}&\frac{\partial^{\xi_1}\mathcal{U}}{\partial t^{\xi_1}}+\frac{\partial^{\xi_2}\mathcal{U}}{\partial t^{\xi_2}}-\beta\frac{\partial}{\partial t}\left(\frac{\partial^2\mathcal{U}}{\partial r^2}+\frac{\partial^2\mathcal{U}}{\partial s^2}+\frac{\partial^2\mathcal{U}}{\partial z^2}\right)-\delta\left(\frac{\partial^2\mathcal{U}}{\partial r^2}+\frac{\partial^2\mathcal{U}}{\partial s^2}+\frac{\partial^2\mathcal{U}}{\partial z^2}\right)\\&+\eta\left(\mathcal{U}\left(\frac{\partial^2\mathcal{U}}{\partial r^2}+\frac{\partial^2\mathcal{U}}{\partial s^2}+\frac{\partial^2\mathcal{U}}{\partial z^2}\right)\right)+\eta\left(\frac{\partial\mathcal{U}}{\partial r}+\frac{\partial\mathcal{U}}{\partial s}+\frac{\partial\mathcal{U}}{\partial z}\right)^2+\gamma\mathcal{U}\\&=F(r,s,z,t),\ \ r,s,z\in\Omega\subset\mathbb{R}^3,\ \ 0<\xi_2\leq\xi_1\leq 1,\ \ t>0,\end{aligned}\tag{2}$$

with the following initial and boundary conditions:

$$\mathcal{U}(\bar{r},0)=\mathcal{U}_0(\bar{r}),\tag{3}$$

$$\mathcal{U}(\bar{r},t)=f_1(\bar{r},t),\ \ \bar{r}\in\partial\Omega\subset\mathbb{R}^d,\ \ d=2,3.\tag{4}$$

where the constants β, δ, η, and γ have known values. Moreover, $\frac{\partial^{\xi_1}}{\partial t^{\xi_1}}$ and $\frac{\partial^{\xi_2}}{\partial t^{\xi_2}}$ denote the Caputo derivatives in accordance with Caputo [12] and applied to $\mathcal{U}(\bar{r},t)$, where $0<\xi_2\leq\xi_1\leq 1$.

Several works delved into the existence and uniqueness of solutions for Sobolev equations, as documented in [13]. Ewing [14] applied the finite difference method to tackle 2D Sobolev equations. The study [15] used a computationally appealing and precise local meshless technique to provide numerical solutions for three-dimensional two- and three-term time-fractional PDE models. Various test problems were employed to assess the accuracy and reliability of the proposed approach. The paper by Luo et al. [16] introduces a reduced-order extrapolated finite difference iterative scheme for 2D Sobolev equations, employing proper orthogonal decomposition to construct a reduced-order solution space model, thus reducing the computational costs. Numerical experiments validated the scheme's efficiency and accuracy, indicating its potential for efficient Sobolev equation solving. An accurate and efficient local meshless technique is used in the article [17] to explore numerical solutions for two-term time-fractional Sobolev models. The method approximates the solution on a uniform or scattered set of nodes, yielding sparse and

well-conditioned coefficient matrices. Another paper by Luo et al. [18] introduces a novel method that employs reduced-order techniques and extrapolation within a Crank–Nicolson finite volume framework for 2D Sobolev equations. It aims to improve the computational efficiency and accuracy, showcasing promising outcomes via numerical simulations. The paper by Li et al. [19] introduces an extended mixed finite element approach for solving 2D Sobolev equations, integrating a novel formulation with stable discretization for accurate solutions and computational efficiency. Numerical experiments highlighted its effectiveness and superiority over existing methods, especially in maintaining stability and convergence properties. Heydari et al. [20] introduced a novel method that employs orthonormal Bernoulli polynomials to solve distributed-order time-fractional 2D Sobolev equations, which demonstrated accuracy through four test problems. Gao et al. [21] used the local discontinuous Galerkin finite element method to solve a particular class of 2D Sobolev equations, while another work [22] applied the weak Galerkin finite element method, providing an error estimate. Abu et al. [23] presented a method for solving time- and space-fractional Sobolev equations with Caputo fractional derivatives in n-dimensional space, utilizing the reproducing kernel Hilbert space method, which is particularly effective for Caputo class derivatives. A meshless RBFs technique for solving 2D time-fractional Sobolev equations was presented by Hussain et al. [24]. This method uses a finite difference formula for time-fractional derivative approximation and RBFs for spatial operator approximation. Using a Liouville–Caputo derivative technique for the time derivative, Ahmad et al. [25] suggested an efficient meshless method for estimating the numerical solution of 3D time-fractional Sobolev equations. Furthermore, Zhang et al. [26] used a characteristic splitting mixed finite element approach to solve convection-dominated Sobolev equations.

In response to its extensive applications, researchers explored a multitude of numerical and analytical methodologies [27,28] for addressing complex PDEs. These methods encompass various techniques, such as the alternating direction implicit method [29], the homotopy perturbation method [30], the Laplace transform technique [31], the variational approach [32,33], finite element methods (FEMs) [34], finite difference methods (FDMs) [16,35], gradient descent iterative method [36], spectral methods [37], the exp-function method [38], the alternating direction method [39], and meshless methods [40]. Notably, the straightforward nature of the FDM, FEM, and meshless techniques is noteworthy. Recently, hybrid methodologies have emerged to enhance the efficiency and accuracy of numerical solutions, including meshless methods, the method of lines utilizing Fibonacci polynomials, and combinations of the FDM and FEM.

This investigation focused on computing numerical solutions for the suggested model using a hybrid methodology based on the Caputo derivative. This approach integrates Fibonacci polynomials with the established Caputo derivative concept, exploiting the relationship between Fibonacci and Lucas polynomials. This integration provides a significant advantage in the straightforward implementation of higher-order derivatives. Moreover, the proposed approach reduces computational costs by enhancing the accuracy, even with a limited number of collocation sites. Remarkably, these polynomials find diverse real-world applications in the realm of differential equations.

Addressing boundary value problems accurately involves exploring the interplay between Chebyshev and Lucas polynomials, as demonstrated in previous studies [41,42]. For instance, the Lucas sequence was utilized to approximate integro-differential equations [43], while Lucas polynomials were applied to solve higher-order differential equations [44]. Additionally, the efficacy of a Fibonacci polynomial methodology in resolving Volterra–Fredholm integral differential equations was demonstrated [45]. Furthermore, a hybrid Taylor–Lucas polynomial approach was introduced for addressing delay difference equations [46]. Notably, novel methodologies for solving time-dependent PDEs were proposed by combining hybrid Fibonacci and Lucas polynomial schemes [47,48]. Moreover, researchers employed finite differences and Lucas polynomials to achieve effective numerical solutions for various PDE models [49,50].

Motivation

The primary objective of this research was to introduce a relatively new numerical approach designed to solve two-term time-fractional PDE models in both two and three dimensions. This method combines the Liouville–Caputo fractional derivative scheme with the Strang splitting algorithm for the temporal component and utilizes a meshless technique for spatial derivatives, incorporating Lucas and Fibonacci polynomials. Below are some of the highlighted key features of the proposed study:

- The complex characteristics of fractional nonlinear PDEs make calculating analytical solutions challenging, driving ongoing research efforts to develop accurate and efficient numerical methodologies, with the two-term fractional order Sobolev model equation in both two and three dimensions holding significant importance across multiple scientific domains.
- This study aimed to introduce an efficient numerical framework specifically designed for solving PDEs with temporal fractions.
- The proposed methodology adopts a hybrid approach, integrating Fibonacci and Lucas polynomials with finite difference techniques, while also addressing the temporal direction through the utilization of the Liouville–Caputo fractional derivative in conjunction with a splitting mechanism.
- Lucas and Fibonacci polynomials, unlike orthogonal counterparts, like Chebyshev polynomials, are non-orthogonal, eliminating the need for interval transformations. Additionally, they facilitate the straightforward approximation of higher-order derivatives for unknown functions.
- Furthermore, the approach is characterized by its simplicity and ability to enhance the accuracy, even in scenarios involving fewer nodal points, with the aim to provide a robust and effective numerical solution to the intricate challenges posed by nonlinear PDEs.

This paper is organized as follows: Section 2 provides an overview of the fundamental terms and concepts. The proposed technique for the underlying model equations is discussed in Section 3, while theoretical results regarding stability and error analysis are presented in Section 4. Section 5 utilizes numerical experiments to validate the method's efficacy, and finally, Section 6 summarizes the outcomes and presents concluding remarks to finalize the work.

2. Basic Concepts in Fractional Calculus and Polynomial Theory

In fractional calculus, fractional derivatives are crucial. Fractional calculus finds applications in various fields, including physics, engineering, biology, and finance, providing a powerful framework for modeling complex phenomena characterized by memory, nonlocality, and fractal behavior. The fundamental definition of fractional calculus involves the generalization of differentiation and integration to non-integer orders. Here are some basic definitions of frequently used fractional derivatives.

Definition 1. *The Riemann–Liouville derivative [51,52] is a mathematical concept used to generalize the notion of a derivative to functions that are not necessarily differentiable in the traditional sense. It is commonly applied in the field of fractional calculus to describe the behavior of functions with fractional orders of differentiation.*

$$\frac{\partial^{\xi}\mathcal{U}(\bar{\mathbf{r}},t)}{\partial t^{\xi}} = \frac{1}{\Gamma(1-\xi)}\frac{d}{dt}\int_{t}^{T}\frac{(\mathcal{U}(\bar{\mathbf{r}},\vartheta)-\mathcal{U}(\bar{\mathbf{r}},T))}{(\vartheta-t)^{\xi}}d\vartheta, \quad 0<\xi<1. \tag{5}$$

Definition 2. *Caputo's fractional derivative [12] is a widely used mathematical tool in fractional calculus, providing a powerful approach for describing and analyzing non-local and memory-dependent phenomena in various scientific and engineering fields.*

$$\frac{\partial^{\xi}\mathcal{U}(\bar{\mathbf{r}},t)}{\partial t^{\xi}}=\frac{1}{\Gamma(1-\xi)}\int_{0}^{t}\frac{\partial\mathcal{U}(\bar{\mathbf{r}},\zeta)}{\partial\zeta}(t-\zeta)^{-\xi}d\zeta,\ \ 0<\xi<1. \tag{6}$$

Definition 3. *The Atangana and Baleanu fractional derivative [53], proposed by Atangana and Baleanu, is a non-local operator that extends the concept of fractional calculus. It provides a novel approach for modeling complex systems that exhibit memory and non-local behavior.*

$${}^{ABC}_{a}\frac{\partial^{\xi}\mathcal{U}(\bar{\mathbf{r}},t)}{\partial t^{\xi}}=\frac{B(\xi)}{1-\xi}\int_{a}^{t}\mathcal{U}'(\bar{\mathbf{r}})E_{\xi}\left(-\frac{\xi(t-\bar{\mathbf{r}})^{\xi}}{1-\xi}\right)d\bar{\mathbf{r}},\ \ 0<\xi<1. \tag{7}$$

Definition 4. *He's fractional derivative [54]:*

$$\frac{\partial^{\xi}\mathcal{U}(\bar{\mathbf{r}},t)}{\partial t^{\xi}}=\frac{1}{\Gamma(1-\xi)}\frac{d}{d\bar{\mathbf{r}}}\int_{t_0}^{t}(t-\zeta)^{-\xi}[\mathcal{U}_0(\zeta)-\mathcal{U}(\zeta)],\ \ 0<\xi<1. \tag{8}$$

2.1. Fibonacci and Lucas Polynomial Theory

Below are explanations outlining the definitions, practical implications, and utilization of Lucas and Fibonacci polynomials, encompassing tasks such as approximating unfamiliar functions and their derivatives.

Fibonacci polynomials [49]:

The Fibonacci polynomial, which is an extension of Fibonacci numbers, is defined through a three-term recurrence relation:

$$F_k(r)=kF_{k-1}(r)+F_{k-2}(r),\ \ k\geq 2, \tag{9}$$

where the sequence begins with $F_0(r)=0$ and $F_1(r)=1$. When $r=1$, Equation (9) generates the familiar sequence of Fibonacci numbers.

Lucas polynomials [49]:

One can define the Lucas polynomials using the three-term recurrence relation:

$$L_k(r)=kL_{k-1}(r)+L_{k-2}(r),\ \ k\geq 2, \tag{10}$$

with $L_0(r)=2$ and $L_1(r)=r$ as initial values. This allows Equation (10) to produce a series of Lucas numbers with $r=1$.

Lemma 1 ([49])**.** *The kth Fibonacci polynomial $F_k(r)$ can be used to define the mth-order derivative of the kth Lucas polynomial $L_k(r)$:*

$$L_k^{(m)}(r)=kF_k(r)D^{m-1},\quad D^{m-1}=\underbrace{D\times D\times D\cdots D}_{(m-1)time} \tag{11}$$

where an $(M+1)\times(M+1)$ matrix is represented by D, which can be described as

$$D=\begin{bmatrix}0 & 0 & \dots & 0\\ 0 & & & \\ \vdots & & d & \\ 0 & & & \end{bmatrix},$$

where d is computed according to [49]:

$$d_{ij} = \begin{cases} i \sin \frac{(j-i)\pi}{2}, & \text{if } j > i, \\ 0, & \text{otherwise.} \end{cases}$$

2.2. Function Approximation

Suppose $\mathcal{U} \in L^2(\mathbb{R})$, and let $\mathcal{U}(\bar{\boldsymbol{r}})$ be continuous. Then, through the linear combination of the kth Lucas polynomials, it is possible to represent $\mathcal{U}$ as

$$\mathcal{U}(\bar{\boldsymbol{r}}) = \sum_{k=0}^{\infty} \Lambda_k L_k(\bar{\boldsymbol{r}}), \tag{12}$$

where the Lucas polynomials are denoted as $L_k(\bar{\boldsymbol{r}})$, with the corresponding unknown coefficients represented by Λ_k.

Likewise, $\mathcal{U}(\bar{\boldsymbol{r}})$ can also be expanded under the same conditions by using a linear combination of the kth Fibonacci polynomials, as demonstrated below:

$$\mathcal{U}(\bar{\boldsymbol{r}}) = \sum_{k=0}^{\infty} \Lambda_k F_k(\bar{\boldsymbol{r}}).$$

In this context, $F_k(\bar{\boldsymbol{r}})$ denotes the Fibonacci polynomials, while Λ_k stands for the coefficients yet to be determined.

The Lucas polynomial series can be used to expand the function $\mathcal{U}(\bar{\boldsymbol{r}})$ and find the first-order derivative:

$$\mathcal{U}'(\bar{\boldsymbol{r}}) = \sum_{k=0}^{\infty} \Lambda_k L_k'(\bar{\boldsymbol{r}}), \tag{13}$$

and the function $\mathcal{U}(\bar{\boldsymbol{r}})$'s associated *mth*-order derivative is given as

$$\mathcal{U}^m(\bar{\boldsymbol{r}}) = \sum_{k=0}^{\infty} \Lambda_k L_k^{(m)}(\bar{\boldsymbol{r}}), \tag{14}$$

where

$$\mathcal{U}^m(\bar{\boldsymbol{r}}) = \frac{\mathrm{d}^m \mathcal{U}(\bar{\boldsymbol{r}})}{\mathrm{d}\bar{\boldsymbol{r}}^m}, \quad L_k^{(m)}(\bar{\boldsymbol{r}}) = \frac{\mathrm{d}^m L_k(\bar{\boldsymbol{r}})}{\mathrm{d}\bar{\boldsymbol{r}}^m}.$$

Equations (13) and (14) can be written by incorporating the relation (11):

$$\mathcal{U}'(\bar{\boldsymbol{r}}) = \sum_{k=0}^{\infty} \Lambda_k k F_k(\bar{\boldsymbol{r}}), \tag{15}$$

and similarly, the mth derivative can be computed as

$$\mathcal{U}^{(m)}(\bar{\boldsymbol{r}}) = \sum_{k=0}^{\infty} \Lambda_k k F_k(\bar{\boldsymbol{r}}) D^{m-1}, \tag{16}$$

in which D and D^{m-1} are defined above.

Remark 1. *In numerical computations, the expansion of $\mathcal{U}(\bar{\mathbf{r}})$ and its mth derivative often involves utilizing truncated Fibonacci and Lucas polynomial series. In other words, we take*

$$\mathcal{U}(\bar{\mathbf{r}}) \simeq \sum_{k=0}^{M} \Lambda_k L_k(\bar{\mathbf{r}}), \quad M \in \mathbb{N},$$

and

$$\mathcal{U}^{(m)}(\bar{\mathbf{r}}) \simeq \sum_{k=0}^{M} \Lambda_k L_k^{(m)}(\bar{\mathbf{r}}) = \sum_{k=0}^{M} \Lambda_k k F_k(\bar{\mathbf{r}}) D^{m-1}, \quad M \in \mathbb{N}, \tag{17}$$

3. Suggested Methodology

This section is devoted to formulating the suggested meshless method for approximating the 2D time-fractional Sobolev model equations given in Equations (20) and (21). To simplify the notation throughout the discussion in this section, we introduce the following:

$$\mathcal{U}^{n+1}(\bar{\mathbf{r}}) = \mathcal{U}(r, s, t^{n+1}), \quad \mathcal{U}_{ij}^{n+1} = \mathcal{U}(r_i, s_j, t^{n+1}),$$

where r_i and s_j are the collocation points specified as follows, and $t^n = n \times \delta t$, with δt representing the time step size:

$$r_i = a + ih_r, \;\; s_j = c + jh_s, \quad (i, j = 1, 2, \cdots, M, \; M \in \mathbb{N}),$$

where $h_r = (b-a)/M$ and $h_s = (d-c)/M$ are the mesh step sizes in the r and s spatial directions throughout the spatial domain $\Xi = [a, b] \times [c, d] \subset \mathbb{R}^2$.

3.1. Time Discretization

The widely recognized $L1$-formula, with $\mathcal{O}(\delta t^{2-\xi_1})$ as the approximation order error, where $0 < \xi_1 \leq 1$, is utilized to derive the discrete representation of the $(n+1)$th time level, as outlined in [55,56].

$$\begin{aligned}
\frac{\partial^{\xi_1} \mathcal{U}(\bar{\mathbf{r}}, t^{n+1})}{\partial t^{\xi_1}} &= \frac{1}{\Gamma(1-\xi_1)} \int_0^{t^{n+1}} \frac{\partial \mathcal{U}(\bar{\mathbf{r}}, \zeta)}{\partial \zeta} (t^{n+1} - \zeta)^{-\xi_1} \mathrm{d}\zeta, \\
&= \frac{1}{\Gamma(1-\xi_1)} \sum_{j=0}^{n} \int_{j\times\delta t}^{(j+1)\times\delta t} \frac{\partial \mathcal{U}(\bar{\mathbf{r}}, \zeta)}{\partial \zeta} (t^{n+1} - \zeta)^{-\xi_1} \mathrm{d}\zeta, \\
&= \frac{1}{\Gamma(1-\xi_1)} \sum_{j=0}^{n} \left[\frac{\mathcal{U}^{j+1}(\bar{\mathbf{r}}) - \mathcal{U}^{j}(\bar{\mathbf{r}})}{\delta t} + O(\delta t) \right] \int_{j\times\delta t}^{(j+1)\times\delta t} ((j+1)\delta t - \zeta)^{-\xi_1} \mathrm{d}\zeta.
\end{aligned}$$

Following integration, it gives

$$\frac{\partial^{\xi_1} \mathcal{U}(s, r, t^{n+1})}{\partial t^{\xi_1}} = \begin{cases} A_{\xi_1} \sum_{j=0}^{n} K_{\xi_1}(j) \left[\mathcal{U}^{n-j+1}(\bar{\mathbf{r}}) - \mathcal{U}^{n-j}(\bar{\mathbf{r}}) \right] + O(\delta t^{2-\xi_1}), & 0 < \xi_1 < 1, \\ \frac{\mathcal{U}^{n+1}(\bar{\mathbf{r}}) - \mathcal{U}^{n}(\bar{\mathbf{r}})}{\delta t} + O(\delta t), & \xi_1 = 1, \end{cases} \tag{18}$$

where $A_{\xi_1} = \frac{\delta t^{-\xi_1}}{\Gamma(2-\xi_1)}$ and $K_{\xi_1}(j) = (j+1)^{1-\xi_1} - (j)^{1-\xi_1}$. Therefore, we may write the following for $0 < \xi_1 < 1$ after ignoring the error term:

$$\frac{\partial^{\xi_1} \mathcal{U}(\bar{\mathbf{r}}, t^{n+1})}{\partial t^{\xi_1}} = A_{\xi_1} \left[\mathcal{U}^{n+1}(\bar{\mathbf{r}}) - \mathcal{U}^{n}(\bar{\mathbf{r}}) \right] + A_{\xi_1} \sum_{j=1}^{n} K_{\xi_1}(j) \left[\mathcal{U}^{n-j+1}(\bar{\mathbf{r}}) - \mathcal{U}^{n-j}(\bar{\mathbf{r}}) \right], \tag{19}$$

with $K_{\xi_1}(j) = 1$ and $j = 0$. The fractional derivative of order ξ_2 can be found above.

Before applying the θ-weighted rule to the suggested Equations (1)–(4), let us rewrite them in compact form as follows:

$$\frac{\partial^{\xi_1}\mathcal{U}(\bar{r},t)}{\partial t^{\xi_1}}+\frac{\partial^{\xi_2}\mathcal{U}(\bar{r},t)}{\partial t^{\xi_2}}-\beta\frac{\partial\nabla^2\mathcal{U}(\bar{r},t)}{\partial t}-\delta\nabla^2\mathcal{U}(\bar{r},t)-\eta\nabla(\mathcal{U}(\bar{r},t)\nabla\mathcal{U}(\bar{r},t))+\gamma\mathcal{U}(\bar{r},t)=f(\bar{r},t),\quad \bar{r}\in\Omega\subset\mathbb{R}^d,\ \ d=2,3,\ \ 0<\xi_2\le\xi_1\le 1,\ \ t>0, \tag{20}$$

with the following conditions:

$$\mathcal{U}(\bar{r},0)=\mathcal{U}_0(\bar{r}),\ \mathcal{U}(\bar{r},t)=f_1(\bar{r},t),\ \ \bar{r}\in\partial\Omega, \tag{21}$$

where the Laplacian and gradient operators are represented by the symbols ∇^2 and ∇, respectively.

The θ-weighted rule is now applied, and Equation (20) becomes

$$\begin{aligned}&A_{\xi_1}\mathcal{U}^{n+1}(\bar{r})+A_{\xi_2}\mathcal{U}^{n+1}(\bar{r})-\beta\left(\frac{\nabla^2\mathcal{U}^{n+1}(\bar{r})-\nabla^2\mathcal{U}^{n}(\bar{r})}{\delta t}\right)-\theta\delta\nabla^2\mathcal{U}^{n+1}(\bar{r})+\theta\gamma\mathcal{U}^{n+1}(\bar{r})\\&-\theta\nabla\left(\mathcal{U}^{n+1}(\bar{r})\nabla\mathcal{U}^{n+1}(\bar{r})\right)=A_{\xi_1}\mathcal{U}^{n}(\bar{r})+A_{\xi_2}\mathcal{U}^{n}(\bar{r})+(1-\theta)\delta\nabla^2\mathcal{U}^{n}(\bar{r})+(1-\theta)\eta\nabla(\mathcal{U}^{n}(\bar{r})\nabla\mathcal{U}^{n}(\bar{r}))\\&-(1-\theta)\gamma\mathcal{U}^{n}(\bar{r})+f_\theta^{n+1}(\bar{r})-Q_\xi^n(\bar{r}),\end{aligned} \tag{22}$$

where

$$f_\theta^{n+1}(\bar{r})=\theta f^{n+1}(\bar{r})+(1-\theta)f^n(\bar{r}),$$

and

$$Q_\xi^n(\bar{r})=A_{\xi_1}\sum_{j=1}^{n}K_{\xi_1}(j)\left[\mathcal{U}^{n-j+1}(r,s)-\mathcal{U}^{n-j}(r,s)\right]+A_{\xi_2}\sum_{j=1}^{n}K_{\xi_2}(j)\left[\mathcal{U}^{n-j+1}(r,s)-\mathcal{U}^{n-j}(r,s)\right].$$

Since

$$\nabla\left(\mathcal{U}^{n+1}(\bar{r})\nabla\mathcal{U}^{n+1}(\bar{r})\right)=\mathcal{U}^{n+1}(\bar{r})\nabla^2\mathcal{U}^{n+1}(\bar{r})+\left(\mathcal{U}_x^{n+1}(\bar{r})\right)^2+\left(\mathcal{U}_y^{n+1}(\bar{r})\right)^2,$$

the nonlinear terms are linearized as follows [24]:

$$\mathcal{U}^{n+1}(\bar{r})\nabla^2\mathcal{U}^{n+1}(\bar{r})\equiv\mathcal{U}^{n+1}(\bar{r})\nabla^2\mathcal{U}^{n}(\bar{r})+\mathcal{U}^{n}(\bar{r})\nabla^2\mathcal{U}^{n+1}(\bar{r})-2\mathcal{U}^{n}(\bar{r})\nabla^2\mathcal{U}^{n}(\bar{r}), \tag{23}$$

$$\left(\mathcal{U}_r^{n+1}(\bar{r})\right)^2\equiv 2\mathcal{U}_r^{n}(\bar{r})\mathcal{U}_r^{n+1}(\bar{r})-(\mathcal{U}_r^{n}(\bar{r}))^2, \tag{24}$$

$$\left(\mathcal{U}_s^{n+1}(\bar{r})\right)^2\equiv 2\mathcal{U}_s^{n}(\bar{r})\mathcal{U}_s^{n+1}(\bar{r})-(\mathcal{U}_s^{n}(\bar{r}))^2. \tag{25}$$

The insertion of Equations (23)–(25) and simple rearrangement reduces Equation (22) to

$$\left(A_{\xi_1}+A_{\xi_2}+\theta\gamma-\theta\nabla^2\mathcal{U}^{n}(\bar{r})\right)\mathcal{U}^{n+1}(\bar{r})-\left(\frac{\beta}{\delta t}+\theta\delta-\theta\eta\mathcal{U}^{n}(\bar{r})\right)\nabla^2\mathcal{U}^{n+1}(\bar{r}) \tag{26}$$

$$=\left(A_{\xi_1}+A_{\xi_2}-(1-\theta)\gamma\right)\mathcal{U}^{n}(\bar{r})-\left(\frac{\beta}{\delta t}-(1-\theta)\delta\right)\nabla^2\mathcal{U}^{n}(\bar{r})+H_\theta^{n+1}(\bar{r})-G_\theta^{n}(\bar{r}), \tag{27}$$

where

$$H_\theta^{n+1}(\bar{r})=\begin{cases}f_\theta^{n+1}-Q_\xi^n\mathcal{U}^n(\bar{r}), & n\ge 1,\\ f_\theta^1, & n=1,\end{cases} \tag{28}$$

and

$$G_\theta^n(\bar{r})=\eta\theta\left(2\mathcal{U}^n(\bar{r})\nabla^2\mathcal{U}^n(\bar{r})+(\mathcal{U}_x^n(\bar{r}))^2+\left(\mathcal{U}_y^n(\bar{r})\right)^2\right)+(1-\theta)\eta\nabla(\mathcal{U}^n(\bar{r})\nabla\mathcal{U}^n(\bar{r})).$$

Let us label

$$p_\theta^n(\bar{\boldsymbol{r}}) = A_{\xi_1} + A_{\xi_2} + \theta\gamma - \theta\eta\nabla^2\mathcal{U}^n(\bar{\boldsymbol{r}}),\ \ q_\theta^n = \frac{\beta}{\delta t} + \delta\theta - \theta\eta\mathcal{U}^n(\bar{\boldsymbol{r}}),$$
$$r_\theta = A_{\xi_1} + A_{\xi_2} - (1-\theta)\gamma,\ \ s_\theta = \frac{\beta}{\delta t} - (1-\theta)\delta,$$

which, when substituted into Equation (26), give us

$$p_\theta^n\mathcal{U}^{n+1}(\bar{\boldsymbol{r}}) - q_\theta^n\nabla^2\mathcal{U}^{n+1}(\bar{\boldsymbol{r}}) = r_\theta\mathcal{U}^n(\bar{\boldsymbol{r}}) + s_\theta\nabla^2\mathcal{U}^n(\bar{\boldsymbol{r}}) + H_\theta^{n+1}(\bar{\boldsymbol{r}}) - G_\theta^n(\bar{\boldsymbol{r}}). \tag{29}$$

We have approximated in the time direction at this point using Equation (29). Furthermore, the time direction is coupled with the splitting technique known as the Strang splitting algorithm, which is given as follows [4,57–59]:

$$\frac{\partial\mathcal{U}_1}{\partial t} = \mathscr{L}_1\mathcal{U}_1(t) \ \text{ with } \ t \in [t^n, t^{n+1/2}] \ \text{ and } \mathcal{U}_1(t^n) = \mathcal{U}_{sp}^n \tag{30}$$

$$\frac{\partial\mathcal{U}_2}{\partial t} = \mathscr{L}_2\mathcal{U}_2(t) \ \text{ with } \ t \in [t^n, t^{n+1}] \ \text{ and } \mathcal{U}_2(t^n) = \mathcal{U}_1(t^{n+1/2}) \tag{31}$$

$$\frac{\partial\mathcal{U}_3}{\partial t} = \mathscr{L}_1\mathcal{U}_3(t) \ \text{ with } \ t \in [t^{n+1/2}, t^{n+1}] \ \text{ and } \mathcal{U}_3(t^{n+1/2}) = \mathcal{U}_2(t^{n+1}) \tag{32}$$

where $\mathcal{L}_1\mathcal{U}(t) = \delta\nabla^2\mathcal{U}(t) - \eta\big(\mathcal{U} * \nabla^2\mathcal{U}(t)\big)$, $\mathcal{L}_2\mathcal{U}(t) = -\eta(\nabla\mathcal{U}(t))^2 - \gamma\mathcal{U}(t)$, and $\mathcal{U}_{sp}^n = \mathcal{U}_0$ is the initial solution defined for Equation (20). The Strang splitting method achieves second-order accuracy. Further information can be found in reference [4].

3.2. Spatial Discretization

We can expand the function $\mathcal{U}(\bar{\boldsymbol{r}})$, which is a two-dimensional function denoted as $\mathcal{U}(r,s)$, into the following truncated series of Lucas polynomials, expressed as a product:

$$\mathcal{U}(r,s) \simeq \sum_{k=0}^{M}\sum_{m=0}^{M}\Lambda_{km}L_k(r)L_m(s) = \sum_{k=0}^{M}\sum_{m=0}^{M}\Lambda_{km}\mathcal{L}_{km}(r,s), \tag{33}$$

where $\mathcal{L}_{km}(r,s) = L_k(r)L_m(s)$. Equation (33) can be expressed in compact form as

$$\mathcal{U}(r,s) \simeq \mathbf{L}^{\mathrm{T}}(r,s)\boldsymbol{\Lambda}, \tag{34}$$

with $\boldsymbol{\Lambda} = [\Lambda_{00}, \Lambda_{01}, \Lambda_{10}, \cdots, \Lambda_{MM}]^{\mathrm{T}}$ and $\mathbf{L}^{\mathrm{T}}(r,s) = [\mathcal{L}_{00}(r,s), \mathcal{L}_{01}(r,s), \mathcal{L}_{10}(r,s), \cdots, \mathcal{L}_{MM}(r,s)]$.

One can compute and briefly represent the consolidated partial derivatives of $\mathcal{U}(r,s)$ as follows:

$$\frac{\partial\mathcal{U}(r,s)}{\partial r} \simeq \sum_{k=0}^{M}\sum_{m=0}^{M}\Lambda_{km}\frac{\mathrm{d}L_k(r)}{\mathrm{d}r}L_m(s) = \sum_{k=0}^{M}\sum_{m=0}^{M}\Lambda_{km}k(F_k(r))L_m(s) = \mathbf{L}_r^{\mathrm{T}}(r,s)\boldsymbol{\Lambda},$$

and

$$\frac{\partial^2\mathcal{U}(r,s)}{\partial r^2} \simeq \sum_{k=0}^{M}\sum_{m=0}^{M}\Lambda_{km}\frac{\mathrm{d}^2L_k(r)}{\mathrm{d}r^2}L_m(s) = \sum_{k=0}^{M}\sum_{m=0}^{M}\Lambda_{km}k(F_k(r)D)L_m(s) = \mathbf{L}_{rr}^{\mathrm{T}}(r,s)\boldsymbol{\Lambda},$$

where

$$\mathbf{L}_r^{\mathrm{T}}(r,s) = \{\frac{\partial}{\partial r}\mathcal{L}_{km}(r,s)\}_{k,m=0}^{M} = \{\frac{\mathrm{d}L_k(r)}{\mathrm{d}r}L_m(s)\}_{k,m=0}^{M} = \{k(F_k(r))L_m(s)\}_{k,m=0}^{M},$$

$$\mathbf{L}_{rr}^{\mathrm{T}}(r,s) = \{\frac{\partial^2}{\partial r^2}\mathcal{L}_{km}(r,s)\}_{k,m=0}^{M} = \{\frac{\mathrm{d}^2L_k(r)}{\mathrm{d}r^2}L_m(s)\}_{k,m=0}^{M} = \{k(F_k(r)D)L_m(s)\}_{k,m=0}^{M}.$$

Similarly

$$\frac{\partial \mathcal{U}(r,s)}{\partial s} \simeq \sum_{k=0}^{M}\sum_{m=0}^{M} \Lambda_{km} L_k(r) \frac{\mathrm{d}L_m(s)}{\mathrm{d}r} = \sum_{k=0}^{M}\sum_{m=0}^{M} \Lambda_{km} m L_k(r)(F_m(s)) = \mathbf{L}_s^{\mathrm{T}}(r,s)\mathbf{\Lambda},$$

and

$$\frac{\partial^2 \mathcal{U}(r,s)}{\partial s^2} \simeq \sum_{k=0}^{M}\sum_{m=0}^{M} \Lambda_{km} L_k(r) \frac{\mathrm{d}^2 L_m(s)}{\mathrm{d}s^2} = \sum_{k=0}^{M}\sum_{m=0}^{M} \Lambda_{km} m L_k(r)(F_m(s)D) = \mathbf{L}_{ss}^{\mathrm{T}}(r,s)\mathbf{\Lambda},$$

with

$$\mathbf{L}_s^{\mathrm{T}}(r,s) = \{\frac{\partial}{\partial s}\mathcal{L}_{km}(r,s)\}_{k,m=0}^{M} = \{L_k(r)\frac{\mathrm{d}^2 L_m(s)}{\mathrm{d}s^2}\}_{k,m=0}^{M} = \{mL_k(r)(F_m(s))\}_{k,m=0}^{M}.$$

$$\mathbf{L}_{ss}^{\mathrm{T}}(r,s) = \{\frac{\partial^2}{\partial s^2}\mathcal{L}_{km}(r,s)\}_{k,m=0}^{M} = \{L_k(r)\frac{\mathrm{d}^2 L_m(s)}{\mathrm{d}s^2}\}_{k,m=0}^{M} = \{mL_k(r)(F_m(s)D)\}_{k,m=0}^{M}.$$

These results can be further refined as

$$\nabla \mathcal{U}(r,s) = \frac{\partial \mathcal{U}}{\partial r} + \frac{\partial \mathcal{U}}{\partial s} \simeq \left(\mathbf{L}_r^{\mathrm{T}}(r,s) + \mathbf{L}_s^{\mathrm{T}}(r,s)\right)\mathbf{\Lambda}. \tag{35}$$

$$\nabla^2 \mathcal{U}(r,s) = \frac{\partial^2 \mathcal{U}}{\partial r^2} + \frac{\partial^2 \mathcal{U}}{\partial s^2} \simeq \left(\mathbf{L}_{rr}^{\mathrm{T}}(r,s) + \mathbf{L}_{ss}^{\mathrm{T}}(r,s)\right)\mathbf{\Lambda}. \tag{36}$$

It is consequently possible to express the time-dependent function $\mathcal{U}(r,s,t)$ and its compact form partial derivatives as follows:

$$\mathcal{U}(r,s,t) \approx \mathbf{L}^{\mathrm{T}}(r,s)\mathbf{\Lambda}(t),\ \frac{\partial^2 \mathcal{U}(r,s,t)}{\partial r^2} \approx \mathbf{L}_{rr}^{\mathrm{T}}(r,s)\mathbf{\Lambda}(t),\ \frac{\partial^2 \mathcal{U}(r,s,t)}{\partial s^2} \approx \mathbf{L}_{ss}^{\mathrm{T}}(r,s)\mathbf{\Lambda}(t), \tag{37}$$

with

$$\nabla \mathcal{U}(r,s,t) \approx \Big(\mathbf{L}_r^{\mathrm{T}}(r,s) + \mathbf{L}_s^{\mathrm{T}}(r,s)\Big)\mathbf{\Lambda}(t),\ \ \nabla^2 \mathcal{U}(r,s,t) \approx \Big(\mathbf{L}_{rr}^{\mathrm{T}}(r,s) + \mathbf{L}_{ss}^{\mathrm{T}}(r,s)\Big)\mathbf{\Lambda}(t), \tag{38}$$

where $\mathbf{\Lambda}(t)$ represents the vector of the time-varying unknown coefficients. Once the information obtained from Equations (37) and (38) is combined with Equation (29), we obtain

$$\begin{aligned} &p_\theta^n \mathbf{L}(r,s)\mathbf{\Lambda}^{n+1} - q_\theta^n \Big(\mathbf{L}_{rr}^{\mathrm{T}}(r,s) + \mathbf{L}_{ss}^{\mathrm{T}}(r,s)\Big)\mathbf{\Lambda}^{n+1} \\ &= r_\theta \mathbf{L}(r,s)\mathbf{\Lambda}^n + r_\theta \Big(\mathbf{L}_{rr}^{\mathrm{T}}(r,s) + \mathbf{L}_{ss}^{\mathrm{T}}(r,s)\Big)\mathbf{\Lambda}^n + \mathbf{H}_\theta^{n+1}(r,s) - \mathbf{G}_\theta^n(r,s), \quad \forall (r,s) \in \Omega. \end{aligned} \tag{39}$$

The boundary conditions are stated as

$$\mathbb{B}\mathbf{L}(r,s)\mathbf{\Lambda}^{n+1} \approx f_1(r,s,t^{n+1}) = f_1^{n+1}(r,s), \quad \forall (r,s) \in \partial\Omega, \tag{40}$$

where $\mathbf{\Lambda}^n = \mathbf{\Lambda}(t^n)$.

3.3. Full Discretization

We collocate Equations (39) and (40) at discrete mesh points r_i and s_j at their respective time levels to derive the discrete form of the time-fractional differential equation as expressed in Equation (20), resulting in the subsequent set of equations:

$$\begin{aligned} &p_\theta^n \mathbf{L}(r_i,s_j)\mathbf{\Lambda}^{n+1} - q_\theta^n \Big(\mathbf{L}_{rr}^{\mathrm{T}}(r_i,s_j) + \mathbf{L}_{ss}^{\mathrm{T}}(r_i,s_j)\Big)\mathbf{\Lambda}^{n+1} \\ &= s_\theta \mathbf{L}(r_i,s_j)\mathbf{\Lambda}^n + r_\theta \Big(\mathbf{L}_{rr}^{\mathrm{T}}(r_i,s_j) + \mathbf{L}_{ss}^{\mathrm{T}}(r_i,s_j)\Big)\mathbf{\Lambda}^n + \mathbf{H}_\theta^{n+1}(r_i,s_j) - \mathbf{G}_\theta^n(r_i,s_j), \quad \forall (r_i,s_j) \in \Omega, \end{aligned}$$

and

$$\mathbb{B}\mathbf{L}(r_i, s_j)\mathbf{\Lambda}^{n+1} \approx f_1(r_i, s_j, t^{n+1}) = f_1^{n+1}(r_i, s_j), \quad \forall (r_i, s_j) \in \partial\Omega,$$

where $i, j = 0, 1, 2, \cdots, M$. This implies the following matrix–vector form:

$$\mathcal{G}\mathbf{\Lambda}^{n+1} = \mathcal{H}\mathbf{\Lambda}^n + \mathcal{Q}^{n+1}. \tag{41}$$

In this case, the matrix entries are provided by

$$(\mathcal{G})_{ij} = \begin{cases} p_\theta^n \mathbf{L}(r_i, s_j) - q_\theta^n \Big(\mathbf{L}_{rr}^{\mathrm{T}}(r_i, s_j) + \mathbf{L}_{ss}^{\mathrm{T}}(r_i, s_j) \Big), & (r_i, s_j) \in \Omega, \\ \mathbb{B}\mathbf{L}(r_i, s_j), & (r_i, s_j) \in \partial\Omega, \end{cases} \tag{42}$$

$$(\mathcal{H})_{ij} = \begin{cases} s_\theta \mathbf{L}(r_i, s_j) + r_\theta \Big(\mathbf{L}_{rr}^{\mathrm{T}}(r_i, s_j) + \mathbf{L}_{ss}^{\mathrm{T}}(r_i, s_j) \Big), & (r_i, s_j) \in \Omega, \\ 0, & (r_i, s_j) \in \partial\Omega, \end{cases} \tag{43}$$

and

$$(\mathcal{Q})_{ij} = \begin{cases} \mathbf{H}_\theta^{n+1}(r_i, s_j) - \mathbf{G}_\theta^n(r_i, s_j), & (r_i, s_j) \in \Omega, \\ f_1(r_i, s_j, t^{n+1}), & (r_i, s_j) \in \partial\Omega. \end{cases} \tag{44}$$

The construction of the scheme for the two-dimensional model equation is finalized. Simplifying it to a one-dimensional form involves eliminating the variable s so that $\bar{r} = r$. The linear system represented by Equation (41) benefits from the assurances provided by [47], ensuring the existence of a solution. Solving Equation (41) allows for the determination of the vector containing unknown coefficients at every time step. The initial condition allows for initialization in the following manner:

$$\mathbf{L}^{\mathrm{T}}(r_i, s_j)\mathbf{\Lambda}^0 = \mathcal{U}(r_i, s_j, 0) = \mathcal{U}_0 \Longrightarrow \mathbf{A}\mathbf{\Lambda}^0 = \mathcal{U}_\mathbf{0}.$$

When solved, it yields $\mathbf{\Lambda}^0$. Utilizing Equation (41), the iteration is subsequently repeated up to the relevant time level. Upon obtaining the coefficients vector, the solution at the corresponding time level can be determined by

$$\mathcal{U}(r_i, s_j, t^n) = \mathbf{L}^{\mathrm{T}}(r_i, s_j)\mathbf{\Lambda}^n, \quad \forall (r_i, s_j) \in \Omega, \ (n \geq 0).$$

A similar procedure can be used in the case of a three-dimensional problem.

4. Analyzing Errors

To conduct the error analysis, we referred to the following theorem.

Theorem 1. *The error can be defined as follows when denoting the exact solution as $\widehat{\mathbb{U}}$ and the computed solution obtained by the suggested meshless method as $\mathcal{U}$ for the underlying problems.*

The error term $\mathcal{E}$ is constrained within the following expression:

$$|\mathcal{E}| \leq \frac{4\exp(2\kappa)\cosh^2(2\mathcal{P})\kappa^{2(N+1)}}{((N+1)!)^2}.$$

Proof. Consider the absolute error between the exact solution and the approximate numerical solution using the proposed hybrid meshless method:

$$|\mathcal{E}| = |\widehat{\mathbb{U}} - \mathcal{U}|,$$

where $\widehat{\mathbb{U}} = \sum_{k=0}^{\infty}\sum_{m=0}^{\infty}\Lambda_k\Lambda_m L_k(r)L_m(s)$ and $\mathscr{U} = \sum_{k=0}^{M}\sum_{m=0}^{M}\Lambda_k\Lambda_m L_k(r)L_m(s)$. Next, the truncated term is as follows:

$$|\mathcal{E}| = \sum_{k=N+1}^{\infty}\sum_{m=N+1}^{\infty}\Lambda_k\Lambda_m L_k(r)L_m(s) \tag{45}$$

In [60], it is demonstrated that

$$L_m(r) \leq 2\vartheta^m,$$

$$|\Lambda_m| \leq \frac{\mathcal{P}^m\cosh(2\mathcal{P})}{m!},$$

where the famous golden ratio is denoted by ϑ. Consequently, Equation (45) suggests that

$$|\mathcal{E}| = 4\cosh^2(2\mathcal{P})\sum_{k=N+1}^{\infty}\sum_{m=N+1}^{\infty}\frac{\kappa^{k+m}}{k!m!},$$

where $\kappa = \mathcal{P}\vartheta$. This inequality can alternatively be expressed as

$$|\mathcal{E}| = 4\exp(2\kappa)\cosh^2(2\mathcal{P})\left[1 - \frac{\Gamma(N+1,\kappa)}{\Gamma(N+1)}\right]^2. \tag{46}$$

The incomplete gamma function in this case is $\Gamma(N+1,\kappa)$, and the complete gamma function is $\Gamma(N+1)$ [61]. Equation (46) can be expressed in integral form as follows:

$$|\mathcal{E}| \leq \frac{4\exp(2\kappa)\cosh^2(2\mathcal{P})}{(N!)^2}\left[\int_0^{\kappa} t^N\exp(-t)dt\right]^2.$$

Since $\exp(-t) < 1, \forall t > 0$, we obtain:

$$|\mathcal{E}| \leq \frac{4\exp(2\kappa)\cosh^2(2\mathcal{P})\kappa^{2(N+1)}}{((N+1)!)^2}.$$

□

Stability Analysis

The stability of the meshless method is crucial for ensuring the accuracy and convergence of numerical solutions over time. By mitigating numerical instabilities, the meshless method maintains the solution quality and reliability across diverse computational domains. The stability analysis was carried out in this work by utilizing a matrix technique. The methodology employed was consistent with that described in previous studies [24,62].

Theorem 2. *Consider w as the computed approximate solution to the underlying problem. In this context, the amplification matrix F is defined as $F = L\mathcal{G}^{-1}\mathcal{H}L^{-1}$. It is essential to confirm that the absolute maximum eigenvalue of F, denoted as $\rho(F)$, stays less than or equal to 1 to ensure stability.*

Proof. We aim to show that $F = L\mathcal{G}^{-1}\mathcal{H}L^{-1}$. From Equation (17), we write

$$\mathbf{\Lambda}^n = L^{-1}\mathscr{U}^n. \tag{47}$$

The relationship can be described utilizing Equation (41):

$$\mathscr{U}^{n+1} = L\mathcal{G}^{-1}\mathcal{H}L^{-1}\mathscr{U}^n + L\mathcal{G}^{-1}\mathcal{Q}^{n+1}. \tag{48}$$

Moreover, the error vector

$$\mathcal{E} = \widehat{\mathbb{U}} - \mathscr{U}, \tag{49}$$

satisfies the following condition:

$$\mathcal{E}^{n+1} = F\mathcal{E}^n.$$

Thus, the amplification matrix is defined as $F = L\mathcal{G}^{-1}\mathcal{H}L^{-1}$. Adherence to the Lax–Richtmyer stability criterion [63], which requires that

$$||F|| \leq 1,$$

ensures the stability of the method. An illustration demonstrating that the spectral radius $\rho(F)$ must not exceed 1 to fulfill this condition is provided in the subsequent section. □

5. Discussion and Numerical Results

The proposed hybrid meshless method (HMM) was assessed for its effectiveness and precision in solving model Equations (1) and (2). The evaluation includes various scenarios with both uniform and scattered nodes in non-rectangular and rectangular domains. The CPU time was measured in seconds for all cases. All computations were performed on an HP PC laptop equipped with an Intel(R) Core(TM) i5-7200U CPU @ 2.50 GHz 2.71 GHz and 8 GB of RAM, using MATLAB (R2012a) software.

The accuracy was measured using error norms, including the following:

$$e_\infty = \max(|\widehat{\mathbb{U}} - \mathcal{U}|),\ \ e_{rms} = \sqrt{\frac{\sum_{i=1}^{N}\left(\widehat{\mathbb{U}}_i - \mathcal{U}_i\right)^2}{N}},\ \ e_{L2} = \sqrt{\delta h \sum_{h=1}^{N}\left(\widehat{\mathbb{U}}_h - \mathcal{U}_h\right)^2}, \tag{50}$$

where the exact solution is $\widehat{\mathbb{U}}$, while the approximate solution is $\mathcal{U}$.

Problem 1. *The exact solution of model* (1) *with* $\delta = 1$ *and* $\eta = \gamma = 0$ *is*

$$\mathcal{U}(\bar{\mathbf{r}}, t) = e^{-t}\sin(\pi r)\sin(\pi s),\quad \bar{\mathbf{r}} = (r, s) \in \Omega. \tag{51}$$

The numerical results of the proposed hybrid meshless method were used to compute the numerical solution of Problem 1, as shown in Table 1. The e_∞ *norm was obtained for the final times* $t = 1$ *and* $t = 5$*. The obtained numerical results were compared with the method reported in [17]. The results using explicit, implicit, and Crank–Nicolson schemes for the proposed method were computed for different time step sizes, and one could conclude that as the time step size* δt *decreased, the accuracy of the proposed method increased. The comparison shows that the HMM was more accurate than the method given in [17]. In Table 2, the numerical results are presented, where they were computed by the proposed method using different fractional orders* ξ*, various nodal points* N*,* $\delta t = 0.001$*, and* $t = 1$*. The results were computed as* e_∞ *and* e_{rms} *norms. It can be observed that increasing the number of nodes improved the accuracy to some extent, whereas changing the fractional order did not significantly affect the accuracy. In this case, the HMM yielded good and accurate results. Additionally, the CPU time is provided in this table, demonstrating the efficiency of the suggested method.*

Comparative results of the HMM and [17] are presented in Figure 1 for various nodes in the form of different error norms. It can be observed that the results produced by the HMM were superior to those of [17]. Furthermore, Figure 2 depicts the comparison of the numerically computed solution with the exact solution, along with the absolute error.

Table 1. Problem 1 numerical results using HMM and [17].

Method	δt	e_∞			
		$t = 1$		$t = 5$	
		MQ [17]	HMM	MQ [17]	HMM
Explicit	0.1	1.8985×10^{-2}	8.5002×10^{-3}	1.5971×10^{-3}	8.3765×10^{-4}
	0.05	9.2780×10^{-3}	5.3215×10^{-3}	8.2371×10^{-4}	5.1759×10^{-4}
	0.025	4.5880×10^{-3}	1.0717×10^{-3}	4.1804×10^{-4}	1.0352×10^{-4}
	0.0125	2.2815×10^{-3}	9.0701×10^{-3}	2.1057×10^{-4}	9.0047×10^{-5}
	0.00625	1.1377×10^{-3}	8.0520×10^{-4}	1.0567×10^{-4}	8.6471×10^{-5}
Implicit	0.1	1.7500×10^{-2}	8.3842×10^{-3}	1.7904×10^{-3}	8.5478×10^{-4}
	0.05	8.9133×10^{-3}	5.2547×10^{-3}	8.7217×10^{-4}	5.5662×10^{-4}
	0.025	4.4982×10^{-3}	1.1406×10^{-3}	4.3024×10^{-4}	1.0639×10^{-4}
	0.0125	2.2594×10^{-3}	9.9320×10^{-4}	2.1364×10^{-4}	9.9331×10^{-5}
	0.00625	1.1323×10^{-3}	8.1481×10^{-4}	1.0645×10^{-4}	8.1101×10^{-5}
Crank–Nicolson	0.1	3.0659×10^{-4}	9.0152×10^{-5}	3.0957×10^{-5}	8.3810×10^{-6}
	0.05	8.4249×10^{-5}	1.2486×10^{-5}	8.4718×10^{-6}	1.1754×10^{-6}
	0.025	2.4213×10^{-5}	6.2692×10^{-6}	2.3901×10^{-6}	3.1455×10^{-7}
	0.0125	7.1414×10^{-6}	8.6427×10^{-7}	6.8938×10^{-7}	8.0157×10^{-8}
	0.00625	2.1392×10^{-6}	1.1503×10^{-7}	2.0203×10^{-7}	5.8023×10^{-8}

Table 2. Problem 1 numerical results using HMM.

N	$\xi_1 = \xi_2 = 0.1$		$\xi_1 = \xi_2 = 0.5$		$\xi_1 = \xi_2 = 0.9$		CPU Time
	e_∞	e_{ems}	e_∞	e_{ems}	e_∞	e_{ems}	
10	3.1204×10^{-9}	2.7813×10^{-9}	4.2101×10^{-9}	3.7823×10^{-9}	5.9105×10^{-9}	3.7930×10^{-9}	15.64
20	2.6534×10^{-9}	2.6591×10^{-9}	3.6587×10^{-9}	3.6901×10^{-9}	3.8257×10^{-9}	3.7133×10^{-9}	18.89
25	2.0673×10^{-9}	2.2873×10^{-9}	3.2510×10^{-9}	3.1246×10^{-9}	3.2780×10^{-9}	3.3854×10^{-9}	19.05

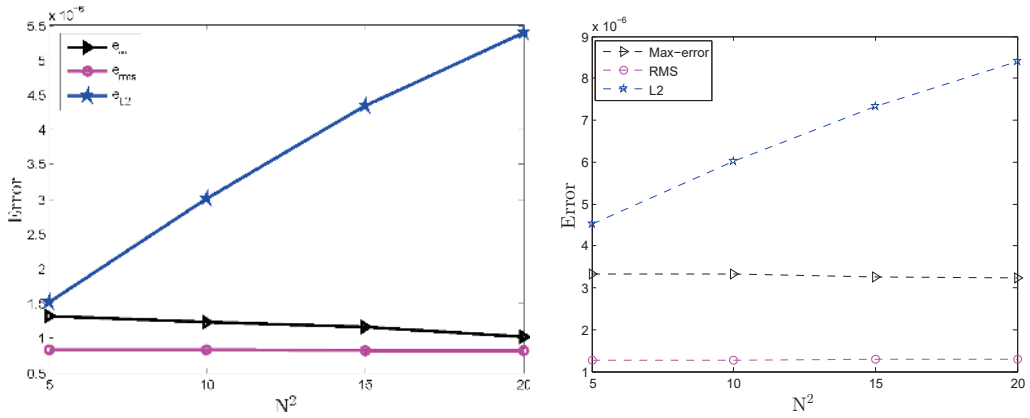

Figure 1. Problem 1 error norms using HMM (**left**) and [17] (**right**).

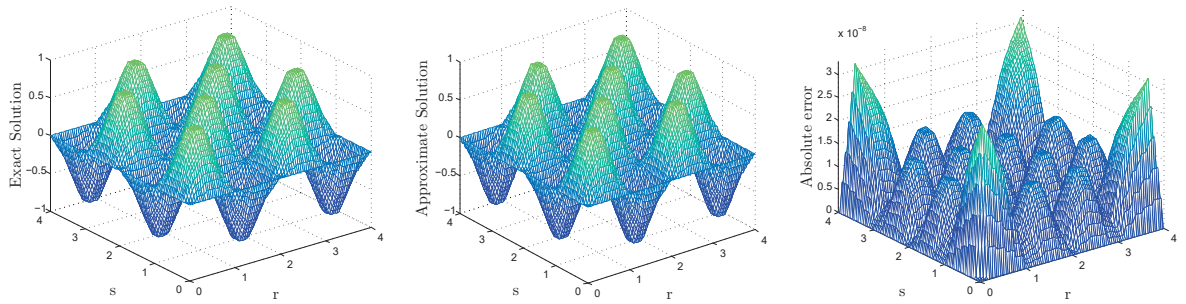

Figure 2. Problem 1 exact and numerical solutions using HMM with absolute error.

Problem 2. *Consider the model Equation* (1) *with* $\beta = 1$ *and* $\gamma = \delta = 0$ *having the exact solution*

$$\mathcal{U}(\bar{\mathbf{r}}, t) = e^{r-s-t}\sin(\pi r)\sin(\pi s), \quad \bar{\mathbf{r}} = (r, s) \in \Omega. \tag{52}$$

Meshless methods offer the advantage of computing solutions without being constrained by the computational geometry. These methods naturally adjust to the geometry of the domain and offer greater flexibility in handling boundary conditions. Additionally, meshless methods often exhibit excellent scalability and parallelizability, making them suitable for large-scale simulations. To assess the true effectiveness of the proposed meshless method, various irregular geometries were examined. To evaluate the performance of the proposed HMM in non-rectangular domains, as shown in Figure 3 for Problem 2, Table 3 presents the numerical results obtained using $\xi_1 = \xi_2 = 0.5$ *and* $\delta t = 0.0001$*, along with various time values, in comparison with the method outlined in [17]. The table illustrates that the HMM achieved greater accuracy compared with [17]. Additionally, in Table 4, the numerical outcomes derived from the proposed HMM were utilized to compute the* e_{L_2} *norm for* δt*, which was then compared with the results obtained using the method reported in [17]. Employing explicit, implicit, and Crank–Nicolson schemes, the proposed method's results were calculated for different time step sizes, demonstrating that decreasing* δt *enhanced the accuracy of the proposed approach. This comparison highlights the superior performance of the HMM over the method described in [17].*

Figure 4 presents a comparison of the HMM results with those in [17] using various error norms for different fractional orders ξ*. Once again, the HMM demonstrated superior performance. Figure 5 illustrates the close agreement between the exact and numerical solutions of Problem 2 with the parameters* $\xi = 0.5$*,* $N = 10^2$*,* $\delta t = 0.001$*, and time* $t = 0.5$ *in terms of the absolute error.*

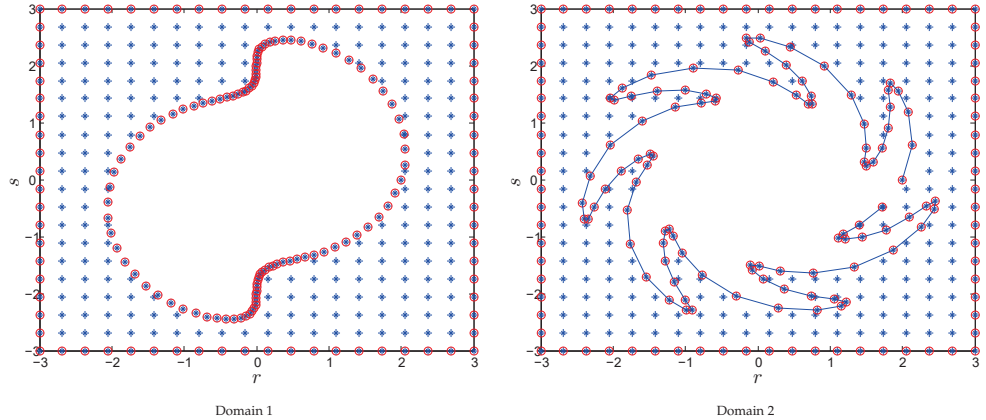

Figure 3. Computational domains.

Table 3. Problem 2 numerical results of HMM using domains given in Figure 3.

Time	Error Norm	Domain 1 HMM	Domain 2 HMM	Domain 2 IQ [17]	Domain 2 MQ [17]	Domain 2 IMQ [17]
t = 1	e_∞	7.0321×10^{-5}	8.1482×10^{-4}	2.8503×10^{-3}	1.0762×10^{-4}	1.6486×10^{-4}
	e_{rms}	6.2456×10^{-6}	8.2453×10^{-5}	5.3969×10^{-4}	1.2498×10^{-5}	1.6465×10^{-5}
	e_{L2}	6.2710×10^{-5}	9.3608×10^{-4}	5.8179×10^{-3}	1.3473×10^{-4}	1.7749×10^{-4}
t = 2	e_∞	3.1438×10^{-5}	4.1930×10^{-5}	6.9177×10^{-3}	7.4827×10^{-5}	1.2021×10^{-4}
	e_{rms}	4.4711×10^{-6}	5.591×10^{-6}	1.1019×10^{-3}	8.9038×10^{-6}	1.2001×10^{-5}
	e_{L2}	5.5379×10^{-5}	5.6283×10^{-5}	1.1879×10^{-2}	9.5983×10^{-5}	1.2937×10^{-4}
t = 3	e_∞	9.3510×10^{-6}	1.8646×10^{-5}	1.9053×10^{-2}	3.9556×10^{-5}	6.5942×10^{-5}
	e_{rms}	1.0392×10^{-6}	2.8366×10^{-6}	2.6854×10^{-3}	4.8116×10^{-6}	6.5818×10^{-6}
	e_{L2}	2.0406×10^{-5}	2.9815×10^{-5}	2.8949×10^{-2}	5.1869×10^{-5}	7.0953×10^{-5}

Table 4. Problem 2 results of HMM and [17] for $\xi_1 = \xi_2 = 0.6$.

		e_{L2}			
		t = 1	t = 1	t = 2	t = 2
Method	δt	HMM	[17]	HMM	[17]
Explicit	0.1	2.0148×10^{-2}	5.1872×10^{-2}	1.3867×10^{-2}	3.7523×10^{-2}
	0.05	9.5461×10^{-3}	2.5444×10^{-2}	8.4984×10^{-3}	1.8637×10^{-2}
	0.025	8.3610×10^{-3}	1.2612×10^{-2}	5.5718×10^{-3}	9.2941×10^{-3}
	0.125	3.4513×10^{-3}	6.2822×10^{-3}	1.9845×10^{-3}	4.6433×10^{-3}
	0.00625	9.3719×10^{-4}	3.1364×10^{-3}	8.3805×10^{-4}	2.3216×10^{-3}
Implicit	0.1	1.3584×10^{-2}	4.8894×10^{-2}	9.7926×10^{-3}	3.7120×10^{-2}
	0.05	9.4241×10^{-3}	2.4862×10^{-2}	7.3200×10^{-3}	1.8657×10^{-2}
	0.025	7.3721×10^{-3}	1.2528×10^{-2}	5.7313×10^{-3}	9.3447×10^{-3}
	0.0125	2.6219×10^{-3}	6.2845×10^{-3}	9.9378×10^{-4}	4.6732×10^{-3}
	0.00125	8.9866×10^{-4}	3.1458×10^{-3}	7.5566×10^{-4}	2.3357×10^{-3}
Crank–Nicolson	0.1	4.3021×10^{-4}	3.5095×10^{-4}	1.5380×10^{-4}	2.5348×10^{-4}
	0.05	7.6320×10^{-5}	9.2813×10^{-5}	7.3817×10^{-5}	7.1868×10^{-5}
	0.025	9.8431×10^{-6}	4.9749×10^{-5}	8.0116×10^{-6}	3.8280×10^{-5}
	0.0125	4.9669×10^{-6}	2.4637×10^{-5}	2.0167×10^{-6}	1.8688×10^{-5}
	0.00625	7.3499×10^{-7}	1.0941×10^{-5}	7.9173×10^{-7}	8.2362×10^{-6}

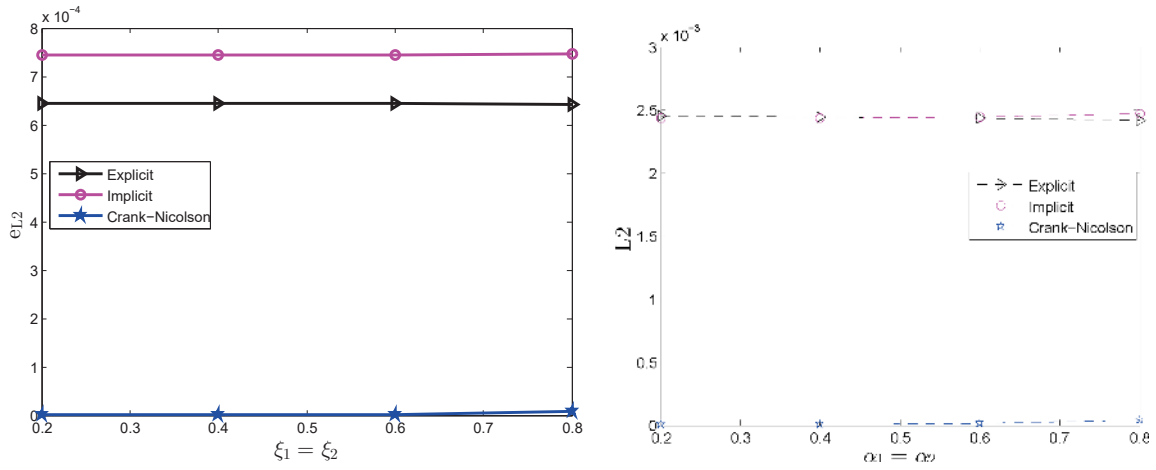

Figure 4. Problem 2 error norms of HMM and [17].

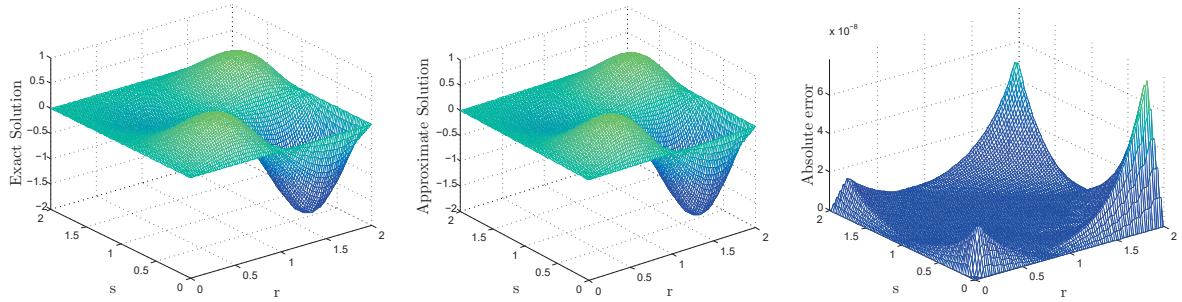

Figure 5. Problem 1 exact and numerical solutions of HMM with absolute error.

Problem 3. *The exact solution of model* (2) *with* $\delta = 1$ *and* $\eta = \gamma = 0$ *is as follows:*

$$\mathcal{U}(\bar{\mathbf{r}}, t) = e^{-t}\sin(\pi r)\sin(\pi s)\sin(\pi z), \quad \bar{\mathbf{r}} = (r, s, z) \in \Omega. \tag{53}$$

The results for Problem 3 were compared with the exact solution and the approach provided in [15] for different values of δt, $N = 10$, *and using* $t = 1$ *and* $\xi_1 = \xi_2 = 0.3$. *This served to illustrate the accurateness and effectiveness of the suggested strategy. These findings are presented in Table 5, along with the CPU time. The table shows that after a few iterations, the suggested meshless technique yielded better results. The accuracy also improved with an increase in the number of iterations, with both error norms reaching as low as* 10^{-10}.

The findings of Problem 3 were computed using the proposed HMM in Table 6, with varying values of fractional order ξ *for* $N = 10$, $t = 1$, *and* $t = 2$. *We evaluated the outcomes in terms of* e_{rms} *and* e_∞. *Accurate results were found for several time-fractional orders in this problem, and these results were also compared with the findings published in [15].*

Table 5. Problem 3 numerical results of HMM and [15].

δt	e_∞	e_{rms}	e_∞ [15]	e_{rms} [15]	CPU Time of HMM
0.1	7.7488×10^{-5}	3.7354×10^{-5}	2.9285×10^{-4}	9.2558×10^{-5}	1.39
0.05	2.6377×10^{-5}	8.5621×10^{-6}	7.3125×10^{-5}	2.3112×10^{-5}	1.54
0.01	6.7313×10^{-7}	3.5478×10^{-7}	2.9195×10^{-6}	9.2271×10^{-7}	2.60
0.005	2.4307×10^{-7}	8.5271×10^{-8}	7.2896×10^{-7}	2.3039×10^{-7}	3.96
0.001	8.1268×10^{-9}	3.2773×10^{-9}	2.9007×10^{-8}	9.1677×10^{-9}	17.73
0.0005	2.4501×10^{-10}	9.9388×10^{-10}	7.2236×10^{-9}	2.2830×10^{-9}	42.14

Table 6. Problem 3 numerical results of HMM and [15].

ξ	$t = 1$				$t = 2$			
	e_∞	e_{rms}	e_∞ [15]	e_{rms} [15]	e_∞	e_{rms}	e_∞ [15]	e_{rms} [15]
0.2	8.69430×10^{-8}	5.3992×10^{-8}	7.3170×10^{-7}	2.3126×10^{-7}	7.9456×10^{-8}	3.9267×10^{-8}	5.3832×10^{-7}	1.7014×10^{-7}
0.4	9.65010×10^{-8}	6.5001×10^{-8}	7.3053×10^{-7}	2.3089×10^{-7}	8.1655×10^{-8}	4.9126×10^{-8}	5.3746×10^{-7}	1.6987×10^{-7}
0.6	9.27650×10^{-8}	8.4952×10^{-8}	7.2584×10^{-7}	2.2940×10^{-7}	7.8037×10^{-8}	5.7601×10^{-8}	5.3402×10^{-7}	1.6878×10^{-7}
0.8	8.72000×10^{-8}	7.3528×10^{-8}	7.0765×10^{-7}	2.2364×10^{-7}	7.6584×10^{-8}	3.9773×10^{-8}	5.2065×10^{-7}	1.6455×10^{-7}

For Problem 3, we considered some non-rectangular domains shown in Figure 6 and in Figure 7 (left) to evaluate the performance of the suggested HMM. In domain 3, scattered nodes were taken into account, as shown in Figure 6 (left). The results obtained in this case are shown in Figure 8, whereas the results for domain 5 are shown in Figure 7 (right) for final times up to $t = 4$. *These results provide evidence of the accurate performance of the HMM in non-rectangular domains.*

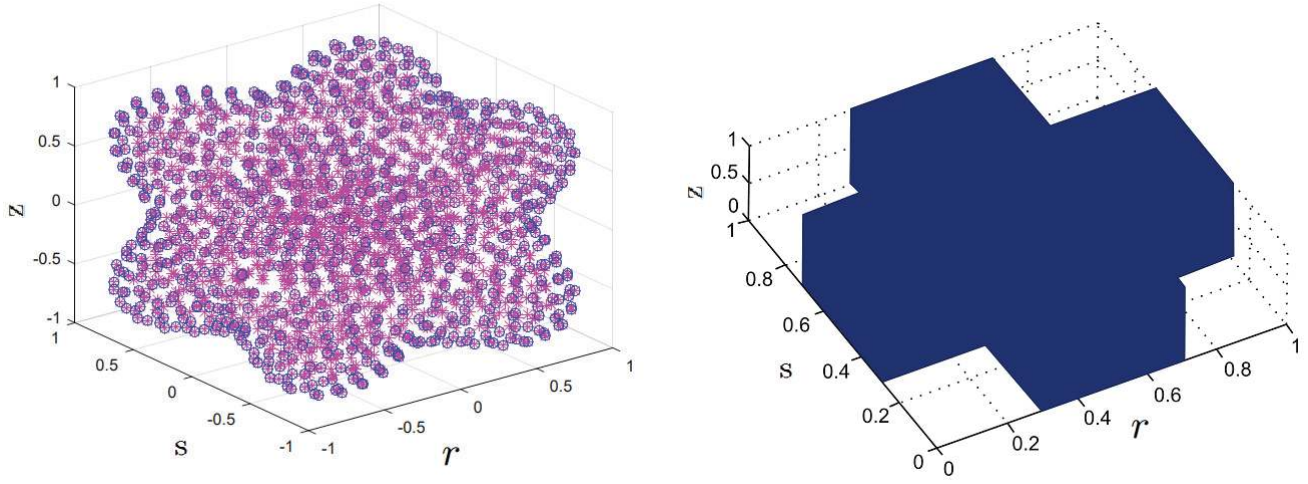

Domain 3 Domain 4

Figure 6. Computational domains.

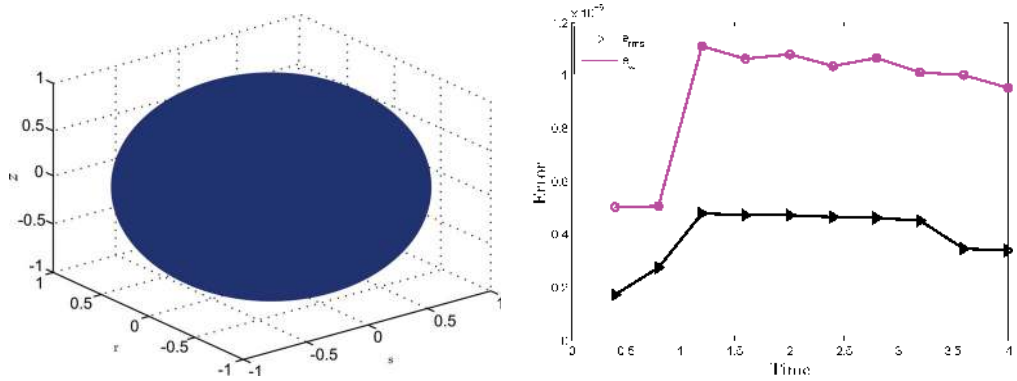

Domain 5

Figure 7. Problem 3 domain 5 (**left**) and error (**right**).

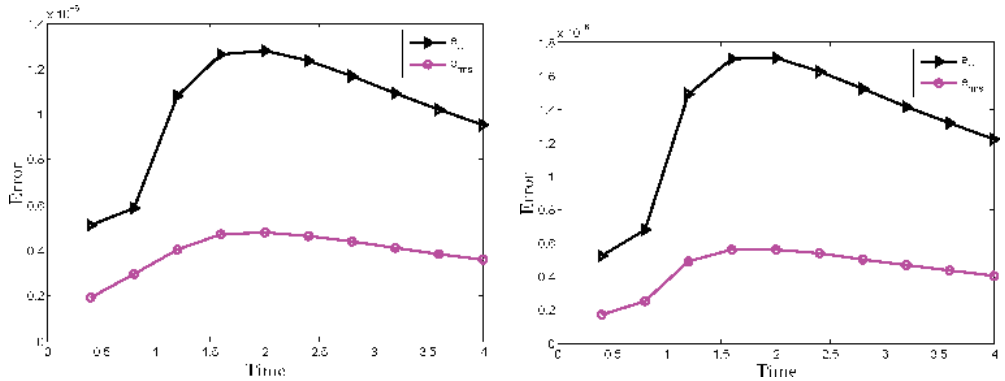

Figure 8. Problem 3 error norms using domain 3 (**left**) and domain 4 (**right**).

Problem 4. *The exact solution for Equation* (2) *with* $\beta = 1$, $\gamma = 1$, *and* $\delta = \pi^2$ *is*

$$\mathcal{U}(\bar{\mathbf{r}}, t) = e^t \sin(\pi r) \sin(\pi s) \sin(\pi z), \quad \bar{\mathbf{r}} = (r, s, z) \in \Omega. \tag{54}$$

For Problem 4, the behavior of the numerical and exact solutions using $N = 21$ *and* $t = 0.01$ *are visualized in Figure 9 at* $z = 0.5$ *and* $\xi_1 = \xi_2 = 0.5$, *along with the absolute error. One can see from these figures that the approximate solution was very compatible with the exact solution. Also, Figure 10 shows the contour graph of the problem at* $\xi_1 = \xi_2 = 0.3$ *and* $\xi_1 = \xi_2 = 0.9$.

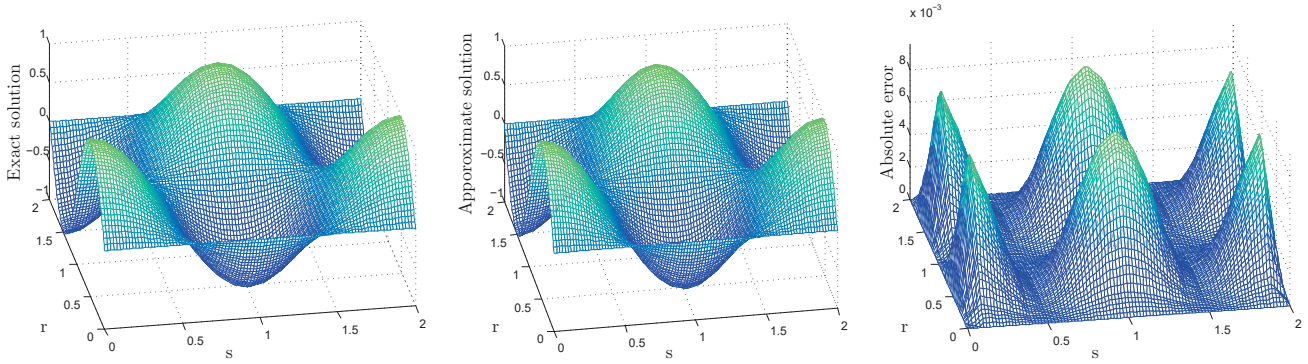

Figure 9. Problem 4 exact and numerical solutions of HMM with absolute error at $z = 0.5$.

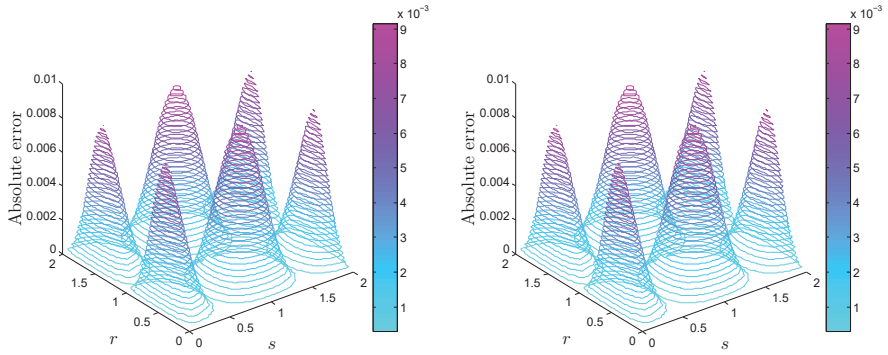

Figure 10. Problem 4 absolute error at $\xi_1 = \xi_2 = 0.3$ (**left**) and $\xi_1 = \xi_2 = 0.9$ (**right**), whereas $z = 0.5$.

6. Conclusions

This paper introduces a relatively new numerical methodology for addressing two-term time-fractional PDE models in two and three dimensions. We combined the Louiville–Caputo fractional derivative scheme with the Strang splitting algorithm for the temporal component and employed a meshless technique for spatial derivatives utilizing Lucas and Fibonacci polynomials. Error norms were utilized to evaluate the accuracy of the methodology across regular and irregular domains. A comparative study was conducted between the exact solution and alternative numerical methods outlined in the contemporary literature. This inquiry illustrated that the proposed approach yielded superior performance while requiring reduced computational resources. Moreover, the study illustrated how minimizing the errors could be accomplished by refining the spatial and temporal stages. With minor modifications, the proposed approach could be applied to various intricate fractional partial differential equations that arise in fields such as fluid dynamics, quantum mechanics, and financial mathematics, where they model phenomena with significant spatial and temporal dependencies.

Author Contributions: Conceptualization, I.A.; Methodology, I.A. and A.O.A.; Software, A.O.A.; Validation, R.J.; Formal analysis, N.N.A.R.; Investigation, I.A. and R.J.; Resources, R.J., N.N.A.R. and S.A.I.; Data curation, N.N.A.R. and S.A.I.; Writing—original draft, I.A. and R.J.; Writing—review & editing, A.O.A., N.N.A.R. and S.A.I.; Visualization, R.J.; Supervision, N.N.A.R. and S.A.I.; Project administration, N.N.A.R.; Funding acquisition, I.A. and S.A.I. All authors read and agreed to the published version of this manuscript.

Funding: The authors extend their appreciation to the Deanship of Scientific Research at King Khalid University for funding this work through Large Groups (project under grant number 2/478/44).

Data Availability Statement: Data are contained within the article and further inquiries can be directed to the corresponding author.

Conflicts of Interest: The authors declare no conflicts of interest.

References

1. Jan, A.; Srivastava, H.M.; Khan, A.; Mohammed, P.O.; Jan, R.; Hamed, Y. In vivo HIV dynamics, modeling the interaction of HIV and immune system via non-integer derivatives. *Fractal Fract.* **2023**, *7*, 361. [CrossRef]
2. Oderinu, R.A.; Owolabi, J.A.; Taiwo, M. Approximate solutions of linear time-fractional differential equations. *J. Math. Comput. Sci.* **2023**, *29*, 60–72. [CrossRef]
3. Ahmad, I.; Ali, I.; Jan, R.; Idris, S.A.; Mousa, M. Solutions of a three-dimensional multi-term fractional anomalous solute transport model for contamination in groundwater. *PLoS ONE* **2023**, *18*, e0294348. [CrossRef] [PubMed]
4. Siraj-ul-Islam; Ahmad, I. A comparative analysis of local meshless formulation for multi-asset option models. *Eng. Anal. Bound. Elem.* **2016**, *65*, 159–176. [CrossRef]
5. Wang, K.L.; He, C.H. A remark on Wang's fractal variational principle. *Fractals* **2019**, *27*, 1950134. [CrossRef]
6. Anjum, N.; He, C.H.; He, J.H. Two-scale fractal theory for the population dynamics. *Fractals* **2021**, *29*, 2150182. [CrossRef]
7. Zheltov, I.; Kochina, I.; Barenblatt, G. Basic concepts in the theory of seepage of homogeneous liquids in fissured rocks (strata). *J. Appl. Math. Mech.* **1960**, *24*, 852–864.
8. Ting, T.W. A cooling process according to two-temperature theory of heat conduction. *J. Math. Anal. Appl.* **1974**, *45*, 23–31. [CrossRef]
9. Rizvi, S.T.R.; Afzal, I.; Ali, K. Chirped optical solitons for Triki–Biswas equation. *Mod. Phys. Lett. B* **2019**, *33*, 1950264. [CrossRef]
10. Attia, R.A.; Lu, D.; MA Khater, M. Chaos and relativistic energy-momentum of the nonlinear time fractional Duffing equation. *Math. Comput. Appl.* **2019**, *24*, 10. [CrossRef]
11. Kelly, J.F.; McGough, R.J.; Meerschaert, M.M. Analytical time-domain Green's functions for power-law media. *J. Acoust. Soc. Am.* **2008**, *124*, 2861–2872. [CrossRef] [PubMed]
12. Caputo, M. Linear models of dissipation whose Q is almost frequency independent—II. *Geophys. J. Int.* **1967**, *13*, 529–539. [CrossRef]
13. Showalter, R. Existence and representation theorems for a semilinear Sobolev equation in Banach space. *SIAM J. Math. Anal.* **1972**, *3*, 527–543. [CrossRef]
14. Ewing, R.E. Numerical solution of Sobolev partial differential equations. *SIAM J. Numer. Anal.* **1975**, *12*, 345–363. [CrossRef]
15. Wang, F.; Ahmad, I.; Ahmad, H.; Alsulami, M.; Alimgeer, K.; Cesarano, C.; Nofal, T.A. Meshless method based on RBFs for solving three-dimensional multi-term time fractional PDEs arising in engineering phenomenons. *J. King Saud Univ.-Sci.* **2021**, *33*, 101604. [CrossRef]
16. Luo, Z.; Teng, F. A reduced-order extrapolated finite difference iterative scheme based on POD method for 2D Sobolev equation. *Appl. Math. Comput.* **2018**, *329*, 374–383. [CrossRef]
17. Li, J.F.; Ahmad, I.; Ahmad, H.; Shah, D.; Chu, Y.M.; Thounthong, P.; Ayaz, M. Numerical solution of two-term time-fractional PDE models arising in mathematical physics using local meshless method. *Open Phys.* **2020**, *18*, 1063–1072. [CrossRef]
18. Luo, Z.; Teng, F.; Chen, J. A POD-based reduced-order Crank–Nicolson finite volume element extrapolating algorithm for 2D Sobolev equations. *Math. Comput. Simul.* **2018**, *146*, 118–133. [CrossRef]
19. Li, N.; Lin, P.; Gao, F. An expanded mixed finite element method for two-dimensional Sobolev equations. *J. Comput. Appl. Math.* **2019**, *348*, 342–355. [CrossRef]
20. Heydari, M.; Rashid, S.; Jarad, F. A numerical method for distributed-order time fractional 2D Sobolev equation. *Results Phys.* **2023**, *45*, 106211. [CrossRef]
21. Gao, F.; Qiu, J.; Zhang, Q. Local discontinuous Galerkin finite element method and error estimates for one class of Sobolev equation. *J. Sci. Comput.* **2009**, *41*, 436–460. [CrossRef]
22. Gao, F.; Cui, J.; Zhao, G. Weak Galerkin finite element methods for Sobolev equation. *J. Comput. Appl. Math.* **2017**, *317*, 188–202. [CrossRef]
23. Abu Arqub, O.; Alsulami, H.; Alhodaly, M. Numerical Hilbert space solution of fractional Sobolev equation in 1+1-dimensional space. *Math. Sci.* **2022**, *18*, 217–228. [CrossRef]
24. Hussain, M.; Haq, S.; Ghafoor, A. Meshless RBFs method for numerical solutions of two-dimensional high order fractional Sobolev equations. *Comput. Math. Appl.* **2020**, *79*, 802–816. [CrossRef]
25. Ahmad, I.; Ahsan, M.; Elamin, A.E.A.; Abdel-Khalek, S.; Inc, M. Numerical simulation of 3-D Sobolev equation via local meshless method. *Therm. Sci.* **2022**, *26*, 457–462. [CrossRef]
26. Zhang, J.; Zhang, Y.; Guo, H.; Fu, H. A mass-conservative characteristic splitting mixed finite element method for convection-dominated Sobolev equation. *Math. Comput. Simul.* **2019**, *160*, 180–191. [CrossRef]
27. Wang, K.L.; Yao, S.W.; Liu, Y.P.; Zhang, L.N. A fractal variational principle for the telegraph equation with fractal derivatives. *Fractals* **2020**, *28*, 2050058. [CrossRef]
28. Wang, K.L.; Wang, K.J.; He, C.H. Physical insight of local fractional calculus and its application to fractional Kdv–Burgers–Kuramoto equation. *Fractals* **2019**, *27*, 1950122. [CrossRef]
29. Dong, G.; Guo, Z.; Yao, W. Numerical methods for time-fractional convection-diffusion problems with high-order accuracy. *Open Math.* **2021**, *19*, 782–802. [CrossRef]
30. He, J.H. Homotopy perturbation method: A new nonlinear analytical technique. *Appl. Math. Comput.* **2003**, *135*, 73–79. [CrossRef]

31. Salama, F.M.; Ali, N.H.M.; Abd Hamid, N.N. Fast O(N) hybrid Laplace transform-finite difference method in solving 2D time fractional diffusion equation. *J. Math. Comput. Sci.* **2021**, *23*, 110–123. [CrossRef]
32. Wang, K.L. A novel variational approach to fractal Swift–Hohenberg model arising in fluid dynamics. *Fractals* **2022**, *30*, 2250156. [CrossRef]
33. Wang, K. New variational theory for coupled nonlinear fractal Schrödinger system. *Int. J. Numer. Methods Heat Fluid Flow* **2022**, *32*, 589–597. [CrossRef]
34. Deng, W. Finite element method for the space and time fractional Fokker–Planck equation. *SIAM J. Numer. Anal.* **2009**, *47*, 204–226. [CrossRef]
35. Li, L.; Jiang, Z.; Yin, Z. Compact finite-difference method for 2D time-fractional convection–diffusion equation of groundwater pollution problems. *Comput. Appl. Math.* **2020**, *39*, 142. [CrossRef]
36. Tansri, K.; Kittisopaporn, A.; Chansangiam, P. Numerical solutions of the space-time fractional diffusion equation via a gradient-descent iterative procedure. *J. Math. Comput. Sci.* **2023**, *31*, 353–366. [CrossRef]
37. Dehghan, M.; Abbaszadeh, M.; Mohebbi, A. Legendre spectral element method for solving time fractional modified anomalous sub-diffusion equation. *Appl. Math. Model.* **2016**, *40*, 3635–3654. [CrossRef]
38. He, J.H.; Wu, X.H. Exp-function method for nonlinear wave equations. *Chaos Solitons Fractals* **2006**, *30*, 700–708. [CrossRef]
39. Guo, T.; Nikan, O.; Avazzadeh, Z.; Qiu, W. Efficient alternating direction implicit numerical approaches for multi-dimensional distributed-order fractional integro differential problems. *Comput. Appl. Math.* **2022**, *41*, 236. [CrossRef]
40. Qiao, H.; Cheng, A. A fast finite difference/RBF meshless approach for time fractional convection-diffusion equation with non-smooth solution. *Eng. Anal. Bound. Elem.* **2021**, *125*, 280–289. [CrossRef]
41. Abd-Elhameed, W.M.; Youssri, Y.H.; El-Sissi, N.; Sadek, M. New hypergeometric connection formulae between Fibonacci and Chebyshev polynomials. *Ramanujan J.* **2017**, *42*, 347–361. [CrossRef]
42. Abd-Elhameed, W.; Youssri, Y. Connection formulae between generalized Lucas polynomials and some Jacobi polynomials: Application to certain types of fourth-order BVPs. *Int. J. Appl. Comput. Math.* **2020**, *6*, 45. [CrossRef]
43. Nadir, M. Lucas polynomials for solving linear integral equations. *J. Theor. Appl. Comput. Sci.* **2017**, *11*, 13–19.
44. Çetin, M.; Sezer, M.; Güler, C. Lucas polynomial approach for system of high-order linear differential equations and residual error estimation. *Math. Probl. Eng.* **2015**, *2015*, 625984. [CrossRef]
45. Mirzaee, F.; Hoseini, S.F. Application of Fibonacci collocation method for solving Volterra–Fredholm integral equations. *Appl. Math. Comput.* **2016**, *273*, 637–644. [CrossRef]
46. Baykuş-Savaşaneril, N.; Sezer, M. Hybrid Taylor-Lucas collocation method for numerical solution of high-order Pantograph type delay differential equations with variables delays. *Appl. Math. Inf. Sci.* **2017**, *11*, 1795–1801.
47. Oruç, Ö. A new algorithm based on Lucas polynomials for approximate solution of 1D and 2D nonlinear generalized Benjamin–Bona–Mahony–Burgers equation. *Comput. Math. Appl.* **2017**, *74*, 3042–3057. [CrossRef]
48. Oruç, Ö. A new numerical treatment based on Lucas polynomials for 1D and 2D sinh-Gordon equation. *Commun. Nonlinear Sci. Numer. Simul.* **2018**, *57*, 14–25. [CrossRef]
49. Ali, I.; Haq, S.; Nisar, K.S.; Baleanu, D. An efficient numerical scheme based on Lucas polynomials for the study of multidimensional Burgers-type equations. *Adv. Differ. Equ.* **2021**, *2021*, 43. [CrossRef]
50. Ahmad, I.; Bakar, A.A.; Ali, I.; Haq, S.; Yussof, S.; Ali, A.H. Computational analysis of time-fractional models in energy infrastructure applications. *Alex. Eng. J.* **2023**, *82*, 426–436. [CrossRef]
51. Jumarie, G. Stock exchange fractional dynamics defined as fractional exponential growth driven by (usual) Gaussian white noise. Application to fractional Black-Scholes equations. *Insur. Math. Econ.* **2008**, *42*, 271–287. [CrossRef]
52. Jumarie, G. Derivation and solutions of some fractional Black-Scholes equations in coarse-grained space and time. Application to Merton's optimal portfolio. *Comput. Math. Appl.* **2010**, *59*, 1142–1164. [CrossRef]
53. Atangana, A.; Baleanu, D. New fractional derivatives with non-local and nonsingular kernel theory and application to heat transfer model. *Therm. Sci.* **2016**, *20*, 763. [CrossRef]
54. He, J.H. A new fractal derivation. *Therm. Sci.* **2011**, *15*, 145–147. [CrossRef]
55. Ali, I.; Haq, S.; Aldosary, S.F.; Nisar, K.S.; Ahmad, F. Numerical solution of one-and two-dimensional time-fractional Burgers' equation via Lucas polynomials coupled with Finite difference method. *Alex. Eng. J.* **2022**, *61*, 6077–6087. [CrossRef]
56. Hussain, M.; Haq, S.; Ghafoor, A.; Ali, I. Numerical solutions of time-fractional coupled viscous Burgers' equations using meshfree spectral method. *Comput. Appl. Math.* **2020**, *39*, 6. [CrossRef]
57. Marchuk, G.I. Some applicatons of splitting-up methods to the solution of problems in mathematical physics. *Aplikace Matematiky* **1968**, *1*, 103–132.
58. Strang, G. On the construction and comparision of difference schemes. *SIAM J. Numer. Anal.* **1968**, *5*, 506–517. [CrossRef]
59. Geiser, J.; Tanoglu, G.; Gucuyenenb, N. Higher order operator splitting methods via Zassenhaus product formula: Theory and applications. *Comput. Math. Appl.* **2011**, *62*, 1994–2015. [CrossRef]
60. Abd-Elhameed, W.; Youssri, Y. Spectral solutions for fractional differential equations via a novel Lucas operational matrix of fractional derivatives. *Rom. J. Phys* **2016**, *61*, 795–813.
61. Ali, I.; Haq, S.; Nisar, K.S.; Arifeen, S.U. Numerical study of 1D and 2D advection-diffusion-reaction equations using Lucas and Fibonacci polynomials. *Arab. J. Math.* **2021**, *10*, 513–526. [CrossRef]

62. Garmanjani, G.; Cavoretto, R.; Esmaeilbeigi, M. A RBF partition of unity collocation method based on finite difference for initial–boundary value problems. *Comput. Math. Appl.* **2018**, *75*, 4066–4090. [CrossRef]
63. Lax, P.D. Weak solutions of nonlinear hyperbolic equations and their numerical computation. *Commun. Pure Appl. Math.* **1954**, *7*, 159–193. [CrossRef]

fractal and fractional

MDPI

Article

A Fast High-Order Compact Difference Scheme for Time-Fractional KS Equation with the Generalized Burgers' Type Nonlinearity

Huifa Jiang [1,*] and Da Xu [2,*]

[1] School of Science, Hunan University of Technology, Zhuzhou 412007, China
[2] School of Mathematics and Statistics, Hunan Normal University, Changsha 410081, China
* Correspondence: huifajiang98@163.com (H.J.); daxu@hunnu.edu.cn (D.X.)

Abstract: This work integrates the fast Alikhanov method with a compact scheme to solve the time-fractional Kuramoto–Sivashinsky (KS) equation with the generalized Burgers' type nonlinearity. Initially, the Alikhanov algorithm, designed to handle the Caputo fractional derivative on non-uniform time grids, effectively avoids the initial singularity. Additionally, the combination of the Alikhanov method with the sum-of-exponentials (SOE) technique significantly reduces both computational cost and memory requirements. By discretizing the spatial direction using a compact finite difference method, a fully discrete scheme is developed, achieving fourth-order convergence in the spatial domain. Stability and convergence are analyzed through energy methods. Several numerical examples are provided to validate the theoretical framework, demonstrating that the proposed algorithm is accurate, stable, and efficient.

Keywords: time-fractional Kuramoto–Sivashinsky equation; fast Alikhanov method; sum-of-exponentials technique; non-uniform time steps; compact difference method

Academic Editor: Luis Manuel Sánchez Ruiz

Received: 17 December 2024
Revised: 22 March 2025
Accepted: 28 March 2025
Published: 30 March 2025

Citation: Jiang, H.; Xu, D. A Fast High-Order Compact Difference Scheme for Time-Fractional KS Equation with the Generalized Burgers' Type Nonlinearity. *Fractal Fract.* **2025**, *9*, 218. https://doi.org/10.3390/fractalfract9040218

1. Introduction

The Kuramoto–Sivashinsky (KS) equation belongs to an important class of chaotic partial differential equations that serve as a bridge between the partial differential equation and dynamical system frameworks. Kuramoto [1] originally proposed the KS equation in his study of phase turbulence in reaction–diffusion systems, while Sivashinsky [2] introduced it in his analysis of flame combustion propagation models. The KS equation has a wide range of applications in simulation science and engineering, such as the evolution of the flow of fluid films on inclined planes [3], flame front instability [4], interfacial turbulence [5], etc.

In this paper, we study the time-fractional KS equation with the generalized Burgers' type nonlinearity:

$$\begin{aligned} {}_0^C D_t^\alpha u(x,t) + u^p(x,t)u_x(x,t) - \mu u_{xx}(x,t) + \lambda u_{xxxx}(x,t) = f(x,t), \\ 0 < x < L, \quad 0 < t \le T, \end{aligned} \tag{1}$$

with the initial condition (IC)

$$u(x,0) = u_0(x), \qquad 0 < x < L, \tag{2}$$

and the boundary conditions (BCs)

$$\begin{aligned} u(0,t) = u(L,t) = 0, \quad 0 \le t \le T, \\ u_{xx}(0,t) = u_{xx}(L,t) = 0, \quad 0 \le t \le T, \end{aligned} \tag{3}$$

where $\mu > 0$ is the viscosity coefficient, $p \ge 1$ is a positive integer, perturbation parameters $0 < \lambda \le 1$, $L > 0, T > 0$ are fixed values, and $u_0(x)$ and $f(x,t)$ are prescribed real functions. The equations are complex, and their combination of fractional-order derivative KS equations and Burgers' nonlinear terms provides them with greater flexibility to capture the intricate dynamical behaviors observed in various physical systems.

- When the fourth-order derivative u_{xxxx} and the source term are not included in the equation, Equation (1) transforms into a time-fractional generalized Burgers equation [6] as follows:

$$ {}_0^C D_t^\alpha u(x,t) + u^p(x,t) u_x(x,t) - \mu u_{xx}(x,t) = 0, \quad 0 < x < L, \quad 0 < t \le T, \tag{4}$$

  where $u^p u_x$ is the generalized Burgers' type nonlinearity.
- When $\alpha = 1$, $p = 1$, Equation (1) is the usual KS equation as follows:

$$ u_t(x,t) + u(x,t) u_x(x,t) - \mu u_{xx}(x,t) + u_{xxxx}(x,t) = 0, \quad 0 < x < L, \quad 0 < t \le T, \tag{5}$$

  and many pioneering studies have been carried out [7–9].
- When $p = 1$, Equation (1) is the generalized fractional KS equation [10] as follows:

$$ {}_0^C D_t^\alpha u(x,t) + u(x,t) u_x(x,t) - \mu u_{xx}(x,t) + u_{xxxx}(x,t) = 0, \quad 0 < x < L, \quad 0 < t \le T, \tag{6}$$

In recent years, numerical computational algorithms for solving the time-fractional KS equation have been developed and become imperative. Many numerical methods are already available for studying KS equations, including those of the form presented in Equation (5). Mittal [11] proposed a quintic B-spline collocation method based on the Crank–Nicolson scheme for temporal discretization, aimed at approximating the solution to the KS equation. In [12], a locally discontinuous Galerkin method is implemented to obtain the numerical solution to the KS equation. The implicit–explicit BDF method was developed by Akrivis and Smyrlis [13] for simulating the KS equation.

However, there are few research studies on effective numerical algorithms for solving fractional KS equations. For the fractional KS equation of the type Equation (6), the weak singularity of the solution generated by the fractional derivative presents a difficult problem to solve. At present, the effective method to solve this problem is to use the variable step numerical method, which concentrates more grid points around the weak singularity and employs a sparse grid where the solution changes slowly. Indeed, the $L1$ formula for the construction of piecewise linear interpolation was proposed by Langlands [14], which leads to a temporal convergence order of $1 + \gamma$ for $0 < \gamma < 1$. Since then, the $L1$ formula has been widely used to deal with Caputo fractional derivatives [15–20]. Furthermore, for the numerical solution to pure sub-diffusion equations, there are several high-order discrete convolution forms for the approximation of the Caputo fractional-order time derivatives, such as the $L1$-2 scheme [21–23] and the $L2$-1_σ formula, which is based on linear interpolation on the last subinterval $[t_{k-1}, t_k]$ and quadratic polynomial interpolation on the rest of the subintervals $[t_{k-1}, t_k]$ (for details, please refer to [24]). These formulas can achieve second-order temporal accuracy for sufficiently smooth solutions.

Due to the advantages of the $L2$-1_σ formula, we will study the approximation of the Caputo fractional derivative by the variable time-step Alikhanov formula. Influenced by [25,26], we also give the regularity assumptions on the exact solution u as follows:

$$\left\| \frac{\partial^k u}{\partial t^k} \right\|_{H^2(0,L)} \leq C\left(1 + t^{\sigma-k}\right), \qquad k = 0, 1, 2, 3, \tag{7}$$

$$\left\| {}_0^C D_t^\alpha u \right\|_{H^6(0,L)} + \|u\|_{H^8(0,L)} \leq C, \tag{8}$$

where $0 < t \leq T$, and $\sigma \in (0,1) \cup (1,2)$ is a regularity parameter. In this paper, we only consider the case of $\lambda = 1$.

In order to obtain a more efficient algorithm for solving the problem and avoid the issue of large computational costs caused by the historical dependence of the fractional derivative, one of the most effective methods is the SOE technique [27–29], which is applied in approximating the convolution kernel $t^{-\alpha}$ with a uniform absolute error ϵ. There have been many research studies on the nonlinear KS equation with a spatial fourth derivative, employing various methods such as the quintic B-spline collocation method [30], cubic Hermite collocation [31], Chebyshev collocation method [10], and Sinc–Galerkin method [32]. The compact difference scheme has good characteristics and high accuracy and is widely used to solve a variety of equations [33–37]. The application of a compact difference scheme to the spatial discretization of fractional KS equations is exactly the starting point of our present work. The theoretical part of the proof makes use of the classical energy method [38–40]. Moreover, the main contributions of this work can be summarized as follows:

- For the complex KS equation, we first apply the non-uniform Alikhanov formula to approximate the Caputo fractional derivative, and then treat the generalized Burgers' nonlinear term. Then, we combine the second-order time scheme and the SOE technique to establish the fast Alikhanov second-order scheme. This approach improves numerical accuracy and reduces computational costs.
- The high-order compact difference scheme is proposed for the first time to be applied to the KS equation with the generalized Burgers' nonlinear term, which can improve the spatial convergence rate to the fourth order.
- We demonstrate in detail the convergence and stability of the fully discrete scheme by the energy argument. In addition, we provide numerical examples to validate the theoretical analysis and demonstrate the efficiency of the algorithm by comparing fast and non-fast Alikhanov schemes.

The outline of this paper is as follows: In Section 2, we introduce some useful notations and lemmas. Additionally, some properties of compact difference formulas and fast Alikhanov formulas are analyzed. In Section 3, the high-order fast Alikhanov compact difference scheme is constructed. The stability and convergence of a full-discrete scheme are investigated. Numerical examples verify the stability and efficiency of the algorithm and the correctness of the theory in Section 4. The conclusion is summarized in Section 5.

2. Preliminaries

In this section, we first recall some basic formulations and useful lemmas. For ease of exposition and proof, we define some notations. To make our analysis extendable, the conditions and properties of the discrete convolution kernel in the Alikhanov formula are also introduced in this section.

2.1. Properties of Compact Difference Scheme

Let the spatial step size $h := L/M$, where M is a given positive integer. We denote $x_j = jh$ $(0 \leq j \leq M)$ and $\overline{\mathcal{U}}_h := \{u | u = (u_0, u_1, \ldots, u_M),\ 0 \leq j \leq M\}$. For any $u,\ v \in \overline{\mathcal{U}}_h$, we denote the following notations:

$$\nabla^+ u_{j+1} = \frac{1}{h}(u_{j+1} - u_j), \quad \nabla^- u_{j-1} = \frac{1}{h}(u_j - u_{j-1}),$$
$$\nabla_h u_j = \frac{1}{2h}(u_{j+1} - u_{j-1}), \quad \Delta_x u_j = \frac{u_{j+1} - 2u_j + u_{j-1}}{h^2}.$$

We also need to introduce the subspace of $\overline{\mathcal{U}}_h$ as $\mathcal{U}_h := \{u \in \overline{\mathcal{U}}_h | u_0 = u_M = 0\}$, and define the inner product and norm as follows:

$$\langle u, v\rangle = h\sum_{j=1}^{M-1} u_j v_j, \quad (u, v) = h\sum_{j=1}^{M}\left(\nabla^+ u_j\right)\left(\nabla^+ v_j\right),$$
$$\|u\| = \sqrt{\langle u, u\rangle}, \quad |u|_1 = \sqrt{(u, u)}, \quad \|u\|_\infty = \max_{0\le j\le M}|u_j|.$$

Furthermore, we denote the following:

$$\mathcal{A}_1 u_j := (1 + \frac{h^2}{6}\Delta_x)u_j, \qquad \mathcal{A}_2 u_j := (1 + \frac{h^2}{12}\Delta_x)u_j.$$

Thus, for the discretization of the second and fourth derivatives of the function $u = u(x, t)$, we have the following formulas:

$$u_x(x_j) = \mathcal{A}_1^{-1}\nabla_h U_j + \mathcal{O}(h^4), \qquad u_{xx}(x_j) = \mathcal{A}_2^{-1}\Delta_x U_j + \mathcal{O}(h^4). \tag{9}$$

The following transformation can be advanced for the nonlinear term:

$$u^p u_x = v u_x = \frac{1}{p+2}[v u_x + (vu)_x], \tag{10}$$

where $v := u^p$, and

$$v_j\frac{\partial u_j}{\partial x} + \frac{\partial u_j v_j}{\partial x} = v_j\mathcal{A}_1^{-1}\nabla_h u_j + \mathcal{A}_1^{-1}\nabla_h(v_j u_j) + \mathcal{O}(h^4) = \varphi(u_j, v_j) + \mathcal{O}(h^4). \tag{11}$$

Lemma 1 ([41]). *For any grid functions $u,\ v \in \mathcal{U}_h$, then the following holds:*

$$\langle \nabla_h u, v\rangle = -\langle u, \nabla_h v\rangle, \qquad \langle \Delta_x u, v\rangle = -(u, v).$$

Lemma 2 ([41]). *For any grid functions $u \in \mathcal{U}_h$, then the following holds:*

$$\|u\|_\infty \le \frac{\sqrt{L}}{2}|u|_1, \quad \|u\| \le \frac{L}{\sqrt{6}}|u|_1, \quad |u|_1 \le \frac{2}{h}\|u\|.$$

Lemma 3 ([42]). *For real symmetric positive-definite matrices $\mathcal{A}_1^{-1}$, $\mathcal{A}_2^{-1}$, and $\omega, u \in \mathcal{U}_h$, we obtain the following:*

$$\left(\mathcal{A}_1^{-1}\omega, u\right) = (\mathcal{V}_1\omega, \mathcal{V}_1 u) = \left(\omega, \mathcal{A}_1^{-1}u\right), \ \left(\mathcal{A}_2^{-1}\omega, u\right) = (\mathcal{V}_2\omega, \mathcal{V}_2 u) = \left(\omega, \mathcal{A}_2^{-1}u\right),$$

where $\mathcal{V}_1$ and $\mathcal{V}_2$ are upper triangular matrices, which can be obtained by the Cholesky factorization of $\mathcal{A}_1^{-1}$ and $\mathcal{A}_2^{-1}$, namely, $\mathcal{A}_1^{-1} = (\mathcal{V}_1)^T\mathcal{V}_1$, $\mathcal{A}_2^{-1} = (\mathcal{V}_2)^T\mathcal{V}_2$.

Proof. The proof of the theorem can be referred to in ([42], Lemma 2.1c). □

Lemma 4 ([43]). *Let $\omega, u \in \mathcal{U}_h$, then we can obtain the following:*

$$\left(\mathcal{A}_1^{-1}\nabla_h\omega, u\right) = \left(\nabla_h\mathcal{A}_1^{-1}\omega, u\right) = -\left(\mathcal{A}_1^{-1}\omega, \nabla_h u\right) = -\left(\omega, \mathcal{A}_1^{-1}\nabla_h u\right),$$
$$\left(\mathcal{A}_2^{-1}\Delta_x\omega, u\right) = \left(\Delta_x\mathcal{A}_2^{-1}\omega, u\right) = -\left(\nabla^+\mathcal{A}_2^{-1}\omega, \nabla^+ u\right) = -\left(\mathcal{A}_2^{-1}\nabla^+\omega, \nabla^+ u\right).$$

Lemma 5. *Let $u,\ v \in \mathcal{U}_h$, we arrive at*

$$\Big\langle \varphi(u,v)\ ,\ u \Big\rangle = 0.$$

Proof. For $u,\ v \in \mathcal{U}_h$, using Lemmas 1 and 4, we can obtain the following:

$$\begin{aligned}\Big\langle \varphi(u,v)\ ,\ u \Big\rangle &= \Big\langle v_j \mathcal{A}_1^{-1}\nabla_h u_j + \mathcal{A}_1^{-1}\nabla_h(v_j u_j)\ ,\ u_j \Big\rangle \\ &= \Big\langle v_j \mathcal{A}_1^{-1}\nabla_h u_j\ ,\ u_j \Big\rangle + \Big\langle \mathcal{A}_1^{-1}\nabla_h(v_j u_j)\ ,\ u_j \Big\rangle, \\ &= \Big\langle \mathcal{A}_1^{-1}\nabla_h u_j\ ,\ v_j u_j \Big\rangle - \Big\langle v_j u_j\ ,\ \mathcal{A}_1^{-1}\nabla_h u_j \Big\rangle, \\ &= 0.\end{aligned}$$

□

Lemma 6 ([43])**.** *For real symmetric positive-definite matrices $\mathcal{A}_1^{-1}$, $\mathcal{A}_2^{-1}$, and $\omega \in \mathcal{U}_h$, we obtain the following:*

$$\|\omega\|^2 \le \Big(\mathcal{A}_1^{-1}\omega,\omega\Big) = \|\mathcal{V}_1\omega\|^2 \le 3\|\omega\|^2,\ \|\omega\|^2 \le \Big(\mathcal{A}_2^{-1}\omega,\omega\Big) = \|\mathcal{V}_2\omega\|^2 \le \tfrac{3}{2}\|\omega\|^2.$$

2.2. Properties of the Fast Alikhanov Scheme

In order to construct the fast Alikhanov scheme, we first consider the time levels $0 = t_0 < t_1 < t_2 < \cdots < t_N = T$, where N is a given positive integer. We define the nth step size $\tau_n := t_n - t_{n-1}$ for $1 \le n \le N$, the maximum step size $\tau := \max\limits_{0\le n\le N} \tau_n$. We set the time level $t_{n-\theta} := \theta t_{n-1} + (1-\theta)t_n$ with a fixed parameter $\theta = \alpha/2$. It is necessary to set the local step-size ratios:

$$\rho_n := \frac{\tau_n}{\tau_{n+1}} \text{ for } 1 \le n \le N-1 \text{ and } \rho := \max_{1\le n\le N-1} \rho_n.$$

For any time sequence $(v^n)_{n=0}^N$, we define $\nabla_\tau v^n := v^n - v^{n-1}$ and the interpolated value $v^{n-\theta} := \theta v^{n-1} + (1-\theta)v^n$. Thus, it is advisable to denote $\Pi_{1,k}u$ as the linear interpolant function of a function, u, with respect to t_{k-1}, t_k, and to denote the quadratic interpolant of u with respect to t_{k-1}, t_k and t_{k+1} as $\Pi_{2,k}u$, respectively. Recalling the definition of $\nabla_\tau u^k$, it follows that for $k \ge 1$, we have the following:

$$\begin{aligned}(\Pi_{1,k}u)'(t) &= \frac{\nabla_\tau u^k}{\tau_k}, \\ (\Pi_{2,k}u)'(t) &= \frac{\nabla_\tau u^k}{\tau_k} + \frac{2(t - t_{k-1/2})}{\tau_k(\tau_k + \tau_{k+1})}\Big(\rho_k \nabla_\tau u^{k+1} - \nabla_\tau u^k\Big).\end{aligned}$$

Next, the Caputo fractional derivative can be approximated by the defined interpolant polynomial at $t_{n-\theta}$ to obtain the Alikhanov approximation:

$$\begin{aligned}(D_\tau^\alpha u)^{n-\theta} &:= \int_{t_{n-1}}^{t_{n-\theta}} \omega_{1-\alpha}(t_{n-\theta} - s)(\Pi_{1,n}u)'(s)\mathrm{d}s + \sum_{k=1}^{n-1}\int_{t_{k-1}}^{t_k} \omega_{1-\alpha}(t_{n-\theta} - s)(\Pi_{2,k}u)'(s)\mathrm{d}s \\ &= a_0^{(n)}\nabla_\tau u^n + \sum_{k=1}^{n-1}\Big(a_{n-k}^{(n)}\nabla_\tau u^k + \rho_k b_{n-k}^{(n)}\nabla_\tau u^{k+1} - b_{n-k}^{(n)}\nabla_\tau u^k\Big), \qquad (12) \\ &= \sum_{k=1}^{n} A_{n-k}^{(\alpha,n)}\nabla_\tau v^k,\end{aligned}$$

we have $A_0^{(1)} := a_0^{(1)}$ if $n = 1$, and for $n \ge 2$,

$$A_{n-k}^{(n)} := \begin{cases} a_0^{(n)} + \rho_{n-1} b_1^{(n)}, & k = n, \\ a_{n-k}^{(n)} + \rho_{k-1} b_{n-k+1}^{(n)} - b_{n-k}^{(n)}, & 2 \le k \le n-1, \\ a_{n-1}^{(n)} - b_{n-1}^{(n)}, & k = 1. \end{cases} \tag{13}$$

Here, $A_{n-k}^{(n)}$ is the discrete convolution kernel of the Alikhanov formula; next, the SOE technique is applied to derive the discrete convolution kernel of the fast Alikhanov formula.

Lemma 7 ([27]). *(SOE) Let $\alpha \in (0,1)$, $\epsilon \ll 1$, and $\Delta t > 0$. Assume there exists a positive integer N_q, and positive quadrature nodes s^l and $\varpi^l > 0$ $(1 \le l \le N_q)$, such that we have the following:*

$$\left| \omega_{1-\alpha}(t) - \sum_{l=1}^{N_q} \varpi^l e^{-s^l t} \right| \le \epsilon, \quad t \in [\Delta t, T],$$

and the quadrature node number N_q satisfies

$$N_q = O\left(\log \frac{1}{\epsilon} \left(\log\log \frac{1}{\epsilon} + \log \frac{T}{\Delta t} \right) + \log \frac{1}{\Delta t} \left(\log\log \frac{1}{\epsilon} + \log \frac{1}{\Delta t} \right) \right).$$

Now, the fractional derivative can be approximated in combination with the SOE technique in Lemma 7 at the time point $t_{n-\theta}$ for $1 \le n \le N$

$$\begin{aligned} {}_0^C D_f^\alpha u(t_{n-\theta}) &\approx \int_{t_{n-1}}^{t_{n-\theta}} \omega_{1-\alpha}(t_{n-\theta} - s)(\Pi_{1,n} u)'(s) \mathrm{d}s + \sum_{k=1}^{n-1} \int_{t_{k-1}}^{t_k} \sum_{l=1}^{N_q} \varpi^l e^{-s^l (t_{n-\theta} - s)} u'(s) \mathrm{d}s \\ &= \hat{\mathbf{a}}_0^{(n)} \nabla_\tau u^n + \sum_{k=1}^{n-1} \left(\hat{\mathbf{a}}_{n-k}^{(n)} \nabla_\tau u^k + \rho_k \hat{\mathbf{b}}_{n-k}^{(n)} \nabla_\tau u^{k+1} - \hat{\mathbf{b}}_{n-k}^{(n)} \nabla_\tau u^k \right) \\ &= \sum_{k=1}^{n} \hat{\mathbf{A}}_{n-k}^{(n)} \nabla_\tau u^k, \end{aligned} \tag{14}$$

where coefficients $\hat{\mathbf{a}}_{n-k}^{(n)}$ and $\hat{\mathbf{b}}_{n-k}^{(n)}$ are defined by the following:

$$\hat{\mathbf{a}}_0^{(n)} := a_0^{(n)}, \qquad \hat{\mathbf{a}}_{n-k}^{(n)} := \frac{1}{\tau_k} \int_{t_{k-1}}^{t_k} \sum_{l=1}^{N_q} \varpi^l e^{-s^l (t_{n-\theta} - s)} \mathrm{d}s, \quad 1 \le k \le n-1,$$

$$\hat{\mathbf{b}}_{n-k}^{(n)} := \frac{2}{\tau_k (\tau_k + \tau_{k+1})} \int_{t_{k-1}}^{t_k} \sum_{l=1}^{N_q} \varpi^l e^{-s^l (t_{n-\theta} - s)} e^{-s^l (t_{k+1-\theta} - s)} (s - t_{k-\frac{1}{2}}) \mathrm{d}s, \quad 1 \le k \le n-1.$$

We reformulate the discrete convolution kernel $\hat{\mathbf{A}}_{n-k}^{(n)}$ as follows: $\hat{\mathbf{A}}_0^{(1)} := a_0^{(1)}$ if $n = 1$ and for $n \ge 2$

$$\hat{\mathbf{A}}_{n-k}^{(n)} := \begin{cases} \hat{\mathbf{a}}_0^{(n)} + \rho_{n-1} \hat{\mathbf{b}}_1^{(n)}, & \text{for} \quad k = n, \\ \hat{\mathbf{a}}_{n-k}^{(n)} + \rho_{k-1} \hat{\mathbf{b}}_{n-k+1}^{(n)} - \hat{\mathbf{b}}_{n-k}^{(n)}, & \text{for} \quad 2 \le k \le n-1, \\ \hat{\mathbf{a}}_{n-1}^{(n)} - \hat{\mathbf{b}}_{n-1}^{(n)}, & \text{for} \quad k = 1. \end{cases} \tag{15}$$

In order to effectively assess some necessary properties of the discrete convolution kernel $\hat{\mathbf{A}}_{n-k}^{(n)}$, the time step needs to satisfy the following two conditions:

M1. The maximum time-step ratio is $\rho = 7/4$.

M2. There exists a positive constant C_γ, such that $\tau_k \le C_\gamma \tau \min\{1, t_k^{1-1/\gamma}\}$ for $1 \le k \le N$, with $t_k \le C_\gamma t_{k-1}$ and $\tau_k / t_k \le C_\gamma \tau_{k-1} / t_{k-1}$ for $2 \le k \le N$.

Lemma 8 ([27]). *Assume that the tolerance error ϵ of the SOE approximation satisfies*

$$\epsilon \leq \min\left\{\frac{\alpha_p}{2(1-\alpha_p)}\omega_{1-\alpha_p}(T), \frac{1}{26}\omega_{1-\alpha_p}(T)\right\},$$

then the discrete kernel $\hat{\mathbf{A}}_{n-k}^{(n)}$ satisfies the following:

(I) *$\hat{\mathbf{A}}_{n-k}^{(n)}$ are bounded, $\hat{\mathbf{A}}_{n-k}^{(n)} \leq \frac{2}{\tau_n}\omega_{2-\alpha_p}(\tau_n)$ and*

$$\hat{\mathbf{A}}_{n-k}^{(n)} \geq \frac{1}{2\tau_k}\int_{t_{k-1}}^{t_k}\omega_{1-\alpha}(t_n-s)\mathrm{d}s, \quad 1 \leq k \leq n;$$

(II) *$\hat{\mathbf{A}}_{n-k}^{(n)}$ are monotone, and*

$$\hat{\mathbf{A}}_{n-k-1}^{(n)} - \hat{\mathbf{A}}_{n-k}^{(n)} \geq (1+\rho_k)\left(\frac{1}{5\rho_k}+1\right)b_{n-k}^{(n)}, \quad 1 \leq k \leq n-1;$$

(III) $\hat{\mathbf{A}}_0^{(n)} - \hat{\mathbf{A}}_1^{(n)} > \theta\left(2\hat{\mathbf{A}}_0^{(n)} - \hat{\mathbf{A}}_1^{(n)}\right)$ *for $n \geq 2$.*

In this case, for the later analysis of global consistency, we introduce the complementary discrete convolution kernels $P_{n-k}^{(n)}$ of $\hat{\mathbf{A}}_{n-k}^{(n)}$ that satisfy

$$\sum_{i=k}^{n} P_{n-i}^{(n)}\hat{\mathbf{A}}_{i-k}^{(i)} \equiv 1. \tag{16}$$

which yields the following recursive formulas:

$$P_0^{(n)} := \frac{1}{\hat{\mathbf{A}}_0^{(n)}}, \quad P_i^{(n)} := \frac{1}{\hat{\mathbf{A}}_0^{(i)}}\sum_{k=i+1}^{n}\left(\hat{\mathbf{A}}_{k-i-1}^{(k)} - \hat{\mathbf{A}}_{k-i}^{(k)}\right)P_k^{(n)}, \quad 1 \leq i \leq n-1.$$

In fact, according to Lemma 8, the complementary discrete kernels are non-negative and satisfy the following:

$$\sum_{i=1}^{n} P_{n-i}^{(n)}\omega_{1+(m-1)\alpha}(t_i) \leq \pi_A\omega_{1+m\alpha}(t_n), \quad m = 0,1, \quad 1 \leq n \leq N. \tag{17}$$

Lemma 9 ([44]). *Let λ_s be nonnegative constants with $0 < \sum_{s=0}^{n}\lambda_s \leq \Lambda$ for $n \geq 1$, where Λ is some positive constant independent of n. Suppose that the nonnegative sequences ξ_n and η_n are bounded, and the nonnegative grid function $\{v_n \mid n \geq 0\}$ satisfies the following:*

$$\sum_{k=1}^{n} A_{n-k}^{(n)}\nabla_\tau(v^k)^2 \leq \sum_{s=1}^{n}\lambda_{n-s}(v^{s,\theta_1})^2 + \xi^n v^{n,\theta_2} + (\eta^n)^2, \quad n \geq 1, \tag{18}$$

where for $i = 1,2$ and each n, we set $v^{n,\theta_1} := \theta_i v^{n-1} + (1-\theta_i)v^n$ for some constant $\theta_i \in [0,1]$. If the nonuniform grid satisfies the maximum time-step criterion $\tau_N \leq [\frac{11}{2}\Gamma(2-\alpha)\Lambda]^{-1/\alpha}$, then we have the following:

$$v^n \leq 2E_\alpha(\frac{11}{2}\Lambda t_n^\alpha)\left[v^0 + \max_{1\leq k\leq n}\sum_{j=1}^{k}P_{k-j}^{(k)}(\xi^j+\eta^j) + \max_{1\leq j\leq n}\eta^j\right], \quad 1 \leq n \leq N,$$

where $E_\alpha(z) := \sum_{k=0}^{\infty} z^k/\Gamma(1+k\alpha)$, and $E_\alpha(\cdot)$ represents the Mittag–Leffler function.

Lemma 10 ([45]). *Under the condition **M1** and Lemma 8, the fast Alikhanov Formula* (14) *satisfies the following:*

$$\left\langle (\mathcal{D}_\tau^\alpha v)^{n-\theta}, v^{n-\theta} \right\rangle \geq \frac{1}{2} \sum_{k=1}^{n} A_{n-k}^{(n)} \nabla_\tau (\|v^k\|^2), \quad 1 \leq n \leq N.$$

3. Establishment and Analysis of Compact Scheme

In this section, we shall derive the second-order fast compact difference scheme for problems (1)–(3). After that, the convergence and stability of the fast compact difference algorithm are rigorously proved.

3.1. Numerical Scheme

First, combined with (11), the temporal direction of Equation (1) at the grid points $(x_j, t_{n-\theta})$ is discretized by the fast nonuniform Alikhanov Formula (14) and the spatial direction is discretized by the compact difference Formula (9), where we obtain the following:

$$\begin{cases} \left(\mathcal{D}_f^\alpha U_j\right)^{n-\theta} + \dfrac{1}{p+2}\varphi(V_j^{n-\theta}, U_j^{n-\theta}) - \mu \mathcal{A}_2^{-1}\Delta_x U_j^{n-\theta} + \mathcal{A}_2^{-1}\Delta_x W_j^{n-\theta} = f_j^{n-\theta} + \Lambda_j^{n-\theta}, \\ \quad 1 \leq j \leq M-1, \qquad 1 \leq n \leq N, \end{cases} \tag{19}$$

$$V_j^n = \left(U_j^n\right)^p, \qquad 0 \leq j \leq M, \quad 0 \leq n \leq N, \tag{20}$$

$$W_j^{n-\theta} = \Delta_x U_j^{n-\theta} + R_3^{n-\theta}, \qquad 0 \leq j \leq M, \quad 0 \leq n \leq N, \tag{21}$$

where $\Lambda_j^{n-\theta}$ and $R_3^{n-\theta}$ denote the truncation errors.

Omitting the small terms $\Lambda_j^{n-\theta}$ and $R_3^{n-\theta}$ in (19), we replace the functions U_j^n, W_j^n, and V_j^n with their numerical approximations u_j^n, ω_j^n, and v_j^n, respectively. Meanwhile, combining IC (2) and BC (3), we can obtain the fully discrete difference scheme:

$$\begin{cases} \left(\mathcal{D}_f^\alpha u_j\right)^{n-\theta} + \dfrac{1}{p+2}\varphi(v_j^{n-\theta}, u_j^{n-\theta}) - \mu \mathcal{A}_2^{-1}\Delta_x u_j^{n-\theta} + \mathcal{A}_2^{-1}\Delta_x \omega_j^{n-\theta} = f_j^{n-\theta}, & (22) \\ 1 \leq j \leq M-1, \quad 1 \leq n \leq N, \\ v_j^n = \left(u_j^n\right)^p, \qquad 0 \leq j \leq M, \quad 0 \leq n \leq N, & (23) \\ \omega_j^{n-\theta} = \Delta_x u_j^{n-\theta}, \qquad 0 \leq j \leq M, \quad 0 \leq n \leq N, & (24) \\ u_j^0 = u_0(x_j), \qquad 1 \leq j \leq M-1, & (25) \\ u_0^n = u_M^n = \omega_0^n = \omega_M^n = 0, \qquad 0 \leq n \leq N. & (26) \end{cases}$$

In what follows, the stability and convergence analysis of the above fully discrete schemes (22)–(26) are carried out by the energy method.

3.2. Stability

Here, we present the stability result as follows:

Theorem 1. *Suppose that $\{u^n\}_{n=0}^N$ is the solution to* (22)–(26)*, and under the conditions of Lemma 8 and **M2**, then we have the following:*

$$\|u^n\| \leq \|u_0\| + \frac{11}{2}\Gamma(1-\alpha) \max_{1 \leq k \leq n} t_k^\alpha \|f^{k-\theta}\|.$$

Proof. Taking an inner product of (22) with $u^{n-\theta}$, we obtain the following:

$$\left\langle \left(\mathcal{D}_f^{\alpha} u\right)^{n-\theta}, u^{n-\theta} \right\rangle + \frac{1}{p+2}\left\langle \varphi(v^{n-\theta}, u^{n-\theta}), u^{n-\theta} \right\rangle - \mu\left\langle \mathcal{A}_2^{-1}\Delta_x u^{n-\theta}, u^{n-\theta} \right\rangle + \left\langle \mathcal{A}_2^{-1}\Delta_x \omega^{n-\theta}, u^{n-\theta} \right\rangle = \left\langle f^{n-\theta}, u^{n-\theta} \right\rangle. \tag{27}$$

By Lemmas 5 and 10, we have the following:

$$\left\langle \left(\mathcal{D}_f^{\alpha} u\right)^{n-\theta}, u^{n-\theta} \right\rangle \geq \frac{1}{2}\sum_{k=1}^{n} A_{n-k}^{(n)} \nabla_\tau (\|u^k\|^2), \tag{28}$$

$$\frac{1}{p+2}\left\langle \varphi(v^{n-\theta}, u^{n-\theta}), u^{n-\theta} \right\rangle = 0, \tag{29}$$

and

$$-\mu\left\langle \mathcal{A}_2^{-1}\Delta_x u^{n-\theta}, u^{n-\theta} \right\rangle = \mu\left\langle \mathcal{A}_2^{-1}\nabla^+ u^{n-\theta}, \nabla^+ u^{n-\theta} \right\rangle \geq \mu \mid u^{n-\theta} \mid_1^2, \tag{30}$$

$$\left\langle \mathcal{A}_2^{-1}\Delta_x \omega^{n-\theta}, u^{n-\theta} \right\rangle = \left\langle \mathcal{A}_2^{-1}\omega^{n-\theta}, \Delta_x u^{n-\theta} \right\rangle = \left\langle \mathcal{A}_2^{-1}\omega^{n-\theta}, \omega^{n-\theta} \right\rangle \geq 0. \tag{31}$$

Under the relations (28)–(31), we have the following:

$$\sum_{k=1}^{n} A_{n-k}^{(n)} \nabla_\tau (\|u^k\|^2) \leq 2\|f^{n-\theta}\|\|u^{n-\theta}\|.$$

Taking $\lambda_s = 0$ for $s \geq 0$, $\eta^n = 0$ and $\xi^n = 2\|f^{n-\theta}\|$ for $n \geq 1$ in Lemma 9 and $\pi_A = \frac{11}{4}$ in Lemma 8, it is easy to obtain

$$\|u^n\| \leq \|u_0\| + \max_{1\leq k\leq n} \sum_{i=1}^{k} 2P_{k-i}^{(k)} \|f^{k-\theta}\| \leq \|u_0\| + 2\pi_A \Gamma(1-\alpha) \max_{1\leq k\leq n} t_k^{\alpha} \|f^{k-\theta}\|.$$

Consequently, we infer the following:

$$\|u^n\| \leq \|u_0\| + \frac{11}{2}\Gamma(1-\alpha) \max_{1\leq k\leq n} t_k^{\alpha} \|f^{k-\theta}\|.$$

□

3.3. Convergence

Before analyzing the convergence of the fast Alikhanov schemes (22)–(26), we first analyze the truncation errors $\Lambda_j^{n-\theta}$ and $(R_3)_j^{n-\theta}$. In fact, $\Lambda_j^{n-\theta}$ is composed of the following four parts:

$$\Lambda_j^{n-\theta} := (R_{t1})_j^{n-\theta} + (R_{t2})_j^{n-\theta} + (R_3)_j^{n-\theta} + (R_s)_j^{n-\theta}, \qquad 1 \leq j \leq M-1, \quad 1 \leq n \leq N,$$

where $(R_s)_j^{n-\theta}$ means that the error is caused by approximating space derivatives; it can easily be seen that $(R_s)_j^{n-\theta} = \mathcal{O}(h^4)$ from (9) and (11). Moreover, we have the following:

$$(R_{t1})_j^{n-\theta} := \left(\mathcal{D}_f^{\alpha} u_j\right)^{n-\theta} - {}_0^C D_t^{\alpha} u(x_j, t_{n-\theta}),$$
$$(R_{t2})_j^{n-\theta} := -\frac{1}{p+2}\varphi((R_v)_j^{n-\theta}, (R_u)_j^{n-\theta}) + \mu \mathcal{A}_2^{-1}\Delta_x (R_u)_j^{n-\theta} - \mathcal{A}_2^{-1}\Delta_x (R_\omega)_j^{n-\theta},$$

where $(R_u)_j^{n-\theta}$, $(R_v)_j^{n-\theta}$ and $(R_\omega)_j^{n-\theta}$ denote the errors of the weighted time approximation at $t_{n-\theta}$, namely, we have the following:

$$(R_u)_j^{n-\theta} := u(x_j, t_{n-\theta}) - [\theta U_j^{n-1} + (1-\theta)U_j^n],$$
$$(R_v)_j^{n-\theta} := v(x_j, t_{n-\theta}) - [\theta V_j^{n-1} + (1-\theta)V_j^n],$$
$$(R_\omega)_j^{n-\theta} := \omega(x_j, t_{n-\theta}) - [\theta W_j^{n-1} + (1-\theta)W_j^n].$$

Based on the mesh condition **M1** and the regularity (7), and consulting Lemma 3.3 and Lemma 3.4 in [25,27], we arrive at the following:

$$\sum_{k=1}^{n} P_{n-k}^{(n)} \left|(R_{t1})_j^{k-\theta}\right| \le C\left(\frac{\tau_1^{\sigma}}{\sigma} + \frac{\epsilon}{\sigma} t_n^{\alpha} \hat{t}_{n-1}^2 + \frac{1}{1-\alpha} \max_{2\le k\le n} t_k^{\alpha} t_{k-1}^{\sigma-3} \tau_k^3 / \tau_{k-1}^{\alpha}\right), \quad 1 \le n \le N, \tag{32}$$

$$\sum_{k=1}^{n} P_{n-k}^{(n)} \left|(R_u)_j^{k-\theta}\right| \le C\left(\frac{\tau_1^{\sigma+\alpha}}{\sigma} + t_n^{\alpha} \max_{2\le k\le n} t_{k-1}^{\sigma-2} \tau_k^2\right), \quad 1 \le n \le N, \tag{33}$$

where $\hat{t}_n = \max\{1, t_n\}$.

Combining (17) and $(R_s)_j^{n-\theta} = \mathcal{O}(h^4)$, we can also obtain the following:

$$\max_{1\le k\le n} \sum_{i=1}^{k} P_{k-i}^{(k)} |(R_s)_j^{i-\theta}| \le C h^4, \quad 1 \le n \le N. \tag{34}$$

Therefore, combining (20)–(22), the following holds:

$$\max_{1\le k\le n} \sum_{i=1}^{k} P_{k-i}^{(k)} \|\Lambda^{i-\theta}\| \le C\left(\frac{\tau_1^{\sigma}}{\sigma} + \frac{\epsilon}{\sigma} t_n^{\alpha} \hat{t}_{n-1}^2 + \max_{2\le i\le k} t_i^{\alpha} t_{i-1}^{\sigma-3} \tau_i^3 / \tau_{i-1}^{\alpha} + t_k^{\alpha} \max_{2\le i\le k} t_{i-1}^{\sigma-2} \tau_i^2 + h^4\right), \quad 1 \le n \le N. \tag{35}$$

To obtain a pointwise error estimate of (22)–(26), we need to apply an important method, namely, the truncated function method. Based on the regularity assumption (8), we denote
$Q := \max_{(x,t)\in[0,L]\times[0,T]} |u(x,t)|$. We can find a second-order smooth function as follows:

$$g(u) := \begin{cases} u^p, & |u| \le Q+1, \\ 0, & |u| \ge Q+2. \end{cases}$$

Furthermore, let $c_1 := \max_{u\in R} |g(u)|$, $c_2 := \max_{u\in R} |g'(u)|$. It is not difficult to verify that the constants c_1 and c_2 depend only on Q and p by the Hermite polynomial interpolant. Clearly, (20) and (23) are equivalent to the following:

$$\begin{cases} V_j^n = g(U_j^n), & 0 \le j \le M, \quad 0 \le n \le N, \end{cases} \tag{36}$$

$$\begin{cases} v_j^n = g(u_j^n), & 0 \le j \le M, \quad 0 \le n \le N. \end{cases} \tag{37}$$

The convergence of the full discrete schemes (22)–(26) is studied below. Subtracting (19)–(21) from (22)–(24), respectively, the error equation can be written as follows:

$$\begin{cases} \left(\mathcal{D}_t^{\alpha} e_j\right)^{n-\theta} + \dfrac{1}{p+2}\left[\varphi(V_j^{n-\theta}, U_j^{n-\theta}) - \varphi(v_j^{n-\theta}, u_j^{n-\theta})\right] - \mu \mathcal{A}_2^{-1}\Delta_x e_j^{n-\theta} + \mathcal{A}_2^{-1}\Delta_x \eta_j^{n-\theta} = \Lambda_j^{n-\theta}, \\ \qquad\qquad 1 \le j \le M-1, \quad 1 \le n \le N, \end{cases} \tag{38}$$

$$\rho_j^{n-\theta} = g(U_j^{n-\theta}) - g(u_j^{n-\theta}), \quad 0 \le j \le M, \quad 0 \le n \le N, \tag{39}$$

$$\eta_j^{n-\theta} = \mathcal{A}_2^{-1}\Delta_x e_j^{n-\theta} + (R_3)_j^{n-\theta}, \quad 0 \le j \le M, \quad 0 \le n \le N, \tag{40}$$

$$e_j^0 = 0, \qquad 1 \le j \le M-1, \tag{41}$$

$$e_0^n = e_M^n = \eta_0^n = \eta_M^n = 0, \qquad 0 \le n \le N, \tag{42}$$

where $e_j^n := U_j^n - u_j^n$, $\varrho_j^n := V_j^n - v_j^n$, $\eta_j^n := W_j^n - \omega_j^n$.

Theorem 2. *Suppose that the exact solution, u, satisfies the regularity property in* (7) *and* (8) *with the parameter $\sigma \in (0,1) \cup (1,2)$. Let* ***M1***, ***M2*** *hold, and $\hat{t}_n = \max\{1, t_n\}$ for $1 \le n \le N$. If $\tau \le ((11/2)\Gamma(2-\alpha)c_3)^{-1/\alpha}$, the following estimate holds:*

$$\|e^n\| \le C(\tau^{\min\{\gamma\sigma,2\}} + h^4 + \epsilon), \quad 0 \le n \le N. \tag{43}$$

Proof. Firstly, according to the differential mean value theorem, from (39), it is clear that

$$|\varrho_j^n| \le c_2 |e_j^n|, \quad 0 \le j \le M, \quad 0 \le n \le N,$$

moreover, we obtain the following:

$$\|\varrho^n\| \le c_2 \|e^n\|, \quad 0 \le n \le N. \tag{44}$$

The next thing to do in the proof is to take an inner product of (38) with $e^{n-\theta}$; we obtain the following:

$$\begin{aligned} &\left\langle (\mathcal{D}_t^{\alpha} e)^{n-\theta}, e^{n-\theta} \right\rangle + \frac{1}{p+2}\left\langle \varphi(V^{n-\theta}, U^{n-\theta}) - \varphi(v^{n-\theta}, u^{n-\theta}), e^{n-\theta} \right\rangle \\ &\quad - \mu \left\langle \mathcal{A}_2^{-1}\Delta_x e^{n-\theta}, e^{n-\theta} \right\rangle + \left\langle \mathcal{A}_2^{-1}\Delta_x \eta^{n-\theta}, e^{n-\theta} \right\rangle = \left\langle \Lambda^{n-\theta}, e^{n-\theta} \right\rangle. \end{aligned} \tag{45}$$

Furthermore, taking an inner product of (40) with $\eta^{n-\theta}$, we obtain the following:

$$\left\langle \eta^{n-\theta}, \eta^{n-\theta} \right\rangle = \left\langle \mathcal{A}_2^{-1}\Delta_x e^{n-\theta}, \eta^{n-\theta} \right\rangle + \left\langle R_3^{n-\theta}, \eta^{n-\theta} \right\rangle. \tag{46}$$

Another step is to analyze the above equation term by term. Using Lemma 10, we have the following:

$$\left\langle (\mathcal{D}_t^{\alpha} e)^{n-\theta}, e^{n-\theta} \right\rangle \ge \frac{1}{2}\sum_{k=1}^{n} A_{n-k}^{(n)} \nabla_\tau (\|e^k\|^2). \tag{47}$$

By the regularity assumption (7), let $c_0 := \max\limits_{(x,t)\in[0,L]\times[0,T]}\{|u(x,t)|,\ |u_x(x,t)|\}$. Applying Lemmas 2–6 and the Cauchy–Schwarz inequality, and noting that $v^{n-\theta} = V^{n-\theta} - \varrho^{n-\theta}$ and $u^{n-\theta} = U^{n-\theta} - e^{n-\theta}$, we have the following:

$$\begin{aligned}
&\Big\langle \varphi(V^{n-\theta}, U^{n-\theta}) - \varphi(v^{n-\theta}, u^{n-\theta}), e^{n-\theta}\Big\rangle \\
=&\Big\langle \varphi(\varrho^{n-\theta}, U^{n-\theta}) + \varphi(V^{n-\theta}, e^{n-\theta}) - \varphi(\varrho^{n-\theta}, e^{n-\theta}), e^{n-\theta}\Big\rangle \\
=&\Big\langle \varphi(\varrho^{n-\theta}, U^{n-\theta}), e^{n-\theta}\Big\rangle \\
=&\Big\langle \varrho^{n-\theta}\mathcal{A}_1^{-1}\nabla_h U^{n-\theta} + \mathcal{A}_1^{-1}\nabla_h(\varrho^{n-\theta}U^{n-\theta}), e^{n-\theta}\Big\rangle \\
=&\Big(\varrho^{n-\theta}\mathcal{A}_1^{-1}\nabla_h U^{n-\theta}, e^{n-\theta}\Big) + \Big(\mathcal{A}_1^{-1}\nabla_h(\varrho^{n-\theta}U^{n-\theta}), e^{n-\theta}\Big) \\
=&\Big(\nabla_h U^{n-\theta}, \mathcal{A}_1^{-1}\Big(\varrho^{n-\theta}e^{n-\theta}\Big)\Big) - \Big(\varrho^{n-\theta}U^{n-\theta}, \mathcal{A}_1^{-1}\nabla_h e^{n-\theta}\Big) \\
\le&\|\mathcal{V}_1\nabla_h U^{n-\theta}\|\|\mathcal{V}_1\Big(\varrho^{n-\theta}e^{n-\theta}\Big)\| + \|\mathcal{V}_1\Big(\varrho^{n-\theta}U^{n-\theta}\Big)\|\|\mathcal{V}_1\nabla_h e^{n-\theta}\| \\
\le&3Lc_0\|\varrho^{n-\theta}e^{n-\theta}\| + 3c_0|e^{n-\theta}|_1\|\varrho^{n-\theta}\| \\
\le&3Lc_0\|\varrho^{n-\theta}\|\|e^{n-\theta}\|_\infty + 3c_0c_2|e^{n-\theta}|_1\|e^{n-\theta}\| \\
\le&3Lc_0c_2\|e^{n-\theta}\|\frac{\sqrt{L}}{2}|e^{n-\theta}|_1 + 3c_0c_2|e^{n-\theta}|_1\|e^{n-\theta}\| \\
\le&3c_0c_2(L^{3/2}+1)\|e^{n-\theta}\||e^{n-\theta}|_1 \\
\le&\frac{9c_0^2c_1^2(L^{3/2}+1)^2}{4\mu}\|e^{n-\theta}\|^2 + \mu|e^{n-\theta}|_1^2,
\end{aligned} \tag{48}$$

as well as

$$-\mu\Big\langle \mathcal{A}_2^{-1}\Delta_x e^{n-\theta}, e^{n-\theta}\Big\rangle = \mu\Big\langle \mathcal{A}_2^{-1}\nabla^+ e^{n-\theta}, \nabla^+ e^{n-\theta}\Big\rangle \ge \mu|e^{n-\theta}|_1^2, \tag{49}$$

$$\Big\langle \Lambda^{n-\theta}, e^{n-\theta}\Big\rangle \le \|\Lambda^{n-\theta}\|\|e^{n-\theta}\|. \tag{50}$$

Substituting the results of (47)–(49) into (34), and adding (46), we have the following:

$$\frac{1}{2}\sum_{k=1}^{n} A_{n-k}^{(n)}\nabla_\tau(\|e^k\|^2) + \Big\langle \eta^{n-\theta}, \eta^{n-\theta}\Big\rangle \le \frac{9c_0^2c_1^2(L^{3/2}+1)^2}{4\mu}\|e^{n-\theta}\|^2 + \|\Lambda^{n-\theta}\|\|e^{n-\theta}\| + \Big\langle R_3^{n-\theta}, \eta^{n-\theta}\Big\rangle.$$

$$\sum_{k=1}^{n} A_{n-k}^{(n)}\nabla_\tau(\|e^k\|^2) \le \frac{9c_0^2c_1^2(L^{3/2}+1)^2}{2\mu}\|e^{n-\theta}\|^2 + 2\|\Lambda^{n-\theta}\|\|e^{n-\theta}\| + \frac{1}{2}\|R_3^{n-\theta}\|^2.$$

According to Lemma 9, $\lambda_0 = \frac{9c_0^2c_1^2(L^{3/2}+1)^2}{2\mu} < c_3, \xi^n = 2\|\Lambda^{n-\theta}\|, \eta^n = \frac{\sqrt{2}}{2}\|R_3^{n-\theta}\|$, we can obtain the following:

$$\|e^n\| \le 2E_\alpha(\frac{11}{2}c_3t_n^\alpha)\left[\|e^0\| + \max_{1\le k\le n}\sum_{j=1}^{k} P_{k-j}^{(k)}(2\|\Lambda^{j-\theta}\| + \frac{\sqrt{2}}{2}\|R_3^{j-\theta}\|) + \frac{\sqrt{2}}{2}\max_{1\le j\le n} R_3^j\right], \quad 1 \le n \le N. \tag{51}$$

Due to $\|e^0\| = 0$, $2E_\alpha(\frac{11}{2}c_3t_n^\alpha) \le C$, and combing (35), we have the following:

$$\|e^n\| \le C\left(\frac{\tau_1^\sigma}{\sigma} + \frac{\epsilon}{\sigma}t_n^\alpha\hat{t}_{n-1}^2 + \max_{2\le i\le k} t_i^\alpha t_{i-1}^{\sigma-3}\tau_i^3/\tau_{i-1}^\alpha + t_k^\alpha\max_{2\le i\le k} t_{i-1}^{\sigma-2}\tau_i^2 + h^4\right). \tag{52}$$

On the other hand, if **M1** and **M2** hold, $\beta = \min\{2, \gamma\sigma\}$, we have the following:

$$\begin{aligned} t_k^{\alpha} t_{k-1}^{\sigma-3} \tau_k^3 \tau_{k-1}^{-\alpha} &\le C_\gamma t_k^{\alpha+\sigma-3} \tau_k^{3-\alpha} \\ &\le C_\gamma t_k^{\alpha+\sigma-3} \tau_k^{3-\alpha-\beta} \Big(\tau \min\Big\{1, t_k^{1-1/\gamma}\Big\}\Big)^{\beta} \\ &\le C_\gamma t_k^{\sigma-\beta/\gamma} (\tau_k / t_k)^{3-\alpha-\beta} \tau^{\beta} \\ &\le C_\gamma t_k^{\max\{0, \sigma-(3-\alpha)/\gamma\}} \tau^{\beta} \quad \text{for } 2 \le k \le n, \end{aligned} \tag{53}$$

$$\begin{aligned} t_{k-1}^{\sigma-2} \tau_k^2 &\le C_\gamma t_k^{\sigma-2} \tau_k^{2-\beta} \Big(\tau \min\Big\{1, t_k^{1-1/\gamma}\Big\}\Big)^{\beta} \\ &\le C_\gamma t_k^{\sigma-\beta/\gamma} (\tau_k / t_k)^{2-\beta} \tau^{\beta} \\ &\le C_\gamma t_k^{\max\{0, \sigma-2/\gamma\}} \tau^{\beta}, \quad \text{for } 2 \le k \le n. \end{aligned} \tag{54}$$

As a result, the discrete solution $u_j^{n-\theta}$ is convergent in the sense that

$$\|e^n\| \le C(\tau^{\min\{\gamma\sigma, 2\}} + h^4 + \epsilon), \quad 0 \le n \le N. \tag{55}$$

This finishes the proof. □

4. Numerical Experiment

In this section, we test the stability and convergence of the fast compact schemes (22)–(26) for three different experiments on a nonuniform grid $\{t_n = T(n/N)^{\gamma}, n = 1, \ldots, N\}$. All experiments were performed on a Windows server with an AMD Ryzen 5 4600H processor of 16GB RAM and 3.00 GHz CPU. In the following experiments, the tolerance accuracy of the SOE algorithm is limited to $\epsilon = 10^{-12}$ in order to balance accuracy and efficiency [6]. The following suitable formulas are given to calculate the error and convergence order of the following numerical solution:

$$E^{SOE}(M, N) = \left\| U^N - u^N \right\|_2 = \sqrt{h \sum_{j=1}^{M-1} (U_j^N - u_j^N)^2},$$

$$Rate_h^{SOE} = \log_2\left(\frac{E^{SOE}(M, N)}{E^{SOE}(2M, N)}\right), \quad Rate_\tau^{SOE} = \log_2\left(\frac{E^{SOE}(M, N)}{E^{SOE}(M, 2N)}\right),$$

where U^N and u^N represent the exact and numerical solutions at the *Nth* time level, respectively.

In addition, we define the following notation to illustrate the numerical implementation of the proposed scheme:

$$U^* = \max_{1 \le n \le N} \|U^n\|.$$

Before proceeding further, let us remark on the numerical scheme setting of the fast Alikhanov approach and Alikhanov approach.

- Alikhanov scheme: The Caputo fractional derivative discretization scheme is (12).
- Fast Alikhanov scheme: The Caputo fractional derivative discretization scheme is (14).

Example 1. *In this example, we consider the following problem:*

$$\begin{cases} {}_0^C D_t^{\alpha} u + u^p u_x - \mu u_{xx} + u_{xxxx} = f(x, t), \quad 0 < x < 1, \quad 0 \le t \le 1, & (56) \\ u(x, 0) = u_0(x), \quad 0 < x < 1, & (57) \\ u_{xx}(0, t) = u_{xx}(1, t), \quad 0 \le t \le 1, & (58) \end{cases}$$

and the exact solution is set as $u(x, t) = \left(1 + \frac{t^{\alpha}}{\Gamma(1+\alpha)}\right) \sin(\pi x)$. *Accordingly, the initial condition* $u_0 = \sin(\pi x)$ *and the source term* $f(x, t)$ *are as follows:*

$$f(x,t) = \sin(\pi x)\left(1+\mu\pi^2+\mu\pi^2\frac{t^\alpha}{\Gamma(1+\alpha)}+\pi^4+\pi^4\frac{t^\alpha}{\Gamma(1+\alpha)}\right)+\pi\left(1+\frac{t^\alpha}{\Gamma(1+\alpha)}\right)^{p+1}(\sin(\pi x))^{p+1}\cos(\pi x).$$

For Example 1, in Table 1, we fix $M = 256$, $\mu = 1$, and $\gamma = 2/\alpha$ to explore the performances of the fast Alikhanov and Alikhanov schemes in terms of errors in the L^2-norm and the convergence order for different α and p cases. It can be found that the errors in the L^2-norm of the Alikhanov and fast Alikhanov schemes are very close and both of them can reach second-order convergence in the temporal direction with $\alpha \in \{0.3, 0.5, 0.7\}$ and $p \in \{2, 3, 4\}$. When $p \in \{2, 3, 4\}$, the value of α keeps on changing, the errors in Alikhanov and fast Alikhanov schemes have the same effect and also achieve second-order convergence. Table 2 shows the errors and convergence orders in the spatial direction for different μ and p when fixing $N = 512$, $\alpha = 0.5$, and $\gamma = 4$. It can be observed that regardless of whether μ changes or p changes, the spatial errors in the L^2-norm of the two schemes are similar and both can achieve fourth-order convergence in agreement with the theoretical prediction.

Table 3 considers the cases where $N = 512$, $p = 2$, $\mu = 1$, and $\gamma = 2$ are fixed, with α changing, which indicates that the fast Alikhanov and Alikhanov schemes can achieve similar spatial errors and fourth-order convergence. The CPU times of the two algorithms are given; it is obvious that the fast Alikhanov scheme is much faster than the Alikhanov scheme. In order to further confirm whether the temporal and spatial convergence orders of the fast Alikhanov scheme remain stable as p increases, the temporal convergence and spatial convergence orders are shown in Figures 1 and 2. Table 4 shows that with the gradual increase in N, the value of U^* tends to stabilize and shows no increasing trend. These results confirm the numerical stability of the proposed scheme in the time direction.

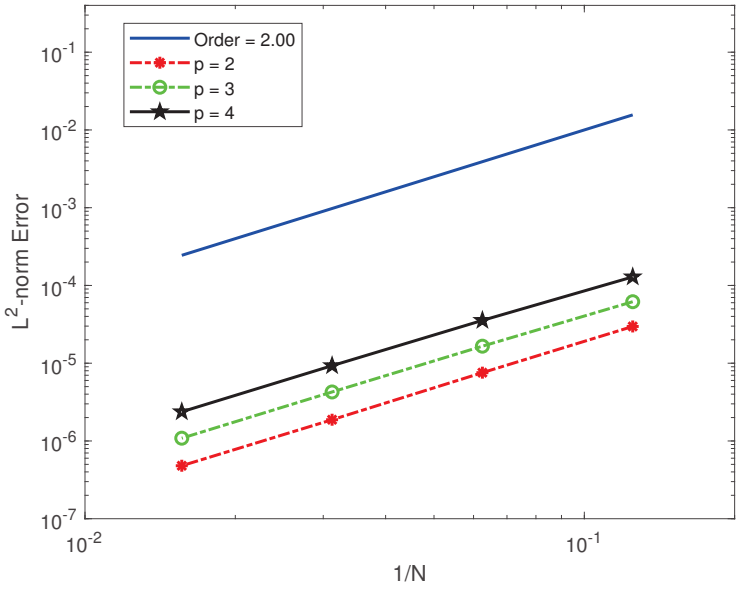

Figure 1. The temporal convergence orders of the fast compact difference scheme when $\alpha = 0.5$, $\mu = 1$, $\gamma = 4$ and $N = 256$.

Table 1. Temporal error and convergence order of Example 1 for different α and p with $M = 256$, $\mu = 1$, $\gamma = 2/\alpha$.

	N	$E^{SOE}(M,N)$	$Rate_\tau^{SOE}$	$E^{SOE}(M,N)$	$Rate_\tau^{SOE}$	$E^{SOE}(M,N)$	$Rate_\tau^{SOE}$
	Alikhanov	$p=2$		$p=3$		$p=4$	
	8	2.6080×10^{-5}	-	4.2294×10^{-5}	-	8.0635×10^{-5}	-
	16	6.2591×10^{-6}	2.0589	1.1197×10^{-5}	1.9173	2.2588×10^{-5}	1.8358
	32	1.4056×10^{-6}	2.1548	2.8265×10^{-6}	1.9861	5.9572×10^{-6}	1.9228
	64	3.2266×10^{-7}	2.1230	7.0951×10^{-7}	1.9941	1.5306×10^{-6}	1.9605
$\alpha = 0.3$	Fast Alikhanov	$p=2$		$p=3$		$p=4$	
	8	2.6081×10^{-5}	-	4.2298×10^{-5}	-	8.0632×10^{-5}	-
	16	6.2657×10^{-6}	2.0575	1.1195×10^{-5}	1.9177	2.2588×10^{-5}	1.8358
	32	1.4042×10^{-6}	2.1578	2.8276×10^{-6}	1.9852	5.9571×10^{-6}	1.9229
	64	3.2485×10^{-7}	2.1119	7.0925×10^{-7}	1.9952	1.5302×10^{-6}	1.9609
	Alikhanov	$p=2$		$p=3$		$p=4$	
	8	2.9692×10^{-5}	-	6.1797×10^{-5}	-	1.2884×10^{-4}	-
	16	7.5590×10^{-6}	1.9738	1.6557×10^{-5}	1.9001	3.5529×10^{-5}	1.8585
	32	1.8727×10^{-6}	2.0131	4.2675×10^{-6}	1.9560	9.2949×10^{-6}	1.9345
	64	4.8342×10^{-7}	1.9537	1.0864×10^{-6}	1.9739	2.3738×10^{-6}	1.9693
$\alpha = 0.5$	Fast Alikhanov	$p=2$		$p=3$		$p=4$	
	8	2.9697×10^{-5}	-	6.1799×10^{-5}	-	1.2884×10^{-4}	-
	16	7.5559×10^{-6}	1.9746	1.6555×10^{-5}	1.9003	3.5529×10^{-5}	1.8585
	32	1.8753×10^{-6}	2.0105	4.2675×10^{-6}	1.9558	9.2949×10^{-6}	1.9345
	64	4.8013×10^{-7}	1.9657	1.0853×10^{-6}	1.9752	2.3737×10^{-6}	1.9693
	Alikhanov	$p=2$		$p=3$		$p=4$	
	8	3.2325×10^{-5}	-	7.1925×10^{-5}	-	1.5150×10^{-4}	-
	16	8.3560×10^{-6}	1.9517	1.8960×10^{-5}	1.9235	4.0683×10^{-5}	1.8968
	32	2.1056×10^{-6}	1.9886	4.8485×10^{-6}	1.9674	1.0492×10^{-5}	1.9552
	64	5.3111×10^{-7}	1.9872	1.2273×10^{-6}	1.9820	2.6629×10^{-6}	1.9782
$\alpha = 0.7$	Fast Alikhanov	$p=2$		$p=3$		$p=4$	
	8	3.2332×10^{-5}	-	7.1927×10^{-5}	-	1.5149×10^{-4}	-
	16	8.3605×10^{-6}	1.9513	1.8961×10^{-5}	1.9235	4.0681×10^{-5}	1.8968
	32	2.1158×10^{-6}	1.9824	4.8494×10^{-6}	1.9672	1.0485×10^{-5}	1.9560
	64	5.2915×10^{-7}	1.9995	1.2265×10^{-6}	1.9833	2.6618×10^{-6}	1.9779

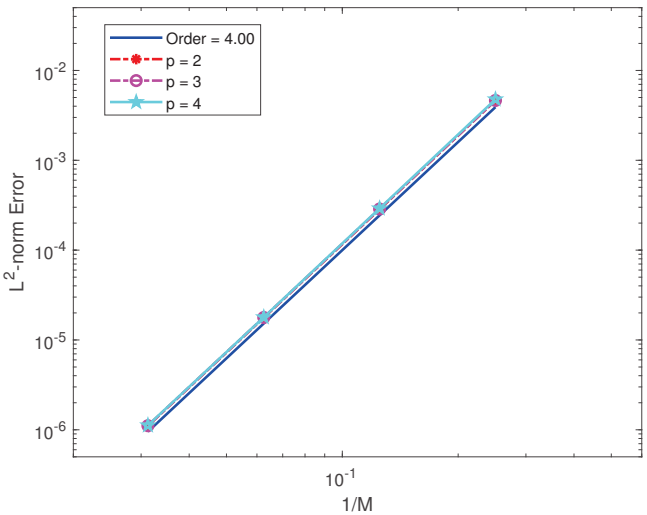

Figure 2. The spatial convergence orders of the fast compact difference scheme when $\alpha = 0.5$, $\mu = 1$, $\gamma = 4$ and $N = 512$.

Table 2. Space error and convergence order of Example 1 for different μ and p with $N = 512$, $\alpha = 0.5$, $\gamma = 4$.

	M	$E^{SOE}(M,N)$	$Rate_h^{SOE}$	$E^{SOE}(M,N)$	$Rate_h^{SOE}$	$E^{SOE}(M,N)$	$Rate_h^{SOE}$
	Alikhanov	$p=2$		$p=3$		$p=4$	
	4	4.8317×10^{-3}	-	4.8272×10^{-3}	-	4.9532×10^{-3}	-
	8	2.9702×10^{-4}	4.0239	2.9925×10^{-4}	4.0118	3.0394×10^{-4}	4.0265
	16	1.8486×10^{-5}	4.0060	1.8543×10^{-5}	4.0124	1.8659×10^{-5}	4.0258
	32	1.1542×10^{-6}	4.0015	1.1572×10^{-6}	4.0021	1.1689×10^{-6}	3.9966
$\mu=0.1$	Fast Alikhanov	$p=2$		$p=3$		$p=4$	
	4	4.8317×10^{-3}	-	4.8272×10^{-3}	-	4.9532×10^{-3}	-
	8	2.9702×10^{-4}	4.0239	2.9925×10^{-4}	4.0118	3.0394×10^{-4}	4.0265
	16	1.8486×10^{-5}	4.0060	1.8543×10^{-5}	4.0124	1.8659×10^{-5}	4.0258
	32	1.1542×10^{-6}	4.0015	1.1572×10^{-6}	4.0021	1.1689×10^{-6}	3.9966
	Alikhanov	$p=2$		$p=3$		$p=4$	
	4	4.6355×10^{-3}	-	4.6325×10^{-3}	-	4.7695×10^{-3}	-
	8	2.8495×10^{-4}	4.0239	2.8705×10^{-4}	4.0124	2.9150×10^{-4}	4.0323
	16	1.7735×10^{-5}	4.0060	1.7788×10^{-5}	4.0123	1.7899×10^{-5}	4.0256
	32	1.1073×10^{-6}	4.0015	1.1102×10^{-6}	4.0021	1.1212×10^{-6}	3.9967
$\mu=1$	Fast Alikhanov	$p=2$		$p=3$		$p=4$	
	4	4.6355×10^{-3}	-	4.6325×10^{-3}	-	4.7695×10^{-3}	-
	8	2.8495×10^{-4}	4.0239	2.8705×10^{-4}	4.0124	2.9150×10^{-4}	4.0323
	16	1.7735×10^{-5}	4.0060	1.7788×10^{-5}	4.0123	1.7899×10^{-5}	4.0256
	32	1.1073×10^{-6}	4.0015	1.1102×10^{-6}	4.0021	1.1212×10^{-6}	3.9967
	Alikhanov	$p=2$		$p=3$		$p=4$	
	4	3.6473×10^{-3}	-	3.6500×10^{-3}	-	3.8049×10^{-3}	-
	8	2.2412×10^{-4}	4.0245	2.2550×10^{-4}	4.0167	2.2849×10^{-4}	4.0576
	16	1.3948×10^{-5}	4.0062	1.3981×10^{-5}	4.0116	1.4058×10^{-5}	4.0227
	32	8.7088×10^{-7}	4.0014	8.7269×10^{-7}	4.0019	8.8006×10^{-7}	3.9976
$\mu=10$	Fast Alikhanov	$p=2$		$p=3$		$p=4$	
	4	3.6473×10^{-3}	-	3.6500×10^{-3}	-	3.8049×10^{-3}	-
	8	2.2412×10^{-4}	4.0245	2.2550×10^{-4}	4.0167	2.2849×10^{-4}	4.0576
	16	1.3948×10^{-5}	4.0062	1.3981×10^{-5}	4.0116	1.4058×10^{-5}	4.0227
	32	8.7088×10^{-7}	4.0014	8.7269×10^{-7}	4.0019	8.8006×10^{-7}	3.9976

Table 3. Errors, convergence orders in space, and CPU times for the Alikhanov scheme and fast Alikhanov scheme by fixing $N = 512$, $p = 2$, $\mu = 1$, and $\gamma = 2$ for Example 1.

		$\alpha = 0.3$		$\alpha = 0.5$		$\alpha = 0.7$	
Alikhanov	M	$E^{SOE}(M,N)$	$Rate_h^{SOE}$	$E^{SOE}(M,N)$	$Rate_h^{SOE}$	$E^{SOE}(M,N)$	$Rate_h^{SOE}$
	4	4.6004×10^{-3}	-	4.6355×10^{-3}	-	4.5792×10^{-3}	-
	8	2.8278×10^{-4}	4.0240	2.8495×10^{-4}	4.0239	2.8149×10^{-4}	4.0240
	16	1.7600×10^{-5}	4.0061	1.7735×10^{-5}	4.0060	1.7555×10^{-5}	4.0031
	32	1.0988×10^{-6}	4.0016	1.1073×10^{-6}	4.0015	1.1327×10^{-6}	3.9541
	CPU(s)	82.777		75.941		82.308	
		$\alpha = 0.3$		$\alpha = 0.5$		$\alpha = 0.7$	
Fast Alikhanov	M	$E^{SOE}(M,N)$	$Rate_h^{SOE}$	$E^{SOE}(M,N)$	$Rate_h^{SOE}$	$E^{SOE}(M,N)$	$Rate_h^{SOE}$
	4	4.6004×10^{-3}	-	4.6355×10^{-3}	-	4.5792×10^{-3}	-
	8	2.8278×10^{-4}	4.0240	2.8495×10^{-4}	4.0239	2.8145×10^{-4}	4.0241
	16	1.7600×10^{-5}	4.0060	1.7735×10^{-5}	4.0060	1.7517×10^{-5}	4.0061
	32	1.0997×10^{-6}	4.0005	1.1073×10^{-6}	4.0015	1.0939×10^{-6}	4.0011
	CPU(s)	3.9295		3.8685		3.9980	

Table 4. Numerical solutions when $M = 256$, $p = 2$, $\mu = 1$, and $\gamma = 2/\alpha$ for Example 1.

	$\alpha = 0.3$	$\alpha = 0.5$	$\alpha = 0.7$
N	U^*	U^*	U^*
4	1.4949	1.5049	1.4853
8	1.4950	1.5050	1.4853
16	1.4950	1.5050	1.4853
32	1.4950	1.5050	1.4853
64	1.4950	1.5050	1.4853
128	1.4950	1.5050	1.4853

Example 2. *In order to verify the wide range of applications of the numerical scheme, the case where the exact solution is unknown is tested in this numerical example. We consider problems* (1)–(3) *in* $\Omega = (0, \pi)$ *to verify the effectiveness and high accuracy of the numerical scheme. Let* $T = 1$*, the initial condition is* $u_0(x) = \sin(x)$*, and the source term is* $f(x, t) = 0$*.*

In Table 5, the errors in the L^2-norm, spatial convergence orders, and CPU times of the Alikhanov scheme and the fast Alikhanov numerical scheme are presented for fixed values of $p = 2$, $\mu = 1$, $\gamma = 2$, and $N = 2048$, with $\alpha \in \{0.3, 0.5, 0.7\}$. It is worth mentioning that both numerical schemes can achieve the same approximation effect, but the CPU time of the fast scheme is much shorter. Table 6 demonstrates that for fixed values of $M = 512$, $\mu = 1$, $\alpha = 0.8$, and $\gamma = 2/\alpha$, the L^2-norm error decreases as the number of temporal subintervals increases. It is expected that the convergence order of the fast approximate scheme is $\mathcal{O}(\tau^2)$. Meanwhile, the error and convergence order remain as expected for changing values of p, suggesting that the approximation scheme is stable for different p. Table 7 shows the errors, temporal convergence orders, and CPU times for different μ, where we take $M = 512$, $p = 2$, and $\gamma = 2/\alpha$. In each row of the table, the errors and convergence orders change very little as μ varies, so the method is stable for the coefficient μ, as predicted by our theoretical analysis. In addition, in order to demonstrate more intuitively the speedup effect of the SOE approximation, taking $\alpha = 0.5$, $p = 2$, $\mu = 1$, $\gamma = 2$, and $M = 4$, we plot the computation time curves of the two schemes for the N increase, as shown in Figure 3. It is clear that the fast Alikhanov scheme saves a lot of computational costs compared to the Alikhanov scheme.

Table 5. Errors, convergence orders in space, and CPU times for the Alikhanov scheme and fast Alikhanov scheme by fixing $p = 2$, $\mu = 1$, $\gamma = 2$, and $N = 2048$ for Example 2.

		$\alpha = 0.3$		$\alpha = 0.5$		$\alpha = 0.7$	
Alikhanov	M	$E^{SOE}(M,N)$	$Rate_h^{SOE}$	$E^{SOE}(M,N)$	$Rate_h^{SOE}$	$E^{SOE}(M,N)$	$Rate_h^{SOE}$
	4	4.3605×10^{-4}	-	4.3568×10^{-4}	-	4.5247×10^{-4}	-
	8	2.6588×10^{-5}	4.0356	2.6570×10^{-5}	4.0354	2.7511×10^{-5}	4.0398
	16	1.6529×10^{-6}	4.0077	1.6517×10^{-6}	4.0078	1.7094×10^{-6}	4.0084
	32	1.0316×10^{-7}	4.0020	1.0308×10^{-7}	4.0021	1.0667×10^{-7}	4.0022
	CPU(s)	1253.8		1197.3		1279.9	
		$\alpha = 0.3$		$\alpha = 0.5$		$\alpha = 0.7$	
Fast Alikhanov	M	$E^{SOE}(M,N)$	$Rate_h^{SOE}$	$E^{SOE}(M,N)$	$Rate_h^{SOE}$	$E^{SOE}(M,N)$	$Rate_h^{SOE}$
	4	4.3605×10^{-4}	-	4.3568×10^{-4}	-	4.5247×10^{-4}	-
	8	2.6588×10^{-5}	4.0356	2.6570×10^{-5}	4.0354	2.7511×10^{-5}	4.0398
	16	1.6529×10^{-6}	4.0077	1.6517×10^{-6}	4.0078	1.7094×10^{-6}	4.0084
	32	1.0316×10^{-7}	4.0020	1.0308×10^{-7}	4.0021	1.0667×10^{-7}	4.0022
	CPU(s)	44.704		45.165		45.322	

Table 6. The E^{SOE}-norm errors and temporal convergence orders with $M = 512$, $\mu = 1$, $\alpha = 0.8$, and $\gamma = 2/\alpha$.

	$p = 1$		$p = 2$		$p = 3$		$p = 4$		$p = 5$	
N	$E^{SOE}(M,N)$	$Rate_\tau^{SOE}$	$E^{SOE}(M,N)$	$Rate_\tau^{SOE}$	$E^{SOE}(M,N)$	$Rate_\tau^{SOE}$	$E^{SOE}(M,N)$	$Rate_\tau^{SOE}$	$E^{SOE}(M,N)$	$Rate_\tau^{SOE}$
10	1.3260×10^{-3}	-	1.3265×10^{-3}	-	1.3266×10^{-3}	-	1.3266×10^{-3}	-	1.3266×10^{-3}	-
20	3.4271×10^{-4}	1.9520	3.4279×10^{-4}	1.9522	3.4281×10^{-4}	1.9522	3.4281×10^{-4}	1.9522	3.4281×10^{-4}	1.9523
40	9.0337×10^{-5}	1.9236	9.0353×10^{-5}	1.9237	9.0356×10^{-5}	1.9237	9.0354×10^{-5}	1.9238	9.0351×10^{-5}	1.9238
80	2.3914×10^{-5}	1.9174	2.3917×10^{-5}	1.9176	2.3917×10^{-5}	1.9176	2.3914×10^{-5}	1.9177	2.3914×10^{-5}	1.9177
160	6.3120×10^{-6}	1.9217	6.3132×10^{-6}	1.9216	6.3131×10^{-6}	1.9216	6.3145×10^{-6}	1.9211	6.3158×10^{-6}	1.9208

Table 7. The E^{SOE}-norm errors, temporal convergence orders, and CPU time (seconds) with $M = 512$, $p = 2$, and $\gamma = 2/\alpha$.

	$\mu = 0.05$			$\mu = 0.1$			
N	$E^{SOE}(M,N)$	$Rate_\tau^{SOE}$	CPU(s)	N	$E^{SOE}(M,N)$	$Rate_\tau^{SOE}$	CPU(s)
4	2.8796×10^{-3}	-	0.4605	4	3.2656×10^{-3}	-	0.4406
8	6.8144×10^{-4}	2.0792	0.7595	8	7.7751×10^{-4}	2.0704	0.8029
16	1.7604×10^{-4}	1.9527	1.5174	16	2.0089×10^{-4}	1.9525	1.5480
32	4.8379×10^{-5}	1.8634	2.5469	32	5.4828×10^{-5}	1.8734	2.7098
64	1.3632×10^{-5}	1.8273	5.0930	64	1.5262×10^{-5}	1.8450	5.3880
	$\mu = 1$			$\mu = 2$			
N	$E^{SOE}(M,N)$	$Rate_\tau^{SOE}$	CPU(s)	N	$E^{SOE}(M,N)$	$Rate_\tau^{SOE}$	CPU(s)
4	8.7476×10^{-3}	-	0.4646	4	9.7976×10^{-3}	-	0.5341
8	2.0697×10^{-3}	2.0794	0.7903	8	2.3022×10^{-3}	2.0894	0.7326
16	5.2813×10^{-4}	1.9705	1.4359	16	5.8600×10^{-4}	1.9741	1.3253
32	1.3868×10^{-4}	1.9291	2.6138	32	1.5258×10^{-4}	1.9413	2.5373
64	3.6684×10^{-5}	1.9185	5.0402	64	3.9897×10^{-5}	1.9353	4.7893

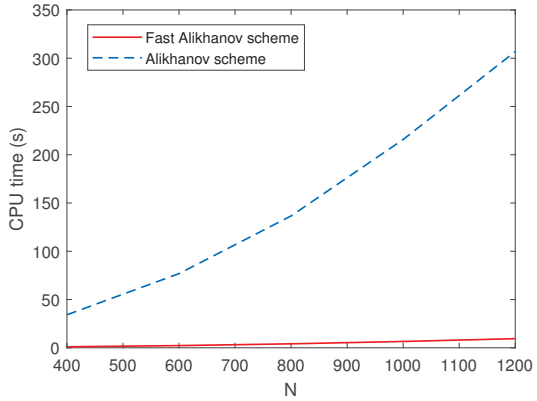

Figure 3. Comparison of the CPU time between the fast Alikhanov and Alikhanov schemes with $\alpha = 0.5$, $p = 2$, $\mu = 1$, $\gamma = 2$, and $M = 4$.

Example 3. *In this example, we consider problem (1) over domains* $\Omega = (0,1)$ *and* $T = 1$. *The analytic solution is* $u(x,t) = \left(\frac{t^\alpha}{\Gamma(1+\alpha)}\right)\sin(\pi x)\cos(\pi x)$, *such that the source term* $f(x,t)$ *is as follows:*

$$f(x,t) = \sin(\pi x)\cos(\pi x) + 2\pi^2\mu\frac{t^\alpha}{\Gamma(1+\alpha)}\sin(2\pi x) + 8\pi^4\frac{t^\alpha}{\Gamma(1+\alpha)}\sin(2\pi x)$$
$$+ \pi\left(\frac{t^\alpha}{\Gamma(1+\alpha)}\right)^{p+1}(\sin(\pi x))^p(\cos(\pi x))^p\cos(2\pi x).$$

Tables 8 and 9 display the temporal and spatial errors, spatial–temporal convergence orders, and CPU times for various α values. Furthermore, the results show that the proposed scheme can reach the second order of convergence in time and the fourth order of convergence in space. Next, we test the stability by fixing $M = 256$, $\mu = 1$, $p = 2$, and

$\gamma = 2/\alpha$ and selecting different T values, which means the time-step sizes are different. The numerical results are listed in Table 10, which shows that the fast Alikhanov scheme is stable and has a relaxed stability restriction. In Table 11, we tested the errors for $\alpha = 0.95, \alpha = 0.99, \alpha = 0.999,$ *and* $\alpha = 0.9999$ by making $M = 256$, $\mu = 1$, $p = 2$, and $\gamma = 2/\alpha$, which also shows that the numerical scheme is stable when $\alpha \to 1^-$.

Table 8. Errors, temporal convergence orders, and CPU times by fixing $p = 2$, $\mu = 1$, $\gamma = 4$, and $M = 256$ for Example 3.

	$\alpha = 0.3$			$\alpha = 0.5$			$\alpha = 0.7$		
N	$E^{SOE}(M,N)$	$Rate_\tau^{SOE}$	CPU	$E^{SOE}(M,N)$	$Rate_\tau^{SOE}$	CPU	$E^{SOE}(M,N)$	$Rate_\tau^{SOE}$	CPU
16	9.5519×10^{-7}	-	0.2818	3.9181×10^{-6}	-	0.2457	8.5622×10^{-6}	-	0.2060
32	2.4356×10^{-7}	1.9715	0.4170	1.0148×10^{-6}	1.9490	0.3583	2.2256×10^{-6}	1.9438	0.4410
64	5.8573×10^{-8}	2.0560	0.7595	2.5816×10^{-7}	1.9748	0.7026	5.6804×10^{-7}	1.9701	0.7078
128	1.6584×10^{-8}	1.8205	1.8818	6.6561×10^{-8}	1.9555	1.4596	1.4255×10^{-7}	1.9946	1.5336

Table 9. Errors, convergence orders in space, and CPU times by fixing $p = 2$, $\mu = 1$, $\gamma = 4$, and $N = 1000$ for Example 3.

	$\alpha = 0.3$			$\alpha = 0.5$			$\alpha = 0.7$		
M	$E^{SOE}(M,N)$	$Rate_h^{SOE}$	CPU	$E^{SOE}(M,N)$	$Rate_h^{SOE}$	CPU	$E^{SOE}(M,N)$	$Rate_h^{SOE}$	CPU
16	7.7546×10^{-5}	-	13.587	7.8530×10^{-5}	-	13.533	7.6592×10^{-5}	-	13.994
32	4.8243×10^{-6}	4.0067	15.856	4.8854×10^{-6}	4.0067	15.493	4.7648×10^{-6}	4.0067	15.609
64	3.0131×10^{-7}	4.0010	19.515	3.0497×10^{-7}	4.0017	19.445	2.9744×10^{-7}	4.0017	19.734
128	1.9031×10^{-8}	3.9848	28.411	1.9111×10^{-8}	3.9962	28.621	1.8807×10^{-8}	3.9833	28.510

Table 10. The E_2-norm errors and temporal convergence orders with $M = 256$, $\mu = 1$, $p = 2$, and $\gamma = 2/\alpha$.

	$T = 0.5$		$T = 1$		$T = 4$		$T = 10$	
N	$E^{SOE}(M,N)$	$Rate_\tau^{SOE}$	$E^{SOE}(M,N)$	$Rate_\tau^{SOE}$	$E^{SOE}(M,N)$	$Rate_\tau^{SOE}$	$E^{SOE}(M,N)$	$Rate_\tau^{SOE}$
16	1.3810×10^{-6}	-	3.9181×10^{-6}	-	3.1501×10^{-5}	-	1.2475×10^{-4}	-
32	3.5931×10^{-7}	1.9424	1.0148×10^{-6}	1.9490	8.1468×10^{-6}	1.9511	3.2269×10^{-5}	1.9507
64	9.0207×10^{-8}	1.9939	2.5816×10^{-7}	1.9748	2.0664×10^{-6}	1.9791	8.2114×10^{-6}	1.9745
128	2.3438×10^{-8}	1.9444	6.6561×10^{-8}	1.9555	5.2247×10^{-7}	1.9837	2.0765×10^{-6}	1.9835
256	6.0047×10^{-9}	1.9647	1.5317×10^{-8}	2.1196	1.3334×10^{-7}	1.9703	5.2527×10^{-7}	1.9830

Table 11. The E_2-norm errors and temporal convergence orders with $M = 256$, $\mu = 1$, $p = 2$, $\alpha = 0.5$, and $\gamma = 2/\alpha$.

	$\alpha = 0.95$		$\alpha = 0.99$		$\alpha = 0.999$		$\alpha = 0.9999$	
N	$E^{SOE}(M,N)$	$Rate_\tau^{SOE}$	$E^{SOE}(M,N)$	$Rate_\tau^{SOE}$	$E^{SOE}(M,N)$	$Rate_\tau^{SOE}$	$E^{SOE}(M,N)$	$Rate_\tau^{SOE}$
16	4.0608×10^{-6}	-	3.8864×10^{-6}	-	3.8417×10^{-6}	-	3.8366×10^{-6}	-
32	1.0171×10^{-6}	1.9973	9.7447×10^{-6}	1.9957	9.6418×10^{-7}	1.9944	9.6071×10^{-7}	1.9977
64	2.5443×10^{-7}	1.9992	2.4199×10^{-7}	2.0097	2.4196×10^{-7}	1.9946	2.3883×10^{-7}	2.0081
128	6.5139×10^{-8}	1.9657	6.0890×10^{-8}	1.9907	6.0593×10^{-8}	1.9975	5.8879×10^{-8}	2.0201
256	1.6078×10^{-8}	2.0184	1.5477×10^{-8}	1.9761	1.7048×10^{-8}	1.8295	1.4500×10^{-8}	2.0217

5. Conclusions

In this work, we propose a fast high-order compact scheme for solving the fractional KS equation with the generalized Burgers' type nonlinearity. To deal with the weak singularity at the initial time, the Alikhanov scheme is implemented to approximate the Caputo fractional derivative in the time direction. With the aid of the SOE technique, the computational efficiency is improved and the storage requirement is reduced. In the space direction, the developed compact difference formulas have been successfully applied for approximating the spatial derivatives. As a result, a fully discrete scheme is constructed.

Meanwhile, the stability and convergence with $\tau^2 + h^4$ of the proposed scheme are proved. Finally, the results of the numerical experiments demonstrate that the convergence orders for temporal and spatial convergence achieve second-order and fourth-order accuracies, respectively. This is highly consistent with the theoretical predictions and effectively verifies the theoretical analysis.

Author Contributions: Conceptualization, D.X.; methodology, H.J.; software, H.J.; validation, H.J.; formal analysis, H.J.; investigation, H.J.; re-sources, H.J.; data curation, H.J.; writing—original draft preparation, H.J.; writing—review and editing, D.X.; visu-alization, D.X.; supervision, D.X. ; project administration, D.X. All authors have read and agreed to the published version of the manuscript.

Funding: The work was supported by Scientific Research Fund of Hunan Provincial Education Department (grant number No. 24C0265).

Data Availability Statement: The manuscript has no associated data.

Conflicts of Interest: The authors declare that they have no conflicts of interest.

References

1. Kuramoto, Y.; Tsuzuki, T. On the Formation of Dissipative Structures in Reaction-Diffusion Systems. *Prog. Theor. Phys.* **1975**, *54*, 687–699.
2. Sivashinsky, G.I. Nonlinear Analysis of Hydrodynamic Instability in Laminar Flames-I. Derivation of Basic Equations. *Acta Astronaut.* **1977**, *4*, 1177–1206.
3. Sivashinsky, G.I.; Michelson, D.M. On Irregular Wavy Flow of a Liquid Film Down a Vertical Plane. *Prog. Theor. Phys.* **1980**, *63*, 2112–2114.
4. Sivashinsky, G.I. Instabilities, Pattern-Formation, and Turbulence in Flames. *Ann. Rev. Fluid Mech.* **1983**, *15*, 179–199.
5. Hyman, J.M.; Nicolaenko, B.; Zaleski, S. Order and Complexity in the Kuramoto-Sivashinsky Model of Weakly Turbulent Interfaces. *Phys. D* **1986**, *23*, 265–292.
6. Peng, X.; Qiu, W.; Hendy, A.; Zaky, M. Temporal Second-Order Fast Finite Difference/Compact Difference Schemes for Time-Fractional Generalized Burgers' Equations. *J. Sci. Comput.* **2024**, *99*, 52.
7. Tadmor, E. The Well-Posedness of the Kuramoto–Sivashinsky Equation. *SIAM J. Math. Anal.* **1986**, *17*, 884–893.
8. Zgliczynski, P. Attracting Fixed Points for the Kuramoto–Sivashinsky Equation: A Computer Assisted Proof. *SIAM J. Appl. Dyn. Syst.* **2002**, *1*, 215–235.
9. Sakthivel, R.; Ito, H. Non-Linear Robust Boundary Control of the Kuramoto–Sivashinsky Equation. *IMA J. Math. Control Inf.* **2007**, *24*, 47–55.
10. Khater, A.H.; Temsah, R.S. Numerical Solutions of the Generalized Kuramoto–Sivashinsky Equation by Chebyshev Spectral Collocation Methods. *Comput. Math. Appl.* **2008**, *56*, 1465–1472.
11. Mittal, R.C.; Arora, G. Quintic B-Spline Collocation Method for Numerical Solution of the Kuramoto–Sivashinsky Equation. *Commun. Nonlinear Sci.* **2010**, *15*, 2798–2808.
12. Xu, Y.; Shu, C.W. Local Discontinuous Galerkin Methods for the Kuramoto–Sivashinsky Equations and the Ito-Type Coupled KdV Equations. *Comput. Methods Appl. Mech. Eng.* **2006**, *195*, 3430–3447.
13. Akrivis, G.; Smyrlis, Y. Implicit—Explicit BDF Methods for the Kuramoto–Sivashinsky Equation. *Appl. Numer. Math.* **2004**, *51*, 151–169.
14. Langlands, T.A.M.; Henry, B.I. The Accuracy and Stability of an Implicit Solution Method for the Fractional Diffusion Equation. *J. Comput. Phys.* **2005**, *205*, 719–736.
15. Sun, Z.Z.; Wu, X.N. A Fully Discrete Difference Scheme for a Diffusion-Wave System. *Appl. Numer. Math.* **2006**, *56*, 193–209.
16. Li, C.; Deng, W.H.; Wu, Y.J. Numerical Analysis and Physical Simulations for the Time Fractional Radial Diffusion Equation. *Comput. Math. Appl.* **2011**, *62*, 1024–1037.
17. Li, L.M.; Xu, D.; Luo, M. Alternating Direction Implicit Galerkin Finite Element Method for the Two-Dimensional Fractional Diffusion-Wave Equation. *J. Comput. Phys.* **2013**, *255*, 471–485.
18. Lin, Y.M.; Xu, C.J. Finite Difference/Spectral Approximations for the Time-Fractional Diffusion Equation. *J. Comput. Phys.* **2007**, *225*, 1533–1552.
19. Qiu, W.L.; Chen, H.B.; Xuan, X. An Implicit Difference Scheme and Algorithm Implementation for the One-Dimensional Time-Fractional Burgers Equations. *Math. Comput. Simulat.* **2019**, *166*, 298–314.
20. Liu, T.; Liu, H.; Ma, Y. Approximate Solution of a Kind of Time-Fractional Evolution Equations Based on Fast L1 Formula and Barycentric Lagrange Interpolation. *Fractal Fract.* **2024**, *8*, 675. [CrossRef]

21. Gao, G.H.; Sun, Z.Z.; Zhang, H.W. A New Fractional Differentiation Formula to Approximate the Caputo Fractional Derivative and Its Applications. *J. Comput. Phys.* **2014**, *259*, 33–50. [CrossRef]
22. Liao, H.L.; Lyu, P.; Vong, S.; Zhao, Y. Stability of Fully Discrete Schemes with Interpolation-Type Fractional Formulas for Distributed-Order Subdiffusion Equations. *Numer. Algor.* **2017**, *75*, 845–878. [CrossRef]
23. Lv, C.W.; Xu, C.J. Error Analysis of a High Order Method for Time-Fractional Diffusion Equations. *SIAM J. Sci. Comput.* **2016**, *38*, 2699–2724. [CrossRef]
24. Alikhanov, A.A. A New Difference Scheme for the Time Fractional Diffusion Equation. *J. Comput. Phys.* **2015**, *280*, 424–438.
25. Liao, H.L.; McLean, W.; Zhang, J.W. A Second-Order Scheme with Nonuniform Time Steps for a Linear Reaction-Subdiffusion Problem. *Commun. Comput. Phys.* **2021**, *30*, 567–601.
26. Zhang, H.X.; Yang, X.H.; Xu, D. An Efficient Spline Collocation Method for a Nonlinear Fourth-Order Reaction Subdiffusion Equation. *J. Sci. Comput.* **2020**, *85*, 7. [CrossRef]
27. Li, X.; Liao, H.L.; Zhang, L.M. A Second-Order Fast Compact Scheme with Unequal Time-Steps for Subdiffusion Problems. *Numer. Algorithms* **2021**, *86*, 1011–1039.
28. Jiang, S.D.; Zhang, J.W.; Zhang, Q.; Zhang, Z.M. Fast Evaluation of the Caputo Fractional Derivative and Its Applications to Fractional Diffusion Equations. *Commun. Comput. Phys.* **2017**, *21*, 650–678. [CrossRef]
29. Lee, S.; Kim, H.; Jang, B. A Novel Numerical Method for Solving Nonlinear Fractional-Order Differential Equations and Its Applications. *Fractal Fract.* **2024**, *8*, 65. [CrossRef]
30. Yang, S.; Yang, X.H. A time two-grid difference method for nonlinear generalized viscous Burgers' equation.*J. Math. Chem.* **2024**, *62*, 1323–1356.
31. Ganaie, I.A.; Arora, S.; Kukreja, V.K. Cubic Hermite Collocation Solution of the Kuramoto–Sivashinsky Equation. *Int. J. Comput. Math.* **2016**, *93*, 223–235. [CrossRef]
32. Al-Khaled, K.; Abu-Irwaq, I. Computational Sinc-Scheme for Extracting Analytical Solution for the Model Kuramoto–Sivashinsky Equation. *Int. J. Electr. Comput. Eng.* **2019**, *9*, 3720–3731.
33. Wang, Y.M.; Zhang, H.B. Higher-Order Compact Finite Difference Method for Systems of Reaction-Diffusion Equations. *J. Comput. Appl. Math.* **2009**, *233*, 502–518.
34. Sari, M.; Gürarslan, G. A Sixth-Order Compact Finite Difference Scheme to the Numerical Solutions of Burgers' Equation. *Appl. Math. Comput.* **2009**, *208*, 475–483.
35. Sutmann, G. Compact Finite Difference Schemes of Sixth Order for the Helmholtz Equation. *J. Comput. Appl. Math.* **2007**, *203*, 15–31.
36. Tian, Z.F.; Liang, X.; Yu, P.X. A Higher Order Compact Finite Difference Algorithm for Solving the Incompressible Navier-Stokes Equations. *Int. J. Numer. Meth. Eng.* **2011**, *88*, 511–532.
37. Kuzenov, V.V.; Ryzhkov, S.V.; Varaksin, A.Y. Development of a Method for Solving Elliptic Differential Equations Based on a Nonlinear Compact-Polynomial Scheme. *J. Comput. Appl. Math.* **2024**, *451*, 116098.
38. Qiu, W.L.; Nikan, O.; Avazzadeh, Z. Numerical Investigation of Generalized Tempered-Type Integrodifferential Equations with Respect to Another Function. *Fract. Calc. Appl. Anal.* **2023**, *60*, 41.
39. Xu, D.; Guo, J.; Qiu, W.L. Time Two-Grid Algorithm Based on Finite Difference Method for Two-Dimensional Nonlinear Fractional Evolution Equations. *Appl. Numer. Math.* **2020**, *152*, 169–184.
40. Qiu, W.L.; Fairweather, G.; Yang, X.H.; Zhang, H.X. ADI Finite Element Galerkin Methods for Two-Dimensional Tempered Fractional Integro-Differential Equations. *Calcolo* **2023**, *60*, 41.
41. Sun, Z.Z. *Numerical Methods of Partial Differential Equations*; Science Press: Beijing, China, 2012.
42. Wang, T.C. Optimal Point-Wise Error Estimate of a Compact Difference Scheme for the Klein–Gordon–Schrödinger Equation. *J. Math. Anal. Appl.* **2014**, *412*, 155–167.
43. Dimitrienko, Y.I.; Li, S.G.; Niu, Y. Study on the Dynamics of a Nonlinear Dispersion Model in Both 1D and 2D Based on the Fourth-Order Compact Conservative Difference Scheme. *Math. Comput. Simulat.* **2020**, *182*, 661–689.
44. Huang, C.B.; Stynes, M. A Sharp α-Robust $L^{\infty}(H^1)$ Error Bound for a Time-Fractional Allen-Cahn Problem Discretised by the Alikhanov $L2-1_{\sigma}$ Scheme and a Standard FEM. *J. Sci. Comput.* **2022**, *91*, 43.
45. Liao, H.L.; McLean, W.; Zhang, J.W. A Discrete Grönwall Inequality with Applications to Numerical Schemes for Subdiffusion Problems. *SIAM J. Numer. Anal.* **2019**, *57*, 218–237.

fractal and fractional

MDPI

Article

Numerical Analysis of a Fractional Cauchy Problem for the Laplace Equation in an Annular Circular Region

José Julio Conde Mones [1], Julio Andrés Acevedo Vázquez [1], Eduardo Hernández Montero [1], María Monserrat Morín Castillo [2], Carlos Arturo Hernández Gracidas [3,*] and José Jacobo Oliveros Oliveros [1,*]

[1] Facultad de Ciencias Físico Matemáticas, Benemérita Universidad Autónoma de Puebla, Boulevard 18 Sur y Avenida San Claudio, Colonia San Manuel, Ciudad Universitaria, Puebla 72570, Mexico; jose.conde@correo.buap.mx (J.J.C.M.); julio.acevedova@alumno.buap.mx (J.A.A.V.); eduardo.hernandezmontero@correo.buap.mx (E.H.M.)

[2] Facultad de Ciencias de la Electrónica, Benemérita Universidad Autónoma de Puebla, Boulevard 18 Sur y Avenida San Claudio, Colonia San Manuel, Ciudad Universitaria, Puebla 72570, Mexico; maria.morin@correo.buap.mx

[3] CONAHCYT-BUAP, Facultad de Ciencias Físico Matemáticas, Benemérita Universidad Autónoma de Puebla, Boulevard 18 Sur y Avenida San Claudio, Colonia San Manuel, Ciudad Universitaria, Puebla 72570, Mexico

* Correspondence: cahernandezgr@conahcyt.mx (C.A.H.G.); jose.oliveros@correo.buap.mx (J.J.O.O.)

Abstract: The Cauchy problem for the Laplace equation in an annular bounded region consists of finding a harmonic function from the Dirichlet and Neumann data known on the exterior boundary. This work considers a fractional boundary condition instead of the Dirichlet condition in a circular annular region. We found the solution to the fractional boundary problem using circular harmonics. Then, the Tikhonov regularization is used to handle the numerical instability of the fractional Cauchy problem. The regularization parameter was chosen using the L-curve method, Morozov's discrepancy principle, and the Tikhonov criterion. From numerical tests, we found that the series expansion of the solution to the Cauchy problem can be truncated in $N = 20$, $N = 25$, or $N = 30$ for smooth functions. For other functions, such as absolute value and the jump function, we have to choose other values of N. Thus, we found a stable method for finding the solution to the problem studied. To illustrate the proposed method, we elaborate on synthetic examples and MATLAB 2021 programs to implement it. The numerical results show the feasibility of the proposed stable algorithm. In almost all cases, the L-curve method gives better results than the Tikhonov Criterion and Morozov's discrepancy principle. In all cases, the regularization using the L-curve method gives better results than without regularization.

Keywords: Cauchy problem; inverse problem; ill-posed problem; Laplace equation; fractional boundary condition; Tikhonov regularization

Academic Editors: Carlo Cattani, Libo Feng, Lin Liu and Yang Liu

Received: 5 February 2025
Revised: 8 April 2025
Accepted: 15 April 2025
Published: 27 April 2025

Citation: Conde Mones, J.J.; Acevedo Vázquez, J.A.; Hernández Montero, E.; Morín Castillo, M.M.; Hernández Gracidas, C.A.; Oliveros Oliveros, J.J. Numerical Analysis of a Fractional Cauchy Problem for the Laplace Equation in an Annular Circular Region. *Fractal Fract.* **2025**, *9*, 284. https://doi.org/10.3390/fractalfract9050284

1. Introduction

The challenge of determining a harmonic function within a bounded annular region based on partial boundary measurements (Cauchy data) is known as the Cauchy problem for the Laplace equation [1]. This problem is notoriously ill-posed in the sense of Hadamard, meaning that small perturbations in the Cauchy data can lead to significant changes in the solution, resulting in numerical instability. Consequently, regularization techniques are essential for solving this problem. To ensure a solution to the Cauchy problem, certain smoothness conditions must be imposed on the Cauchy data (refer to Theorem 1 in [2]).

Various methods have been developed to analyze the Cauchy problem. For instance, ref. [3] utilized singular value decomposition to find the solution in a circular annular region,

employing the spectral cut-off of the pseudo-inverse method to manage the numerical instability. In Refs. [4,5], a novel regularization method was introduced using the method of fundamental solutions to address the Cauchy problem in both annular and multi-connected domains. To effectively solve the discrete ill-posed problem arising from a boundary collocation scheme, Tikhonov regularization and L-curve methods were applied in [5]. Additionally, the technique of layer potentials was used in [3,6,7] to derive an equivalent system of integral equations. The moment problem approach, based on Green's formula, was employed in [8] to solve the Cauchy problem in more complex annular regions. A similar technique was proposed for the three-dimensional Cauchy problem in [9], where the solution was expressed using spherical harmonics and Tikhonov regularization. In [10], a variational formulation was introduced, minimizing the cost functional through conjugate gradient iterations combined with boundary element discretization. In [1], the potential on the interior boundary of the annular region was treated as a control function to match the Cauchy input data on the exterior boundary, incorporating a penalized term in the cost function. This approach allowed for the determination of the optimal solution using an iterative conjugate gradient algorithm, with the computational cost involving the solution of two elliptic problems per iteration, solved by the finite element method. Similar techniques have been applied to other control problems, as seen in [10–14].

The Cauchy problem holds significant importance due to its numerous applications, such as estimating pipeline deterioration, calculating solutions or potentials in inaccessible regions or boundaries, and studying cracks in plates [15,16]. Furthermore, the Cauchy problem is utilized in inverse electrocardiography problems [17–19] and in solving inverse problems in electroencephalography (EEG) [14]. EEG signals are known to exhibit fractal characteristics [20–22]. Additionally, fractional derivatives can model voltage propagation in axons using a fractional cable geometry to study human neural networks [23]. In the context of EEG, these fractal characteristics may be related to the sources generating the signal. One potential approach to relate these fractal characteristics to EEG signals is through the use of fractional operators, which warrants further investigation in future studies.

In this work, we consider one variant of the Cauchy problem. More precisely, we consider that we know the action of a fractional operator on the potential on the exterior boundary instead of the potential itself. We apply the Tikhonov regularization to handle the numerical instability that presents this variant, which we call the fractional Cauchy problem. Since we consider circular geometry, we use the Fourier series method to solve the normal equations. The adjoint operator was found using its definition. From this, we found a stable algorithm for some of the parameters defining the fractional operator. To illustrate the results presented in this work, we elaborate synthetic examples and programs in MATLAB.

Regarding the fractional Cauchy problem, we found no work on it. Therefore, as a validation of the results from our proposal, we include results for the classical case that considers a Dirichlet condition, which has been extensively studied, as we attempted to demonstrate in our literature review, which included a substantial number of articles. We obtain the same results as in the classical case using our method.

The paper is organized as follows: In Section 2, the definition and some results of the classical Cauchy problem, as well as the Sturm–Liouville operator, are presented. Section 2 also finalizes the definition of the fractional Cauchy problem. Section 3 applies the Tikhonov regularization to find an algorithm to recover the potential on the interior boundary. Section 4 presents numerical examples to illustrate the algorithm presented in this work. In Section 5, we discuss the stability of the proposed algorithm. In Section 6, we give the conclusions.

2. Problem Formulation

2.1. The Cauchy Problem

Let Ω be a bounded annular region in $\mathbb{R}^2$ with sufficiently smooth interior boundary S_1 and exterior boundary S_2, as shown in Figure 1.

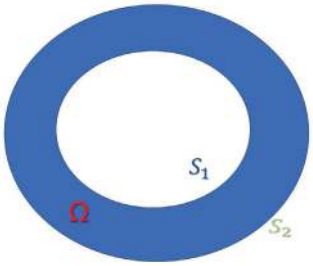

Figure 1. Bi-dimensional circular annular region Ω.

We consider the following boundary value problem: Find ω, such that

$$\begin{aligned} \Delta w &= 0, \text{ in } \Omega, \\ w &= \Phi, \text{ on } S_2, \\ \sigma \frac{\partial w}{\partial n} &= \Psi, \text{ on } S_2, \end{aligned} \tag{1}$$

where $\Phi \in \mathrm{H}^{1/2}(S_2)$, $\sigma \frac{\partial w}{\partial n}\Big|_{S_2} = \Psi \in \mathrm{H}^{-1/2}(S_2)$, n is the outward unitary vector defined on $\partial\Omega$, and $\partial w/\partial n$ denotes the outward normal derivative of w on S_2. For simplicity, we consider (1) with $\Psi \equiv 0$ by the change in variable $u = w - w_1$, where w_1 is the unique harmonic function satisfying $\sigma\, \partial w_1/\partial n|_{S_2} = \Psi$ on S_2, and $w_1|_{S_1} \equiv 0$. Then,

$$\begin{aligned} \sigma \Delta u &= 0, \text{ in } \Omega, \\ u &= V, \text{ on } S_2, \\ \sigma \frac{\partial u}{\partial n} &= 0, \text{ on } S_2, \end{aligned} \tag{2}$$

where $V = \Phi - w_1|_{S_2} \in \mathrm{H}^{1/2}(S_2)$. For the analysis of the Cauchy problem (2), the following problem is employed (see [15]):

Given a function φ defined on S_1, find u such that

$$\begin{aligned} \sigma \Delta u &= 0, \text{ in } \Omega, \\ u &= \varphi, \text{ on } S_1, \\ \sigma \frac{\partial u}{\partial n} &= 0, \text{ on } S_2. \end{aligned} \tag{3}$$

This problem is well-posed, and we will call it the *auxiliary problem*.

The inverse problem associated with the Cauchy problem can be formulated in the following way:

Recover the potential $u = \varphi$ on S_1 from the measurements $u = V$ on S_2, where u is the solution to the auxiliary problem (3).

Definition 1. *A function $u \in V_\varphi$ is a weak solution to the auxiliary problem (3) if*

$$\int_\Omega \sigma \nabla u \cdot \nabla v \, d\Omega = 0, \quad \text{for all} \quad v \in V_0, \tag{4}$$

where

$$V_\varphi \;=\; \Big\{ v \in H^1(\Omega) : v \;=\; \varphi \; on \; S_1 \Big\}, \tag{5}$$

$$V_0 \;=\; \Big\{ v \in H^1(\Omega) : v \;=\; 0 \; on \; S_1 \Big\}. \tag{6}$$

Theorem 1 given in [1] guarantees the existence and uniqueness of the weak solution and allows us to define the lineal, injective, and compact operator $K : H^{m-1/2}(S_1) \to L_2(S_2)$ that associates to each $\varphi \in H^{m-1/2}(S_1)$ the trace over S_2 of the weak solution u to the auxiliary problem (3). Operator K is compact because it is the composition of the continuous operator $T : H^{m-1/2}(S_1) \to H^1(\Omega)$, which associates to each $\varphi \in H^{m-1/2}(S_1)$ the weak solution to the auxiliary problem (3), with the trace operator Tr from $H^m(\Omega)$ into $L_2(\partial\Omega)$, which is compact. The relationship between problem (2) and auxiliary problem (3) can be described by the operator K as follows:

A solution to the auxiliary problem (3) is also a solution to the problem (2) if we choose ϕ on S_1, such that

$$K\varphi := \; u(\varphi)|_{S_2} \;=\; V, \tag{7}$$

where $u(\varphi)$ denotes the solution to the auxiliary problem (3), and V is the known measurement in problem (2), so we have $\varphi \;=\; K^{-1}(V)$.

The following result is very important for the statement of the minimization problem presented in Section 3, and its demonstration can be found in [10].

Theorem 1. *$Im(K)$ is dense in $L_2(S_2)$.*

Equation (7) does not have a solution for all $V \in L_2(S_2)$. However, if we impose some smoothness conditions on V, we can find global conditions of the existence of the solution, as in [10]. As K is an injective and well-defined [15] operator, it ensures uniqueness when a solution is available. Since the operator K is linear, injective, and compact, its inverse K^{-1} is not continuous. Therefore, the inverse problem is ill-posed due to its numerical instability.

2.2. Fractional Boundary Operator

The following material has been obtained from [24]. Let $\Omega_1 \;=\; \{x : |x| < 1\}$ be a unit ball, $2 \leq n$. The $\partial\Omega$ corresponds with the unit sphere; $r \;=\; |x|$, $\overline{x} \;=\; \frac{x}{r}$, let $\delta \;=\; r\frac{d}{dr}$ be a Dirac operator, where $r\frac{d}{dr} \;=\; \sum\limits_{j\,=\,1}^{n} x_j \frac{\partial}{\partial x_j}$. Let $u(x)$ be a smooth function on the domain $\overline{\Omega}$. For any $\alpha > 0$, the following expression

$$J^\beta[u](x) \;=\; \frac{1}{\Gamma(\beta)} \int_0^r \Big(ln\frac{r}{s} \Big)^{\beta-1} \frac{u(s\overline{x})}{s} ds, \quad x \in \Omega_1 \tag{8}$$

is called an operator of integration of the order β in the Hadamard sense. Furthermore, we will assume that $J^0[u](x) \;=\; u(x), x \in \Omega$.

We consider the following modification of the Hadamard operator:

$$D_m^\beta[u](x) \;=\; J^{m-\beta}[\delta^m u](x) \;=\; \frac{1}{\Gamma(m-\beta)} \int_0^r \Big(ln\frac{r}{s} \Big)^{m-1-\beta} \Big(s\frac{d}{ds} \Big)^m \frac{u(s\overline{x})}{s} ds, \tag{9}$$

where m is a positive integer.

Properties and applications of the operators J^β y D^β have been studied in [24]. In that paper, the authors studied a certain generalization of the classical Neumann problem with the fractional order of boundary operators. Let $0 < \beta_n < \ldots < \beta_1 < \beta \leq 1$,

$P_N(D) = D_m^\beta + \sum_{j=1}^{N} a_j D_m^{\beta j}$. In the domain Ω_1, the authors consider the following problem:

$$\Delta u(x) = 0, \quad x \in \Omega_1, \tag{10}$$

$$P_N(D)u(x) = f(x), \quad x \in \partial\Omega_1. \tag{11}$$

As a solution to the last problem, the authors consider a function $u \in C^2(\Omega_1) \cap C(\overline{\Omega_1})$ satisfying Equation (10) and the boundary condition (11) in a classical sense. Since $J^0[u](x) = u(x)$, then $D^1[u](x) \mid_{\partial\Omega_1} = r\frac{du}{dr} \mid_{\partial\Omega_1} = \frac{du}{dn} \mid_{\partial\Omega_1}$, where n is a normal vector to the boundary of the domain Ω. Therefore, in the case $\beta = 1$ and $a_j = 0$, $j = 1, \ldots, n$, we obtain the classical Neumann problem.

2.3. Fractional Cauchy Problem

We consider the following fractional Cauchy problem

$$\begin{aligned} \Delta u &= 0, \quad \text{in} \quad \Omega, \\ D_m^\beta u\Big|_{S_2} &= V, \ \text{on} \quad S_2, \\ \frac{\partial u}{\partial n} &= 0, \ \text{on} \quad S_2, \end{aligned} \tag{12}$$

where the operator D_m^β is given in (9).

In this case, the operator $D_m^\beta u(x) = \frac{1}{\Gamma(m-\beta)} \int_{R_1}^{r} \left(ln\frac{r}{s}\right)^{m-1-\beta} \left(s\frac{d}{ds}\right)^m \frac{u(s\bar{x})}{s} ds$. We note that the operator is linear and continuous, and it has no singularities since $R_1 \leq r, s \leq R_2$. For the analysis of the fractional Cauchy problem (12), we also consider the auxiliary problem (3). We define the operator $K_m^\beta(\varphi) = \left(Tr \circ \left(D_m^\beta T\right)\right)(\varphi) = D_m^\beta u|_{S_2}$, which is a compact operator. We have the following two definitions to study the problem that concerns us.

Definition 2. *The Forward Problem (FP) related to the fractional Cauchy problem consists of finding the potential $V = K_m^\beta(\varphi)$ when ϕ is known.*

We can consider other fractional Cauchy problems by changing the boundary operator. We can consider different kernels for the integral operator. For example, we can take the kernel of the Riemann–Liouville and Caputo fractional derivative, which can be found in [25].

Definition 3. *Given $V \in L_2(S_2)$, the Inverse Problem (IP) related to the fractional Cauchy problem consists of finding $\varphi \in L_2(S_1)$ such that $K_m^\beta(\varphi) = V$.*

3. Methods

3.1. Tikhonov Regularization of the Fractional Cauchy Problem

To find an approximate solution $\varphi \in L_2(S_1)$ of Equation (7) for $K = K_m^\beta$ when we have a measurement with error V_δ, the minimization of the following Tikhonov functional is proposed in [26]:

$$J_\alpha(\varphi) := \frac{1}{2} \| K_m^\beta \varphi - V_\delta \|_{L_2(S_2)}^2 + \frac{\alpha}{2} \| \varphi \|^2, \quad \forall \varphi \in L_2(S_1), \tag{13}$$

where α is the Tikhonov regularization parameter, which will be chosen by the L-curve method, Morozov's discrepancy principle, and numerical tests. The first and second Fréchet derivatives are given by (see Appendix A):

$$\begin{aligned} DJ_\alpha(\varphi) &= \left(\left(K_m^\beta\right)^* K_m^\beta + \alpha I\right)\varphi - \left(K_m^\beta\right)^* V_\delta, \\ D^2 J_\alpha(\varphi) &= \left(K_m^\beta\right)^* K_m^\beta + \alpha I \end{aligned}$$

This least squares procedure is equivalent to solving the normal equation

$$\left(\left(K_m^\beta\right)^* K_m^\beta + \alpha I\right)\varphi \;=\; \left(K_m^\beta\right)^* V, \tag{14}$$

where $\left(K_m^\beta\right)^*$ is the adjoint operator.

According to Theorem 2.12 given in [26], the operator $\left(K_m^\beta\right)^* K_m^\beta + \alpha I$ is boundedly invertible. Given $\varphi \in L_2(S_1)$, the exact solution to the auxiliary problem (3) in a circular annular region $R_1 \le r \le R_2$, in polar coordinates, is given by

$$\begin{aligned} u(r,\theta) \;=\; \varphi_0 + \sum_{k=1}^{\infty} \frac{(R_2/R_1)^{2k}}{(R_2/R_1)^{2k}+1} \Bigg\{ &\left[\left(\frac{R_1}{R_2}\right)^k \left(\frac{r}{R_2}\right)^k + \left(\frac{R_1}{r}\right)^k\right]\varphi_k^1 \cos(k\theta) \\ &+ \left[\left(\frac{R_1}{R_2}\right)^k \left(\frac{r}{R_2}\right)^k + \left(\frac{R_1}{r}\right)^k\right]\varphi_k^2 \sin(k\theta)\Bigg\}, \end{aligned} \tag{15}$$

where $0 \le \theta < 2\pi$. The values φ_0, φ_k^1, φ_k^2, $k = 1, 2, \ldots$, are the Fourier coefficients of φ. The solution to the FP, called *measurement*, is given by $V = K_m^\beta \varphi$, which is obtained by applying the operator D_m^β, the identities

$$\left(s\tfrac{d}{ds}\right)^m \left(s^k \cos(k\theta)\right) \;=\; k^m s^k \cos(k\theta),\; \left(s\tfrac{d}{ds}\right)^m \left(s^{-k} \cos(k\theta)\right) \;=\; (-1)^m k^m s^{-k} \cos(k\theta),$$
$$\left(s\tfrac{d}{ds}\right)^m \left(s^k \sin(k\theta)\right) \;=\; k^m s^k \sin(k\theta),\; \left(s\tfrac{d}{ds}\right)^m \left(s^{-k} \sin(k\theta)\right) \;=\; (-1)^m k^m s^{-k} \sin(k\theta),$$

and then evaluating in $r = R_2$, i.e.,

$$\begin{aligned} V(\theta) \;=\; K_m^\beta \varphi(\theta) \;&=\; \left(Tr \circ \left(D_m^\beta T\right)\right)\varphi(\theta) \;=\; D_m^\beta u|_{S_2}(\theta) \\ &= \sum_{k=1}^{\infty} G_{m,k}^\beta \left(\varphi_k^1 \cos(k\theta) + \varphi_k^2 \sin(k\theta)\right), \end{aligned} \tag{16}$$

where the Fourier coefficients V_k^i of exact measurement V are given by $V_k^i = G_{m,k}^\beta \varphi_k^i$, for $i = 1, 2$, in which

$$G_{m,k}^\beta \;=\; \frac{k^m}{\Gamma(m-\beta)} \int_{R_1}^{R_2} \left(ln\frac{R_2}{s}\right)^{m-1-\beta} \left[\left(\frac{R_1}{R_2}\right)^k \frac{s^{k-1}}{R_2^k} + (-1)^m R_1^k s^{-k}\right] ds. \tag{17}$$

In the numerical examples, the integrals are calculated using the function *quadl* of MATLAB.

The '*exact solution*' u and the '*exact measurement*' $V = v|_{S_2}$ are generated taking $2N+1$ terms of the Fourier series (15) and (16), with $N = 15$, which is obtained from numerical tests. To find the solution to the IP, we must solve the normal equations. To do this, we calculate the adjoint operator using its definition:

$$\left\langle \left(K_m^\beta\right)^* W\right), \varphi\rangle_{L_2(S_1)} \;=\; \left\langle V, K_m^\beta \varphi\right\rangle_{L_2(S_2)}. \tag{18}$$

Without loss of generality, we consider functions in which the constant term of their series expansion is null. Using (16) and (18), we found

$$\begin{aligned}
&\left\langle W, K_m^\beta \varphi \right\rangle_{L_2(S_2)} = \\
&\left\langle \sum_{j=1}^{\infty} W_j^1 \cos(j\theta) + W_j^2 \sin(j\theta), \sum_{k=1}^{\infty} G_{m,k}^\beta \varphi_k^1 \cos(k\theta) + G_{m,k}^\beta \varphi_k^2 \sin(k\theta) \right\rangle_{L_2(S_2)} \\
&= \left\langle \frac{R_2}{R_1} \sum_{j=1}^{\infty} G_{m,k}^\beta W_j^1 \cos(j\theta) + G_{m,k}^\beta W_j^2 \sin(j\theta), \sum_{k=1}^{\infty} \varphi_k^1 \cos(k\theta) + \varphi_k^2 \sin(k\theta) \right\rangle_{L_2(S_1)} \\
&= \left\langle \left(K_m^\beta\right)^* W, \varphi \right\rangle_{L_2(S_1)}.
\end{aligned} \tag{19}$$

Thus, the adjoint operator is defined by $\left(K_m^\beta\right)^* : L_2(S_2) \to L_2(S_1)$,

$$\left(K_m^\beta\right)^*(W) = \frac{R_2}{R_1} \sum_{k=1}^{\infty} G_{m,k}^\beta \Big(W_k^1 \cos(k\theta) + W_k^2 \sin(k\theta) \Big). \tag{20}$$

After some calculations, the regularized solution $\varphi_{\alpha(\delta)}$ that minimizes the functional (13) or that solves normal Equation (14) is given by

$$\varphi_{\alpha(\delta)}(\theta) = \sum_{k=1}^{\infty} \Big(\varphi_{k,\alpha(\delta)}^1 \cos(k\theta) + \varphi_{k,\alpha(\delta)}^2 \sin(k\theta) \Big), \text{ on } S_1, \tag{21}$$

where

$$\varphi_{k,\alpha(\delta)}^i = \frac{R_2 G_{m,k}^\beta}{\left(G_{m,k}^\beta\right)^2 R_2 + \alpha R_1} V_{k,\delta}^i, \text{ for } i = 1,2, \text{ and } k = 1,2,\ldots,N,$$

and $V_{k,\delta}^i$ are the Fourier coefficients of measurement with error V_δ.

3.2. Tikhonov Regularization for the Classical Cauchy Problem

Given $\varphi \in L_2(S_1)$, the exact solution $u(r,\theta)$ to the auxiliary problem (3) in a circular annular region $R_1 \le r \le R_2$ is given, in polar coordinates, by (15). Therefore, the measurement $V = u|_{S_2}$ is obtained with $r = R_2$ in (15):

$$V(\theta) = u(r,\theta)|_{r=R_2} = \varphi_0 + 2 \sum_{k=1}^{\infty} \frac{(R_2/R_1)^k}{(R_2/R_1)^{2k} + 1} \Big\{ \varphi_k^1 \cos(k\theta) + \varphi_k^2 \sin(k\theta) \Big\}, \tag{22}$$

which is the solution to the FP. The Fourier coefficients of V are given by

$$V_0 = \varphi_0 \text{ and } = V_k^i = \frac{2(R_2/R_1)^k}{(R_2/R_1)^{2k} + 1} \varphi_k^i, \text{ for } i = 1,2.$$

Therefore, the solution to the IP from the measurement with error

$$V_\delta(\theta) = V_{0,\delta} + \sum_{k=1}^{\infty} \Big(V_{k,\delta}^1 \cos(k\theta) + V_{k,\delta}^2 \sin(k\theta) \Big) \text{ on } S_1, \tag{23}$$

is given by the regularized solution

$$\varphi_{\alpha(\delta)}(\theta) = \varphi_{0,\alpha(\delta)} + \sum_{k=1}^{\infty} \Big(\varphi_{k,\alpha(\delta)}^1 \cos(k\theta) + \varphi_{k,\alpha(\delta)}^2 \sin(k\theta) \Big) \text{ on } S_1, \tag{24}$$

where

$$\varphi^i_{k,\alpha(\delta)} \;=\; \frac{\left(\frac{R_2}{R_1}\right)^k\left[1+\left(\frac{R_2}{R_1}\right)^{2k}\right]}{2\left(\frac{R_2}{R_1}\right)^{2k}+\frac{\alpha R_1}{2R_2}\left[1+\left(\frac{R_2}{R_1}\right)^{2k}\right]^2}V^i_{k,\delta},\; i\;=\;1,2,\; k\;=\;1,2,3,\ldots \tag{25}$$

where $V^i_{k,\delta}$ are the Fourier coefficients of V_δ and α is the Tikhonov regularization parameter. Thus, the solution to the IP (of the classical Cauchy problem) applying the Tikhonov regularization method (TRM) is given by (15), replacing the coefficients φ^i_k by the coefficients $\varphi^i_{k,\alpha(\delta)}$ given by (25).

4. Numerical Results

In this section, we illustrate the method proposed in this work using synthetic examples. We know the exact φ defined on S_1 in this case. Then, we calculated the measurement with and without noise by solving the FP for the classical and fractional Cauchy problem.

The exact measurement is calculated by solving the FP. To generate the measurements with error V_δ, we added to the exact measurement a Gaussian error using the function *random* of MATLAB. The exact measurement was calculated by solving the FP. Therefore, we define

$$V_\delta \;=\; V+E, \tag{26}$$

where $E \;=\; random(\text{'}Normal\text{'},\mu_0,\sigma_0,1,m)$ is a vector of random numbers of length m (numbers of nodes on S_2) with a normal distribution. The corresponding numerical solutions are denoted by $\varphi_{\alpha(\delta)}$.

In this section, we obtain the relative error between the exact source φ and the recovered source $\varphi_{\alpha(\delta)}$ shown in tables and denoted by $RE\left(\varphi,\varphi_{\alpha(\delta)}\right)$. The relative error is given by

$$RE\left(\varphi,\varphi_{\alpha(\delta)}\right) \;=\; \|\;\varphi-\varphi_{\alpha(\delta)}\;\|_{L_2(S_1)}/\|\;\varphi\;\|_{L_2(S_1)},$$

and the relative error between the exact measurement V and the measurement with error V_δ is denoted by $RE(V,V_\delta)$, which is given by

$$RE(V,V_\delta) \;=\; \|\;V-V_\delta\;\|_{L_2(S_2)}\;/\|\;V\;\|_{L_2(S_2)},$$

where $\|\cdot\|_{L_2(S_i)}$ is the norm of the space $L_2(S_i)$, $i\;=\;1,2$.

4.1. Solution to the IP Related to the Classical Cauchy Problem

In the following two examples, we consider a circular annular region $R_1 \le r \le R_2$ with $R_1 \;=\; 1$ and $R_2 \;=\; 1.2$; then S_1 and S_2 are two circumferences of radii $R_1 \;=\; 1$ and $R_2 \;=\; 1.2$ (see Figure 1), respectively.

Example 1. *We take the 'exact potential' $\varphi(x,y) \;=\; x^2-y^2$, $(x,y)\in S_1$, that in polar coordinates is $\varphi(\theta) \;=\; \cos(2\theta)$. In this case, $V_0 \;=\; \varphi_0 \;=\; 0$, and the solution to the forward problem, that is, the solution to the auxiliary problem (3), is given by*

$$V(\theta) \;=\; K\varphi(\theta) \;=\; u(r,\theta)|_{r\;=\;R_2} \;=\; \left[\frac{2\left(\frac{R_2}{R_1}\right)^2}{1+\left(\frac{R_2}{R_1}\right)^4}\right]\varphi^1_2\cos(2\theta),\;\; \theta\in[0,2\pi],$$

where $\varphi^1_2 \;=\; 1$. Then, the 'exact solution' V and the 'measurement with error' V_δ are generated with the first N terms of the Fourier series (22) and (23), respectively. In this case, we take values of $N \;=\; 20$, 25, and 30 terms. For smooth functions in the Cauchy data, these values of N are obtained by combining numerical tests and the following ideas:

$K(\varphi) = V$ is approximated by a truncation $K_N(\varphi) = V_N$ choosing N such that we can guarantee that $\| V - V_N \|^2_{L_2(S_2)} = \| K(\varphi) - K_N(\varphi) \|^2_{L_2(S_2)} < \frac{\delta^2}{4}$, where the approximation $K_N(g) = \sum_{k=1}^{N} \left[V_k^1 \cos k\theta + V_k^2 \sin k\theta \right]$. From the Parseval equality and (22), where we found that the Fourier coefficients of V decay at least as $1/k^2$, we infer

$$\| V - V_N \|^2_{L_2(S_2)} < 2\pi/N < \delta^2/4. \tag{27}$$

From this, we can take $N > \frac{8\pi}{\delta^2}$ for obtaining the inequality. With this, we obtain an error regarding the truncation of the series expansion.

Now, the measurement error is simulated by adding a random error to each Fourier coefficient V_k^1, V_k^2, $k = 1, 2, \ldots, N$, such that $\| V_N - V_{\delta,N} \|^2_{L_2(S_2)} < \frac{\delta^2}{4}$, which guarantees that $\| V - V_{\delta,N} \|_{L_2(S_2)} \leq \delta$.

For other functions, such as absolute value and the jump function, we have to choose other values of N. This is shown in Examples 3 and 4, which are included in Section 4.2.6 .

Thus, we consider synthetic examples; that is, we examine the fundamental elements of the problems studied, such as how real data are generated and the inherent error within them. In this way, we attempt to emulate the characteristics of real-world problems so that our proposal is closely aligned with providing a solution to them.

Therefore, the measurement with error V_δ is given by the series

$$V_\delta(\theta) = \sum_{k=1}^{N} \left(V_{k,\delta}^1 \cos(k\theta) + V_{k,\delta}^2 \sin(k\theta) \right) \text{ on } S_1, \tag{28}$$

where $V_{k,\delta}^i$ are the Fourier coefficients of V_δ. The regularized solution $\varphi_{\alpha(\delta)}$ to the inverse problem is given by the series (24) truncated to N terms. The solution without regularization φ_δ to the IP is given by

$$\varphi_\delta(\theta) = \sum_{k=1}^{N} \left(\varphi_{k,\delta}^1 \cos(k\theta) + \varphi_{k,\delta}^2 \sin(k\theta) \right) \text{ on } S_1, \tag{29}$$

where the coefficients $\varphi_{k,\delta}^i$ are given by

$$\varphi_{k,\delta}^i = \frac{\left[1 + \left(\frac{R_2}{R_1} \right)^{2k} \right]}{2\left(\frac{R_2}{R_1} \right)^k} V_{k,\delta}^i, \; i = 1, 2. \tag{30}$$

Remark 1. *In all tables associated with the classical case, if $\alpha(\delta) = 0$, then the solution $\varphi_{\alpha(\delta)}$ is the solution without regularization φ_δ given by (29), where the coefficients $\varphi_{k,\delta}^i$ are given by (30).*

Table 1 shows the numerical results for data with and without error, applying TRM to solve the IP of the classical Cauchy problem (2). In this case, we observe that the solutions with regularization $\varphi_{\alpha(\delta)}$ have a percentage of relative errors around 10%, equal to the percentage of error included in the data with error V_δ for $\delta = 0.1$. The regularization parameter was chosen as $\alpha(\delta) = \delta$ for $N = 20$, 25, and 30. Also, we can see that the $RE\left(\varphi, \varphi_{\alpha(\delta)} \right)$ decreases when the error δ tends to zero, while the $RE(\varphi, \varphi_\delta)$ increases for each value of N. In particular, the $RE(\varphi, \varphi_\delta)$ increases faster when $N = 30$, for $\delta = 0.1$, 0.01, and y 0.001. In this case, the regularization parameter $\alpha(\delta)$ depends on V_δ.

Table 1. Numerical results applying TRM to solve the IP related to the classical Cauchy problem (2), for $\varphi(x,y) = x^2 - y^2$, $(x,y) \in S_1$, and different values of δ and N.

δ	N	$\alpha(\delta)$	$RE(V,V_\delta)$	$RE(\varphi,\varphi_{\alpha(\delta)})$	$RE(\varphi,\varphi_\delta)$
0	20	0	0	0	0
0.1	20	0.1	0.1069	0.1465	0.8224
0.1	25	0.1	0.1034	0.1471	1.6048
0.1	30	0.1	0.1126	0.1435	3.0063
0.01	20	0.01	0.0102	0.0342	0.0663
0.01	25	0.01	0.0112	0.0360	0.2137
0.01	30	0.01	0.0114	0.0362	0.4820
0.001	20	0.001	9.0770×10^{-4}	0.0050	0.0057
0.001	25	0.001	8.8517×10^{-4}	0.0068	0.0122
0.001	30	0.001	9.5479×10^{-4}	0.0083	0.0354

Figure 2a,b show the graphs of the exact measurement V and with error V_δ, the graphs of the exact potential φ and its approximations $\varphi_{\alpha(\delta)}$ (with regularization) and φ_δ (without regularization) taking $\alpha(\delta) = 0.1$ and $N = 30$, corresponding to Example 1, for $\delta = 0.1$ (see Table 1). In Figure 2b, we can see the ill-posedness of the inverse problem if we do not apply regularization, where $RE\left(\varphi, \varphi_{\alpha(\delta)}\right) = 0.1435$ and $RE(\varphi, \varphi_\delta) = 3.0063$.

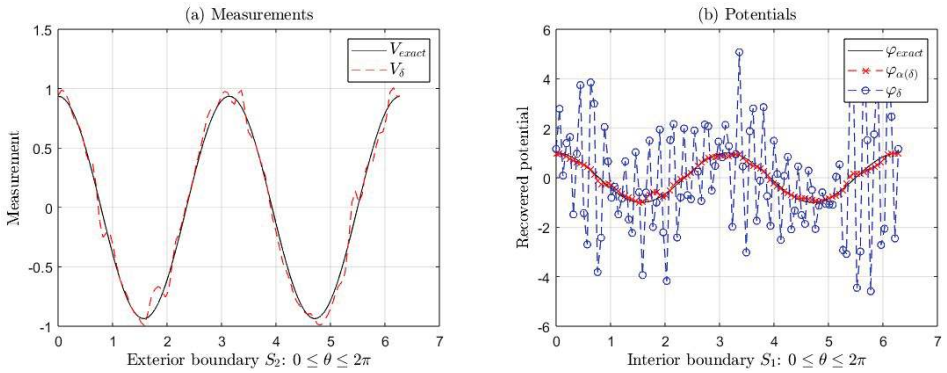

Figure 2. (**a**) Exact measurement V (black line) and with error V_δ (red line). (**b**) Exact potential φ and its approximations $\varphi_{\alpha(\delta)}$ and φ_δ applying regularization and without regularization, corresponding to Example 1 for $\delta = 0.1$ (see Table 1). We take $\alpha(\delta) = 0.1$ and $N = 30$ in this case.

Example 2. *We consider the 'exact potential' $\varphi(x,y) = e^x \sin(y)$, for $(x,y) \in S_1$. Similar to the first example, the 'exact measurement' V and the 'measurement with error' V_δ are generated with the first N terms of the Fourier series (22) and (23), respectively, such that $\| \varphi_N - \varphi \|_{L_2(S_1)} \le \epsilon_F$, with $0 < \epsilon_F < 10^{-14}$. In this case, $V_0 = \varphi_0 = 0$ and the Fourier coefficients φ_k, $1 \le k \le N$, are obtained numerically using the intrinsic function quadl of MATLAB. Here, we take values of $N = 18$, 25, and 30 terms.*

Table 2 shows the numerical results for data with and without error, applying TRM to solve the IP of the classical Cauchy problem (2). Analogous to Example 1, we can observe that the solutions with regularization $\varphi_{\alpha(\delta)}$ have a percentage of relative errors around 10%, equal to the percentage of error included in the data with error V_δ for $\delta = 0.1$. Also, we can see that the $RE\left(\varphi, \varphi_{\alpha(\delta)}\right)$ decreases when the error δ tends to zero, while the $RE(\varphi, \varphi_\delta)$ increases for each value of N. In particular, the $RE(\varphi, \varphi_\delta)$ increases when $N = 30$ for each

$\delta = 0.1$, 0.01, and 0.001. As in the previous example, the regularization parameter $\alpha(\delta)$ depends on V_δ, and we take $\alpha(\delta) = \delta$ for each value of $N = 18$, 25, and 30.

Table 2. Numerical results applying TRM to solve the IP related to the classical Cauchy problem (2), for $\varphi(x,y) = e^x \sin(y)$, $(x,y) \in S_1$ and different values of δ and N.

δ	N	$\alpha(\delta)$	$RE(V,V_\delta)$	$RE(\varphi,\varphi_{\alpha(\delta)})$	$RE(\varphi,\varphi_\delta)$
0	18	0	0	2.5338×10^{-17}	2.4537×10^{-17}
0.1	18	0.1	0.1161	0.1590	0.8005
0.1	25	0.1	0.1125	0.1571	1.6366
0.1	30	0.1	0.1340	0.1512	5.7825
0.01	18	0.01	0.0117	0.0357	0.0509
0.01	25	0.01	0.0105	0.0392	0.1485
0.01	30	0.01	0.0112	0.0364	0.3478
0.001	18	0.001	8.8274×10^{-4}	0.0046	0.0048
0.001	25	0.001	9.9199×10^{-4}	0.0095	0.0162
0.001	30	0.001	0.0011	0.0099	0.0423

Figure 3a,b show the graphs of the exact measurement V and with error V_δ, the graphs of the exact potential φ and its approximations $\varphi_{\alpha(\delta)}$ (with regularization) and φ_δ (without regularization) taking $\alpha(\delta) = 0.1$ and $N = 30$, corresponding to Example 2, for $\delta = 0.1$ (see Table 2). In Figure 3b, we can see the ill-posedness of the inverse problem if we do not apply regularization. In this case, $RE\left(\varphi, \varphi_{\alpha(\delta)}\right) = 0.1512$ and $RE(\varphi, \varphi_\delta) = 5.7825$.

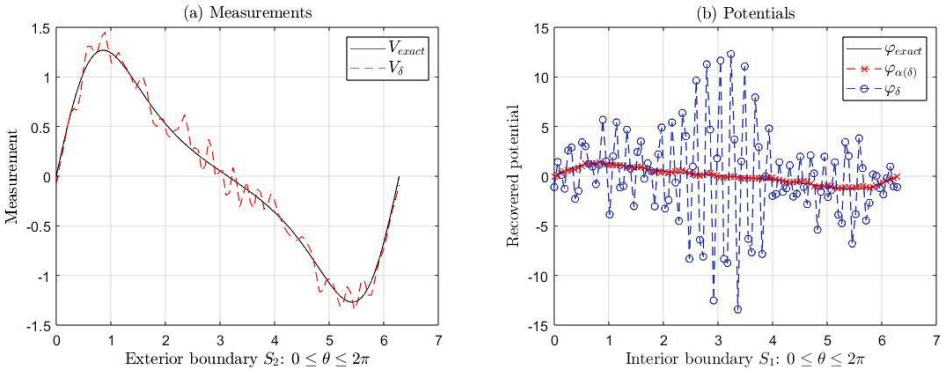

Figure 3. (**a**) Exact measurement V (black line) and with error V_δ (red line). (**b**) Exact potential φ and its approximations $\varphi_{\alpha(\delta)}$ and φ_δ applying regularization and without regularization, corresponding to Example 2 for $\delta = 0.1$ (see Table 2). In this case, we take $\alpha(\delta) = 0.1$ and $N = 30$.

4.2. Solution to the IP Related to the Fractional Cauchy Problem

In this section, we look into the performance of the TRM to solve the IP of the fractional Cauchy problem (12) in a circular annular region $R_1 \le r \le R_2$ with $R_1 = 1$ and $R_2 = 1.2$. Then, S_1 and S_2 are two circumferences of radii $R_1 = 1$ and $R_2 = 1.2$ (see Figure 1), respectively. In this case, we consider as '*exact potentials*' the two functions from the previous subsection: $\varphi(x,y) = x^2 - y^2$ and $\varphi(x,y) = e^x \sin(y)$, for $(x,y) \in S_1$.

Similar to the previous subsection, the '*exact solution*' V and the '*measurement with error*' V_δ are obtained by truncating the series (16) and (23) up to N terms, respectively; furthermore, the Fourier coefficients φ_k^1, φ_k^2, and $G_{m,k}^\beta$ (given by (17)) are obtained numerically using the function *quadl* of $MATLAB$.

In this case, we take values of $N = 18$, 20, 25, and 30 terms. Therefore, the measurement with error V_δ is given by the series (23) truncated to N terms. The regularized solution

$\varphi_{\alpha(\delta)}$ to the IP is given by the series (21) truncated to N terms. Also, the solution without regularization φ_δ to the IP is given by (29), where

$$\varphi^i_{k,\delta} = \frac{1}{G^\beta_{m,k}} V^i_{k,\delta},\ i = 1,2,\ k = 1,2,\ldots,N. \tag{31}$$

Remark 2. *In all tables from the fractional case, if $\alpha(\delta) = 0$, the solution $\varphi_{\alpha(\delta)}$ is the solution without regularization φ_δ given by (29), where the coefficients $\varphi^i_{k,\delta}$ are given by (31).*

4.2.1. Case 1: $\beta = 0.5$ and $m = 1$, When δ Tends to Zero

In this section, we consider the case when $\beta = 0.5$, $m = 1$, and for different values of δ close to zero. Tables 3 and 4 show the relative errors of the approximations $\varphi_{\alpha(\delta)}$ and φ_δ, when δ tends to zero, for the two exact functions φ considered in Section 4.1. In both cases, we observe that the $RE\left(\varphi, \varphi_{\alpha(\delta)}\right)$ of the solutions with regularization $\varphi_{\alpha(\delta)}$ is less than the $RE(V, V_\delta)$ for each value of δ and N given in these tables. Additionally, the $RE\left(\varphi, \varphi_{\alpha(\delta)}\right)$ and $RE(\varphi, \varphi_\delta)$ are of the same order, i.e., the solutions without regularization φ_δ are close to regularized solutions $\varphi_{\alpha(\delta)}$ for $\beta = 0.5$ and $m = 1$. In both cases, the measurements with errors V_δ do not have much impact on recovered solution φ_δ, and they are close to $\varphi_{\alpha(\delta)}$. We observe from the relative errors that regularized approximations $\varphi_{\alpha(\delta)}$ are better than those without regularization. In this case, the regularization parameter $\alpha(\delta)$ depends on V_δ, N, m, and β.

Table 3. Numerical results applying TRM to solve IP related to the fractional Cauchy problem (12), for $\varphi(x,y) = x^2 - y^2$, $(x,y) \in S_1$, and different values of δ and N.

δ	N	$\alpha(\delta)$	β	m	$RE(V,V_\delta)$	$RE(\varphi,\varphi_{\alpha(\delta)})$	$RE(\varphi,\varphi_\delta)$
0	20	0	0.5	1	0	1.1102×10^{-16}	0
0.1	20	1×10^{-2}	0.5	1	0.0970	0.0617	0.0880
0.1	25	1×10^{-2}	0.5	1	0.0979	0.0719	0.0990
0.1	30	1×10^{-2}	0.5	1	0.1038	0.0775	0.1217
0.01	20	1×10^{-4}	0.5	1	0.0093	0.0037	0.0039
0.01	25	1×10^{-4}	0.5	1	0.0091	0.0070	0.0070
0.01	30	1×10^{-4}	0.5	1	0.0127	0.0072	0.0073
0.001	20	1×10^{-6}	0.5	1	9.6950×10^{-4}	8.9805×10^{-4}	8.9826×10^{-4}
0.001	25	1×10^{-6}	0.5	1	8.3006×10^{-4}	3.4557×10^{-4}	3.4620×10^{-4}
0.001	30	1×10^{-6}	0.5	1	9.8327×10^{-4}	5.4898×10^{-4}	5.4925×10^{-4}

Considering $\delta = 0.1$, $\beta = 0.5$, and $m = 1$, we show the graphs for the following potentials $\varphi(x,y) = x^2 - y^2$ (Figure 4) and $\varphi(x,y) = e^x \sin(y)$ (Figure 5) for $(x,y) \in S_1$ where the following is true:

(a) The exact measurement V and the measurement with error V_δ.
(b) The exact potential φ and its approximations $\varphi_{\alpha(\delta)}$ (with regularization) and φ_δ (without regularization) taking $\alpha(\delta) = 10^{-2}$ and $N = 30$.

Table 4. Numerical results applying TRM to solve IP related to the fractional Cauchy problem (12), for $\varphi(x,y) = e^x \sin(y)$, $(x,y) \in S_1$, and different values of δ and N.

δ	N	$\alpha(\delta)$	β	m	$RE(V,V_\delta)$	$RE(\varphi,\varphi_{\alpha(\delta)})$	$RE(\varphi,\varphi_\delta)$
0	18	0	0.5	1	0	2.4537×10^{-17}	2.4537×10^{-17}
0.1	18	1×10^{-4}	0.5	1	0.1292	0.1196	0.1212
0.1	25	1×10^{-4}	0.5	1	0.1732	0.1238	0.1296
0.1	30	1×10^{-4}	0.5	1	0.1921	0.0624	0.0672
0.01	18	1×10^{-5}	0.5	1	0.0147	0.0126	0.0129
0.01	25	1×10^{-5}	0.5	1	0.0166	0.0124	0.0129
0.01	30	1×10^{-5}	0.5	1	0.0177	0.0069	0.0071
0.001	18	1×10^{-6}	0.5	1	0.0012	8.6623×10^{-4}	9.1811×10^{-4}
0.001	25	1×10^{-6}	0.5	1	0.0017	8.6801×10^{-4}	9.1904×10^{-4}
0.001	25	1×10^{-6}	0.5	1	0.0018	7.3211×10^{-4}	7.7961×10^{-4}

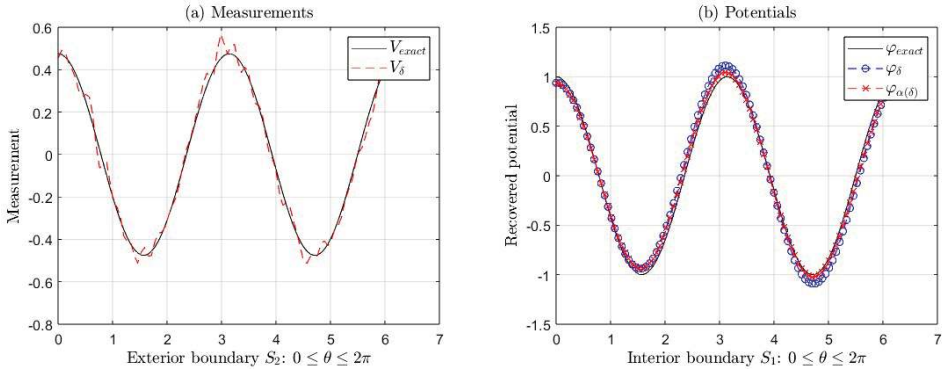

Figure 4. (**a**) Exact measurement V (black line) and with error V_δ (red line). (**b**) Exact potential φ and its approximations $\varphi_{\alpha(\delta)}$ and φ_δ, corresponding to Example 1 for $\delta = 0.1$ (see Table 3). In this case, we take $\alpha(\delta) = 10^{-2}$ and $N = 30$.

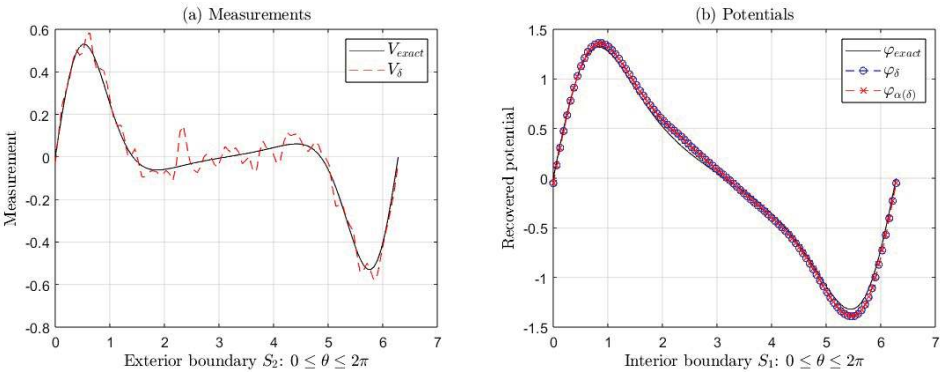

Figure 5. (**a**) Exact measurement V (black line) and with error V_δ (red line). (**b**) Exact potential φ and its approximations $\varphi_{\alpha(\delta)}$ and φ_δ, corresponding to Example 2 for $\delta = 0.1$ (see Table 4). In this case, we take $\alpha(\delta) = 10^{-4}$ and $N = 30$.

See Tables 3 and 4 for other values of the parameters N and δ.

In Figure 4b, the $RE\left(\varphi, \varphi_{\alpha(\delta)}\right) = 0.0775$ is less than $RE(\varphi, \varphi_\delta) = 0.1217$ for $\delta = 0.1$ (see Table 3). In Figure 5b, the $RE\left(\varphi, \varphi_{\alpha(\delta)}\right) = 0.0624$ is less than $RE(\varphi, \varphi_\delta) = 0.0672$ for $\delta = 0.1$ (see Table 4).

4.2.2. Case 2: $\beta \in (m-1, m)$, for $m = 2, \ldots, 12$ and $\delta = 0.1$

Tables 5 and 6 show the relative errors of the approximations $\varphi_{\alpha(\delta)}$ and φ_δ when $\delta = 0.1$ for the two exact functions φ considered in Section 4.1.

Table 5. Case 2: Numerical results applying TRM to solve IP related to the fractional Cauchy problem (12) for $\delta = 0.1$ and different values of β and m, where $\varphi(x,y) = x^2 - y^2$, $(x,y) \in S_1$.

N	$\alpha(\delta)$	β	m	$RE(V,V_\delta)$	$RE(\varphi,\varphi_{\alpha(\delta)})$	$RE(\varphi,\varphi_\delta)$
20	1×10^{-1}	1.5	2	0.1027	0.0360	0.0392
25	8×10^{-1}	1.5	2	0.1017	0.0518	0.0819
30	5×10^{-1}	1.5	2	0.1136	0.0597	0.0718
20	2×10^{-1}	2.5	3	0.0936	0.0508	0.4857
20	1×10^{1}	3.5	4	0.0969	0.0474	0.3523
20	1×10^{0}	4.5	5	0.0915	0.0421	1.5924
20	1×10^{2}	5.5	6	0.1112	0.0248	1.2606
20	1×10^{1}	6.5	7	0.1078	0.0366	5.8758
20	1×10^{2}	7.5	8	0.1045	0.0351	2.2946
20	1×10^{2}	8.5	9	0.0916	0.0197	16.6149
20	1×10^{3}	9.5	10	0.0996	0.0274	21.0258
20	1×10^{3}	10.5	11	0.0939	0.0176	46.6720
20	1×10^{3}	11.5	12	0.0861	0.0407	33.8060

Table 6. Case 2: Numerical results applying TRM to solve IP related to the fractional Cauchy problem (12) for $\delta = 0.1$ and different values of β and m, where $\varphi(x,y) = e^x \sin(y)$, $(x,y) \in S_1$.

N	$\alpha(\delta)$	β	m	$RE(V,V_\delta)$	$RE(\varphi,\varphi_{\alpha(\delta)})$	$RE(\varphi,\varphi_\delta)$
18	1×10^{-2}	1.5	2	0.1279	0.0342	0.0411
25	1×10^{-2}	1.5	2	0.1780	0.0258	0.0264
30	1×10^{-2}	1.5	2	0.1732	0.0439	0.0509
18	9×10^{-4}	2.5	3	0.1629	0.1437	0.1504
18	4×10^{-1}	3.5	4	0.1461	0.0931	0.3543
18	1.4×10^{-1}	4.5	5	0.1466	0.1385	7.4132
18	1×10^{1}	5.5	6	0.1757	0.3306	9.1616
18	1×10^{1}	6.5	7	0.1512	0.3654	478.6290
18	4.2×10^{2}	7.5	8	0.1643	0.3822	310.6255
18	3×10^{5}	8.5	9	0.1732	0.8982	633.1135
18	2×10^{7}	9.5	10	0.2062	0.9546	4.0208×10^{3}
18	2×10^{7}	10.5	11	0.1712	0.8948	1.9672×10^{5}
18	8×10^{8}	11.5	12	0.1636	0.9326	2.2607×10^{5}

In Table 5, we observe that $RE\left(\varphi, \varphi_{\alpha(\delta)}\right) < RE(V, V_\delta)$ for each value of N, β, and m given in the mentioned table. Also, the $RE\left(\varphi, \varphi_{\alpha(\delta)}\right)$ and $RE(\varphi, \varphi_\delta)$ are of the same order, i.e., the solutions without regularization φ_δ are close to regularized solutions $\varphi_{\alpha(\delta)}$, for $\delta = 0.1$, $N = 20, 25, 30$, $\beta = 1.5$, and $m = 2$. We can see similar results in Table 6 for $\delta = 0.1$, $N = 18, 25, 30$, $\beta = 1.5, 2.5$, $m = 2$, and 3; however the regularized approximates $\varphi_{\alpha(\delta)}$ are better than the solutions without regularization. Furthermore, $RE(\varphi, \varphi_\delta) < RE(V, V_\delta)$ and these increase suddenly, starting at $m = 3$ and $m = 4$ (see Tables 5 and 6) for the functions $\varphi(x,y) = x^2 - y^2$ and $\varphi(x,y) = e^x \sin(y)$ for $(x,y) \in S_1$, respectively. As in the previous case, the regularization parameter $\alpha(\delta)$ changes depending on V_δ, N, m, and β.

We show the graphs for the following functions:

- $\varphi(x,y) = x^2 - y^2$ (Figure 6 with parameters $\beta = 1.5$, $m = 2$, $\delta = 0.1$, $\alpha(\delta) = 5 \times 10^{-1}$, and $N = 30$; and Figure 7 with parameters $\beta = 2.5$, $m = 3$, $\delta = 0.1$, $\alpha(\delta) = 2 \times 10^{-1}$, and $N = 20$).
- $\varphi(x,y) = e^x \sin(y)$ (Figure 8 with parameters $\beta = 7.5$, $m = 8$, $\delta = 0.1$, $\alpha(\delta) = 4.2 \times 10^2$, and $N = 18$).

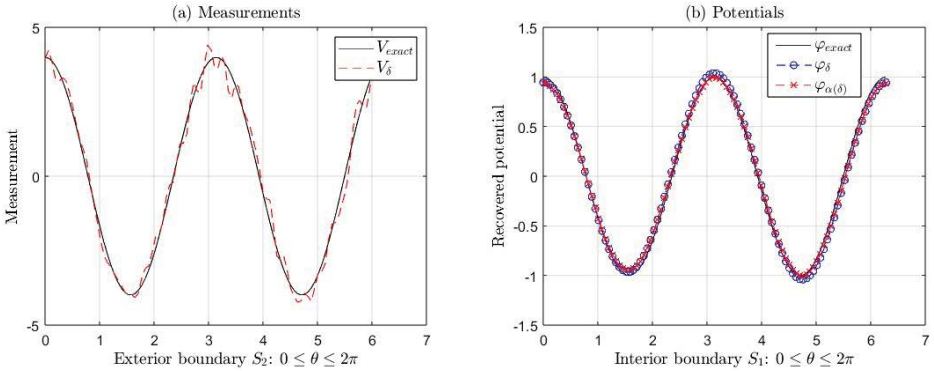

Figure 6. (**a**) Exact measurement V (black line) and with error V_δ (red line). (**b**) Exact potential φ and its approximations $\varphi_{\alpha(\delta)}$ and φ_δ, corresponding to Example 1 for $\beta = 1.5$, $m = 2$, and $\delta = 0.1$ (see Table 5). In this case, we take $\alpha(\delta) = 5 \times 10^{-1}$ and $N = 30$.

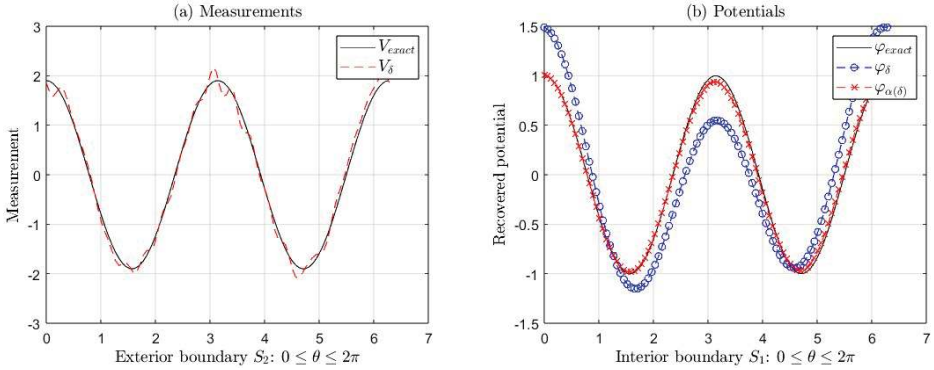

Figure 7. (**a**) Exact measurement V (black line) and with error V_δ (red line). (**b**) Exact potential φ and its approximations $\varphi_{\alpha(\delta)}$ and φ_δ, corresponding to Example 1 for $\beta = 2.5$, $m = 3$, and $\delta = 0.1$ (see Table 5). In this case, we take $\alpha(\delta) = 2 \times 10^{-1}$ and $N = 20$.

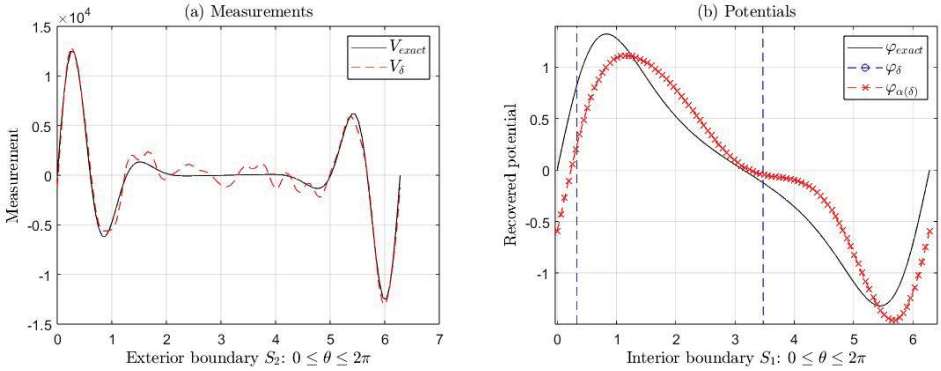

Figure 8. (**a**) Exact measurement V (black line) and with error V_δ (red line). (**b**) Exact potential φ and its approximations $\varphi_{\alpha(\delta)}$ and φ_δ, corresponding to Example 2 for $\beta = 7.5$, $m = 8$, and $\delta = 0.1$ (see Table 6). In this case, we take $\alpha(\delta) = 4.2 \times 10^2$ and $N = 18$.

For $(x,y) \in S_1$. These figures show the following:

(a) The exact measurement V and the measurement with error V_δ.

(b) The exact potential φ and its approximations $\varphi_{\alpha(\delta)}$ (with regularization) and φ_δ (without regularization).

In both cases, as mentioned in the previous paragraph, the errors increase suddenly, starting at $m = 3$ for the first function and $m = 4$ for the second one, as can be seen in Figures 7b and 8b, where we can see the ill-posedness of the IP if we do not apply regularization. For example, for the second function, the $RE\left(\varphi, \varphi_{\alpha(\delta)}\right) = 310.6255$ is much greater than $RE(\varphi, \varphi_\delta) = 0.3822$ for $\beta = 7.5$, $m = 8$, and $\delta = 0.1$ (see Table 6). However, in this same example, for $m = 9$, 10, 11, and 12, the $RE\left(\varphi, \varphi_{\alpha(\delta)}\right)$ increases around 90%. Nevertheless, $RE(\varphi, \varphi_\delta)$ is bigger than $RE\left(\varphi, \varphi_{\alpha(\delta)}\right)$. In this case, we could use the regularized solution as an initial point of an iterative method to recover a better solution to the IP.

4.2.3. Case 3: $\beta \in (m-1, m)$, When β Is Next to $m-1$ or m and $\delta = 0.1$

This section considers the case when $m - 1 < \beta < m$ and β is next to $m-1$ or m. Tables 7 and 8 show the relative errors of the approximations $\varphi_{\alpha(\delta)}$ and φ_δ when $\delta = 0.1$ for the same two exact functions φ considered in Section 4.1.

Table 7. Case 3: Numerical results applying TRM to solve the IP related to the fractional Cauchy problem (12) for $\delta = 0.1$ and different values of β and m, where $\varphi(x, y) = x^2 - y^2$, $(x, y) \in S_1$.

N	$\alpha(\delta)$	β	m	$RE(V,V_\delta)$	$RE(\varphi,\varphi_{\alpha(\delta)})$	$RE(\varphi,\varphi_\delta)$
20	1×10^{-3}	0.1	1	0.1093	0.0565	0.0765
20	1×10^{-5}	0.0001	1	0.1032	0.0699	0.0705
20	1×10^{-12}	0.0000001	1	0.1040	0.0394	0.0394
20	1×10^{-3}	0.9	1	0.0922	0.0809	0.0817
20	1×10^{-8}	0.9999	1	0.0988	0.0581	0.0583
20	1×10^{-12}	0.9999999	1	0.0967	0.0921	0.1277
20	1×10^{-1}	1.1	2	0.1081	0.0563	0.0647
20	5×10^{-2}	1.0001	2	0.0931	0.0791	0.0984
20	1×10^{-2}	1.0000001	2	0.0979	0.0901	0.0953
20	1×10^{-1}	1.9	2	0.0980	0.0726	0.0746
20	1×10^{-5}	1.9999	2	0.0971	0.0449	0.0488
20	1×10^{-11}	1.9999999	2	0.1033	0.0997	0.1105
20	1×10^{-2}	2.1	3	0.0998	0.0392	0.2108
20	1×10^{-2}	2.0001	3	0.0905	0.0479	0.3250
20	1×10^{-2}	2.0000001	3	0.0894	0.0264	0.1021
20	1×10^{-1}	2.9	3	0.1110	0.0860	0.1731
20	1×10^{-5}	2.9999	3	0.0999	0.0804	0.4756
20	1×10^{-11}	2.9999999	3	0.1027	0.0672	0.3546
20	1×10^{0}	3.1	4	0.1061	0.0328	0.1583
20	1×10^{2}	3.9	4	0.1061	0.0738	0.5624
20	1×10^{-1}	4.1	5	0.0863	0.0421	1.8856
20	1×10^{0}	4.9	5	0.1030	0.0401	0.2528
20	1×10^{1}	5.1	6	0.0751	0.0368	1.5197
20	1×10^{2}	5.9	6	0.0957	0.0438	1.0323
20	1×10^{0}	6.1	7	0.0917	0.0267	5.3155
20	1×10^{0}	6.9	7	0.1020	0.0600	5.5627
20	1×10^{2}	7.1	8	0.0935	0.0199	3.3483
20	1×10^{2}	7.0000001	8	0.0827	0.0206	1.7258
20	1×10^{3}	7.9	8	0.0870	0.0212	4.5019
20	1×10^{-8}	7.9999999	8	0.0986	0.0454	4.2454

Table 7. *Cont.*

N	$\alpha(\delta)$	β	m	$RE(V,V_\delta)$	$RE(\varphi,\varphi_{\alpha(\delta)})$	$RE(\varphi,\varphi_\delta)$
20	1×10^{1}	8.1	9	0.1155	0.0276	14.3075
20	1×10^{2}	8.9	9	0.0953	0.0342	34.0155
20	1×10^{2}	9.1	10	0.1013	0.0508	20.6047
20	1×10^{4}	9.9	10	0.0972	0.0095	24.1306
20	1×10^{2}	10.1	11	0.0941	0.0271	35.0730
20	1×10^{3}	10.9	11	0.0956	0.0090	90.0697
20	1×10^{3}	11.1	12	0.0951	0.0226	65.9229
20	1×10^{4}	11.9	12	0.0967	0.0475	101.7022

Table 8. Case 3: Numerical results applying TRM to solve IP related to the fractional Cauchy problem (12) for $\delta = 0.1$ and different values of β and m, where $\varphi(x,y) = e^x \sin(y)$, $(x,y) \in S_1$.

N	$\alpha(\delta)$	β	m	$RE(V,V_\delta)$	$\delta RE(\varphi,\varphi_{\alpha(\delta)})$	$RE(\varphi,\varphi_\delta)$
30	1×10^{-5}	0.1	1	0.1429	0.0210	0.0230
30	1×10^{-6}	0.0001	1	0.1849	0.0396	0.0401
30	1×10^{-13}	0.0000001	1	0.1762	0.0314	0.0314
30	1×10^{-4}	0.9	1	0.1674	0.0448	0.0452
30	1×10^{-8}	0.9999	1	0.1299	0.0544	0.0575
30	1×10^{-15}	0.9999999	1	0.1748	0.0271	0.0272
30	1×10^{-5}	1.1	2	0.1613	0.0454	0.0454
30	1×10^{-5}	1.0001	2	0.1829	0.0492	0.0493
30	1×10^{-5}	1.0000001	2	0.1842	0.0584	0.0585
30	1×10^{-1}	1.9	2	0.1739	0.0353	0.0431
30	1×10^{-6}	1.9999	2	0.1870	0.0380	0.0413
30	1×10^{-12}	1.9999999	2	0.1690	0.0609	0.0674
30	1×10^{-4}	2.1	3	0.2071	0.0760	0.1016
30	1×10^{-8}	2.0001	3	0.2114	0.1688	0.1689
30	1×10^{-9}	2.0000001	3	0.1877	0.1176	0.1176
30	3×10^{-2}	2.9	3	0.2256	0.1156	0.2868
30	1×10^{-6}	2.9999	3	0.1676	0.0761	0.4059
30	5×10^{-13}	2.9999999	3	0.2155	0.1581	0.1751
30	5×10^{-2}	3.1	4	0.2057	0.1258	0.1717
30	1×10^{0}	3.9	4	0.2001	0.0881	0.3453
30	5×10^{-2}	4.1	5	0.2545	0.3090	16.5294
30	1×10^{0}	4.9	5	0.2011	0.2408	6.8619
30	4×10^{0}	5.1	6	0.1983	0.4226	12.4482
30	5×10^{1}	5.9	6	0.2049	0.3878	7.9340
30	7×10^{-1}	6.1	7	0.2124	0.4678	243.7232
30	6×10^{1}	6.9	7	0.2553	0.5497	363.0725
30	4×10^{1}	7.1	8	0.2463	0.4505	123.0513
30	5×10^{1}	7.0001	8	0.2452	0.2910	240.1527
30	2×10^{1}	7.0000001	8	0.2335	0.1839	119.2328
30	2×10^{3}	7.9	8	0.2184	0.1710	402.7594
30	1.3×10^{-2}	7.9999	8	0.2308	0.3440	181.8997
30	2×10^{-8}	7.9999999	8	0.1833	0.5806	164.4764

Table 8. *Cont.*

N	$\alpha(\delta)$	β	m	$RE(V,V_\delta)$	$\delta RE(\varphi,\varphi_{\alpha(\delta)})$	$RE(\varphi,\varphi_\delta)$
30	3×10^4	8.1	9	0.2548	0.8971	3.4981×10^3
30	2×10^6	8.9	9	0.2054	0.9059	2.8978×10^3
30	2×10^6	9.1	10	0.2260	0.8857	6.8133×10^3
30	7×10^7	9.9	10	0.2241	0.8896	6.2431×10^3
30	4×10^6	10.1	11	0.2233	0.9011	2.5172×10^5
30	2×10^8	10.9	11	0.2069	0.8934	1.9773×10^5
30	5×10^8	11.1	12	0.2479	0.9212	1.1346×10^5
30	5×10^9	11.9	12	0.2372	0.8996	3.4904×10^5

In Table 7, we observe that the $RE\left(\varphi, \varphi_{\alpha(\delta)}\right)$ are less than the $RE(V, V_\delta)$ for each value of N, β, and m given in this table. We can see that $RE\left(\varphi, \varphi_{\alpha(\delta)}\right)$ and $RE(\varphi, \varphi_\delta)$ are of the same order for $m = 1, 2$, i.e., the solutions without regularization φ_δ are close to regularized solutions $\varphi_{\alpha(\delta)}$. However, the regularized approximates $\varphi_{\alpha(\delta)}$ are better than the solutions without regularization for $m = 1, 2$. Nonetheless, $RE\left(\varphi, \varphi_{\alpha(\delta)}\right)$ increases more than $RE(V, V_\delta)$ starting at $m = 3$. Furthermore, we can observe similar results in Table 8, where the $RE\left(\varphi, \varphi_{\alpha(\delta)}\right)$ are less than the $RE(V, V_\delta)$ for $m = 1, 2, 3, 4$, with $\delta = 0.1$, $N = 30$, and the different values of β are close to m or $m - 1$ given in this table. For the values of $m = 5, 6, 7$, and 8, the $RE\left(\varphi, \varphi_{\alpha(\delta)}\right)$ are around the percentage of the $RE(V, V_\delta)$. For the other values of $m = 9, 10, 11$, and 12, given in Table 8, the corresponding $RE\left(\varphi, \varphi_{\alpha(\delta)}\right)$ increases around 90%, but no more than $RE(\varphi, \varphi_\delta)$, i.e., the TRM does not provide a good approximate solution to the IP. In this case, we could use the regularized solution $\varphi_{\alpha(\delta)}$ as an initial point of an iterative method to recover a better solution to the IP. Furthermore, the relative errors of the recovered solutions φ_δ without applying regularization increase suddenly, starting at $m = 7$ and $m = 5$ (see Tables 7 and 8) for the functions $\varphi(x, y) = x^2 - y^2$ and $\varphi(x, y) = e^x \sin(y)$ for $(x, y) \in S_1$, respectively. As in the previous cases, the regularization parameter $\alpha(\delta)$ changes depending on V_δ, N, m, and β.

We show the graphs for the following functions:

- $\varphi(x, y) = x^2 - y^2$ (Figure 9 with parameters $\beta = 7.1$, $m = 8$, $\delta = 0.1$, $\alpha(\delta) = 10^2$, and $N = 20$).
- $\varphi(x, y) = e^x \sin(y)$ (Figure 10 with parameters $\beta = 7.9999999$, $m = 8$, $\delta = 0.1$, $\alpha(\delta) = 2 \times 10^{-8}$, and $N = 30$).

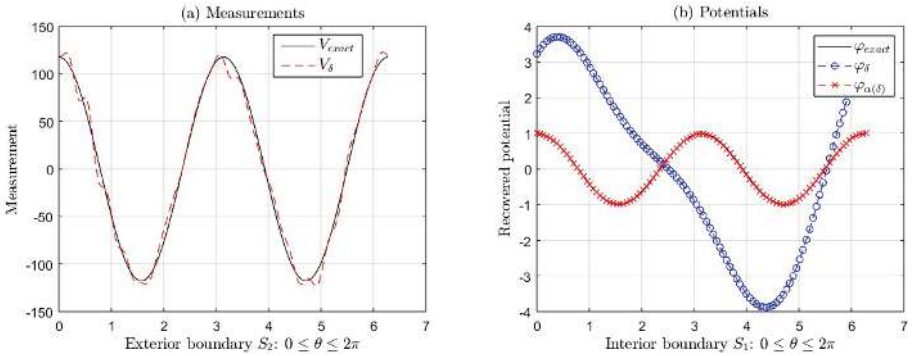

Figure 9. (**a**) Exact measurement V (black line) and with error V_δ (red line). (**b**) Exact potential φ and its approximations $\varphi_{\alpha(\delta)}$ and φ_δ, corresponding to Example 1 for $\beta = 7.1$, $m = 8$, and $\delta = 0.1$ (see Table 7). In this case, we take $\alpha(\delta) = 10^2$ and $N = 20$.

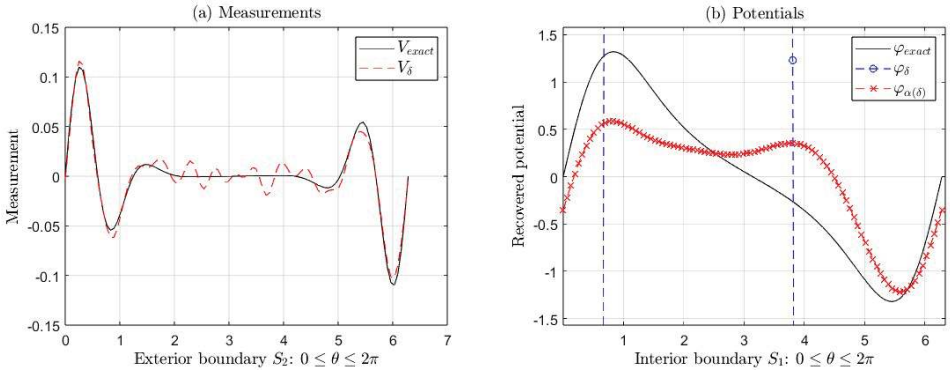

Figure 10. (**a**) Exact measurement V (black line) and with error V_δ (red line). (**b**) Exact potential φ and its approximations $\varphi_{\alpha(\delta)}$ and φ_δ, corresponding to Example 1 for $\beta = 7.9999999$, $m = 8$, and $\delta = 0.1$ (see Table 8). In this case, we take $\alpha(\delta) = 2 \times 10^{-8}$ and $N = 30$.

For $(x, y) \in S_1$. These figures show the following:

(a) The exact measurement V and the measurement with error V_δ.
(b) The exact potential φ and its approximations $\varphi_{\alpha(\delta)}$ (with regularization) and φ_δ (without regularization).

In both cases, as mentioned in the previous paragraph, the errors increase starting at $m = 7$ for the first function and starting at $m = 5$ for the second one, as can be seen in Figures 9b and 10b for $m = 8$, where we can see the ill-posedness of the IP if we do not apply regularization. For example, for the first function, the $RE(\varphi, \varphi_\delta) = 3.3483$ is greater than $RE\left(\varphi, \varphi_{\alpha(\delta)}\right) = 0.0199$ for $\beta = 7.1$, $m = 8$, and $\delta = 0.1$ (see Table 7). For the second one, the $RE(\varphi, \varphi_\delta) = 164.4764$ is greater than $RE\left(\varphi, \varphi_{\alpha(\delta)}\right) = 0.5806$ for $\beta = 7.9999999$, $m = 8$, and $\delta = 0.1$ (see Table 8). In this latter function, the approximate solution $\varphi_{\alpha(\delta)}$ is far from the exact solution φ. In this case, we could apply an iterative method to obtain a better solution, taking $\varphi_{\alpha(\delta)}$ as an initial point.

4.2.4. Case 4: $\beta < m - 1$, for $m = 2,\ldots,12$ and $\delta = 0.1$

In this Section, we consider the case when $\beta < m - 1$ for $m = 2, 3, \ldots, 12$ and $\delta = 0.1$. Tables 9 and 10 show the relative errors of the approximations $\varphi_{\alpha(\delta)}$ and φ_δ when $\delta = 0.1$, with the same two exact functions φ considered in the Section 4.1.

In Table 9, we observe that the $RE\left(\varphi, \varphi_{\alpha(\delta)}\right)$ from solutions with regularization $\varphi_{\alpha(\delta)}$ are less than the $RE(V, V_\delta)$. For some values of N, β, and m given in this same table, we can see that $RE\left(\varphi, \varphi_{\alpha(\delta)}\right)$ and $RE(\varphi, \varphi_\delta)$ are of the same order, i.e., the solutions without regularization φ_δ are close to regularized solutions $\varphi_{\alpha(\delta)}$; however, the regularized solutions $\varphi_{\alpha(\delta)}$ are better than the solutions without regularization. The $RE(\varphi, \varphi_\delta)$ increases faster than the $RE(V, V_\delta)$ starting at $m = 3$. Furthermore, we can observe similar results in Table 10, where the $RE\left(\varphi, \varphi_{\alpha(\delta)}\right)$ are of the same order as $RE(V, V_\delta)$ for $m = 2, 3, 4$, with $\beta = 0.5, \delta = 0.1$, except for $m = 5, 6, \ldots, 12$. Nevertheless, the $RE(\varphi, \varphi_\delta)$ increases faster than the $RE(V, V_\delta)$ starting at $m = 5$. For the values of $m = 8$, 9, 10, 11, and 12, the $RE\left(\varphi, \varphi_{\alpha(\delta)}\right)$ increases between 40% and 90%, but no more than $RE(\varphi, \varphi_\delta)$. In this case, the TRM does not provide a good approximate solution to the IP. However, as mentioned before, we could use the regularized solution $\varphi_{\alpha(\delta)}$ as an initial point of an iterative method to recover a better solution to the IP. Also, the relative errors of the recovered solutions φ_δ without applying regularization increase suddenly, starting at $m = 7$ and $m = 5$ (see Tables 9 and 10) for the functions $\varphi(x, y) = x^2 - y^2$ and $\varphi(x, y) = e^x \sin(y)$ for $(x, y) \in S_1$, respectively. Here also, as in the previous cases, the parameter of regularization $\alpha(\delta)$ changes depending on V_δ, N, m, and β.

Table 9. Case 4: Numerical results applying TRM to solve the IP related to the fractional Cauchy problem (12) for $\delta = 0.1$ and different values of β and m, where $\varphi(x,y) = x^2 - y^2$, $(x,y) \in S_1$.

N	$\alpha(\delta)$	β	m	$RE(V,V_\delta)$	$RE(\varphi,\varphi_{\alpha(\delta)})$	$RE(\varphi,\varphi_\delta)$
20	1×10^{-4}	0.5	2	0.1037	0.0369	0.0371
25	1×10^{-4}	0.5	2	0.1043	0.0846	0.0850
30	1×10^{-4}	0.5	2	0.1123	0.0947	0.0952
20	1×10^{-7}	0.1	3	0.0953	0.0558	0.3293
20	1×10^{-5}	0.8	3	0.0928	0.0397	0.1176
20	1×10^{-3}	1.6	4	0.1031	0.0692	0.3781
20	1×10^{0}	2.9	4	0.0988	0.0550	0.2616
20	1×10^{-10}	0.5	5	0.1063	0.0493	2.3272
20	1×10^{-2}	3.5	5	0.1002	0.0479	0.6521
20	1×10^{-10}	0.5	6	0.0824	0.0664	1.0640
20	1×10^{-3}	3.4	6	0.1156	0.0541	1.0860
20	1×10^{-16}	0.5	7	0.1093	0.0251	11.3550
20	1×10^{-5}	4.2	7	0.0871	0.0203	4.0183
20	1×10^{-16}	0.5	8	0.0915	0.0280	3.7583
20	1×10^{-6}	3.7	8	0.1097	0.0212	4.3335
20	1×10^{-22}	0.5	9	0.0969	0.0195	21.9486
20	1×10^{-6}	5.2	9	0.0841	0.0345	9.1221
20	1×10^{-22}	0.5	10	0.1022	0.0290	22.9009
20	1×10^{-5}	7.6	10	0.1073	0.0181	7.2447
20	1×10^{-28}	0.5	11	0.0936	0.0300	122.7548
20	1×10^{-8}	6.6	11	0.0886	0.0121	91.7074
20	1×10^{-28}	0.5	12	0.0926	0.0149	30.3739
20	1×10^{-8}	6.3	12	0.1007	0.0329	36.2964

Table 10. Case 4: Numerical results applying TRM to solve IP related to the fractional Cauchy problem (12) for $\delta = 0.1$, $\beta = 0.5$ and different values of m, where $\varphi(x,y) = e^x \sin(y)$, $(x,y) \in S_1$.

N	$\alpha(\delta)$	β	m	$RE(V,V_\delta)$	$RE(\varphi,\varphi_{\alpha(\delta)})$	$RE(\varphi,\varphi_\delta)$
20	1×10^{-4}	0.5	2	0.1422	0.0274	0.0284
25	1×10^{-4}	0.5	2	0.1537	0.0496	0.0551
30	1×10^{-4}	0.5	2	0.1524	0.0585	0.0627
30	9×10^{-10}	0.5	3	0.1619	0.1437	0.1438
30	5×10^{-8}	0.5	4	0.1960	0.1656	0.2199
30	7×10^{-12}	0.5	5	0.2014	0.1376	13.9836
30	4×10^{-12}	0.5	6	0.2265	0.2261	8.6601
30	5×10^{-17}	0.5	7	0.2419	0.2709	209.3490
30	5×10^{-17}	0.5	8	0.2131	0.4002	205.2009
30	3×10^{-19}	0.5	9	0.2154	0.8873	2.6220×10^{3}
30	1.4×10^{-19}	0.5	10	0.2010	0.8863	4.1567×10^{3}
30	6×10^{-24}	0.5	11	0.2148	0.9054	1.3299×10^{5}
30	3×10^{-24}	0.5	12	0.2021	0.8935	1.6833×10^{5}

Figures 11 and 12 show the graphs of the exact measurement V and with error V_δ with $\delta = 0.1$, the graphs of the exact potential φ and its approximations $\varphi_{\alpha(\delta)}$ (with regularization) and φ_δ (without regularization), corresponding to the functions $\varphi(x,y) = x^2 - y^2$ and $\varphi(x,y) = e^x \sin(y)$ for $(x,y) \in S_1$, respectively. In both cases, as mentioned in the previous paragraph, the errors increase suddenly, starting at $m = 7$ for the first function and starting at $m = 5$ for the second one, as can be seen in Figures 11b and 12b, where we can see the ill-posedness of the IP if we do not apply regularization. For example, for the first function, the relative error $RE(\varphi,\varphi_\delta) = 36.2964$ is greater than $RE\left(\varphi,\varphi_{\alpha(\delta)}\right) = 0.0329$ for $\beta = 6.3$,

$m = 12$, and y $\delta = 0.1$ (see Table 9). For the second one, the $RE(\varphi, \varphi_\delta) = 205.2009$ is greater than $RE\left(\varphi, \varphi_{\alpha(\delta)}\right) = 0.4002$ for $\beta = 0.5$, $m = 8$, and $\delta = 0.1$ (see Table 10). In this case, we could use the regularized solution $\varphi_{\alpha(\delta)}$ as an initial point of an iterative method to recover a better solution to the IP.

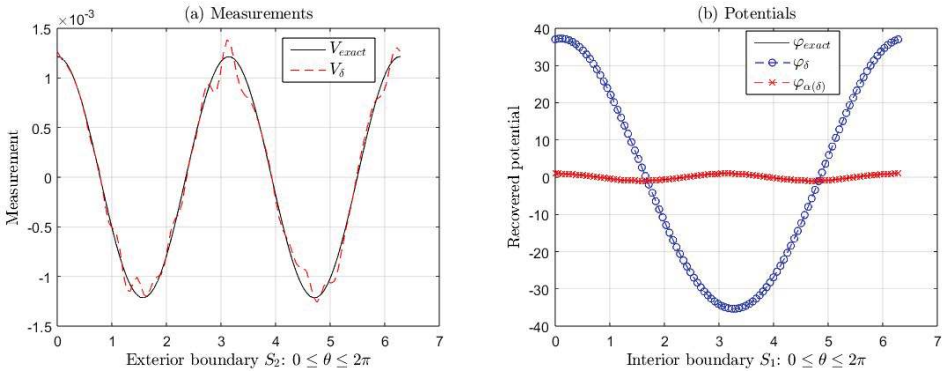

Figure 11. (**a**) Exact measurement V (black line) and with error V_δ (red line). (**b**) Exact potential φ and its approximations $\varphi_{\alpha(\delta)}$ and φ_δ, corresponding to Example 1 for $\beta = 6.3$, $m = 12$, and $\delta = 0.1$ (see Table 9). In this case, we take $\alpha(\delta) = 10^{-8}$ and $N = 20$.

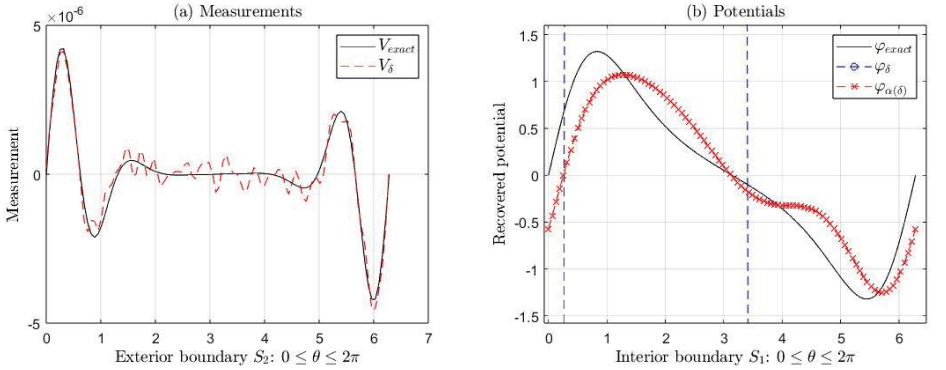

Figure 12. (**a**) Exact measurement V (black line) and with error V_δ (red line). (**b**) Exact potential φ and its approximations $\varphi_{\alpha(\delta)}$ and φ_δ, corresponding to Example 2 for $\beta = 0.5$, $m = 8$, and $\delta = 0.1$ (see Table 10). In this case, we take $\alpha(\delta) = 5 \times 10^{-17}$ and $N = 30$.

4.2.5. Case 5: $\beta < m - 1$, When β Is Next to n or $n - 1$, Where $0 < n \le m - 1$, for $m = 2, \ldots, 12$ and $\delta = 0.1$

In this section, we consider the case when $\beta < m - 1$, when β is next to n or $n - 1$, where $0 < n \le m - 1$, for $m = 2, \ldots, 12$ and $\delta = 0.1$. Tables 11 and 12 show the relative errors of the approximations $\varphi_{\alpha(\delta)}$ and φ_δ when $\delta = 0.1$ for the same two exact functions φ considered in Section 4.1.

Table 11. Case 5: Numerical results applying TRM to solve the IP related to the fractional Cauchy problem (12) for $\delta = 0.1$ and different values of β and m, where $\varphi(x, y) = x^2 - y^2$, $(x, y) \in S_1$.

N	$\alpha(\delta)$	β	m	$RE(V,V_\delta)$	$RE(\varphi,\varphi_{\alpha(\delta)})$	$RE(\varphi,\varphi_\delta)$
20	1×10^{-4}	0.1	2	0.0981	0.0294	0.0312
20	1×10^{-4}	0.0001	2	0.0880	0.0665	0.0702
20	1×10^{-4}	0.0000001	2	0.0877	0.0420	0.0436
20	1×10^{-2}	0.9	2	0.0825	0.0252	0.0301
20	1×10^{-2}	0.9999	2	0.0896	0.0355	0.0383
20	1×10^{-2}	0.9999999	2	0.0988	0.0497	0.0524

Table 11. *Cont.*

N	$\alpha(\delta)$	β	m	$RE(V,V_\delta)$	$RE(\varphi,\varphi_{\alpha(\delta)})$	$RE(\varphi,\varphi_\delta)$
20	1×10^{-7}	0.1	3	0.0984	0.0736	0.4041
20	1×10^{-7}	0.0001	3	0.0988	0.0556	0.2586
20	1×10^{-7}	0.0000001	3	0.1063	0.0633	0.5828
20	1×10^{-5}	0.9	3	0.0824	0.0632	0.2671
20	1×10^{-4}	0.9999	3	0.0940	0.0747	0.4997
20	5×10^{-5}	0.9999999	3	0.0843	0.0582	0.2323
20	1×10^{-2}	2.1	4	0.1133	0.0813	0.4297
20	1×10^{0}	2.9	4	0.1097	0.0494	0.2746
20	1×10^{-4}	3.1	5	0.0841	0.0521	0.5721
20	1×10^{-1}	3.9	5	0.0923	0.0284	0.9725
20	1×10^{-1}	4.1	6	0.0982	0.0441	1.3912
20	1×10^{1}	4.9	6	0.1192	0.0261	0.2905
20	1×10^{-2}	5.1	7	0.1027	0.0331	12.2005
20	1×10^{0}	5.9	7	0.0926	0.0324	2.2300
20	1×10^{-3}	5.1	8	0.0928	0.0306	2.3248
20	1×10^{-3}	5.0001	8	0.0936	0.0312	5.2064
20	1×10^{-18}	5.0000001	8	0.1020	0.0174	1.3253
20	1×10^{0}	5.9	8	0.0967	0.0113	3.4116
20	1×10^{0}	5.9999	8	0.0946	0.0260	7.0605
20	1×10^{-15}	5.9999999	8	0.0907	0.0275	1.9174
20	1×10^{-1}	7.1	9	0.0849	0.0118	9.9754
20	1×10^{0}	7.9	9	0.0916	0.0224	16.5564
20	1×10^{-13}	3.1	10	0.0930	0.0114	20.7949
20	1×10^{-11}	3.9	10	0.1054	0.0197	31.4437
20	1×10^{-10}	6.1	11	0.0978	0.0207	79.4649
20	1×10^{-7}	6.9	11	0.1048	0.0109	59.7459
20	1×10^{-15}	4.1	12	0.1035	0.0133	108.9786
20	1×10^{-12}	4.9	12	0.0978	0.0278	131.9629

Table 12. Case 5: Numerical results applying TRM to solve the IP related to the fractional Cauchy problem (12) for $\delta = 0.1$ and different values of β and m, where $\varphi(x,y) = e^x \sin(y)$, $(x,y) \in S_1$.

N	$\alpha(\delta)$	β	m	$RE(V,V_\delta)$	$RE(\varphi,\varphi_{\alpha(\delta)})$	$RE(\varphi,\varphi_\delta)$
30	1×10^{-5}	0.1	2	0.1918	0.0633	0.0669
30	1×10^{-5}	0.0001	2	0.1747	0.0510	0.0551
30	1×10^{-5}	0.0000001	2	0.1932	0.0408	0.0466
30	1×10^{-3}	0.9	2	0.1678	0.0267	0.0338
30	1×10^{-2}	0.9999	2	0.1879	0.0538	0.0996
30	1×10^{-3}	0.9999999	2	0.1757	0.0330	0.0352
30	7×10^{-9}	0.1	3	0.2035	0.1269	0.3288
30	3×10^{-9}	0.0001	3	0.1945	0.0741	0.2384
30	6×10^{-10}	0.0000001	3	0.1863	0.2035	0.2102
30	7×10^{-7}	0.9	3	0.2208	0.1301	0.2493
30	2×10^{-6}	0.9999	3	0.2057	0.0770	0.2885
30	5×10^{-7}	0.9999999	3	0.2013	0.1809	0.2036

Table 12. *Cont.*

N	$\alpha(\delta)$	β	m	$RE(V,V_\delta)$	$RE(\varphi,\varphi_{\alpha(\delta)})$	$RE(\varphi,\varphi_\delta)$
30	1×10^{-5}	2.1	4	0.2001	0.1393	0.1397
30	3×10^{-2}	2.9	4	0.1984	0.1061	0.2367
30	2×10^{-4}	3.1	5	0.2106	0.2788	14.4371
30	6×10^{-3}	3.9	5	0.1827	0.2914	6.9833
30	1×10^{-2}	4.1	6	0.2299	0.3008	4.2311
30	5×10^{-1}	4.9	6	0.1770	0.2723	3.9078
30	3×10^{-3}	5.1	7	0.2095	0.1755	297.5818
30	5×10^{-2}	5.9	7	0.1969	0.3580	51.0331
30	2×10^{-3}	5.1	8	0.2424	0.2924	216.7317
30	3×10^{-3}	5.0001	8	0.2004	0.3714	452.3457
30	1.4×10^{-3}	5.0000001	8	0.1747	0.3650	239.9826
30	2×10^{2}	5.9	8	0.2001	0.3549	263.7365
30	1.3×10^{-1}	5.9999	8	0.1829	0.3781	78.5332
30	5×10^{-1}	5.9999999	8	0.2137	0.2490	311.6103
30	1.5×10^{2}	7.1	9	0.2263	0.8972	4.5033×10^{3}
30	1×10^{4}	7.9	9	0.2228	0.8943	4.3085×10^{3}
30	1×10^{-10}	3.1	10	0.2658	0.8914	7.9703×10^{3}
30	8×10^{-8}	3.9	10	0.2642	0.8948	5.5828×10^{3}
30	1×10^{-4}	6.1	11	0.2378	0.9312	2.8572×10^{5}
30	5×10^{-3}	6.9	11	0.2089	0.8950	5.1113×10^{4}
30	2×10^{-11}	4.1	12	0.2311	0.8945	7.0888×10^{4}
30	4×10^{-9}	4.9	12	0.1994	0.9057	7.9818×10^{4}

In Table 11, we observe that $RE\left(\varphi, \varphi_{\alpha(\delta)}\right) < RE(V, V_\delta)$. For $m = 2$, we can see that $RE\left(\varphi, \varphi_{\alpha(\delta)}\right)$ and $RE(\varphi, \varphi_\delta)$ are of the same order when β is next to 1 or 0 (taking $n = 1$), i.e., the solutions without regularization φ_δ are close to regularized solutions $\varphi_{\alpha(\delta)}$. However, the regularized approximates $\varphi_{\alpha(\delta)}$ are better than the solutions without regularization. The $RE\left(\varphi, \varphi_{\alpha(\delta)}\right)$ increases faster than the $RE(V, V_\delta)$ starting at $m = 3$, as shown in Figure 13b for $\beta = 0.0001$, $m = 3$, and $\delta = 0.1$, where $RE\left(\varphi, \varphi_{\alpha(\delta)}\right) = 0.0556$ and $RE(\varphi, \varphi_\delta) = 0.2586$. These approximations, $\varphi_{\alpha(\delta)}$ and φ_δ, are recovered from measurements with error V_δ, shown in Figure 13a. Also, we can observe similar results in Table 12, where $RE\left(\varphi, \varphi_{\alpha(\delta)}\right)$ and $RE(\varphi, \varphi_\delta)$ are of the same order for $m = 2, 3, 4$, and when β is next to n or $n-1$ (taking $n = 1, 1$, and 3, respectively), for $\delta = 0.1$, nevertheless the $RE\left(\varphi, \varphi_{\alpha(\delta)}\right)$ increases between 17% and 38%, but no more than the $RE(\varphi, \varphi_\delta)$ for $m = 5, 6, 7$, and 8. For the values of $m = 9, 10, 11$, and 12, the $RE\left(\varphi, \varphi_{\alpha(\delta)}\right)$ increases around 90%, but no more than $RE(\varphi, \varphi_\delta)$. In this case, we could use the regularized solution $\varphi_{\alpha(\delta)}$ as an initial point of an iterative method to recover a better solution to the IP. Nevertheless, the relative errors of the recovered solutions φ_δ without applying regularization increase suddenly, starting at $m = 7$ and $m = 5$ (see Tables 11 and 12) for the functions $\varphi(x, y) = x^2 - y^2$ and $\varphi(x, y) = e^x \sin(y)$ for $(x, y) \in S_1$, respectively. Here, the regularization parameters $\alpha(\delta)$ also change depending on V_δ, N, m, and β.

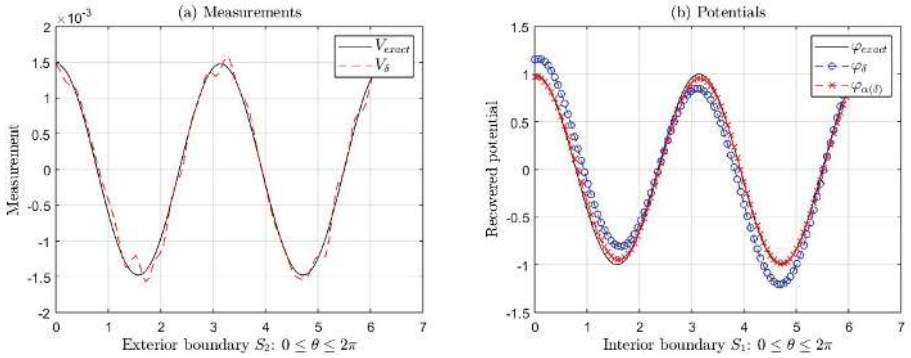

Figure 13. (**a**) Exact measurement V (black line) and with error V_δ (red line). (**b**) Exact potential φ and its approximations $\varphi_{\alpha(\delta)}$ and φ_δ, corresponding to Example 1 for $\beta = 0.0001$, $m = 3$, and $\delta = 0.1$ (see Table 11). In this case, we take $\alpha(\delta) = 10^{-7}$ and $N = 20$.

Figures 13–16 show the graphs of the exact measurement V and with error V_δ with $\delta = 0.1$, the graphs of the exact potential φ and its approximations $\varphi_{\alpha(\delta)}$ (with regularization) and φ_δ (without regularization), corresponding to the functions $\varphi(x, y) = x^2 - y^2$ and $\varphi(x, y) = e^x \sin(y)$ for $(x, y) \in S_1$, respectively. In both cases, as mentioned in the previous paragraph, the errors increase suddenly, starting at $m = 7$ for the first function and starting at $m = 5$ for the second one, as can be seen in Figure 14b, Figure 15b, and Figure 16b, where we can see the ill-posedness of the IP if we do not apply regularization for $m = 12, 8$, and $m = 11$, respectively. For example, for the approximations φ_δ and $\varphi_{\alpha(\delta)}$ shown in Figure 14b of the first function, the $RE(\varphi, \varphi_\delta) = 131.9629$ is much greater than $RE\left(\varphi, \varphi_{\alpha(\delta)}\right) = 0.0278$ for $\beta = 4.9$, $m = 12$, and $\delta = 0.1$ (see Table 11). For the approximations φ_δ and $\varphi_{\alpha(\delta)}$ shown in Figure 15b of the second one, the $RE(\varphi, \varphi_\delta) = 78.5332$ is much greater than $RE\left(\varphi, \varphi_{\alpha(\delta)}\right) = 0.3781$, for $\beta = 5.9999$, $m = 8$, and y $\delta = 0.1$ (see Table 12). Lastly, for the approximations φ_δ and $\varphi_{\alpha(\delta)}$ shown in Figure 16b of the second one, the $RE(\varphi, \varphi_\delta) = 2.8572 \times 10^5$ is greater than $RE\left(\varphi, \varphi_{\alpha(\delta)}\right) = 0.9312$ for $\beta = 6.1$, $m = 11$, and $\delta = 0.1$ (see Table 12). In these last two examples, when the approximate solutions $\varphi_{\alpha(\delta)}$ are not close to the exact solution φ, we could use the regularized solution $\varphi_{\alpha(\delta)}$ as an initial point of an iterative method to recover a better solution to the IP.

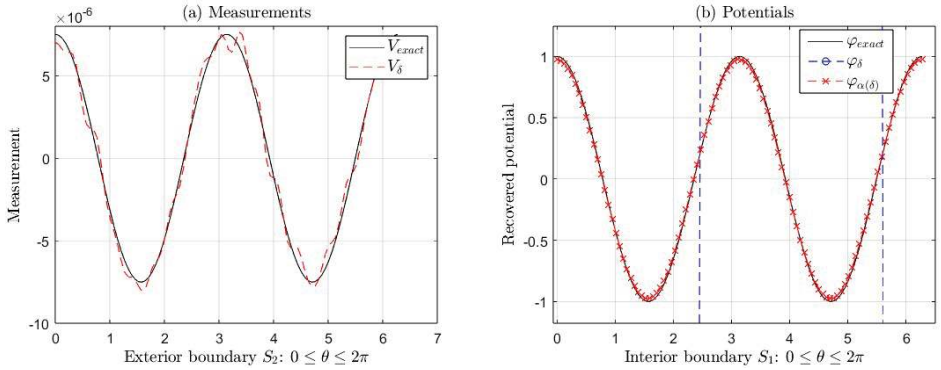

Figure 14. (**a**) Exact measurement V (black line) and with error V_δ (red line). (**b**) Exact potential φ and its approximations $\varphi_{\alpha(\delta)}$ and φ_δ, corresponding to Example 1 for $\beta = 4.9$, $m = 12$, and $\delta = 0.1$ (see Table 11). In this case, we take $\alpha(\delta) = 10^{-12}$ and $N = 20$.

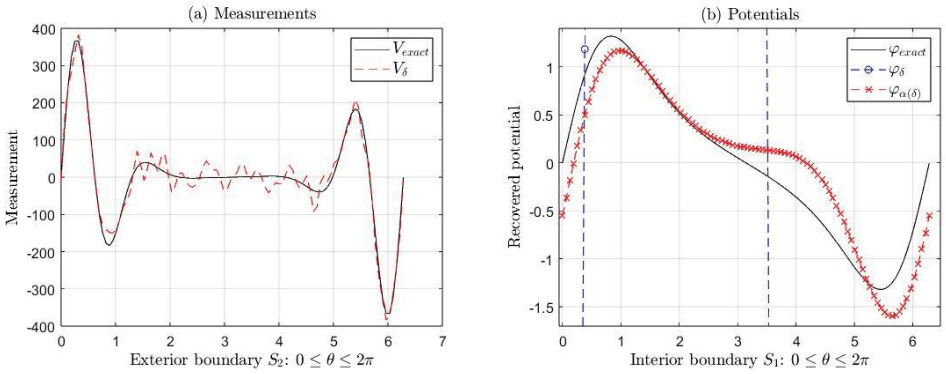

Figure 15. (**a**) Exact measurement V (black line) and with error V_δ (red line). (**b**) Exact potential φ and its approximations $\varphi_{\alpha(\delta)}$ and φ_δ, corresponding to Example 2 for $\beta = 5.9999$, $m = 8$, and $\delta = 0.1$ (see Table 12). In this case, we take $\alpha(\delta) = 1.3 \times 10^{-1}$ and $N = 30$.

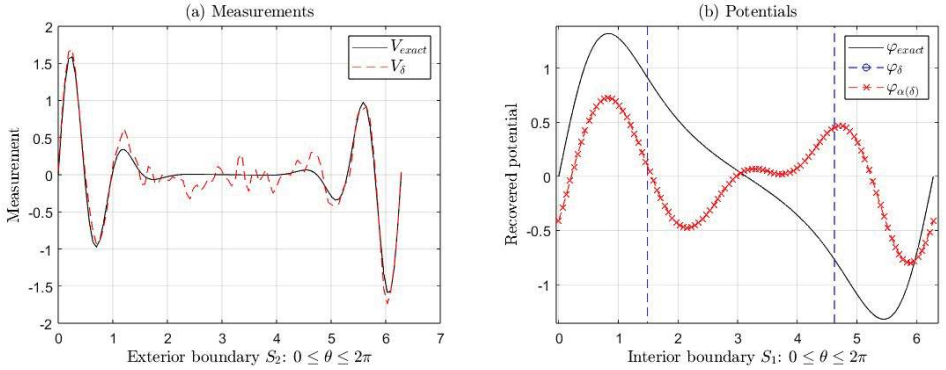

Figure 16. (**a**) Exact measurement V (black line) and with error V_δ (red line). (**b**) Exact potential φ and its approximations $\varphi_{\alpha(\delta)}$ and φ_δ, corresponding to Example 2 for $\beta = 6.1$, $m = 11$, and $\delta = 0.1$ (see Table 12). In this case, we take $\alpha(\delta) = 10^{-4}$ and $N = 30$.

4.2.6. Case 6: $\beta > m$, for $m = 1, 2, \ldots, 13$ and $\delta = 0.1$

In this case, we consider the case when $\beta > m$, with $m = 1, 2, \ldots, 13$. for $\delta = 0.1$. Tables 13 and 14 show the relative errors of the approximations $\varphi_{\alpha(\delta)}$ and φ_δ when $\delta = 0.1$ for the same two exact functions φ considered in Section 4.1.

Table 13. Case 6: Numerical results applying TRM to solve IP related to the fractional Cauchy problem (12) for $\delta = 0.1$ and different values of β and m, where $\varphi(x, y) = x^2 - y^2$, $(x, y) \in S_1$.

N	$\alpha(\delta)$	β	m	$RE(V, V_\delta)$	$RE(\varphi, \varphi_{\alpha(\delta)})$	$RE(\varphi, \varphi_\delta)$
20	1×10^{-6}	1.001	1	0.0949	0.0430	0.0432
20	1×10^{14}	1.5	1	0.0860	0.0825	0.0965
20	1×10^{-6}	2.0001	2	0.0911	0.0574	0.0581
20	1×10^{32}	3.1	2	0.0809	0.0783	0.0863
20	1×10^{-1}	3.01	3	0.0894	0.0278	0.1076
20	1×10^{45}	4.5	3	0.1048	0.0639	0.2370
20	1×10^{5}	4.1	4	0.0942	0.0294	0.1592
20	1×10^{95}	7.1	4	0.1051	0.0495	0.2588
20	1×10^{-4}	5.0001	5	0.0792	0.0298	1.3533
20	1×10^{33}	6.1	5	0.0946	0.0165	0.4475
20	1×10^{6}	6.1	6	0.0907	0.0277	0.9987
20	1×10^{48}	7.5	6	0.0867	0.0276	0.6014
20	1×10^{5}	7.1	7	0.0932	0.0109	3.5379
20	1×10^{50}	8.6	7	0.1024	0.0131	3.1745

Table 13. *Cont.*

N	$\alpha(\delta)$	β	m	$RE(V,V_\delta)$	$RE(\varphi,\varphi_{\alpha(\delta)})$	$RE(\varphi,\varphi_\delta)$
20	1×10^{1}	8.001	8	0.1135	0.0277	2.2757
20	1×10^{46}	9.4	8	0.0877	0.0180	3.6123
20	1×10^{-2}	9.0001	9	0.0935	0.0163	22.9725
20	1×10^{53}	10.7	9	0.0979	0.0342	3.1946
20	1×10^{-1}	10.0001	10	0.1046	0.0345	50.3389
20	1×10^{49}	11.5	10	0.0979	0.0179	12.7233
20	1×10^{0}	11.001	11	0.0834	0.0164	12.8627
20	1×10^{53}	12.6	11	0.0915	0.0331	44.9837
20	1×10^{1}	12.0001	12	0.1136	0.0195	121.2423
20	1×10^{47}	13.4	12	0.0822	0.0165	113.4837
20	1×10^{1}	11.5	13	0.0941	0.0155	420.7545
20	1×10^{3}	12.0001	13	0.0950	0.0280	319.2454
20	1×10^{4}	12.5	13	0.1188	0.0187	701.4226
20	1×10^{1}	12.9999	13	0.0925	0.0198	183.4905
20	1×10^{29}	13.5	13	0.0938	0.0219	400.2461
20	1×10^{51}	14.5	13	0.1112	0.0295	319.4336

Table 14. Case 6: Numerical results applying TRM to solve IP related to the fractional Cauchy problem (12) for $\delta = 0.1$ and different values of β and m, where $\varphi(x,y) = e^x \sin(y)$, $(x,y) \in S_1$.

N	$\alpha(\delta)$	β	m	$RE(V,V_\delta)$	$RE(\varphi,\varphi_{\alpha(\delta)})$	$RE(\varphi,\varphi_\delta)$
30	3×10^{-5}	1.001	1	0.1942	0.0575	0.1229
30	3×10^{13}	1.5	1	0.1687	0.0687	0.0965
30	6×10^{-6}	2.0001	2	0.1681	0.0606	0.1017
30	1×10^{32}	3.1	2	0.1800	0.0660	0.0763
30	2×10^{-2}	3.01	3	0.1855	0.1200	0.5139
30	5×10^{44}	4.5	3	0.2034	0.1517	1.0728
30	3×10^{3}	4.1	4	0.1930	0.0226	0.3616
30	5×10^{93}	7.1	4	0.2236	0.1517	0.4427
30	3.1×10^{-5}	5.0001	5	0.2254	0.1550	13.8261
30	1.1×10^{32}	6.1	5	0.2046	0.1057	3.5558
30	6.3×10^{-4}	6.0001	6	0.1984	0.1863	8.7178
30	6.4×10^{46}	7.5	6	0.2036	0.1233	4.9854
30	6.5×10^{4}	7.1	7	0.2188	0.3310	253.4635
30	4.4×10^{36}	8.2	7	0.1844	0.2976	36.0590
30	3.4×10^{-4}	8.00001	8	0.1944	0.4695	460.0541
30	1.1×10^{57}	9.8	8	0.2512	0.4601	157.1510
30	3×10^{1}	9.0001	9	0.2299	0.8871	7.2299×10^{3}
30	5.1×10^{57}	10.7	9	0.2143	0.8912	4.4110×10^{3}
30	5×10^{2}	10.0001	10	0.2151	0.8907	2.0204×10^{4}
30	1×10^{53}	11.5	10	0.2191	0.8920	2.4527×10^{3}
30	6×10^{3}	11.0001	11	0.2632	0.8857	3.6429×10^{5}
30	9×10^{50}	12.4	11	0.2290	0.9571	1.8509×10^{5}
30	1.3×10^{5}	12.0001	12	0.2451	0.9564	3.7314×10^{5}
30	2.1×10^{52}	13.4	12	0.2211	0.9192	4.5936×10^{5}
30	5.9×10^{10}	11.5	13	0.2168	0.9964	1.3190×10^{7}
30	5×10^{11}	12.0001	13	0.2607	0.9994	1.0836×10^{5}
30	9×10^{11}	12.5	13	0.2326	0.9904	1.0214×10^{7}
30	1.1×10^{9}	12.9999	13	0.2439	0.9890	1.3107×10^{7}
30	1.3×10^{29}	13.5	13	0.2338	0.9895	5.7405×10^{6}
30	1.7×10^{59}	14.5	13	0.2424	0.9899	1.3997×10^{7}

In Table 13, we observe that $RE\left(\varphi, \varphi_{\alpha(\delta)}\right) < RE(V, V_\delta)$. For $m = 1, 2$, we can see that $RE\left(\varphi, \varphi_{\alpha(\delta)}\right)$ and $RE(\varphi, \varphi_\delta)$ are of the same order when $\delta = 0.1$, i.e., the solutions without regularization φ_δ are close to regularized solutions $\varphi_{\alpha(\delta)}$. However, the regularized approximates $\varphi_{\alpha(\delta)}$ are better than the solutions without regularization. Additionally, the relative errors of the solutions without regularization φ_δ increase faster, starting at $m = 3$. Furthermore, we can observe similar results in Table 14. In this case, the relative errors from solutions with regularization $RE\left(\varphi, \varphi_{\alpha(\delta)}\right)$ are less than the $RE(V, V_\delta)$ for $m = 1, 2, \ldots, 6$, and increase between 29% and 46% for $m = 7, 8$, when $\delta = 0.1$. Nevertheless, the corresponding relative errors of the solutions with regularization increase between 88% and 96% for $m = 9, 10, 11, 12$, but no more than the corresponding $RE(\varphi, \varphi_\delta)$. The relative errors of the recovered solutions φ_δ without regularization increase suddenly, starting at $m \geq 5$. For example, for $\beta = 10.7$ and $m = 9$, the $RE(\varphi, \varphi_\delta) = 4.4110 \times 10^3$. For $m = 13$, the $RE\left(\varphi, \varphi_{\alpha(\delta)}\right)$ increases between 91% and 99%, but no more than the $RE(\varphi, \varphi_\delta)$), for $\beta > m$, as well as for $\beta < m$ and $m - 1 < \beta < m$ with $\delta = 0.1$. Moreover, as in the previous cases, the regularization parameters $\alpha(\delta)$ change depending on the data with error V_δ, the values N, m, and β. Analogous results can be obtained for values $m \geq 14$, as those obtained for $m = 13$, which are not included in this work.

In the following two examples, we have considered non-smooth functions.

Example 3. *We consider the 'exact potential'* $\varphi(x, y) = \sqrt{(x^2 + y^2)} - \pi/2$, *for* $(x, y) \in S_1$, *which in polar coordinates is given by* $\varphi(\theta) = |\theta| - \pi/2$, *for* $\theta \in [-\pi, \pi]$. *Resembling the first example, the 'exact measurement' V and the 'measurement with error'* V_δ *are generated with the first N terms of the Fourier series (22) and (23), respectively, such that* $\| \varphi_N - \varphi \|_{L_2(S_1)} \leq \epsilon_F$, *with* $0 \leq \epsilon_F$. *For* $N = 30$, $\epsilon_F = 0.0056$. *In this case,* $V_0 = \varphi_0 = 0$ *and the Fourier coefficients* φ_k, $1 \leq k \leq N$, *are obtained numerically using the intrinsic function quadl of MATLAB.*

Table 15 shows the numerical results for data without error, applying TRM to solve the IP of the classical Cauchy problem (2), where $N = 20$, 25, and 30. In this table, we can observe similar results to the previous examples where the regularized solutions $\varphi_{\alpha(\delta)}$ are better.

Table 15. Numerical results applying TRM to solve the IP related to the classical Cauchy problem (2), for $\varphi(\theta) = |\theta| - \pi/2$, $\theta \in [-\pi, \pi]$ and different values of δ and N.

δ	N	$\alpha(\delta)$	$RE(V, V_\delta)$	$RE(\varphi, \varphi_{\alpha(\delta)})$	$RE(\varphi, \varphi_\delta)$
0.1	20	0.1	0.1080	0.1545	1.1839
0.1	25	0.1	0.0953	0.1314	2.1403
0.1	30	0.1	0.1342	0.1630	5.5998
0.01	20	0.01	0.0121	0.0409	0.1102
0.01	25	0.01	0.0114	0.0425	0.1676
0.01	30	0.01	0.0128	0.0370	0.5224
0.001	20	0.001	8.1891×10^{-4}	0.0043	0.0046
0.001	25	0.001	9.1866×10^{-4}	0.0088	0.0139
0.001	30	0.001	0.0014	0.0117	0.0557

Table 16 shows the numerical results for data without error, applying TRM to solve the IP of the fractional Cauchy problem (12) for different values of β, m, and N.

Table 16. Numerical results applying TRM to solve IP related to the fractional Cauchy problem (12) for $\delta = 0.1$ and different values of β and m, where $\varphi(\theta) = |\theta| - \pi/2, \theta \in [-\pi, \pi]$.

N	$\alpha(\delta)$	β	m	$RE(V,V_\delta)$	$RE(\varphi,\varphi_{\alpha(\delta)})$	$RE(\varphi,\varphi_\delta)$
20	2×10^{-3}	0.5	1	0.3124	0.1870	0.2188
20	2×10^{-5}	0.1	1	0.1347	0.1118	0.1121
20	1×10^{-2}	0.9	1	0.1180	0.1919	0.2229
20	2×10^{-4}	0.1	2	0.1524	0.0594	0.0974
20	1×10^{-3}	1.1	2	0.1362	0.1985	0.1989
20	1×10^{-3}	1.5	2	0.1047	0.2133	0.2141
20	4.7×10^{0}	1.9	2	0.2123	0.3425	1.3020
10	4.9×10^{-3}	2.1	3	0.0523	0.2633	1.9458
10	5×10^{-3}	2.5	3	0.0527	0.1430	0.3773
10	2.8×10^{-1}	2.9	3	0.0495	0.2678	2.7599
10	2.1×10^{0}	3.5	4	0.0463	0.2386	1.8027
8	1×10^{-1}	4.1	5	0.0397	0.4832	48.7338
8	4.2×10^{-1}	4.5	5	0.0378	0.3875	24.7968
8	2.8×10^{0}	4.9	5	0.0269	0.4535	27.6306
8	1×10^{2}	5.9	6	0.0281	0.2041	23.2792
6	1×10^{1}	6.9	7	0.0207	0.2113	105.7357
6	7.2×10^{1}	7.1	8	0.0257	0.5941	280.7669
4	2.2×10^{1}	9.1	10	0.0416	0.2823	79.7393
4	3.3×10^{0}	10.1	11	0.0265	0.1181	1.4592×10^{3}
4	2.5×10^{2}	11.1	12	0.0306	0.1032	1.0285×10^{3}
4	2.2×10^{2}	12.5	13	0.0348	0.7974	1.0332×10^{4}

Figure 17a,b show the graphs of the exact potential φ and its approximations $\varphi_{\alpha(\delta)}$ (with regularization) and φ_δ (without regularization), corresponding to the function $\varphi(\theta) = |\theta| - \pi/2$, for $\theta \in [-\pi, \pi]$, for different values of β, m, and N, respectively.

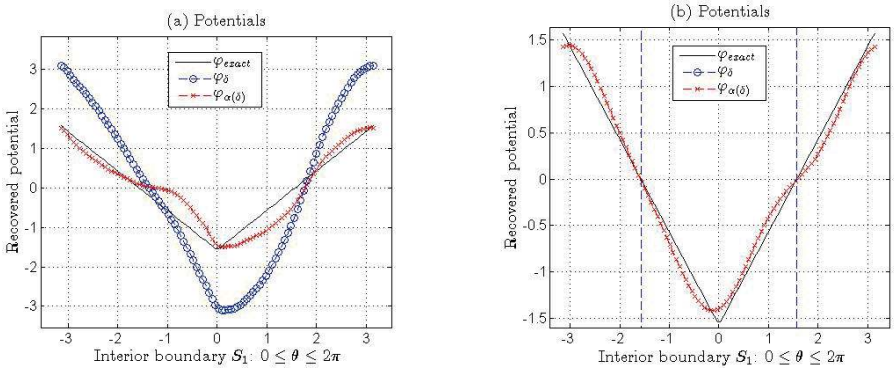

Figure 17. (**a**) Exact potential φ and its approximations $\varphi_{\alpha(\delta)}$ and φ_δ, corresponding to Example 3 for $\beta = 1.9$, $m = 2$, $N = 20$, and $\delta = 0.1$. (**b**) Exact potential φ and its approximations $\varphi_{\alpha(\delta)}$ and φ_δ, corresponding to Example 3 for $\beta = 11.1$, $m = 12$, $N = 4$, and $\delta = 0.1$ (see Table 16).

Example 4. *We consider the 'exact potential' in polar coordinates given by* $\varphi(\theta) = -1$ *if* $\theta \in [-\pi, 0)$ *and 1 if* $\theta \in [0, \pi]$. *Similar to the first example, the 'exact measurement' V and the 'measurement with error'* V_δ *are generated with the first N terms of the Fourier series (22) and (23), respectively, such that* $\| \varphi_N - \varphi \|_{L_2(S_1)} \le \epsilon_F$, *with* $0 \le \epsilon_F$. *For* $N = 30$, $\epsilon_F = 0.2913$. *In this case,* $V_0 = \varphi_0 = 0$, *and the Fourier coefficients* φ_k, $1 \le k \le N$, *are obtained numerically using the intrinsic function quadl of MATLAB.*

Table 17 shows the numerical results for data without error, applying TRM to solve the IP of the classical Cauchy problem (2), where $N = 20$, 25, and 30. In this table, we can observe similar results to the previous examples where the regularized solutions $\varphi_{\alpha(\delta)}$ are better.

Table 17. Numerical results applying TRM to solve the IP related to the classical Cauchy problem (2), for $\varphi(\theta) = -1$ if $\theta \in [-\pi, 0)$ and 1 if $\theta \in [0, \pi]$, and different values of δ and N.

δ	N	$\alpha(\delta)$	$RE(V,V_\delta)$	$RE(\varphi,\varphi_{\alpha(\delta)})$	$RE(\varphi,\varphi_\delta)$
0.1	20	0.1	0.0666	0.1608	0.7217
0.1	25	0.1	0.0638	0.1702	0.7641
0.1	30	0.1	0.0767	0.1827	2.6840
0.01	20	0.01	0.0080	0.0544	0.0659
0.01	25	0.01	0.0068	0.0761	0.0998
0.01	30	0.01	0.0078	0.0946	0.3552
0.001	20	0.0001	7.6172×10^{-4}	0.0044	0.0048
0.001	25	0.0001	7.2529×10^{-4}	0.0099	0.0118
0.001	30	0.0001	9.2391×10^{-4}	0.0195	0.0353

Table 18 shows the numerical results for data without error, applying TRM to solve the IP of the fractional Cauchy problem (12) for different values of β, m, and N.

Table 18. Numerical results applying TRM to solve IP related to the fractional Cauchy problem (12) for $\delta = 0.1$ and different values of β and m, where $\varphi(\theta) = -1$ if $\theta \in [-\pi, 0)$ and 1 if $\theta \in [0, \pi]$.

N	$\alpha(\delta)$	β	m	$RE(V,V_\delta)$	$RE(\varphi,\varphi_{\alpha(\delta)})$	$RE(\varphi,\varphi_\delta)$
20	4.5×10^{-2}	0.5	1	0.1062	0.2731	1.9413
10	3.9×10^{-4}	0.1	1	0.0645	0.0729	0.1759
10	3.2×10^{-3}	0.5	1	0.0640	0.1624	0.2390
10	4×10^{-3}	0.9	1	0.0609	0.0841	0.0934
10	2.1×10^{-2}	1.2	2	0.0910	0.1530	0.1636
10	1.5×10^{-3}	1.5	2	0.0549	0.2629	0.2699
6	2.1×10^{-2}	2.5	3	0.0352	0.3415	1.3513
6	1.5×10^{0}	3.5	4	0.0523	0.5428	1.1704
6	1×10^{3}	4.2	5	0.0472	0.9410	88.1158
6	3.6×10^{4}	5.2	6	0.0483	0.9354	41.0394
6	1.5×10^{7}	7.2	8	0.0400	0.9343	1.7546×10^{3}
6	4.2×10^{16}	12.8	13	0.0606	0.9825	2.1740×10^{7}

Figure 18a,b show the graphs of the exact potential φ and its approximations $\varphi_{\alpha(\delta)}$ (with regularization) and φ_δ (without regularization), corresponding to the function $\varphi(\theta) = -1$ if $\theta \in [-\pi, 0)$ and 1 if $\theta \in [0, \pi]$, for $\theta \in [-\pi, \pi]$, for different values of β, m, and N, respectively.

Examples 3 and 4 show numerical results analogous to the previous examples for both the classical and fractional cases. However, when we have piecewise constant functions, we truncate the series of approximate solutions $\varphi_{\alpha(\delta)}$ to find a better approximation of the solution to the fractional Cauchy problem.

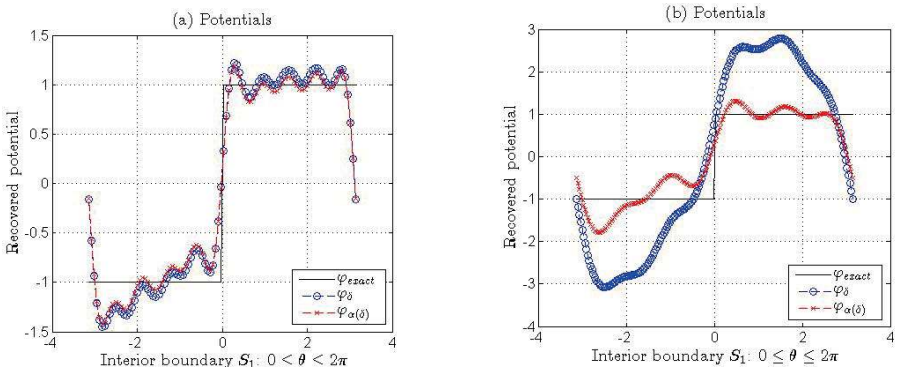

Figure 18. (**a**) Exact potential φ and its approximations $\varphi_{\alpha(\delta)}$ and φ_δ, corresponding to Example 4 for $\beta = 1.2$, $m = 2$, $N = 10$, and $\delta = 0.1$. (**b**) Exact potential φ and its approximations $\varphi_{\alpha(\delta)}$ and φ_δ, corresponding to Example 4 for $\beta = 2.5$, $m = 3$, $N = 6$, and $\delta = 0.1$ (see Table 18).

4.3. Solution to the IP Related to the Fractional Cauchy Problem Morozov Discrepancy Method and the Criterion of Tikhonov

In this subsection, the numerical results of the approximate solutions of the four examples presented above are calculated by the proposed method, choosing the regularization parameter by Morozov's discrepancy method and by the Tikhonov criterion. The relative errors of the approximations given in Tables 19–26 show that the best approximate solutions to the inverse problem are obtained by the *L-curve criterion*, as shown in Table 13, Table 14, Table 16, and Table 18, taking the same values of N, α, β, and m from these same examples for Tables 19–26, respectively.

Table 19. Numerical results choosing the regularization parameter $\alpha(\delta)$ with the discrepancy principle of Morozov to solve IP related to the fractional Cauchy problem (12) for $\delta = 0.1$ and different values of β and m, where $\varphi(x, y) = x^2 - y^2$, $(x, y) \in S_1$. According to the results of the table and additional experiments, the discrepancy method fails when $\beta > (m + 1)$ and $m > 1$, as well as for some values of $\beta < (m - 1)$.

N	$\alpha(\delta)$	β	m	$RE(V,V_\delta)$	$RE(\varphi,\varphi_{\alpha(\delta)})$	$RE(\varphi,\varphi_\delta)$
20	0.1613	1.001	1	0.0959	1.0470	0.0972
20	7.5089×10^6	1.5	1	0.0983	0.1328	0.1328
20	1.03×10^3	2.0001	2	0.0827	1.0000	0.0418
20	NaN	3.1	2	0.0870	NaN	0.0259
20	0.3137	3.01	3	0.0921	0.0526	0.1290
20	NaN	4.5	3	0.0994	NaN	0.4877
20	17.79	4.1	4	0.1069	0.5115	0.5102
20	NaN	7.1	4	0.0949	NaN	0.1675
20	6.53×10^7	5.0001	5	0.0901	1.0000	1.2477
20	NaN	6.1	5	0.0965	NaN	1.4885
20	4.7570	6.1	6	0.0860	1.9250	1.9237
20	NaN	7.5	6	0.0932	NaN	1.9387
20	0.2678	7.1	7	0.0922	6.1441	6.1514
20	NaN	8.6	7	0.0983	NaN	8.3501
20	0.0909	8.001	8	0.1113	0.0995	1.4459
20	NaN	9.4	8	0.0947	NaN	3.8687
20	0.1659	9.0001	9	0.0913	0.0497	9.9648
20	NaN	10.7	9	0.1018	NaN	21.7190
20	3.7653×10^{-5}	10.0001	10	0.0818	23.2250	36.9474
20	NaN	11.5	10	0.0980	NaN	34.1752
20	3.1198×10^{-5}	11.001	11	0.0828	50.0333	57.7211
20	NaN	12.6	11	0.0827	NaN	105.6237
20	1.0869×10^{-5}	12.0001	12	0.0892	80.4548	94.1772

Table 19. *Cont.*

N	$\alpha(\delta)$	β	m	$RE(V,V_\delta)$	$RE(\varphi,\varphi_{\alpha(\delta)})$	$RE(\varphi,\varphi_\delta)$
20	NaN	13.4	12	0.0852	NaN	13.4034
20	NaN	11.5	13	0.0984	NaN	517.1635
20	5.1280×10^{-6}	12.0001	13	0.1027	780.2431	783.2423
20	4.8277×10^{-5}	12.5	13	0.1031	292.2405	293.0910
20	1.03160×10^{-6}	12.9999	13	0.0971	148.1006	226.6417
20	3.4578×10^{3}	13.5	13	0.1041	597.4911	597.4911
20	NaN	14.5	13	0.0747	NaN	105.6650

Table 20. Numerical results choosing the regularization parameter $\alpha(\delta)$ with the Tikhonov criterion to solve IP related to the fractional Cauchy problem (12) for $\delta = 0.1$ and different values of β and m, where $\varphi(x,y) = x^2 - y^2$, $(x,y) \in S_1$. Similar results have been obtained for other values of α using this criterion.

N	$\alpha(\delta)$	β	m	$RE(V,V_\delta)$	$RE(\varphi,\varphi_{\alpha(\delta)})$	$RE(\varphi,\varphi_\delta)$
20	$\delta^{\frac{3}{2}}$	1.001	1	0.0994	0.9040	0.0769
20	$\delta^{\frac{3}{2}}$	1.5	1	0.0965	0.0938	0.0938
20	$1 + 1 = 2\delta^{\frac{99}{50}}$	2.0001	2	0.1046	0.9022	0.0702
20	δ	3.1	2	0.0984	0.1345	0.1345
20	δ	3.01	3	0.0812	0.0852	0.3750
20	$\delta^{\frac{1}{3}}$	4.5	3	0.0862	0.3665	0.3665
20	$\delta^{\frac{1}{100}}$	4.1	4	0.1050	0.3914	0.3914
20	δ	7.1	4	0.0971	0.8561	0.8561
20	$\delta^{\frac{99}{50}}$	5.0001	5	0.0893	0.5591	1.5529
20	$\delta^{\frac{99}{50}}$	6.1	5	0.0934	1.2559	1.2559
20	$\delta^{\frac{1}{3}}$	6.1	6	0.0929	1.5055	1.5056
20	$\delta^{\frac{1}{2}}$	7.5	6	0.0994	2.0076	2.0076
20	$\delta^{\frac{99}{50}}$	7.1	7	0.0949	2.5857	2.5858
20	$\delta^{\frac{99}{50}}$	8.6	7	0.0913	2.4924	2.4924
20	$\delta^{\frac{1}{100}}$	8.001	8	0.0957	0.0431	5.6199
20	$\delta^{\frac{1}{100}}$	9.4	8	0.0971	13.6930	13.6930
20	$\delta^{\frac{1}{10000}}$	9.0001	9	0.0893	0.3169	24.8451
20	$\delta^{\frac{1}{10000}}$	10.7	9	0.1057	8.4227	8.4227
20	δ	10.0001	10	0.1031	0.0334	25.1034
20	δ	11.5	10	0.0990	28.5194	28.5194
20	$\delta^{\frac{99}{10000}}$	11.001	11	0.0834	0.0225	36.1203
20	$\delta^{\frac{99}{10000}}$	12.6	11	0.0988	66.3421	66.3421
20	$\delta^{\frac{1}{100}}$	12.0001	12	0.1022	0.0279	95.8910
20	$\delta^{\frac{1}{100}}$	13.4	12	0.0926	31.8654	31.8654
20	$\delta^{\frac{1}{10000}}$	11.5	13	0.1099	0.0552	457.5273
20	$\delta^{\frac{1}{10000}}$	12.0001	13	0.1133	0.5851	438.2230
20	$\delta^{\frac{1}{10000}}$	12.5	13	0.1097	4.5644	279.6731
20	$\delta^{\frac{1}{10000}}$	12.9999	13	0.0982	0.0249	358.7193
20	$\delta^{\frac{1}{10000}}$	13.5	13	0.0925	183.5626	183.5626
20	$\delta^{\frac{1}{10000}}$	14.5	13	0.1027	789.7150	789.7150

Table 21. Numerical results applying Morozov discrepancy principle to solve IP related to the fractional Cauchy problem (12) for $\delta = 0.1$ and different values of β and m, where $\varphi(x,y) = e^x \sin(y)$, $(x,y) \in S_1$. According to the results, the discrepancy principle has problems when $\beta > m+1$ and $m > 1$, and for $\beta = 1.001$ and $m = 1$.

N	$\alpha(\delta)$	β	m	$RE(V,V_\delta)$	$RE(\varphi,\varphi_{\alpha(\delta)})$	$RE(\varphi,\varphi_\delta)$
30	NaN	1.001	1	0.1245	NaN	0.0962
30	2.0984×10^{6}	1.5	1	0.1910	0.1082	0.1082
30	1.03×10^{3}	2.0001	2	0.0954	1.0000	0.0244
30	NaN	3.1	2	0.1075	NaN	0.0402
30	0.2289	3.01	3	0.1118	0.0657	0.4844
30	NaN	4.5	3	0.1218	NaN	1.4902
30	49.9604	4.1	4	0.1040	0.1739	0.1726
30	NaN	7.1	4	0.1200	NaN	0.3234
30	6.46×10^{7}	5.0001	5	0.1222	1.0000	1.5949
30	NaN	6.1	5	0.1098	NaN	1.8066
30	0.0725	6.0001	6	0.1133	0.1997	1.9133
30	NaN	7.5	6	0.1058	NaN	1.5889
30	0.1979	7.1	7	0.1126	8.3170	8.3243
30	NaN	8.2	7	0.1207	NaN	4.1606
30	0.0471	8.00001	8	0.1245	0.5043	5.9603
30	NaN	9.8	8	0.1132	NaN	6.3306
30	0.1675	9.0001	9	0.1027	0.0679	15.9717
30	NaN	10.7	9	0.0961	NaN	9.3670
30	0.8716	10.0001	10	0.0954	0.0099	5.1670
30	NaN	11.5	10	0.1075	NaN	8.4426
30	2.7508×10^{-8}	11.0001	11	0.2068	5.0164×10^{4}	5.0171×10^{4}
30	NaN	12.4	11	0.1218	NaN	125.4177
30	6.7362×10^{-9}	12.0001	12	0.2635	1.1476×10^{5}	1.1477×10^{5}
30	NaN	13.4	12	0.1200	NaN	82.7087
30	1.6116×10^{-10}	11.5	13	0.2236	5.6345×10^{6}	5.6345×10^{6}
30	9.6113×10^{-8}	12.0001	13	0.2251	3.6801×10^{5}	3.6801×10^{5}
30	3.7943×10^{-9}	12.5	13	0.2458	3.2872×10^{6}	3.2872×10^{6}
30	1.2925×10^{-11}	12.9999	13	0.2276	1.0450×10^{7}	1.0450×10^{7}
30	NaN	13.5	13	0.2413	NaN	8.8855×10^{6}
30	NaN	14.5	13	0.2454	NaN	9.6411×10^{6}

Table 22. Numerical results choosing the regularization parameter $\alpha(\delta)$ with the Tikhonov criterion to solve IP related to the fractional Cauchy problem (12) for $\delta = 0.1$ and different values of β and m, where $\varphi(x,y) = e^x \sin(y)$, $(x,y) \in S_1$. In almost all cases, the L-curve method gives better results.

N	$\alpha(\delta)$	β	m	$RE(V,V_\delta)$	$RE(\varphi,\varphi_{\alpha(\delta)})$	$RE(\varphi,\varphi_\delta)$
30	δ	1.001	1	0.1760	0.9884	0.1546
30	$\delta^{\frac{1}{10000}}$	1.5	1	0.1562	0.1227	0.1227
30	$\delta^{\frac{99}{50}}$	2.0001	2	0.1783	0.9696	0.1104
30	$\delta^{\frac{99}{50}}$	3.1	2	0.1806	0.0813	0.0813
30	$\delta^{\frac{99}{50}}$	3.01	3	0.1774	0.4170	0.5684
30	$\delta^{\frac{1}{10000}}$	4.5	3	0.1939	0.3294	0.3294
30	$\delta^{\frac{1}{10000}}$	4.1	4	0.2089	0.6294	0.6294
30	$\delta^{\frac{1}{10000}}$	7.1	4	0.2157	0.9195	0.9195
30	$\delta^{\frac{99}{50}}$	5.0001	5	0.2132	0.9217	6.2925
30	$\delta^{\frac{1}{10000}}$	6.1	5	0.1985	10.2345	10.2345
30	$\delta^{\frac{99}{50}}$	6.0001	6	0.2047	0.8225	11.8088
30	$\delta^{\frac{1}{10000}}$	7.5	6	0.1893	8.5339	8.5339
30	$\delta^{\frac{1}{10000}}$	7.1	7	0.2272	66.4146	66.7074

Table 22. *Cont.*

N	$\alpha(\delta)$	β	m	$RE(V,V_\delta)$	$RE(\varphi,\varphi_{\alpha(\delta)})$	$RE(\varphi,\varphi_\delta)$
30	$\delta^{\frac{1}{10000}}$	8.2	7	0.2041	65.2733	65.2733
30	$\delta^{\frac{5}{3}}$	8.00001	8	0.1768	1.1965	97.2722
30	δ	9.8	8	0.1955	90.8875	90.8875
30	$\delta^{\frac{5}{3}}$	9.0001	9	0.2093	2.2232	2.6794×10^3
30	$\delta^{\frac{1}{10000}}$	10.7	9	0.2038	3.7798×10^3	3.7798×10^3
30	$\delta^{\frac{1}{10000}}$	10.0001	10	0.2252	4.4215	7.1864×10^3
30	$\delta^{\frac{1}{100}}$	11.5	10	0.2077	4.0842×10^3	4.0842×10^3
30	$\delta^{\frac{1}{100}}$	11.0001	11	0.2059	80.7421	2.1991×10^5
30	$\delta^{\frac{1}{10000}}$	12.4	11	0.2496	3.1294×10^5	3.1294×10^5
30	$\delta^{\frac{1}{2}}$	12.0001	12	0.2130	93.2559	4.0135×10^5
30	$\delta^{\frac{1}{3}}$	13.4	12	0.2228	3.0318×10^5	3.0318×10^5
30	$\delta^{\frac{1}{100}}$	11.5	13	0.2128	785.0281	5.2143×10^6
30	$\delta^{\frac{1}{3}}$	12.0001	13	0.2471	6.1257×10^3	2.1351×10^6
30	$\delta^{\frac{1}{8}}$	12.5	13	0.2025	2.3802×10^5	1.0999×10^7
30	$\delta^{\frac{1}{50}}$	12.9999	13	0.2472	583.7069	2.0067×10^7
30	$\delta^{\frac{1}{100}}$	13.5	13	0.2477	1.8405×10^7	1.8405×10^7
30	$\delta^{\frac{1}{10000}}$	14.5	13	0.2120	1.3707×10^7	1.3707×10^7

Table 23. Numerical results choosing the regularization parameter $\alpha(\delta)$ with the discrepancy principle of Morozov to solve IP related to the fractional Cauchy problem (12) for $\delta = 0.1$ and different values of β and m, where $\varphi(\theta) = |\theta| - \pi/2$, $\theta \in [-\pi, \pi]$. In almost all cases, the L-curve method gives better results.

N	$\alpha(\delta)$	β	m	$RE(V,V_\delta)$	$RE(\varphi,\varphi_{\alpha(\delta)})$	$RE(\varphi,\varphi_\delta)$
20	0.0320	0.5	1	0.2693	0.7013	0.3930
20	6.8073	0.1	1	0.2790	0.9988	0.2787
20	0.0595	0.9	1	0.2171	0.5500	0.2910
20	2.3795	0.1	2	0.2306	0.9972	0.3700
20	0.0297	1.1	2	0.2421	0.4419	0.6114
20	0.0993	1.5	2	0.1942	0.7216	0.7481
20	0.1561	1.9	2	0.2055	1.0241	1.0477
10	0.0079	2.1	3	0.0840	0.8154	1.8753
10	0.0096	2.5	3	0.0958	2.0322	2.6709
10	0.0122	2.9	3	0.0965	2.6035	2.8554
10	0.0231	3.5	4	0.0992	4.7034	4.7820
8	6.6817×10^{-5}	4.1	5	0.0688	59.6092	61.4116
8	1.9688×10^{-4}	4.5	5	0.0577	55.5120	56.1750
8	5.4635×10^{-4}	4.9	5	0.0623	48.1493	48.4213
8	0.0013	5.9	6	0.0620	127.5673	127.6119
6	1.3725×10^{-4}	6.9	7	0.0225	196.1122	196.3843
6	1.2394×10^{-4}	7.1	8	0.0316	342.3864	342.5589
4	4.6244×10^{-4}	9.1	10	0.0577	92.5918	92.7644
4	2.3783×10^{-6}	10.1	11	0.0451	1.7044×10^3	1.7062×10^3
4	2.4299×10^{-5}	11.1	12	0.0491	1.7439×10^3	1.7441×10^3
4	1.0631×10^{-6}	12.5	13	0.0401	1.0360×10^4	1.0361×10^4

Table 24. Numerical results choosing the regularization parameter $\alpha(\delta)$ with the Tikhonov criterion to solve IP related to the fractional Cauchy problem (12) for $\delta = 0.1$ and different values of β and m, where $\varphi(\theta) = |\theta| - \pi/2, \theta \in [-\pi, \pi]$. In almost all cases, the L-curve method gives better results.

N	$\alpha(\delta)$	β	m	$RE(V,V_\delta)$	$RE(\varphi,\varphi_{\alpha(\delta)})$	$RE(\varphi,\varphi_\delta)$
20	$\delta^{\frac{1}{3}}$	0.5	1	0.3117	0.9521	0.5185
20	$\delta^{\frac{1}{3}}$	0.1	1	0.2942	0.9921	0.4911
20	$\delta^{\frac{1}{3}}$	0.9	1	0.2614	0.7377	0.5011
20	$\delta^{\frac{3}{2}}$	0.1	2	0.2944	0.9571	0.4833
20	$\delta^{\frac{3}{2}}$	1.1	2	0.2224	0.5438	0.5251
20	$\delta^{\frac{5}{4}}$	1.5	2	0.2703	0.7070	0.6965
20	δ	1.9	2	0.2060	0.9825	1.3020
10	$\delta^{\frac{99}{50}}$	2.1	3	0.0105	0.1151	1.0675
10	$\delta^{\frac{99}{50}}$	2.5	3	0.0790	1.7172	2.2671
10	$\delta^{\frac{99}{50}}$	2.9	3	0.0935	2.4815	2.6475
10	$\delta^{\frac{1}{3}}$	3.5	4	0.0992	3.7011	5.0290
8	$\delta^{\frac{3}{2}}$	4.1	5	0.0725	2.3038	32.4249
8	$\delta^{\frac{3}{2}}$	4.5	5	0.0822	26.8355	76.0308
8	$\delta^{\frac{1}{5}}$	4.9	5	0.0696	7.6778	60.6948
8	$\delta^{\frac{99}{10000}}$	5.9	6	0.0538	34.4968	43.7691
6	$\delta^{\frac{99}{10000}}$	6.9	7	0.0418	25.5161	284.8013
6	$\delta^{\frac{99}{50}}$	7.1	8	0.0514	414.7308	432.4166
4	$\delta^{\frac{99}{50}}$	9.1	10	0.0432	39.8856	41.6149
4	$\delta^{\frac{1}{100}}$	10.1	11	0.0440	2.1960	1.1303×10^3
4	$\delta^{\frac{1}{100}}$	11.1	12	0.0485	306.1543	1.5216×10^3
4	$\delta^{\frac{1}{10000}}$	12.5	13	0.0387	75.5346	4.6817×10^4

Table 25. Numerical results choosing the regularization parameter $\alpha(\delta)$ with the discrepancy principle of Morozov to solve IP related to the fractional Cauchy problem (12) for $\delta = 0.1$ and different values of β and m, where $\varphi(\theta) = -1$ if $\theta \in [-\pi, 0)$ and 1 if $\theta \in [0, \pi]$. In almost all cases, the L-curve method gives better results. In this Table, $m - 1 < \beta < m$.

N	$\alpha(\delta)$	β	m	$RE(V,V_\delta)$	$RE(\varphi,\varphi_{\alpha(\delta)})$	$RE(\varphi,\varphi_\delta)$
20	0.0084	0.5	1	0.1321	1.1988	1.4773
10	0.1198	0.1	1	0.0763	0.9065	0.3944
10	0.0480	0.5	1	0.0641	0.7212	0.2595
10	0.0292	0.9	1	0.0780	0.1942	0.2717
10	0.0556	1.2	2	0.0905	0.4162	0.4471
10	0.1325	1.5	2	0.0808	0.3404	0.2828
6	0.0026	2.5	3	0.0542	3.2590	3.8754
6	0.0184	3.5	4	0.0555	3.8072	3.8819
6	1.8758×10^{-4}	4.2	5	0.0402	25.9293	27.2371
6	0.0016	5.2	6	0.0417	30.6892	30.8212
6	2.1013×10^{-5}	7.2	8	0.0454	2.3159×10^3	2.3161×10^3
6	1.1443×10^{-9}	12.8	13	0.0415	1.8147×10^7	1.8147×10^7

Table 26. Numerical results choosing the regularization parameter $\alpha(\delta)$ with the Tikhonov criterion to solve IP related to the fractional Cauchy problem (12) for $\delta = 0.1$ and different values of β and m, where $\varphi(\theta) = -1$ if $\theta \in [-\pi, 0)$ and 1 if $\theta \in [0, \pi]$. In almost all cases, the L-curve method gives better results.

N	$\alpha(\delta)$	β	m	$RE(V,V_\delta)$	$RE(\varphi,\varphi_{\alpha(\delta)})$	$RE(\varphi,\varphi_\delta)$
20	$\delta^{\frac{5}{4}}$	0.5	1	0.1447	1.3444	2.7243
10	$\delta^{\frac{3}{2}}$	0.1	1	0.0882	0.8467	0.3194
10	$\delta^{\frac{3}{2}}$	0.5	1	0.0584	0.7281	0.5733
10	$\delta^{\frac{99}{50}}$	0.9	1	0.0602	0.8434	0.3127
10	$\delta^{\frac{99}{50}}$	1.2	2	0.0711	0.5848	0.5872
10	$\delta^{\frac{99}{50}}$	1.5	2	0.0624	0.5957	0.6053
6	$\delta^{\frac{3}{2}}$	2.5	3	0.0334	1.1740	1.6434
6	$\delta^{\frac{1}{10000}}$	3.5	4	0.0602	1.1241	1.2573
6	$\delta^{\frac{1}{50}}$	4.2	5	0.0437	1.0155	88.8735
6	$\delta^{\frac{1}{100}}$	5.2	6	0.0551	23.6302	86.1879
6	$\delta^{\frac{1}{10000}}$	7.2	8	0.0359	387.4002	1.4405×10^3
6	$\delta^{\frac{1}{10000}}$	12.8	13	0.0425	2.0636×10^6	3.2829×10^7

5. Discussion

The numerical tests show that the proposed algorithm usually gives good results. Even if the numerical results are unsatisfactory, they are enough to start an iterative method. In all cases, the regularized method is worth more than the method without regularization. After some numerical tests, we found that the series expansion of the solution to the fractional Cauchy problem can be truncated in $N = 20$, $N = 25$, or $N = 30$.

When $\beta < m$ for $m = 1, 2 \ldots, 7$, the results obtained are similar, i.e., the results obtained with and without regularization almost coincide. One possible explanation can be associated with the smoothing properties of the integral operator to have similar results when $\beta > m$, for $m = 1, 2$. In the other cases, the regularized case is better.

When $m > 7$, the regularized method loses precision. However, the approximate solution obtained can be used as an initial point of a stable iterative method. From the numerical results, we want to emphasize that the solution by the Tikhonov regularization method of the classical Cauchy problem works adequately in all cases.

The Tikhonov regularization parameter was very large in some cases. We do not have an explanation for this situation, but we consider this an interesting topic that must be studied in future works. According to numerical results, in almost all cases, the best approximate solutions to the inverse problem are obtained by the L-curve criterion. According to the results, the discrepancy principle has problems when $\beta > m + 1$ and $m > 1$.

In the classical Cauchy problem, the adjoint operator is associated with a boundary value problem called the adjoint problem. In the fractional Cauchy problem, we calculate the adjoint operator using its definition. One interesting question is whether a boundary value problem is associated with the adjoint operator. If the answer is positive, the following question arises: Can the adjoint operator be used in irregular regions? This is an interesting question whose answer can help us apply numerical methods to find the minimum of the functional since we have to solve boundary value problems. One of the most used methods to find such a minimum is the conjugate gradient method in combination with the finite element method.

6. Conclusions

This work proposes an algorithm to solve the fractional Cauchy problem obtained from the Tikhonov regularization and the circular harmonics. The regularization was obtained using the L-curve method, Morozov's discrepancy principle, and numerical tests by the Tikhonov criterion. The numerical results show that the algorithm is feasible for various parameters. The discrepancy principle presents some problems in finding the regularization parameter for some values of the parameters appearing in the fractional Cauchy problem.

In almost all cases, the L-curve method gives better results than the Tikhonov Criterion and Morozov's discrepancy principle. In all cases, the regularization using the L-curve method gives better results than without regularization. In some cases, despite not being a good approximation, the regularized solution is much better than the solution without regularization. Since the algorithm does not give good results in some cases, it must be improved using an iterative method, which takes the regularized solution as an initial point. This point might be future work.

Author Contributions: Conceptualization, J.J.C.M., J.A.A.V., E.H.M., M.M.M.C., and J.J.O.O.; methodology, J.J.C.M., J.A.A.V., E.H.M., M.M.M.C., and J.J.O.O.; software, J.J.C.M., J.A.A.V. and E.H.M.; validation, J.J.C.M., J.A.A.V., and J.J.O.O.; formal analysis, J.J.C.M., J.A.A.V., E.H.M., M.M.M.C., C.A.H.G., and J.J.O.O.; investigation, J.J.C.M., J.A.A.V., E.H.M., M.M.M.C., C.A.H.G., and J.J.O.O.; resources, J.J.C.M., J.A.A.V., E.H.M., M.M.M.C., C.A.H.G., and J.J.O.O.; data curation, J.J.C.M., J.A.A.V., and J.J.O.O.; writing—original draft preparation, J.J.C.M., J.A.A.V., E.H.M., M.M.M.C., C.A.H.G., and J.J.O.O.; writing—review and editing, J.J.C.M., J.A.A.V., E.H.M., M.M.M.C., and J.J.O.O.; visualization, J.J.C.M., J.A.A.V., E.H.M., M.M.M.C., C.A.H.G., and J.J.O.O.; supervision, J.J.C.M. and J.J.O.O.; project administration, J.J.C.M. and J.J.O.O.; funding acquisition, J.J.C.M., J.A.A.V., E.H.M., M.M.M.C., and J.J.O.O. All authors have read and agreed to the published version of the manuscript.

Funding: This research was funded by VIEP-BUAP withthe support provided, to research project number 151. The National Council for Humanities, Sciences, and Technologies in Mexico (CONAHCYT) also provided partial funding through a PhD scholarship for the second author, with CVU number 1030555.

Data Availability Statement: Data are contained within the article.

Conflicts of Interest: The authors declare that they have no competing interests.

Appendix A. Computation of the Derivatives of J_α

If $J_\alpha(\varphi) = \frac{1}{2} \parallel K_m^\beta \varphi - V_\delta \parallel^2_{L_2(S_2)} + \frac{\alpha}{2} \parallel \varphi \parallel^2_{L_2(S_1)}$, then

$$
\begin{aligned}
J_\alpha(\varphi+h)-J_\alpha(\varphi) &= \frac{1}{2}\|K_m^\beta(\varphi+h)-V_\delta\|^2_{L_2(S_2)}+\frac{\alpha}{2}\|\varphi+h\|^2_{L_2(S_1)}-\left(\frac{1}{2}\|K_m^\beta\varphi-V_\delta\|^2_{L_2(S_2)}+\frac{\alpha}{2}\|\varphi\|^2_{L_2(S_1)}\right)\\
&= \frac{1}{2}\|K_m^\beta(\varphi+h)-V_\delta\|^2_{L_2(S_2)}-\frac{1}{2}\|K_m^\beta\varphi-V_\delta\|^2_{L_2(S_2)}+\frac{\alpha}{2}\|\varphi+h\|^2_{L_2(S_1)}-\frac{\alpha}{2}\|\varphi\|^2_{L_2(S_1)}\\
&= \frac{1}{2}\langle K_m^\beta\varphi-V_\delta+K_m^\beta h, K_m^\beta\varphi-V_\delta+K_m^\beta h\rangle_{L_2(S_2)}-\frac{1}{2}\langle K_m^\beta\varphi-V_\delta, K_m^\beta\varphi-V_\delta\rangle_{L_2(S_2)}\\
&+\frac{\alpha}{2}\langle\varphi+h,\varphi+h\rangle_{L_2(S_1)}-\frac{\alpha}{2}\langle\varphi,\varphi\rangle_{L_2(S_1)}\\
&= \frac{1}{2}\Big[\cancel{\langle K_m^\beta\varphi-V_\delta, K_m^\beta\varphi-V_\delta\rangle_{L_2(S_2)}}+\langle K_m^\beta h, K_m^\beta h\rangle_{L_2(S_2)}+\langle K_m^\beta\varphi-V_\delta, K_m^\beta h\rangle_{L_2(S_2)}\Big]\\
&-\cancel{\frac{1}{2}\langle K_m^\beta\varphi-V_\delta, K_m^\beta\varphi-V_\delta\rangle_{L_2(S_2)}}+\frac{1}{2}\langle K_m^\beta h, K_m^\beta\varphi-V_\delta\rangle_{L_2(S_2)}\\
&+\frac{\alpha}{2}\Big[\cancel{\langle\varphi,\varphi\rangle}+\langle\varphi,h\rangle_{L_2(S_1)}+\langle h,\varphi\rangle_{L_2(S_1)}+\langle h,h\rangle_{L_2(S_1)}\Big]-\cancel{\frac{\alpha}{2}\langle\varphi,\varphi\rangle_{L_2(S_1)}}\\
&= \frac{1}{2}\|K_m^\beta h\|^2_{L_2(S_2)}+\langle(K_m^\beta)^*(K_m^\beta\varphi-V_\delta),h\rangle_{L_2(S_1)}+\langle\alpha\varphi,h\rangle_{L_2(S_1)}+\frac{\alpha}{2}\|h\|^2_{L_2(S_1)}\\
&= \frac{1}{2}\|K_m^\beta h\|^2_{L_2(S_2)}+\langle((K_m^\beta)^*K_m^\beta+\alpha I)\varphi-(K_m^\beta)^*V_\delta,h\rangle_{L_2(S_1)}+\frac{\alpha}{2}\|h\|^2_{L_2(S_1)}
\end{aligned}
$$

Thus, $DJ_\alpha(\varphi) = \left(\left(K_m^\beta\right)^*K_m^\beta+\alpha I\right)\varphi-\left(K_m^\beta\right)^*V_\delta$. For the second derivative, we have

$$
\begin{aligned}
DJ_\alpha(\varphi+h)-DJ_\alpha(\varphi) &= ((K_m^\beta)^*K_m^\beta+\alpha I)(\varphi+h)-(K_m^\beta)^*V_\delta-[((K_m^\beta)^*K_m^\beta+\alpha I)\varphi-(K_m^\beta)^*V_\delta]\\
&= \cancel{((K_m^\beta)^*K_m^\beta+\alpha I)\varphi}+((K_m^\beta)^*K_m^\beta+\alpha I)h-\cancel{(K_m^\beta)^*V_\delta}-[\cancel{((K_m^\beta)^*K_m^\beta+\alpha I)\varphi}-\cancel{(K_m^\beta)^*V_\delta}]\\
&= ((K_m^\beta)^*K_m^\beta+\alpha I)h.
\end{aligned}
$$

Hence, $D^2J_\alpha(\varphi) = \left(K_m^\beta\right)^*K_m^\beta+\alpha I$.

Appendix B. Proof That the Functional $J_\alpha(f) = \frac{1}{2}\| K_m^\beta(f)-V_\delta \|^2_{L_2(S_2)_{L_2(S_2)}}+\frac{\alpha}{2}\| f \|^2_{L_2(S_1)}$ Is Convex

Theorem A1. *The functional*

$$J_1(f) = \frac{\alpha}{2}\| f \|^2_{L_2(S_1)}$$

is convex.

Proof. We want to show that

$$J_1(\lambda f+(1-\lambda)g)\le\lambda J_1(f)+(1-\lambda)J_1(g),$$

for all $f,g\in L_2(S_1)$, with $f\neq g$, and for all $\lambda\in(0,1)$.

Starting with the left-hand side,

$$
\begin{aligned}
J_1(\lambda f+(1-\lambda)g) &= \frac{\alpha}{2}\| \lambda f+(1-\lambda)g \|^2_{L_2(S_1)}\\
&= \frac{\alpha}{2}\langle\lambda f+(1-\lambda)g,\lambda f+(1-\lambda)g\rangle_{L_2(S_1)}\\
&= \frac{\alpha}{2}\langle\lambda f,\lambda f\rangle_{L_2(S_1)}+\alpha\langle\lambda f,(1-\lambda)g\rangle_{L_2(S_1)}\\
&\quad+\frac{\alpha}{2}\langle(1-\lambda)g,(1-\lambda)g\rangle_{L_2(S_1)}\\
&= \frac{\alpha}{2}\lambda^2\| f \|^2+\alpha\lambda(1-\lambda)\langle f,g\rangle_{L_2(S_1)}\\
&\quad+\frac{\alpha}{2}(1-\lambda)^2\| g \|^2_{L_2(S_1)}
\end{aligned}
$$

By the Cauchy–Schwarz inequality:

$$|\langle f, g\rangle_{L_2(S_1)}| \leq \| f \|_{L_2(S_1)} \| g \|_{L_2(S_1)}, \quad \forall f \neq g$$

we obtain

$$\begin{aligned} J_1(\lambda f + (1-\lambda)g) \leq \lambda^2 \frac{\alpha}{2} \| f \|^2_{L_2(S_1)} + (1-\lambda)^2 \frac{\alpha}{2} \| g \|^2_{L_2(S_1)} \\ + \alpha\lambda(1-\lambda) \| f \|_{L_2(S_1)} \| g \|_{L_2(S_1)} \end{aligned}$$

Applying the inequality: $a \cdot b \leq \frac{a^2+b^2}{2}$, if $a, b \in \mathbb{R}$. Considering that $a = ||f||_{L_2(S_1)}$ and $b = ||g||_{L_2(S_1)}$, then,

$$\alpha\lambda(1-\lambda)||f||_{L_2(S_1)}||g||_{L_2(S_1)} \leq \alpha\lambda(1-\lambda)\frac{1}{2}\left[||f||^2_{L_2(S_1)} + ||g||^2_{L_2(S_1)}\right]$$

Then

$$\begin{aligned} J_1(\lambda f + (1-\lambda)g) &\leq \lambda^2 \frac{\alpha}{2}||f||^2_{L_2(S_1)} + (1-\lambda)^2 \frac{\alpha}{2}||g||^2_{L_2(S_1)} + \lambda(1-\lambda)\frac{\alpha}{2}\left[||f||^2_{L_2(S_1)} + ||g||^2_{L_2(S_1)}\right] \\ &= \lambda^2 \frac{\alpha}{2}||f||^2_{L_2(S_1)} + \left(1 - 2\lambda + \lambda^2\right)\frac{\alpha}{2}||g||^2_{L_2(S_1)} + \left(\lambda - \lambda^2\right)\frac{\alpha}{2}\left[||f||^2_{L_2(S_1)} + ||g||^2_{L_2(S_1)}\right] \\ &= \lambda^2 \frac{\alpha}{2}||f||^2_{L_2(S_1)} + \frac{\alpha}{2}||g||^2_{L_2(S_1)} - \lambda\alpha||g||^2_{L_2(S_1)} + \lambda^2\frac{\alpha}{2}||g||^2_{L_2(S_1)} + \lambda\frac{\alpha}{2}||f||^2 \\ &\quad + \lambda\frac{\alpha}{2}||g||^2_{L_2(S_1)} - \lambda^2\frac{\alpha}{2}||f||^2_{L_2(S_1)} - \lambda^2\frac{\alpha}{2}||g||^2_{L_2(S_1)} \\ &= \lambda\frac{\alpha}{2}||f||^2_{L_2(S_1)} + \frac{\alpha}{2}||g||^2_{L_2(S_1)} - \lambda\frac{\alpha}{2}||g||^2_{L_2(S_1)} \\ &= \lambda\frac{\alpha}{2}||f||^2_{L_2(S_1)} + (1-\lambda)\frac{\alpha}{2}||g||^2_{L_2(S_1)} \\ &= \lambda J_1(f) + (1-\lambda)J_1(f). \end{aligned}$$

Therefore, $J_1(f) = \frac{\alpha}{2}(||f||^2_{L_2(S_1)}$ is convex. □

Theorem A2. *The functional*

$$J_2(f) = \frac{1}{2}\| K^\beta_m(f) - V_\delta \|^2_{L_2(S_2)}$$

is convex.

Proof. Assuming the operator K^β_m is linear, we have

$$\begin{aligned} J_2(\lambda f + (1-\lambda)g) &= \frac{1}{2}\| K^\beta_m(\lambda f + (1-\lambda)g) - V_\delta \|^2_{L_2(S_2)} \\ &= \frac{1}{2}\| \lambda\left(K^\beta_m(f) - V_\delta\right) + (1-\lambda)\left(K^\beta_m(g) - V_\delta\right) \|^2_{L_2(S_2)} \\ &= \frac{\lambda^2}{2} \| K^\beta_m(f) - V_\delta \|^2_{L_2(S_2)} + \frac{(1-\lambda)^2}{2}\| K^\beta_m(g) - V_\delta \|^2_{L_2(S_2)} \\ &\quad + \lambda(1-\lambda)\left\langle K^\beta_m(f) - V_\delta, K^\beta_m(g) - V_\delta \right\rangle_{L_2(S_2)}, \end{aligned}$$

where $\lambda \in (0, 1)$.

By the Cauchy–Schwarz inequality:

$$\left\langle K^\beta_m(f) - V_\delta, K^\beta_m(g) - V_\delta \right\rangle_{L_2(S_2)} \leq \|K^\beta_m(f) - V_\delta \|_{L_2(S_2)} \| K^\beta_m(g) - V_\delta \|_{L_2(S_2)}$$

and using the inequality $ab \leq \frac{1}{2}(a^2+b^2)$ if $a, b \in \mathbb{R}$. Considering that $a = \|K_m^\beta(f) - V_\delta\|_{L_2(S_2)}$ and $b = \|K_m^\beta(g) - V_\delta\|_{L_2(S_2)}$, we obtain

$$\lambda(1-\lambda)\left\langle K_m^\beta(f) - V_\delta, K_m^\beta(g) - V_\delta \right\rangle_{L_2(S_2)} \leq \frac{\lambda(1-\lambda)}{2}\left(\| K_m^\beta(f) - V_\delta \|^2_{L_2(S_2)} + \| K_m^\beta(g) - V_\delta \|^2_{L_2(S_2)} \right)$$

Combining these results,

$$\begin{aligned} J_2(\lambda f + (1-\lambda)g) \leq & \frac{\lambda^2}{2} \| K_m^\beta(f) - V_\delta \|^2_{L_2(S_2)} + \frac{(1-\lambda)^2}{2} \| K_m^\beta(g) - V_\delta \|^2_{L_2(S_2)} \\ & + \frac{\lambda(1-\lambda)}{2}\left(\| K_m^\beta(f) - V_\delta \|^2_{L_2(S_2)} + \| K_m^\beta(g) - V_\delta \|^2_{L_2(S_2)} \right) \\ = & \frac{\lambda}{2} \| K_m^\beta(f) - V_\delta \|^2_{L_2(S_2)} + \frac{1-\lambda}{2} \| K_m^\beta(g) - V_\delta \|^2_{L_2(S_2)} \\ = & \lambda J_2(f) + (1-\lambda) J_2(g). \end{aligned}$$

Therefore, $J_2(f) = \frac{1}{2}\| K_m^\beta(f) - V_\delta \|^2_{L_2(S_2)}$ is convex. □

Thus, from the last two theorems, we have that the functional $J_\alpha(f) = \frac{1}{2} \| K_m^\beta(f) - V_\delta \|^2_{L_2(S_2)} + \frac{\alpha}{2}\| f \|^2_{L_2(S_1)}$ is convex.

References

1. Conde Mones, J.J.; Juárez Valencia, L.H.; Oliveros Oliveros, J.J.; León Velasco, D.A. Stable numerical solution of the Cauchy problem for the Laplace equation in irregular annular regions. *Numer. Methods Partial Differ. Equ.* **2017**, *33*, 1799–1822. [CrossRef]
2. Oliveros, J.; Morín, M.; Conde, J.; Fraguela, A. A regularization strategy for the inverse problem of identification of bioelectrical sources for the case of concentric spheres. *Far East J. Appl. Math.* **2013**, *77*, 1–20.
3. Lee, J.Y.; Yoon, J.R. A numerical method for Cauchy problem using singular value decomposition. *Commun. Korean Math. Soc.* **2001**, *16*, 487–508.
4. Wei, T.; Chen, Y.G. A regularization method for a Cauchy problem of Laplace's equation in an annular domain. *Math. Comput. Simul.* **2012**, *82*, 2129–2144. [CrossRef]
5. Zhou, D.; Wei, T. The method of fundamental solutions for solving a Cauchy problem of Laplace's equation in a multi-connected domain. *Inverse Probl. Sci. Eng.* **2008**, *16*, 389–411. [CrossRef]
6. Chang, J.R.; Yeih, W.; Shieh, M.H. On the modified Tikhonov's regularization method for the Cauchy problem of the Laplace equation. *J. Mar. Sci. Technol.* **2001**, *9*, 113–121. [CrossRef]
7. Gong, X.; Yang, S. A local regularization scheme of Cauchy problem for the Laplace equation on a doubly connected domain. *Bound. Value Probl.* **2023**, *2023*, 30. [CrossRef]
8. Cheng, J.; Hon, Y.C.; Wei, T.; Yamamoto, M. Numerical computation of a Cauchy problem for Laplace's equation. *ZAMM-J. Appl. Math. Mech. Angew. Math. Mech. Appl. Math. Mech.* **2001**, *81*, 665–674. [CrossRef]
9. Borachok, I.; Chapko, R.; Tomas Johansson, B. Numerical solution of a Cauchy problem for Laplace equation in 3-dimensional domains by integral equations. *Inverse Probl. Sci. Eng.* **2016**, *24*, 1550–1568. [CrossRef]
10. Hào, D.N.; Lesnic, D. The Cauchy problem for Laplace's equation via the conjugate gradient method. *IMA J. Appl. Math.* **2000**, *65*, 199–217. [CrossRef]
11. Caubet, F.; Dardé, J.; Godoy, M. On the data completion problem and the inverse obstacle problem with partial Cauchy data for Laplace's equation. *ESAIM Control Optim. Calc. Var.* **2019**, *25*, 30. [CrossRef]
12. Amdouni, S.; Ben Abda, A. The Cauchy problem for Laplace's equation via a modified conjugate gradient method and energy space approaches. *Math. Methods Appl. Sci.* **2023**, *46*, 3560–3582. [CrossRef]
13. León-Velasco, A.; Glowinski, R.; Juárez-Valencia, L.H. On the controllability of diffusion processes on the surface of a torus: A computational approach. *Pac. J. Optim.* **2015**, *11*, 763–790.
14. Conde Mones, J.J.; Estrada Aguayo, E.R.; Oliveros Oliveros, J.J.; Hernández Gracidas, C.A.; Morín Castillo, M.M. Stable identification of sources located on interface of nonhomogeneous media. *Mathematics* **2021**, *9*, 1932. [CrossRef]
15. Berntsson, F.; Lars, E. Numerical solution of a Cauchy problem for the Laplace equation. *Inverse Probl.* **2001**, *17*, 839–853. [CrossRef]
16. Kress, R. Inverse Dirichlet problem and conformal mapping. *Math. Comput. Simul.* **2004**, *66*, 255–265. [CrossRef]

17. Clerc, M.; Kybic, J. Cortical mapping by Laplace-Cauchy transmission using a boundary element method. *Inverse Probl.* **2007**, *23*, 2589–2601. [CrossRef]
18. Denisov, A.M.; Zakharov, E.V.; Kalinin, A.V.; Kalinin, V.V. Numerical solution of an inverse electrocardiography problem for a medium with piecewise constant electrical conductivity. *Comput. Math. Math. Phys.* **2010**, *50*, 1172–1177. [CrossRef]
19. Kalinin, A.; Potyagaylo, D.; Kalinin, V. Solving the inverse problem of electrocardiography on the endocardium using a single layer source. *Front. Physiol.* **2019**, *10*, 58. [CrossRef]
20. Ruiz de Miras, J.; Derchi, C.-C.; Atzori, T.; Mazza, A.; Arcuri, P.; Salvatore, A.; Navarro, J.; Saibene, F.L.; Meloni, M.; Comanducci, A. Spatio-Temporal Fractal Dimension Analysis from Resting State EEG Signals in Parkinson's Disease. *Entropy* **2023**, *25*, 1017. [CrossRef]
21. Sirpal, P.; Sikora, W.A.; Refai, H.H.; Yang, Y. Association between Opioid Dependence and Scale Free Fractal Brain Activity: An EEG Study. *Fractal Fract.* **2023**, *7*, 659. [CrossRef]
22. Perez-Sanchez, A.V.; Valtierra-Rodriguez, M.; Perez-Ramirez, C.A.; De-Santiago-Perez, J.J.; Amezquita-Sanchez, J.P. Epileptic Seizure Prediction Using Wavelet Transform, Fractal Dimension, Support Vector Machine, and EEG Signals. *Fractals* **2022**, *30*, 2250154. [CrossRef]
23. Karaoulanis, D.; Lazopoulou, N.; Lazopoulos, K. On A-Fractional Derivative and Human Neural Network. *Axioms* **2023**, *12*, 136. [CrossRef]
24. Turmetov, B.K.; Nazarova, K.D. On a generalization of the Neumann problem for the Laplace equation. *Math. Nachrichten* **2019**, *293*, 169–177. [CrossRef]
25. Kadirkulov, B.J.; Kirane, M. On solvability of a boundary value problem for the Poisson equation with a nonlocal boundary operator. *Acta Math. Sci.* **2015**, *35B*, 970–980. [CrossRef]
26. Kirsch, A. *An Introduction to the Mathematical Theory of Inverse Problems*, 2nd ed.; Springer: New York, NY, USA, 2011; Volume 120, Applied Mathematical Sciences.

fractal and fractional

MDPI

Article

On a Preloaded Compliance System of Fractional Order: Numerical Integration

Marius-F. Danca

STAR-UBB Institute, Babes-Bolyai University, 400084 Cluj-Napoca, Romania; m.f.danca@gmail.com

Abstract: In this paper, the use of a class of fractional-order dynamical systems with discontinuous right-hand side defined with Caputo's derivative is considered. The existence of the solutions is analyzed. For this purpose, differential inclusions theory is used to transform, via the Filippov regularization, the discontinuous right-hand side into a set-valued function. Next, via Cellina's Theorem, the obtained set-valued differential inclusion of fractional order can be restarted as a single-valued continuous differential equation of fractional order, to which the existing numerical schemes for fractional differential equations can be applied. In this way, the delicate problem of integrating discontinuous problems of fractional order, as well as integer order, is solved by transforming the discontinuous problem into a continuous one. Also, it is noted that even the numerical methods for fractional-order differential equations can be applied abruptly to the discontinuous problem, without considering the underlying discontinuity, so the results could be incorrect. The technical example of a single-degree-of-freedom preloaded compliance system of fractional order is presented.

Keywords: switch dynamical systems of fractional order; Caputo's derivative; fractional differential equations

1. Introduction

Generally, integer-order (IO) systems with a discontinuous right-hand side are mostly ideal due to the presence of switch-type functions like sgn or Heaviside H. Discontinuity can generally be found in two-dimensional mechanical systems: oscillating systems combined with dry and viscous damping; systems with dry friction; systems with stick and slip modes, forced vibrations, brake processes with locking phases, control synthesis for uncertain systems, and elastoplasticity; and in control theory, game theory, optimization, calculus of variations, physiological, biological systems, electrical (chaotic) circuits, complex networks, power electronics, etc. (see [1], the workshop on the "Nonlinear Dynamics of Mechanical Systems", an attempt to give a standard textbook devoted to nonlinear dynamical systems with discontinuities).

It is important to note that there are two main strategies to approach numerically discontinuous systems of IO: the first one is to ignore the discontinuities ("time stepping" methods) and to rely on a local error estimator such that the error remains acceptably small; the other strategy is to determine a scalar event function defining the discontinuity. In this way, the intersection point serves as the new starting point for continuing the numerical solution ("event-driven" methods).

To integrate discontinuous Ordinary Differential Equations (ODEs) of IO, there are dedicated numerical methods (see [1,2]). However, it is important to note that numerical methods for discontinuous systems could be either inaccurate or even inefficient in the

Academic Editor: António Lopes

Received: 4 December 2024
Revised: 7 January 2025
Accepted: 21 January 2025
Published: 26 January 2025

Citation: Danca, M.-F. On a Preloaded Compliance System of Fractional Order: Numerical Integration. *Fractal Fract.* **2025**, *9*, 84. https://doi.org/10.3390/fractalfract9020084

region of the discontinuity. Also, the error analysis often fails if there is not sufficient local smoothness.

On the other hand, in recent years, FO dynamical systems have received increasing attention due to their broad range of applications, such as real-life applications, [3], viscoelastic materials [4], control engineering [5], fractional electrical circuits [6], chaotic FO dynamical systems [7,8], and Lyapunov exponents of FO systems [9]. Fractional differential equations are presented in [10], while for a review of definitions of fractional derivatives, see [11].

FO models can describe complex physics problems more clearly and concisely compared with their IO variant.

Therefore, considering the FO variants of discontinuous is a subject of interest. Most known examples of discontinuous systems are defined as IO. In this paper, we consider their FO variants, a fact that could represent a novel approach. For this purpose, by using the differential inclusions theory, the problem modeling the underlying discontinuous problem is transformed into a continuous one.

The manuscript is organized as follows: Section 2 introduces the class of switch dynamical systems of IO. Section 3 deals with a class of discontinuous dynamical systems of FO, discusses notions and results on differential inclusions used to transform a discontinuous problem into a continuous one and considers the preloaded compliance system of FO. Special attention is paid to the correctness of the numerical integration of underlying IVP. This paper ends with the Conclusion Section.

2. Switch Dynamical Systems of IO

The class of systems analyzed in this paper, with a discontinuous right-hand side (Piece-Wise Continuous (PWC), see Definition 1), usually called "switch" or "relay systems", are modeled by the following discontinuous with respect to the state variable, autonomous Initial Value Problem (IVP):

$$\dot{x} = f(x) := g(x) + As(x), \quad x(0) = x_0, \quad t \in I = [0, T], \tag{1}$$

where $g : \mathbb{R}^n \to \mathbb{R}^n$ is a nonlinear Lipschitz continuous function and $s : \mathbb{R}^n \to \mathbb{R}^n$ is a piecewise function with piecewise constant components $s_i : \mathbb{R} \to \mathbb{R}$, usually sgn or Heaviside $H(x) = (1 + \operatorname{sgn}(x))/2$. $T \in \mathbb{R}, T > 0$, and the real matrix $A \in \mathbb{R}^{n \times n}$ is supposed to have at least one nonzero element.

The considered system, briefly described below, which comes from real applications and is called a preloaded compliance system with a single degree of freedom [1], is modeled by the following IVP:

$$m\ddot{y} + c\dot{y} + h(y) = P\cos\omega t, \quad y(0) = y_0, \quad \dot{y}(0) = y_1, \tag{2}$$

where m is the mass of the system, k is the stiffness and c is the viscous damping coefficient (see Figure 1a). The restoring force that has discontinuity at $y = 0$, where its value is $2ky_0$, the segment of the values at the discontinuity point, $[-ky_0, ky_0]$ (presented in [12]), will be rigorously studied in Section 3. The system is excited by the periodic external force $P\cos\omega t$. The preloaded force ky_0 is defined by the function (Figure 1b)

$$h(y) = \begin{cases} k(y + y_0), & y \geq 0 \\ k(y - y_0), & y \leq 0 \end{cases}$$

which outlines the switch character of the system.

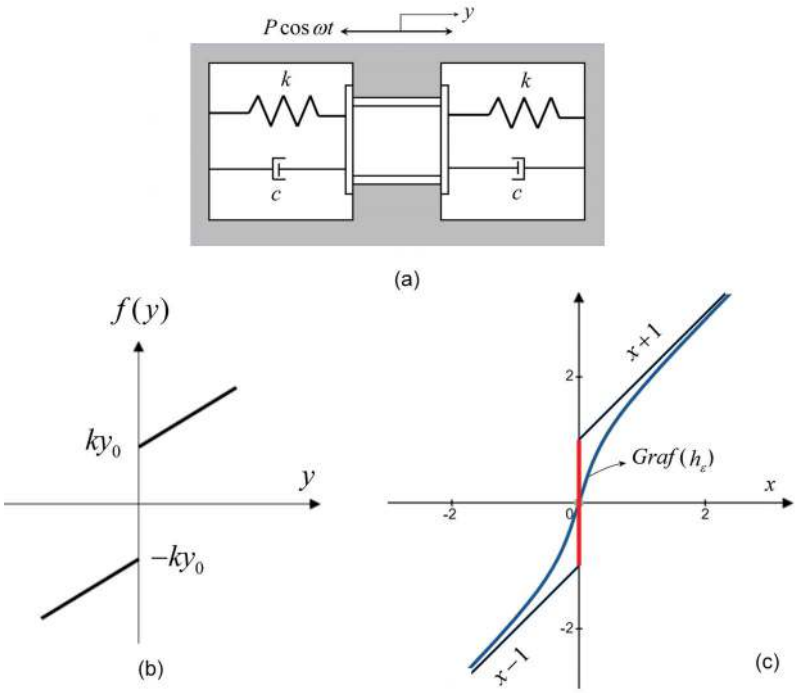

Figure 1. (**a**) A model of the preloaded system (3); (**b**) the characteristic of the restoring force f; (**c**) a graph of the approximate function h_ε.

With the change in the variables $x = y/y_0$ and $\tau = \omega_n t$, after some notations and substitutions (see the details in [12]), the dimensionless form of the system (2) becomes

$$\ddot{x} + 2\gamma\dot{x} + h(x) = P\cos\nu\tau, \tag{3}$$

where $h(x)$, after the mentioned substitutions, has the following form:

$$h(x) = \begin{cases} x+1, & y \geq 0, \\ x-1, & y \leq 0, \end{cases} \tag{4}$$

which can be written as $h(x) = x + \operatorname{sgn}(x)$.

Finally, the standard form of the preloaded compliance system (3) becomes

$$\begin{aligned} \dot{x}_1 &= x_2, \\ \dot{x}_2 &= -2\gamma x_1 - x_1 - \operatorname{sgn}(x_1) + P\cos(x_3), \quad x(0) = x_0. \\ \dot{x}_3 &= \nu. \end{aligned} \tag{5}$$

As can be seen, the system is in the form of the general switch system (1) with

$$A = \begin{pmatrix} 0 & 0 & 0 \\ -1 & 0 & 0 \\ 0 & 0 & 0 \end{pmatrix}, \quad g(x) = \begin{pmatrix} x_2 \\ -2\gamma - x_1 + P\cos(x_3) \\ \nu \end{pmatrix}, \quad s(x) = \begin{pmatrix} \operatorname{sgn}(x_1) \\ \operatorname{sgn}(x_2) \\ \operatorname{sgn}(x_3) \end{pmatrix}.$$

The dynamics of the system are presented in [1] and are not considered here.

A few other switch dynamical systems are presented in Table 1. Note that the presence of the term $x_1\operatorname{sgn}(x_1)$ in the function g of the variant of the Shimizu–Morioka system [13] (see Table 1) does not affect the continuity of g.

Table 1. Examples of switch dynamical systems of IO modeled by the IVP (1).

System	Equations	$g(x)$	A
Steam turbine [14]	$\dot{x}_1 = p(x_3 - x_1 + \text{sgn}(x_2))$, $\dot{x}_2 = x_1 - x_2$, $\dot{x}_3 = -x_2$	$\begin{pmatrix} px_3 - px_1 \\ x_1 - x_2 \\ -x_2 \end{pmatrix}$	$\begin{pmatrix} 0 & p & 0 \\ 0 & 0 & 0 \\ 0 & 0 & 0 \end{pmatrix}$
Sprott system [15]	$\dot{x}_1 = x_2$, $\dot{x}_2 = x_3$, $\dot{x}_3 = -x_1 - x_2 - x_3 + p\text{sgn}(x_3)$	$\begin{pmatrix} x_2 \\ x_3 \\ -x_1 - x_2 - x_3 \end{pmatrix}$	$\begin{pmatrix} 0 & 0 & 0 \\ 0 & 0 & 0 \\ 0 & 0 & p \end{pmatrix}$
Shimizu–Morioka [13] system	$\dot{x}_1 = x_2$, $\dot{x}_2 = (1 - x_1)\text{sgn}(x_1) - p_1 x_2$, $\dot{x}_3 = x_1^2 - p_2 x_3$	$\begin{pmatrix} x_2 \\ -x_1\text{sgn}(x_1) - p_1 x_2 \\ x_1^2 - p_2 x_3 \end{pmatrix}$	$\begin{pmatrix} 0 & 0 & 0 \\ 1 & 0 & 0 \\ 0 & 0 & 0 \end{pmatrix}$

Due to the broad range of applications of fractional calculus in real-life applications and in diverse and widespread fields of engineering and science [16], considering the fractional approaches of some systems like switch systems represents an open research direction.

3. Switch Dynamical Systems of FO

Considering the FO counterpart of the PWC systems, the counterpart of the autonomous systems modeled by the IVP (1) is as follows:

$$D_*^q x = f(x) := g(x) + A(x)s(x), \quad x(0) = x_0, \quad t \in I = [0, T], \tag{6}$$

where g and A are described in Section 2 and the Caputo derivative is considered, as in usual examples, with a lower limit $t = 0$ as follows:

$$D_*^q x(t) = \frac{1}{\Gamma(n-q)} \int_0^t (t-\tau)^{n-q-1} x^{(n)} \tau d\tau$$

where for $x : [0, T] \to \mathbb{R}$, $q \in (m-1, m)$, $m \in \mathbb{Z}^+$ is a smooth enough function, and $x^{(n)}$ is the classical derivative of the integer order n. Even more restrictive compared to other fractional-order derivatives, Caputo's derivative with a lower limit of 0 has the great advantage of using the initial conditions, like for IO systems, making it fully justified in practical examples.

One of the main restrictions on the numerical implementation of fractional derivatives is the memory-dependent characteristic, i.e., every state variable depends on all previously calculated values. Due to this effect, integration is time-consuming. On the other hand, the variation in real systems where the instantaneous change rate depends on the past state can be better described by the memory effect. In this context, with its entire (full) memory effect, Caputo's derivative describes better the real dynamics of an FO system but to the detriment of the integration time (see e.g., [17]. Compared with Caputo's derivative, the Gründwald–Letnikov derivative, which is the basic extension of the derivative in fractional calculus [18], follows the short memory principle, and its numerical implementation offers a relatively short time integration in numerical problems.

In this paper, the Adams–Bashforth–Moulton (ABM) method is used [19].

As observed in the previous sections, discontinuous ODEs and FDEs might not have classical solutions. Therefore, even though the dedicated numerical methods used to solve ODEs, as well as FDEs, can be used directly to integrate such problems, the numerical results can be wrong, as stated by the following example:

Consider the IVP

$$D_*^q x = f(x) := 2 - 3\text{sgn}(x), \quad x(0) = x_0. \tag{7}$$

For $t \in [0, \infty)$, there are no solutions in the classical sense that start from x_0. If $x_0 = 0$, the right-hand side of the equation $D_*^q(0) = 0$ is different from the right-hand side $2 - \text{sgn}(0) = 2$. In the case of $x_0 > 0$, there is the solution $x(t) = x_0 - t^q/\Gamma(1+q)$, defined only on the interval $[0, T')$, $T' = (\Gamma(1+q)x_0)^{1/q}$. This solution cannot be extended over a larger interval $[0, T')$. If $x_0 < 0$, there is the solution $x(t) = x_0 + 5t^q/\Gamma(1+q)$, defined only on $[0, T'')$, with $T'' = (\Gamma(1+q)x_0/5)^{1/q}$. Both these solutions tend toward the line $x = 0$, but they cannot extend along this line $x = 0$, whose equation, $x(t) = 0$, does not verify the equation (in Figure 2a, the cases $q = 0.8$ with $x_0 = \pm 1$ are presented). Note that by using a numerical method to solve this FDE, it is possible to obtain some numerical solutions even for $t > T', T''$, but they could be incorrect since we cannot verify the equation for $t \in [0, \infty)$. This aspect will be analyzed below. Therefore, a special approach for solutions to FDEs is required.

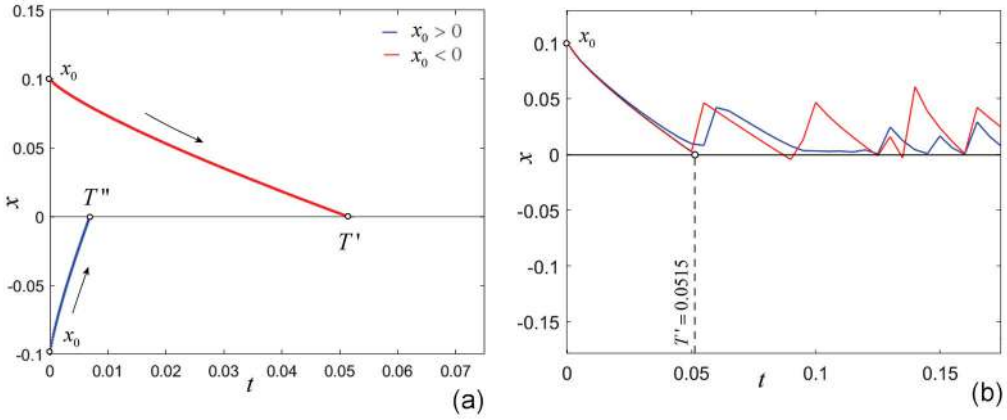

Figure 2. (**a**) Nonclassical solutions of the IVP (7), existing for $t < T', T''$; (**b**) a graph of the exact solution of the discontinuous FO problem (7) with $x_0 >$, on $[0, T']$, with $T' = 0.0505$ (black plot), the solution of the approximated problem (16) (blue plot), and the solution of the discontinuous IVP (7) (red plot) obtained with numerical integration for $t \in [0, T^*]$, $T^* > T'$ (without considering the problem of discontinuity).

3.1. Notions and Utilized Results

Notation 1. *Denote using $\mathcal{M}$ the set of discontinuity points of f.*

The set $\mathcal{M}$ has a zero Lebesgue measure and divides $\mathbb{R}^n$ to several $m > 1$ open disjuncts and connected sub-domains $\mathcal{D}_i \subset \mathbb{R}^n$, $i = 1, 2, ..., m$, $\mathbb{R}^n = \cup_{i=1}^m \overline{\mathcal{D}_i}$ on which f is continuous. Thus, discontinuity points belong to the union of the boundaries of $\mathcal{D}_i$. In Example (7)*, $\mathcal{M} = \{0\}$, which determines in $\mathbb{R}$ the sub-domains $\mathcal{D}_1 = (-\infty, 0)$ and $\mathcal{M}_2 = (0, \infty)$, where f is continuous.*

Definition 1. *$f : \mathbb{R}^n \to \mathbb{R}^n$ is called PWC if it is continuous throughout $\mathbb{R}^n \setminus M$ and, at $\mathcal{M}$, has finite (possible different) limits.*

Definition 2. *A set-valued function $F : \mathbb{R}^n \rightrightarrows \mathbb{R}^n$ is a function that associates with any element $x \in \mathbb{R}^n$, a subset of $\mathbb{R}^n$, $F(x)$ (see the sketch in Figure 3).*

For more details on set-valued functions, see [20–22].

Definition 3. *The graph of a set-valued function $F : X \rightrightarrows Y$, where X, Y are non-empty sets, is defined as follows (see Figure 3):*

$$Graph(F) = \{(x, y) \in X \times Y | y \in F(x)\}.$$

To overcome the difficulty of finding solutions for PWC systems, IVP problems can be restarted by using the Filippov approach [23], as a set-valued Fractional Differential Inclusion (FDI) of

$$D_*^q x(t) \in F(x(t)), \quad \text{for a.e. } t \in I, \tag{8}$$

where F is a set-valued function.

The existence and uniqueness of solutions of DIs of IO are studied in [20,21], while numerical schemes can be found, e.g., in [24–28].

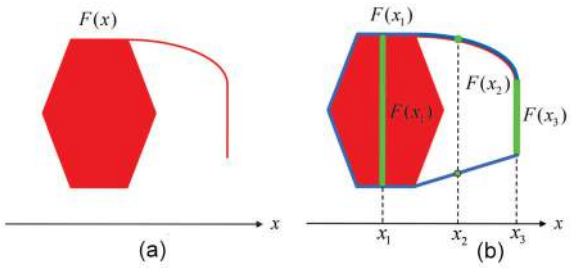

Figure 3. (**a**) The graph of a set-valued function F; (**b**) the values of $F(x)$ for different values of x.

The set-valued function F can be defined in several ways, the most known being Filippov's regularization [23]:

$$F(x) = \bigcap_{\varepsilon>0} \overline{conv}(f(\{z \in \mathbb{R}^n : \|z - x\| \leq \varepsilon\} \setminus M)). \tag{9}$$

$F(x)$ defined by (9) is a convex function, its values representing the convex hull of f, and ε represents the radius of the ball centered in x. At the points x where f is continuous, $F(x) = f(x)$, i.e., $F(x)$, consists of a single point $\{f(x)\}$ (see Figure 3), while for $x \in \mathcal{M}$, $F(x)$ is given by (9). It is important to note that for physical meanings, ε should have as many small values as possible (ideally $\varepsilon \to 0$, when the solution of the DI tends to the real motion of the underlying physical system modeled by the discontinuous IVP (6)).

The regularization applied to one of the most used functions to define switch systems, sgn, generates the so-called sigmoid function, denoted usually as Sgn (see Figure 4a,b):

$$\text{Sgn}(x) = \begin{cases} \{-1\}, & x < 0, \\ [-1,1], & x = 0, \\ \{+1\}, & x > 0. \end{cases} \tag{10}$$

Therefore, in the case of example (7), the discontinued problem transforms into the following FDI (Figure 4c,d) for *a.e.* $t \in I$.:

$$\text{Sgn}(x) - 2 \in \begin{cases} \{5\}, & x < 0, \\ [-1,5], & x = 0, \\ \{-1\}, & x > 0. \end{cases} \tag{11}$$

Now, the problem transforms into the FDI, $D_*^q x \in [-1,5]$. When the solutions starting from negative or positive initial conditions reach the axis $x = 0$, the derivative $D_*^q x$ can now take an infinite number of values within the segment of values $[-1,5]$, so that the problem can be solved, even for $x_0 = 0$ (see [20,21]). For $x_0 \neq 0$, the problem reads as a continuous problem: $D_*^q x = 2 - 3\text{sgn}(x) = 5$, for $x_0 \in \mathcal{D}_1 = (-\infty, 0)$ and $D_*^q x = 2 - 3\text{sgn}(x) = -1$ for $x_0 \in \mathcal{D}_2 = (0, \infty)$.

Therefore, Filippov regularization opens the door for the possible existence of solutions to discontinuous systems of IO and even of FO.

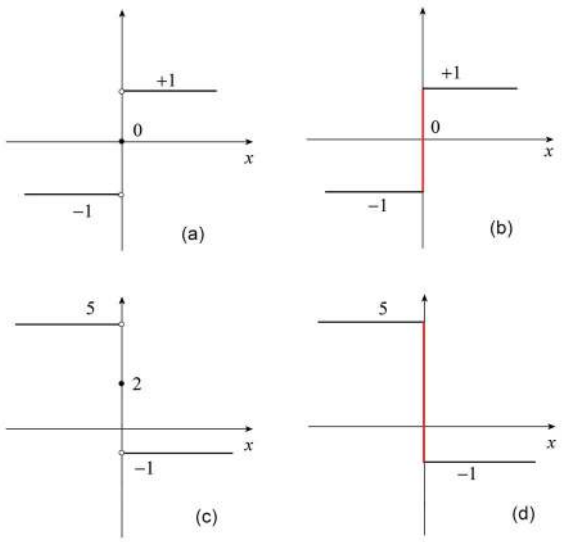

Figure 4. (**a**) A graph of the sgn function; (**b**) a graph of the set-valued function Sgn; (**c**) a graph of the discontinuous right-hand side of (7); (**d**) a graph of the set-valued function of (7).

Definition 4. *The map F is upper-semi-continuous (USC) on $\mathbb{R}^n$ if for each $x \in \mathbb{R}^n$, the set $F(x)$ is a non-empty and closed subset of R^n, and for each open set N of $\mathbb{R}^n$ containing $F(x)$, there is an open neighborhood B of x such that $F(B) \subset N$.*

Remark 1. *Filippov's approach* (9) *ensures enough regularity so that if f is continuous at x, then a solution to the IVP* (8) *satisfies the IVP* (6) *and any classical solution to the IVP* (6) *is a solution to the IVP* (8). *On mild assumptions, DIs of IO, obtained with Filippov regularization, admit generalized (Filippov) solutions [23]. As stipulated in [23], it is justified to call a solution for the IVP* (6) *a solution for the IVP* (8). *For FDIs, existence results are presented in [29].*

Definition 5. *The single-valued function $f : \mathbb{R}^n \to \mathbb{R}^n$ is a selection (approximation) of a set-valued function F, if $f(x) \in F(x)$ for every $x \in \mathbb{R}^n$ (see, e.g., [20,21]).*

Finding numerical solutions for DIs of IO represents a complex task (see e.g., [24–26,30]), while numerical solutions for FDIs are, based on our knowledge, an even more challenging and less studied topic. Therefore, proposing continuous approximation via selection theory represents a successful approach.

Theorem 1. *Cellina's Theorem [20,21]: Let a USC set-valued function $F : \mathbb{R}^n \rightrightarrows \mathbb{R}^n$ with non-empty convex values. Then, for every $\varepsilon > 0$, there is a local Lipschitz selection $f_\varepsilon : \mathbb{R}^n \rightrightarrows \mathbb{R}^n$ such that*

$$Graph(f_\varepsilon) \subset Graph(F) + \varepsilon B$$

showing the sphere of radius ε (see the sketch in Figure 5a).

Generally, a set-valued function admits infinitely many selections, a fact that represents a major advantage in approaching discontinuous systems coming from practical problems.

Remark 2 ([20,21])**.** *Because of the symmetric interpretation of a set-valued map as a graph, we can say that a set-valued function satisfies a property if and only if its graph satisfies it. For instance, a set-valued function is said to be closed if and only if its graph is closed. For a function f that is locally bounded, its set-valued map obtained with Filippov regularization enjoys the following properties:*

it is USC and has non-empty closed and convex values (Péano functions ([20], Proposition 1, p. 102, [21], Lemma 3, p. 67), which satisfies the existence result of solutions to DIs. For FDIs, similar results can be found in [29].

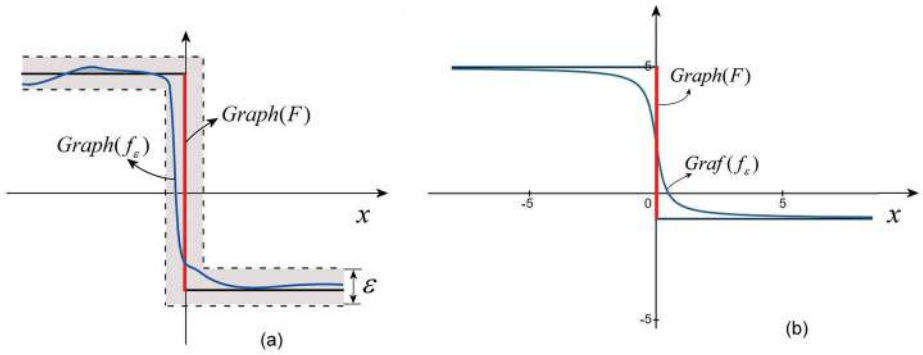

Figure 5. (**a**) A sketch of a continuous approximation f_ε within a ε-neighborhood of the set-valued function F; (**b**) a graph of the continuous ε-approximation for system (7).

The set-valued function defined with Fillipov's regularization verifies Theorem 1 [31].

3.2. Numerical Integration of FO Switch Systems

Consider the FO counterpart of the IVP (1) defined with Caputo's derivative:

$$D_*^q x = f_\varepsilon(x) := g(x) + As(x), \quad x(0) = x_0, \quad t \in I = [0, T]. \tag{12}$$

The steps required to restart the PWC problem into a continuous problem are the following:

(I) Firstly, the set-valued right-hand side, obtained with Filippov's regularization, is

$$F(x) = g(x) + AS(x), \quad x(0) = x_0, \quad t \in I = [0, T], \tag{13}$$

with $S(x) = [\mathrm{Sgn}(x_1), \mathrm{Sgn}(x_2), ..., \mathrm{Sgn}(x_n)]^T$ being the set-valued sigmoid functions given by (10).

(II) Next, the continuous approximation of the component $\mathrm{Sgn}(x)$ (Theorem 1) is

$$S_\varepsilon(x) = [S_\varepsilon(x_1), S_\varepsilon(x_2), ..., S_\varepsilon(x_n)]^T,$$

where $S_\varepsilon(x_i)$, $i = 1, 2, ..., n$, are continuous approximations of the set-valued functions $\mathrm{Sgn}(x_i)$ given by, e.g., (15).

(III) The result regarding the continuous approximation of the IVP (12) is

Theorem 2 ([31]). *The PWC IVP* (6) *can be restarted as the following continuous IVP of FO*

$$: \mathrm{D}_*^q x = g(x) + A(x)\mathrm{S}_\varepsilon(x), \quad x(0) = x_0, \quad t \in I, \tag{14}$$

Theorem 2 represents the main result according to which it is demonstrated how a PWC problem of IO can be transformed into a continuous one of FO. Thus, by applying the algorithm in Figure 6, the discontinuous preloaded compliance system of FO (12) is transformed into a continuous problem of FO (14), which can be studied both analytically and numerically.

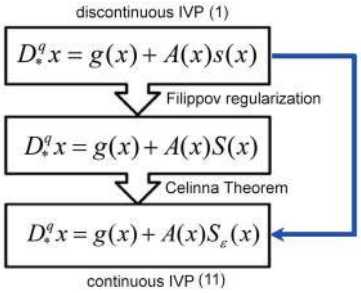

Figure 6. The algorithm of the continuous approximation of the discontinuous IVP (6).

The algorithm described above is presented in Figure 6. It is important to note that in the examples, step II can be omitted and the discontinuous function approximated directly (step III).

One of the used approximations S_ε of the set-valued functions sgn function, which provides enough flexibility, has the following form:

$$S_\varepsilon(x) = \frac{2}{\pi}\arctan\frac{x}{\delta}, \tag{15}$$

where δ is a positive parameter that controls the slope of the approximation in the ε-neighborhood of $x = 0$. A cubic polynomial approximation is presented in [32], where a discussion on the δ influence of the approximation can be found. While approximations like (15) are defined on I, in [32], the polynomial approximation is defined only in a chosen local ε-neighborhood around the discontinuity, a fact that confers better properties to the approximated function.

Once the continuity of the underlying problem is ensured by Theorem 2, the obtained IVP can be numerically integrated via some numerical schemes for FDEs, like the ABM method [19] used in this paper.

Reconsider example (7) by using approximation (15). Then, the discontinuous problem is transformed via Theorem 2 into the following continuous IVP of FO:

$$D_*^q x = 2 - \frac{6}{\pi}\arctan\frac{x}{\delta} \approx 2 - 3S_\varepsilon(x), x(0) = x_0, \quad t \in I, \tag{16}$$

with the approximation of the right-hand side presented in Figure 5b. Now, the problem admits numerical solutions for $t \in I$, which can be determined with numerical schemes for FDEs. In Figure 2b are the exact solution of the discontinuous FO problem on $[0, T']$, $T' = 0.0505$ (black plot), the solution of the approximated problem (16) (blue plot), and the solution of the discontinuous IVP (7) (red plot) obtained with numerical integration for $t \in [0, T^*]$, with $T^* > T'$, without considering the discontinuity $x = 0$. The differences can be seen in Figure 2b.

3.3. Preloaded Compliance System of FO

Consider now the FO of the system modeling the preloaded compliance system (5). Via Theorem 2, by applying the continuous approximation algorithm (see Figure 6) with h_ε approximation presented in Figure 1c), one obtains the single-valued continuous FO system:

$$\begin{aligned} &D_*^q x_1 = x_2, \\ &D_*^q x_2 = -2\gamma x_1 - x_1 - S_\varepsilon(x_1) + P\cos(x_3), \quad x(0) = x_0, \quad t \in I. \\ &D_*^q x_3 = \nu. \end{aligned} \tag{17}$$

Despite the fact that the form (17) is defined with three FDEs (see Figure 7a), required to transform the standard form into an autonomous one, the dynamics of the system are graphically described in the plane (x_1, x_2) (Figure 7b–d).

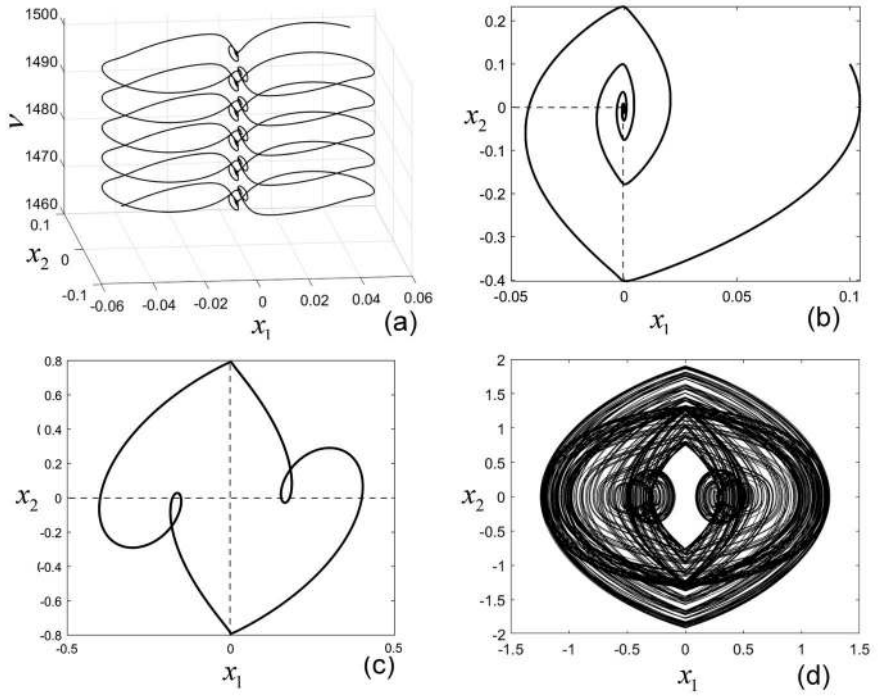

Figure 7. (**a**) The trajectory of the system (17) in space (x_1, x_2, v); (**b**) attractive fixed point-like. The zoomed-in detail reveals the influence of the sgn function; (**c**) periodic-like trajectory; (**d**) chaotic trajectory.

Remark 3. *Compared with the IO variant of the preloaded compliance system* (2)*, its obtained FO counterpart* (17) *presents several advantages: (1) The first one is that by applying the proposed algorithm, the obtained problem is a continuous one, thus taking advantage of the existing tools to study continuous systems. (2) The second one is the fact that with this approach, numerical integration is more accessible compared with the IO case, which, as can be seen, e.g., in [1], does not exit a clear unified way to integrate discontinuous systems. Thus, generally, at the discontinuity surface, $\mathcal{M}$, the considered solutions obtained (incorrectly) with some standard methods for continuous systems are just "glued". The third argument in favor of the proposed algorithm, i.e., to transform the IO problem into a FO one, is the fact that, as mentioned in the previous sections, FO variants generally offer a better characterization of the underlying IO system.*

Note: *(1) As known now, FO systems (continuous or discrete) cannot have periodic non-constant solutions [33]. Besides the analytical proof in [33], this property can be explained due to the fact that all the past history has to be taken into account (time-memory of FO systems is continuous-time or discrete). Also, any equilibrium of a general FO nonlinear system described by Caputo's derivative can never be finite-time stable in the sense that the trajectory will never reach the equilibrium in finite time [34].*

(2) Numerical schemes for FDEs (and also for DEs),require at least the continuity of the underlying equations [19]. However, the numerical methods can directly (abruptly) be applied to discontinuous problems too, but this method, which is still poorly understood, can lead to questionable results. Therefore, the correct results for the integration of IVP (6) *should be obtained, e.g., after the continuous approximation of the underlying problem.*

While in the IO variant of the preloaded compliance system (2), there are periodic solutions abruptly changing the stability [12], in (17), this does not happen anymore (see Note 1).

Consider $q = 0.95$ and $\delta = 1e-3$ and integrate the system (17). In Figure 7b, an attractive fixed point-like element is presented (see Note 1). For $p = 2$, in Figure 7c, a periodic-like trajectory is presented. Even though visually, the orbit looks periodic, it is not (see Note 1). A chaotic trajectory is presented in Figure 7d. The apparent corners, visible in Figure 7b–d, are due to the sgn function. However, due to the continuous approximations, these corners are in fact smooth (see the zoomed-in Figure 7b).

4. Discussion and Conclusions

In this paper, the continuous approximation of discontinuous (switch) IVPs of IO is proposed as a novel technique to approach a class of dynamical systems of FO. Using the theory of differential inclusions and Cellina's Theorem, the discontinuous IVP is restarted as a continuous problem of FO, which can be integrated with some numerical scheme for FDEs. First, it is shown that the Filippov regularization applied to the discontinuous function allows the existence of a sufficiently regular set-valued map, so that the underlying FDI verifies Cellina's Theorem. As a consequence, the discontinuous problem can be restarted as a continuous one. Also, the problem of using numerical integration, without considering the discontinuity, is treated on a concrete example.

In the case of a practical example, a preloaded compliance system is considered.

Funding: This research received no external funding.

Data Availability Statement: The original contributions presented in this study are included in the article. Further inquiries can be directed to the corresponding author.

Conflicts of Interest: The author declares no conflicts of interest.

References

1. Wiercigroch, M.; de Kraker, B. *Applied Nonlinear Dynamics and Chaos of Mechanical Systems with Discontinuities*; Marian Wiercigroch and Bram de Kraker, World Scientific Series on Nonlinear Science; Chua, L.O., Ed.; World Scientific: Singapore, 2000.
2. Acary, V.; Brogliato, B. *Numerical Methods for Nonsmooth Dynamical Systems: Applications in Mechanics and Electronics*; Lecture Notes in Applied and Computational Mechanics; Springer: New York, NY, USA, 2008.
3. Ray S.S.; Atangana, A.; Noutchie, S.C.O.; Kurulay, M.; Bildik, N.; Kilicman, A. Fractional calculus and its applications in applied mathematics and other sciences. *Math. Probl. Eng.* **2014**, *2014* , 849395. [CrossRef]
4. Bagley, R.; Torvik, P. On the fractional calculus model of viscoelastic behavior. *J. Rheol.* **1986**, *30*, 133–155. [CrossRef]
5. Oustaloup, A.; Mathieu, B.; Lanusse, P. The CRONE control of resonant plants: Application to a flexible transmission. *Eur. J. Control* **1995**, *1*, 113–121. [CrossRef]
6. Nakagawa, M.; Sorimachi, K. Basic characteristics of a fractance device. *IEICE Trans. Fundam. Electron. Commun. Comput. Sci.* **1992**, *75*, 1814–1819.
7. Danca, M.-F. Fractional order logistic map: Numerical approach. *Chaos Soliton. Fract.* **2022**, *157*, 111851. [CrossRef]
8. Danca, M.-F. Chaotic hidden attractor in a fractional order system modelling the interaction between dark matter and dark energy. *Commun. Nonlinear Sci.* **2024**, *131*, 107838 [CrossRef]
9. Danca, M.F.; Fečkan, M. Memory Principle of the MATLAB Code for Lyapunov Exponents of Fractional-Order. *Int. J. Bifurcat. Chaos* **2024**, *34*, 2450156. [CrossRef]
10. Podlubny, I. *Fractional Differential Equations*; Academic Press: New York, NY, USA, 1999.
11. Teodoro, G.S.; Machado, J.A.T.; de Oliveira, E.C. A review of definitions of fractional derivatives and other operators. *J. Comput. Phys.* **2019**, *388*, 195–208. [CrossRef]
12. Yoshitake, Y.; Sueoka, A. Forced Self-Excited Vibration with Dry Friction. In *Applied Nonlinear Dynamics and Chaos of Mechanical Systems with Discontinuities*; Marian Wiercigroch and Bram de Kraker, World Scientific Series on Nonlinear Science; Chua, L.O., Ed.; World Scientific: Singapore, 2000.
13. Shimizu, T.; Morioka, N. On the bifurcation of a symmetric limit cycle to an asymmetric one in a simple model. *Phys. Lett. A* **1980**, *76*, 201–204. [CrossRef]

14. Belea, C. *Automatica Neliniara; Teorie, Exemple si Aplicatii*; Editura Tehnica: Bucuresti, Romania, 1983. (In Romanian)
15. Sprott, J.C. A new class of chaotic circuit. *Phys. Lett. A* **2000**, *266*, 19–23. [CrossRef]
16. Tenreiro Machado, J.A.; Silva, M.F.; Barbosa, R.S.; Jesus, I.S.; Reis, C.M.; Marcos, M.G.; Galhano, A.F. Some Applications of Fractional Calculus in Engineering. *Math. Probl. Eng.* **2010**, *2010*, 639801. [CrossRef]
17. Wang, J.-L.; Li, H.-F. Surpassing the fractional derivative: Concept of the memory-dependent derivative. *Comput. Math. Appl.* **2011**, *62*, 1562–1567. [CrossRef]
18. Podlubny, I. *Fractional Differential Equations. An Introduction to Fractional Derivatives, Fractional Differential Equations, to Methods of their Solution and Some of their Applications*; Academic Press: San Diego, CA, USA, 1999.
19. Diethelm, K.; Ford, N.J.; Freed, A.D. A predictor-corrector approach for the numerical solution of fractional differential equations. *Nonlinear Dyn.* **2002**, *29*, 3–22. [CrossRef]
20. Aubin, J.-P.; Cellina, A. *Differential Inclusions Set-Valued Maps and Viability Theory*; Springer: Berlin/Heidelberg, Germany, 1984.
21. Aubin, J.-P.; Frankowska, H. *Set-Valued Analysis*; Birkhuser: Boston, MA, USA, 1990.
22. Deimling, K. *Multivalued Differential Equations*; de Gruyter: Berlin, Germany; New York, NY, USA, 1992.
23. Filippov, A.F. *Differential Equations with Discontinuous Right-Hand Sides*; Kluwer Academic: Dordrecht, The Netherlands, 1988.
24. El-Sayed, A.M.A.; Ibrahim, A.G. Multivalued fractional differential equations of arbitrary orders. *Appl. Math. Comput.* **1995**, *68*, 15–25.
25. Elliot, C.M. On the convergence of a onestep method for the numerical solution of an ordinary differential inclusion. *IMA J. Numer. Anal.* **1985**, *5*, 3–21. [CrossRef]
26. Lempio, F. Modified Euler methods for differential inclusions. In *Set-Valued Analysis and Differential Inclusions*; A Collection of Papers Resulting from a Workshop; Kurzanski, A.B., Veliov, V.M., Eds.; Birkhäuser: Boston, MA, USA, 1993.
27. Lempio, F.; Veliov, V. Discrete approximations of differential inclusions. *Bayreuth. Math. Schr.* **1998**, *54*, 149–232.
28. Dontchev, A.; Lempio, F. Difference Methods for Differential Inclusions: A Survey. *SIAM Rev.* **1992**, *34*, 263–294. [CrossRef]
29. Agarwal, R.; Benchohra, M. A Survey on Existence Results for Boundary Value Problems of Nonlinear Fractional Differential Equations and Inclusions. *Acta Appl. Math.* **2010**, *109*, 973–1033. [CrossRef]
30. Kastner-Maresch, A.; Lempio, F. Difference methods with selection strategies for differential inclusions. *Numer. Funct. Anal. Optim.* **1993**, *14*, 555–572. [CrossRef]
31. Danca, M.-F. On a Class of Discontinuous Dynamical Systems. *Miskolt Math. Notes* **2001**, *2*, 103–116.
32. Danca, M.-F. Continuous approximations of a class of piecewise continuous systems. *Int. J. Bifurcat. Chaos*, **2015**, *25*, 1550146. [CrossRef]
33. Tavazoei, M.S.; Haeri, M. A proof for non existence of periodic solutions in time invariant fractional order systems. *Automatica* **2009**, *45*, 1886–1890. [CrossRef]
34. Shen, J.; Lam, J. Non-existence of finite-time stable equilibria in fractional-order nonlinear systems. *Automatica* **2014**, *50*, 547–551. [CrossRef]

MDPI AG
Grosspeteranlage 5
4052 Basel
Switzerland
Tel.: +41 61 683 77 34

Fractal and Fractional Editorial Office
E-mail: fractalfract@mdpi.com
www.mdpi.com/journal/fractalfract

Academic Open
Access Publishing

mdpi.com

ISBN 978-3-7258-4112-7